TESIS DE LA UNIVERSIDAD
DE ZARAGOZA

2023

92

Mario Peláez Fernández

Optoelectronic properties and in-situ transformations of 1D and 2D materials studied by transmission electron microscopy

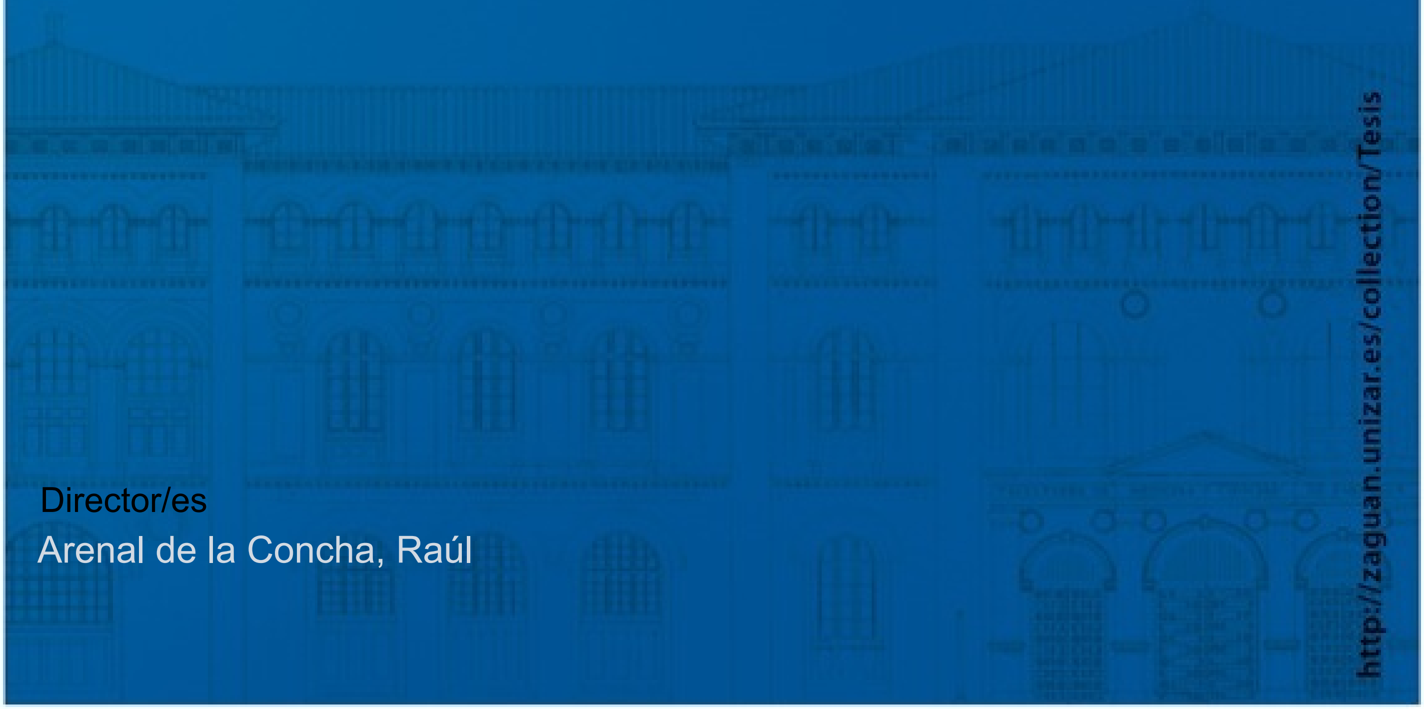

Director/es
Arenal de la Concha, Raúl

ISSN 2254-7606

Prensas de la Universidad
Universidad Zaragoza

Servicio de Publicaciones

ISSN 2254-7606

Tesis Doctoral

OPTOELECTRONIC PROPERTIES AND IN-SITU TRANSFORMATIONS OF 1D AND 2D MATERIALS STUDIED BY TRANSMISSION ELECTRON MICROSCOPY

Autor

Mario Peláez Fernández

Director/es

Arenal de la Concha, Raúl

UNIVERSIDAD DE ZARAGOZA
Escuela de Doctorado

Programa de Doctorado en Física

2020

Tesis Doctoral Programa de Doctorado en Ciencias Físicas
Universidad de Zaragoza

Facultad de Ciencias Universidad de Zaragoza

Mario PELÁEZ FERNÁNDEZ

Optoelectonic properties and in-situ transformations of 1D and 2D materials studied by transmission electron microscopy

2020

Director de tesis: Raul ARENAL

General summary

In the past 30 years, materials science has observed a change of paradigm where more and more research interest has started to focus on nanomaterials. This change of paradigm has become evident with the isolation of graphene in 2004 and the wave of nanomaterial research it has brought along with it.

One of the main properties for which nanomaterials are of increasing interest for the research community are their optoelectronic properties. These properties have brought along applications in photovoltaics, nanophotonics, sensors and fields as biology or medicine. The tuning of these optoelectronic properties offers even further applications for this kind of materials.

On the other hand, the investigation of property tuning in materials *in situ* offers a much more detailed picture than any other possible kind of study.

In this sense, electron microscopy and spectroscopy (EELS) offer the possibility to gather a myriad of information on different properties at once, such as thickness, mass density or optoelectronic properties (such as the band gap, features on its density of states or plasmonic response).

Furthermore, the merging of all the possibilities that TEM/STEM/EELS can provide along with the possibility of modifying the sample *in situ*, whether it is by applying a bias, heating the sample up or by electron irradiation, offers the possibility for dynamic studies not just on the properties of a certain material, but on their evolution.

This manuscript exists at the intersection between TEM/STEM/EELS studies, optoelectronic properties, creative data analysis for challenging conditions and *in situ* experiments.

This thesis has been developed within the context of Initial Training Network Marie Slodowska-Curie 'Enabling Excellence'. The essential works of this thesis are condensed in this manuscript.

The optoelectronic properties in atomically thin 2D $Mo_xW_{1-x}S_2$ alloys have been investigated. Their band gap, excitonic features and features deriving from Van Hove points in the density of states have been measured as a function of the alloying degree (Mo content) and thickness (number of layers) of the flakes.

Plasmonic analyses of high aspect-ratio Au nanostructures using STEM-EELS have also been performed. This analysis focuses both on the materials aspect of the study (the plasmonic properties of these high aspect-ratio Au nanostructures) as well as on the data analysis aspect of it, providing a promising analysis routine that can potentially be used for other types of characterisation.

Finally, the *in situ* thermal reduction of GO flakes has been investigated within a TEM. The TEM/EELS analysis at various temperatures allow for the gathering of enough information to properly devise a hypothesis of which groups desorb from the sample at which temperature, and what this desorption entails for the sample itself.

In conclusion, these works have furthered the understanding of the diverse 1D and 2D materials present in it, as well as the possible changes they can undergo; which can be beneficial for the conceiving of different kinds of future applications.

Resumen general

Durante los últimos 30 años, la ciencia de materiales ha contemplado un cambio de paradigma, donde se ha generado cada vez más interés dentro de la investigación en torno a los nanomateriales. Este cambio de paradigma se ha vuelto evidente a partir de la síntesis del grafeno en 2004 y la ola de investigación en nanomateriales que trajo consigo.

Unas de las principales propiedades por las que los nanomateriales tienen cada vez más interes para la comunidad investigadora son sus propiedades optoelectrónicas. Estas propiedades han traído consigo aplicaciones en fotovoltaica, nanofotónica, sensores y campos como la biología o la medicina. La modificación de estas propiedades optoelectrónicas ofrece aún más posibilidades de aplicaciones para este tipo de materiales.

Por otra parte, la investigación de la modificación de propiedades de materiales *in situ* ofrece un análisis más completo que cualquier otro tipo posible de estudio.

De esta manera, la microscopía y espectroscopía de electrones (EELS) ofrece la posibilidad de aunar una vasta cantidad de información sobre diferentes propiedades de forma simultánea, como el espesor, la densidad másica o propiedades optoelectrónicas (como el *band gap*, características de la densidad de estados o respuesta plasmónica).

Asimismo, la unión de todas las posibilidades que el TEM/STEM/EELS pueden ofrecer junto con la posibilidad de modificar una muestra *in situ*, ya sea aplicándole un voltaje, calentándola o a través de la irradiación de electrones, permite la posibilidad de estudios dinámicos no sólo sobre las propiedades de un material concreto, sino también en su evolución.

Este manuscrito existe en la intersección entre los estudios de TEM/STEM/EELS, las propiedades optoelectrónicas, el análisis de datos creativo para condiciones difíciles, y los experimentos *in situ*.

Esta tesis se ha desarrollado dentro dle contexto de la *Initial Training Network* Marie Slodowska-Curie 'Enabling Excellence'. Los trabajos más esenciales de esta tesis se han plasmado en este manuscrito.

Se han investigado las propiedades optoelectrónicas de aleaciones 2D atómicamente finas de $Mo_xW_{1-x}S_2$. Hemos medido su band gap, características espectrales relacionadas con excitones y otros fenómenos espectrales que derivan de puntos de Van Hove en la densidad de estados; tanto en función de el grado de aleación (el contenido de Mo) como en función del espesor (número de capas) de los copos.

También se han realizado análisis plasmónicos de nanoestructuras de oro con una alta relación de aspecto. Este análisis se centra tanto en la parte de materiales del estudio (las propiedades plasmónicas de estas nanoestructuras de oro de alta relación de aspecto) como en el aspecto relacionado con el análisis de datos, ofreciendo una rutina de análisis prometedora que podría en principio ser usada para otros tipos de caracterización.

Por último, la reducción termal *in situ* de copos de óxido de grafeno se ha estudiado dentro de un TEM. Los análisis TEM/EELS a varias temperaturas han permitido aunar suficiente información como para poder elaborar una hipótesis completa sobre qué grupos se desorben de la muestra a qué temperaturas, y qué implica esta desorción para la muestra en sí.

Para concluir, estos trabajos han hecho avanzar el entendimiento sobre los diversos materiales 1D y 2D presentes en ellos, así como sobre los posibles cambios que pueden sufrir; lo cual puede ser beneficioso para el desarrollo de diferentes tipos de aplicaciones en el futuro.

Contents

1

Introduction to this manuscript: From electron microscopy to nanomaterials

In this introductory chapter, we will cover the motivation of this whole manuscript. There are three main axes that intertwine along the studies: Electron microscopy, electron energy loss spectroscopy and nanomaterials. These three subjects are presented and discussed in a proper manner, although we provide a briefer explanation of the latter since each nanomaterial of interest is detailed in their corresponding experimental chapters.

1.1 Motivation of this manuscript

The motivation for all of these works can essentially be divided into two different but converging lines of work. On the one hand, we have the study of fundamental properties in nanomaterials, which has been the core of a vast amount of research in the past few decades. However, for this purpose the analytic techniques related to the transmission electron microscope sometimes need to be taken up a notch to provide further information on the study of these fundamental properties. Here we provide some insight on both these concepts.

1.1.1 Nanomaterials: fundamental research for future applications

As we have stated, research on nanomaterials is a field that has attracted a great deal of research interest over the last few decades for its many possible applications. Thanks to these applications, nanomaterials have obviously revolutionised the world of physics, chemistry and material science, but also that of disciplines so seemingly far as medicine, biotechnology and engineering. However, in order to know what those applications are and how to get to them, it is vital to perform fundamental research on these materials and their properties. Along this manuscript, the main properties focused on have been the optoelectronic response of nanomaterials, as well as their response to in-situ modifications either by means of temperature or by means of beam irradiation. A brief summary of these experiments is shown in Section 1.8

1.1.2 Electron microscopy and spectroscopy: taking the techniques a step further

As we have said in this section, as the need for a better understanding of nanomaterials arises, it is accompanied by an increasing urge for the analysis techniques used to study them to catch up in a way. There is a myriad of different and novel analytic techniques for the characterisation of nanomaterials. Out of these techniques, two of the most prominent technique families are microscopies (including, but not limited to, optical microscopy, focused ion beam, electron microscopies, scanning probe microscopy, etcetera) and spectroscopies (including energy-dispersive x-ray spectroscopy, x-ray photoelectron spectroscopy, electron/ion energy loss spectroscopy, infrared, ultraviolet, cathodoluminescence, and many more). Our work will be focused on transmission electron microscopy in various forms, as well as electron energy loss spectroscopy. Both techniques are pushed forward in several different ways:

- First and foremost, the combination of electron microscopy and EELS, in and of itself, offers a better amount of information when compared to both techniques separately. This is discussed in detail in Section 1.5.2.
- Secondly, both the electron microscopy and the electron spectroscopy techniques shown in this manuscript have had their own individual improvements, by means, for example, of aberration corrected microscopy or monochromated EELS. These improvements are discussed in sections 1.3.2 and 1.4.1.
- An additional improvement to these techniques comes after the gathering of the pertaining data. Novel or more accurate ways to analyse our data, especially our EEL spectra, greatly improve the quality of our research. This is especially visible in the experimental results in chapter 3.
- Finally, the opportunity to actually modify our nanomaterials within the electron microscope allows to not only perform static studies of a sample with specific environmental parametres, but also to study the evolution of said materials when modifying these parametres.

However, in order to achieve such feats in the different techniques and materials used, one must start by knowing about them in depth, starting by the main technique of this manuscripte with no doubt whatsoever: the transmission electron microscope.

1.2 The transmission electron microscope

The main driving force behind most , if not all of the research shown in this manuscript, is that it has either been performed in a transmission electron microscope or related to it. Understanding its working principle and how it has been improved over the years is key to fully comprehend the subject of this thesis. In this section, we try to give a detailed explanation of every technique related to this manuscript that can be performed within an electron microscope, from their working principle to their implementation and applications.

1.2.1 Brief history of the transmission electron microscope

The history of transmission electron microscopy can be traced back to a bit less than a centrury ago. In 1924, Louis DeBroglie initially proposed a dual character of electrons as both particles and waves [1], which was confirmed in two different experiments by Davisson and Germer on the one hand and Thompson and Reid on the other hand, two years later [2]. This proposition had many different applications, one of them being that particles could, in theory, be used to image samples in the same way as electromacnetic waves, such as light.

However, in order to achieve this, it was necessary to be able to guide beams of moving electrons in a similar way lenses guide light. The basis for this kind of technology came from the study from Busch in 1926, who calculated the trajectories of charged particle beams under different sorts of magnetic and electric fields [3]. This would eventually evolve into the development of the first electron lenses, which were the thesis subject of Ernst Ruska, who would become one or the fathers of electron microscopy [4]. Two years after this dissertation, the first electron microscope was built by Ruska and Knoll [5, 6], which would eventually earn Ruska the Nobel Prize in 1986. This first-ever micrsocope can be seen in Figure 1.1.

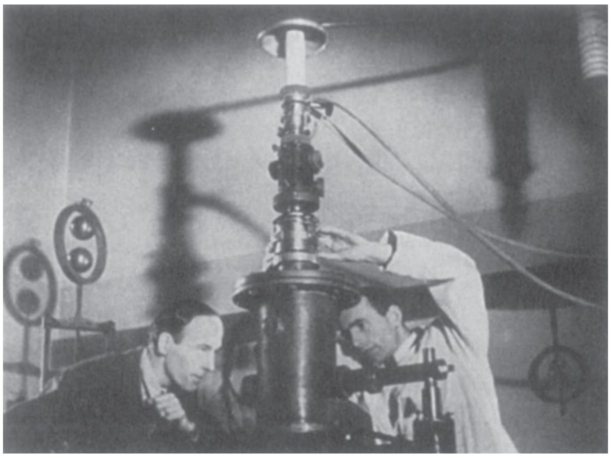

Figure 1.1: *The electron microscope built by Ruska and Knoll in Berlin in the early 1930s. Source: [2].*

In only three years, developments in this kind of microscope made it surpass the resolution of conventional light microscopes, with 40 nm in resolution [7]. By 1939, the first commercial TEMs were available, with a spatial resolution around 10 nm, which can be seen in Figure 1.2 and just one year later RCA systems offered 2.5 nm in resolution. The next decade brought with it an increase in resolution that left it below the nanometre limit [8]; and in the mid 1970s, many commercial TEMs were already able to resolve individual atomic columns in crystals, which originated the concept of high resolution TEM or HRTEM, which we will focus on in Section 1.3.2.

From then on, different routes have been used to improve the resolution in TEM, from higher accelerating voltages to the MeV range, obtaining better resolution but damaging in turn the samples measured. The true revolution for the increasing of spatial resolution in transmission electron microscopy would come with the advanced aberration correction of the microscope electron lenses. This topic had been worked on since the 1940s [9], but it did not achieve an actual improvement of the resolution of an electron microscope until the studies by Zach and Haider in 1995 [10].This will be seen in section 1.3; as well as improvements in data analysis, which will be seen throughout this work. Even though there is still a long path before us, much more has already been developed with regard to this technique.

1.2.1.1 Interactions between electrons and matter: a brief review

To properly understand electron microscopy, as well as many of the techniques derived from it, it is vital to understand the interactions that take place between an electron beam and a sample.

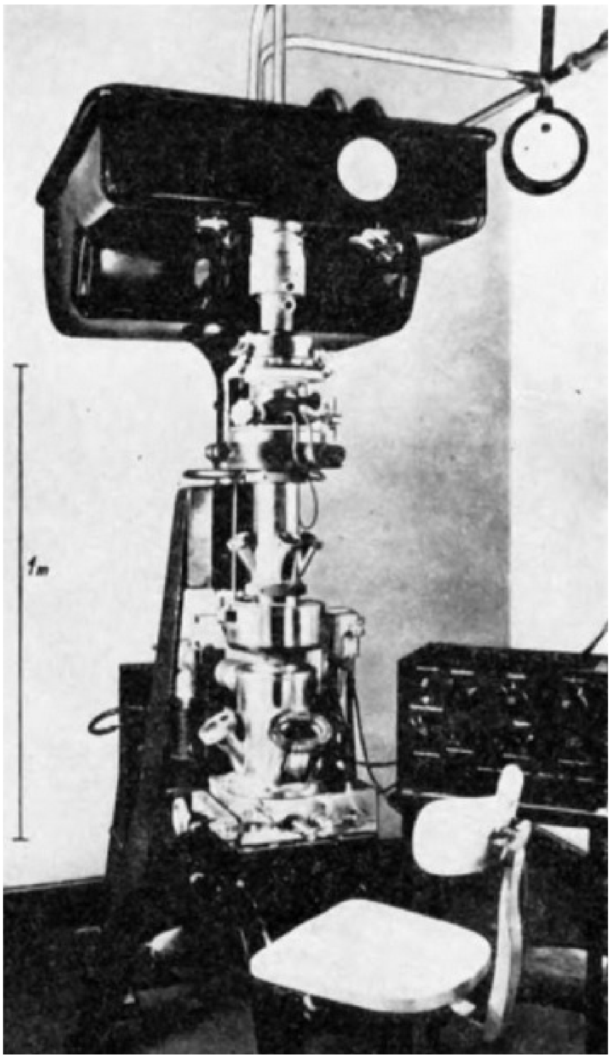

Figure 1.2: *Siemens' first commercial electron microscope, 1939. Source: [8].*

The first notion that is important to understand, is which kind of sample can be imaged in a TEM. The first and most important aspect for a sample to be imaged is its thickness. Due to the diffusion of electrons in thick samples, it is important that the sample is thin enough that most of the electron beam can get through the it. We use the term "electron transparent" for samples that are thin enough for this. The thickness below which a sample is electron transparent is not a fixed value, but it ranges from a few nanometres to a few tenths of nanometres, depending on the density of the sample.

The interaction of high energy electrons with matter has been extensively studied in the past [11].There is a considerable amount of phenomena taking place when a high-kV electron beam impacts a sample, as it can be seen in Figure 1.3. This comes from the electron beam being an "ionising radiation", that is, a radiation capable of removing one of the inner-shell electrons from the sample atoms [2]. We can group these radiation interactions (or lack thereof) in five main categories:

- The first category comprises the electrons that do not interact with the sample in any way. This forms the sometimes wrongfully denominated "transmitted beam", where the electrons follow the same trajectory and have the same energy as the incident beam.

- The second category deals with the electrons that do interact with the sample, being scattered by it. This scattering encompasses transmitted elastically scattered electrons (which we will delve into in Section 1.2.1.2, inelastically scattered electrons (which we will talk about in the same section) and backscattered electrons (BSE), which scatter back to the same side of the sample that the incident beam focuses on. Backscattered electrons are not a part of transmission electron microscopy per se, since they are not, by definition, transmitted electrons. However, in some TEM systems, BSE detectors exist as an additional feature. Nevertheless, in the case of scanning electron microscopy (SEM), BSE are of great importance both for imaging and analysis.

- Inelastic scattering implies a transfer of energy from the electrons to the specimen, which in turn excites the atoms of said specimen producing a myriad of different phenomena. These include the emission of secondary electrons from the sample (electrons that were within the atomic structure of the sample), the emission of different optical radiations coming from different characteristic transitions in the sample (both X-Rays and visible light), as well as the emission of Auger electrons. These eletrons, discovered by Lise Meitner in 1923, are emitted after an inner shell electron is ejected from an atom due to an inelastic scattering. An electron from an outer shell replaces it, and the energy from this level transition is given to a different outer shell electron, which can, in turn, either emit light or be ejected from the sample atom. Within this category we can also include Brehmsstralung X-Rays, produced by the energy lost by electrons decelerating due to their interactions with the sample. These X-Rays are not of direct importance to electron microscopy itself, but they hold importance for other techniques that can be performed in an electron microscope, such as EDX.

- Finally, the last category refers to the phenomena taking place within the excited sample. On the one hand, the sample can get negatively charged, especially if it is non-conducting. In other words, some samples are susceptible of absorbing electrons. On the other hand, this kind of excitation can also produce electron-hole pairs, also known as excitons, which will be of importance during several parts of this manuscript.

1.2.1.2 Electron Scattering

In the previous subsection we have hinted the concept of scattering, which we will focus on in this part of the chapter. Scattering is, without a doubt, the main interaction between an electron beam and a thin sample and, much like light scattering is responsible in one way or another for all light optical systems, from microscopes to telescopes, a similar statement can be made of electron optical systems such as TEM. Furthermore, in the same way as light, for something to be ”visible” using TEM, it is needed that this object scatters electrons in some way[12]. From a wave point of view, we can think of a uniform electron beam as a planar wave front upon our sample. The transmitted wave contains the information necessary for the imaging of the sample [11].

From the different types of phenomena shown in Figure 1.3, we will focus on the electron signals transmitted through the sample. This comprises the direct beam, that is, the beam formed by the electrons that do not undergo any kind of scattering, electrons that are elastically scattered through the sample, diffracted electrons, refracted electrons and inelastically scattered electrons.

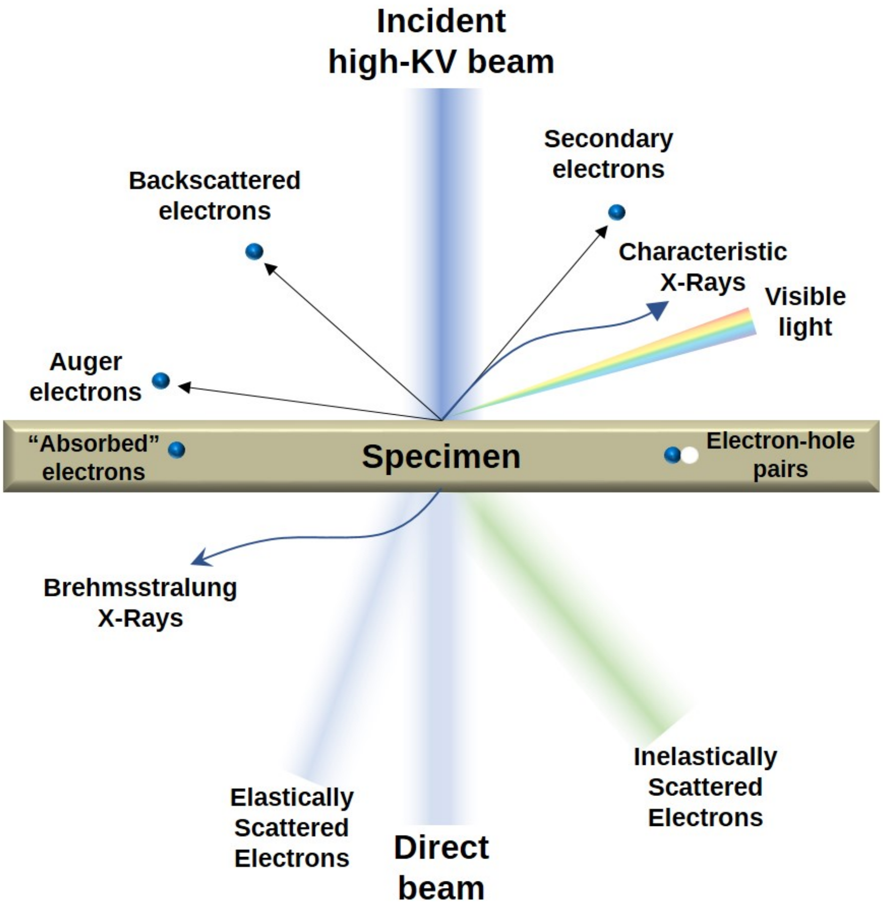

Figure 1.3: *interactions generated when a high-energy beam of electrons interacts with a thin specimen. Most of these interactions can be detected in different types of transmission electron microscope. The directions shown for each signal do not always represent the actual direction of the signal but indicate, in a relative manner, where the signal is strongest or where it is detected. Edited from [2].*

Electron scattering concepts

In order to define electron scattering, it is important to define the following parametres:

The **point-spread function** (PSF) of a certain scattering at the image plane could be interpreted as the image of a point source after undergoing a certain type of scattering [13]. This point spread function can also include aberrations affecting each sort of scattering, so it is a relevant parametre to take into account to describe scattering phenomena. This point spread function can be seen as the projection of the scattering function of the source on a plane that is perpendicular to the scattered beam. A good approximation for this scattering function is a Lorentzian angular distribution that terminates bruptly at a cutoff angle θ_c.

For inelastic scattering, literature shows there is a characteristic angle θ_E for each phenomenon of inelastic scattering [13], where there is a relationship between this angle, the energy E transferred during the scattering phenomenon and the beam energy following the expression $\theta_E \approx E/(2E_0)$ without taking into account any relativistic corrections. This angle is, in other words, the median angle of the scattering distribution, and therefore the center of the point spread function is situated at this precise angle.

The **Rayleigh diffraction limit** is a common parametre of any sort of image formed through scattering, whether it is light or electron scattering. This diffraction limit is defined as:

$$\Delta x = \frac{0.6\lambda}{\sin\beta} \approx \frac{0.6\lambda}{\beta} \tag{1.1}$$

Where β is the aperture semi-angle of the optical system that is used for the imaging in question and λ is the wavelength associated with the scattering in question.

Finally, an interesting parametre to describe an inelastic scattering phenomenon is its **median scattering angle** $< \theta >$; that is, the angle within which half of the inelastic scattering is contained.

Elastic scattering Elastically scttered electrons are the main source of contrast in TEM images and electron diffraction patterns.

There are two main notions in elastic scattering, and they are both important for different parts of this manuscript. These two notions are high-angle elastic scattering by a single atom by an atom nucleus and low-angle elastic scattering by a thin surface, either monocrystalline, polycrystalline, amorphous or a combination of the above. The latter will be called diffraction from now on, even though some of the elastic interactions between the beam and the sample might not fall under this catergory as we will define it.

When it comes to single atom scattering by an atom nucleus, a good starting point is the Rutherford scattering equation, which relates the differential cross section for this kind of high-angle scattering by a nucleus alone as a function of the scattering angle θ:

$$\sigma_R(\theta) = \frac{e^4 \cdot Z^2}{16(4\pi\epsilon_0 E_0)^2} \cdot \frac{d\Omega}{sin^4\frac{\theta}{2}} \tag{1.2}$$

Where e is the electron charge, Z is the atomic number of the nucleus, E_0 is the energy of the incoming beam and dΩ is the differential of solid angle. Electron screening can have an effect of diminishing the effective charge seen by the incoming electrons and correction factors arise from this event, but the main notion to be had is that this differential cross-section is dependent on the atomic number of the nucleus scattering the incoming electrons. This will be of importance when explaining HAADF STEM imaging.

When it comes to diffraction, we can understand this phenomenon, much like with light, by treating the incident electron beam as a planar wave. The concept of using waves with a shorter wavelength (e.g., a higher energy) would undergo a diffraction process by the sample atoms themselves. In this sense, each atom that interacts with the incident beam can be thought of as a source of secondary spherical wavelets [14]. The interference between these wavelets depends on the atomic structure of the sample. This is the origin of one of the two main contrast sources in TEM imaging, diffraction contrast. The electrons conforming this diffracted beams are scattered at low angles. In the case of crystalline materials, these angles are characteristic for the crystalline structure being imaged [12].

It is known from light optics that two diffracted rays are in phase (and therefore, interfere constructively) if their path difference is equal to the wavelength of said rays multiplied by an integer number. Although Laue proposed a successful mathematical model for this phenomenon, nowadays we use the simpler approach developed by Bragg and Bragg (father and son). This approach describes diffraction as a reflection of a plane wave incident at a certain angle by two atomic planes spaced out by a distance d. This is the general notion used not only in electron diffraction, but in any kind of optical diffraction, and is valid not only for reflected waves but also for transmitted waves, since the condition for constructive interference is the same. A scheme of this approach is shown in Figure 1.4

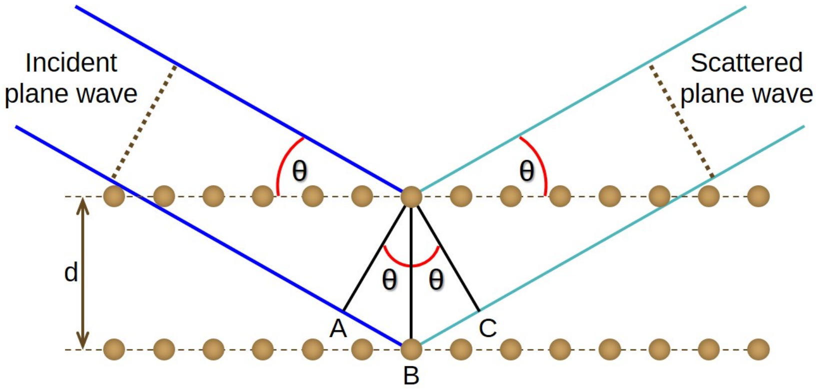

Figure 1.4: *Bragg's description for diffraction in terms of the reflection of a plane wave of wavelength λ, incident at an angle θ to atomic planes with a spacing d among them. Source: [14].*

As we can see in this image, the difference in path between the incident and the scattered wave is the segment AB plus the segment AC, which we can derive from the interplanar distance and the incidence angle:

$$\overline{AB} = \overline{BC} = d \cdot \sin\theta \tag{1.3}$$

And by applying the constructive interference condition previously described:

$$n \cdot \lambda = 2 \cdot d \cdot \sin\theta \tag{1.4}$$

In other words, for a specific crystalline material, only the angles that fulfill this condition (also called Bragg angles, θ_B) will have constructive interference and therefore a high scattering cross-section. This will be delved into in Section 1.2.5 and 1.2.3.

Inelastic scattering Along with elastic scattering, there are scattering phenomena taking place simultaneously that do imply an energy exchange. This energy exchange is appreciable, as hinted by the similarity in mass between the projectiles in the electron beam and the target, that is, the sample atoms and nuclei [15]. In ascending order of energy, here are several different excitations that can give rise to this kind of scattering [16] [12] :

- The least energetic phenomena consists on the collective vibration of the atoms in a certain sample, commonly known as **phonons**. They did not use to be visible in terms of EEL spectroscopy, but new monochromators have rendered these features visible.
- \- Some electronic properties like a semiconductor band gap can induce scattering phenomena when overcoming the conduction band energy, producing intraband transitions. This is explained in detail in chapter 2.
- \- The creation of electron-hole pairs, also known as **excitons**, is a possible outcome of inelastic scattering as well. This kind of phenomenon happens at different energies from sample to sample, and it can rule other electronic properties in the sample such as the band gap. This is further discussed in section 1.4.3.1 and chapter 2.
- \- An adittional phenomenon that can result from this sort of scattering is the collective oscillations of electrons in the sample, commonly known as **plasmons**. These will be a crucial part of this manuscript, and we will come back to them in depth in Section 1.4.3,

chapter2 and chapter4. Plasmons can occur in pretty much any material with weakly bound or free electrons, but they tend to occur mainly in metals.

- - Finally, as long as spectroscopy goes, we also have inner-shell ionisations, which happen when a beam electron transfers enough energy to a core-shell electron (that is, an electron in the inner shells of the atom) to move it outside the attracting field of the nucleus of said atom. It is the basis for high energy EELS, as well as many other phenomena from the ones shown in Figure 1.3, such as light and X-ray scattering, Auger electrons or secondary electrons.

With the exception of the last mentioned phenomena, in general terms the other four phenomena mentioned result from the interaction between the electrons in the incident beam and the conduction electrons in the sample. We will go back to these concepts and how they relate to electron spectroscopy in Section 1.4.3.

The delocalisation of inelastic scattering Generally speaking, all of the phenomena mentioned take place between the incident beam and the electron beam. This kind of electron-electron interaction comes from electrostatic forces, which present quite a long-range nature with respect to the typical sizes in these sort of experiments. This implies there is a basic limit for the spatial resolution we can obtain using techniques related to inelastic scattering.

If we consider the inelastic scattering phenomena to be defined by their distribution of scattering probability [13], also called object function [17], we can define the delocalisation of each inelastic phenomenon as the width of its correspondent distribution in the real space.

The mean free path There are several ways to describe a particular interaction (elastic scattering, inelastic scattering, etc) between electrons and a particular sample. One of the most employed ones, and the one we will use for the purpose of this manuscript, is the mean free path.

Simply put, the mean free path of a specific electron scattering interaction is the average distance an electron travels between scattering events of a specific kind [11, 12]. This means that there are both elastic and inelastic mean free paths. The latter can be used to estimate the thickness of a sample using EEL spectra, as it is shown in Section 4.2.3.1 of this manuscript.

Generally speaking, these parametres are important in the realm of TEM studies, since it provides an estimate of the maximum thickness a sample can have without having a significant amount of plural scattering (which could have negative effects in terms of TEM and EELS resolution).

1.2.1.3 Electron diffraction and the reciprocal space

In a similar way to other scattering diffraction interactions in matter, such as X-rays or other charged particles, in order to talk about electron diffraction and the importance of the analysis of electron diffraction patterns in microscopy works, it is important to address how this diffraction process occurs from a geometrical point of view. For this purpose, we offer a brief explanation on the reciprocal space in crystallography and how it relates to electron diffraction [18].

For the subject of our studies (that is, crystalline and amorphous thin samples) we can think of them as atomic sets that can present some sort of periodical arrangement (such as graphene or TMDs, crystalline materials) or more of a disordered structure (such as amorphous carbon or GO). For the first kind (crystals), we can conceive two different representations for the arrangement of the atoms in these materials. The first one has to do with the specific position of each atom. We call this representation the real lattice of a crystal.

The second kind of representation is an array of points which is specifically defined for each particular crystal but does not relate to the position of the different atoms; instead, each point is related to a particular set of planes in the crystal. We call this the 3D reciprocal lattice of a crystal.

In a more general way, instead of speaking only of real and reciprocal lattices, we can refer to real and reciprocal spaces, the vectorial spaces where these lattices take form.

We can picture a sphere in the reciprocal space centered at the origin of coordinates an with a diametre of $1/\lambda$ (which is generally called the Ewald sphere for its inventor P. P. Ewald [19]. If we superimpose the reciprocal lattice of a sample and the Ewald sphere, we can see that, for the points where the lattice and the sphere intersect, the Bragg condition (see equation 1.4) is met and constructive interference is achieved. For high energies, such as the ones shown in these works, λ is very small and the Ewald sphere has a much bigger radius, therefore having a flatter edge and intersecting more points.

This comes of interest if we think about electron diffraction patterns in the TEM. A diffraction pattern is, on the one hand, the intensity distribution of the scattered beams at the diffraction plane, but it is also the projection of the intersection between the Ewald sphere and the reciprocal lattice. This implies that there is a lot of information about the atomic structure of a material that can be gathered from its electron diffraction pattern.

1.2.2 Working principle of a transmission electron microscope

The working principle of a TEM can be thought as an analogous path to the working principle of a conventional transmission optical microscope. The radiation beam (in this case the accelerated electron beam) is produced at a source, a lamp of sorts. This beam is then conveyed onto the sample by means of a set of lenses. After the radiation goes through the sample in question, an additional set of lenses convey the transmitted beam in order to form an image.

However, this parallelism has to be taken within context, and it is important to understand how each of these processes happen in order to better understand electron microscopy.

1.2.2.1 Elements of an electron microscope

In order to understand the working principle of TEM, it is necessary to know of its different parts first. Following the previous analogy, an electron microscope needs to have an electron source, a way of conveying said electrons onto a sample and forming an image with it, and a way of visualising said image. This section is dedicated to these different parts.

Electron sources
A reliable electron source is key for electron microscopy of any kind. Much like with its light counterpart, a good electron source must produce an electron beam of high intensity and coherence, concept that will be delved into in this section.

There are mainly two mechanisms for the production of an electron beam, both based on giving the electrons enough energy to overcome the natural barrier that keeps them within a solid, called the work function of a material [20]:

- The first mechanism is called thermionic emission. By heating up any material to a high enough temperature, it is possible to give the electrons in said material enough energy to ”leak out” from it by overcoming the work function threshold. In most materials this amount of energy would either melt or vaporise it, so the only viable materials for thermionic sources are either those with a high melting point or those with a really low work function. In modern microscopes, the electron sources using this mechanism are mainly made of LaB_6 or W.

- The second mechanism is called field emission (FE). This mechanisms is based on two very well known concepts in fundamental physics: The tunnel effect and the tip-induced effects on electric fields, which are explained in detail in Section 3.2.3. These tip-induced effects imply that the strength of an electric field E is importantly increased at sharp points. Applying a high potential to an extremely fine metallic tip increases the electric field at the tip greatly, lowering the work-function enough so that the electrons of the material can tunnel out of the tip. A vital factor for field emission to occur is that the surface of the tip has to be pristine. One way to achieve this is to operate in ultra-high vacuum (UHV) conditions (pressures under 10^{-9} Pa). This is what is commonly known as cold FEGs. The other way to achieve this is to keep the surface pristine in worse vacuum conditions by heating it.

In order for an electron source to produce an electron beam, it is necessary to build a device commonly known as an electron gun. Simply put, this device accelerates and focuses the electrons coming from the different electron sources. There are electron guns that produce an electron beam using either thermoionic or field emission mechanisms, and a third kind that uses both mechanisms at once, also called Schottky electron sources.

In the case of thermionic guns, the electrons coming out of the heated filament need to be focused somehow before accelerating them. This is done by means of an electrostatic lens known as Wehnelt. After this, the focused electrons undergo acceleration by means of an anode, applying the desired acceleration voltage between this anode and the Wehnelt and the source, which act as a cathode.

As for FEG, their working principle is much simpler than that of thermionic guns. In order to get a FEG to work, the FEG source acts like the cathode for two different anodes. The first anode is charged several KV with respect to the tip, providing the extraction voltage needed to generate the high electric fields mentioned before. The second anode is used to accelerate the extracted electrons to the desired energy. It is important to know that the spatial coherency of these guns is dependent on the size source, so new research is being made of smaller sources for FEG such as nanowires [21] or carbon nanotubes [22, 23].

Interaction of electrons and magnetic fields

The interaction between a moving charge and a magnetic field can be derived from the Lorentz force law for a charge moving at a speed v and subjected to an electric field E and a magnetic field B:

$$\vec{F} = q \cdot \vec{E} + q\vec{v} \times \vec{B} \tag{1.5}$$

From the magnetic contribution to this law, we can deduce that the magnetic force acting on an electron is perpendicular to both its velocity vector and the applied field on each point. We can also deduce that the magnitude of this force for a specific electron in an electron beam is:

$$F_e = e \cdot v \cdot B_e \cdot \sin\theta_e \tag{1.6}$$

Where v is the velocity of v is the electron velocity, B_e is the magnitude of the magnetic field at the point where the electron is, and θ_e is the angle between the magnetic field and the velocity vector of the electron at said point.

Knowing the interaction between electrons and a magnetic field means it is possible to produce magnetic fields in a way that can focus an electron beam in an analogous way glass lenses can focus light. This kind of device is known as an electron lens.

Electron lenses

During this chapter, the analogy between optical and electron microscopy has been brought up several times. When it comes to electron lenses, this is still very much the case. The name electron lense derives from optical lenses, in the sense that they can do to electron beams what glass lenses can do to light beams, that is:

- Take the rays coming from a certain point A in a sample and recreate a single point A' in a specific image plain.
- Focusing electrons with parallel trajectories in the focal plane of the lens.

However, unlike glass lenses, this kind of lenses can vary in magnification or focus, as we will see in this section.

An electron lens consists of two main parts. On the one hand, we have a cylinder (sometimes a cone) made of a magnetically soft material (that is, easily magnetisable and demagnetisable, such as soft iron) with a hole through its centre. A lense can have several polepieces, which can be part of the same soft iron or completely detatched. A respresentation of an electron lens with two connected polepieces (upper and lower) can be seen in Figure 1.5.

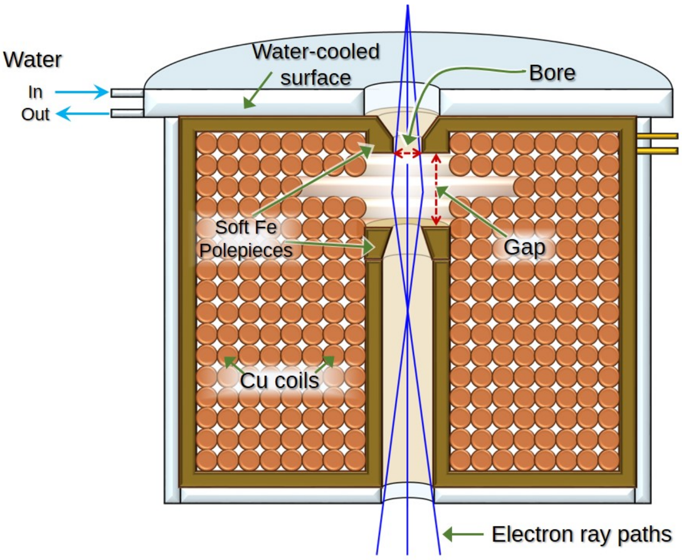

Figure 1.5: *Schematic diagram of a magnetic lens. The magnetically soft iron polepieces sit in the hole down the middle of the lens and are surrounded by copper coils. Current runs through these copper coils in order to magnetize the polepieces. This cross section allows the bore and the gap between the polepieces to be visible.*

The distance between the upper and lower polepieces is called the gap, and the size of the hole within the polepiece is called the bore. In this kind of lense, the bore-to-gap ratio controls to an extent the focusing of the lens.

The second part of these lenses is a coil of copper wire that surrounds each polepiece, which basically acts as solenoid when we pass an electric current through it creating a magnetic field that magnetises the polepieces. This field is inhomogeneous on the plane perpendicular to the electron beam, but homogeneous on the direction parallel to the beam. On the beam axis, this magnetic field has the weakest value, and it increases in strength the closer a point is to the sides of the polepiece.

In simple terms, this means that the more the electrons travel off axis the more strongly they are going to be deflected, which is an analogous behaviour to the interaction between light and a spherical glass lens. However, there is a very important difference between the two: in the case of electron lenses, we can change focus, the intensity of illumination or the magnification an optical system provides by changing the strength of the lenses at will, which can be done by changing the current in the coil.

Apertures

Another fundamental part of an electron microscope are apertures. They consist of interchangeable metallic disk structures with holes of various diametres that are placed along the column of an electron microscope. The aperture is the name for the hole in said disk, while the disk itself is called a diaphragm. Their function is mainly selecting to what extent off-axis electrons will be used for the construction of an image.

For example, the collection aperture on the objective lens of an electron microscope determines its collection semiangle, which in turn limits the scattered intensity that is collected by the microscope. This can affect the resolution of the image formed by the lens. An aperture closer to the sample can also be used to select the region of a specimen (or its diffraction pattern) that is going to be analysed, like the case of the aperture at the entrance of EEL spectrometres. This can correct effects due to scattering in the sample (such as beam broadening) or even solve problems caused by lens aberrations to some extent, since the electrons closest to the optic axis are the least affected by lens aberrations [24]. However, these pieces can contribute to aberrations as well, as we will see in Section 1.3 [13].

Screens, cameras and detectors

In order to form an image from the electrons that go through the sample, it is vital to have some way of detecting them. This is done by means of screens, cameras and detectors.

There are two main types of transmission electron microscopy images. On the one hand, TEM images and diffraction patterns are both, in principle, electron density distributions. A way of translating this electron distribution into an image that can be analysed and interpreted. This is the function of screens and cameras. On the other hand, as we will see in Section 1.2.4, STEM imaging employs a scanning electron probe that moves along the sample, and the image is taken by detecting the electron intensity gathered in each point of the sample. For this purpose, electron detectors offer the best solution.

Regarding the first kind of electron images (TEM), images and diffraction patterns are static; which means they can be projected onto a viewing screen or camera. TEM images are representations of the electron density variations at the image plane, and diffraction patterns the same type of representations at the object plane.

Viewing screens in TEM are coated with a cathodoluminescent material, that is, a material that emits photons when hit by high energy electrons, usually copper-doped ZnS, which produces light around the visible green wavelengths. This means that the viewing screen will emit light in proportion to the intensity of electrons impacting it [25, 26]. This has the advantage of a live analog viewing of the images before the actual recording of an image. This was especially important back in the day when images were recorded by photographic means and each image recorded implied a resource expense. However, an analogic viewing of these images might be decreasing in favor of digital cameras, which offer several advantages, such as not needing the lights to be out (viewing screens are best used in the dark) and the possibility for remote viewing, which means the electron column does not even need to be in the same room as the person performing the study.

In the context of this mansucript, we will understand the term "camera" as a type of serial electron detector, that is, one that can detects several values of intensity at once and therefore can "see" an electron density distribution. The current devices being used for this purpose are the so-called charge-couple device (CCD) and complementary metal-oxide semiconductor (CMOS) detectors. These detectors are able to digitally store the charge generated by light or electrons. They consist of a series of arrays of pixels where each pixel is a capacitor electrically isolated from its neighbouring pixels by means of potential wells under each cell. In other words, these devices accumulate charge proportionally to the incident electron radiation intensity [27, 26] and therefore can construct, by means of specialised software, a digital TEM image. This detection used to precise of an intermediate scintillator to convert the electron distribution onto a light distribution, since detectors were not resistent enough for high energy electrons. However, nowadays direct electron detection using CMOS has started to be implemented in TEMs, which offer a detection method involving less steps [28]. This is of interest for the development of ultrafast electron microscopy [29]

As for STEM imaging, the devices used for image recording are sequential electron detectors, that is, detectors that take one single reading of electron intensity but do so periodically. These are not limited to forward scattered electrons, secondary electron and backscattered electron detectors are used in SEM imaging, but we will focus on those used in transmission electron microscopy since this is the technique that concerns this manuscript.

There are two main kinds of annular sequential electron detectors. First we have semiconductor detectors (generally a p-n junction) where the incoming electrons create electron-hole paris that are separated by the p-n junction internal bias, therefore converting the impacting electrons onto a current between the surface contacs of the detector. The second kind are based on CL just as the fluorescent screens. However, here the scintillator material needs to have a much lower decay time [27]. This signal is then amplified by a photomultiplier.

An additional type of detectors are segmented detectors, generally in 4 quadrants, which are used for Integrated differential phase contrast (iDPC) which allows for direct phase imaging in STEM, increasing the effective resolution and contrast in thin samples[30, 31].

There are several kinds of STEM detector configurations in a STEM optical system, which we will delve into in Section 1.2.4. These are used depending on the type of sample that is being analysed and the sort of image that we want to take of it.

Spectrometres

Performing diverse types of spectroscopy within a TEM is one of its many advantages with respect to other techniques. In this sense, spectrometres are not a fundamental part of an electron microscope in the sense that a TEM can perfectly work without the need for spectrometres, but they do open a new world of analytic possibilities within the instrument.

There are mainly two kinds of spectrometres to be found in TEM optic systems. The first one is related to the photons the sample can produce when excited by an electron beam. This interaction generally produces X-rays, but in some materials we can see a cathodoluminescence phenomenon, where the sample produces light in the visible spectrum in an analogous way to a photoluminescent sample when hit by white light [32]. For these two phenomena, X-ray detectors and cathodoluminescence detectors exist as part of some optic TEM systems.

The second kind of spectrometre found in these systems will be explained in detail in Section 1.4.1, and it has to do with the energy loss of the electrons that undergo inelastic scattering when going through the sample. This, along with X-ray spectroscopy, are the two most used spectroscopic techniques in the TEM.

Aberration correctors

These elements are also not a fundamental one in electron microscopy in the sense that we can find current microscopes that do not feature this element, but it has revolutionised the reach of electron microscopy in the last two decades.

Transmission electron microscopes are not perfect optical systems, and like any other real optical system, there are aberrations that arise from an imperfect working of the lenses in the microscope. As it will be delved into in Section 1.3.2, there are certain devices that can be included in a TEM to compensate for these aberrations.

Monochromators

In a similar way that aberration correctors compensate for the imperfections the optical system has that affect the spatial resolution of the microscope, monochromators do a similar function for the imperfections the electron source has that affect the energy resolution of the beam, that is, the width of the energy distribution in the incident beam. To do so, the monochromator builds an energy spectrum off the electrons ejected by the electron source and projects them onto an energy-selecting slit, which defines the energies of the electrons that will form the final electron beam. This working principle is very similar to the EFTEM mechanism and the EELS spectrometer, which will be seen in following sections [33].

As with any other aperture in the TEM system, the inclusion of a monochromator, although having the advantage of greatly reducing the energy spread of the electron beam, includes some optical aberrations of its own. Recent works, of which the ones by Krivanek *et al* are particularly remarkable, have dealt with the improvement of monochromators in TEM systems to the point of arriving to an energy resolution around $\sim$ 10 meV [34, 35, 36]. This is not only a remarkable improvement in terms of chromatic aberration, but also a very important step forward for EELS in terms of resolution.

1.2.2.2 Basic optics of an electron microscope

Now that we know what are the different parts that conform a TEM, we can have a look at the general optics of an electron microscope using these parts. These concepts are summarised in Figure 1.6

The electron beam is produced and focused in the electron gun. From there it is conveyed to the sample by means of one or several condenser lenses. A condenser aperture is set between the condenser lenses and the sample, which allows us to choose the collection angle of the electron beam. From there, the electrons impact the sample either with a parallel or a focused beam depending on the configuration being used (that is, conventional TEM, CTEM, or scanning TEM, STEM). This is the region of the microscope where phenomena like X-ray scattering and cathodoluminescence take place, so the detectors for the analysis of these features are located on this section of the microscope.

From there on the transmitted electron beam is conveyed by an objective lens, which also features an objective aperture that serves to choose which section of the transmitted beam is used for imaging. After this, the electron beam goes through an imaging system, that is different

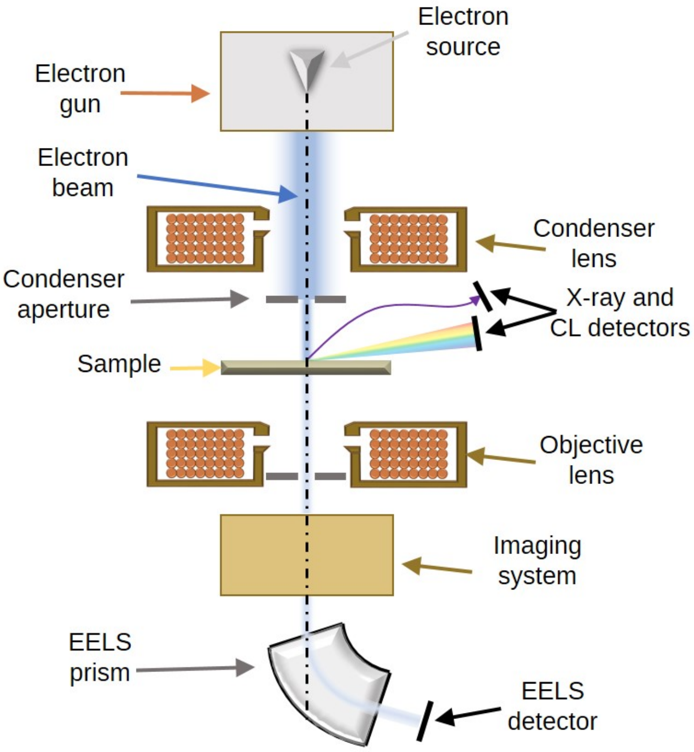

Figure 1.6: *General scheme of the assembly of the optical system of a transmission electron microscope. Elements are not shown to scale.*

depending on whether we have a CTEM or a STEM and will be delved into in sections 1.2.3 and 1.2.4.

Below the imaging system, in the electron microscopes that feature it, we can find an EELS setting to perform this sort of spectroscopic analysis. This device will be explained in detail in Section 1.4.1.

After we have explained the basic working principle of the transmission electron microscope, it is time to focus on its two main working configurations: the parallel beam TEM imaging and the focused beam STEM imaging.

1.2.3 Parallel beam TEM imaging

The first configuration to take into account is the one commonly known as conventional TEM, where we use a ”parallel beam” to interact with the sample. It is important to notice that, in this section, parallel does not necessarily mean completely parallel but rather a beam that is not very convergent [37].

A beam that is almost parallel can be achieved with two condenser lens, which we will from now on call C1 and C2. C1 forms an image of the electron gun crossover, and C2 is set to form an underfocused image of this, hence producing a beam of low convergence.

However, nowadays all TEMs have an additional lens that allows for a much more parallel beam. This last lens can also switch a microscope from CTEM configuration to STEM configuration, hence the name of upper objective lens (an objective lens that is situated before the sample in question), that is also called a condenser-objective lens or, in this particular configuration, C3. Here, C1 and C2 are used to create an image of the crossover of the electron gun at

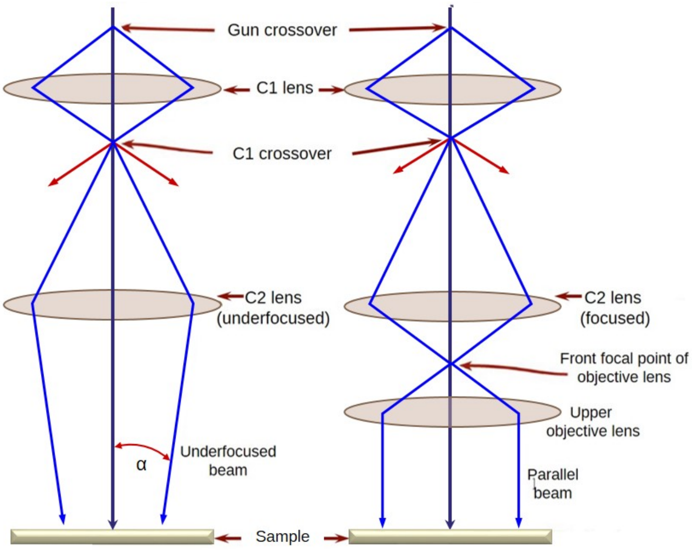

Figure 1.7: *Parallel-beam operation in the TEM. Left: Two lens configuration, using just the C1 and an underfocused C2 lens. Right: The practical situation in most TEMs; using the C1 and C2 lenses to image the source at the FFP of the condenser-objective lens, and therefore creating a truly parallel beam. Edited from [37]*

the focal point of C3, hence producing a parallel beam. The optical arrangement of the CTEM configuration with two and three lenses can be seen in Figure 1.7

Nevertheless, this is only half of the structure of a CTEM. After being transmitted through the sample, this electron beam needs a second set of lenses in order to be able to form an image with it. For this purpose, we use objective lenses, along with objective apertures that serve the purpose of selecting electrons that have been scattered through a particular angle[37]. This allows for image formation using not only the paraxial electron beam (CTEM bright field mode), but also a specific diffracted beam (CTEM dark field mode), as shown in Figure 1.8

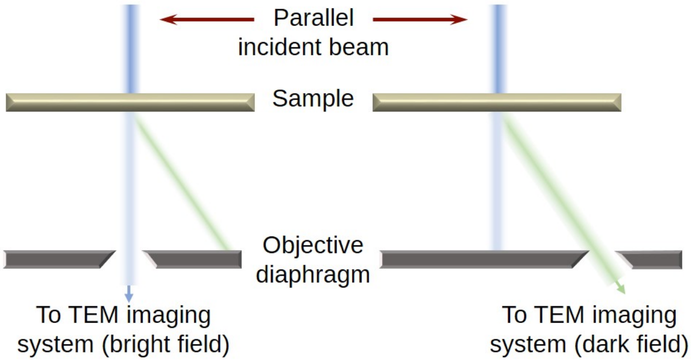

Figure 1.8: *Comparison of the use of an objective aperture in C hbn TEM in two different positions to select either the direct beam, forming BF images (left); or the scattered electrons, forming DF images (right). Edited from [37].*

After the first image is formed by the objective lens, there is the possibility of improving the quality of this first image by means of an aberration corrector, which we will describe in detail in Section 1.3.2. This image can then be magnified by a set of lenses, ending with a

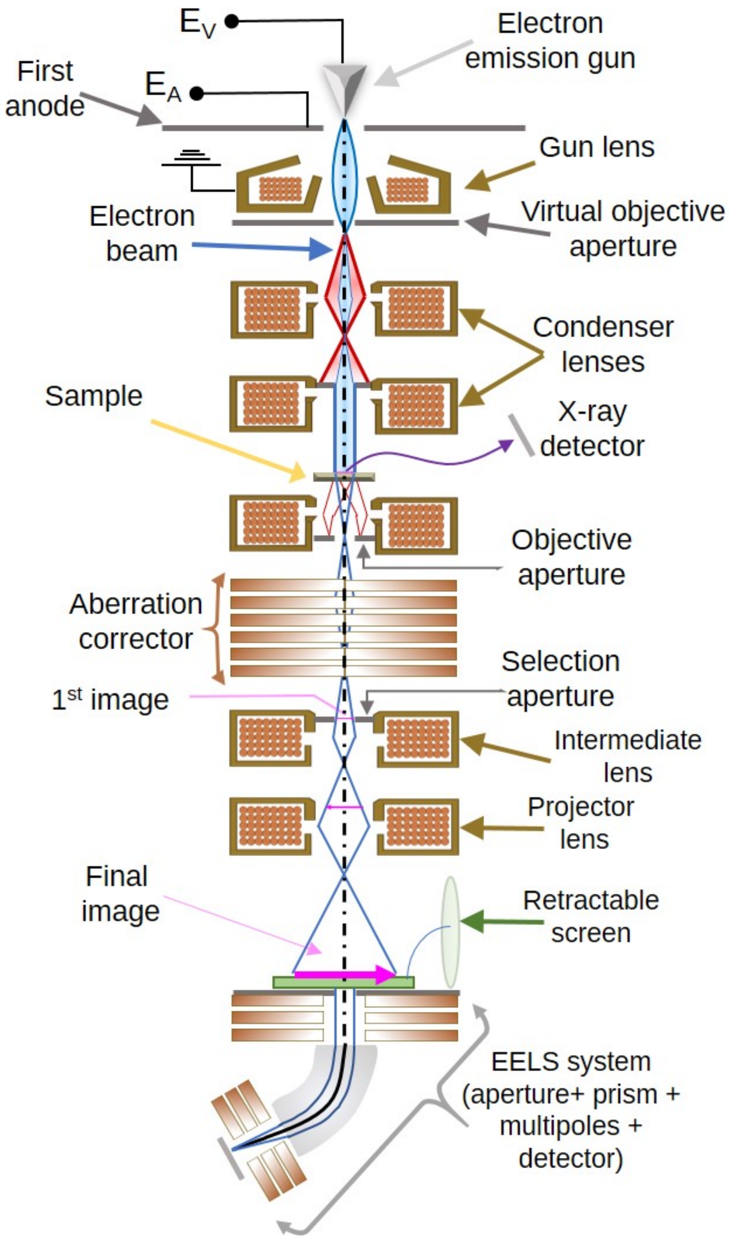

Figure 1.9: *Scheme of the CTEM structure used for the works presented in this manuscript.*

projector lens. An additional aperture is found in these intermediate lenses, with the purpose of being able to select a specific area for a TEM or TEM/EELS study. After being magnified, this electron density can either be projected onto a TEM viewing screen or camera for imaging. Finally, EEL spectroscopic analysis can be performed if the microscope in question features an EEL spectroscopic system, which encompasses yet another aperture to use electrons as paraxial as possible, along with a magnetic prism, a multipole system able to convey the electron beam onto the magnetic prism and focus it properly on its way out, and an EELS detector. A scheme of this complete TEM structure can be seen in Figure 1.9, and it is a simplified scheme of the image-corrected TEM used for this work, which will be described in Section 1.6.

Origin of contrast in TEM imaging: Amplitude and phase contrast

In order to form an image in any kind of optical system, there is a need for a difference in intensity between the points of said image. We call this difference in intensity contrast.

In TEM imaging, contrast comes from the scattering of the incident beam by the sample. If we think of the electron beam as a wave set, this wave can change both its amplitude and its phase as it goes through the sample. Both of these changes are the source of image contrast in TEM, hence the distinction in this kind of microscopy between amplitude contrast and phase contrast. In general, both kinds of contrast can contribute to the overall contrast of an image, although we can selec experimental setups where one will rule over the other.

We will focus on the first of the two, since it is the most relevant for the purpose of this manuscript.

In CTEM configuration, the amplitude contrast can be differentiated into two very clear sources: mass-thickness contrast and diffraction contrast. We will briefly delve deeper into these two concepts.

Mass-thickness contrast

This first source for amplitude contrast is simply related to the amount of scattering phenomena an electron beam will undergo when going through a sample, as well as the deviations these scattering phenomena will induce.

Let us picture two different regions within our imaging area, namely A and B. If area B has a higher thickness than area A, or, in the case that their thickness is the same, in the case that area B is more dense (that is, it has a higher mass and therefore its atoms are more tightly compactec) region B is supposed to host a higher number of scattering events than area A, and the deviations of the scattered electrons coming out of region B should be higher than in region A. As we have seen in section 1.2.3 there is an aperture at the entrance of the objective lens in CTEM systems. This means that, in bright field configuration, some of the "highly scattered" electrons from region B will not be able to get past this aperture, therefore the image intensity for region A will be higher than in region B, hence creating a contrast between the two. A scheme of this process can be seen in Figure 1.10

However, if we choose a diffracted beam (TEM dark field mode), region B will have a higher amount of scattering and therefore diffract a higher amount of electrons, having a higher intensity than region A. In any case, a change of mass or thickness in a sample represents a change of this type of contrast.

In terms of applications, this sort of contrast is the basis of most of CTEM imaging, allowing us to discern between regions with and without matter in them. Furthermore, this sort of contrast also indicates abrupt changes of composition or thickness on a sample. A good example of this would be the imaging of metallic nanoparticles on a carbon matrix, where the high density of the metallic nanoparticles show as a dark contrast in bright field CTEM images. This example is shown in Figure 1.11

Diffraction contrast There is a second sort of contrast that arises from the diffraction of the electron beam, which has been explained in Section 1.2.1.2. We have seen that the angle at which electrons scatter from a material is related to the structure of said material. In the case of crystalline materials, the scattering angles are reduced to those that fulfill the Bragg condition. We can think of the direct beam and the different diffracted beams as a set of different waves that are focused on the same point of the image plane. When this happens, the direct beam and

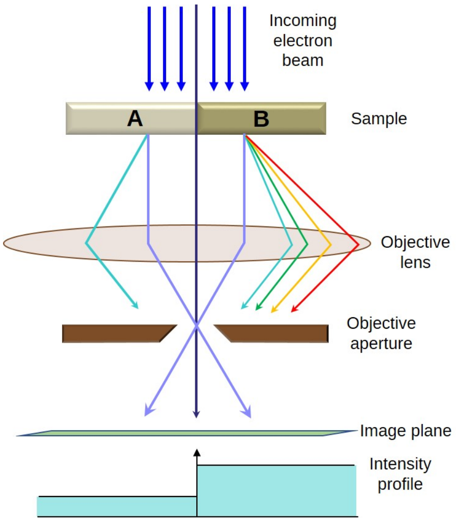

Figure 1.10: *Mass-thickness contrast in a BF image. Thicker or higher-Z areas of the sample (darker, marked with a B in the figure) will scatter more electrons off axis than thinner, lower mass (lighter, marked with an A in the figure) areas. That means fewer electrons from the darker region get to the image plane and therefore, the intensity of the TEM signal is lower. Source: Williams et al [38]*

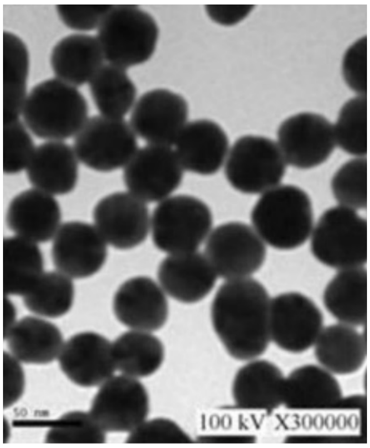

Figure 1.11: *TEM images of Au nanoparticles. Source: Meen et al [39]*

the scattered beams produce an interference phenomenon, which gives rise to what is known in optics as an interference pattern. Since each θ_B is related to a different atomic plane and atomic distance, the wavelength of this interference pattern is, in fact, the interplanar atomic distance of the sample. However, this is merely an interference pattern and not an actual image of the atomic planes in the sample[38, 37].

The combination of these two contrasts generally constitutes what we know as an TEM micrograph.

Structure studies: the Fourier transform An important kind of information that can be inferred from a TEM micrograph relates to the atomic structure in the samples. Since the early models by Ewald in the 1930s and 1940s [40], which dealt with X-ray diffraction and its mathematical approach, it has been seen that the reciprocal lattices explained in section 1.2.1.3 are just a fraction of the information of a specific sample in the reciprocal space, and that the most accurate depiction of an object in the reciprocal spaces is the Fourier transform of said object

In this sense, TEM micrographs allow insight onto the general morphology and shape of a certain sample, but high resolution TEM can offer real information about the general atomic structure of a sample. This, on the one hand, can help identify the type of sample at hand, whether it is amorphous, polycrystalline or monocrystalline. On the other hand a quantification of the Fourier transforms of TEM micrographs can be performed in a similar way to the quantification of electron diffraction patterns. this quantification can lead to the determination of the lattice parametres in crystalline materials, which in turn can help identify a specific sample.

1.2.4 Focused beam TEM imaging: STEM

The other main imaging mode in transmission electron microscopy is known as scanning transmission electron microscopy or STEM. Instead of using a parallel beam, this imaging mode forms a "probe", or focused beam, to image samples by rastering them. This scanning is achieved by the use of macnetic coils that deflect the electron probe slightly, with a spatial accuracy that goes below atomic resolution.

The optic system to obtain this convergent beam is not too far from the one that has been explained for a parallel beam. In essence, it is possible to produce a convergent beam using the same two condenser lenses (C1 and C2) as in parallel beams.

In order to understand this optical scheme, it is important to understand the principle of reciprocity when it comes to electron imaging. If we consider scattering so that all the electron waves have the same energy, we can say that the propagation of electrons from A to B is equivalent to the popagation of electrons from B to A. The application of this principle to STEM [41] indicates that the condenser optics in STEM are equivalent to the objective optics in CTEM. In a similar way, the detector plane in STEM is analogous to the illumination configuration in CTEM [17].

However, by turning off or minimising the intensity of C2 and including a condenser-objective lens such as the one mentioned in the previous section, it is possible to form a more convergent, smaller probe. This is due to the distance between the lens and the sample being much smaller compared to the distance between C1 and C3, which lowers the magnification of the gun crossover (in this case we aspire to have a probe as small as possible)[24, 37].

After the probe is rastered along the the sample, a different mechanism is used to be able to form an image. In this case, we do not have an electron distribution, such as the one found for CTEM, but rather intensity values on each position where the probe scans the sample.

After the electron probe is scattered by the sample, it is possible to collect the electron intensity that is scattered at different angles. As we have seen in Section 1.2.1.2, electrons that interact with the atomic nucleus are scattered at higher angles that those that are not, so in STEM systems there are three kinds of detectors:

- A detector on the optic axis of the system, set in place to collect the electrons that are not scattered by the sample. These electrons will conform what is known as STEM bright field images, where regions where electrons have been scattered (e.g., a sample is present) will appear darker.

- an annular detector for scattered electrons at low or medium angles $\theta <\sim 3^\circ$. These electrons will conform annular dark field or ADF STEM images.

- An annular detector for scattered electrons at high angles $\theta > 5^\circ$. These are the electrons

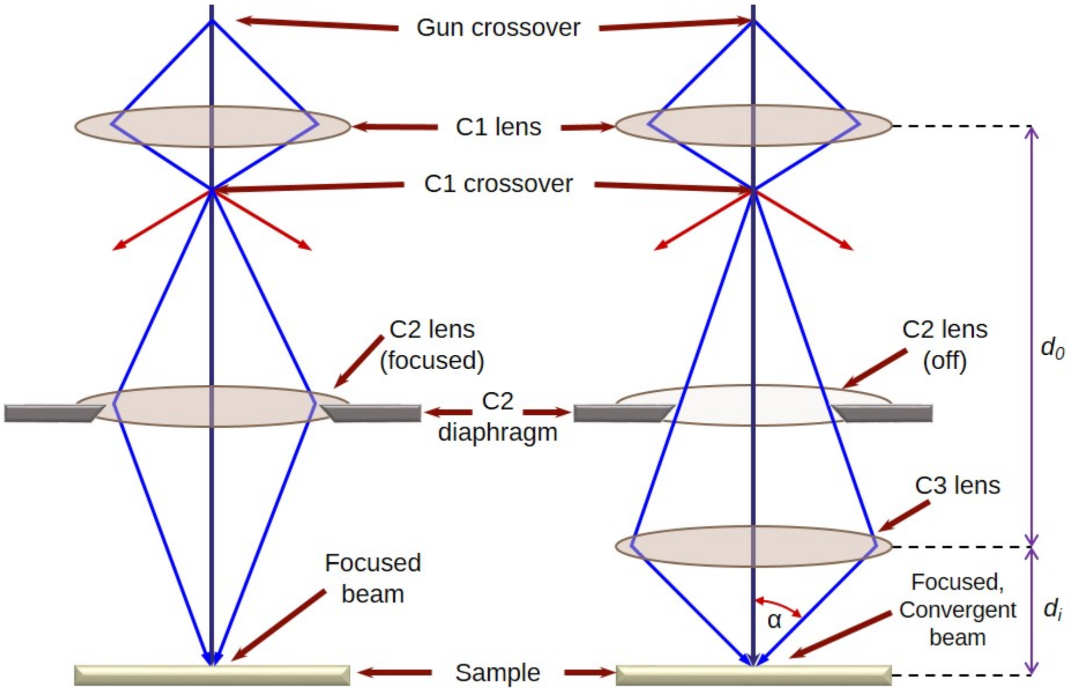

Figure 1.12: *Focused-beam operation in the TEM. Left: Two lens configuration, using just the C1 and an focused C2 lens. Right: The actual situation in most TEM-STEM systems; turning off the C2 lens and using a lower C3 lens to obtain a more convergent beam. Edited from [37]*

that hold the most information about the sample, and their collection results in the construction of high-angle annular dark field STEM images (HAADF STEM images).

A scheme of the different detectors present in a STEM system can be seen in Figure 1.13. As we have seen previously with CTEM, an actual microscope scheme is not as simple as the ones shown in this section. Current STEM systems can provide aberration correction, which, contrary to what is seen for CTEM, is performed not on the electron image but on the electron probe. This means that, in this case, the aberration corrector will be situated between the condenser lenses and the sample, and not between the sample and the imaging collection system. A complete scheme for STEM system that is much close to the one used in this manuscript can be seen in Figure 1.14.

Origin of contrast in HAADF STEM imaging: mass-thickness and HAADF contrast

The origin of the difference in intensity between different points of a sample in STEM has an origin in common with that of CTEM imaging, which is related to the density and thickness of the sample.

With relation to thickness, In a similar way to what we have seen in Section 1.2.3, if we take two regions of a sample that has the same composition but a difference in thickness, the amount of electrons scattered to high angles by this sample will be proportional to the thickness of said sample and their HAADF intensities will be proportional to the thickness as well. In this sense, we can identify regions down to the nanoscale with differences in thickness, which has been what has allowed us to distiguish atomic flakes with a different number of layers in Chapter 2. Another important notion, which we have already mentioned in Section 1.2.1.2, is that the cross-section of atoms scattering to higher angles due to electron-nucleus interaction is

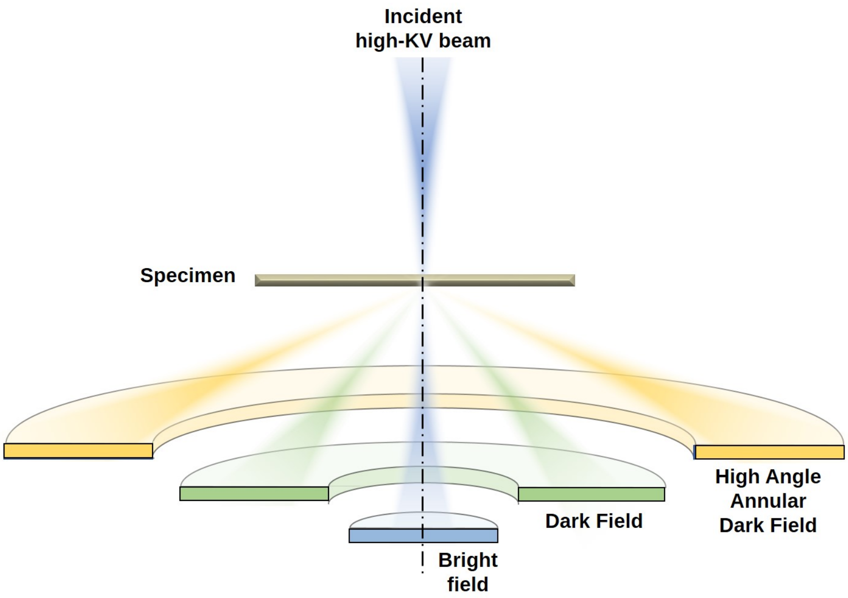

Figure 1.13: *On-axis and annular forward-scattered and high-angle dark field detectors. This scheme is not depicted on scale. Edited from [27].*

proportional to the size of said nucleus, that is, to the atomic number of the element in question. The expression for the screening contrast is not as simple as the one given by Rutherford given the influence of electron screening in this scattering process, so the proportionality between the measured HAADF intensity and the atomic number of the nucleus scattering the electron probe is $I \propto Z^{\xi}$, with ξ taking a value between 1.5 an 2 and being generally approximated as 1.7 [42].

This means that STEM imaging, and especially aberration-corrected STEM imaging, offers the possibility for a quick chemical identification at the atomic scale, given that we know the composition of the sample beforehand. This has been used for the alloying degree quantification of the samples in Chapter 2.

1.2.5 Electron diffraction in a TEM

In Section 1.2.2.1, we referred to the fact that what we call image within the optical system of an electron microscope is just an electron distribution. However, this distribution can be represented as a spatial distribution (that is, a conventional TEM image) or as an angular distribution, which is commonly known as a diffraction pattern. We will only be covering parallel beam electron diffraction because convergent beam diffraction is not of interest for the purpose of this manuscript.

We have seen in Section 1.2.1.2 that one of the forms of elastic scattering in CTEM is by diffraction. Diffraction in the TEM provides information on the atomic structure of the samples being analysed, specifically the cristallinity of the sampple (or lack thereof), the type of crystallinity in the case of cristalline samples, and whether or not there are different crystalline orientations (or even materials) within a certain area [43].

If we go back to the optics of parallel beam TEM, it is possible to see that there is a plane

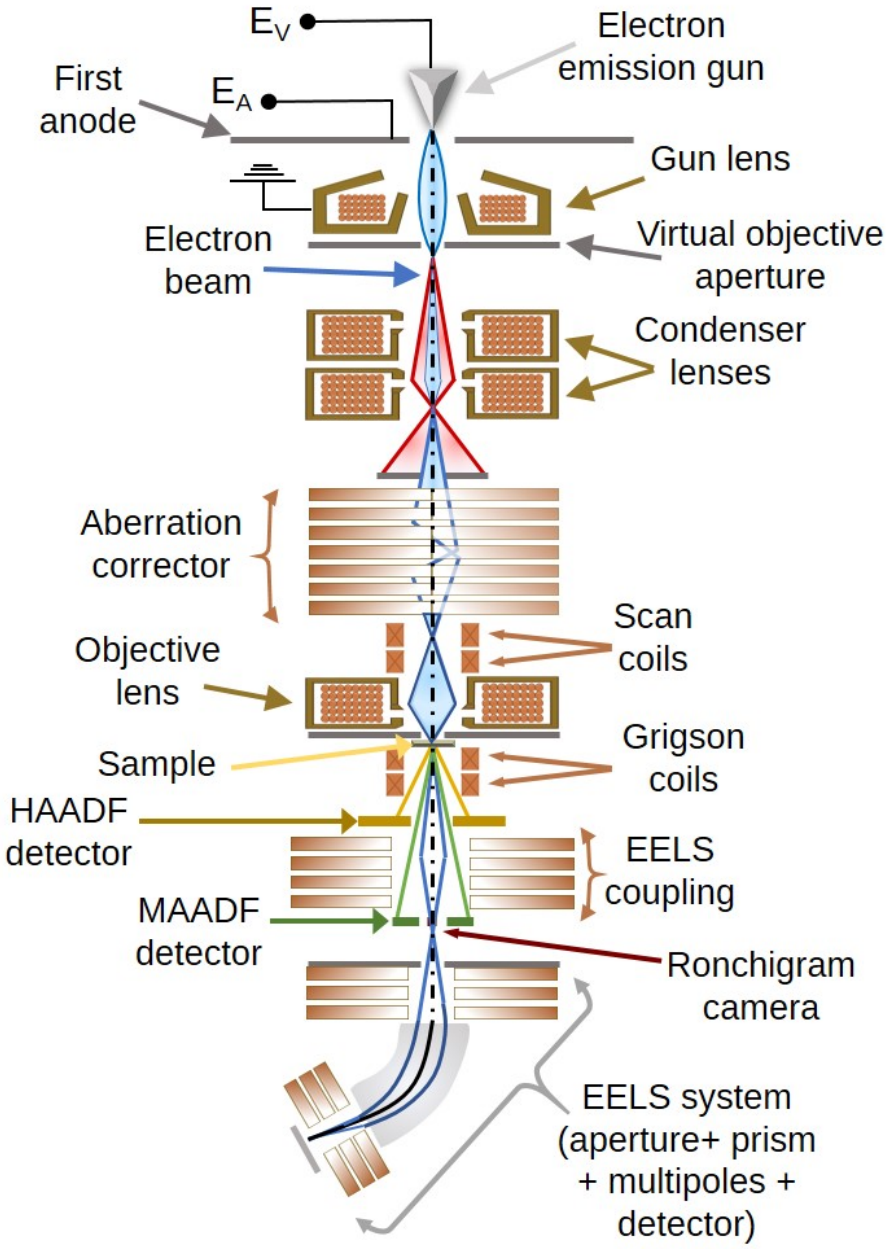

Figure 1.14: *Structure of a STEM with probe correctors and an EELS spectrometre, similar to the one used for these works.*

above the image plane where rays coming out of the sample with the same angle are focused, the diffraction plane. A scheme of this process can be seen in Figure 1.15

Now, with this in mind, in the electron microscope it is possible to take an image of this diffraction plane, which can be done either by lifting the camera up to the diffraction plane (which is not recommended) or by tuning the focus of the different objective lenses so that the diffraction plane of the optical system will coincide with the camera or viewing screen. The image taken in these conditions is known as a diffraction pattern. It consists of a central bright spot coming from the part of the beam that has not been diffracted and a set of features that hold qualitative and quantitative information about the structure of the sample being imaged.

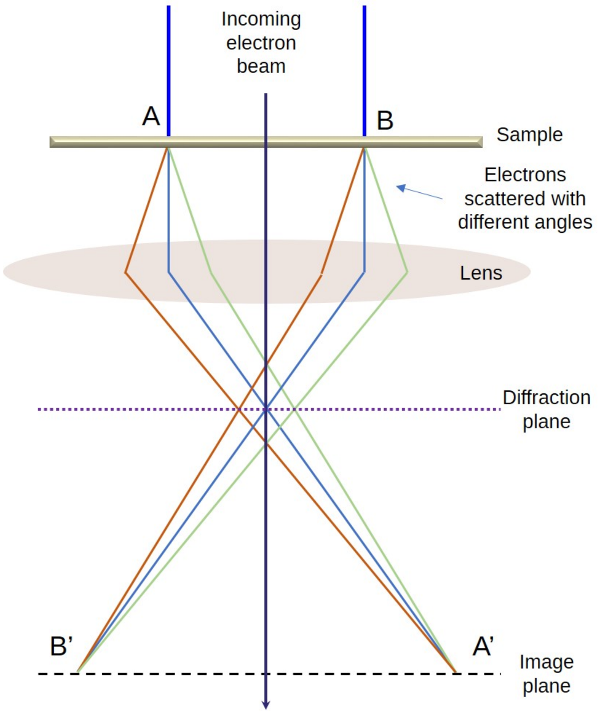

Figure 1.15: *Scheme of the diffraction plane of an optical system. The lens focuses the rays coming out of point A and point B into two different points in the image plane A' and B'. At the same time, there is an intermediate plane, the diffraction plane, where rays that are scattered out of the sample at a specific angle are focused. Source: Williams and Carter [20].*

Bragg's law has been covered in Section 1.2.1.2 (see equation 1.4). If we think of this law in 3 dimensions, in a crystalline material there are specific Bragg angles for each of the atomic planes present in the sample (we will not take the structure factors into account for this introduction because they are not of importance for the studies shown here). This provides the diffraction contrast shown in Section 1.2.3, but in diffraction mode, the fact that electrons are diffracted following different Bragg angles implies that their diffraction patterns are going to be a set of spots that hold relation to the different atomic planes in the sample. The distance between these spots and the central spot (the direct beam spot) is directly related to the Bragg angle at which the electrons have been scattered, and these angles in turn are related to the interplanar distance for a specific diffraction. In other words, the diffraction pattern of a crystalline material allows us to reconstruct its structure.

We can think of the diffraction patterns of polycristalline materials as a linear combination of the diffraction patterns of the different monocrystalline materials composing them. If there is only one kind of material, this means there will be visible spots at a certain distance from the central spot, but it will not be as easy to understand the structure of the material itself.

As for amorphous materials, we can consider it as a polycristalline material with an infinitely small grain size. In this case the diffraction pattern of the materials show rings around the central spot with a certain diametre.

Other types of imaging in a transmission electron microscope

Throughout the years, new technical approaches have been developed within the TEM realm. Here we provide a very brief description of some of them.

Electron tomography has been developed throughout the years as other kinds of tomography (such as MRI) was developed. In essence, it is known that any TEM or STEM micrograph is a two-dimensional projection of a 3D specimen. By gathering images from more than one direction, it is possible to computationally reconstruct the 3D object from the 2D projections of it [44].

Another technique that creates a 3D image of an object is **electron holography**, a process that uses the information of both the intensity and the phase information of the scattered electrons to reconstruct a 3D image. For this, a reference beam from the same source is guided outside the sample and then deflected by a biprism so it interferes with the beam that has gone through the sample. From this interference, the holographic image of the sample is built [45].

It is possible to image magnetic samples in the TEM, as long as there is a correction for the magnetic field introduced by the sample. When this happens, it is possible to image the magnetic domains using a form of phase-contrast microscopy, generally called **Lorentz microscopy**, which plays with the different ways a magnetic sample with different domains deviates the electron beam [44].

Geometrical phase analysis, or GPA is a technique used to quantify the strain in different nanostructures from their HRTEM micrographs. This method consists on placing a small aperture around a strong reflection in the Fourier transform of an HRTEM micrograph (which, as we have seen, is to some extent equivalent to its diffraction pattern) and performing an inverse Fourier transform to this filtered image. The phase component of the complex image resulting from this inverse transform holds information on local displacements of atomic planes. Local strain components can be inferred by analysing the derivative of the displacement field of these atomic planes [46, 45].

Electron ptychography is a computational method for electron imaging. When a sample is imaged using electron microcopy, there is phase information that is encoded in the form of interference patterns between overlapping scattered beams. As the sample is being scanned, this phase information changes and therefore the interference patterns change in a predictable manner, whcih can then be used to obtain the phase differences between regions in a sample [47, 48].

Precession-assisted crystal orientation electron mapping is a somewhat novel technique that scans a precessed electron beam in nanoprobe mode (STEM mode) over the area of the sample, creating a series of precession electron diffraction patterns. The analysis and indexing of these diffraction patterns can provide information on the structure of the sample being imaged.

1.3 Aberration correction in the transmission electron microscope

One of the main turnaround points, if not the main one, for both CTEM and STEM image has been the incorporation of aberration correction into these microscopes [49, 42, 10]. As with any other optical system, elements like electron lenses and apertures can produce optical aberrations that, in turn, can lower the resolution of the imaging or distort the image itself. This section will be divided into two main concepts: First, we will try to explain the cause and the shape of the different aberrations in the electron microscope. Then, we will delve into how these aberrations are corrected and the results of said correction.

1.3.1 Aberrations in an electron optical system

The aberrations in an electron optical system can be mainly grouped into two catergories. On the one hand, we have geometrical aberrations, caused by geometrical imperfections in the TEM system, particularly lenses and apertures. These aberrations, and particularly the spherical aberation and the astigmatism, are responsible for the spatial resolution of the sample [50], the chromatic aberration limits the "*information transfer of high-frequent object information*" [50, 51]. Here we delve a little deeper into these different kinds of aberrations.

Spherical aberration

Spherical aberration is an aberration linked to the very working principle for electron lenses shown in Section 1.2.2.1. This aberration occurs when the lens and its magnetic field behaves differently for on-axis and off-axis electrons. As it has been mentioned before, in electromagnetic lenses, the further off-axis an electron is, the more it is bent toward the axis, not just in direction but also with a different force. as a result, a point would be imaged as a disk of finite size, which would limit the resolution.

Chromatic aberration

Chromatic aberration can the next in importance after spherical aberration. This aberration is due to the electrons in the beam having slight variations in energy among them. An electron gun can produce an electron beam accelerated to a specific energy, but always with some sort of uncertainty. As it was explained in Section 1.2.2.1, the force exerted by the magnetic field of a lens on an electron is proportional to the velocity of said vector, which is in turn higher the higher the energy to which it has been accelerated. A lower velocity in the axis region means the magnetic field from the objective lens will bend these electrons more than the rest. This would mean the image of a single point in the sample would become a small circle when projected.

Astigmatism

Astigmatism is arguably one of the most important aberrations in the TEM. This aberration occurs when the electrons go through a non-uniform magnetic field in the electron lenses. It is not possible to fabricate perfectly center-symmetrical polepieces to the microscopic level, which means the magnetic field in the lens will not be completely center-symmetrical with respect to the central axis of the microscope. Even if these issues could be fixed, off-centering of the apertures can disturb the field even if it is just by a few Angstroms. Astigmatism, in first order, distorts the image by an amount R_{A_1}, where:

$$R_{A_1} = \beta \cdot \Delta f \tag{1.7}$$

Where β is the collection angle and Δf is the maximum difference in focus that is induced by the astigmatic aberration.

Coma

Coma is an aberration that might not be as important in terms of resolution as the abovementioned ones, but it becomes more and more important as the other aberrations are corrected. Generally speaking, this aberration relates to a set of rays emerging from a point in the sample plane, which passes an aperture in a given angle, leading to a circle in the image plane. Without this aberration, the circles of a set of off-axis rays in the image plane are concentric. However, the effects of this aberration induces a translation between the circles for on-axis rays and those for off-axis rays, so the image of a single point in the sample plane would appear as a comet-like feature in the image plane, hence the name of the aberration. Unlike with light optics, due to the helical trajectory of electrons under a magnetic field, the coma aberration related to magnetic electron lenses has two different contributions, radial coma and azimuthal comma [50].

These are just the most intense aberrations within TEM microscopy, without taking into account other higher order aberrations such as star aberration or rosette aberration [52].

In order to counteract the effects of these aberrations on electron microscopy, aberration correctors have been devised.

1.3.2 Aberration correction

In some modern electron microscopes, aberration correctors are set in place for the improvement of the images obtained by counteracting the effects of the different optical aberrations. There is not just one corrector for all of the different aberrations that exist in the electron microscope, so we will briefly delve into the different routes taken for these corrections.

Astigmatism is corrected by means of stigmators, which are small octupoles (8-fold polepieces) that produce a magnetic field to compensate for the effects inhomogeneities have on the magnetic field of the lens. There are stigmators both in the condenser lenses and in the objetive lens, and they are used both for image and for probe aberration corrections. Second order stigmators are used not only for the correction of astigmatism in the TEM, but also for the correction of the coma aberration.

As for the spherical aberration correction, the correction system has two main variants, one using multiple quadrupole and octupole lenses (used by Nion mostly for STEMs), and another one using hexapoles and other transfer lenses (used by CEOS both for image and probe correction) [24]. Since it had been proven since the 1930s that the spherical aberration cannot be corrected in an axyally symmetrical problem [10], they both base their correction on the displacement of the whole optical system off-axis and a further correction by means of polepieces. Modern quadrupole-octupole correctors also account for the correction of the chromatic aberration, which is also helped by the incorporation of monochromators into TEM systems.

HRTEM

The application of aberration correction, under a set of specific conditions has allowed for an instrumentation, theory and computational tools that allow for the characterisation of certain materials at an atomic resolution, which conforms the field of study known as high resolution transmission electron microscopy or HRTEM. Nowadays, the challenges presented are not only those related to the instrumentation itself, but also the theory used to describe the way images are formed[52].

Some novel studies allow for the fine-tuning of the aberration correction by means of software alone [53, 54].

HRSTEM

In the case of STEM, aberration correction has allowed for the formation of probes with a size comparable to atomic sizes. Providing atomic resolution to STEM has also implied providing atomic resolution to the implicit chemical quantification provided by the contrast of HAADF imaging [45] as well as their potential combination with spectroscopic techniques such as EELS. Thanks to this increase in resolution, it is now possible to perform STEM-EELS analyses with a resolution that allows not only for the identification of specific species within a matrix to an atomic level (such as dopants), but that also allows for the in-depth study of these species with all the information EELS can offer [55].

1.4 Spectroscopy in a transmission electron microscope: EELS

There are several kinds of spectroscopies that can be performed within a TEM. However, for the purpose of this manuscript, we will focus on one in particular, electron energy loss spectroscopy (EELS).

1.4.1 Working principle of an EEL spectrometre

The main device that allows for EEL spectrometry is known as a magnetic prism. To some extent, it works in a similar way to the polepiece lenses shown in Section 1.2.2.1, only with an added factor: magnetic prisms provide an additional uniform magnetic field that interacts with electrons, of the order of 0.01 T, which is generated by an electromagnet with carefully shaped polepieces [15]. As it has been seen in Section 1.2.2.1, The interaction between accelerated electrons and a uniform magnetic field is for the electrons to follow circular paths of radius R, where said radius follows an expression that is dependent on the energy of each electron. This expressions comes from the magnetic part of equation 1.5 for magnetic fields that are perpendicular to the velocity vector of the electrons (that is, $\theta_e = 90\,\mathrm{deg}$. The Lorentz principle states that that the magnetic force on the particle is equal to its centripetal force

$$B \times q \times v = \frac{m \times v^2}{R} \tag{1.8}$$

Where B is the magnetic field, q is the charge of the particle (which we call e in this case for its being an electron), m is the mass of the particle (here, m_e),v is the velocity of the particle, and R is the radius of the curvature of the particles. The expression fo R would be as follows::

$$R = \frac{m_e}{e} \times B \times v \tag{1.9}$$

and by equating the energy coming from the acceleration of the electrons in the column, E_V, and the kinetic energy of the sample, $\frac{1}{2} m_e \times v^2$ we obtain: 2ev/m

$$R = \frac{m_e}{e} \times B \times \sqrt{\frac{2 \times E_V}{m_e}} = \frac{\sqrt{2 \times m_e \times E_V}}{e} \times B \tag{1.10}$$

Since the rest of the parametres in this equation are constant, we have a 1-to-1 relationship between energy and curvature radius. This means that, for an electron beam with a constant acceleration, we also have a 1-to-1 relationship between energy loss and curvature radius. This is the working principle of EELS.

The optics of this working principle and its inclusion in a TEM system, adapted from [15], can be seen in Figure 1.16

In this figure, the purple beam represents the whole of the electrons that go through the sample. After going through the spectrometre aperture, that limits the maximum angle at which the electrons can get through, the magnetic prism is able to form an image where electrons with different energies are focused in different points. This is here represented by the blue beam, focusing on the point ***I***, and the red beam, focusing on the point ***I'***. In other words, this is able to build an EEL spectrum. It is imporant to know that, in this schematic, the points ***I*** and ***I'***

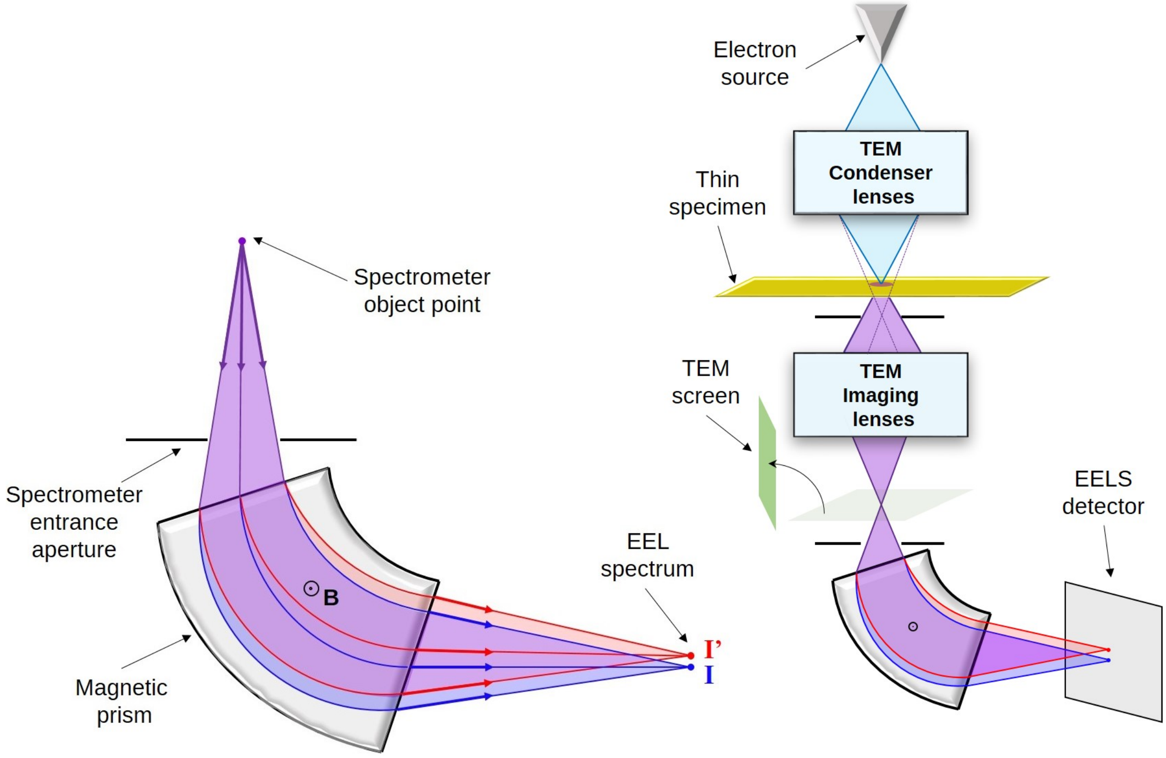

Figure 1.16: *EELS working principle. Left: Dispersive and focusing properties of a magnetic prism in a plane perpendicular to the magnetic field. Right: implementing of a magnetic prism in a TEM optic system. TEM parts not represented to scale. Source: [15].*

would be on the same vertical line, since the prism acts as a lense as well, focusing the dispersion that will later be the EEL spectrum onto a single line.

There are other kinds of spectrometers for EELS, like the electrostatic ones or some that combine magnetic fields and their electrostatic character. However, magnetic prism spectrometres in EELS (also known in this configuration as parallel-collection EELS or PEELS for the Gatan devices) offers advantages with respect to these other kinds of spectrometers, in terms of resolution and in ease of implementation [56].

Now that we have seen the working principle that allows for this kind of spectroscopy, it is time to dive into the EEL spectra, their characteristics and their analysis.

1.4.2 General notions of EELS: Zero loss, low-loss and core-loss

Figure 1.17, taken from [57], displays a complete energy loss spectrum with different signaled features.

There are several features signaled in this figure, which will be explained in depth along this section. Out of these, there are three that relate to different energy windows in the EEL spectra:

- The **zero-loss peak (ZLP)** is mainly conformed by electrons that have suffered elastic scattering or have not undergone scaterring at all. This feature is the most intense one and its contribution renders dificult the analysis of the following low-loss EELS, as we will see in chapter 3. It is generally considered within the low-loss region of the EEL spectra for proximity reasons, so we will delve into it a little bit in Section 1.4.3.

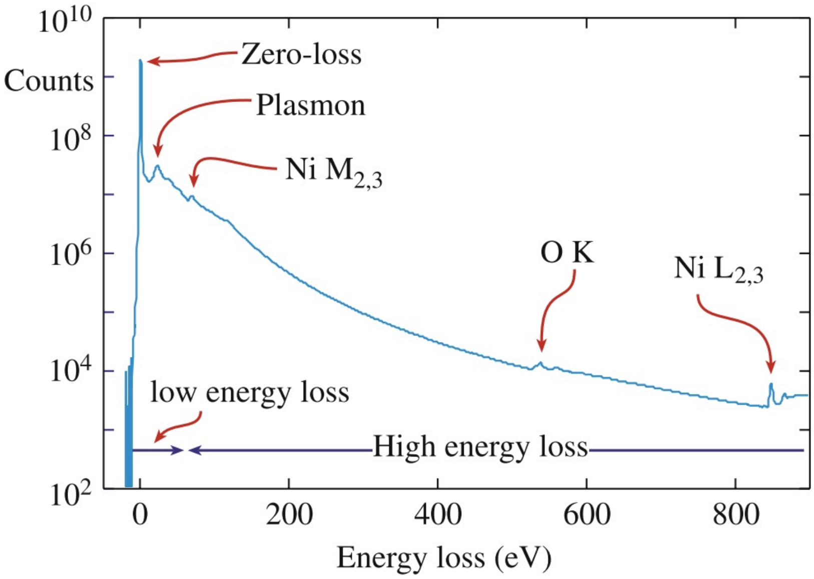

Figure 1.17: *A typical EELS spectrum displayed in logarithmic scale. The zero-loss peak is an order of magnitude more intense than the low energy-loss portion (characterized by the plasmon peak), which is many orders of magnitude more intense than the small ionization edges identified in the high energy-loss range. figure taken from the bibliography [56].*

- The **low-loss region of the EEL spectra** goes up to a few tenths of eV in energy, with a general consensus of an upper limit of this region around ∼ 50 eV. This region comprises the electrons which have interacted with the outer-shell electrons of the atoms in the sample, in other words, the conduction electrons of the sample. It contains information about the optoelectronic properties of the sample and, as we will delve into in Chapter 4, we can obtain information about the thickness of a sample and the mass density from the analysis of this spectral region.

- The **core-loss region of the EEL spectra** (above ∼ 50 eV in energy) contains information from the inelastic interactions between the electron beam and the inner or core shells of the sample, that is the nucleus and the valence electrons. Generally speaking, it contains information about the chemical composition and atomic configuration of the sample.

1.4.3 Low-loss EELS: features, properties and applications

As we have mentioned in the previous section, this subsection of the manuscript focuses on the spectral window that goes from 0 to ∼50 eV in energy loss, which is a reasonable low estimate for the energy of inner-shell ionisations.

The low energy at which this spectroscopy interacts means that we will only be measuring the response of the valence electrons in the sample [58], although, to be completely precise, we will be measuring the combined response of the valence electrons and the electromagnetic field [59]. This is why, for example, in chapter 3, we are able to measure the effects of surface plasmons even when we are not probing directly on top of our sample. In other words, low-loss EELS is *"a direct measure of the dielectric response of the sample to the external electromagnetic excitation"* [60]

From this we can deduce that we will be able to analyse the electronic properties mentioned in Section 1.2.1.2 from the low loss EELS. Additionally,this energy window covers plasmons and phonons as well, although the latter cannot be seen in most EEL spectra due to its low energy (around 10 meV) [58].

1.4.3.1 The low-loss EEL spectrum

Here we introduce the main phenomena and features related to the low-loss EEL spectrum.

The predominant feature in any low loss EEL spectrum is the zero-loss peak, or **ZLP**. As we have mentioned, this feature consists mainly of electrons that have not suffered any energy loss when being transmitted through the sample. This includes, in a broad sense, any electron within the energy resolution of the EEL spectrometer; from those who did not undergo any scattering events, to those who were elastically scattered and, in most cases, phonon-scattered electrons. The have an energy loss so little that most EEL spectrometers do not have an energy resolution good enough to discern their features, even when monochromated [58].

The resolution of a given EEL spectrum is typically given by the full width alt half maximum (FWHM) of the ZLP, and its signal, along with the plasmonic contributions, constitutes the most part of the background signal in the spectra. This resolution depends mainly on two factors: the nature of the electron gun and whether there is a monochromator in the optical system of the electron microscope or not. In order to minimize an additional tail due to the point-spread function of the electron detector, which can also influence the resolution of an EEL spectrum, these are generally recorded with a high dispersion, that is, with a small energy window per channel in the spectrometre [13].

After the ZLP, and in suitable samples, features related to **plasmonic phenomena** are the most intense feature of a LL-EEL spectra. These peaks come from collective excitations of the free electrons in said samples. This phenomena translate into somewhat wide peaks that depend on the nature of the material, as well as its geometry. There can be a single plasmon phenomenon in a sample (a bulk plasmon) along with one or more surface plasmons, in the case of samples with a high surface-to-volume ratio. The bulk plasmon contains information about the density and the mechanical properties of a material, a large value of the energy related to the plasmon feature implies a higher valence-electron density, which is both related to a higher atomic density and a stronger interatomic bonding [15]. These phenomena will be delved into in detail in chapter 3 and, to some extent, in chapter 4.

Excitonic transitions due to electron-hole pair creation, characteristic of each material, can also play a part in the LL-EEL spectra. When the energy exchange between an electron from the beam and the sample is high enough, this promotes an electron from one of the sample atoms from its valence band to its conduction band. Every different material has their own characteristic excitonic transitions, which means the features associated with them can be a fingerprint of sorts for their corresponding samples. In some materials their optical gap is defined by these excitonic transitions, so their study is also of importance when it comes to optoelectronic properties.

Finally, in certain samples that fulfill a series of conditions (which we will get into in chapter 2), and if there are no visible features going on below this energy value, it is possible to see features in the LL-EEL spectra related to the **density of states** of a sample. This allows, for example, for the determination of the optical gap [13] as well as other optoelectronic features, such as Van Hove discontinuity points in the density of states, which also reflect as features in the LL-EEL spectra [61, 62].

1.4.3.2 Interpretation of low-loss EELS: feature analysis, information and applications

Here we present a classic routine for the analysis of LL-EELS, along with the information that can be gathered from it and even some application this analysis could have.

When it comes to the analysis of LL-EEL spectra, the first feature to analyse is the ZLP. This intense peak has a tail either side of it, which intensity is tied to the energy resolution. On the negative part of the ZLP, its tail is only due to the energy spread of the incoming beam, whereas the positive part of the peak may have additional components coming from phononic resonances [58]. However, these contributions are generally much less intense than the ZLP itself and, for the case of our studies (monochromated beam), we can consider the ZLP to be pretty much symmetric. The center of this peak is used for calibration, since, even with previous experimental calibrations, the spectrum in question might have shifted slightly from its correct position (that is, with the ZLP centered around 0).

The tail of the ZLP goes far beyond its FWHM. In other words, the ZLP can have an observable effect even at energies that are eV apart from it. This tail is mostly composed of backscattered electrons that have then been reabsorbed by the sample and find their way to the electron detector by means of multiple backscattering [13]. However, in most cases, at high energies it is the tail of other features, such as plasmons, that dominate the background.

To remove the tail of the ZLP there are two main routes: either fitting it using a specific function (power-law, polynomial, gaussian+lorentzian, etc) or to fit it using a ZLP obtained in a region where the absence of our signal or signals of interest is assured [63]. During the experiments of this manuscript, for several reasons, we have been in need of both approaches. However, the one that has been used more often has been a fitting using a power-law function, which is a command already implemented in our analysis software, Digital Micrograph.

The noise and the high dynamic range of the low loss spectra (the high variation of intensity along the spectra) make the background fitting window a crucial parametre for an optimal fitting of the ZLP. This is why we have paid special attention to this window for every ZLP fitting in this manuscript, especially in chapter 2, where an optimal fit of the ZLP was crucial for a correct analysis of the optoelectronic properties in the alloy samples.

Another possible use for the ZLP is as an estimation of the non-scattered electron intensity. This, along with an estimation of the total transmitted electron intensity (an integration over the ZLP as well as the rest of the features in the LL-EEL spectra, can be used for the estimation of the thickness of a specific sample using the log-ratio method [64]. This method is explained in detail in chapter 4.

The analysis of plasmonic components is also a key procedure for the studies in this manuscript, especially in chapter 3 but also to a lower extent in chapter 4. There are many different ways this features can be analysed, but there are two that have been used for our studies. In chapter 3, in view of the difficult experimental conditions for the plasmonic component analysis, multivariate analysis has been set in place, which is discussed vastly in said chapter. This has allowed for a very complete description of the plasmonic behaviour of our samples. On the other hand, in chapter 4, the Drude model has been used to fit our plasmonic spectral features, as it has been used before in the literature for this sort of features [13, 65]. The expression for this kind of fit is:

$$Im\left(-\frac{1}{\epsilon(E)}\right) = \frac{E_p^2 \times E \times \Delta E_p}{(E^2 - E_p^2) + (E \times \Delta E_p)} \tag{1.11}$$

Where, in this case, we approximate the energy loss function by $Im\left(-\frac{1}{\epsilon(E)}\right)$ and use this expression to fit our plasmon peaks. This has been useful for estimations of the mass density of our samples, as well as a rough estimation of the surface-to-volume ratio in our samples by checking the ratio between the surface plasmon in the GO and its bulk plasmon, which essentially was an indicator of the increasing surface effects that were taking place in the sample as it thinned out.

For the purpose of this manuscript, all other properties measured on the LL-EEL spectra (band gap, excitonic transitions and Van Hove features) have been measured by means of either linear fitting (band gap) or multi-peak gaussian fitting (excitonic and Van Hove features).

1.4.4 Core-loss EELS: features, properties and applications

In this section of the manuscript, we will focus on the section of EELS that focues on the spectral region from 50 eV and up, even though depending on the elements being analysed the threshold energy for this energy window can be lower. This spectral window shows features related to the interactions between the electron beam and the inner-shell electrons in the sample shown in Section 1.2.1.2. This spectral window can go up to a few thousands of eV [15], although for the purpose of our core-loss studies (mainly used in chapter 4 for the analysis of GO samples) we will be focusing on the spectral window between 200 and 600 eV, since the signatures of all the elements of interest for this study are located within this spectral window. [66]

1.4.4.1 Working mechanism

As we have mentioned, the high-loss part of EEL spectra is produced by the inelastic interactions between the electron beam and the electrons located at inner levels of atoms, also called core levels. In these kinds of interactions, a beam electron transfer sufficient energy to one of these core-shell electrons to pull it out of the nucleus Coulombic attractive field. The deionisation of these atoms produce the characteristic X-rays measured in EDS, so we could say these two techniques measure two processes that are closely related.

The ionisation process that takes place with the interaction that yields the high-loss EEL spectra is characteristic to the atom said ionisation is taken place in, as well as the core shell where the ionisation takes place (named K, L, M, N... in ascending order as they are further apart from the atom nucleus), so this part of the spectra is essential for the determination of the chemical composition of a sample, and as it will be explained in this section, for the quantification of said chemical composition.

Compared to the low loss excitations mentioned in Section 1.4.3, core-loss features have much smaller cross-sections and, as a result, the intensity of said features are much smaller than low-loss features such as the plasmonic peaks. These features become fainter for higher characteristic energies. We will focus on the two main features taking place at these energies: ionisation edges and fine peak structures.

1.4.4.2 General shape of a core-loss EEL spectrum: Ionisation edges and fine peak structures

Taking into account the structure of any given atom, it is possible to see that atom ionisation via displacement of their core shell electrons is a process that requires a certain minimum energy, a threshold of sorts from which said ionisation will take place. In this regard, we can categorise the threshold ionisation energies of all different atoms, which will in turn provide an energy map of the localisation of the different ionisation peaks, something extremely useful for qualitative chemical composition determination.

It is possible to ionise a core-shell electron with an energy higher than its ionisation threshold energy. However, it is important to notice that the ionisation cross section of a certain electron is lower the higher the energy transfer. This means that the contribution to the energy loss distribution of the electrons corresponding to a certain ionisation process have a very distinctive shape, with a sharp rise to a maximum intensity at the threshold energy and a decreasing ”tail” at higher energies. An example of this sort of edge, before and after the removal of plural scattering background, can be seen in Figure 1.18.[57] This distribution, of course, is framed within a full EEL spectra, so there are several other contributions taking place simultaneously, which have to be taken into consideration, such as plural scattering and plasmonic contributions. However, there is a second kind of features in core-loss EEL spectra that is remarkably important not only for EELS analysis in general, but also for this manuscript in particular. This is what we know as fine structure peaks.

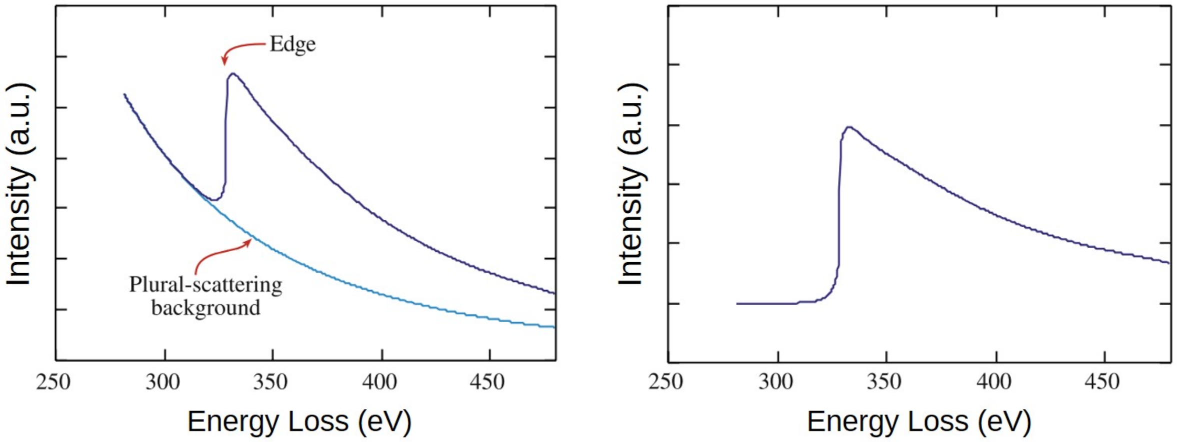

Figure 1.18: *Shape of an ideal core-loss EELS ionisation edge, both with a plural scattering background (left) and after background removal (right). Edited from [57]*

Fine structure peaks

Besides the ideal ionisation edges here explained, there are a second kind of features to core-loss EEL spectra that are of extreme importance for EELS analyses. These EELS features are denominated fine structure peaks.

These processes arise from the energy transferred from the beam electrons to the core-shell electrons being higher than the threshold ionisation energy of the atoms in the sample, that is, the energy needed by the core electron to be ejected from this inner shell.

Depending on the energy excess of the electron after being ejected from this inner shell, we can have two different phenomena taking place. This gives rise to the two types of fine structure peaks: energy-loss near-edge structure features (ELNES) and extended energy-loss fine structure features (EXELFS). We will provide a brief description of their working mechanism, focusing mainly on the ELNES features since they are a key part of the studies in this manusctript.

Electrons with only a few eV of energy excess are ejected from their core shell but their energy is not enough to be ejected to the vacuum level. In other words, the final state of this ejected electron is set on the ”empty” energy levels above the Fermi energy (E_F) of the atom in question. In other words, these electrons probe the unoccupied density of states (DOS) of the material, hence their uniqueness and their importance for studies related to the chemistry of the sample. These features (ELNES features) can yield unique information on the internal bonds of the different atoms in the materials.

ELNES electrons undergo multiple elastic scattering interactions with the atoms surrounding our ionised one, which means the analysis of these features is more challenging than it could seem at first sight. This will be briefly explained in Section 1.4.4.3.

On the other hand, electrons with enough energy after ionisation to escape the atom can be considered as free electrons, which can in turn be diffracted by its neighbouring atoms. Given the cross-section of these interactions is smaller the larger the energy, it is sensible to consider these interactions as single scattering events. These scattering events produce oscillations on the "ideal" ionisation edge, which are also known as EXELFS features. These features are analogous to the oscillations in extended X-ray absorption fine structures (EXAFS) seen in synchroton x-ray spectroscopy, which is one reason why it has been said that EELS has been able to place a synchroton within a TEM[67].

1.4.4.3 Analysis in core-loss EEL spectra

As far as this manuscript goes, there are three main areas of application that are of interest for EELS analysis: elemental analysis, chemical quantification and fine structure peak analysis.

Elemental analysis in EELS It has been said in the previous section that one of the main features of core-loss EEL spectra are the ionisation edges. These edges are characteristic for each element present in the sample, so by identifying the different ionisation edges present in an EEL spectrum we can discern different elements conforming our sample.

Chemical quantification in EELS

The theoretical basis of relative chemical quantification of samples using core loss EELS has been extensively covered in the literature [57, 13, 68]. Here we present a succint explanation on how relative elemental quantification works.

An adequate way to discern how this quantification process works is with the expression for the probability of ionisation of a certain edge in a certain atom, which we can name P_E. Assuming single ionisation events, this probability can be described in a similar way to the scattering probability mentioned in Section 1.2.1.2:

$$P_K = N \cdot \sigma_E \cdot e^{-t/\lambda_E} \tag{1.12}$$

Where t is the thickness of our sample, N is the surface density of atoms of the specific kind that contributes to the edge in question, σ_E is the ionisation cross section for this particular edge and λ_E is the mean free path for this ionisation phenomenon.

If we know the probability for this phenomenon to happen, this could be defined as the ratio between the amount of electrons that undergo this ionisation phenomenon and the total amount of transmitted electrons. In other words, this probability represents the ratio between the intensity of a given ionisation edge (I_E) and the total transmitted intensity(I_t:

$$P_E = \frac{I_E}{I_t} \tag{1.13}$$

If the sample is thin enough, or if multiple scattering events are corrected somehow, the exponential term in equation 1.12 is approximated by 1, given the large mean free path this kind of interaction has. This leaves us with a simplified expression for the number of atoms of a certain kind in a specific area:

$$N_E = \frac{I_E}{\sigma_E \cdot I_t} \tag{1.14}$$

However, from an experimental point of view, there is an important experimental challenge in taking EEL spectra that cover both the core-loss ionisation edges and the ZLP, which represents the majority of the transmitted intensity. This is the reason why in this manuscript we will be representing relative compositions of different elements instead of absolute ones. If we calculate the ratio between edges coming from different atoms A and B, we can obtain a composition ratio, in other words, a relative atomic quantification:

$$\frac{N_A}{N_B} = \frac{I_E^A \cdot \sigma_E^B}{I_E^B \cdot \sigma_E^A} \tag{1.15}$$

It is important to notice that the collection of the intensity corresponding to a specific ionisation edge is not taken over the whole spectrum, but a spectral window that generally ranges between 20 and 100 eV. Another important fact is that not all of the electrons coming out of the sample are collected, therefore the collection angle in the experimental setup has to be taken into consideration as well. Both this energy window and this collection angle will have an effect on the values both of the measured intensities and the ionisation cross-sections. Both of these will be taken into account when dealing with the actual experimental treatments shown in this manuscript.

ELNES peaks analysis

The other cornerstone of core-loss EELS analysis in this manuscript is the analysis of fine structure peaks, in this case those corresponding to ELNES, which is extensively used in Chapter 4.

The plural scattering giving rise to ELNES features, along with the possibility of not knowing the unoccupied DOS of a certain sample, make this kind of analysis quite challenging. If the composition and structure of a sample is known, it is possible to model the behaviour of ELNES features [69]. However, if that is not the case, the only viable route is fingerprinting the ELNES features of a certain spectrum based on previous data on similar samples.

This previous data, in the form of EEL spectra where we actually know the composition of the sample and how its atoms are arranged, can come from samples from a previous study, from the literature and, nowadays, even from EELS databases [70].

There is an additional technique that can be extremely helpful for this sort of analyses. We have seen in this section that ELNES features are caused by electrons that receive enough energy to escape a core shell but not to be expelled to the vacuum level. This can be achieved not only by means of an electron beam, but with any sort of excitation that transfers the same amount of energy. X-Ray excitations are a good candidate to produce similar states to the ones that cause ELNES features, and X-Ray photoelectron spectroscopy (XPS) can be used to an extent to better understand ELNES features.

In this sense, it is possible to somewhat establish a correlation between features at a certain energy in an XP spectra and ELNES features in a core-loss EEL spectra. Due to the different natures of the two spectroscopy techniques, both spectra do not have to be similar in shape, but when analysing the same sample it is possible to see at least some features in common for both spectra. This has been one of the main keys for the ELNES analysis shown in Chapter 4.

1.4.4.4 Applications

Core-loss EELS gathers a remarkable amount of information not only about the elemental composition of a sample, but also about how these elements are chemically arranged within the sample. some examples of this are the studies performed on oxydation states in transition metal oxides [71] or complex boron nitride samples [72], or the quantification of sp^2 hybridised C atoms in the analyses performed in chapter 4.

In conjunction with STEM, this kind of spectroscopy has allowed for an elemental characterisation down to the atomic level [73]. It has also become more used than EDS, since it is better suited for the detection of light elements [56].

Some unusual applications of this kind of spectroscopy relate to magnetic measurements. Specific areas in the diffraction plane of magnetic materials have a different amount of inelastic interference that is dependent on the spin direction and the location of the detector. By substracting two spectra taken at regions with different spin direction, it is possible to obtain a signal that relates to the spin behaviour of the material [13].

Other types of spectroscopy in the electron microscope

Besides EELS, there are other kinds of spectroscopy that can be used within a TEM, mostly for chemical quantification reasons but also for the analysis of the optic response of a material.

With the exception of EELS, the most known type of spectroscopy within TEM is energy-dispersive X-ray spectroscopy (EDX), which, within the TEM context, relates to the characteristic X-rays emitted by the sample when relaxing after its being ionised by the electron beam.

An additional spectroscopic technique that has gathered more and more interest throughout the years has been **cathodoluminescence**, which analyses the visible light emitted by a photoactive species after it has been excited with an external source, in this case, an electron beam, which in terms of photoluminescence can be thought of as a perfect white light [32].

Both of these spectroscopies need specific instruments to be placed within the TEM, namely spectrometers and, for the case of CL, a specific set of mirrors for a better gathering of the emitted photons. It is also important to notice that both of these techniques can be coupled with STEM (STEM-EDX and STEM-CL, respectively), whcih combines the remarkable spectroscopic properties of these techniques with the very high spatial resolution provided by STEM.

1.5 Intersection of EELS and other microscopy techniques

EELS is a very poweful technique in and of itself, but perhaps some of its most interesting applications come from the intersection between this spectrometry and the imaging techniques an electron microscope can offer. In this section, we focus on the two main intersections between EELS and electron microscopy, which can be seen as complimentary with one another: energy-filtered TEM (EFTEM) and STEM-EELS.

1.5.1 EFTEM

The first of this intersections stems from a principle simple in theory but rather complicated in practice. We have seen the optics of TEM imaging extensively in Section 1.2. We have also discerned the way EEL spectrometres work by focusing electrons with different energies on different points in Section 1.4.1. In theory, by using apertures centered on the points where electrons of a certain energy are focused, we could use only said electrons to form a CTEM image in the same way shown in Section 1.2.3. These are known as energy-filtred TEM images (EFTEM).

There are two main ways to obtain these images experimentally, both with an energy filter. The first one is known as an in-column filter or Omega (Ω) filter. This filter is set between the intermediate and projector lenses (see Figure 1.9) and consists of a set of four magnetic prisms arranged in a shape that reminds of a Ω, hence its name. This filter moves the electron beam off-axis but, thanks to its geometry, it brings it back on axis. By means of selecting a particular region in the filter, it is possible to produce an EFTEM image.[56]

The second kind of energy filter for this purpose, and the one used for the studies presented here is what is known as a post column filter, specifically a Gatan Image Filter (GIF). In essence, this system can be seen as a development for the magnetic prism shown in Figure 1.4.1. An aperture can be set at any given point of the prism focusing plane, selecting only the electrons with a specific energy value which we can name E_1 (and therefore a specific energy loss). This electron beam with energy E_1 can then be treated as any other incident beam and produce an image by means of an electron lense optical system, in a similar way to the one shown in Section 1.2.3.

A simplified scheme of these EFTEM filters working principle, along with a cross-section of a modern GIF, can be seen in Figure 1.19.

This technique is especially useful for the analysis of samples when we know their elemental compositions, since it can provide morphological distributions of each particular element by selecting energy losses close to their ionisation edges, for example. It can also be used to increase contrast when imaging atomically thin samples such as fullerenes or nanotubes. Selecting an energy loss slit around the ZLP filters out most of plural scattering, which in turn enhances the imaging contrast.

1.5.2 Spatially-resolved-EELS

The other side of this intersection between TEM imaging and EELS also stems from principles that we have covered in previous sections, which are the principles of STEM imaging and detection as well as the basic principles of EEL spectroscopy. This intersection consists on simultaneous STEM-EELS data acquisition, a technique first conceived and named ”spectrum image” (SPIM)in 1989 [74] and experimentally proven in 1991 [75]. It offers the combined spatial resolution of STEM with the energy resolution of EELS, making it a unique tool for analyses at the nanoscale. Here we present a brief explanation of this technique, which is of great importance for the understanding of chapters2 and 3.

Working principle

As we have seen in Section 1.2.4, STEM imaging can be performed using a variety of detectors depending on the angle at which the transmitted electrons are scattered (see Figure 1.13). These detectors work independently, and the beam corresponding to the detector for which the scattering angle is either 0 or very close to 0 (bright field detectors) can be considered as an incident beam for EEL spectroscopy. This means that, using the scanning coils, the electron probe can scan a point array in the sample, taking an EEL spectrum in each of the points. Furthermore, since the electron detectors are independent among them, it is possible to gather a value for the HAADF intensity at the same time as the EEL spectrum. This three-dimensional array, with a set of points with a spectra on each point, is what is known as a data cube.

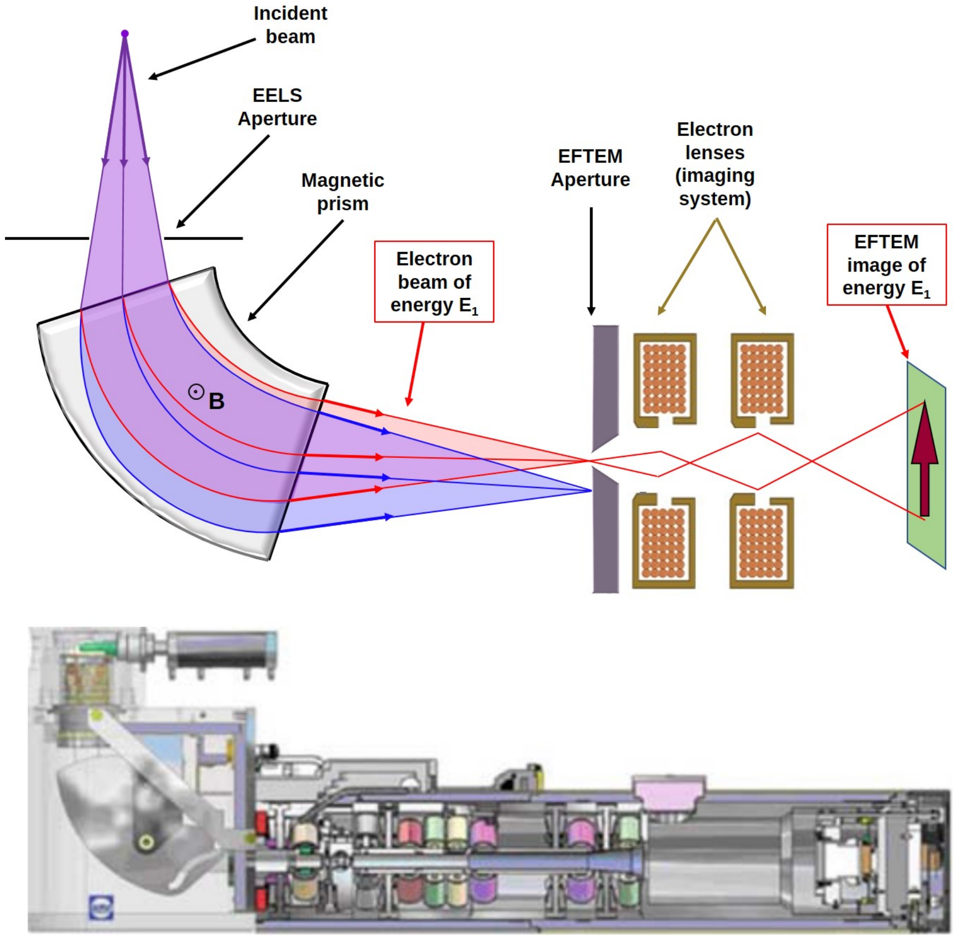

Figure 1.19: *General notions of a post-axis energy filter for EFTEM. Top: simplified scheme of the working principle of a post-axis energy filter and EFTEM image formation. Bottom: Cross section of a Gatan Tridiem imaging filter (GIF) showing the actual experimental complexity of real GIFs. Source: [56]*

The datacube

The data cube is the basis of STEM-EELS analysis and, to some extent, of EFTEM analysis too. We can think of this data cube as a three-dimensional cube in the x and y spatial dimensions, where to each (x,y) point there would be an additional dimension in energy loss with its corresponding EEL spectrum. Other way of thinking about this datacube is a three-dimensional matrix where there exists a certain intensity value for each (x,y,E) point [63].

In this sense, STEM-EELS and EFTEM can both be used for the obtention of a datacube. In STEM-EELS, the collection of an EEL spectrum for each (x,y) point would add an additional ”pixel row” to this data cube, whereas a collection of EFTEM images taken at continuously growing energy losses would add a new ”pixel plane” to this data cube per EFTEM image gathered. A scheme showing this equivalency can be seen in Figure 1.20

In a similar way, a datacube can be interpreted in two different ways, either by showing the spatial distribution of energy loss intensity at a specific energy, or by showing the EELspectra corresponding to a specific area.

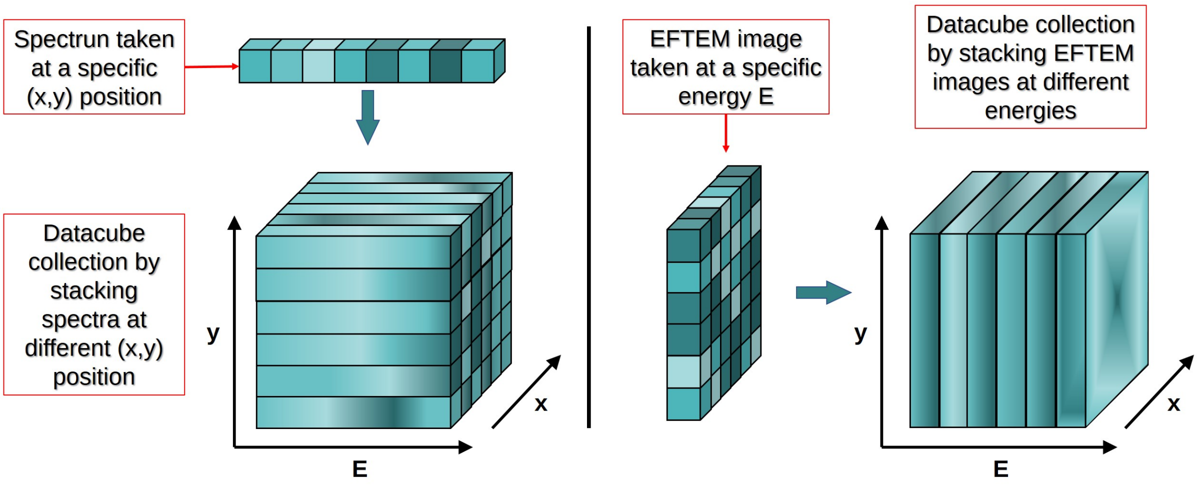

Figure 1.20: *Acquisition of a datacube using STEM-EELS and EFTEM. Left: EEL spectrum at a (x,y) position as a 1-dimensional matrix of energy loss intensity values; and construction of the datacube by stacking of the different spectra taken at different (x,y) positions. Right: EFTEM image at a specific energy loss as a 2-dimensional distribution of energy loss intensity values, and construction of the datacube by stacking EFTEM images taken at different energy loss values. Edited from [63].*

The spectrum profile mode

A spectrum profile can be thought as a data cube with a thickness of 1 pixel in one of its spatial dimensions. This would not be something optimally achieved by EFTEM methods, so it is a mode exclusively used in STEM-EELS.

In spectrum profile mode, the STEM probe takes EEL spectra rastering over a straigt line, leaving a preset distance between measures and thus creating the 1D datacube. A representation of this process can be seen in Figure 1.21. This is the main technique used in chapter 2.

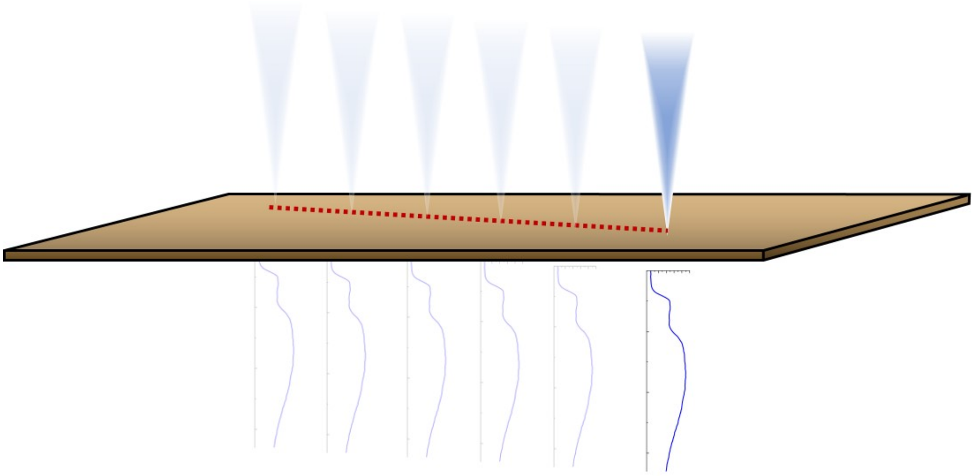

Figure 1.21: *Acquisition process for a STEM-EELS spectrum profile. The electron probe rasters the sample, taking an EEL spectrum and possibly the value for HAADF at each of the measuring points. The example spectra on the Figure are shown after ZLP extraction, showing the characteristic C-K edge.*

The spectrum image mode (SPIM-EELS)

If we think of a spectrum profile as a data cube that is 1 pixel wide, we can think of a spectrum image as a datacube that is, at least, several pixels wide in each of its dimensions. It can be thought of as a collection of EEL spectra along a 2D array of equidistant points. This is the acquisition mode shown in Figure 1.20 for STEM-EELS. This mode is the cornerstone for the studies shown in Chapter 3.

1.5.2.1 Applications of STEM-EELS

STEM-EELS is, without a doubt, one of the most prolific techniques in TEM microscopy. We have previously seen in sections 1.4.3 and 1.4.4 that EEL studies can be used for a variety of possible applications, from measuring changes in the dielectric function and plasmonic studies in low-loss EELS; to elemental analysis and bond identification in core-loss EELS. STEM-EELS adds the possibility, on the one hand, to obtain a spatial distribution of any of these properties, and, on the other hand, to group and integrate spectra based on their spatial positions, in order to obtain better signal-to-noise ratios.

Applications of STEM-EELS to show the spatial distribution of plasmonic modes are exhaustively delved into in chapter 3. Other possible applications include elemental mapping with high spatial resolution, even getting to atomic resolution [76] as well as mapping different coordination values and different types of bonding for a single element [77].

1.5.2.2 Electron delocalisation

STEM-EELS offers a uniquely accurate technique in many ways for the analysis of thin samples, given its potential high resolution both in terms of energy and in terms of spatial resolution. However, there are some potential issues that come with this technique. Aside from acquisition issues, such as adjusting acquisition times to have a good enough SNR over a whole region, some of the most important issues with regard to this manuscript are those arising from electron delocalisation.

As we have seen in Section 1.2.1.2, inelastic scattering implies spatial delocalisation, which can affect the resolution of this technique as well as that of EFTEM. A common parametre for this sort of resolution when there is an aperture present, which collection angle we will call β, is the Rayleigh diffraction limit which, as shown in equation 1.1, follows the expression $\Delta x = 0.6\lambda/\beta$.

However, for the case of inelastic scattering, β is not a characteristic angle of the interaction. We have defined a characteristic median angle for a certain electron scattering phenomenon $< \theta >$ as that which contains half of the inelastic scattering. Based on this angle, we can give an estimation of the object width containing 50% of the inelastically scattered electrons (L_{50}), which is a good indicator of the delocalisation induced by said inelastic scattering. Given the angular distribution for the scattering phenomenon that we have specified in section , that is, a Lorentzian angular distribution with a specific cutoff angle θ_c, we know from the bibliography [13] that:

$$< \theta > \approx \sqrt{\theta_E \theta_c} \tag{1.16}$$

Where θ_E is the characteristic angle from the scattering interaction in question. We also now from the bibliography that a good approximation for the cutoff angle is the Bethe-ridge angle, which follows the expression $\theta_R = \sqrt{2\theta_E}$. This means that, taking only into account the scattering interactions, the estimation for the object width L_{50} would follow the following expression:

$$L_{50} \approx \frac{0.6\lambda}{< \theta >} \approx \frac{0.5\lambda}{\theta_E^{3/4}} \tag{1.17}$$

And if we were to take into account the effects of a given aperture, the expression would be calculated the same way as any standard error:

$$L_{50} \approx \sqrt{\left(\frac{0.5\lambda}{\theta_E^{3/4}}\right)^2 + \left(\frac{0.6\lambda}{< \theta >}\right)^2} \tag{1.18}$$

As it can be seen, given the fact that $\theta_E$is smaller the lower the energy, and that λ is higher the lower the energy, it seems evident that in enrgies close to that of the ZLP, the effect of this delocalisation effects will be especially noticeable. This is one of the main discussions given in chapter 2, where we have been working at energies close to 0 eV. For the energies in this study (1-2 eV), the literature sets L_{50} in a few nanometres [13].

1.6 Equipment used in these works

Here we present the main equipment used for the experiments shown in this manuscript, that is, the microscopes used and the transfer setup employed for the fabrication of the HOPG reference samples in Chapter 4.

1.6.1 Image-corrected FEI Titan3 60-300

The instrument used for the TEM and TEM-EELS presented in this manuscript has been a FEI Titan 3 60-300. This instrument is devoted to sub-angstrom high-resolution TEM imaging (HRTEM), atomic resolution low-voltage HRTEM and aberration corrected field-free Lorentz microscopy and off-axis electron holography. It works at acceleration voltages between 60 and 300 kV, although our experiments have been carried out at 80 kV to have a good resolution-damage trade-off. The microscope is fitted with a standard Field Emission Gun (FEG) emitter and a Cs-objective corrector allowing a maximum point resolution of 0.08 nm in TEM mode. For TEM image acquisition, it features a 2Kx2K CCD camera. This TEM is also equipped with a Lorentz lens, and a motorized electrostatic biprism, allowing Lorentz and electron holography experiments to be carried in magnetic field free conditions. The spherical aberration of the Lorentz lens can be compensated with the Cs corrector to reach a spatial resolution of 1 nm in Lorentz mode. In addition, this microscope can also be used for un-corrected STEM imaging, and is fitted with a GIF Tridiem for EELS and EFTEM experiments

1.6.2 Probe-Corrected FEI Titan Low Base 60-300

All STEM-EELS studies performed for this manuscript have been performed in this microscope. This instrument is dedicated to atomic resolution STEM imaging, atomic resolution EELS spectroscopy and low-loss EELS spectroscopy and off-axis electron holography. For these purposes, this instrument can be operated at acceleration voltages from 60 and 300 kV (although, again, we have kept the acceleration voltage at 80 kV for our experiments). It is fitted with a high-brightness Schottky Field Emission Gun (X-FEG) emitter, a Wien-filter monochromator, and a Cs-probe corrector allowing a ultimate spatial resolution of 0.08 nm in STEM mode. For analytical studies, it is equipped with Gatan Energy Filter (GIF) Tridiem 866 ERS (which combined with the monochromator provides a maximum energy resolution of 110 meV), and an EDS detector. This TEM also features a dedicated Lorentz lens and an electrostatic biprism which, coupled with a 2Kx2K CCD camera for TEM imaging. It is also equipped with a tomography set-up to perform 3D analysis.

1.6.3 Transfer Setup

A custom-built transfer setup for 2D materials has been built following the setup presented by Castellanos-Gomez *et al* in [78], where they offered a very detailed explanation on how to build this equipment. In this setup, a micromanipulator is used to be able to stamp comercial elastomeric films with mechanically exfoliated 2D materials onto diverse substrates, including TEM grids. It is possible to see the manipulation of the stamps and the stamping region in real time by means of a digital camera and a lens tube, which offers a precision in the stamping process down to micrometres. An image of our transfer setup can be seen in Figure 1.22

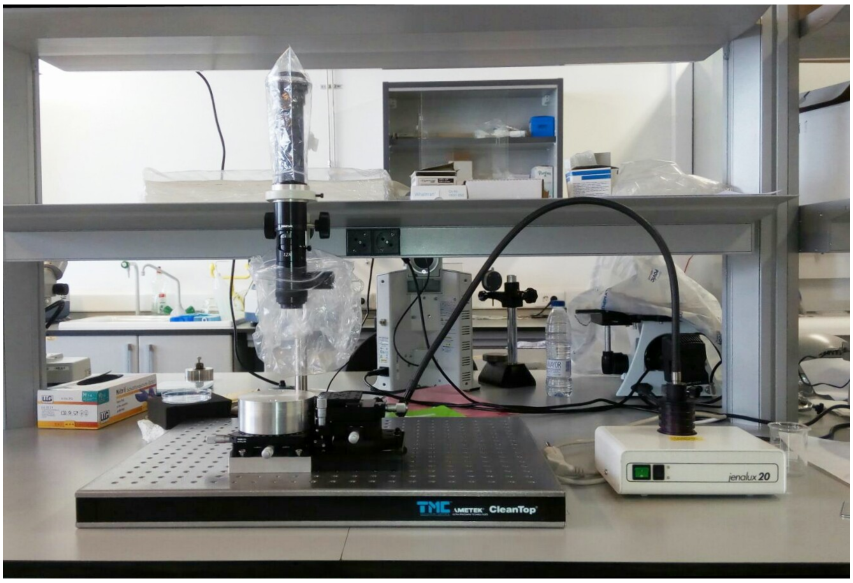

Figure 1.22: *Transfer setup used for the experiments in this manuscript.*

1.7 Advanced 0D, 1D and 2D materials: from graphene sheets to lego bricks

The second main axis for this manuscript, and directly related to that of electron microscopy, is that all the studies presented in this manuscript have nanomaterials as their field of study.

More specifically, this manuscript verses on two different kind of materials: atomically thin 2D nanomaterials (transition metal dichalcogenides, graphene oxide, reduced graphene oxide and graphene) and plasmonic 1D materials (high aspect-ratio gold nanostructures, to be precise). There is, thus, a need for some context with respect to these materials, namely a bit of historical context and a word on their properties and its modification, which will help understand the role this manuscript plays on its current context.

1.7.1 A brief history of atomically thin nanomaterials

In this section of the manuscript, we would like to provide a historical context for the materials that are at the very core of the studies presented here, as well as a brief description of said materials. In this context, the history of atomically thin nanomaterials is bound to the history of carbon-based nanomaterials.

Carbon is a fairly abundant element in our planet. It makes up a sizable amount of our own composition, and carbon-based materials have been a pillar for the development our societies since their very beginning and up to our very days.

However, in the past decades and with the rising of nanomaterials as a new field of study, carbon has not only been a part of this feat: it has become one of its main pillars.

The earliest research on nanocarbons, to the best of our knowledge, dates back to the structure of carbon formed during the thermal decomposition of carbon monoxide on a Fe contact, almost seventy years ago[79], finding some sort of elongated nanostructures with a diametre under 200 nm

However, it is sensible to consider that the study of carbon and carbon-related nanomaterials as a field started in 1960 in the MIT with the research by M. S. Dresselhauss [80]. This research was focused mainly on accurately determining electronic and structural properties of graphite for the most part of the 1960s.

In the 1970s, intercalation started to be used as a way to separate individual ”graphite monolayers”, or a specific number of graphite layers in general, and modify them [81]. This could be considered as the first cases of tuning for carbon nanomaterials, if we consider the separated graphitic monolayers as independent at least to some extent.

By the 1980s, thanks to the myriad of advances in surface sciences, smaller samples could start to be studied. By this time it was possible to study carbon atom clusters and not only that, but knowing the amount of carbon atoms in them. In 1984, a study by Rohlfing, Cox and Kaldor achieved the fabrication of molecularly heavy carbon clusters by pulsed laser vaporisation of a laser target combined with a pulsed helium expansion source [82]. A year later, a very similar yet completely independent study performed by Smalley, Kroto and Curl would yield similar results, but their interpretation would eventually give rise to the discovery of the very first atomically thin carbon nanostructure: the fullerene.

1.7.1.1 The 0D discovery: Fullerenes

The atomic clusters in the aforementioned studies were analysed by time-of-flight mass spectroscopy. Since the original samples were composed exclusively of carbon, these time-of flight mass distributions could be reinterpreted as a cluster size distributions. These resulting atomic size distributions for both studies can be seen in Figure 1.23.

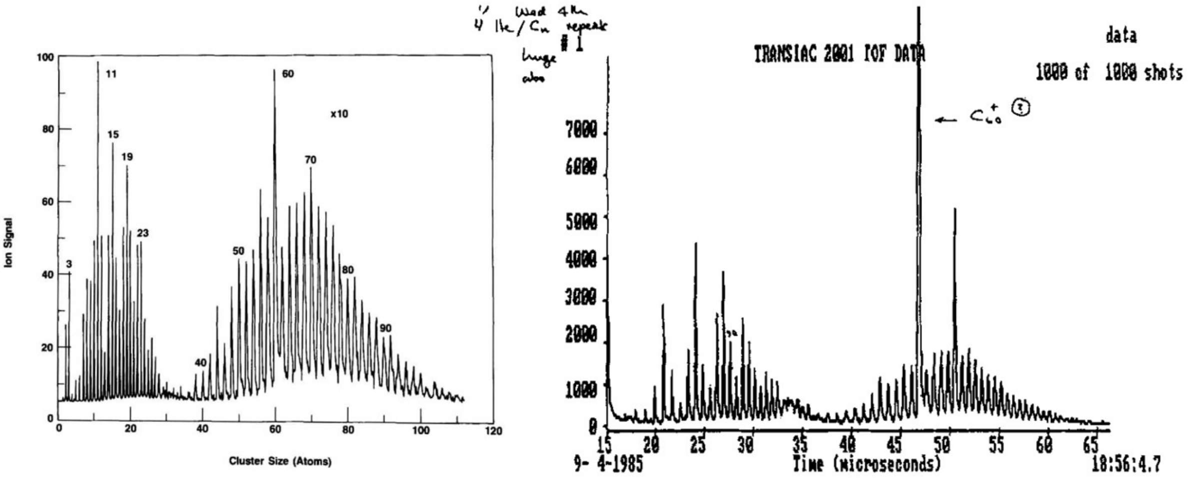

Figure 1.23: *Original TOF-MS of carbon clusters from the study by Rohlfing, Cox and Kaldor [82](left); and from the study by Kroto, Smalley and Curl [83] (right). Both studies show an exceptionally high peak for C clusters having 60 atoms*

Besides other interesting conclusions, the most important one concerning this subject was the unusually high intensities of the peak corresponding to 70 atom clusters and, especially, to 60 atom clusters. The group of Rohlfing *et al* did not comment this anomaly in any way, but Kroto, Smalley, Curl and co-workers theorised that this unusually stable 60 atom cluster corresponded to a truncated carbon icosaedral cage. This geometry would contain 20 hexagons and 12 pentagons in a similar way to a soccer ball. This way, all carbons were sp^2 hybridised (were bound to other 3 carbons) with no dangling bonds. This discovery would eventually grant Kroto, Smalley and Curl the Nobel Prize in Chemistry in 1996.

In time, a big enough amount of this molecule was prepared in order to perform a full characterisation, confirming this structure, shown in Figure 1.24 This amount of fullerenes were prepared by arcing two graphite electrodes in a heliun atmosphere which produced soot containing the molecule [84]. This device would play a role in the continuity of the history of carbon materials as well.

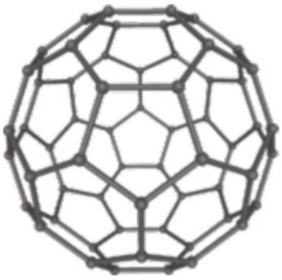

Figure 1.24: *Schematic representation of a fullerene. Source: [85].*

As for C_{70}, it was considered an enlarged, although stable, version of C_{60}. This would actually play a role in carbon materials in the years to come.

1.7.1.2 1D: Carbon nanotubes

In a conference organised by the US Department of Defense in 1990 to discuss fullerenes and carbon fibers, a hypothesis was made that, if $C_{70}$was an enlarged version of C_{60}, it could be possible for the process to keep on going, eventually forming a single wall carbon nanotube. With this in mind, in 1991 Ijima published a study on the structure of "Helical microtubules of graphilic carbon"[86], which are now known as multi-walled carbon nanotubes or MWNTs. These were being produced at the same reactor where a big quantity of fullerenes was first obtained. The structure of these nanotubes corresponds to a single layer of graphite (known today as graphene) rolled up in a seamless way. The structure can be seen in Figure 1.25. It is important to acknowledge that, in retrospective, it is most probable that other groups had found either single or multi-walled carbon nanotubes before Ijima. However, he was the first one to propose a molecular structure for these materials.

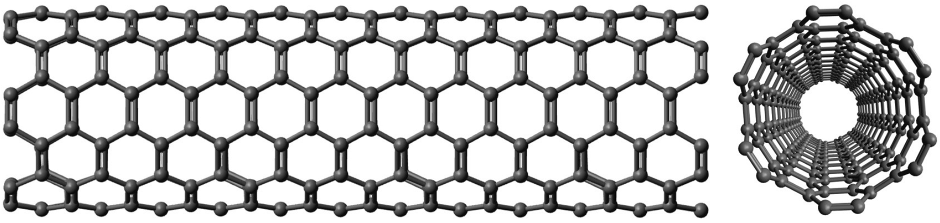

Figure 1.25: *Schematic representation of a single-walled carbon nanotube.*

The year after, a very important study was published by Fujita and Saito that did not only clarify that the preparation of SWCNT was experimentally possible (which would be confirmed a year later, in 1993, by two independent groups), but most importantly delved into the electronic structure of carbon nanotubes. In this publication they showed that nanotubes would be either semiconducting or metallic depending on the orientation of their hexagons with respect to the central axis of the nanotube. These properties are delved into in Section 1.7.2 and are the basis of an important part of their applications. During the 1990s and 2000s, and even to this day, research on CNTs was increased and improved, which increased the interest in the research world on the possible behaviour of carbon monolayers, which would in turn result in the discovery of a new kind of material: graphene.

1.7.1.3 2D: graphene, GO and TMDs

Along with the discovery of fullerenes and nanotubes, the third turning point for nanomaterials was the discovery of graphene in 2004 by Geim and Novoselov [87] and the remarkable properties it showed, which will be explained in Section 1.7.2 and chapter 4. Motivated by previous work on SWNT [88, 89] They achieved this by mechanical exfoliation of highly oriented pyrolitic graphite using a piece of scotch tape.

The aforementioned myriad of properties and potential applications attracted an incredible amount of interest to graphene research in particular and 2D materials in general, such as graphene oxide, transition metal dichalcogenides or boron nitride.

This field of study has been coined "beyond graphene" research and it is a very active research subject nowadays [80]. A good amount of the research shown in this manuscript could be considered as part of this particular field. Numerous new 2D materials have been synthesised to date. A brief summary of these can be found in the literature [90, 91]

1.7.1.4 Other carbon nanomaterials

We have covered the history of the main three axes of carbon nanomaterial research, but in time this field has evolved beyond these three types of material. Here we offer a very brief review on other kinds of carbon nanomaterials

The sp^3 nanocarbon: nanodiamonds

Even though they are not a part of the same family as the rest of the materials in this section (in the sense that these cannot be atomically thin), it would be incomplete without mentioning the existence of carbon nanodiamonds, that is, nanoparticles consisting of sp^3 hybridised carbon, with their edges passivated somehow in order not to have any dangling bonds [92]. This material was first discovered in 1963 when analysing carbon from explosion products [93], although they would not be really known worldwide until the 1980s. A scheme of their structure can be seen in Figure 1.26

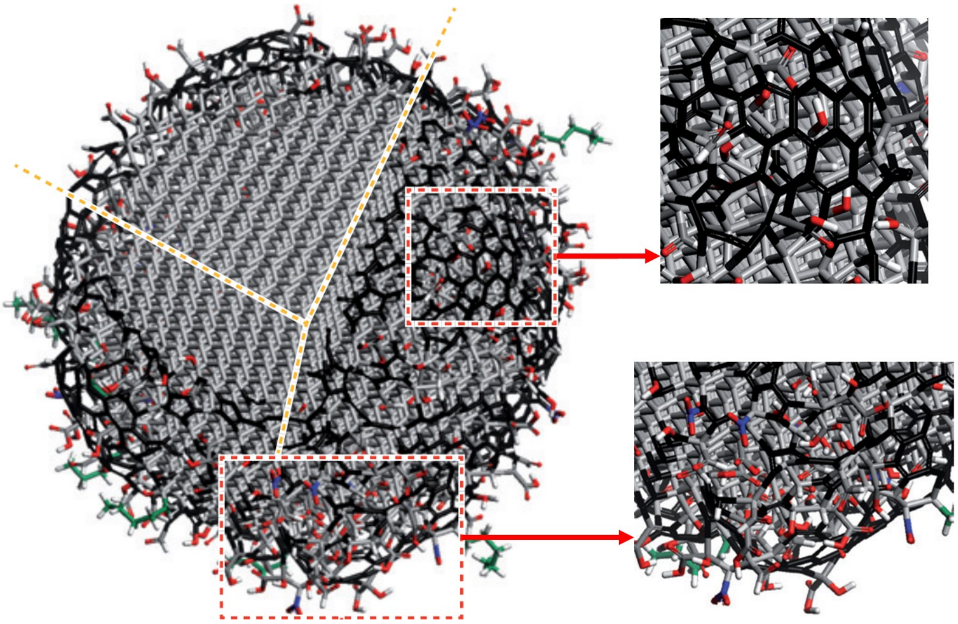

Figure 1.26: *Structure of a nanodiamond particle. Schematic model illustrating the structure of a 5-nm nanodiamond after oxidative purification. The diamond core can be passivated either by converting the sp^3 carbon on the edges onto sp^2 carbon, or by having the diamond core covered by a layer of surface functional groups. A section of the particle has been cut along the amber dashed lines and removed to illustrate the inner diamond structure of the particle. The two insets show close-up views of two regions of the nanodiamond. The sp^2 carbon (shown in black) forms chains and graphitic patches, but the majority of surface atoms are terminated with oxygen-containing groups (oxygen atoms are shown in red, nitrogen in blue). Some hydrocarbon chains (green) and hydrogen terminations (shown in white) can also be seen. Source: [92].*

Besides the ones mentioned in this section, there has been a wide range of carbon nanomaterials that have been synthesised in the few past decades, such as carbon nanoribbons, carbon nanocones or carbon peapods. A comprehensive review of all these different materials can be found in the literature [85].

1.7.2 Brief description of the properties and applications of carbon-related nanomaterials

After this brief piece of history to contextualise the research presented in this manuscript, it is important to understand that said discoveries were not only relevant from a fundamental point of view (obtaining new and interesting materials that further expand our insight on how carbon, as well as other elements, can form different structures). These discoveries were also remarkably important from the point of view of their different properties, the possible modification of said properties, and the myriad of fields these materials have had applications in.

Starting with their electronic properties , carbon nanomaterials cover literally every possible response to electron conduction depending on their structure, from semimetals (graphene) to metals and semiconductors (CNTs) and insulators (nanodiamonds), to give an example of each [85]. No other element can produce such a vast array of electronically different materials on its own.

Graphene shows a really high electron mobility, with an electric behaviour known as semimetal. As we can see in Figure 1.27, the band structure of graphene is what is known as a Dirac cone, where the E(k) dispersion in the electronic band structure follows a linear relation that intersects at the Fermi level (shown as a cone when using a three-dimensional representation). This implies that graphene will behave as a semiconductor with zero band gap, or as it is best known, as a semimental. This greatly increases its electron mobility, which can get up to 100000 cm^2 and could arguably still be improved, since impurities and corrugations of the graphene surface have a significant effect on said mobility [94].

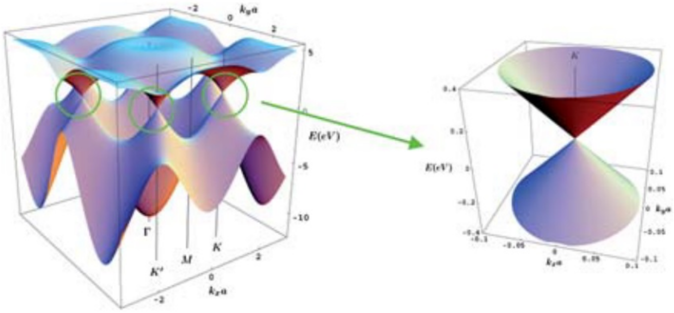

Figure 1.27: *3D representation of graphene band structure. Inset: region near the Fermi level. Source: [90].*

The difference in electronic behaviour of CNTs depending on their particular helicity can be explained using the E(k) dispersion of graphene. We could understand the process of a seamless rolling of a graphene sheet anbd the electron confinement it represents as an intersection of the E(k) dispersion with vertical planes, which would give cutting lines from which we can deduce its density of states. As it can be seen in Figure shown in 1.28, depending on the orientation of the CNT this cutting line can either go through the K-point (Dirac point) or the electronic band structure, resulting in a metallic CNT; or it can go through a section where a gap is created around the Fermi level, resulting in a semiconducting CNT. The typical DOS of this kind of systems show very well defined peaks coming from the discontinuity of the electronic band structure. These features are known as Van hove peaks, which will be one of the subjects treated in chapter 2. The seizing of this different character of CNTs as well as the ability to separate both has been an important point for nanotube research in the past decades.

As for mechanical properties, carbon nanomaterials have offered some of the most mechani-

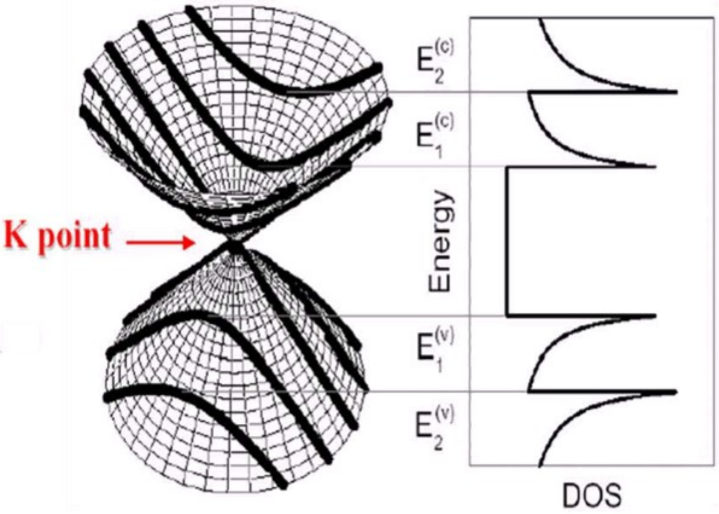

Figure 1.28: *Cutting lines showing the confinement of the electronic density of states for a 1-D system, such as carbon nanotubes. Here the 1-D singularities in the electronic density of states are also shown. Source: [80].*

cally resistant materials ever made, with Young's modulus on the 1 TPa order for both MWCNT and SWCNT [95]. Graphene presents an exceptionally high Young modulus on the order of 1 TPa as well[96]. An important fact is that both materials have such high mechanical resistance while keeping a high elasticity. Both properties stem from the strong but flexible covalent sp^2 bonding among the C atoms in these materials.

Most of these nanocarbon materials also offer exceptional thermal conductivity, a characteristic in comon with other nanocarbons [97].

The relevance of atomically thin nanomaterials

As we have mentioned, In the past couple of decades, research in material science has had a peaking interest in carbon and carbon-related nanomaterials, due mainly to its variety of possible applications, which stems both from the unique properties of these materials as well as the possibility of tuning said properties. As an example of this growing interest, we provide in Figure 1.29 the yearly amount of publications found for the terms "fullerene", "nanotube", "graphene" and "graphene oxide", showing that the interest in these materials is not only remarkable, but still growing to this very day.

However, in order to understand these materials, as well as the possible properties and applications that can be obtained from their tuning, it is critical to offer an in-depth study of said tuning processes.

1.7.3 Plasmonic nanomaterials

The counterpart to this study, that is, the only part of it that distances itself from carbon and carbon-related nanomaterials, is the one related to plasmonic nanostructures. Chapter 3 offers a very comprehensible review on the history, structure, composition and working principle of this kind of materials. Plasmonics are also used to an extent in the analyses performed in Chapter 4, and their relationship to EEL spectroscopy has been delved into in Section 1.4.3.

Explained in a very brief way, nanomaterials with a dielectric constant that shows a large and negative real component and a small and positive imaginary component (usually metals) are

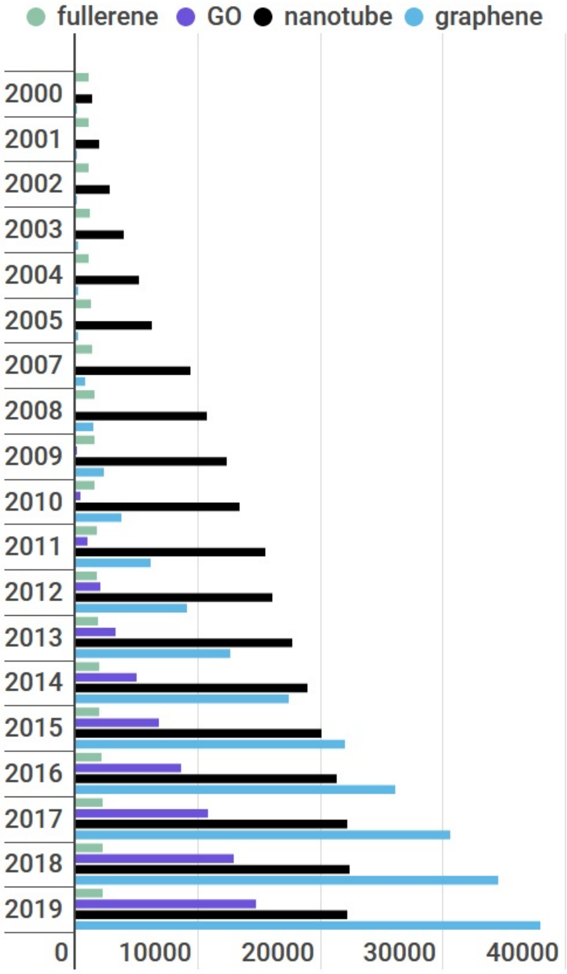

Figure 1.29: *Number of publications per year since the year 2000 in the areas of fullerenes, nanotubes, graphene and graphene oxide. The data were gathered from the Web of Knowledge (Science Citation Index). The exact search terms were "fullerene", "nanotube", "graphene" and "graphene oxide". This graph is inspired by the one shown in [80], offering an up-to-date version that takes more into account the nature of this manuscript.*

prone to take part into plasmonic phenomena. These phenomena have to do with the collective oscillations of the otherwise free conduction electrons in the sample when being excited by an external electromagnetic source, whether it be a light beam or an electron beam. As we have seen in Section 1.5.2, the combination of STEM and EEL spectroscopy allows for spectroscopic studies with a remarkable spatial resolution, being the perfect tool for this kind of studies.

1.7.4 The importance of property tuning

We have mentioned in this section that one of the most interesting aspects of this sort of nanomaterials is their ample possibilities for tunability. Through means such as doping, chemical functionalisation, thermal treatments, straining, laser ablation, electron and ion bean irradiation, synthesis of heterostructures and composite materials, alloying, and, as we have seen, intercalation; it is possible to change properties in carbon and carbon-related nanomaterials. These changes range from its chemical reactivity to its optoelectronical properties or their mechanical ones. An extensive review on property tuning is given in Chapter 2 for the case of transition metal dichalcogenides, but the same can be said about any of the carbon-related nanomaterials mentioned in this section.

As for plasmonic materials, their resonances and therefore their optoelectronic properties are not only correlated with their composition, but also their actual geometry and morphology. In other words, morphology-changing processes like laser manipulation are a form of property tuning for these kind of structures.

Both the unique properties of all of these nanomaterials and the possibility to tune said properties have been the reason for these materials to have applications in fields as far appart as medicine, photovoltaics, electronic devices, mechanic devices or sensors.

This manuscript is, to a big extent, centered on the study of this sort of property tuning in materials. On the one hand, in Chapter 2, the optoelectronic properties of several different kinds of TMD alloys are studied while changing the alloying degree. Alternatively, in Chapter 4 we do not only look at the effects of thermal reduction on graphene oxide, but on each part of the reduction process and how it affects the sample. Finally, Chapter 3 also has to do with the tuning of properties in nanomaterials, where we change their morphology instead of their composition.

Now that both the main techniques and the main materials for these studies have been properly into context, it is important to explain how these two worlds will merge in the context of this manuscript.

1.8 Structure of this work

The structure of this manuscript is divided in four differentiated sections:

- An introduction to the fundamental concepts of transmission electron microscopy, electron energy loss spectroscopy as well as a brief history of nanomaterials, which is completed by this structure section.
- An experimental section on optoelectronic properties of nanomaterials using the aforementioned techniques.
- A second experimental section on in-situ TEM and EELS studies
- A conclusions section where the main points of the research shown in this manuscript are brought up.

This section tries to briefly get into each one of these sections in order to better understand the structure of this text.

1.8.1 Fundamental concepts: materials and techniques

First and foremost, with this work being almost entirely related to some form of electron microscopy and/or spectroscopy, it is vital to understand the working principle of these techniques. This includes a brief historical introduction, as well as an in-depth explanation on how transmission electron microscopes and EEL spectrometers work, the different kinds of imaging, how aberration correction has set a turning point for electron microscopy, the information we can gather from the different features on EEL spectra, the combination of STEM and EELS, and, last but not least, a brief description of our own equipment and how it fits within the theoretical background provided. We also offer a brief insight into the world of nanomaterials and, more specifically, carbon nanomaterials, since they are the starting point from where most of the research in this manuscript has emerged from.

1.8.2 Optoelectronic properties using STEM-EELS

Once we have seen the different possible features of a Low loss EEL spectrum, as well as how STEM and EELS can be performed as a combined technique to obtain all the information from EEL spectra with the spatial resolution of a STEM, we can now see how we can use this knowledge for the analysis of different nanomaterials.

Band gap and Van Hove measurements of TMD alloys

The first material to be analysed using these techniques are transition metal dichalcogenide alloys, specifically $Mo_xW_{1-x}S_2$ alloys. In this section, we delve into what transition metal dichalcogenides, and how alloying has allowed, among others, for a finer tuning of the optoelectronic properties of these materials. By means of STEM-EELS measurements using the spectrum-line configuration, which is explained in detail in Section 1.5.2, it has been possible to provide direct measurements of the band gap of these alloys, as well as other optoelectronic properties such as exciton features and Van Hove features. This study is shown in detail in chapter 2.

Plasmonic measurements of high aspect-ration Au nanostructures

The second study related to optoelectronic properties of nanomaterials and STEM-EELS relates to the plasmonic properties of novel high aspect-ratio gold nanostructures. This section offers insight on plasmonics and its applications, as well as how STEM-EELS can be a technique that offers remarkable insight on the study of these properties. After having challenging experimental conditions, this section also tackles the use of multivariate analysis, among other data analysis methods, in order to try to gather as much information as possible from the raw data. This can be seen in chapter 3.

1.8.3 In-situ TEM and EELS studies

The second main experimental focus of this work is the use of TEM and TEM-EELS techniques for the purpose of in-situ experiments. In this sense, the principal subject of this section is the thermal studies on the reduction of graphene oxide, althouh an added annex is provided on an ongoing work related to in-situ studies on chemically modified carbon peapods.

In-situ TEM-EELS studies on the thermal reduction of GO

The main section concerning in-situ studies using TEM-EELS focuses on the reduction of graphene oxide, or GO. After properly introducing this material, its possible models, its properties and its reduction mechanisms, a thorough thermal study has been performed where we have been able to measure properties from the oxydation degree to the sp^2 bond ratio in the samples along a series of temperatures. This kind of study allows for an in-depth knowledge of the sample not only before and after complete reduction, but on every step of the reduction process, which also means a more intricate knowledge on the reduction mechanism itself. This can be seen in chapter **??**.

1.8.4 Conclusions

The final section of this manuscript focuses on the general conclusions drawn from the studies shown in it. From sample preparation to data analysis optimisation, this section covers how these studies fit on the current scientific panorama surrounding these materials and techniques.

2

Optoelectronic properties and Van Hove singularities in few-layer $Mo_xW_{1-x}S_2$ alloys: a STEM-EELS study

Transition metal dichalcogenides have been on the spotlight of nanomaterial research for decades. Futhermore, as we have mentioned in Section 1.7, one of the main appeals of the research in this 2D material, as well as many other atomically thin nanomaterials, is the possibility to tune their properties using a diverse variety of methods.

In this chapter, we will delve into the history of TMDs, the differend kinds of TMD materials and their properties, as well as the different methods that have been used for tuning said properties. The study presented here focuses on a specific tuning method, alloying, which is literally a millenary technique that can nowadays be applied to nanomaterials.

The study presented in this chapter focuses on the optoelectronic properties of atomically thin TMD alloys, specifically MoS_2-WS_2 alloys, which are a kind of material that has been somewhat recently synthesised. This is the reason why a full study of its properties is needed, and, as we have seen in Section 1.5.2, STEM-EELS allows for the study of these properties at the nanoscale.

An additional aspect of alloy study, that is explained in this chapter but has been done previously to this study, has been the identification of the alloying degrees of different $Mo_xW_{1-x}S_2$ alloys using STEM imaging. In atomically thin flakes of these alloys, using the spectrum profile explained in Section 1.5.2, and several data analysis techniques that we will explain in detail in this chapter, it has been possible to study the evolution of several optoelectronic properties in alloy regions showing a different thickness or a different alloying degree.

The properties studied in this chapter cover the dielectric function of the different samples and several aspects dealing with the electronic density of states of said materials. Specifically, we will be performing direct measurements of the bandgap, as well as estimations of features related to Van Hove singularities in the density of states of the alloys, and features related to electron-hole pairs that appear in the samples when excited by a TEM beam.

However, in order to fully understand the research performed in this study, we shall start by understanding the history of this family of materials, transition metal dichalcogenides.

2.1 Introduction to transition metal dichalcogenides (TMDs) and the tuning of their optoelectronic properties

In the introduction of this work, specifically in Section 1.7, the importance of 2D materials for modern research has been highlighted. Among them, as we will see, one of the most interesting ones are transition metal dichalcogenides (or TMDs). This section focuses on these materials: what they are, their history, their properties and the way they can be tuned.

2.1.1 What are transition metal dichalcogenides?

Transition metal dichalcogenides are layered materials with a stochiometry MX_2, with X being a chalcogen(X=S, Se, Te) and M being a transition metal.

There is no date of synthesis of the first TMD due to the fact that some of these materials can exist in nature as minerals. However, the atomic structure of a TMD was first determined by Dickinson and Pauling in 1923 using X-Ray diffraction (XRD). This TMD was molybdenum disulfide (MoS_2), also known as the mineral molybdenite, and the structure discerned by Dickinson and Pauling was not far from one of the structures known for MoS_2 nowadays. This structure can be seen in Figure 2.1

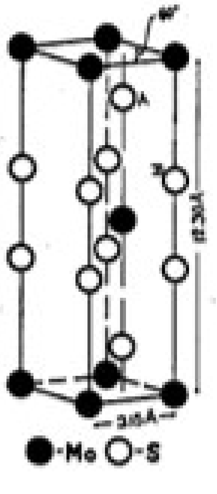

Figure 2.1: *Arrangement of atoms in molybdenite, MoS_2. Source: [98].*

Transition Metal Dichalcogenides became a growing interest for the scientific community, and a vast diversity of TMDs were discovered over the next decades. A study by Wilson and Yoffe in 1969 about TMDs reported over 60 types of TMDs, of which around two thirds were known to have layered structures [99]. This study also showed a meticulous clasification of the different TMDs found to that date, including their composition, crystallographic structure or structures and some electrical properties.

Unlike graphene, TMDs, and more specifically MoS_2, was fabricated as a 2D material decades before graphene had even seen the light; with the first reports of the scotch tape mechanical cleavage method being used to try and produce ultrathin MoS_2 films dating all the way back to 1963 in the study by Frindt and Yoffe. These ultrathn films were reported to be less than 10 nm in thickness. It was the same Frindt, along with Joensen and Morrison, who first reported a solution of single layers of MoS_2, produced by liquid exfoliation of MoS_2 previously intercalated with lithium atoms [100]; a phenomenon that will be delved into in Section 2.1.3

The 1990s and 2000s were, within the realm of nanomaterials, the golden years of nanotubes and fullerenes. It makes complete sense that it was these years that saw the first synthesis of TMDs fullerenes and nanotubes, specifically WS_2, in the study by Tenne *et al* from 1992 [101]. This was followed by similar synthesis on other TMDs such as MoS_2 [102].

TMDs gathered a vast amount of research interest again during the discovery of graphene and the beginning of the "2D revolution", that is, after 2004. There are two crucial moments for this resurge research interest on 2D TMDs.

The first moment, circa 2010, was the fabrication of the first monolayer MoS_2 transistor using a hafnium oxide gate. This device had an on/of current ratio of 10^8, and it opened the door to a new development in 2D nanodevices [103]. The second moment was the discovery of a very strong photoluminescence behaviour in MoS_2 monolayers. This would mean that MoS_2, considered an indirect bandgap material, would undergo an indirect to direct bandgap transition when thinning it down to a single atomic layer [104, 105]. A similar property would be discovered for WS_2 three years later [106]. This study also reported a much higher luminescence at the edges of WS_2 monolayers, related to the the structure, the chemical composition and probably some excitonic effects that have been presented in Section 1.4.3 and will be explained in detail in this chapter.

An additional advantage of this kind of materials was that, in time, 2D nanosheets were able to be fabricated with a really high yield and large scale, which make TMDs an ideal candidate for industrial scale applications[107].

For the purpose of this chapter, and for their being arguably the most worked-on TMDs to date, we will focus on two specific cases among the different TMDs: molybdenum disulfide (MoS_2) and tungsten disulfide (WS_2).

2.1.2 MoS_2 and WS_2

Although there is a vast number of layered TMDs discovered to date [108, 109], as far as we know there are only two layered TMDs that exist in nature: MoS_2 and WS_2, in the form of molybdenite and tungstenite, respectively. This has kickstarted their research with respect to others, since synthesis was important but not essential to the development of further studies on these materials. For example, the first transistors with high mobility made of monolayer MoS_2 were actually fabricated using material gathered from molybdenite [103] using the scotch-tape micromechanical cleavage method commonly known for being used for the fabrication of few-layer graphene.

Since this study focuses on alloys between MoS_2 and WS_2, it makes sense to delve deeper into the properties of these two materials

2.1.2.1 Atomic structure and phases

Although TMDs exist in different structures, MoS_2 and WS_2 have the two most common structural phases in TMDs: trigonal prismatic (2H) and octahedral (1T) coordination of the transition metal atoms, the first one being the most stable one. These two structures can be seen in Figure 2.2. A third option, a distorted 1T phase, is given as well. Finally, two different stacked superstructures are given, which will be studied in detail in Section 2.1.3

A monolayer of MX_2 consists of a sandwich structure formed by three superposed layers, X-M-X, the 2H structure (1H in the case of monolayers) would represent an A-B-A stacking among these layers (the atoms of the two chalcogen layer are in the same positions in their respective planes) and the 1T would represent an A-B-C stacking.

For the case of TMDs formed by Mo and W with either Se or S (that is, the family of TMDs that is most common), both DFT and experimental studies show the two aforementioned phases.

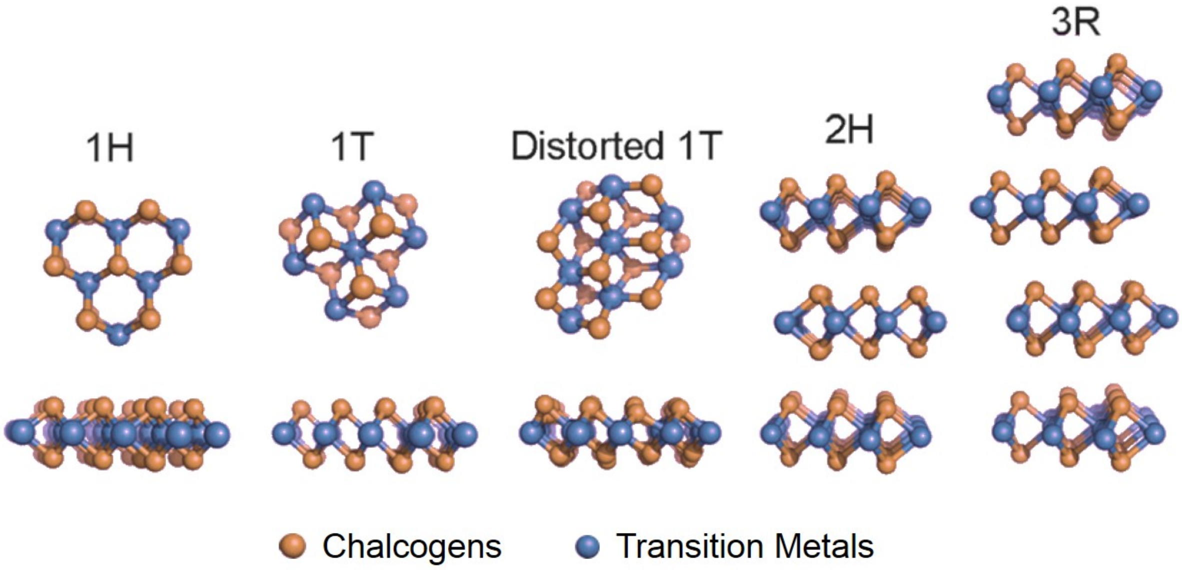

Figure 2.2: *Atomic structure of single layers and simple stacks of TMDs in different phases. From left to right: trigonal prismatic (2H), ideal octahedral (a×a)(1T) and distorted octahedral (2a×a) phases; 2H ABA stacking and 3R ABC stacking. Edited from [110]*

The 2H phases are semiconductors; and the 1T are metals. We will delve deper into these studies in Section 2.1.2.2. This has sparked a lot of interest, research-wise [111, 112, 113].

As it has been mentioned, the most stable structure for these materials is the 2H structure. However, several processes can be used to transition the materials from one phase to the other, something that belongs to a somewhat new discipline for TMDs called phase engineering, which will be studied more thoroughly in Section 2.1.3

2D TMDs are oftentimes thought of as perfect lattices. however, grain boundaries and are not uncommon, and chalcogen vacancies are fairly common as well. This is interesting from an application point of view, since grain boundaries, defects and other structural disorders like terraces between regions of different atomic thickness is vital for the catalysis applications of TMDs. This is due to the fact that both chalcogen vacancies (which generally imply a dangling bond) and grain boundaries (which can imply a certain amount of structural disorder that can increase reactivity) are both used as active sites for these catalytic applications, especially in the case of chalcogen vacancies [114, 115]

2.1.2.2 State of the art

As we will see in Section 2.1.4.1, MoS_2 and WS_2 are currently used in a variety of studies, mostly as a part of some sort of heterostructure or composite, or using new approaches for their property tuning, such as doping or, of course, alloying. These are shown in depth in Section 2.1.3. However, studies are being performed to this very day on the properties of these materials on their own, and the possible applications of these properties.

When it comes to MoS_2 and WS_2 monolayers, a lot of recent studies have focused on the study of its excitons (which we will delve deeper into in Section 2.1.2.3. These studies range from probing this excitonic behaviour by exciting the TMDs with photons above the lowest energy exciton [116] to the studies of excitonic effects under high magnetic fields [117, 118]. Additionally, we have seen the role defects and grain boundaries in 2D TMDs when it comes to its applications, but these structural defects also play a role on their excitonic behaviour[119]. Excitonics have also been a subject of study for large scale batches of TMDs presenting a varied array of thicknesses [120].

As we have seen in Section 2.1.1, photoluminescence is a big research interest when it comes to TMD monolayers like MoS_2 and WS_2. An important notion that will be explained in detail in chapter 3 is that the plasmonic behaviour of a material can enhance the the photoresponse of a material as well as its luminescence. This has been a main reason for the study of surface plasmon-mediated enhancements of these properties [121], which have already yielded some applications in the form of photosensors [122].

Another vast field within TMD applications, which we will see in detail in Section 2.1.4.1 for the case of TMD alloys, is catalysis and specifically hydrogen evolution reaction (HER) applications. In this sense, MoS_2 and WS_2 have both been used on their own for this purpose, in order to study the role of its phase, defects and edge effects in this type of catalysis [123].

In recent years, one of the biggest research interests in terms of properties of 2D materials has been the behaviour of twisted bilayers. When it comes to MoS_2 and WS_2, plenty of new studies have focused on the properties of these twister bilayers, from the vibrational properties of their Moiré patterns [124, 125] to the dependence of their coupling as a function of the twisting angle [126, 127]. This interface coupling has found applications in photodetector sensors as well [128].

In conclusion, despite being two materials that have been long known, the relevance of MoS_2 and WS_2 for research is still quite high, as is the research interest in materials that derive from them.

2.1.2.3 Physical Properties

There is a vast number of interesting physical properties in these materials, from mechanical to thermal and, especially, optoelectronic properties. We will briefly delve into these different kind of properties.

As we have seen in the previous section, this type of TMDs consists of interacting sandwich structures (S-X-S, where X=Mo or W). Generally speaking, the average thickness for a layer is ≈ 6.5Å [129], which makes for a material with a very high mechanical anisotropy. When it comes to the internal bonds in TMDs in general, it is known that the intralayer bonds, regardless of their being among transition metals, among chalcogens or between one and the other, are covalent bonds. As for the bonds between two MX_2 layers, they are generally van der Waals bonds [130]. This is the main reason why this material can be exfoliated, in a similar manner as other 2D materials such as graphene or boron nitride [131, 132, 133].

However, differently from what we will see for carbon materials in chapter 4, where the electronic properties stem from the hybridization of *s* and *p* orbitals, the electronic properties of TMDS depend on the transition metals in question, specifically the filling of their *d* orbitals [110].

We can deduce the oxydation state of the chalcogens is the same one as oxygen, as they are on the same column of the periodic table; that is, -2. Since the material is not charged at equilibrium, this would take the oxidation state of the transition metals to be +4. If we take into account that both Mo and W are in the group VI, with electronic configurations with 6 valence atoms each, we get to the conclusion that these TMDs have a total of 2 d orbital electrons

For both our case studies, the naturally ocurring phase in the materials without any kind of doping nor treatment is the trigonal prismatic one (2H). In other words, both MoS_2 and WS_2 are, in principle, semiconductors. Due to their general structure, explained in Section 2.1.2.1, layered TMDs are extremely anisotropic, both mechanically (which allows for exfoliation) and electrically, with a conductivity perpendicular to the planes that can be up to orders of magnitude higher than its in-plane conductivity [99]. In terms of mechanical properties, MoS_2 and WS_2 offer rather interesting properties, with MoS_2 being a very flexible material, with a Young modulus of 270 GPa for monolayer MoS_2 and 240 for bulk MoS_2 [134]. It is not as high as graphene but it still makes for a very flexible and resistent material. Its fracture strain has been modeled to be between 25 and 33%, and it has been measured at 23% for monolayers [134].

With relation to their thermal properties, both MoS_2 and WS_2 offer good thermal stability [135], but very poor values of thermal conductivity, with a value of 40 W m^{-1} K^{-1} for monolayer MoS_2 and a value of 50 W m^{-1} K^{-1} in the intraplanar direction and 4 W m^{-1} K^{-1} in the interplanar direction for bulk MoS_2. Bulk MoS_2 offers a coefficient for thermal expansion of 1.1 $\cdot 10^{-5}$ K^{-1} in the in-plane direction [134].

Optoelectronic properties

Even though other properties of the material are of importance, this study focuses particularly on the optoelectronic properties of TMDs.

Due to their general structure, explained in Section 2.1.2.1, layered TMDs are extremely anisotropic, both mechanically (which allows for exfoliation) and electrically, with a conductivity perpendicular to the planes that can be up to orders of magnitude higher than its in-plane conductivity [99]. Briefly put, these kind of materials offer a high electrical conductivity [135], with an in-plane carrier mobility of 200 to 500 cm^2 V^{-1} s^{-1} for MoS_2 [136]

As we have seen in Section 2.1.2.1, the electrical properties of both MoS_2 and WS_2 are heavily influenced by their structure, with two main structural phases that are metallic and semiconductor, respectively. However, as we will see in Section 2.1.3, many other factors can have an effect on the electrical properties of these materials; like strain, temperature or thickness. This is why we can see values for the bandgap of semiconducting MoS_2 that range from 1.25 eV [137, 138] to 1.83 eV for MoS_2 [139]; and from 1,35 eV [138] to 2 eV in WS_2 [140]. In general terms, there is consensus that MoS_2 has a lower bandgap than WS_2.

As we have mentioned, thickness plays a part on the electrical properties of both semiconducting MoS_2 and WS_2, especially when it comes down to an atomic thickness. As an example, we can see the calculated band structure for bulk MoS_2 as well as samples of a specific atomic layer thickness in Figure 2.3 [104].

As we can see, bulk MoS_2 is characterized by an indirect bandgap, as are 4-layer and bilayer MoS_2. The direct excitonic transitions still occur at high energies at K point. However, as the atomic thickness goes down to a few layers, the indirect bandgap becomes larger, while the direct excitonic transition barely changes. For monolayer MoS_2 (see plot d in Figure 2.3), this material turns into a direct bandgap semiconductor. This dramatic change of electronic structure in monolayer MoS_2 is related to the increase of photoluminescence for monolayer MoS_2, which has been previously covered in this chapter.

The main phenomena that rules over this electronic band structure and its lowest energy transitions, and therefore the bandgap of the sample, are excitons. The dielectric confinement present in TMDs allows for the formation of highly stable, strongly bound excitons [117, 141].

The spin-orbit interaction in TMDs is much stronger than in other 2D materials like graphene. This interaction comes from the heavier elements in TMDs compared to graphene and from the transition metals *d* orbitals as well. As a consequence, there is a spin splitting at the valence band, which has been seen to be around 0.2 eV for monolayer MoS_2 and 0.4 eV for WS_2 [142, 143]. In turn, this coupling creates a splitting of the valence band into two subbands. This means there are two different types of excitons involving transitions from the upper and lower energy spin states, which we call A and B.

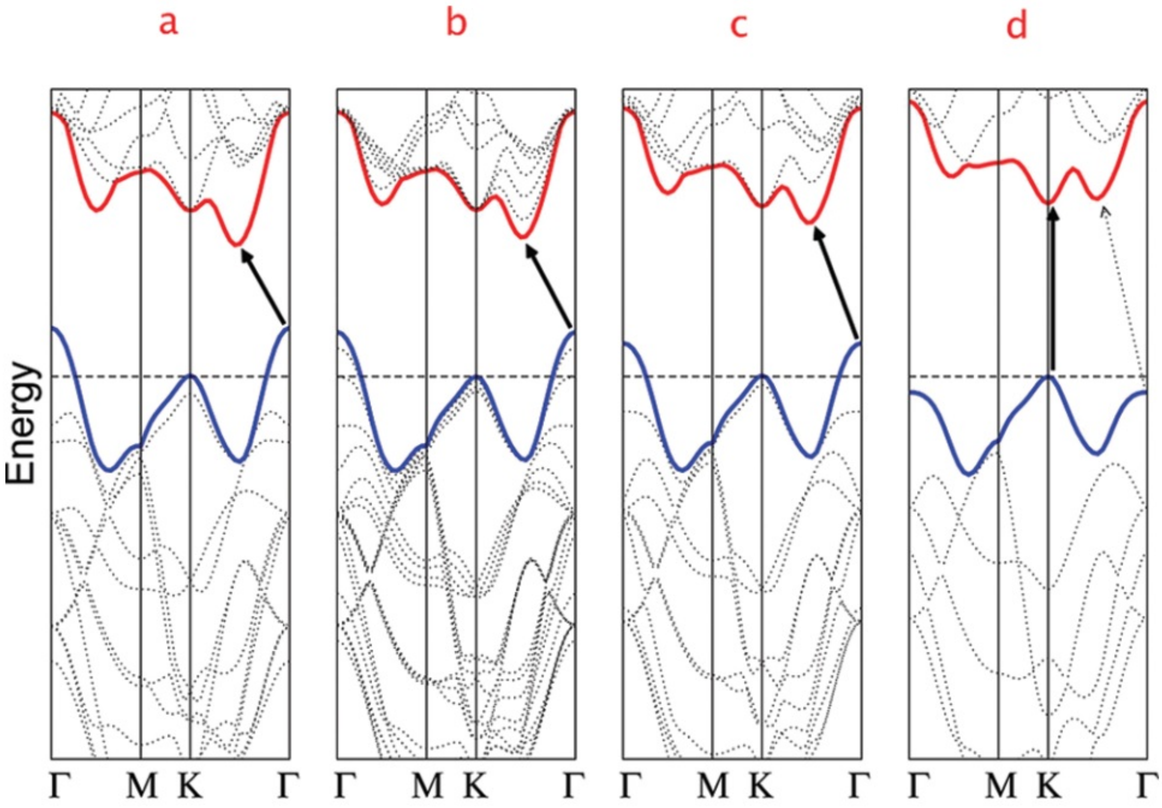

Figure 2.3: *Theoretically calculated band structures of (a) bulk* MoS_2*, (b) 4-layer* MoS_2*, (c) bilayer* MoS_2*, and (d) monolayer* MoS_2*. The solid arrows indicate the lowest energy transitions, responsible for the bandgap. Source: [104]*

For the purpose of this study we will also focus on higher energy excitonic transitions. There is an additional excitonic feature in EELS, which we call C feature, that comes from several of these higher energy excitonic transitions.

An additional property of these materials, which will be delved into a lot deeper in chapter 3, are its plasmonic optoelectronic properties. These do not only have to do with the material itself, but also with the morphology of it and with the technique we have used for these studies. These properties arise from the excitation of the material, in this case with an electron beam, which in turn produces collective excitations of the materials valence electrons. In few-layer flakes of MoS_2, for example, it has been seen in the literature [144] that these excitations take two forms:

- On the one hand, we have the bulk plasmons, which affect the whole sample and are somewhat constant for a given thickness of the sample. It is situated at somewhat high energies (approximately 20 eV).
- On the other hand, we have surface plasmons, which are a lot more spatially localised. Their energy is much lower (under 4 eV) and they are hard to analyse because there are several features in a similar spectral window. According to the literature, these plasmons tend to concentrate at the edges of the different steps of the flakes. However, it has been seen that this effect could not be the only one that is spatially localised in MoS_2; suggesting that maybe excitonic behaviour also showed some edge effects [144].

These are not our main focus for the purpose of this study, but just as a cautionary measure we will avoid any EEL spectra taken at the edges of the alloy flakes, since these are regions with an enhanced plasmonic activity.

An additional property of these materials, and one that is clearly of interest for the purpose of our study, is the existence of discontinuities in their density of states. This kind of discontinuities are called Van Hove singularities, and their effect can be seen in the EEL spectra as peaks around this discontinuity in the DOS, since these discontinuities serve as triggers for transitions at a very specific energy. In the case of our materials, they both exhibit two distinct Van Hove singularities, which in turn produce two separate features in the EEL spectra which we will denominate α and β from now on.

2.1.3 Tuning properties of 2D TMDs at the nanoscale

Additionnally to having really interesting properties by themselves, one of the most attractive features of 2D TMDs, as with most of 2D materials, is the versatility they can have in terms of modifying and tuning said properties. This section is focused on the different ways this property tuning can be performed on 2D TMDs, including the one being the subject of this study, that is, alloying.

Phase engineering

As we have seen in Section 2.1, 2D TMDs have a layered structure where each unit layer is 3 atoms thick. The intralayer bonds are covalent, whereas the bonds among layers are usually van der Waals bonds ,which are the ones allowing for exfoliation. The main different phases in which these TMDs can appear have already been explained in Section 2.1.2.1. The phase of single-layer TMDs depends quite a lot on the electron density of the d orbital of the transition metal. Tuning the filling in said orbital allows for phase engineering in TMDs [110].This phase engineering can be achieved through several different paths, some of them already mentioned in this section.

The actual structural process taking place in the transition from 2H to 1T phase has been seen *in situ* by means of electron microscopy. When heating the sample up to 600 °C and combining this with the energy given by the interaction between the electron beam and the sample, it can also undergo this phase transition [113].

However, the most common path for phase engineering is alkali metal intercalation. For example, lithium intercalation has been used for decades for chemical exfoliation of different TMDs [111]. The effects of Li intercalation on the structural phase of MoS_2 were known to be a change from a 2H to a 1T phase [145, 146, 147]. This is due to tan electron transfer from the reducing agent to the TMD during the intercalation, increasing the electron density of the 4d orbital in the transition metal [110, 148]. This is not the case for all TMDs. For example, the lithiation of TaS_2 induces the opposite phase change, from 1T phase to 2H phase [149].

Generally, single-layer TMDs are not phase stable and end up having a regions of several phases, most commonly 2H and 1T. This creates grain boundaries, which have been previously mentioned in Section 2.1.2.1 and will be delved into later in this section.

Another way of tuning the phase of TMD compounds is the generation of heterostructures, which will be discussed later in this section. For example, the stacking of 1H TMDs can generate an ABA sequence (2H in Figure 2.2) or an ABC sequence (3R in Figure 2.2). This sort of restacking gives the TMDs different properties from their non-stacked equivalents. For example, bilayer MoS_2 and folded MoS_2 show different properties from one another.

As we will see in this section, both hot electrons coming from plasmonic nanostructures and mechanical strain can also provide the necessary energy for this phase transition [150, 151].

Heterostructures

Heterostructures are a commonly used technique for property tuning in different 2D materials, especially graphenic ones [152, 153]. Heterostructures are stackings of two or more 2D materials. In the case of TMDs, these stackings can consist of two layers of the same TMD (in which case we speak of TMD homostructures), different kinds of TMDs or a mixture of TMDs and other 2D materials.

The stacking of two layers of the same TMD is essential for the study of twisted bilayers mentioned in Section 2.1.2.2 [154, 125, 127] for the study of the properties mentioned in said section, especially the coupling of the two layers in question depending on the twisting angle among them.

TMDs have been built as well into heterostructures with a variety of 2D materials, resulting in various applications. Materials like graphene, rGO and black phosphorous enhance the electrical conductivity of TMDs [155, 156, 157], and graphene has even been used to tune spin injection and transport in TMDs [158]. These kind of heterostructures have had a wide array of applications, mostly in sensors [159, 160] but also in transistor-like devices. Hexagonal boron nitride (h-BN) can also be used for this purpose despite its being an insulator. When put together with a TMD in a heterostructure, its high smoothness reduces the TMD carrier mobility barriers caused by sample roughness if we compare it with other sorts of substrate [161]

As we will see in Section 2.1.4.1, one of the main applications of TMD nowadays is in hydrogen evolution reaction catalysis (HER). In this sense, heterostructures combining TMDs and other layered nanomaterials such as a Ni-Co layered double hydroxide (LDH)[162] or $Co(OH)_2$ [163] can increase the performativity of TMDs in this reaction, and it is a prominent field of study nowadays[164].

Another possible use of heterostructures can be the tuning of the TMD phase, a property tuning covered in this section as well. This can be achieved through excitation via hot electrons coming from plasmonic sources [165]. This can be used to obtain a plasmon-induced HER reactio n[150].

An important matter when it comes to 2D materials and property tuning is that the substrate does not just play a part in the efficiency of the property tuning, but can be a part of this tuning itself. In other words, we can think of the combination of the sample and the substrate as a heterostructure itself. Choosing a particular substrate over another can modify chemical or electrical properties at will [166]. This is one of the reasons why the studies on this chapter are performed on free-standing TMD alloys.

It is possible to use several property tuning methods simultaneously to obtain a higher control over the final properties of the material. In this sense, alloying and heterostructures have already been used together for a better tuning over the final optoelectronic properties of the material, like for example building heterostructures out of pure MoS_2 and $MoS_{2(1-x)}Se_{2x}$ with a tunable alloying degree [167].

Composites can be seen as a specific kind of heterostructures. As it has been explained at the beginning of this chapter, TMDs can be currently synthesised with hihg yield and in large batches. This along with their interesting properties, has made them a perfect candidate for their hybridization with other materials in order to fabricate new composites [107].

Functionalisation

In order to modify their properties for the optimisation of their applications, routes towards their chemical functionalisation have been developed. Within this functionalisation, we distinguish two very different areas, namely chemical and non-chemical functionalisation.

Chemical functionalisation refers to the kind that implies a chemical bond formation between the functionality and our TMD. Despite their promising properties, 2D TMDs are rather intert, chemically speaking, which difficults this type of functionalisation. This is due to the chalcogen atoms in the basal planes of charge neutral TMDs being saturated and therefore not highly reactive [168] leaving only the edges of the 2D TMD flakes as reactive sites. However, several routes have been found to chemically functionalise TMDs not only on the edges but also on the basal plane.

One of the first examples of chemical functionalisation of 2D TMDs was the functionalisation of 1T-MoS_2, WS_2 and $MoSe_2$ using diazonium salts and organoiodides. This kind of covalent fucntionalisation seemed to be based on the cration of defects in the TMD nanosheets to which the functionality could attatch to. This study also had to do with the previously explained phase engineering [169]. Other examples include thiol/sulphur functionalization. In fact, a study on this kind of functionalisation (dibenzothiophene adsorption on MoS_2) seems to be the first covalent TMD fucntionalisation of which there was direct evidence [170, 171].

With regard to this last example of TMD chemical functionalisation, it is imporant to highlight a study performed within the context of this PhD, of which the object of study was the functionalisation of MoS_2 with 1,2-dithiolanes with organic electron donor units for energy conversion applications [172]. The TEM microscopy shown in said study was also performed as a part of this doctorate.

On the other hand, **non-chemical functionalisation** relates to the sort of functionalisation where the functionality is attatched to our TMD without the need of a chemical bond, for example by physisorption or Van der Waals forces. Some examples include the functionalisation of WS_2 monolayers with small fullerenes in order to tune their electronic properties and photoactivity [173] which has been calculated using DFT; although this could be considered as a Van der Waals heterostructure.

A more recent approach consists on tuning the surface charge density of MoS_2 nanosheets by exfoliating MoS_2 with various exfoliants, namely pyridinium tribromide, imidazole, and chlorophyll. Non-covalent functionalisation of MoS_2 is caused by said exfoliation processes, and these functionalisations seem to improve the performance of MoS2 in HER reactions, which will be delved into in Section 2.1.4.1

Doping

Following the path of other atomically thin nanomaterials, another common method for tuning the properties of TMDs is doping.

One of the first kinds of doping regarding TMDs deals with the topic of phase engineering, which we will delve into later. In this sense, Li intercalation (which can be considered a kind of doping) has been used extensively for the phase transition of layered TMDs [111].

One of the most known applications of doping for TMDs is the doping of MoS_2 and WS_2 for the improvement of HER catalytic performance[137]. This will be delved into in depth in Section 2.1.4.1.

A very comprehensive review on the different doping methods and their possible applications is shown in [135]. These application range from optoelectronic sensors, biological imaging and sensing applications, photodetectors or data storage memories.

Alloying

Alloying is a technique that has been used for the improvement of bulk materials for millenia. When it comes to the tuning of optoelectronic properties in bulk materials, alloying has been a technique vastly used [174]. These bulk alloys have been studied for decades now, with studies on any possible property of these materials. Regarding optoelectronic properties, there have been studies in these alloys with subjects ranging from from elasto-optic effects, to "Electro-optic constants", and even some specific effects under electrical fields such as the Franz-Keldysh effect, which measures the changes in optical absorption under said fields [175, 176].

The study of these bulk semiconductor alloys was especially focused on "*Tuning the magnitude of the band-gap energy and other material properties so as to optimize and widen the application of semiconductor devices*" [174]. With respect to the case of binary alloys in semiconductors, it is commonly the case that the bandgap of the alloy has a gradual behaviour with the alloying degree, if not always within the energy window marked by the individual bandgaps of its parent compounds. However, this method does provide a way of tuning the bandgap of a material within a certain energy range, wich makes it a perfect candidate for doing the same in 2D materials.

Even though there were some bulk TMD alloys around the same time as $Mo_xW_{1-x}S_2$ [177] (so we cannot know for sure if this was the first bulk alloy to be synthesised), the first time this method was successfully employed to produce a crystal of a $Mo_xW_{1-x}S_2$ alloy was reported on the study by Bonneau *et al*, in 1993 [178]. In this study, they used a common reaction that had already been used for the synthesis of other materials. This technique, a modification of the one introduced by Bouchard in 1968 [179], had two different steps. First, high-quality $(Mo,W)S_2$ solid solutions were synthesised by reacting a mixture of $MoCl_5$ and WCl_6 with Na_2S. This mixed-metal dichalcogenide solutions were reduced in a H_2 atmosphere at 900°C. The 2D approach to these alloys will be later discussed in Section 2.1.4.

Other forms of tuning properties in 2D TMDs

Strain In Section 2.1.2.1, there was reference to a distorted 1T phase in TMD structures. The strain in this distortion changes the metal-metal bond distance in the TMD, hence modifying the electronic structure. For example, in the case of ReS_2, studies show that the distorted layers create an energy gap instead of its being metallic, as expected by its 1T structure[180, 181].

This seems to be applicable as well to other TMDs, where DFT calculations are predicting a small gap opening of a few tenths of meV in 1T MoS_2 due to the distortion of 1T phase[182, 183]. Tensile strain has been predicted to red-shift the bandgap of semiconducting TMDs, and experimentally a decrease has been found in the bandgap, of about 70 meV per percent of applied strain[184]. Strain has also been shown to improve the catalytic activity of TMDs[185]. All in all, this makes strain engineering a very interesting field for this type of materials.

Gating Electric field gating of TMDs, in other words, controlling the amount of charge carriers in a sample by applying an electric field of a certain intensity, is a method for property tuning that has been used vastly with metallic and semiconductor 2D materials, and TMDs are no exception. In fact, due to their electronic properties, an increase in charge carriers in layered TMDs can have rather exceptional effects, most notably superconductivity. This has been a phenomenon known for more than 50 years, but still relevant to this very day [99].

2.1.4 Alloying in 2D TMDs

Even though TMD alloys have existed for decades now, 2D TMD alloys have all been synthesised in the past ten years. New and novel methods like optimised chemical vapor deposition[186], physical vapor deposition [187], chalcogen exchange [186], and colloidal solution synthesis[188][189]

The synthesis of these alloys has also been succesful by combining several techniques. This includes transport vapor deposition and mechanical exfoliation [166], Electrochemical coating and annealing [190]

These techniques have made it possible to create new and novel alloys within this realm. The alloys that have been synthesised to date (that we know of), along with measurements related to the bandgap, are shown in table 2.1:

Alloy	**Reference**	**Gap value estimation (eV)**
$Mo_xW_{1-x}S_2$	[113, 191, 192]	≈ 1.85 - 1.93 eV [113] Excitonic peak ruling bandgap at 1.93 eV for $Mo_{0.33}W_{0.67}S_2$ and Exc. peaks from 1.87 to 2.03 eV depending on alloying degree [191]
$Mo_xW_{1-x}Se_2$	[188]	A exciton ranging from 1.61 eV (x=0) to 1.50 eV (x=1)
$WS_{2x}Se_{2(1-x)}$	[188]	A exciton ranging from 1.61 eV (x=0) to 1.93 eV (x=1)
$MoS_{2x}Se_{2(1-x)}$	[186, 187]	1.86 eV - 1.57 eV [186] Band g in PL ranging from 1.55 (x=0) to 1.86 (x=1) [187]
$Mo_xW_{1-x}Te_2$	[193]	Possiby 0 (semimetal candidate)
$WS_{2x}Se_{2(1-x)}$	[194]	1.62 (x=0) to 1.97 (x=1)
$V_xMo_{1-x}S_2$	[190]	(unpublished)

Table 2.1: *Brief review of different TMD alloys discovered in the last years.*

2.1.4.1 Applications of 2D TMD alloys

The development in the last years of all the abovementioned TMD alloys has given raise to a myriad of possible applications. Here we try to give a brief explanation of the most notable ones.

Electronic properties

Optoelectronic properties The 2D TMD family presents a wide variety of optoelectronic properties, with bandgaps going from 0 to ≈2 eV, with a majority of these bandgaps ranging from the infrared to the near ultraviolet energy range [195]. This, along with the presence of direct and indirect transitions depending on the number of layers, make these materials ideal candidates for applications in optoelectronic devices, both as photodetectors [196] and as LED emitters. In the photodetector field, they have even managed to achieve spectral response from ultraviolet to infrared using a single kind of TMD (in this case, MoS_2) [197]. Alloying allows for tuning of these optoelectronic properties, tailoring them to the application needed .

Hydrogen evolution reaction catalysts In the current energy context, it is an increasing interest to employ hydrogen as a sustainable, green carbon-free energy carrier. For the production of this hydrogen, it is vital to find new catalysts with good performance on electrochemical water reduction, also known as hydrogen evolution reaction (HER). For global scaling purposes, another significant factor is that these catalysts are not fabricated from precious materials.

In this regard, there have been studies on the high performance of TMD-based catalysts for this purpose, with the first report on HER activity for TMDs published in 1977 [198]. However, it would take three decades and a 2D materials revolution to significantly advance HER catalysis using TMDs. in 2005, the free energy of H adsorption on MoS_2 was calculated by DFT, showing that this free energy was close to that of hydrogenase and platinum. The edges of MoS_2 were considered as potential active sites in catalysts for HER reactions [199]. This was experimentally proven two years later using MoS_2 NPs on Au(111), finding a linear correlation between the electroacatalytic activity for hydrogen evolution and the number of edge sites on the MoS_2 catalyst [200]. The results from this study were completely different from the ones of bulk MoS_2 and focused the research effors on TMDs for HER applications on nanostructures where surface phenomena were enhanced.

Four main approaches are being taken with respect to improving the HER activity of these materials [201]:

- The first approach has to do with the electronic properties of TMDs. As we have seen in Section 2.1.2.3, different TMDs have quite different electronic properties, going from being semimetals semiconductors with a bandgap of ≈2eV. Furthermore, as it has been explained in Section 2.1.3, these electronic properties can be tuned using a vast amount of procedures. Given that the electronic properties of the TMDs involved in HER, it makes sense that tuning these electronic properties would be a way of improving the HER activity of these materials.

- A second approach has been the improvement of the catalytic activity of these TMDs. For this purpose, one of the possible routes to go is doping TMDs with Co, which has been used before as a catalysis promoter of MoS_2 in hydrosulfurization reactions. In this regard, different approaches for an even higher HER performance have been studied using co-doped MoS_2 as one of its main elements. These approaches include amorphous Co-do ped MoS_2 nanosheets coated on metallic CoS_2 nanocubes [202], Co-doped MoS_2 annealed thermally with a CoMoS phase (which was shown to be crucial for the enhance HER activity)[203], as well as Co-doped MoS_2 nanosheets on CdS [204]. In all of these cases, the HER activity has been increased with respect to plain MoS_2.

- A third approach for this optimisation has to do with increasing the amount of active sites in the catalysts, which have a direct correlation among others with the surface area of the different morphologies in which we can find TMDs. For example, changing the dimensions of MoS_2 from bulk sizes to single-layer structures lead to special surface properties that could enhance HER performance [205, 206].

- Finally, the last approach is to improve the electron transport from these active sites to the electrodes. This has been attempted by synthesising core-shell structures including TMDs and other materials with better electrical conduction such as metallic multi-walled carbon nanotubes [207]; as well as hybrid structures using other materials in the 2D realm such as reduced graphene oxide [208], mesoporous graphene foams [209] or graphene itself.

Alloying can play a role in several of these optimisation approaches. For example, monolayer WS_2-WSe_2 alloys have been shown to offer a better HER performance than both of their precursors. This improved performance is thought to be caused by crystal distortions produced by the different atomic radii of S and Se in the crystal lattice, which in turn create localised electron fields that can help break the bonds in the molecules adsorbed on the alloy basal plane [194]. Similarly, calculations show that hydrogen adsorption is a bit weak on the Mo edges of MoS_2

($\Delta G_H \approx 80$ meV)and slightly too strong on the Mo edges of $MoSe_2$ ($\Delta G_H \approx -140$ meV). Alloys between these two materials can improve hydrogen adsorption by having a value for ΔG_H that is as close to 0 as possible, improving HER catalytic activity [210].

In conclusion, TMDs, both as alloys [211, 210, 194, 212, 213] and in and of themselves [214, 201, 215, 216, 217], has been as a new source of catalyst materials for hydrogen evolution reaction.

We will delve deeper into the alloy being subject of our study, $Mo_xW_{1-x}S_2$, in the next section.

2.1.5 $Mo_xW_{1-x}S_2$ alloys

Out of all the possible TMD alloys that have been discovered so far (see table 2.1), this study focuses on the behaviour of MoS_2-WS_2 alloys with a variable alloying degree. This section focuses on these alloys, their structure and their properties

2.1.5.1 Structure

Much like its predecessors (MoS_2 and WS_2), it was assumed that $Mo_xW_{1-x}S_2$ could have either the 2H or the 1T structure from its parent compounds, as explained in Section 2.1.2.1. The first TEM images seemed to support this assumption, since it showed images that were very close to those of MoS_2 or WS_2, with the exception of the difference in contrast due to the variation in atomic number between Mo and W [166]. These images can be seen in Figure 2.4

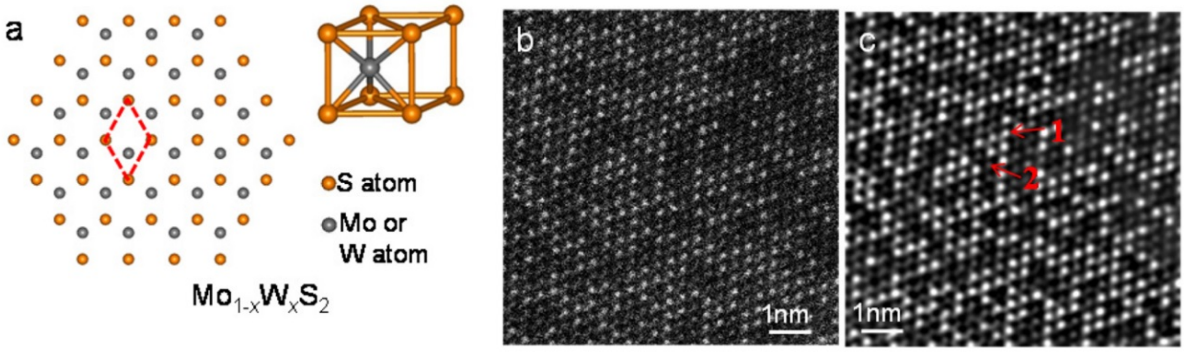

Figure 2.4: *(a) Top view of $Mo_xW_{1-x}S_2$ monolayer and a side view of a unit cell. (b) STEM image of $Mo_{0.47}W_{0.53}S_2$ monolayer. (c) STEM image in panel (b) after FFT filtering. Source: [166]*

Simply put, we can think of these alloys as having the exact same structure as MoS_2 or WS_2, with either an atom of Mo or W in each unit cell, depending on the proportion of both elements. this proportion, numerically represented by the Mo fraction in each alloy, will be called alloying degree from now on.

Our particular alloy sample presents a semiconducting 2H phase. However, much like with its predecessors, it is possible to meddle with the phases of a certain alloy . For example, in the case of the subject of this study, $Mo_xW_{1-x}S_2$, it has been found that, after its fabrication via CVD, the difference between thermal expansion coefficients between TMD monolayers and different substrates produces in-plane thermal strains during cooling that can in turn produce a phase transition from 1H to 1T [192]. This further enriches the amount of properties that can be tuned using phase engineering and alloying (explained in Section 2.1.3) by being able to use both approaches simultaneously.

2.1.5.2 Properties

Since these materials were conceived with applications in optoelectronics, these properties have been the one that have gathered the most interest from the research community, and other properties have not been delved into as much. For example, there are no studies to our knowledge evaluating the mechanical properties of these alloys, even if some structural strain could be present in the sample due to the different atomic radii of Mo and W. However, there have been extensive theoretical and experimental studies on the optoelectronic properties of these materials.

Much like we have seen in Section 2.1.2.3, 2H-phase $Mo_xW_{1-x}S_2$ is a semiconductor, much like their precursor materials, and just like with them excitons play a crucial role on the value of the bandgap of the material. In other words, these stable excitonic states represent the lowest unoccupied states of the material. In other words, the value of the bandgap for a $Mo_xW_{1-x}S_2$ flake of a specific alloying degree is directly related to the energy position of the A exciton (the lowest energy exciton) for that alloying degree. This is a phenomenon that has been seen for both MoS_2 and WS_2 [144], so it is reasonable to see it as well in alloys of both materials.

Previous studies on excitons in $Mo_xW_{1-x}S_2$ alloys have been made using two main techniques, theoretical simulations [218] and experimental photoluminescence studies [219]. The studies on the A excitonic peak, the lowest one in energy, throw light on the behaviour of the bandgap in these alloys [218]. Furthermore, a deconvolution of this photoluminescence peaks into neutral excitons and trions delve further into the behaviour of the bandgap and the nature of the excitons in each material [219]. A summary of these studies can be found in Figure 2.5, taken from a study in the literature that employs the x value of the alloying degree as the amount of W in the sample and not as the amount of Mo, which is important to understand this figure.

What these studies infer is that, as far as the bandgap goes, is a bowing effect. This means there is a small decrease of the bandgap ocurring at low W amounts (x over 0.7) and then an increase as the amount of W in the sample goes up. Furthermore, these studies show that the amount of trionic excitons, as well as the excessive charge densities go down as the amount of W increases .

2.1.6 The importance of EELS for the measurement of optoelectronic features in few-layer TMDs

As we have seen in the previous section, the studies concerning the bandgap of $Mo_{1-x}W_xS_2$ alloys are based on PL experiments. However, this is a direct measurements of the low energy empty states of the materials, which are related to the material bandgap but not a direct measurement of said bandgap, even though some studies have actually made an equivalence between the two [220].

However, as we have seen in Section 1.4.3, low-loss EELS does offer the opportunity to directly probe the dielectric function of materials. Furthermore, as we have seen in Section 1.5.2, it is possible to perform these studies while having a spatial resolution that allows for the study of these alloys down to the nanoscale. Additionally, as we will see both in this chapter and chapter 4, it is possible to estimate the thickness of our samples based on their scattered and unscattered electron ratio, and as we have seen in Section 1.2.4, the HAADF intensity, assuming a homogeneous composition, is proportional to the thickness of a sample. So, in conclusion, STEM HAADF imaging can be used to find alloy flakes showing regions with a different amount of layers, and STEM-EELS spectrum lines, along with the HAADF intensity value of each of the pixels in the spectrum line, holds all the information needed to study the optoelectronic behaviour of $Mo_{1-x}W_xS_2$ alloys not only as a function of the alloying degree, but also as a

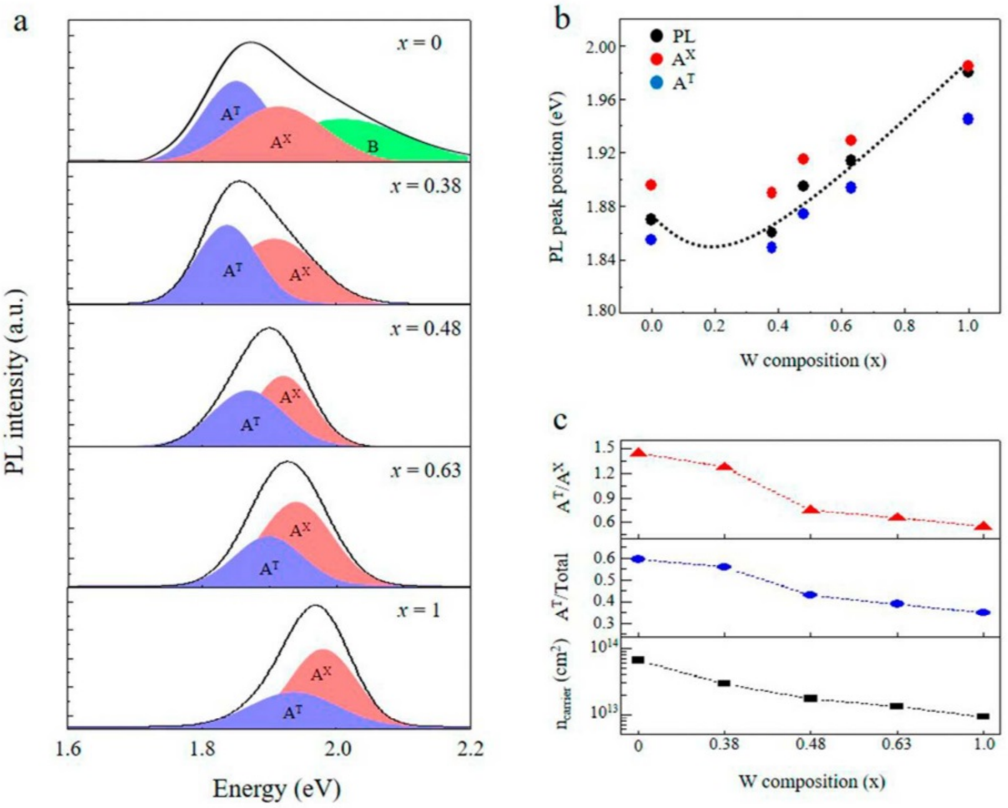

Figure 2.5: *PL studies on $Mo_{1-x}W_xS_2$ alloys. (a) The PL spectra for the single-layer $Mo_{1-x}W_xS_2$ (x = 0, 0.38, 0.48, 0.63, and 1) alloys. The spectra are fitted with peaks corresponding to neutral excitons (A^X) and trions (A^T). (b) The peak maximum positions of PL intensity, the A^X component, and the A^T component as a function of the alloy composition. (c) From top to bottom: The intensity ratios of A^X to A^T, A^X to total excitons, and the excessive charge density calculated by both the mass action model and three-level model. Source: [219]*

function of the sample thickness; in other words, the number of layers in each region.

This section focuses on how low-loss EELS has been used for the measurement of optoelectonic properties in 2D materials, especially MoS_2 and WS_2, and what we can learn from it for the purpose of this study. A good starting point for this is to analyse EELS studies on these materials found in the bibliography, in order to get familiar with the general shape of the low-loss EEL spectra on these samples, the features present in said spectra and their interpretation.

2.1.6.1 EEL spectrum analyses of MoS_2

In Figure 2.6, we can see the EEL spectra of MoS_2 samples presenting different numbers of layers. These spectra come from the literature [62], but the Figure has been modified to include the three main regions from the spectra from an analysis point of view, which are the following in ascending energy:

- The first region of interest for our analysis contains information about the bandgap of the material, as well as features corresponding to the A exciton (which rules the bandgap behaviour) and the B exciton. In Figure 2.6, as well as in our case, both peaks are to close among them to be resolvable from one another. However, we know them to be two different peaks from both theoretical studies [61] and PL studies [220].

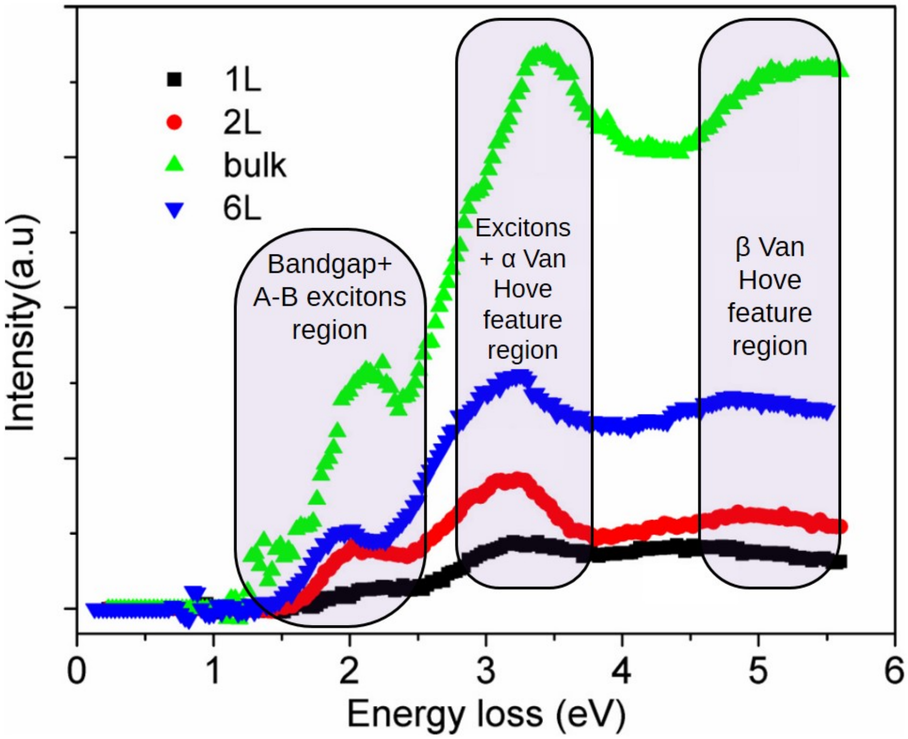

Figure 2.6: *Angle-integrated low loss EEL spectra of* MoS_2 *samples showing 1, 2 and 6 layers, as well as a sample thick enough to be considered bulk MoS2. Regions containing the main features of these spectra have been highlighted. Modified from [62]*

- The second region of interest for this analysis contains information about the C excitonic features of the sample as well as the α Van Hove feature. These two are really close in energy and they are not easy to discern from one another, but our data analysis seems to have resolved them well enough.
- The third region of interest contains the feature related to the β Van Hove feature in the sample. However, since this feature is really wide in energy, it is sensible to analyse this region along with the previous one to account for any overlapping effect.

We will see the physical phenomena lying behind these features, as well as how they impact the EEL spectra, in the remainder of this section.

2.1.6.2 The bandgap

One or the main objectives of these works is the direct measurement of the bandgap for the different alloys present in the studies. The mechanism through which these measurements can be performed is explained in this section.

Usually, optical absorption spectroscopy is the technique chosen for measuring the optical gap of a bulk material. This technique probes the frequency dependance of the imaginary part of the dielectric function ($\varepsilon(\omega)$) [221]. In the case of EELS, an EEL spectrum is proportional to the energy loss function (Im(-1/$\varepsilon(\omega)$)) [13]. In a penetrating geometry, when the electron beam is going through the sample, this energy loss function, neglecting the surface loss contributions, is expressed as:

$$Im(-1/\varepsilon(\omega)) = \varepsilon_2/(\varepsilon_1^2+\varepsilon_2^2) \tag{2.1}$$

where ε_1 and ε_2 are, respectively, the real and imaginary parts of this complex dielectric response function. Kramers-Kronig transformation allows to determine this dielectric function from the measured energy-loss function [13]. Thus, optical properties at the local scale can be measured [13, 222, 223]. However, as the dimensions of the objects decrease, the surface effects get more importance, and this energy loss function is not a correct response function anymore. Under these circumstances, the response function is different from the bulk one, as it depends on the geometry of the object.

One of the advantages of STEM-EELS is that allows to investigate the surface effects and to work in a non-penetrating ("aloof spectroscopy" (Howie & Milne, 1985 [224]) or "near field" spectroscopy), where the electron beam is focused at a grazing incidence to the nanostructure, no intersecting it. In this case, the only excited modes in the EEL spectra correspond to surface contributions. Under these conditions, a successful approach for investigating these optical responses by EELS is the continuous dielectric model [225, 226, 227, 228, 229, 230, 231, 232, 77]. It is a macroscopic semi-classical model based on the resolution of Maxwell's equations for fixed boundary conditions. In particular, for different nanostructures (spheres-onions, fullerenes, nanotubes...), it has been shown that for the aloof geometry, an EELS spectrum is a weighted sum of the imaginary part of the multipolar polarisabilities (γ) [229, 231]. Two different regimes can be distinguished depending of the dimensions (thickness - number of layers in lamellar-based systems (including nanotubes, nanoonions, 2D planar materials) of the nanostructures: (1) strong-coupling and (b) week-coupling regimes, respectively. In our case, as we will deal with a reduced number of layers (1-3 layers), the strong-coupling between the two surface modes existing in the flakes regime is considered. Therefore, the imaginary part of the polarizability can be written:

$$Im(\gamma(\omega) = (Im(\varepsilon_{\perp}(\omega) - 1/\varepsilon_{\|}(\omega))) \qquad (2.2)$$

where $\varepsilon_{\perp}$ and $\varepsilon_{//}$ are respectively the in-plane (perpendicular to the anisotropy axis) and out-of-plane (parallel to the anisotropy axis) components of the dielectric tensor of a planar $Mo_xW_{1-x}S_2$ sheet. This is interesting because, as we can see from the analysis of the dielectric constants for MoS_2 and WS_2, below 3 eV the two terms do not overlap, and then, a direct measurement of a quantity proportional to the optical absorption perpendicular to the anisotropy axis can thus be obtained [228, 229, 231]. Thus, the bandgap of the flakes can be directly measurable by aloof spectroscopy as previously has been done for BNNTs [233, 232, 77].

2.1.6.3 The excitons

As we have seen in section 2.1.5.2, both precursors to our alloy and our alloy itself present stable empty states in their electronic structure where electrons from the valence band can go to if they are excited. This is known as excitonic transitions or excitons [144].

In the low-loss EELS spectra in MoS_2, there are two features related to excitons at a very low energy, around 1.5-2 eV. These excitons have been vastly probed by a wide set of techniques, namely optical absorption, photoluminescence, cathodoluminescence and EELS [234, 235, 191, 186, 188, 236, 237]. It is known that their origin is found on the transitions between the maxima of split valence bands and the minimum of the conduction band, which are all located at the K point of the Brillouin zone according to the simulation of the electronic structure of MoS2 in the literature [104]. As we have seen in Section 2.1.2.3, the splitting of this excitonic feature comes from spin-orbit coupling effects. The name of the two features for this study will be A and B, although our spectra do not have a resolution good enough to discern between both features.

These features have also been observed for WS_2 in a similar manner [237], as well as $Mo_xW_{1-x}S_2$ alloys, which have been probed by means of IR spectroscopy. The comparison between the DFT simulations of the bandgap of the alloys and the A exciton position of the same alloys showed a correlated behaviour between one and the other with the alloying degree [166]. In other words, the bandgap of the sample is heavily influenced by the A exciton in said sample and follows its behaviour when varying the alloying degree of the samples.

This is the reason that the measurements of the excitonic peak behaviour and the behaviour of the bandgap are considered equivalent in a portion of the literature [187, 188, 189]. However, this equivalence is inaccurate since the excitonic peak is centered around the maximum number of transitions, not the lowest ones in energy, which would be the ones ruling the bandgap. In this sense,no previous direct measurements of the bandgap of these alloys have been performed.

There is a third excitonic feature present in the EELS spectra that was not gathered as such in recent literature [62]. Recent studies show this appearing on theoretical simulations [144] and it is coherent with our data. This feature was first predicted in 2013 [238] and evidence of it has only been found in recent years [239]. Full *ab-initio* modelling of these features has been performed[144, 240], which is quite useful to put this study into context.

This excitonic feature does not correspond to a single exciton, but rather from "*six nearly degenerate exciton states made from transitions between the highest valence band and the first three lowest conduction bands near, but not directly at,* Γ, *reflecting the fact that the lowest transitions are degenerate at multiple points near* Γ" [238]. However, in terms of data analysis, all these 6 excitons overlap and we treat the feature as a whole.

2.1.6.4 The Van Hove features

As we have seen in Section 2.1.2.3, these kind of TMDs show what is known as Van Hove singularities that appear on the EEL spectra as energy loss features or peaks. For the purpose of our study, much like the one shown in Figure 2.6 [62], we will focus on both the α feature, situated around $\approx$3.5 eV; and the β feature, situated around $\approx$5.5 eV. The analysis of these two features will not only provide further information about the optoelectronic properties of the sample, but it will also ease the analysis of the C excitonic feature, since it is quite overlapped with the α Van Hove feature.

2.1.6.5 state of the art

There have been several studies using low-loss EELS and theoretical simulations to delve deeper into what we know about out precursor materials, MoS_2 and WS_2. here we present

Excitons and bandgap In fact, a similar study to ours has been performed for MoS_2 and Re_2 by Dileep *et al* [61], using high resolution EELS to try and calculate the indirect and direct bandgaps of these materials. This gives us a starting point in terms of results in MoS_2. However, this measurements were not performed for the alloys that are the subject of our study. They used Tauc plots to determine the direct and indirect gaps.

A second study by Nerl *et al* focused on high resolution STEM-EELS studies on MoS_2, this time focusing on the one hand on the distance to steps, edges and number of layers and their role on the excitonic features (which they managed to resolve) and, on the other hand, with theoretical calculations on the excitonic behaviour of MoS_2, which made it clear that there was an additional excitonic feature at an energy $\approx$2.8 eV. Both of these points are of extreme importance for a correct understanding of the analysis of our data.

Van Hove features The study by Hong *et al* on MoS_2 versed not only on momentum-dependent spectra of monolayer MoS_2 but also on the behaviour of the Van Hove features in the spectra as a function of the layer thickness of the sample. However, even though it is a signal that an be sort of seen in the spectra, they did not take the C excitonic features into account for their analyses.

2.2 Experiment

Now that we know the starting point for this study, it is time to focus on how it has been performed. This section focuses on all the different experimental parametres, from the sample preparation as a whole to the data gathering and analysis. These explanations will be crucial for the understanding of the results yielded by the experiment.

2.2.1 Sample preparation

In order to obtain a STEM measurable sample of the different $MoS_xW_{1-x}S_2$, there is a series of steps to be followed, from the synthesis of the alloy to the transfer of alloy flakes onto a TEM grid and ht selection of optimal flakes for their study. Here we focus on each one of these steps.

2.2.1.1 Synthesis of the sample: chemical vapour transport

The bulk sample has been prepared using the chemical vapour transport method (CVT), a technique that has been used far and wide for the creation of crystalline materials [241]. This process was discovered by Bunsen more than 150 years ago while studying the vulcanic eruptions of the Vesuv [242]. In this study, he noticed the formation of hematites in the presence of hydrogen chloride. This, along with confirmation laboratory experiments, made Bunsen develop the concept of ”pneumatolysis” and pneumatolytic reactions. In this kind of reactions, a solid could be transfered to a gas phase material and then redeposited somewhere else.

After its discovery, and some modelling approaches, the biggest breakthrough in the development of this technique was done by Schäfer, in his study ” *Über den Transport des Bodenkörpers im Temperaturgefälle mit Hilfe heterogener Gleichgewichte*”. In this study, Schäfer studied the migration of iron oxide when put in a hydrogen chloride atmosphere in a temperature gradient from 100°C to 800°C in a sealed ampoule. A general scheme for the set-up of this kind of experiments can be seen in Figure 2.7

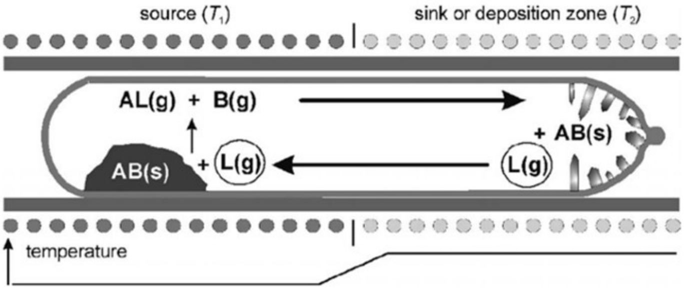

Figure 2.7: *CVT synthesis method. Sketch of a transport ampoule in the temperature gradient of a two-zone tubular furnace. In an exothermic reaction solid AB and the transport agent [L(g), which might be regarded as solvent] form the transporting gas species AL(g) and B(g). At the sink, which is for the chosen example at the higher temperature, the reaction is reversed. Source: [241]*

His conclusions allowed a reproductible and versatile method for the production of different crystals.

In CVT, generally, a condensed phase (normally a solid) is heated up and volatilised with a gas present in its medium (called a transport agent), and then redeposited in the form of a crystal in a different location. The volatilisation, the transport and the redeposit all take place within a sealed container where there is a temperature gradient. The three steps of a CVT reaction are perfectly explained in the historical review done by Binnewies *et al* [241]:

> ”*It is the characteristic of a chemical vapor transport reaction that only gaseous products are formed off a condensed phase and a gaseous transport agent. [...] Three steps are distinguished:*
>
> 1. *Forward reaction (the condensed phase reacts with the transport agent; first phase-transfer reaction).*
> 2. *Gas flow*
> 3. *Back reaction (deposition of the condensed phase under release of the transport agent; nucleation, crystal growth; second phase-transfer reaction)*”

This method has previously been used for the preparation of a variety of crystalline materials, mainly pyrites [243], a variety of oxides [244], and, most notably, transition metal chalcogenides in various forms (including TMDs)as well as mixed crystals, which could be considered as alloys nowadays [245, 246]. This would later be used for the preparation of a variety of TMDs [247, 248, 249, 108].

In the context of this study, bulk $Mo_xW_{1-x}S_2$ alloys have been synthesised using this method in previous studies by our collaborators [250] as well as other independent studies [136]. They had been previously synthesised twenty years before using chemical reactions as stated in Section 2.1.3, so a stable phase of this alloy was known to exist. However, chemical vapor transpot ensured a single phase crystal.

Nowadays, alternative bottom-up techniques are being used for the production of these alloys, such as Chemical Vapor Deposition (CVD) [251]; as well as bottom-up plus top-down approaches, such as CVD plus laser thinning [219]. This allows for a better control of the sample thickness, allowing for the growth of a specific number of layers. However, in terms of TEM samples, these two methods are not ideal since an effective transfer from the substrates employed for these synthesis methods to a TEM grid is more challenging than the exfoliation and transfer from a single phase crystal.

Preparation of the grid

After the synthesis of the material in the form of single crystals using CVT, these crystals were exfoliated using the scotch tape method, much like the original exfoliation of graphene [**?**]. After exfoliation, the alloy flakes were transfered onto a TEM grid. Optical microscopy was used to determine areas with flakes showing a high degree of transparency, in other words, few layers. These regions of interest were the ones studied using STEM-EELS.

2.2.2 STEM-EELS measurements

Once the samples have been brought into the microscope, it is time to perform the necessary measurements to ensure, on the one hand, that we are choosing regions that offer what we are looking for; i.e., flakes with distinct regions of different number of layers, and on the other hand, that we have a truly alloyed sample. Additionally, this section covers the treatment of the EEL spectra in this study to obtain a better spectral resolution.

Initial STEM measurements

For each region of interest, an initial STEM micrograph has been gathered to fulfill several different purposes:

- Initial STEM micrographs in several different areas were taken by our collaborators for the determination of their alloying degree. The method for this will be explained in detail below.
- These same micrographs proved that all of our alloys have a 2H structure, and are therefore semiconducting.
- Another goal is to correlate the results from the optical microscopy to actual STEM micrographs, where the specific morphology of each flake is more evident.

From the regions of interest mentioned here, several have been chosen where there was an evident change in layer stacking that could be gathered in a single line. These selected areas have been subjected to STEM-EELS measurements.

2.2.2.1 Calculation of the alloying degree using STEM micrographs

Several different ways have been used to analyse the alloying degree of alloys throughout the years, most of which focused on chemical quantification [178]. However, a study by Dumcenco *et al* from 2013 offered a simple alternative when it comes to atomically thin dichalcogenide alloys [250]. The technique for the calculation of the Mo and W ratio (what we define in this manuscript as the alloying degree) is pretty straight-forward.

As we have seen in Section 1.2.4, the contrast of an atom in HAADF imaging is proportional to $Z^{1.7}$. by taking a simple STEM-HAADF micrograph, they proved that it is possible to distinguish the intensity profiles corresponding W, Mo and stacked S atoms. in other words, just by analysing a big enough micrograph of a monolayer of a certain $\mathrm{Mo}_x\mathrm{W}_{1-x}\mathrm{S}_2$ sample, one can quantify the ratio of Mo atoms in the sample x. The procedure for this quantification is shown in Figure 2.8

The same study provided a great tool not just to analyse the ratio of Mo and W in the sample, but also to determine what they define as the "alloying degree", which could be understood as a level of homogeneity of the sample at the atomic level.

This calculation comes from the observation of heteroatoms in neighbouring sites for a specific species (either Mo or W), also known as its coordination number. An analysis of the different coordination numbers of each W atom in a micrograph of a $\mathrm{Mo}_{0.5}\mathrm{W}_{0.5}\mathrm{S}_2$ sample can also be seen in Figure 2.8. Once we have measured the coordination numbers of all the atoms of a certain species, the quantification of the alloying homogeneity of Mo and W atoms can be calculated. For example, the homogeneity of W atoms can be expressed as:

$$J_W = \frac{P_{observed}}{P_{random}} \times 100\% \tag{2.3}$$

In this expression, and for this example, $\mathrm{P}_{observed}$ is defined as the average coordination number of all the W atoms measured, divided by the total coordination number (in this case, six). P_{random} is the same ratio for a sample with a random distribution of atoms, which coincides with the ratio of the species of interest in the sample being studied, in other words, what we call the alloying degree. in a sample with perfectly random distribution of W atoms, $\mathrm{P}_{observed}$=P_{random} and J_W=100%. a value of J_W under 100% is indicative of a homophilic configuration for this species, while a value of J_W over 100% indicates a configuration that favours heteroatoms.

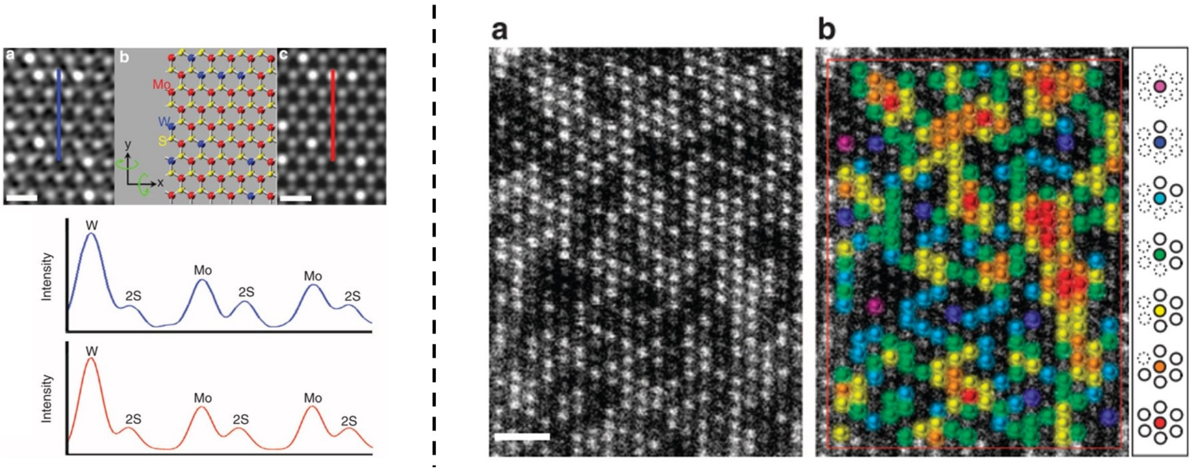

Figure 2.8: *Alloying degree quantification and coordination number calculation for these alloys.* ***Left****: An ADF image of a* $Mo_xW_{1-x}S_2$ *single layer with x=0.2 (filtered), in which the atomic positions of sulphur are also visible. (b,c) Modelled structure and simulated ADF image (red: Mo, blue: W, yellow: S). Note that the two sulphur atoms are overlapped with a small inclination of (5°in x axis and 6°in y axis). (d,e) Profiles of the experimental and simulated ADF counts for lines indicated in a and c. They confirm the W, Mo and 2S atomic sites, that is, the brighter spots correspond to W and the less bright ones to Mo.* ***Right****: (a) Example for ADF image of* $Mo_xW_{1-x}S_2$ *single layer (x=0.5). The W atoms are shown in different colours on the same image (b): purple, blue, light blue, green, yellow, orange and red for six-, five-, four-, three-, two-, one- and zero- coordinate sites. Source: [250]*

The alloys measured in the study by Dumcenco *et al* have been prepared in the same conditions and using the exact same equipment, so for the purpose of this study we will assume a somewhat random distribution of Mo and W atoms in our samples.

STEM-EELS measurements- experimental conditions

Finally, in the selected aforementioned regions, HAADF intensities and EELS spectra have been gathered using the spectrum profile technique explained in Section 1.5.2. An image of a micrograph of our sample, as well as an explanatory image of a spectrum profile, can be seen in Figure 2.9.

These studies have been performed with an electron beam energy of 80 KeV, to prevent beam damage and reduce Cherenkov effects. The convergence semi-angle of the measurements has been of 25 mrad, and the collection semi-angle has been of 35 mrad. Spectrum profiles of 40 spectra were taken where a 2 ms spectrum was collected for each probe position. The energy resolution was found to be around 180 meV.

2.3 Analysis

2.3.1 Selection and preparation of the spectral data

The two main variables of this study are the number of layers of the different analysed regions, as well as the alloying degree of the samples being analysed. The latter has been calculated in our samples with the method explained in Section 2.2.2.1. For our spectral data, as it has been explained in Section 2.2.2.1, we have measured profiles gathering data both about the EELS spectra and the general HAADF intensity. An example of a sample with their HAADF–STEM micrograph along with their HAADF intensity can be seen in Figure 2.9.

[h!]

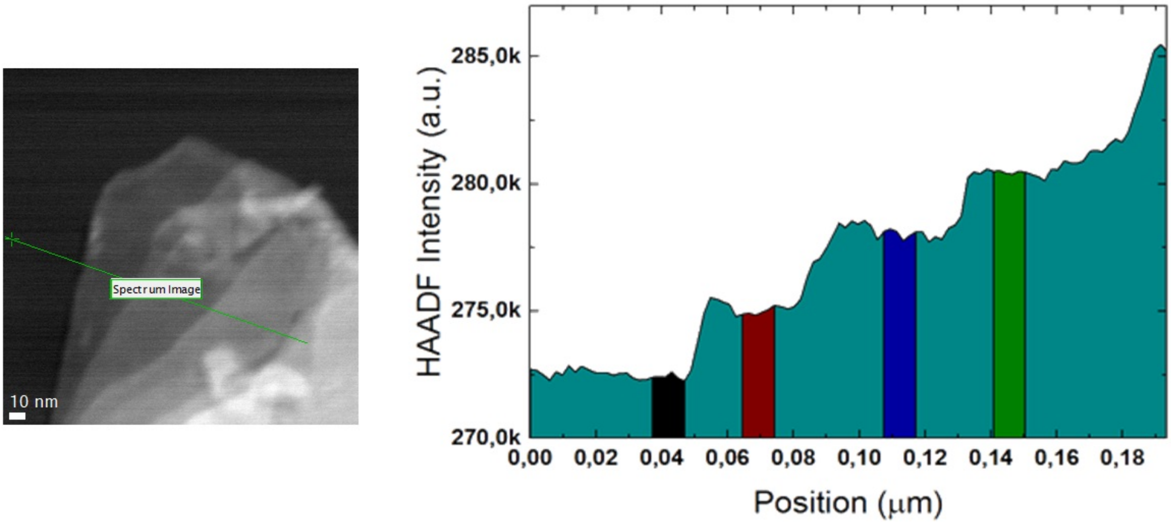

Figure 2.9: *Left: STEM micrograph of a $Mo_{0.5}W_{0.5}S_2$. The spatial location of the STEM-EELS spectrum line is shown with a green line. Right: HAADF intensity of the profile indicated on the left. The regions appartaining to areas with the same number of layers where we have integrated the spectra are highlighted.*

In order to have a study as accurate as possible, and to optimise the signal to noise ratio in the spectra, we opted for integrating several spectra corresponding for each measurement. For this purpose, we analysed the HAADF intensity related to each point of the STEM-EELS spectrum-line. As we have seen in Section 1.2.4, the HAADF intensity changes mainly with two parametres: the chemical composition and the thickness. We assume a homogeneous chemical composition; which would be the case given that we have a grain size that is only a few atoms wide and therefore we can consider the sample as homogeneous in terms of atomic distribution of the transition metals.

The HAADF intensity profile shown in Figure 2.9 seems to have some sort of steps, as does the HAADF micrograph. This corresponds to a change in the number of layers of the sample. Based on the HAADF microgrpah, we know there is no sample on the left of this profile. We will integrate 6 spectra over this "background" signal from the vacuum, as reference in each of the samples analysed. The spectra chosen for this sample are the ones in the black area highlighted in Figure 2.9.

The flat steps on the HAADF profile correspond to regions with a constant number of layers. We will integrate 6 spectra over these regions as well (as highlighted in Figure 2.9). The choice of 6 as the number of spectra to integrate comes simply from the fact that, for this study, this was the biggest spectral window that could be used without getting too close to the edge of each layer for most of the spectrum profiles in the study.

The need to not get too close to the edge spectra comes from the possible plasmonic influence of the edges of the flakes. This has been proven for MoS_2, both by DFT calculations [252, 253] as well as spatially-resolved EELS. This plasmonic behaviour [254] happens at low losses, and could therefore interfere with our measurements.

For the specific case of the optical gap measurements, since it was vital to choose a region that was as close as possible to the sample without actually being over the sample, a different approach was taken in order to avoid possible offsets between the point of the sample where the HAADF profile was taken and the point of the sample where the EEL spectra had been taken.

These offsets are generally under a pixel long, but in this particular case this was a big enough offset.

For this particular case, a thickness profile was extracted from the spectrum profile by analysing the relative thickness estimated from each single spectrum. This provided a much more reliable way of choosing the integration window for our gap measurements.

The spectra have also been removed of their Zero Loss Peak (ZLP) by means of a power-law fitting of the ZLP and its subsequent substraction from the spectra, as explained in chapter 3.3.3.

Finally, in order to improve the resolution of the features in the spectra, these have been subjected to a Richardson-Lucy deconvolution.

2.3.1.1 Spectral preparation: The Richardson-Lucy deconvolution

In order to improve the accuracy of the measurements, a matter of importance is to improve the energy resolution of the EEL spectra taken. Here we present a technique that has been widely used for this purpose in EEL spectroscopy. We will discuss the effectivity of this technique for the purpose of this study in Section 2.4.1.

This technique originates in the analysis of astrophysical data. In these cases, there is a large point spreading caused by telescopes and different numerical approaches have been used to try to inverse this spreading. One of the techniques that has been used the most is the one known as the Richardson-Lucy deconvolution [255, 256].

As it has been seen previously in the bibliography, this is also applicable to EEL spectroscopy, as it has been seen in previous studies which offer a comprehensive explanation on the matter [257]. In this case, the point spread function (PSF) comes from the aberration of the spectrometer, the energy spread of the electron beam itself and the PSF of the CCD camera used to take said spectra. Since the spectra taken by the CCD is an integration over a number of pixels in the CCD in the non-dispersive axis of the EEL spectra, the treatment of EEl spectra, provided that a CCD camera is used (which is our case) can be treated as an image reconstruction.

This image reconstruction algorithm begins with the imaging equation of any sort of image, including the one formed in the CCD camera by the EEL spectra. This equation is a mathematical approach to the blurring of an object by a PSF when forming an image:

$$I(i) = \sum_j P(i/j) O_{(j)} \tag{2.4}$$

Where O_j is the signal coming from the original unblurred object in its location j, $I(i)$ is the intensity measured on the image at the pixel i, and $P(i/j)$ is the PSF of the system with respect to the pixel i and the location j in the image and the object, respectively. We assume the PSF not to vary at different energy losses, which means $P(i/j) = P(i-j)$ and this sum becomes a convolution.

Assuming a Poissonian distribution for the noise, the probability to get N counts in a specific pixel when the mean expected number of counts is N_m is:

$$P\left(N/N_{\mathrm{m}}\right) = \frac{\mathrm{e}^{-N_{\mathrm{m}}} N_{\mathrm{m}}^{N}}{N!} \tag{2.5}$$

Given these past two equations, one can deduce the expression for the joint likelihood of getting the the observed $D(i)$ in a pixel given the expected intensity $I(i)$ by substituting equation 2.4 into the logarithm of equation 2.5:

$$\ln L = \sum_i [D(i)\ln(I(i)) - I(i) - \ln(D(i)!) \tag{2.6}$$

The Richardson-Lucy deconvolution applies an iterative method to approach the maximum of this likelihood:

$$O_{(j)}^{k+1} = \partial_{(j)}^{k}\left(\sum_i \frac{P(i/j)D(i)}{\sum_l P(i/l)O_{(i)}^{k}}\right) / \left(\sum_i P(i/j)\right) \tag{2.7}$$

This method starts with the observed image, and calculates the the k+1 object taking the object k as the basis. Following this iterative method, The image O should end up converging to something closer to the original object before the blurring of the PSF. In the case of EEL spectra, this implies an enhancement of the resolution.

2.3.2 Thickness analysis and number of layers

For the analysis of the thickness of the samples, we have employed a log-ratio method as the one used in chapter 4. Since we assume the composition of each sample is constant, we can use a more direct implementation of this method. This implementation needs the experimental parametres of the data acquisition, shown in Section 2.2.2.1, and the effective atomic number of the sample, which we can calculate from the alloying degree of the sample,

The effective atomic number Z_{eff} is defined as the average atomic number of the sample. This is easy to know given the alloying degree (taken as the x in $Mo_xW_{1-x}S_2$) . Knowing the atomic number of Mo, W and S, N_{Mo}=42, N_W =74 and N_S=16, the effective atomic number is calculated as a function of the alloying degreeas follows:

$$Z_{eff} = \frac{x \times N_{Mo} + (1-x) \times N_W + 2\times_S}{3} = \frac{x \times 42 + (1-x)74 + 2 \times 16}{3} = \frac{106 - 32x}{3} \tag{2.8}$$

It is important to notice that, in the vacuum spectra we have selected where we are only nm apart from the sample, there are some medium-range interactions taking place between the beam and the sample, mostly due to the delocalisation effects explained in Section 1.5.2.2. This causes some of the electrons to interact with the sample and therefore lose energy, thus we obtain a non-zero value for the sample thickness of this vacuum area, since it was dependent on the scattered beam intensity. (see chapter 4 for details). This "background thickness" has a value between 0.5 and 1 nm.

As for the number of layers, we estimate them from the thickness of the sample. Taking into account the interlayer distance for MoS_2 and WS_2, ≈6.5Å [129], we can estimate the number of layers of the different regions of the samples based on their thickness.

2.3.3 Estimation of the bandgap

For the estimation of the bandgap, and based on the shape of the spectra, we have chosen a linear fit to analyse a spectral window located between the onset of the spectra and the feature corresponding to the A and B excitons.

The intersection between this linear fit and the X-axis is considered as the onset point of the spectra, in other words, the point where we start having signal. We consider the energy value of this onset point to be the bandgap value of the sample being measured. In other words, we fit the spectral region with a linear fit $y = a \times x + b$, and we choose the value $x_{onset} = -\frac{b}{a}$ as our bandgap value. An example of this analysis can be seen in Figure 2.10.

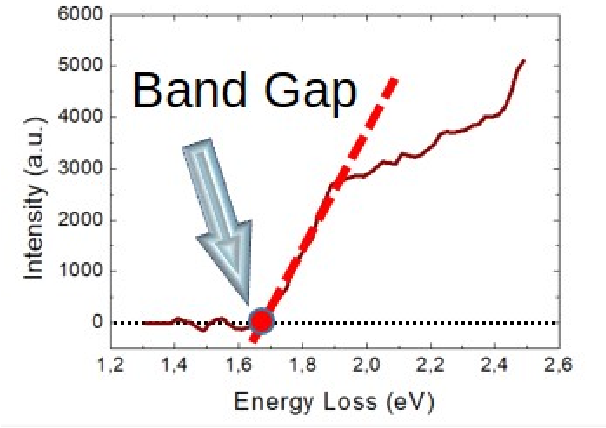

Figure 2.10: *Scheme of the method used for the estimation of the bandgap.*

The energy window for performing these fits has been kept at a width of 0.2 eV; except for a few cases where the noise of that specific spectrum was too high to obtain a regular behaviour over the whole window. . The position of the window has varied depending on the spectra.

2.3.4 Estimation of the Van Hove features and the C exciton peak: 2 vs 3 Gaussian analysis

The initial analysis performed for the spectral window from 2 to 6 eV was a two feature fitting, since the literature at the time did not account for the presence of the C excitonic peak. This initial analysis used a double Gaussian to try to locate only the peaks in the EELS spectra related to the α and the β Van Hove features.

However, recent experimental studies and simulations [240, 238, 258], as well as calculations performed by our collaborators acknowledge the presence of a feature in the EELS spectra of a peak corresponding to a C exciton in the sample. Furthermore, for most spectra, a three Gaussian analysis seems to yield a much more accurate result than a two Gaussian analysis, as it can be seen in Figure 2.11.

Based on this information, the analysis of this spectral region has been performed using a three Gaussian analysis. The assignment of the peaks, from lower to higher energy, is: C exciton, α Van Hove feature, and β Van Hove feature. An example of this fit is shown in Figure 2.11.

As we can see, the three Gaussian fit does not only make more sense from a purely physical point of view, but it also performs better in terms of how close the fit is to the actual shape of the spectra, as shown by the reduced difference between the fit and the original using the three-Gaussian approach.

The Gaussian widths We have tried to do the 3 Gaussian analysis without a fixed width for any of the Gaussians and it seems that it influences the rest of the analysis. Small changes in dominant features can have great effects on smaller features and this seems to be the case. As the number of layers go up, so does the width of the β feature, which greatly complicates the analysis of the alpha feature and the C exciton since it is much more intense. For the purpose of this analysis, we have set the width of the β feature to the mean value of the width of the β feature for each alloying degree, namely w(β)=3.1, 3.9, 2.8, 2.7 and 2.1 for an alloying degree x= 1, 0.7, 0.5, 0.3, and 0; respectively.

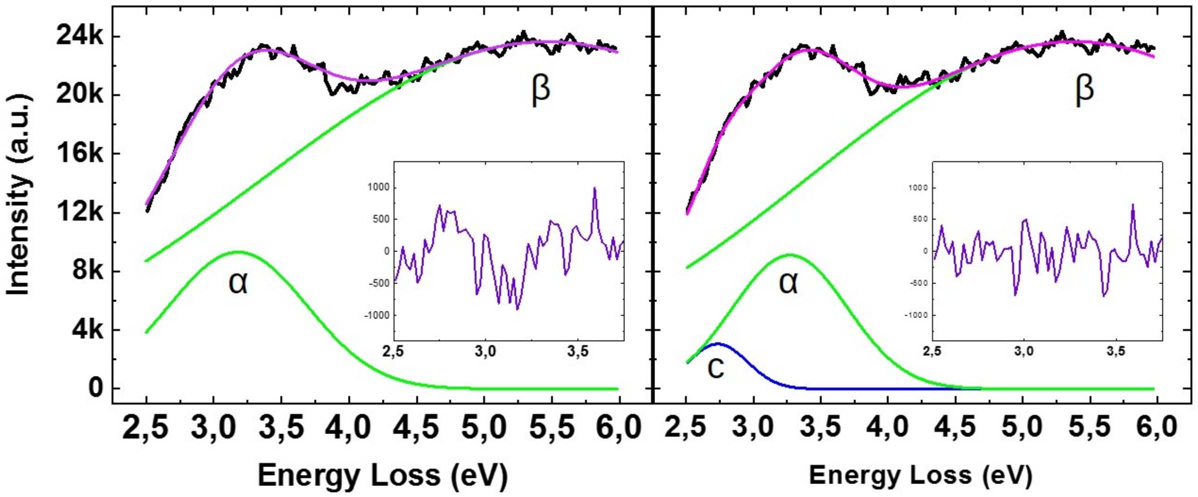

Figure 2.11: *Side-by-side comparison of the 2 Gaussian vs 3 Gaussian fit for the spectral region of interest in this study. The two Gaussian approach contains fits accounting for the α and β Van Hove features in the sample(green); and the three Gaussian approachs contains fits accounting for the C excitonic features (blue) as well as the α and β Van Hove features. The sum of all the different Gaussian fits is shown in each case (pink) and the difference between the original data and the fit is shown as well (purple inset).*

2.3.5 Error calculation and propagation

For the calculation of errors, and its propagation, several methods have been employed depending on the error being calculated.

For the bandgap measurements, we consider the error in the measurement as the error of $-\frac{b}{a}$, which we can calculate from the error values of a and b, respectively:

$$\delta x^2 = \sum_i \left(\frac{\partial x}{\partial x_i}\right)^2 \delta x_i^2 \tag{2.9}$$

$$\frac{\partial x}{\partial a} = \frac{b}{a^2} \tag{2.10}$$

$$\frac{\partial x}{\partial b} = -\frac{1}{a} \tag{2.11}$$

$$\delta x^2 = \frac{\delta b^2}{a^2} + \frac{\delta a^2 b^2}{a^4} = \frac{\delta b^2 a^2 + \delta a^2 b^2}{a^4} \tag{2.12}$$

$$\delta x = \frac{1}{a^2}\sqrt{\delta a^2 b^2 + \delta b^2 a^2} \tag{2.13}$$

For average values in the bandgap, the standard deviation of the measurement set has been used as the error in the measurement.

In the case of C excitons and α and β Van Hove features, the error values of the position of these peaks come directly fron the Gaussian analysis. For the average C exciton and α and β Van Hove features, the error value shown in their respective figures is calculated using equation 2.16:

$$x = \frac{\sum_{i=1}^{n} x_i}{n} \tag{2.14}$$

$$\frac{\partial x}{\partial x_i} = \frac{1}{n} \tag{2.15}$$

$$\delta x = \frac{1}{n}\sqrt{\sum_{i=1}^{n} \delta x_i^2} \tag{2.16}$$

2.4 Results and discussion

Here we present the results regarding this study, as well as the conclusions we can draw from them.

Thickness and layers

The histogram on the number of layers of the different samples in this study can be seen in Figure 2.12.

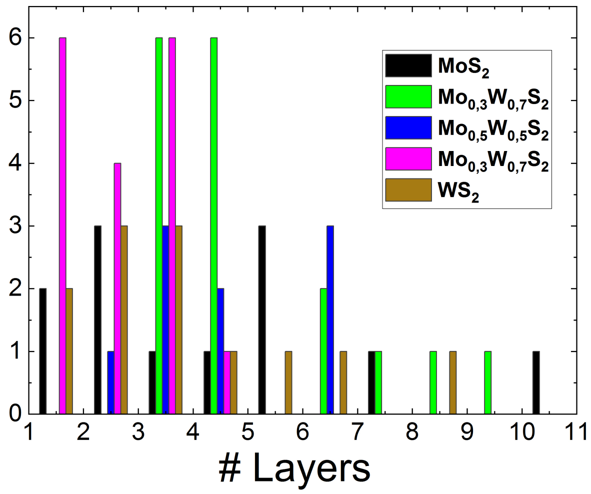

Figure 2.12: *Histogram containing the number of layers of each measurement performed in each alloy for this study.*

The difficulty to perform the measurements needed for this study has not allowed us to have a stable amount of measurements for each number of layers of each sample, and for some of the samples no regions containing monolayers have been found. However, as we can see, there are enough different thicknesses on each sample to talk in general about the variation of the different optoelectronic properties of these samples both with the alloying degree and with the number of layers.

2.4.1 Bandgap studies

Influence of the Richardson-Lucy deconvolution on the determination of the bandgap

The Richardson-Lucy deconvolution, explained in Section 2.3.1.1, has been used, in principle, to enhance the different features present in the EELS spectra of the alloys. a comparative study of both the average bandgap values for the raw spectra compared to the deconvoluted spectra can be seen in Figure 2.13b.

As we can see, the deconvoluted spectra do not only yield a bandgap behaviour that is much more coherent with previous bibliography on the matter [218], but it also presents smaller errors

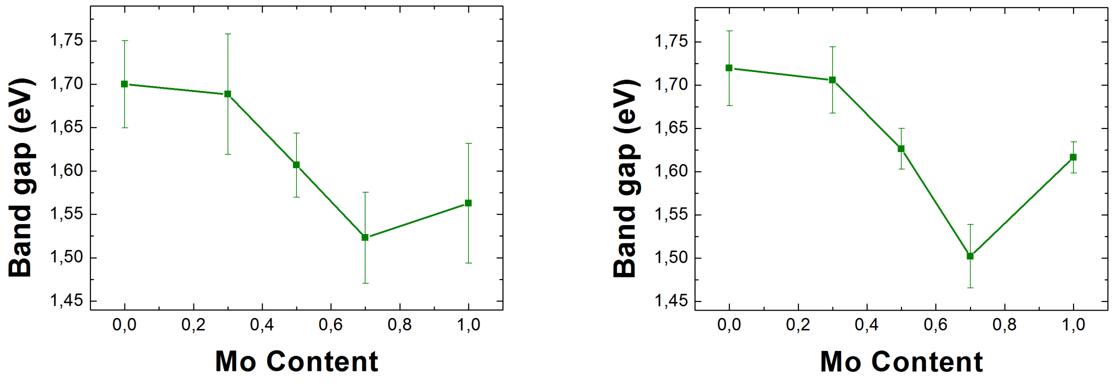

(a) (b)

Figure 2.13: *Comparison between raw and deconvoluted spectra for a selection of spectrum profiles. a) Average estimation of the bandgap for raw EELS spectrum profiles. b) Average estimation of the bandgap for Richardson-Lucy deconvoluted EELS spectrum profiles. The error bars represent the statistical deviation among measurements.*

in their measurements. This is why, as far as the bandgap studies are concerned, we will be analysing the values taken from the deconvoluted spectra.

These results represent the first direct measurement of this property that we have been able to find in the literature. The found values are lower than those shown in the literature for PL studies, but it is coherent, since generally the value given for the optical gap for these materials is the value of the A exciton peak, which dominates the bandgap but is slightly higher in energy than the bandgap itself.

Bandgap vs number of layers

The individual measurements of the bandgap, as well as the average measurements for different numbers of layers and for different alloying degrees can be seen in Figure 2.14

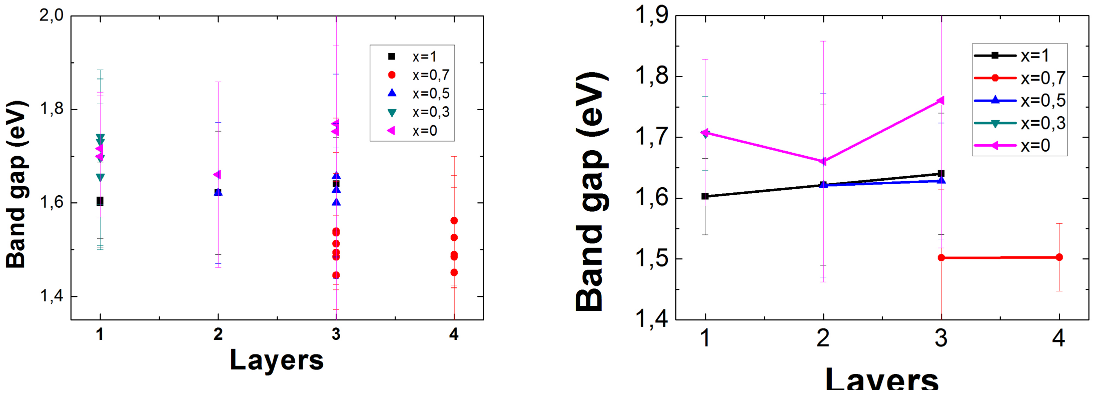

(a) (b)

Figure 2.14: *a) Individual estimation of the bandgap for all raw EELS spectrum profiles. b)average estimate of the bandgap for all raw EELS spectrum profiles.*

As it can be seen, there are no clear tendencies in the behaviour of the babd gap, either seen individually or averaged. Our hypothesis is not that the bandgap does not shift with the number of layers, but rather that we cannot confirm it. This may have to do with our energy resolution, the role of the exciton peaks in the EELS spectra or even with our linear fit not being the most accurate tool for this study. In other words, the inaccuracy in the measurements coming from this fit is too big to be sure of any changes in the sample, although if we were to estimate based on the given data we would probably say there is a slight decrease in the bandgap as the number of layers goes up. It is important to notice, however, that for each individual number of layers, the average bandgap for each alloy seems to follow the same tendency as the average bandgap of the alloy for all thicknesses.

2.4.2 The C excitonic feature

The results corresponding to the values of the individual measurements of the C exciton, plotted against the number of layers of the selected region for all of the alloying degrees in this study, can be seen in Figure 2.15a. The average value of these measurements of the C exciton for each number of layers can also be seen in this figure.

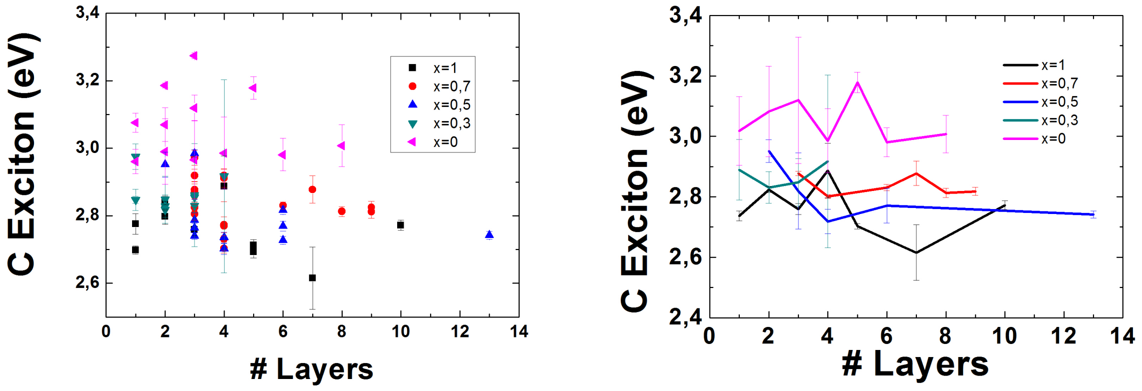

(a) (b)

Figure 2.15: *a) Individual measurements of the position of the Gaussian fit corresponding to the C exciton for different number of layers and different alloying degrees. b) Average measurements of the position of the Gaussian fit corresponding to the C exciton for different number of layers and different alloying degrees.*

The results show a somewhat clear tendency from the C exciton to decrease with the number of layers for a specific alloying degree. This behaviour seems to be more evident for some alloying degreees than for others. As for the general behaviour with the alloying degree, the position of the C exciton seems to decrease with the alloying degree as well.

2.4.3 α Van Hove Feature

The measurements corresponding to the position of the Gaussian fit assigned to the α Van Hove feature can be seen in Figure 2.16

The average results seem to confirm what the individual measurements seem to indicate. The results for a low number of layers seem to show a slight decrease for lower values of the alloying degree. Besides that, there is a general, albeit slight, increase of the α Van Hove feature with the number of layers. As for the variation of this feature with the alloying degree, it seems to go down as the alloying degree goes up. However, within this trend, the only thing we can

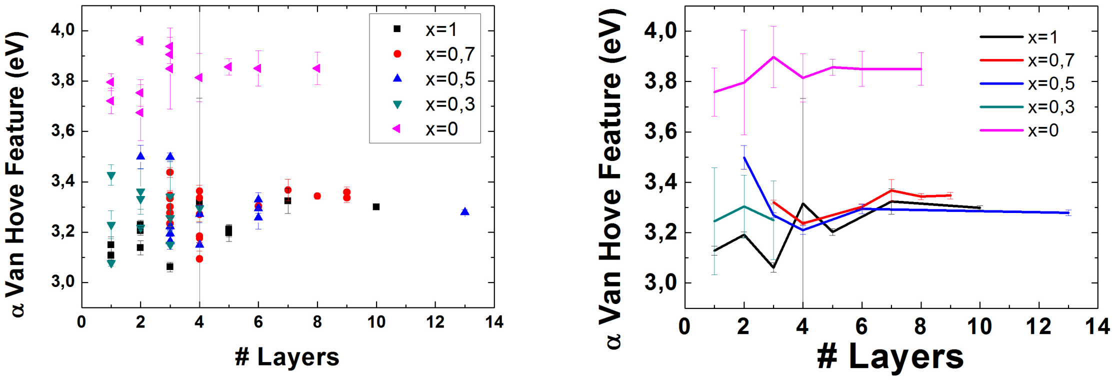

(a)

(b)

Figure 2.16: *a) Individual measurements of the position of the Gaussian fit corresponding to the α Van Hove feature for different number of layers and different alloying degrees. b) Average measurements of the position of the Gaussian fit corresponding to the α Van Hove feature for different number of layers and different alloying degrees.*

assure taking into account our error propagation is the great difference in this value between WS_2 and the rest of the alloys.

2.4.4 β Van Hove Feature

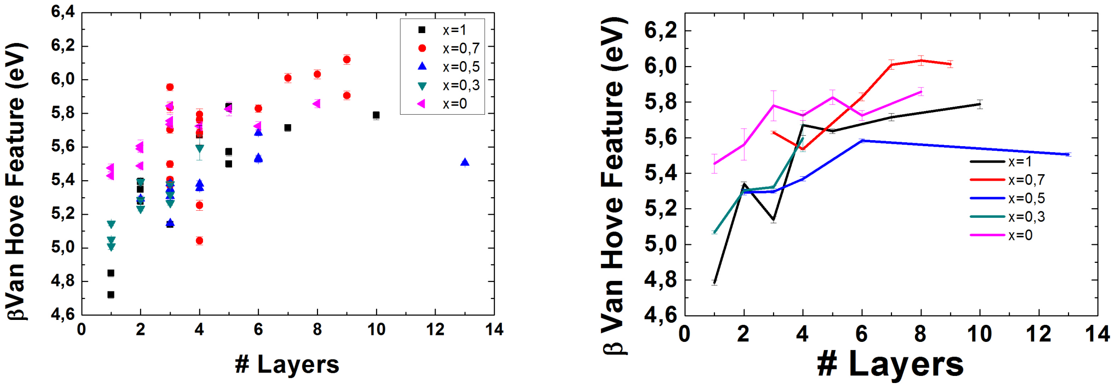

(a)

(b)

Figure 2.17: *a) Individual measurements of the position of the Gaussian fit corresponding to the β Van Hove feature for different number of layers and different alloying degrees. b) Average measurements of the position of the Gaussian fit corresponding to the β Van Hove feature for different number of layers and different alloying degrees.*

For this feature, whether we focus on the individual measurements or the average values, it is pretty straight-forward to see that there is an increase on the value of the β Van Hove feature as the number of layers increases. However, in this case, it is not as easy to discern the behaviour of this feature with the alloying degree of the sample. This can be due to the setting of a specific width for the Gaussian fitting this feature. The other possible explanation is that this feature changes abruptly with the alloying degree several times, so the aforementioned explanation seems more plausible.

2.5 Theroetical modelling

Preliminary GW-BSE calculations on this subject have been performed by our collaborators L. Wirtz and E. Torun from the University of Luxembourg, calculating the density of states for monolayer, bilayer and trilayer MoS_2 and WS_2, as well as modelling the LL-EEL spectra for these cases.

The results of these calculations can be seen in Figures 2.18 and 2.19

There are two main points of interest for these calculations when comparing them to our experimental results. First, the modelling of the band structure of MoS_2 and WS_2 confirms that the C excitonic feature that we have measured corresponds to the sum of several contributions, highlighted in figures 2.18 and 2.19.

The second important point relates to the simulation of the EEL spectra in the calculations. As we can see, the C excitonic feature in the model seems to decrease as the number of layers increases, which further confirms our experimental results.

2.6 Discussion

There are several points of discussion when it comes to this study, that we can group up in experimental discussion and analytical discussion.

When it comes to the data analysis, there are several issues that come to mind. First of all, we do not have a measurement of the extinction distance for the plasmonic resonances taking place at the edges of the alloys, so our choice of spectra to integrate is an estimate that these resonances only span in a non-negligible way over a few nanometres.

When it comes to the analysis of the data using the triple Gaussian fit, it is clear that, even though this approach is more complete than the analysis using only two Gaussians, there are still some issues with this new analysis. This is manifested in the relative behaviour of the C exciton and the α Van Hove feature as we increase the number of layers. even though the general behaviour of the C exciton is a slight decrease and the general behaviour of the α feature is a slight increase, if we compare the two sets of data side-by-side, it seems like their behaviour is somewhat correlated. This could be due to our resolution being just good enough to gather data using a 3 Gaussian fit but not good enough to actually be able to discern the specific behaviour of the C exciton and the α feature as we increase the number of layers.

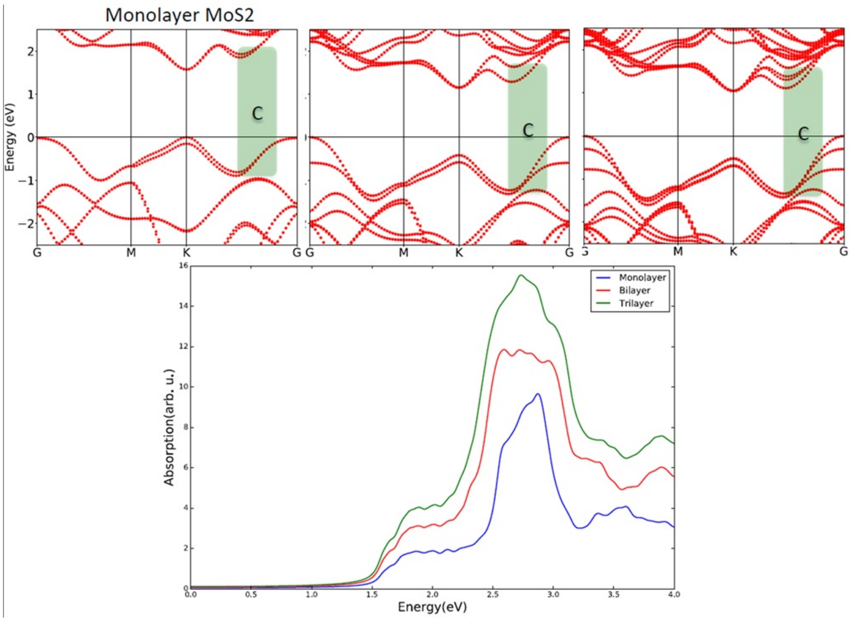

Figure 2.18: *Top: band structure modelling for monolayer (left), bilayer (centre) and trilayer (right) MoS_2. The contributions to the C excitonic feature are highlighted. Bottom: Simulated EEL spectra for monolayer, bilayer and trilayer MoS_2 including the C excitonic feature.*

[h!]

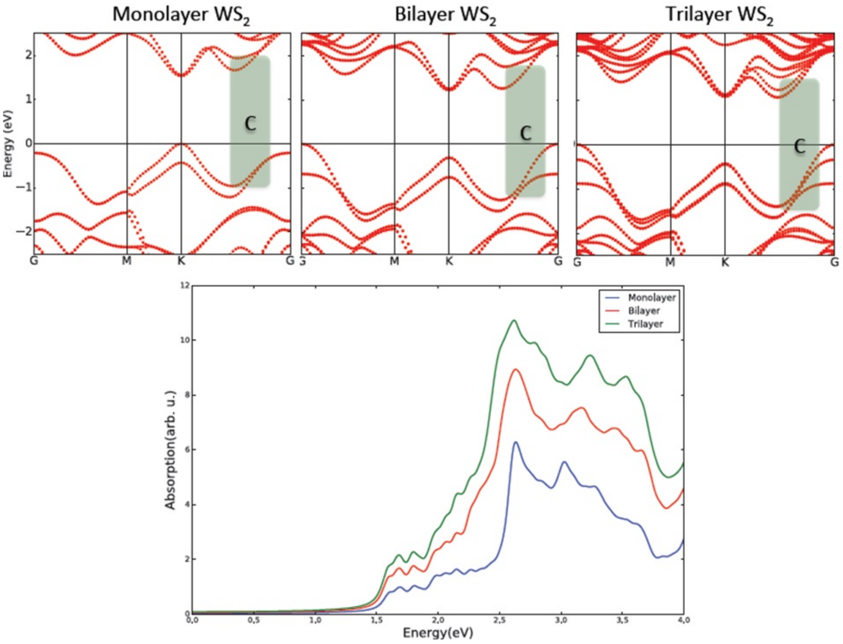

Figure 2.19: *Top: band structure modelling for monolayer (left), bilayer (centre) and trilayer (right) WS_2. The contributions to the C excitonic feature are highlighted. Bottom: Simulated EEL spectra for monolayer, bilayer and trilayer WS_2 including the C excitonic feature.*

2.7 Conclusion

In these works, we have succesfully managed to delve into the optoelectronic properties of $Mo_xW_{1-x}S_2$ alloys, more specifically its optical gap, a feature related to excitonic transitions (that we have called C) and two features related to discontinuities in the density of states (α and β van Hove features, respectively).

The most interesting results are arguably those on the optical bandgap, which have been obtained using a direct measuring method by aloof EELS. The average results for the bandgap seem very coherent with what the bibliography stated on the matter [218], although our values are lower, which is coherent since we are measuring the band gap onset and not the A exciton peak, which rules the bandgap. The results show a decrease in the band gap from x=1 to x=0.7 (with x being the alloying degree) and a continous increase in the band gap value from x=0.7 to x=0. This provides a guide for the tuning of the band gap in this kind of alloys.

The behaviour of the gap with the number of layers remains unclear, although for a specific number of layers our studies suggest that the behaviour follows the same patterns as the average behaviour for any number of layers.

When it comes to the C exciton features, which come from different excitonic transitions, the results within a specific alloying degree show a somewhat clear tendency for these features to decrease with the number of layers in the sample. The average position of the C exciton signature for each alloy seems to show a tendency for these features to decrease as the Mo content in the sample increases. Both of these results seem to be supported by the preliminar theoretical modelling on the matter.

The α van Hove feature seems to have a slight decrease for alloys high in Mo as the number of layers go up. For the other alloys, there is a general increase of this feature with the number of layers. Regarding the average variation of this feature with the alloying degree, the average value for WS_2 is remarkably higher compared to the rest of the alloys.

Regarding the β van Hove feature, for any alloying degree, the value for this feature increases with the number of layers. However, probably due to this variable character within each alloy, it is not possible to discern as clearly how the average value of this feature behaves as a function of the Mo content.

3

High aspect-ratio Au nanostructures: Plasmonic studies via EELS

> *"It is during our darkest moments that we must focus to see the light."*
>
> – Aristotle

The possibility of studying plasmons (collective vibrations of charge) using EELS has been introduced in Chapter 1. This field of study, related to the interactions of light and matter, has developed importantly during the past years, mainly for their applications on sensing [259] and photovoltaics [260].

The field of study regarding the properties of new plasmonic nanostructures is an evolving one, and EELS can play an important part in these studies. However, some structures can be challenging when it comes to the analysis of the EEL spectra.

Here we delve into the plasmonic properties of novel high aspect-ratio Au nanostructures, fabricated using templated electrodeposition and laser irradiation. These samples are challenging in terms of EELS analysis. We propose a method involving custom-scripted background removals and multi-variate analysis to show how the qualitative plasmonic analysis in these samples can be improved, and, potentially, how this could be applied to other microscopy systems.

The plasmonic behaviour of these samples has also been modelled using DDEELS. A comparative study between the modelled and the experimental data, as well as some drawn conclusions with respect to the differences between the two, is shown in this study.

3.1 Introduction

This section may serve as a theoretical introduction, as well as a historical context review, for most of the concepts appearing on this chapter related to plasmonics. We focus especially on the subject of this study, that is, localised surface plasmon resonances, or LSPRs and, to a lesser extent, surface plasmon polaritons (SPPs). The application for these two phenomena is shown, with special attention to SERS and waveguiding. Finally, the main motivation for this study, a previous work that encompasses LSPRs and SPPs for remote sensing, is put into context.

3.1.1 Plasmonics: a novel antique field

This study is focused on plasmonics, a field of study that got its name a little over twenty years ago. As one of the authors of the presentation where it was coined stated in [261]:

> *[...] The term "plasmonics" was coined for a promising new device technology that aims to exploit the unique optical properties of metallic nanostructures to enable routing and active manipulation of light at the nanoscale.*

This term was, in fact, coined at a conference presentation on the MRS symposium in Boston, USA[262]. However, it is a subject that got started a long time before that, with first reports of plasmonic activity being reported more than a century before [263, 264].

Even though plasmonics is considered a rather novel field, first reports of what we know now to be a plasmonic behaviour were first noted by Faraday in 1857, when he was studying on the ondulatory character of light and its interactions with gold and other metals [265]. However, at the time there was not a correct explanation for this phenomena, nor was there for studies showing plasmonic effects even 50 years later, such as the one by Wood in 1902 where he tried to make sense of the distribution of light after reflecting on a grated surface [266]:

> *It is a well-known fact that in the spectra formed by a diffraction-grating the light is unevenly distributed, that is the total light in any one spectrum will not recombine to form white light. I have been examining a most remarkable grating recently [...]in which this uneven distribution is carried to a degree almost incomprehensible. If the spectra of an incandescent lamp are viewed directly in the grating without any other optical appliance, at certain angles of incidence perfectly sharp monochromatic images of the filament appear in different parts of the first order spectra. Sometimes these images are nearly black, and sometimes they are far brighter than the rest of the spectrum. [...] Under certain conditions the drop from maximum illuinination to minimum, a drop certainly of from 10 to 1, occurred within a range of wave-lengths not greater than the distance between the sodium lines.*

The mathematical description of surface waves was established by Sommerfeld a few years later, by explaining the behaviour of radio waves propagating along the surface of a conductor (along a wire) following previous works by Hertz [267]. Around the same time, Mie developed an analytical solution to Maxwell's equations for the specific case of the scattering and absorption of light by particles of a diametre smaller than the wavelength of said light [268], which will be discussed in depth in Section 3.1.2.

However, it would take a long time before the experimental and the theoretical work were connected, more than thirty years later, in the theory shown in the study of Fano in 1941. This publication consisted on trying to explain Wood's diffraction gratings using quasi-stationary waves on metallic surfaces, in other words, Sommerfeld's "surface waves" [269].

Around this time, studies involving interactions between metallic surfaces and electron beams started to increase, and electron energy loss phenomena were recorded at metallic surfaces by Ritchie in 1957 [270]. This is an extensive analysis that had electron energy loss at its core, much like the study explained here. A deeper explanation of this study can be seen in Section 3.1.2. However, it would not be until ten years later [271] that this was related to the grating studies started by Wood more than sixty years before. With this, along with other important studies on the matter around the same time [272, 273], the field of plasmonics started to become more of a unified field as we know it today.

The applications of plasmonics evolved until becoming an important part of the field of nanophotonics, which focuses on the confinement of electromagnetic fields on structures on the order of or smaller than its wavelength [263, 274, 153]. In this sense, nowadays this discipline finds applications in fields such as medicine [275], photovoltaics[260], sensing[259, 276] and spectroscopy [277, 278].

Explained the most succint way possible, plasmonics is the discipline focused on the study and applications of plasmons and their different effects. Plasmons are commonly defined as collective vibrations of charge within a certain material, most commonly but not limited to noble metals. These vibrations can occur for the whole of a certain nanostructure (bulk plasmons) or at the interface between a metal and a dielectric medium (surface plasmons). The work of the study presented on this chapter is focused on the latter.

To understand the notion of what a plasmon is, it is important to explain the concept of electron sea. In this regard, the subatomic structure of metals can be described as a somewhat rigid lattice of cations embedded in a sea of delocalised conduction electrons (also called the plasma sea) [263]. A plasmon can be interpreted simply as an oscillation of this electron sea, whtere the incident electic force (which can come from different electromagnetic sources such as light or an electron beam) act as a driving force, and the coulombic attraction from the cations in the metal act as a restoring force.

The free electron gas model: Volume plasmons

The electrons in the plasma sea oscillate in response to an applied electromagnetic field E, and their motion is damped by collisions of this very electrons, occurring at a specific frequency $\gamma = 1/\tau$, where τ is the relaxation time of the free electron gas [263]. When it comes to the motion of a specific electron of mass m on the plasma sea, we can describe its motion as:

$$m\ddot{x} + m\gamma\dot{x} = -e \cdot E \tag{3.1}$$

Assuming a harmonic time dependence of the electric field, $E(t) = E_0 \cdot e^{-i\omega t}$, from there we can deduct the oscillation equation for the motion of the electrons:

$$x(t) = \frac{e}{m(\omega^2 + i\gamma\omega)} \cdot E(t) \tag{3.2}$$

From here we can calculate the polarization produced by the isplacement of a specific electron, given by $P = -n \cdot e \cdot x$. Since we know from basic electromagnetism that $D = \varepsilon_0 E + P$:

$$D = \varepsilon_0 E - \frac{ne^2}{m(\omega^2 + i\gamma\omega)} \cdot E = \varepsilon_0 \cdot E \cdot \left(1 - \frac{ne^2}{m\varepsilon_0(\omega^2 + i\gamma\omega)}\right) = \varepsilon_0 \cdot E \cdot \left(1 - \frac{\omega_p^2}{\omega^2 + i\gamma\omega}\right) \tag{3.3}$$

With $\omega_p = \sqrt{\frac{ne^2}{\varepsilon_0 m}}$ being the *plasma frequency* of the free electron gas. Knowing that the complex dielectric function $\varepsilon(\omega)$ is defined as $\frac{D}{\varepsilon_0 E}$, we can easily deduce the value for this property:

$$\varepsilon(\omega) = 1 - \frac{\omega_p^2}{\omega^2 + i\gamma\omega} \tag{3.4}$$

Where the term $i\gamma\omega$ is taken as negligible for high values of relaxation time.

When it comes to EELS, we can translate this expression in terms of energies, using the relation $E = \hbar\omega$:

$$\varepsilon(E) = 1 - \frac{E_p^2}{E^2 + i\gamma E} \tag{3.5}$$

Where E_p is the characteristic *bulk/volume plasmon energy.*

3.1.2 Surface plasmons, LSPRs and SPPs

The subject of this study is a specific kind of plasmonic resonances. We have talked about plasmons in Section 3.1.1 as collective oscillations of electrons inside a metallic material. However, there is a particular kind of plasmonic modes that is characteristic of an interface between a metallic material and a dielectric material [279, 280].

These excitations were first theoretically identified by Ritchie in 1957 [270]. This study was trying to make sense of energy losses in fast electrons that were occurring at energies different to the *"plasma energy"* of the material in question (which would be the energy related to the bulk plasmon in modern terms) in previous energy loss studies, such as the one shown in reference [281]. In this previous study, they had assigned these features in the energy loss spectrum as possibly due to interband transistions in the material being studied.

Describing the conduction electrons in metals using hydrodynamical equations, Ritchie showed that, for very thin films, energy losses could indeed be found at an energy values lower than the bulk plasmon energy. However, it would not be until 1959 that Powell and Swan confirmed these surface plasmons [272] (named by Stern and Ferrell for their being *"surface plasma oscillations"*[282]). The technique used for the experimental confirmation of this plasmons was, indeed, electron energy loss spectroscopy.

Powell and Swan used EELS from electrons reflected on thin films of aluminum, which had been a heavily extended material for low-loss EELS studies. Their spectra, showing what we know today as a surface plasmon feature and a bulk plasmon feature, can be seen in Figure 3.1

As it can be seen in the figure, there was a set of two very distinctive features at low energies, one at 10.3 eV and another one at 15.3 eV. It was known at the time that the bulk plasmon energy of the sample was causing the latter feature. As for the feature at lower energies, studies were performed where they measured the energy loss related to the bulk plasmon and this second feature at different thicknesses, finding a variation on the ratio between both energy losses as the thickness changed. Even though they had not been the first ones to find features at energies lower than the bulk plasmon, they were the first ones to interpret this feature and to correlate it to some sort of surface effect in the sample.

In terms of energy, on the interface of materials with opposite sign Re[ε] and for the case of high relaxation times, we can deduce the frequency for the surface plasmon resonance from their bulk plasmon resonance, using the continuity rules on the interface between the plasmonic material and the medium [263]:

$$\omega_{sp} = \frac{\omega_p}{\sqrt{1+\varepsilon_m}} \tag{3.6}$$

Where ω_{sp} is the surface plasmon resonance frequency of the interface, ω_p is the bulk plasmon frequency of the plasmonic material, and ε_m is the imaginary part of the dielectric constant in the medium. For samples measured in vacuum, $\varepsilon_m = 1$ and $\omega_{sp} = \frac{\omega_p}{\sqrt{2}}$.

When a surface plasmon is confined to a nanostructure presenting a size that is comparable to the wavelength of light in at least one of its dimensions, the free conduction electrons in the nanostructure participate in collective, stationary oscillations. These type of oscillations are called localised surface plasmon resonances (LSPR) [283]. This is the kind of resonances that our study is focused on.

Surface Plasmon Polaritons

Now that we have established a somewhat general definition of what a surface plasmon is, it is time to define what is known as surface plasmon polaritons or SPPs.

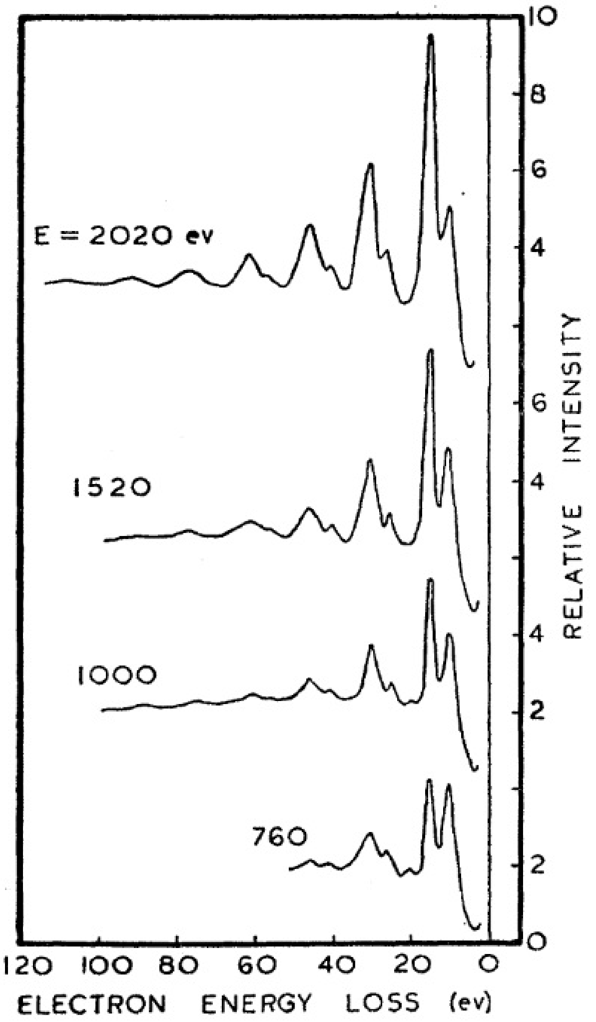

Figure 3.1: . *Original EELS spectra in the study by Powell and Swan. This figure shows the EELS spectra from beam energies of 760, 1000, 1520 and 2020 eV. The ZLP has been adjusted in each spectrum to 25 units to normalise all spectra. Source: Powell et al [272].* **Note to the reader: these spectra are shown as they were plotted in the original source, which means the energy loss axis is mirrored with respect to the current way of plotting this kind of spectra. Please take this into account.*

In general lines, SPPs are defined as the coupling between surface plasmons and their resulting confined electromagnetic field, here called polariton. This confinement appears in the direction perpendicular to the interface between the metal and the dielectric, has an evanescent character and can propagate non-radiatively along the aforementioned interface [284]. The length of this propagation will depend on several parameters, such as the dielectric constants of the metal and the medium it shares its interface with, as well as the geometry of said interface and even the temperature at which it is kept [285]. This propagation length has been extensively calculated for metals such as gold and silver at different energies [286, 287, 288]. Within the visible spectrum, the values of this propagation length are generally in the micrometres for gold and silver, which is generally orders of magnitude over the typical size for nanostructures.

This phenomenon is the one responsible for EELS being able to image plasmonic modes and study their dispersion. The dispersion relation (Energy vs moment) for plasmonic nanostructures has been studied as well for several different nanostructures, namely nanoparticles [289] and nanowires[288], which is of great importance for our works. One of this examples in the literature [287] shows a general dispersion relation for different studies performed on Au NW, which can be seen in Figure 3.2.

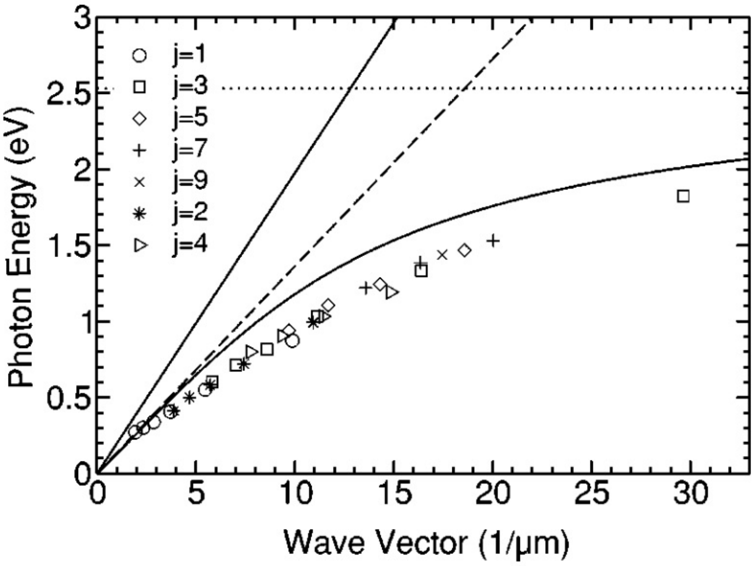

Figure 3.2: *SPP dispersion relations for Au. Solid line: light line in vacuum. Dashed line: light line in quartz glass. Solid curve: SPP of a thin gold layer on a flat quartz surface. Dotted line : limiting frequency* ω_{sp}*. Symbols: experimental wavevectors for Au NW,* w_z *= 91 nm, h= 17 nm. Wave vectors for the symbols are calculated as* $j \times \pi / w_y$*. Source: Schider et al [287].*

As we can see, the E-k dispersion of Au NW is close to the surface dispersion of a Au planar surface, with a linear beginning for small wavevectors that separates further away from the light line the closer we are to the surface plasmon energy ω_{sp}. This will be of interest for the interpretation of our results.

3.1.2.1 Localised Surface Plasmon Resonances

Within the surface plasmonic resonsances, LSPR are the ones that conform the subject of our study. We have seen in the section above that SPPs are propagating electromagnetic waves coupled to the plasmons of a conducting material. LSPRs, on the other hand, are stationary excitation of the conduction electrons of this material.

Both for the case of SPPs and LSPRs, we can differenciate between two different kinds of modes:

- On the one hand, we have the modes where the coupling between the electromagnetic waves and the plasmons of a conducting material does not need a momentum transfer. This is the kind of modes that can be activated using light.

- On the other hand, we have the modes where this coupling needs a momentum transfer from the electromagnetic wave to the plasmons in the material. This can only be achieved using charged particles as the source of our electromagnetic wave, and these modes cannot be accessed using light, hence why they are called dark modes.

The distribution of LSPR modes, as well as their resonant energy, depend on the structure of the plasmonic device in question, its composition and environment [290]. Here we present an approximation for the behaviour of these LSPRs that explain how they can be used for some of their applications.

The Mie theory: a brief approach to plasmonic scattering in nanoparticles

It is of interest to explain the plasmonics in nanoparticles and their relation to external parametres in order to better understand both the phenomena taking place and the potential application this field of study has.

This theory assumes a plane wave incident on a homogeneous metallic sphere.Mie theory defines the total scattering (σ_{sca}), extinction(σ_{ext}) and absorption (σ_{abs}) cross-sections of light as follows [283, 268]:

$$\sigma_{\mathrm{sca}} = \frac{2\pi}{|k|^2} \sum_{L=1}^{\infty} (2L+1) \left(|a_L|^2 + |b_L|^2 \right) \tag{3.7}$$

$$\sigma_{\mathrm{ext}} = \frac{2\pi}{|k|^2} \sum_{L=1}^{\infty} (2L+1) \left[\mathrm{Re}\,(a_L + b_L) \right] \tag{3.8}$$

$$\sigma_{\mathrm{abs}} = \sigma_{\mathrm{ext}} - \sigma_{\mathrm{sca}} \tag{3.9}$$

where k is the wavevector of the incoming wave and L are integer numbers representing the multipoles of the scattering. In the above expressions, a_L and b_L are parameters that include Riccati-Bessel functions dependent on m (where $m = \tilde{n}/n_{\mathrm{m}}$, where $\tilde{n} = n_{\mathrm{R}} + in_{\mathrm{I}}$ is the complex refractive index of the material, and n_{m} is the real refractive index of the surrounding medium) and x ($x = k_{\mathrm{m}}r$, where r is the radius of the particle). In this context, $k_{\mathrm{m}} = 2\pi/\lambda_{\mathrm{m}}$ is defined as the wavenumber in the medium.

In order to simplify these expressions, a power approximation has been done for a nanoparticle of a size considered very small in comparison to the wavelength of the inciding wave, $x << 1$. This yields a much simpler expression for a_L and b_L. By taking only terms up to x^3, the terms b_L are approximated by zero, as are all a_L with $L > 1$. The term a_1 takes the form:

$$a_1 \approx -\frac{12x^3}{3} \frac{m^2 - 1}{m^2 + 2} \tag{3.10}$$

we can obtain an expression of a_1 as a function of the complex metal dielectric function $\tilde{\varepsilon} = \varepsilon_1 + i\varepsilon_2$. Given our previous definition of m, and the relations $\varepsilon_1 = n_{\mathrm{R}}^2 - n_1^2$, as well as $\varepsilon_2 = 2n_R n_1$ and $\varepsilon_m = n_{\mathrm{m}}^2$, the expression for a_1 is as follows:

$$a_1 = \frac{2x^3}{3} \frac{-i\varepsilon_1^2 - i\varepsilon_1\varepsilon_m + 3\varepsilon_2\varepsilon_m - i\varepsilon_2^2 + i2\varepsilon_m^2}{\left(\varepsilon_1 + 2\varepsilon_m\right)^2 + \left(\varepsilon_2\right)^2} \tag{3.11}$$

By substituting this into equation 3.8, and taking only the dipolar term, we obtain the very well known formula for the extinction cross-section for nanoparticle plasmon resonances :

$$\sigma_{\mathrm{ext}} = \frac{18\pi\varepsilon_{\mathrm{m}}^{3/2}V}{\lambda} \frac{\varepsilon_2(\lambda)}{\left[\varepsilon_1(\lambda) + 2\varepsilon_{\mathrm{m}}\right]^2 + \varepsilon_2(\lambda)^2} \tag{3.12}$$

Now, these concepts might seem a bit apart from the main subject of this chapter, but they are essential to understand one of the main applications of LSP resonances: estimation of the dielectric function in dielectric media using the analysis of the plasmonic resonances.

Even though this approximation is taken for small particles, it has been experimentally quantified that the predictions related to dielectric sensitivity (which will be discussed in this section when talking about applications) are still accurate for bigger sizes [291].

Applications of SPPs and LSPRs

According to the bibliography [292], there are five main characteristics that have attracted interest to surface plasmons from an application point of view: their concentration of light beyond the diffraction limit their potential to modify the local density of photonic states as well as the local electric field, their envireomental sensitivity to the refraction index of the medium the samples are in (among others), as well as their flexibility in design, which has been a source of constant growth in this field and will be delved into in Section 3.1.4.1.

Refractive index sensitivity As it has been explained in this section, LSPR phenomena are heavily dependent on the refractive index both of the material conforming the plasmonic nanostructure, as well as the refractive index of the surrounding medium. It can be inferred from this that, by studying the LSPR of a certain interface and knowing the refractive index of our nanostructure, it is possible to discern the refractive index of the surrounding medium. This brings up one of the main applications of LSPR: Refractive index sensing[283].

The LSPR mode in a nanoparticle will appear at the energy corresponding to the wavelength λ that maximises equation 3.12. This will happen when the denominator in the equation is minimised. By derivating this denominator, we can find out that the resonance condition for these modes is $\varepsilon_1 = -2\varepsilon_m$.

In the Drude model, explained in this section there is a frequency-dependent way to express the real part of the dielectrical constant of the material conforming our nanostructure (ε_1) as a function of the plasma frequency of the material and a damping parametre γ, that is negligible for the energy range in this study:

$$\varepsilon_1 = 1 - \frac{\omega_p^2}{\omega^2 + \gamma^2} \approx 1 - \frac{\omega_p^2}{\omega^2} \tag{3.13}$$

by applying the resonance condition $\varepsilon_1 = -2\varepsilon_m$, we obtain a set of equivalent equations, one for predicting the resonance frequency if the dielectric constant of a medium is known, and another one to discern said dielectric constant, and hence the refraction index of a medium, by measuring the resonance frequency of the LSP resonances:

$$\omega_{\max} = \frac{\omega_{\mathrm{P}}}{\sqrt{2\varepsilon_{\mathrm{m}} + 1}} = \frac{\omega_{\mathrm{P}}}{\sqrt{2n_{\mathrm{m}}^2 + 1}} \tag{3.14}$$

$$n_m^2 = \varepsilon_m = -\frac{1}{2} \cdot \left(1 - \frac{\omega_p^2}{\omega_{\max}^2}\right) \tag{3.15}$$

Due to this possibility of measuring the refraction index of a medium, this has become one of the biggest applications for LSP resonances.

Surface-Enhanced Raman Spectroscopy Raman scattering is a widely known type of vibrational spectroscopy. In this type of spectroscopy, the Raman spectra are related to the molecular structure, the composition and the geometry of the analyte in question [276]

One of the main drawbacks for Raman spectroscopy is that it has quite a low yield, more than 10 orders of magnitude lower than other similar analytical techniques such as fluorescence[293].

This means that regular Raman spectroscopy is not suitable for the detection of molecules in low concentrations.

The dipole moment induced by the Raman scattering of light is proportional to the amplitude E of the electric field used to excite these photoelectric species:

$$P = \alpha \cdot E_{applied} \tag{3.16}$$

With α beint the polarisability of the material. The intensity of the Raman signal is defined as the square of this dipole moment.

This is where LSPR comes into place. As we have seen in Section 3.1.2, in the case of surface plasmons there is an enhancement of the amplitude of the electric field close to the interface between the metal and the medium. This has an effect on the photoactive species that are close to the surface of the nanoparticle, enhancing their Raman signal.

This effect, name surface-enhanced Raman spectroscopy, or SERS, was first discovered by Fleischmann and his coworkers in 1974 [294]. It has been since then one of the main applications of LSPRs [295, 278, 276, 296, 297]

Generally speaking, there are two main phenomena taking place in SERS: the enhancement of the incident electric field at the vicinity of the plasmonic nanostructure and the enhancement of the Raman scattering, also called re-radiation.

In the case of LSPRs, previous literature [296] shows a proportionality between the incident electric field on a plasmonic surface E_0 and the electric field at the surface of a metallic sphere:

$$E^2 \propto E_0^2 \left| \frac{\varepsilon_\mathrm{m} - \varepsilon_0}{\varepsilon_\mathrm{m} - 2\varepsilon_0} \right|^2 \tag{3.17}$$

with ε_m the wavelength-dependent dielectric constant of the material in the plasmonic device.

Provided we excite a plasmonic structure with an electric field of amplitude E_0, the local electric field at the surface of the plasmonic structure E_{LOC} will be proportional to this incident electric field, with an enhancement factor that will depend on the excitation wavelength λ_0 since ε_m is wavelength-dependent:

$$E_{LOC} = f(\lambda_0) \cdot E_0 \tag{3.18}$$

Now, considering this is the situation where the first Raman phenomenon occurs, the photoactive species close to the surface of the nanostructure will be excited by this enhanced local field E_{LOC}. As a result, these analytes will produce a Raman scattering at a shifted wavelength, λ_R. The amplitude of the Raman scattering can be calculated by applying equation 3.16:

$$P = \alpha \cdot E_{LOC} = \alpha \cdot f(\lambda_0) \cdot E_0 \tag{3.19}$$

At this point, a second process takes place. The Raman scattered light can interact with the plasmonic nanostructure in the same way as our incident radiation. We follow what has been explained in equation 3.18, but taking several things into account. First of all, now the incident field is $P = \alpha \cdot f(\lambda_0) \cdot E_0$. Second, the Raman scattering has a different wavelength λ_R and therefore a different enhancement factor $f(\lambda_R)$:

$$E_{SERS} = f(\lambda_R) \cdot f(\lambda_0) \cdot \alpha \cdot E_0 \tag{3.20}$$

And since $I_{SERS} = E_{SERS}^2$ and taking into account that I_0 is the original Raman intensity, $I_0 = \alpha^2 \cdot E_0^2$,

$$I_{SERS} = f^2(\lambda_R) \cdot f^2(\lambda_0) \cdot \alpha^2 \cdot E_0^2 = f^2(\lambda_R) \cdot f^2(\lambda_0) \cdot I_0 \tag{3.21}$$

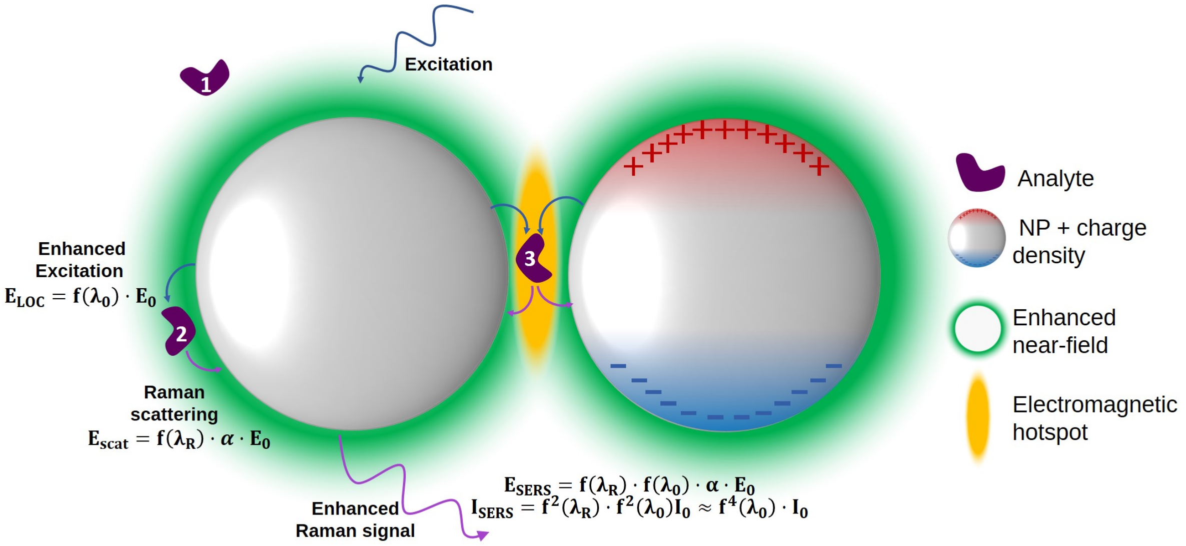

Figure 3.3: *Adapted from [264]and [276].*

A scheme of the working principle of this technique can be seen in Figure 3.3.

A particular case of this phenomenon is the study of the molecules located in areas like the one marked in yellow in Figure 3.3. Because this area has a combination of the enhanced local field of both the nanoparticles around it, it is what is called an ”electromagnetic hot spot”. Molecules in this region will have an even greater Raman signal [298].

Waveguides and remote sensing As it has been said in Section 3.1.2, SPP are propagative in nature. In other words, structures that control this propagation can be used as light waveguides with a smaller size than the wavelength of the light they are propagating. This has been an extensive application for plasmonics throughout the years [299].

By combining structures that allow the propagation of an SPP forth and back along a certain axis, and the combination of these structures with closely located photoactive species, it is possible as well to use this sub-wavelength wave-guiding for remote sensing. In this context, remote sensing would apply to a sensing mechanism where the photoactive species is not located at the point where the signal measurement is being taken, yet the signal measured at said point comes from the photoactive species. It is also possible to create remote switches, where SPPs trigger a certain phenomenon, like the remote activation of catalytic reactions shown in reference [21].

A good example for this kind of application is shown in our collaborative study in Section 3.1.5 [300]. As it is seen in that study, this waveguiding, as well as the remote sensing applications, can be coupled with other plasmonic applications such as SERS. This study serves as a base for the works presented in this chapter.

3.1.3 STEM-EELS, a tool for spatially localised plasmonic analysis

As we have seen in Section 3.1.2, EELS had been a technique for the study of plasmons even before the discovery of surface plasmons, and played a key role on the experimental confirmation of the existence of surface plasmons by Powell and Swan[272]. However, there is a key aspect of this kind of spectroscopy that makes this technique, along with cathodoluminescence (spectroscopy performed on the photons that are emitted from the sample when said sample is under an electron beam)[280], two of the most promising techniques for the study of the spatial distribution of different plasmonic modes.

As it has been reported in chapter 1, the combination of STEM and EELS allows the study of localised excitations, being able to achieve a sub-nanometric spatial resolution and an energy resolution that can go down to a few meV [223, 301]. As we have seen in Section 3.1.2, the study of this distribution can provide further information on the plasmonic device being imaged. On top of this, as we have seen in section 3.1.2, there are certain modes (dark modes) that precise a momentum transfer from the exciting electromagnetic waves and therefore can only be imaged using charged particle beams.

There are studies dating back to 1980 describing the measurement of surface plasmons on nanoparticles using STEM-EELS [302], and even on the coupling effects of several nanoparticles [303]. However, these studies, as well as the ones that followed for two decades, focused more on the spectroscopic component of the plasmonic behaviour and deduced from it. The main constraints for these experiments were, on the one hand, the lack of monochromaticity of the beam, which resulted on a larger ZLP and therefore made the analysis of the peaks at low energy (where surface plasmon resonaces appear) [58] much more challenging. In addition, the field of plasmonics had not yet flourished along with all its possible applications. Finally, there were some aberrations that had to do with the EELS detector that also played a part on the inaccuracy of the results.

With this in mind, the STEM-EELS technique was improved over the years, and in time, several EELS measurements could be performed on the same sample, thus being able to differenciate different sections of the same nanostructure [304]. A few years later, the first studies mapping the energy loss at low losses coming from Ag nanotriangles [305, 306] (see Figure 3.4)as well as different geometries of Ag NP[307](see Figure 3.5). This, in and of itself, provided a new tool for the analysis of surface plasmons that offered a unique advantage to it: the possibility to study the electric field perturbations caused by LSPRs in nanostructures at a lower scale than the size of said nanostructures. In other words, this provided a tool for the measurement of the spatial distribution of the different LSPRs within a single nanostructure.

As we can see in Figure 3.5, this tool provides information about all the different types of plasmonic resonances taking place in the sample (the Ag NP in this case) simultaneously, whether they are surface longitudinal resonances, surface transversal resonances or bulk resonances. However the latter will only be visible for samples that are thin enough to be ”electron transparent” [11]. This will be of importance when explaining the study performed on this chapter. This was also a turning point for plasmonics, since EELS allowed for an analysis of the spatial distribution of all the plasmonic resonances in the sample with a single spectrum image.

STEM-EELS has even provided to be a powerful technique for the analysis of plasmonic features at the nanoscale in three dimensions, by combining the possibilities of plasmonic feature imaging of STEM-EELS with the three-dimensional analysis possibilities of electron tomography [308, 309, 310]

3.1.4 EELS, nanostructures and plasmonics

In this section we focus on the state of the art when it comes to plasmonic nanostructures, especially those that have been studied by means of STEM/EELS. for this purpose, we will focus on the different geometries that have been studied over the years, especially those that are close to the samples studied in this chapter. On a second subsection we will focus as well on the different preparation methods that have allowed the growth of plasmonics to the extent we know it today.

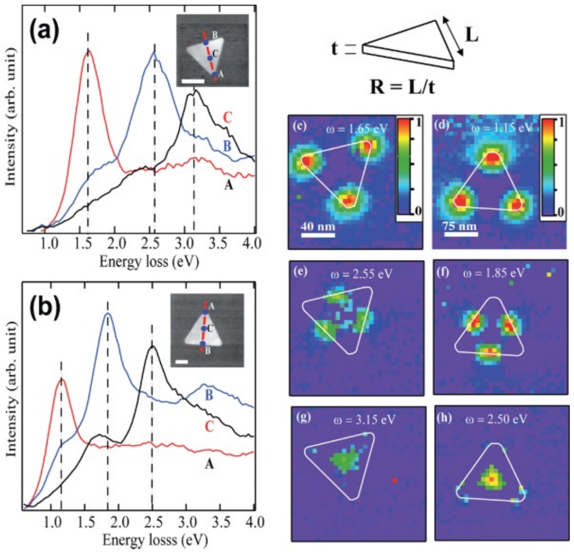

Figure 3.4: *Mapping of plasmons for two different sizes in silver nano- prisms. EELS spectra acquired at a corner (A), the middle point of an edge (B) and the center (C) of (a) a 97 nm edge-long (thickness 4 nm) (b) and a 176 nm edge-long (thickness 6 nm) nanoprisms, respectively. The corresponding insets show the HAADF images of each nanoprism and the exact positions at which the EEL data were measured. In each case, three main resonances were identified. The energies of these modes vary from one prism to another. P anels (c,e,g) present maps of the intensity distributions of the main resonances detected on the prism in (a). Similarly, panels (d,f,h) show the intensity maps of the three modes on the prism in (b) Source: Nelayah et al [306]*

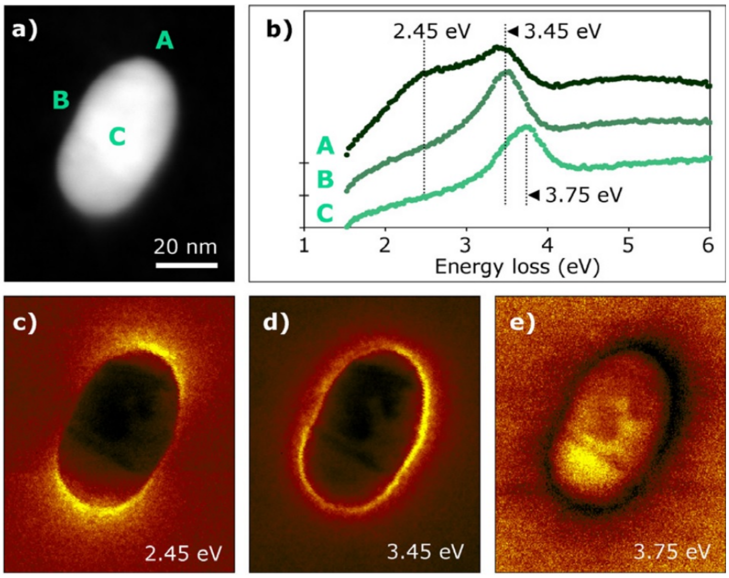

Figure 3.5: *(a) Annular dark field STEM image of an ellipsoidal silver particle. (b) Spectra from the three regions indicated in (a). (c) Map of the plasmon intensity at 2.45 eV (λ = 506 nm), showing the longitudinal resonance mode. (d) Map of the plasmon intensity at 3.45 eV (λ =360 nm), showing the transverse resonance mode. (e) Intensity map of the bulk plasmon resonance at 3.75 eV (λ =330 nm). The intensity in the last map further than about 10 nm off the ellipsoid is caused by spectral noise. Source: Bosman et al [307].*

Sample	**Material(s)**	**References**
Al voids	Al	[318]
Bypiramids	Ag, Au	[308, 316]
Chiral star-like structure	Au	[312]
Cubes	Ag	[319]
Decahedra	Au	[320]
Disks	Ag	[321]
Meta-atoms (curved antennae)	Ag, Au	[322, 323, 324]
Nanoantennae (NW and NR of a high-enough aspect-ratio)	Ag, Au	[325, 326, 327, 328]
Nanocarrots	Ag	[329, 330]
Nanospheres or short rods	Au	[331]
Other nanoparticles	Au, Mg	[317, 332]
Nanostars	Au,	[333, 334]
Nanorings	Au	[335]
Tapers	Au	[313]
Triangles	Al	[336, 337, 338, 339, 340, 341]
Hollow structures	Ag, AuAg	[309, 310]
Bimetallic structures	AuAg, AuPd	[315, 316, 342]
Coupled structures	Au, Ag	[324, 343, 344, 345, 346, 347, 348, 349, 350]
Flower-like structures	Ag/ZnO	[314]

Table 3.1: *Brief review of plasmonic nanostructures studied using EELS in the last years.*

3.1.4.1 Geometries

In the past few years, many different nanostructures have been fabricated with novel plasmonic properties. For many of these nanostructures, such as the ones presented in the previous section, EELS has been a key technique to gather a deeper understanding of their plasmonic components. A review by Kociak *et al* in 2014 gave a quite complete list of geometries of plasmonic nanostructures analysed using EELS to that date [311]. This section aims to provide a brief updated version of this list.

The initial nanostructures used for the study of plasmonic materials have been nanoparticles and nanorods, which are considered the most simple structure for this kind of study [311]. Along with new studies on this kind of structures, such the works presented here, several new geometries have been created for these studies. These structures have evolved into more and more complex structures through the development of their fabrication techniques, which we will see in section 3.1.4.2. Nowadays, structures as complex as star-like chirals structures [312], u-shaped structures[313], hollow nanoparticles [309], flower-like structures [314] or bi-metallic structures [315, 316] have increased the different properties of these plasmonic systems, hence opening new possibilities for future applications. New materials are being used as well for these structures, such as magnesium [317] or zinc oxide [314]. A comprehensive list of these different geometries, along with the materials they have been fabricated with, is shown in Table 3.1.

The applications of these recent structures have been extensive, from photocatalysis [314] to the fine-tuning of nanophotonic devices [316], hydrogen sensors [342] or wavelength tunability using new materials [332].

3.1.4.2 Preparation methods

In order to achieve this myriad of structures, several preparation methods have been needed. This methods include, but are not limited to, nanosphere lithography or colloidal lithography [335, 351], thermal synthesis [318], templated electrodeposition [300, 264] (which we will delve into in section 3.2.1, coaxial lithography [352], and chemical synthesis [315, 351], to name a few. On top of this, secondary fabrication techniques to produce core-shell nanostructures such as evaporation [353],

However, the world of plasmonics developed quite fast after the use of electron lithography to obtain different types of samples, becoming arguably the most used preparation method when it comes to plasmonic samples [353, 347, 315, 340, 332, 323]. This method offered the possibility to fabricate plasmonic devices at the nanoscale with a never before seen precision.

An additional state of the art technique used nowadays for this kind of fabrication that also offers a high amount of precission is Focused Ion Beam (FIB) [354, 355]. This technique, along with electron beam-induced deposition also offer a uniquely precise technique for the fabrication of plasmonic nanostructures.

Modification methods for nanowires: dumbbell fabrication

Much like with any other kind of nanostructures, there are methods to modify previously fabricated samples. In this sense, our works take into consideration a specific one regarding the modification of Au NW. In this sense, recent studies [356, 357] show the possibilities to modify the morphology of Au NW using laser irradiation.

These studies show that, given a certain amount of laser irradiation, the Au NW starts to melt, and if given enough energy, it can even break apart, forming an Au NP on one of the broken edges. A figure showing this change in morphology can be seen in figure 3.6

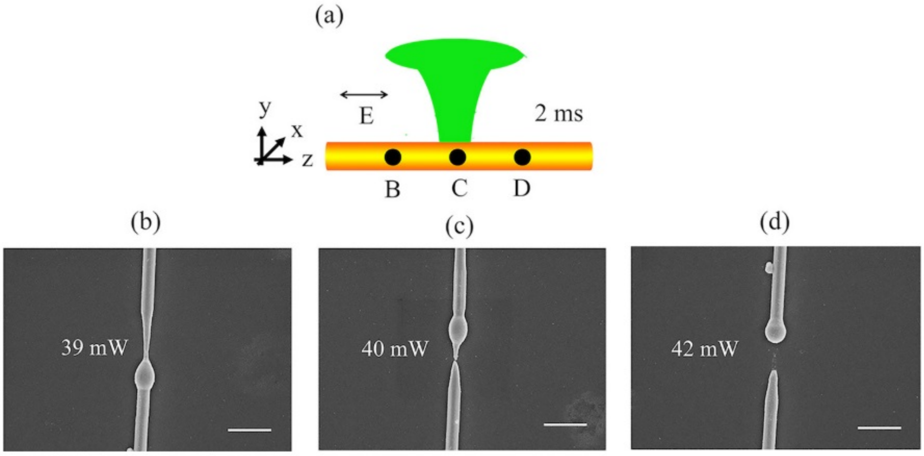

Figure 3.6: *Morphological changes undergone on a 300-nm-diameter gold NW after light irradiation using different powers (a) Scheme of a focused light irradiated on different positions. The irradiation power is (b) 39 mW (47 mJ/cm2), (c) 40 mW (48 mJ/cm2), and (d) 42 mW (51 mJ/cm2) for positions "B", "C", and "D", respectively. Inset scale bars are 1 μm. Source: Zhou et al [357]*

This technique has been the one used to fabricate the dumbbell shaped samples of these works, as we will see in Section 3.2.1.

3.1.5 Motivation for this study: Au high aspect-ratio nanowires as effective remote SERS tools

One of the most interesting applications of plasmonic nanostructures is in remote sensing, as it has been explained in Section 3.1.1 . In this regard, a collaborative study within the framework of the Enabling Excellence ITN, along with the Institut de Matériaux Jean Rouxel and the Renishaw company has been the starting point for the studies found in this chapter [300]. The PhD subject of one of the students within this ITN has been one of the main sources for the studies shown in this chapter [264].

In this study, 1D plasmon-mediated Raman nanosensor was crafted by creating a coaxial Au@PEDOT NW following a similar procedure as the one stated in Section 3.2.1, but with an intermediate step after the fabrication of the Au NW core. This step consisted on enlarging the pore by a few nm as reported in previous studies [358] and covering the etched space in the porous membrane with a 3,4-ethylenedioxythiophene (EDOT) monomer. After carrying out an oxydative electropolymerization a core-shell Au-PEDOT system was formed. In order to have a better-suiting sample for the remote Raman experiments, core-shell Au@PEDOT NW with PEDOT present in just one of the tips of the Au NW were fabricated by not enlarging the AAO membrane pore completely and following the rest of the procedure in a similar way.

Thanks to a novel approach to the Raman optics within the experiment, succintly explained in images a and b of Figure 3.7, it was possible to acquire a signal present at a remote point with respect to the excitation taking place.

After performing an initial map to be sure about which part of the Au@PEDOT NW had a Raman signal corresponding to that of PEDOT, it was possible to find signal corresponding to PEDOT at the opposite NW tip to the one with PEDOT present, as it is shown in images d and e of Figure 3.7. This served as a proof-of-concept for the possible application of these structures for remote Raman sensing of delicate photoactive species.

Au nanodumbbells: A possible enhancement

As we have seen in Section 3.1.2, the excitation of a SPP with light needs momentum matching between the incident light and the SPP. In the case of metallic NWs, a simple way to satisfy this criterion consists in irradiating one of the tips of the NW in order to excite the SPP, which can then propagate toward the opposite tip of the NW.

The polarisation in said excitation is extremely important, since it allows to control the type of plasmonic modes that will be excited [359] and it can even route an SPP towards a specific branch of a branched nanowire [360]. We know that the propagation length of SPPs strongly depends on several properties such as the material of the nanostructure, its shape and its size [361], but, in the case of NWs, it also depends on the shape of its tips [362]. In our case, the dumbbell and half-dumbbell sample of this study have been fabricated as explained in Section 3.2.1.

Acquiring a better understanding of the plasmonic phenomena taking place in these different nanostructures, as well as how they correlate with their SPP propagation, has been the main motivation for the development of the study shown in this chapter.

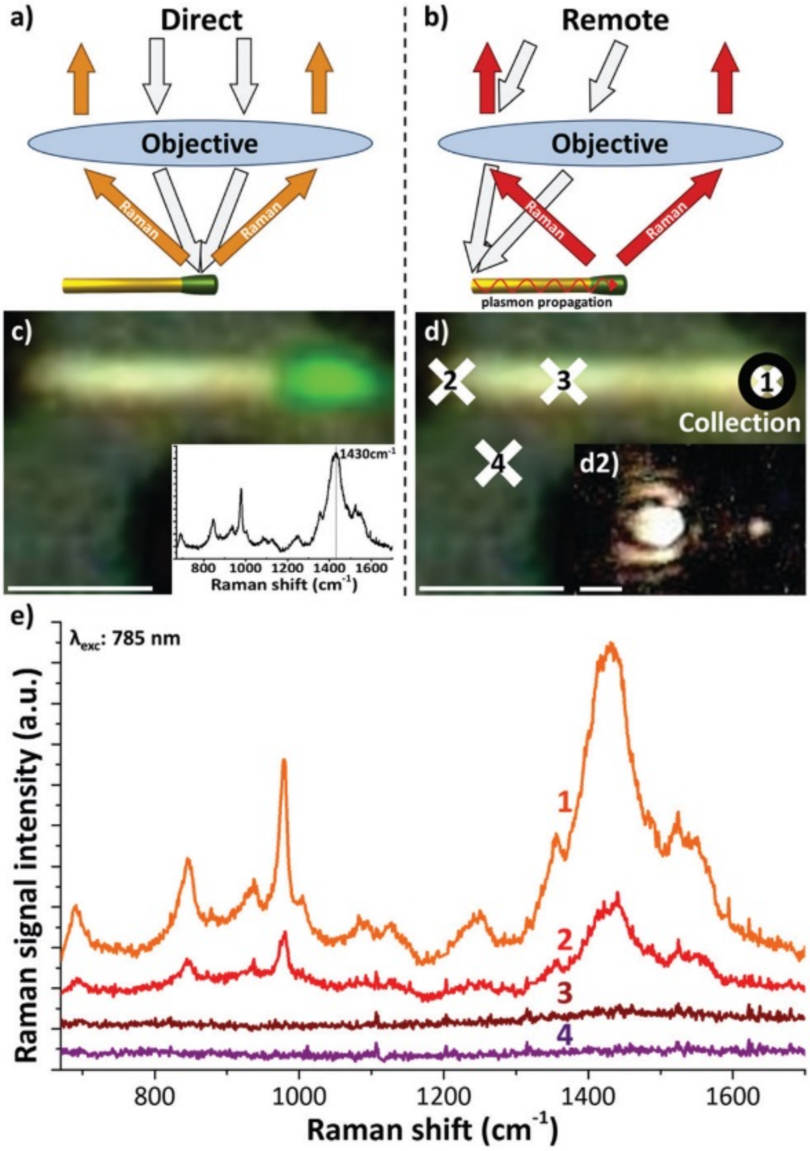

Figure 3.7: *Schematic view of the optical configuration (laser source, objective, sample and collected light) for measuring the standard (a) and the remote (b) Raman signals. (c) Optical microscopy view (objective Ã—100 LF) with superposed Raman spectroscopy mapping (intensity at 1430 cmâˆ’1 appears green) of a single gold nanowire (diameter: 114 nm) partially covered with PEDOT close to the right tip. (d) Four excitation configurations (X symbol labelled 1 to 4) and maintained collection area (O) of the Raman signal plotted in (e) at 785 nm. (d2) Optical microscopy image without back light when exciting in 2 with a 785 nm laser. Scale bars are 2 Î¼m. Source: Funes-Hernando et al [300].*

3.2 Experiment

After having set a general notion of surface plasmonics, their mechanism and their importance, this section focuses on the experimental part of this study. First, a short description of the sample preparation, namely the growth of Au NW and their irradiation into dumbbells, is shown. Initial TEM studies are shown, which confirmed the crystalline character of the Au NW prepared with this method. Finally, the STEM-EELS gathering of our data SPIMs is shown, and experimental drawbacks are brought to the spotlight.

3.2.1 Sample preparation

The preparation of these samples was performed by Daniel Funes-Hernando as part of his thesis project, directed by Jean-Luc Duvail and taking place at the Institut de Matériaux de Nantes. Among the various preparation methods stated above, the Au NW used for this study have been prepared using a bottom-up approach, to be specific, by electrodeposition by means of a hard template, in this case a porous template made of anodic aluminum oxide (AAO). This method has been discussed in depth in Section 3.1.4.2 and a schematic of the complete preparation can be seen in Figure 3.9.

For these particular Au NW, an AAO membrane was sputtered on its barrier layer with gold, and was then introduced into a home-made electrochemical cell providing three electrodes, one (the working electrode) connected to the Au sputtered layer, and the other two (the counter electrode and a reference electrode) in contact with the electrolyte within the electrochemical cell. A schematic cross-section of this electrochemical cell can be seen in Figure 3.8, coming from the thesis manuscript of Dr. Funes-Hernando [264]. A table containing the composition of the initial chloroauric acid aqueous electrolyte solution, as well as the reason for each of the components to be in said solution, are displayed in table 3.2.

Species	Concentration	Role
$HAuCl_4$	0.03 M	Electrolyte to reduce
K_2HPO_4	0.1 M	Buffer at pH = 7.6
KCl	0.1 M	Enhances the conductivity of the solution

Table 3.2: *Composition of the electrochemical solution for Au plating prior to mixing. Source: D. Funes-Hernando PhD thesis manuscript [264]*

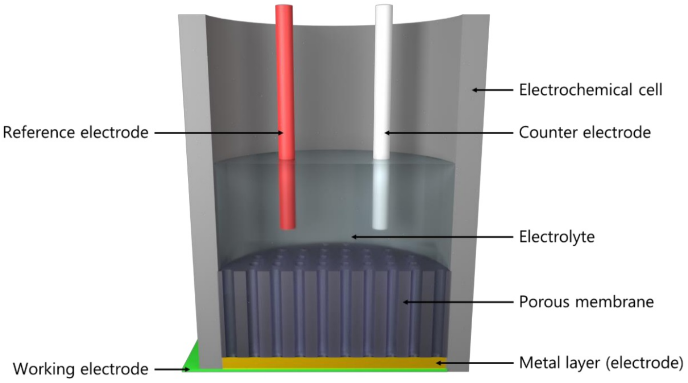

Figure 3.8: *Schematic of setup for confined electrochemistry within a nanoporous membrane. Source: D. Funes-Hernando PhD thesis manuscript [264]*

The counter electrode, a platinum foil, was inserted, along with the reference elctrode, in the electrolyte aqueous solution. Then, a cyclic voltammetry was performed in the potential window 0.75-0 eV with respect to a saturated calomel electrode (SCE) reference electrode. This voltammetry was performed at a rate of 50 mV/s, which prompted the reduction of $[AuCl_4]^-$ into Au^0. This gold started to deposit at the bottom of the pores.

The cyclic voltammetry starts at 0.75 V, the equilibrium potential of this reaction, so that the process is not started by means of a spontaneous reaction. As the potential different went down, specifically when crossing the 0.46 v threshold, the electrolyte solution was reduced into gold. After getting to 0 V, the potential was brought up again to allow the electrolyte to refill the nanopores of the AAO membrane, and with this a single cycle of the deposition would be complete.

The diametre of the AAO membrane pore determined the diametre of the Au NW, and the number of cycles in this voltammetry determined the length of the Au NW, since this length and the number of cycles mantain a linear relation. Taking into account the time for a single cycle, the growth rate of these Au NW was around 4.7nm/s.

After the NW synthesis, the membrane and the Au NW were thoroughly rinsed with ultrapure water. This was done to remove any possible residue of the electrolyte solution. After this, the AAO template was etched by immersing the AAO template along with the Au NW in a 4.9 M H_3PO_4 solution for 48 hours.

The remaining gold film was then rinsed with ultrapure water several times and stored in water into small glass containers. When the TEM study started, this gold film in water was sonicated during 0.5 s, the nanowires broke off from the gold film and got dispersed in ultrapure water. From then on, the TEM samples were prepared by drop-casting this water dispersion onto a 20 nm thick SiO_x TEM grid.

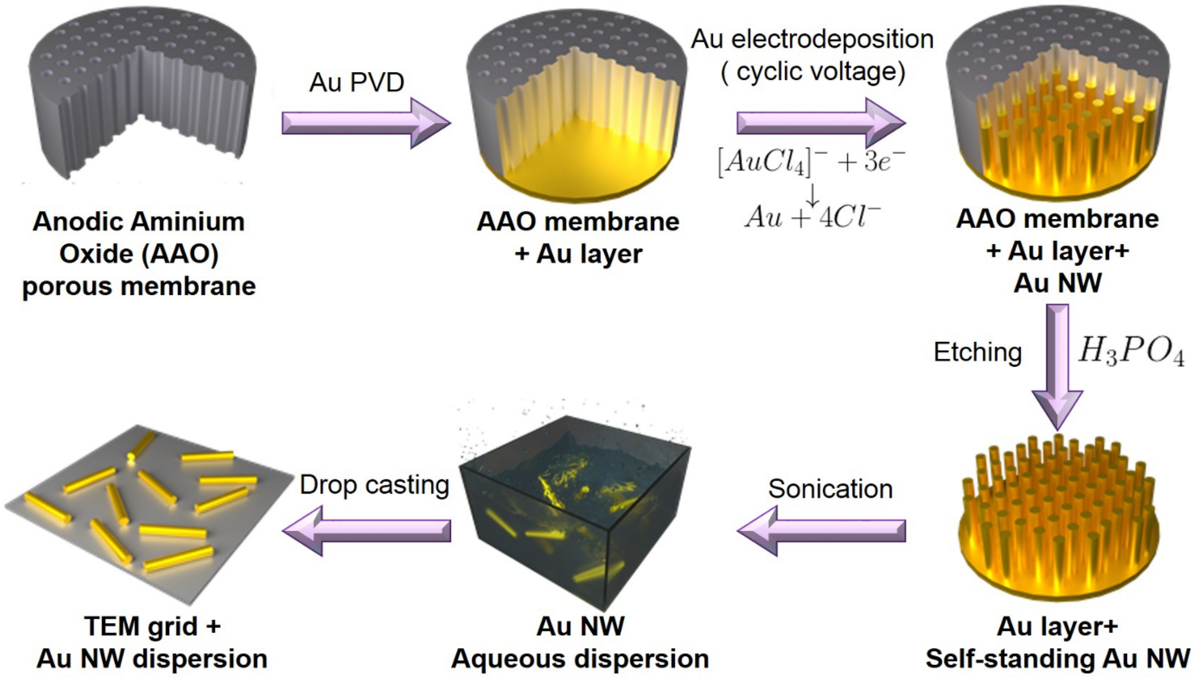

Figure 3.9: *Detailed preparation of the Au NW using templated electrodeposition. Edited from [264]*

The dumbbell fabrication

After the study shown in Section 3.1.5, and the idea for a possible geometrical filter that is explained within, it was of great interest to fabricate samples that combined nanoparticles and nanowires. Out of the different modification techniques shown in Section 3.1.4.2, the one that has been chosen by our partners at the IMN for this part of the study has been laser irradiation at the tips of the nanowires, melting the metal due to temperature increase [356]. These samples were part of a bigger study, which has been explained in Section 3.1.5 and can be seen as a whole in references [264] and [300]. Due to this reason, the original samples for this fabrication were Au NW with PEDOT shells on their tips. For this reason, the PEDOT in the samples had to be taken off using laser dry etching before fabricating our dumbbells.

For the fabrication of the specific dumbbells shown in our study, the tips of the Au NW were irradiated using a green laser ($\lambda = 488nm$, power = 14 mW) for 3 seconds on the tips of our half-dumbbell and dumbbell samples. In the case of our half-dumbbell, both tips were irradiated but one of them got volatilised. An in-depth description of these and all of the other samples fabricated for this study can be seen in Section 3.2.3

3.2.2 Initial TEM studies

During the studies prior to this one, which have already been published [300] and have been delved into in Section 3.1.5, several preliminary HRTEM studies have been performed on samples fabricated using the method explained in detail in Section 3.2.1. These studies focused on the crystalline quality of the Au NW, as well as the homogeneity of the coaxial Au-PEDOT NW.

The results concerning the presence and even distribution of the PEDOT shells in these systems has already been shown in Section 3.1.5. using TEM and EELS we were able to determine that the Au-PEDOT NW was, indeed, coaxial and that the Au surrounding shell had an EELS sulphur signal, which gave us proof that it was not carbon residue but PEDOT. However, an additional study was performed to check the crystallinity of the sample. A TEM micrograph showing the high crystallinity of the sample can be seen in Figure 3.10

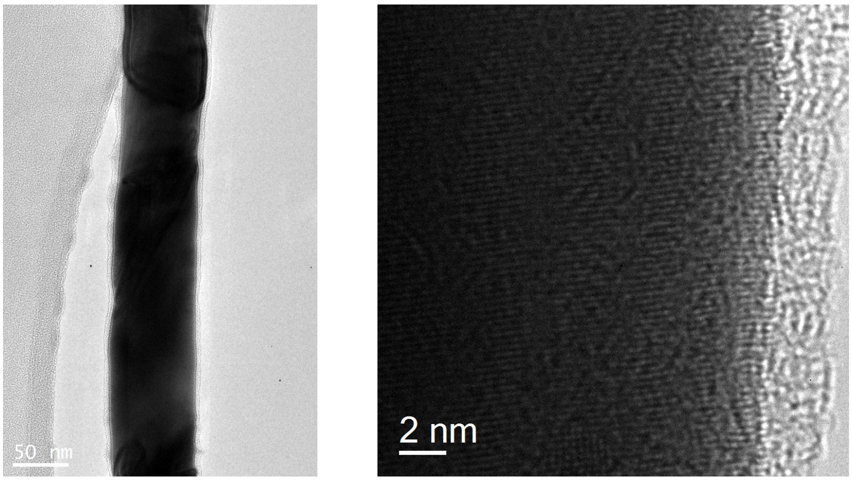

Figure 3.10: *TEM studies on Au NW. Left: TEM micrograph showing a protion of an Au NW, with a thin carbon layer coming from sample pollution. Right: HRTEM micrograph of the Au NW on the left, showing the planar diffraction due to the high cristallinity degree of the Au NW used in this study.*

3.2.3 STEM-EELS experiments

This section focuses on the main experiment of this chapter, that is, the STEM-EELS spectrum images taken over several different Au nanostructures. We provide an in-depth explanation of these samples, the experimental conditions as well as the experimental drawbacks associated with these studies. The as-taken SPIMs for this study can be seen in the videos in the supplementary information.

Experimental conditions

The STEM-EELS studies shown in these works have been performed using the monochromated FEI Titan Low-Base microscope shown in Section 1.6.2. The accelerating potential has been kept at 80 keV to avoid damage to the samples during the STEM-EELS studies. The convergence angle α has been kept at 25 mrad, and the collection angle β has been kept at 35 mrad

As for the SPIM-EELS acquisitions, the acquisition time has been set at 0.01 s/pixel. The pixel size has been chosen individually for each sample, depending on the area to be analysed. The energy step for this experiment has been set at 0.02 eV, and the energy resolution has been estimated by measuring the full width half maximum of the ZLP, resulting in an energy resolution of 160 meV.

The analysed samples

Five samples have been selected from the analysis of these studies. A scheme for the morphology of these different samples is displayedin Figure 3.11. In this description, we will provide a general explanation of the morphology of each one of the Au nanostructures in the study, as well as the number of spectra gathered in their corresponding SPIM. This last parametre will be of interest, since NMF is a statistical analysis method and should therefore be more accurate for a higher number of spectra.

- The first sample consists of a half-dumbbell. This half-dumbbell consists of a NW of 110±5 nm in diameter. To this nanowire, using the abovementioned laser irradiation (see Section 3.2.1), a nanoparticle measuring an average of 340±10 nm in diametre has been attatched. The total length of the sample amounts to 3.6 ± 0.1 μm. Its corresponding SPIM has a total of $538 \times 65 = 34970$ spectra

- The second and third samples are, respectively, of a single NW and a double NW where two NW have been joint during the drying process after the drop-casting of the Au NW solution. These high aspect-ratio Au NW make 3±0.1 μm long with a diameter of 30 ± 1 nm. The SPIMs used to study these two samples have $379 \times 37 = 14023$ and $288 \times 37 = 10656$ spectra, respectively. This means that the amount of spectra in these samples is between half and a third of the number of spectra in the aforementioned one.

- The fourth sample consists on a nanowire with an increase in diametre following its transversal edge. The diametre of the NW goes from 120 ± 5 nm to 225 ± 5 nm in a quite homogeneous way. This could also be understood as a high aspect-ratio conical section. The size of its SPIM is $578 \times 55 = 31790$ spectra, that is, on the same range as the half-dumbbell. This sample makes 4±0.1 μm long.

- The fifth sample consisted of a full dumbbell, resulting of joining a NW 4.1±0.1 μm long and 110±5 nm in diameter, with one nanoparticle in each end, each measuring an average of 300±10 nm and 210±10nm in diameter, respectively. The full dumbbell initally had a little 60±5 nm diameter Au particle attached to it. Its associated SPIM presents a size of $538 \times 40 = 21520$ spectra, which means a decrease over a 30% with respect to the half-dumbbell.

This variety of geometries give us a vast range of responses we can gather from these studies, such as the coupling between Au NP of different diametres with Au NW presenting the same diametre (samples *a* and *e* in Figure 3.11), the effects of coupling between two Au NW with respect to a single NW of the same characteristics (samples *b* and *c* in Figure 3.11) and finally, and arguably most interestingly, the variation of both the EEL spectra and the plasmonic components on a Au NW with a varying diametre (sample *d* in the aforementioned figure).

This sample with a varying diametre offers a very interesting set of properties due to its geometry, since the response of the sample to the electron beam at a specific point of this NW is

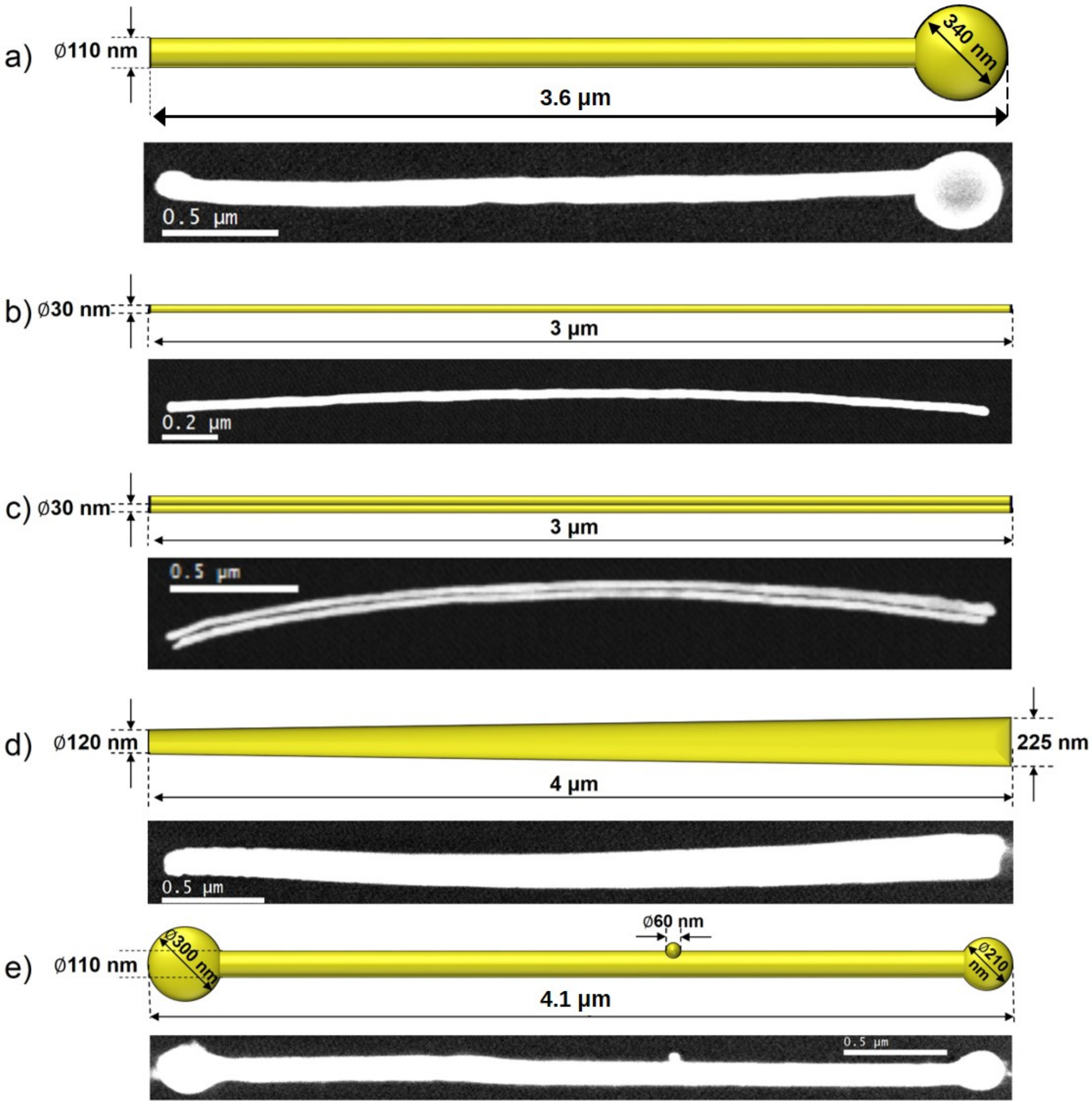

Figure 3.11: *In-depth morphological descriptions of the analysed samples. Geometrical schemes (top) and HAADF micrographs (bottom) of: a) Au half-dumbbell b) Single NW c) Double joint NW d) Varying diametre NW and e) Au dumbbell.*

correlated to the diametre of the NW at said point in what is commonly called the electrostatic tip-induced effect.

This is a direct derivation of the Coulomb Law. For simplicity purposes when integrating, we will compare two spheres of a different radius when they are both subjected to the same potential to explain this phenomenon, since our whole sample is subjected to the same potential.

Deriving from the expression of the electrostatic potential, on the surface of each particle, $V_i = \frac{K \times Q_i}{R_i}$, where $K = \frac{1}{4\pi\varepsilon_0}$. Taking into account that our particles 1 and 2 are at the same potential at their surface, we can deduce:

$$\frac{KQ_1}{R_1} = \frac{KQ_2}{R_2} \tag{3.22}$$

And, defining the variable n as the ratio between these two radii, we obtain:

$$\frac{Q_1}{Q_2} = \frac{R_1}{R_2} = n \tag{3.23}$$

Now, by applying the same law as before, we know we can define the electric field E_i at a distance d from its center as:

$$E_i(d) = \frac{K \cdot Q_i}{d^2} \tag{3.24}$$

And thus comparing the electric field at the surface of both spheres we obtain:

$$\frac{E_1\left(R_1\right)}{E_2\left(R_2\right)} = \frac{Q_1}{Q_2} \cdot \frac{R_2^2}{R_1^2} = \frac{n}{n^2} = \frac{1}{n} \tag{3.25}$$

In other words, if the radius of particle 1 is n times higher than that of particle 2, the electrical field will be n times stronger at the surface of this second particle. This can be extrapolated to our specific case, where the electrical field in the thinner parts of the Au NW is stronger than that of the thicker parts of the NW, hence having a higher energy loss.

With respect to the EELS plasmonic studies shown in this section, there is an additional subject that is necessary to address when it comes to these samples. Even though the samples have different diametres, they all have diametres that are higher than the electron quasi-transparency limit in TEM for materials this dense. Simply put, the vast majority of the electrons going through the Au NW will be dispersed and hence not retrieved by the STEM nor EELS detectors. This poses a problem when measuring the bulk plasmon in the samples.

As we have seen in Section 3.1.4, there are two types of plasmonic resonances going on in these sort of plasmonic nanostructures: surface plasmon resonances and bulk plasmon resonances. since the surface plasmon resonances happen at the interface between the nanostructure and vacuum, EELS is a very adequate technique for its study. However with samples as thick as ours, EELS cannot be used to study bulk plasmons simply because the electron beam disperses when going through the sample. This is clearly seen in the TEM micrographs taken by integrating each SPIM, such as the one for the half-dumbbell shown in figure 3.12.

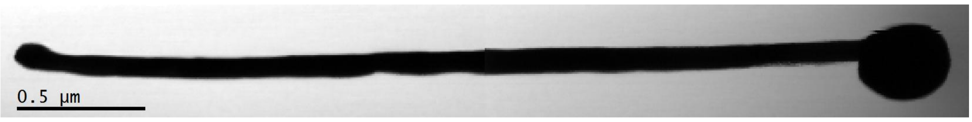

Figure 3.12: *Intensity micrograph built by integrating the half-dumbbelll SPIM. The black area shows almost no electrons from the electron beam are able to get through the sample.*

At the edges of the nanostructures, since there are areas where the thickness of the sample is much lower, this signal could in theory be retrieved. However, the map for this plasmonic resonance would be, in principle, indistinguishable from the one for the transversal surface plasmon. This is the reason why bulk plasmons are not shown in the results of this study.

The noise issue

Due to an unknown experimental cause, there has been some unexpected electronic noise in the spectrometre for all of the SPIMs gathered for this experiment, with the exception of the SPIM related to the Au half-dumbbell. This noise can especially be seen in the background-extracted SPIMs shown in the videos in the supporting information for this manuscript. An example of this noise can be found in Figure 3.13.

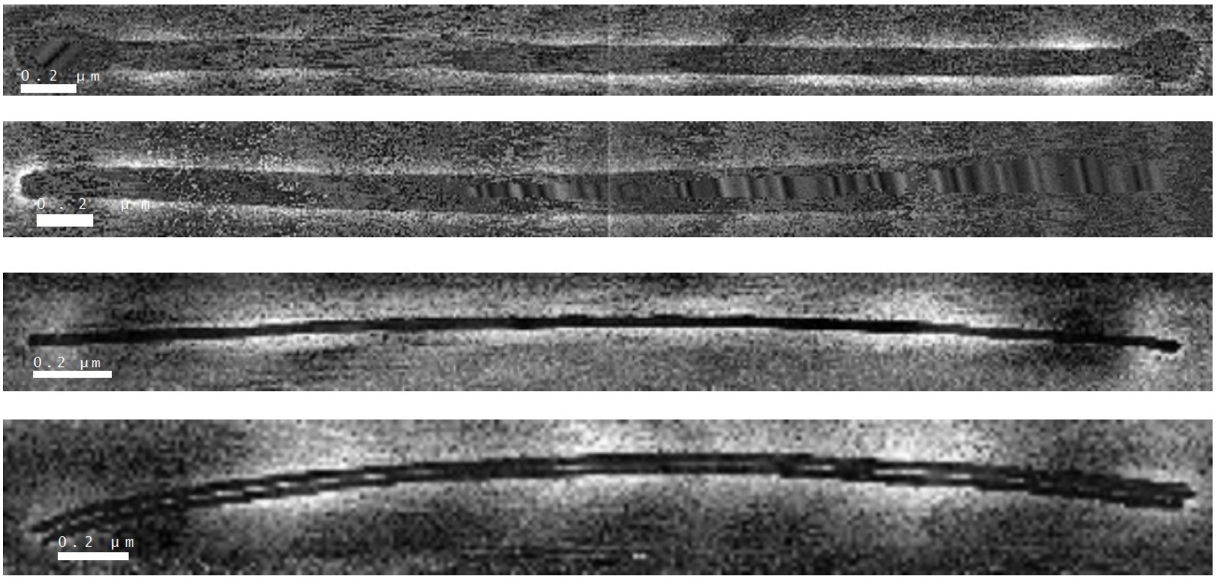

Figure 3.13: *Energy loss intensity maps representing examples of the experimental noise. From top to bottom, intensity maps of: the Au dumbbell at 1.17 eV, the increasing diametre NW at 1.15 eV, the single NW at 0.51 eV and the double NW at 0.5 eV.*

We can group the samples in three main catergories depending on the signal-to-noise ratio (SNR) they present: the one with a high SNR (the half-dumbbell), the ones with a medium SNR (the single and double Au NW) and the ones with a very poor SNR (the Au dumbbell and, especially, the increasing diametre nanowire). An important thing to take into account is that, with the exception of the increasing diametre NW, the plasmonic components are visible for most of the energies in the SPIM, even with the noise effects. This will be of importance, as it will be explained in Section 3.3.2.

A Richardson-Lucy deconvolution [255, 13, 256, 257], like the one presented in chapter 2, was tried to be used in order to try and improve the quality of the different spectra. However, at least for the purpose of this analysis, this deconvolution was unfruitful. After performing this deconvolution, the spectra seemed to have even more noise than it had before performing this analysis.

On top of this, the noise levels in the SPIMs make it impossible to use the somewhat traditional Reflected Tail method for the extraction of the background [15]. This consists on assuming the ZLP as symetrycal with respect to the 0 eV point, which it should be. using the negative part of the ZLP as a reflection of its positive part, it is possible to extract the background from the spectra. However, in this case and with this level of noise, it would not be advised, since noise is randomly distributed and extracting a noisy background from a noisy signal would only decrease the SNR.

3.3 Methods: Data analysis

3.3.1 Challenges in the EELS spectra analysis

When it comes to the analysis of these samples, after aligning the spectra in the SPIMs around its ZLP,there are several issues to be taken considered into account besides the experimental noise reported in Section 3.2.3. These issues can be divided into two main groups: those having to do with the removal of the background of the EEL spectra, and those having to do with the plasmonic features themselves. This section aims to explain them in detail.

The background issue

As seen in section 1.4.3, generally speaking, when an analiysis of an EEL spectrum needs to be performed, generally one of the first steps is the removal of the zero-loss peak (ZLP) of the spectrum, which can be considered a background for the purpose of the analysis of low-loss EELS. In general, the ZLP is removed from the EEL spectra by fitting it using a power-law function.

An EEL spectra for the ZLP with no sample present has been taken at the beginning of each measuring day, which could have been used as a background to extract from each one of the EELS SPIMs taken. However, the ideal case would be to be able to extract the background from the particular SPIM being analysed.

However, as it has been seen in Section 3.1.4, high aspect-ratio nanostructures tend to have plasmonic components that are more closely packed in energy, with this packing being tighter the higher the aspect ratio [329]. In the particular cases of this study, the plasmonic features in the EEL spectra are so tightly packed that the ones at lower energies are overlapped with the lowest energy region that could be used for the fitting of the ZLP. In other words, there is no energy window in the spectra that fulfills these two conditions:

- Being far enough from 0 eV that the behaviour of the ZLP can be fitted using a power law. For our particular experimental conditions, this would mean a few thenths of eV far from the ZLP, minimum.
- Not having any sort of plasmonic features present in the spectral window.

Furthermore, and also because of this reason, the results yielded by the in-built background extraction routines in our data analysis software (Digital Micrograph) are far from optimal, and not enough of the negative part of the ZLP has been gathered to be able to perform a background extraction using the *reflected tail model*, where the negative section of the ZLP is mirrored with respect to zero and used as the background to be extracted from each spectrum. This complicates greatly the data analysis for these samples.

The plasmonic components issues

As we have stated in Section 3.1.3, the energy resolution of our experimental system was about 160 meV. With this in mind, a second effect raising from the high aspect-ratio of the sample is that the different longitudinal plasmonic components will start to be indistinguishable from each other once the difference in energy between two consecutive components starts to be in the same order of magnitude as the spectral resolution or our system. This is the case for all of our samples. In other words, even after hypothetically removing the background from the spectrum images, we are still facing the issue that we cannot distinguish the different spectral features of each plasmonic mode.

On top of this, as with any other kind of metal nanowire [328], we encounter a transversal plasmonic mode at an energy that, for our samples, has been between 2.5 and 2.8 eV. In general, this transversal mode depends on the specific material the nanowire is made of as well as its size and aspect ratio. This plasmonic component is substantially more spread in energy than its longitudinal counterparts, which is coherent with the literature [325, 327]. In our particular case, we have been able to find this component at energies more than 1.5 eV away from the center of the feature. As a result, a non-negligible part of our longitudinal plasmonic features in our samples are mixed to some degree with their transversal features, difficulting even more this spectral analysis.

3.3.2 Multivariate analysis and EELS: a brief review

As we have stated in sections 3.2.3 and 3.3.1, the SPIMs we have gathered for this study present, on the one hand, a very high level of noise. On the other hand, these SPIMs also present plasmonic components that are so close in energy to each other that they overlap. This creates a necessity to implement some sort of data analysis that de-noises the spatial distributions of the different plasmonic modes and at the same time separates the different plasmonic modes independently.

This is not necessarily a novel problem, since there are plenty of EELS studies where SPIMs with various phenomena taking place at once are dealt with [363]. This is where the so-called hyperspectral analysis comes into play. These kind of methods analyse the whole SPIM at once, which make it easier to discern different components within the whole SPIM.

A very interesting part of hyperspectral analysis, concerning our study, is multivariate analysis (MVA). A very good general definition for this sort of analysis is given in [364]:

> The EELS dataset is regarded as an N×M matrix, where M is the total number of pixels and N is the spectral size. For instance, a spectrum image dataset is **D***(x, y,E)*, with N equal to the pixel-area covered by x and y. One way to sort this data array is to solve the matrix factorization problem in the linear mixing model, by proposing a new representation of **D** as a combination of components,
>
> $$\mathbf{D}(x,y,E) = \sum_n \mathbf{S}_n(x,y)\mathbf{L}_n^T(E) \tag{3.26}$$
>
> where n is the component index, that runs up to the minimum between N and M. Moreover, each $\mathbf{S}$ is a score matrix and $\mathbf{L}^T$ is the transpose of the loading matrix. Notice that score and loading matrices keep the spatial and spectral dimensions, respectively

Simply put, when applied to an SPIM-EELS, this kind of analysis decomposes a given SPIM (which can be understood as a matrix in 3 dimensions) into a sum of different components. Each component is the product of two different matrices, one that contains all of the spatial information of the component ($\mathbf{S}_n(x,y)$), and another matrix that contains all of the spectral information of the component ($L_n^T(E)$). This means that, even though this component is in and of itself a 3D matrix, for any given point *(x,y)*, the spectrum associated in the component will mantain the same relative intensity between any two given energies. This relative intensity (in other words, the shape of the spectrum) is the information stored in $L_n^T(E)$. The only factor that will change among points will be the intensity of the spectral component at each point *(x,y)* (in other words, the spatial distribution of the component), which is an information stored in $\mathbf{S}_n(x,y)$.

Principal component analysis decompositions

Principal component analysis (PCA) is a possible solution to equation 3.26. This is a method mathematically found more than a century ago by Karl Pearson [365]. The different analysis methods under the PCA umbrella have one particular aspect in common, which is that they solve equation 3.26 by imposing orthogonality on the loadings [364]. A very comprehensive review on

PCA and its general use can be seen in [366]. In other words, applied to our system this would impose orthogonality between the different spectral components, or said otherwise: if we consider two spectral components as two vectors, their scalar product would be 0. In simple words, the PCA analysis tries to provide a solution tot his problem that will minimise the distance between the solution proposed and the different points contained in the experimental data.

To the best of our knowledge, the first reports on the use of PCA for the analysis of EELS spectrum images (although with a different kind of data acquisition) date back to 1990 [367], although here is reported as a simplification of another multivariate analysis, factorial analysis of correspondence (FAC). The only difference between this method and PCA is the technique used to calculate the distance between the experimental points and the solution. While PCA used a regular euclidean distance, FAC uses χ^2 as a measure of distance.

Generally speaking, algorithms using PCA evaluate the amount of information shown in a specific component by the value of their explained variance. If the variance of the signal is higher than that of the noise (an assumption on which basis the whole PCA method is sustained [368]) , it is possible to set a number of components for the analysis by setting a variance threshold.

It is of interest to notice that the orthogonality imposed by PCA, when applied to our EELS signal (which is always positive for any energy), implies that some of our components might have negative values for some energies. This makes it really hard to be able to discern the physical phenomena taking place from the data given by the analysis; which means it complicates greatly the initial objective of the study. This objective was to discern the different plasmonic modes from one another.

The use of PCA as a hyperspectral EELS analytic tool has been quite extensively used in the last twenty years, especially since a PCA-based method was offered in Digital Micrograph, one of the main analytic software for TEM-EELS data, in 1999 [363]. Since then, PCA has shown some remarkable results, going from early EELS component analysis [369] to being able to map chemical components by PCA analyses of SPIM-EELS [370] and even played a part as a noise reduction algorithm in EEL spectroscopy tomography studies [371]. One of its main perks is that it is somewhat cheap in terms of computational cost. Another main perk is that, even though the components given by the analysis will not be something that can be interpreted right away, the elimination of low-variance components do make PCA a valuable algorithm for noise reduction, hence its vast use as such.

Many studies over the years have performed modifications on the original PCA method in order to make its final components more intuitively interpretable, for example by scaling the EELS data so that both matrices out of the PCA method would be orthogonal and then rotating them to maximise their mutual simplicity [372], or as a first denoising step before a different sort of MVA [373]. This is where blind source separation comes into play.

Blind source separation: Independent Component Analysis and Non-negative Matrix Factorisation

Blind source separation (or BSS) refers to the decomposition of a mixed set of signals and noise into the different denoised signals that compose it, in a way that the final product is as close as possible to the real components as possible, that is, the final components mantain as much as possible of their physical significance. In our specific set, this relates to obtaining the individual components for each plasmonic resonance.

BSS is built on the basis of PCA and there are two main variations to this method: Independent component analysis (ICA) and non-negative matrix factorisation (NMF).

Indepenedent Component Analysis

The concept of independent component analysis (ICA) is not far from that of PCA in the sense that it searches in a random source of data for "*a linear transformation that minimizes the statistical dependence between its components*" [374]. In other words, the constraint that is imposed on the different components for this analysisss is not their orthogonality but their independence from one another. In this case we define two scalar-value random variables y_1 and y_2 as independent "*if information on the value of* y_1 *does not give any information on the value of* y_2 *and viceversa*"[375], which is a property that can be defined by the probability densities of these two variables.

This analysis was first addressed by Herault and Jutten around 1983. They worked on trying to solve this problem algorithmically using a recursive neural network even before providing a theoretical explanation for it. Their method can be seen thoroughly explained in [374], as well as an initial proof-of-concept of this analysis that consisted on straightening text lines. At the same time, a myriad of different studies working on this issue started to be done. A very comprehensive review of these first studies can be seen in [376].

Nowadays, it is possible to perform an ICA decomposition on a system without the need for any special sort of neural circuit, by reducing the dimensionality of the sample. This is done by performing a first decomposition using PCA and only retaining the components over a certain variance threshold [375]. Then, it is possible to perform a transformation on these PCA components trying to minimise the dependence among them, in other words, imposing mutual independence to the source components [364].

To this day there are plenty of studies that employ ICA with relation to EELS hyperspectral studies [363, 368, 371], but a very clear example of why ICA offers a better performance than PCA is the study performed by de la Peña *et al* in 2011 [368]. This study used EELS mapping over a sample consisting of a thin foil of separated TiO_2-SnO_2 phases. By using a PCA-treated dataset, and the combination of the resulting components, they were able to create maps corresponding to the different elements present in the sample. Nevertheless, the interpretation of said components and their linear combination was something performed by the research team from three components with no physical value. However, when applying ICA to the PCA components, three new independent components were found with a clear physical meaning: the spectral background, a component that seem to correspond to the spectrum of TiO_2 and another one that was thought to be related to SnO_2. However, it is important to notice that this is not always the case and the ease of interpretation and amount of physical meaning of the ICA components depends heavily on the dataset analysed.

To sum up, even though this method poses many advantages with respect to PCA for certain datasets, there are two main throwbacks to this analysis. The first one is the computational cost of performing two different analysis, first PCA and then ICA. The second one is more relevant for our study: a characteristic that ICA inherits from PCA is that their results can also not refer to actual physical phenomena, therefore making their interpretation more dificult [364]. Since our main goal with this analysis is obtaining components as close as possible to our plasmonic modes, this method is not the most recommended either.

Non-Negative Matrix Factorisation

The other main BSS method currently being used in EELS, and the one used in this study, is non-negative matrix factorisation, or NMF. In general terms, we can think of this technique as a solution for equation 3.26 for a data set $\mathbf{D}(x,y,E)$ that has positive values in energy for the whole SPIM (which is the case for EELS). The two constrains that we apply to this specific method is the number of constraints, which we must set beforehand, and the non-negativity of all the components for all their energy values. A more general mathematical definition can be found in the bibliography [377]:

> Given an M dimensional random vector x with non-negative elements, whose N observations are denoted as $\mathrm{x}_{j,j=1,2,...,N}$, let data matrix be $\boldsymbol{X}$ =[x_1, x_2,..., x_N] $\in \mathbb{R}^{M\times N}_{\geq 0}$, NMF seeks to decompose $\boldsymbol{X}$ into non-negative $M \times L$ basis matrix $\boldsymbol{U}$=[u_1, u_2,..., u_N] $\in \mathbb{R}^{M\times L}_{\geq 0}$ and non-negative $L \times N$ coefficient matrix $\boldsymbol{V}$=[v_1, v_2,..., v_N]$\in \mathbb{R}^{L}_{\geq 0}$ such that that $\boldsymbol{X} \approx \boldsymbol{UV}$, where $\mathbb{R}^{M\times N}_{\geq 0}$ stands for the set of $M \times N$ element-wise non-negative matrices. [...] Hence NMF decomposes each data into the linear combination of the basis vectors. [...] In other words, this approach tries to represent the high dimensional stochastic pattern with far fewer bases, so the perfect approximation can be achieved successfully only if the intrinsic features are identified in $\boldsymbol{U}$

This definition is entirely coherent both with our simplified definition and with the general introduction on MVA in this section. It also states an important issue with this method: The intrisic features of our system (plasmonic resonances) need to be visible at least to some extent for this method to work. Just like with ICA, it can be interpreted as a neural network learning algorithm, which aims to depict the parts a certain additive dataset is made of [377].

The concept of NMF was first introduced by Paatero and Tapper with the name of positive matrix factorisation [378, 379]. These studies focused on a very specific application and therefore did not offer a generalised version of the algorithms, which made it more difficult to apply it to other fields. Later on, Lee and Seung focused on the potential of NMF to perform parts-based representation, which played a key role on the popularisation of this analysis [380]. In this first study, they performed two proofs-of-concept for NMF as a method for parts-based representation, one applied to faces and another one applied to words semantics. The first one was a clear example of how this method was, in principle, more intuitive than PCA, since it managed to represent face pictures using a set of basis images (its components) that actually resembled parts of faces.

An additional study, a year later, delve deeper into the formulation of NMF as recursive algorithms, discussing the cost functions to estimate the quality of the approximation, the proof of convergence to interpret a result as valid, and the formulation that could be given to NMF as optimisation problems [381]. Given the approximation problem set in equation 3.26, here noted as $D \approx SL$, one of the formulations is set on the basis of minimising the square of the euclidean distance between the matrix D and the factorisation product SL. In other words, finding a minimum for equation 3.27 with the constraint that $D_{ijk}, S_{ij}, L_k \geq 0 \forall i, j, k$ within the dimensions of their respective matrices:

$$\|D - SL\|^2 = \sum_{ijk} (D_{ijk} - S_{ij} \cdot L_k)^2 \tag{3.27}$$

An alternative method mentioned in this study consists in defining a "divergence" of A from B that also fulfills the conditions that it is always non-negative and it is only zero if and only if A and B are the same. The one proposed in this study is described in equation 3.28:

$$\mathbf{D}(D\|SL) = \sum_{ijk} \left(D_{ijk} \log \frac{D_{ijk}}{S_{ij} \cdot L_k} - D_{ijk} + S_{ij} \cdot L_k \right) \tag{3.28}$$

Briefly explained, these two studies put NMF in the spotlight for parts-based decomposition by not only giving proofs-of-concept centered in vastly different applications, but also paved the way for an actual implementation of this analysis.

As of lately, NMF has become more of a family of methods than a method in and of itself, with new catergories of NMF appearing, each one with new constraints applied to said NMF, from orthogonality (whenever it is applicable) to weights or sparseness [377], although the latter usually comes naturally from the non-negativity constraint [380]. This sparsity can be define in our study as the fact that, for a specific energy window, we do not always need all the components given by the algorithm to reconstruct our energy loss spatial distribution.

Some approaches, like semi-NMF, only subjects a specific factor matrix to the non-negativity constraint, which is useful for the cases where we know some of the sources in the additive dataset are always positive, while others are not [377]. However, for this study, we will be using the most basic form of NMF, where the only constraint imposed is the non-negativity one.

The applications of NMF, just like with the rest of MVA, cover a vast array of different fields. As it has been said, one of the main perks of this kind of analyses is their versatility. This analysis method has been used for subjects that fall under completely different catergories. Apart from the two proofs of concept presented before [380], NMF has also been used, to name a few, for document clustering [382], text data mining (using orthogonal constraints and tri-factorisations) [383], chemometrics(its original usage) [378], face recognition [384], audio pattern separation [385] and, obviously, for spectrosopic analysis.

Within spectroscopic analysis, we will focus on the use of NMF for the analysis of hyper-spectral datasets in EELS, although it has been used as well for other sorts of spectroscopy such as EDX [386, 387]. This sort of analyses have gathered a considerable amount of interest, especially in the past few years. Both core-loss EELS [386, 387, 388, 389] and low-loss EELS [290, 308, 312, 318, 328, 342, 350, 390, 391, 392] have been the subject of these studies.

NMF in EELS has been used for a variety of applications besides plasmonic analysis, such as separating the low-loss EELS spectra of silicon nanotcrystals in a dielectric matrix from EELS signal coming both from the dielectric matrix and from instrument-related signals, in order to study the electronic properties of said silicon nanocrystals [393], studying the local chemical morphology of single metal-organic framework glass bend nanoparticles from the precursors of said metal-organic framework [392], or chemical mapping going down to the atomic resolution [386, 387, 388].

Within the plasmonic field of study, there has been an increasing amount of studies in the past 7 years, which range from the study of single SPIMs of different types of geometries and noble metals such as the ones explained in Section 3.1.4.1 [312, 328, 342, 350, 391], as well as other types of structure such as topologically enclosed aluminum voids [318]; to three-dimensional EELS studies combining SPIM-EELS with tomography techniques [290, 308]. The study presented on this chapter builds on this previous work and applies it to arguably even more challenging datasets, with higher aspect ratios, more closely packed components, different geometries and low-SNR experimental noise conditions.

As it is explained in Section 3.3.3, in terms of implementation, we have implemented our NMF method using a custom script on the Hyperspy software [394], which already includes an NMF package. A more detailed explanation can be seen in Section 3.3.3.

The noise effects

There is an issue with NMF and in general with MVA that has been briefly mentioned in this section but needs to be taken as one of the most important factors to take into account when performing an MVA decomposition. This kind of analyses are extremely sensitive to the noise level, in other words, to the signal-to-noise ratio of the specific data being decomposed [395, 396]. We know from our raw data that we have a variable SNR in the different SPIMs that conform this study (see Section 3.2.3 and joint videos), but it is clear that all of them have a considerable amount of noise and some of them have a way too poor SNR. This has already been mentioned in the aforementioned section and will be explained again in detail in Section 3.4.

3.3.3 Creative data analysis solutions for the EELS challenges

As we have seen in sections 3.3.1 and 3.2.3, all the different challenging conditions happening all at once in our SPIMs (with different degrees of noise) make almost impossible to apply somewhat traditional methods to our EELS analysis. These methods include power-law background extraction, integration of the SPIMs on small spectral windows around the plasmonic features, or even multi-peak analysis, although the latter could in theory be of use for samples with even less noise than our high signal-to-noise ratio sample.

In consequence, more novel, out-of-the-box methods have been had to be put into action. These two methods consist, on one hand, of a custom background extraction, and on the other hand, on the use of NMF to perform a component analysis that is coherent with the physical reality taking place in the samples.

Zero Loss Peak - background extraction

The custom ZLP extraction does not rely on the fitting of the ZLP at low energies like most traditional ZLP extractions. Inspired by the component analysis applied for the plasmonic features, we have implemented a method that uses the ZLP itself as a component, which is then subtracted from each and every spectrum in the SPIM-EELS. This ZLP component is gathered from the SPIM itself, by integrating an average of ∼200 spectra from the edges of the SPIM. The SPIM edges chosen for this integration do not show any plasmonic activity, at least at first glance. This tells us that, even if there were some plasmonic activity, it would be negligible with respect to the rest of the SPIM.

Once we have our SPIM and our corresponding background, we can start our customised background extraction routine, using a custom-made script in our TEM analysis software, Digital Micrograph. A scheme of this routine can be seen in Figure 3.14.

First of all, we take our SPIM and get its size, which will be parametres of this routine. Secondly, we get our background spectrum and re-bin it, in our case by three. This will minimise the effects of the noise on our routine, which will increase the accuracy of the background extraction. We also get only the first 20 channels of our re-binned spectrum for the calculations we are going to perform. We name this reduced and re-binned background B_{red}.

Then we repeat the process in this list for every spectrum of the SPIM one by one:

- We get the spectrum in question, and we apply the same procedure as we have applied to the background: we re-bin it and get only the first 20 channels in the spectrum. The spectrum of the (i,j) pixel in the SPIM is defined as $S_{red}(i,j)$.

- We divide each of the reduced spectra by the background, channel by channel. In other words,

$$C(i,j) = S_{red}(i,j)/B_{red} \tag{3.29}$$

  where $C(i,j)$ is the result of this fraction.

- We obtain the global minimum point of $C(i,j)$. The energy loss and the intensity of this point are defined as $E_{min}(i,j)$ and $I_{min}(i,j)$, respectively. We also obtain the intensity of each of $S_{red}(i,j)$ at $E_{min}(i,j)$; which we define as $S_{min}(i,j)$. We do the same for the background spectrum. The intensity obtained for the background is labeled IB_{min}.

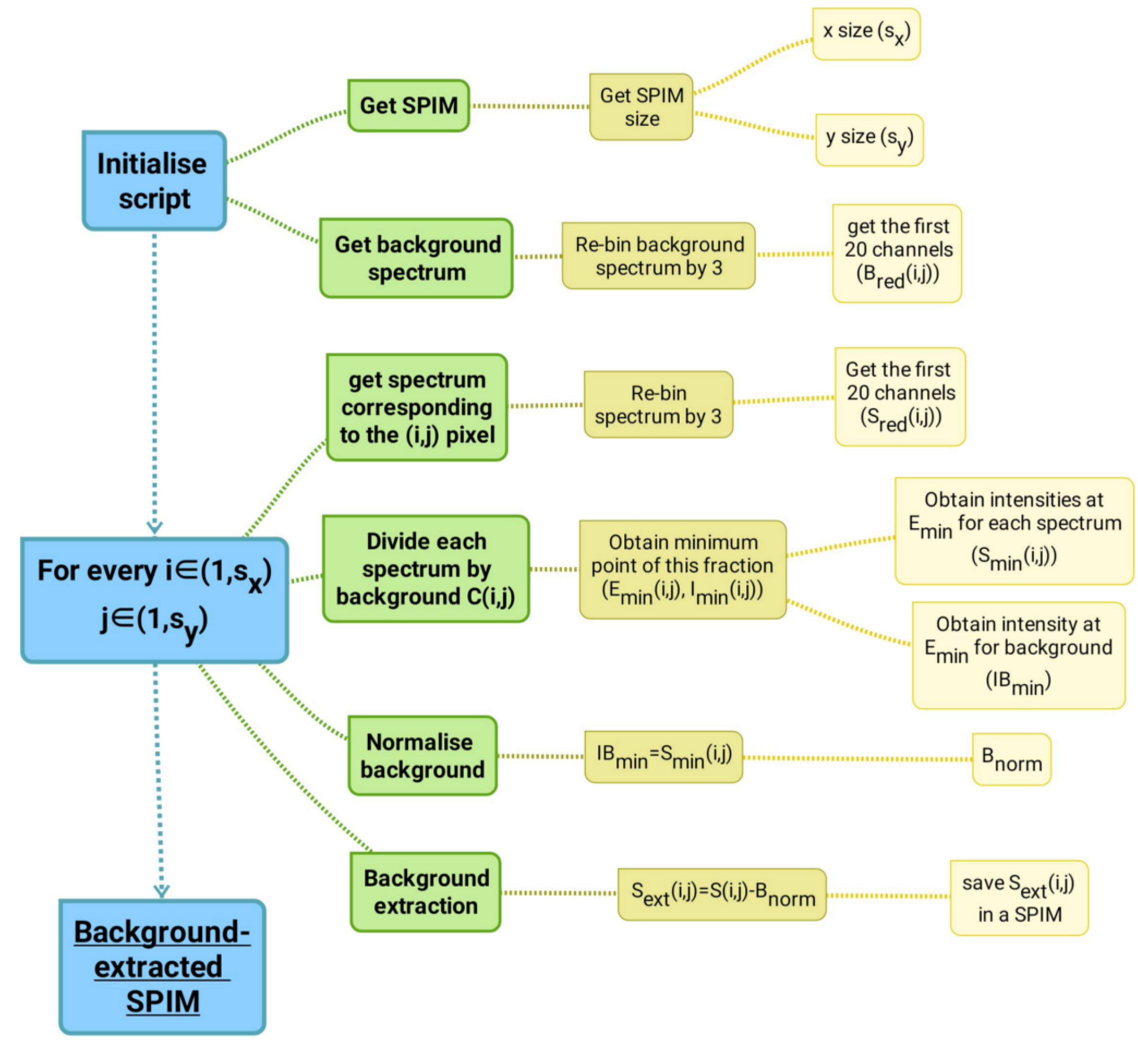

Figure 3.14: *Step By step scheme of our custom background extraction.*

- We normalise the background with respect to each one of the spectra in the SPIM. For this, we put as a condition that the intensity of the background at $E_{min}(i,j)$ (IB_{min}) has to be equal to the intensity of the given spectrum at $E_{min}(i,j)(S_{min}(i,j))$. This way, we ensure that the background will be lower than the spectrum for all the energy window being analysed except for $E_{min}(i,j)$. In other words, the background-subtracted spectra will be positive for all energies except for $E_{min}(i,j)$, which we consider to be an energy point with no plasmonic activity that depends on the spectrum being analysed. The operation to achieve this is
$$B_{norm}(i,j) = B \times \frac{S_{min}(i,j)}{IB_{min}} \tag{3.30}$$
where $B_{norm}(i,j)$ is the normalised background with respect to $S(i,j)$

- We subtract the normalised background in every spectrum of the SPIM, and we label it S_{ext}:
$$S_{ext}(i,j) = S(i,j) - B_{norm} \tag{3.31}$$

- Finally, we save each of the bacground-subtracted spectra in a new SPIM.

An integrated spectrum after background extraction from one of our SPIM-EELS can be seen in Figure 3.15. As we can see, what this background extraction does is just subtracting the background component so that the remaining spectrum is positive for all energies, which is coherent with the physics taking place in the mentioned spectrum.

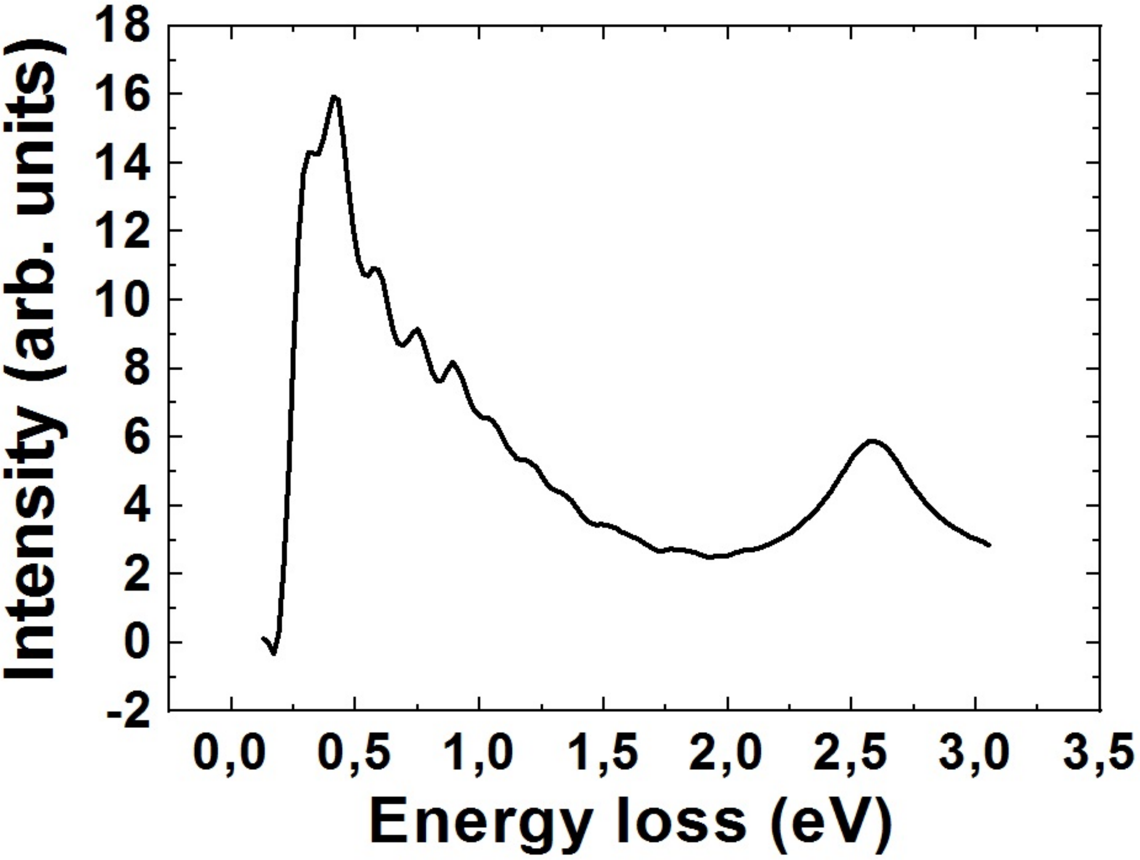

Figure 3.15: *Integrated EEL spectrum from the half-dumbbell SPIM-EELS after background extraction. The different plasmonic components can be seen in the spectrum.*

Using only this background routine, we are able to obtain a SPIM where we can already observe some of the spatial distributions of the different plasmonic features, especially those at low energies, where the SNR is the lowest and there is almost no influence from the transversal component of each NW. An example for these components, visible right after the background extraction with no further analyisis, can be seen in Figure 3.16. However, for other components at lower and higher energies, where either the background extraction has not been as successful, the different features start to not be discernible from one another or there is an undeniable part of the spectrum coming from the transversal plasmonic mode, a more accurate analysis is needed. This is where NMF is needed.

Component analysis: Non-negative Matrix Factorisation

After the background has been subtracted, it is time to discern the different features present in the low-loss EEL spectra. Since the traditional approach for this analysis (isolating different

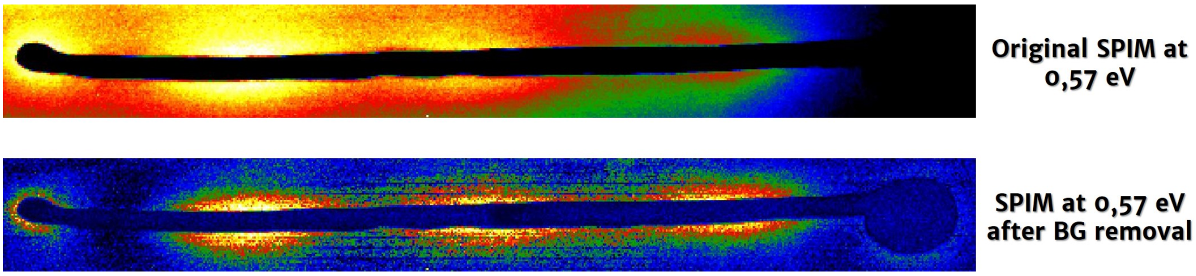

Figure 3.16: *Comparison between the original SPIM of the Au half-dumbbell at 0.57 eV before and after the background extraction.*

spectral windows where we only have one specific feature) cannot be used, and multi-peak fitting without constraints has not worked, a statistical multivariate analysis using NMF has been put in place, as explained in Section 3.3.2.

As it has been stated in Section 3.3.2, to implement this component analysis, we have used the Hyperspy interface. In here, we have created a custom algorithm that reads our SPIM files, performs an NMF decomposition, and then gives individual data for each component of the decomposition. Instead of saving our scores and our loadings as two separate matrices, one containing the spatial distribution of all of the different components and another one containing the spectral data of said components, we have set our custom algorithm to provide one SPIM-like dataset for each component.

Analysis using a different number of components have been tried, as well as several spectral windows. Due to the noisy character of this data, large spectral windows did not work well for this analyis. On the other hand, spectral windows that were too small did not have enough energy channels to be able to perform a statistic analyis on them.

As stated in Section 3.3.2, NMF requires a number of components to be given before the analysis itself. When performing this analysis in data sets with high amounts of noise and an unknown number of sources, this has been tackled by setting a high number of components. It has been observed that a number of components close to the actual number of features in the sample (roughly estimated from the SPIMs) yields acceptable results, but using more components to account for noise, as well as components we migh not know to be there, yielded more accurate results. However, as a result, in a few cases some of the plasmonic resonances are spread over several components. In a few other cases, two resonances are intertwined over two or more components. In these cases, the NMF components have had to be integrated in order to retrieve the actual plasmonic resonances. The output of each component as an independent SPIM-like dataset has eased this process greatly.

Finally, we have considered spectral windows 1 eV in width, moving up by 0.5 ev. This is, if the first window is from 0 to 1 eV, the second one will be from 0.5 to 1.5, and so on. The only exception to these spectral windows will be the initial one, which will go from 0.2 to 1 eV since the noise, as well as the residue signal from the background extraction, is especially concentrated at very low energies.

The number of components per decomposition has been set at 16 to account for residual low energy components and noise, although calculations have been done with a few less components for some of the samples yielding similar results.

We have mostly taken into account components that appear in at least two overlapping spectral windows, since that shows that the feature is physically present and not a product of the NMF decomposition and the noise in the SPIM.

In very few cases, and probably due to noise in the SPIM, two components have appeared for the same plasmonic feature. In this case, we have taken both components, summed them and integrated them for a spectral window between 0.8 and 1.2 eV wide around the main spectral feature.

A visual representation of two integrated background-extracted spectra taken from a SPIM, as well as their component analysis, can be seen in Figure 3.17. Here, we can see that the two background-extracted spectra, integrated over two different areas of the same size in the SPIM, present completely different characteristics at the same energy. We also see that the shape of the different components is not as sharp as it should be for some of the components. This could be due to the noise in the different SPIMs, a small error in the background extraction, or just an effect of the component analysis itself. However, the components are a lot more differentiable than they were prior to this analysis and, as we will see in Section 3.4, so are their spatial distributions.

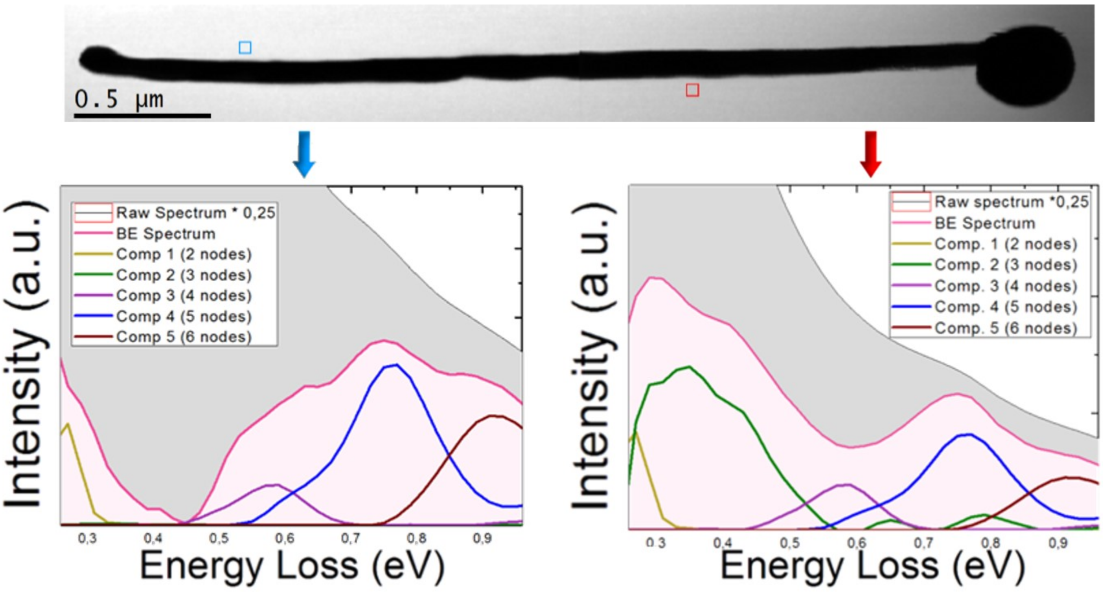

Figure 3.17: *Component analysis comparison between two areas in a SPIM. Top: STEM bright field micrograph corresponding to our Au half-dumbbell sample. The two areas where the spectra have been integrated have been marked in blue and red, respectively. Bottom: Plots showing the raw spectrum in each of the aforementioned areas, as well as their background extracted spectra and the intensity of the components present in that energy window.*

3.4 Results

An example of the joint analysis of the background extraction and the NMF decomposition can be seen in Figure 3.18. For this example, at 2.05 eV, we can see the intensity map at this energy of the original SPIM, as well as the same map after the background removal. For this specific energy, we can see two different components: on the one hand, a feature corresponding to a longitudinal mode that peaks at 2.05 ev, and the tail of the transversal mode, which peaks at 2.7 eV for this sample.

It is easy to see that the map of the SPIM after the background removal corresponds to

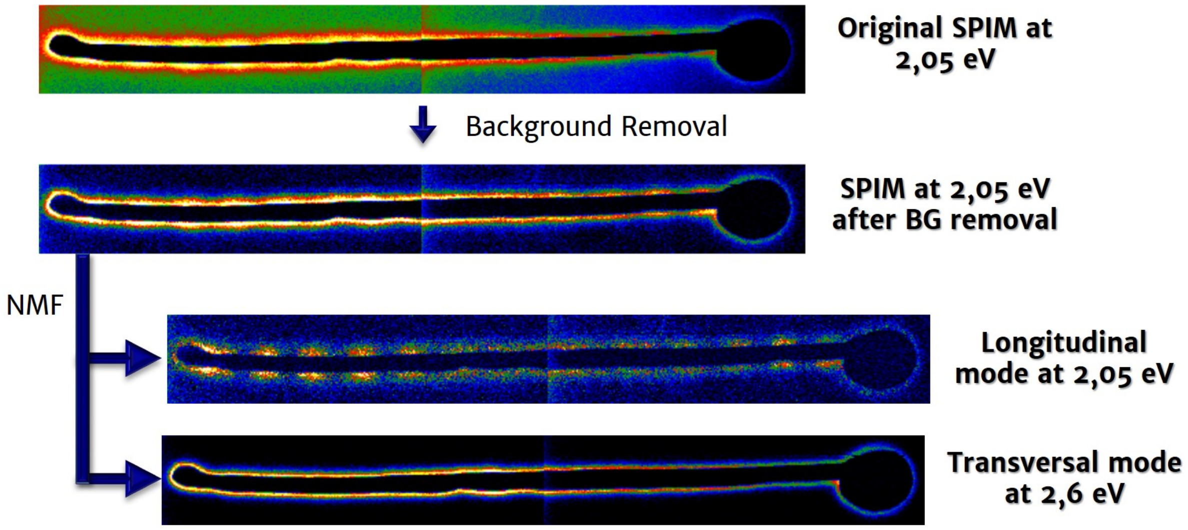

Figure 3.18: *Joint background removal and component analysis in a SPIM, result example at 2.05 eV. From top to bottom: Intensity map of the original SPIM, SPIM after background removal, and the components for the longitudinal mode, which has a peak at 2.05 eV, and for the transversal mode, which peaks at 2.6 eV, respectively.*

a combination of the longitudinal and the transversal mode. By being able to discern both modes, we can perform an analysis that yields much more accurate spatial distributions for the longitudinal modes at energies clsoe to the transversal mode. This is of great importance for the analysis of the plasmonic behaviour of these samples.

For the purpose of this study, and since we are testing the combination of our custom background extraction and the NMF analysis, we will be looking at the results from the different analysis ordering them by an increasing amount of noise in the SPIM-EELS, regradless of their morphology.

3.4.1 High SNR: the Au half-dumbbell

The results concerning the plasmonic response of the Au half-dumbbell can be seen in Figure 3.19. Due to the higher SNR in this SPIM, this is the most accurate of the analyses shown in this study. Several characteristics are to be pointed out from these results:

- The first important remark is the accurate discerning of the different components, in some cases going below the spectral resolution of the study($\sim$ 160 meV). The nodes and antinodes shown in the spatial distribution of these plasmonic features are clearly differentiated, providing an in-depth information for the plasmonic behaviour of this system.

- Another remarkable concept concerning these results is the spectral window that we have been able to cover using this technique. At low energies, we have been able to discern plasmonic modes down to 250 meV, quite an astounding result given that the spectral resolution of the EELS spectra during this study has been $\sim$ 160 meV. As for the energies closer to the transversal mode, we have been able to discern energy modes up to 2.2 eV. If we see the integrated spectrum shown in Figure 3.15, we can observe that the spectral components are not discernible at this energies even when integrating the spectra, let alone when studying the spatial distribution of said component.

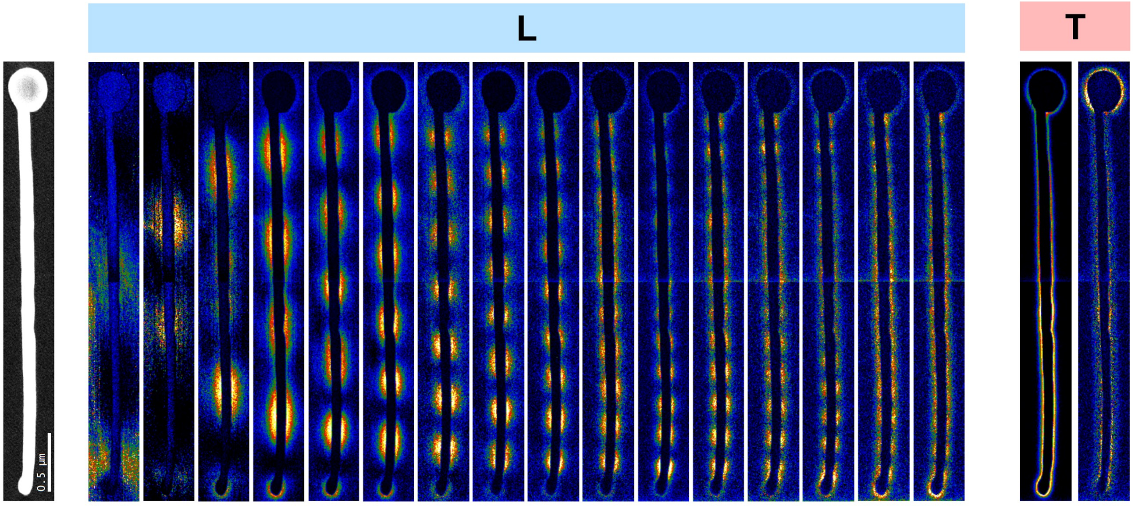

Energy (eV)	0,25	0,35	0,6	0,7	0,9	1,1	1,2	1,35	1,5	1,65	1,75	1,85	1,95	2,05	2,15	2,2	2,6	2,7
Energy (nm)	4960	3540	2070	1770	1240	1130	1030	930	830	750	710	670	630	600	580	560	480	460

Figure 3.19: *Spatial distribution of the plasmonic modes for the Au half-dumbbell. From left to right: STEM-HAADF micrograph of the area where the SPIM has been taken, spatial distribution of the different longitudinal modes in ascending order of energy of the plasmonic resonance, and spatial distribution of the transversal plasmonic mode corresponding to the NW (at 2.6 eV) and the NP attatched to the NW (at 2.7 eV).*

- Finally, this analysis lets us discern the transversal components coming from the Au NW (peaking at 2.6 eV) and the ones coming from the Au NP (peaking at 2.7 eV). Given the intensity and width of the Au NW transversal mode, and the fact that the energy difference between the two transversal modes is below the energy resolution of our study, it is quite an interesting result to have. Furthermore, this answers our initial inquiry about this system (whether the Au NW and the Au NP are coupled), showing proof that they are indeed not coupled at all.

3.4.2 Medium SNR: The Au nanowire

As it has been explained in Section 3.2.3, there has been one SPIM with a SNR high enough to present more challenges in the data analysis than the Au half-dumbbell, but low enough that, to some extent, a complete plasmonic analysis can be performed. This SPIM comprises a very high aspect-ratio Au NW. It is of importance to notice that, for this SPIM, the number of spectra taken has been a 40% of the spectra present in the SPIM described in Section 3.4.1. This has been an added handicap to the analysis on top of the noise in these EELS SPIMs.

The Au NW

Results concerning the Au NW SPIM can be seen in Figure 3.20.

First and foremost, the presence of a lower SNR is evident, as the plasmonic components resulting from the NMF analysis are sensibly noisier than in the previous case. The components at low energies appear irregular due to this noise, and at higher energies the intensity of the modes closer to the tips of the Au NW are much more intense than the ones in the central part of said NW. This could be due to the curvature of this sample. However, this lower intensity, combined with the higher SNR, makes the analysis of the central longitudinal modes of this

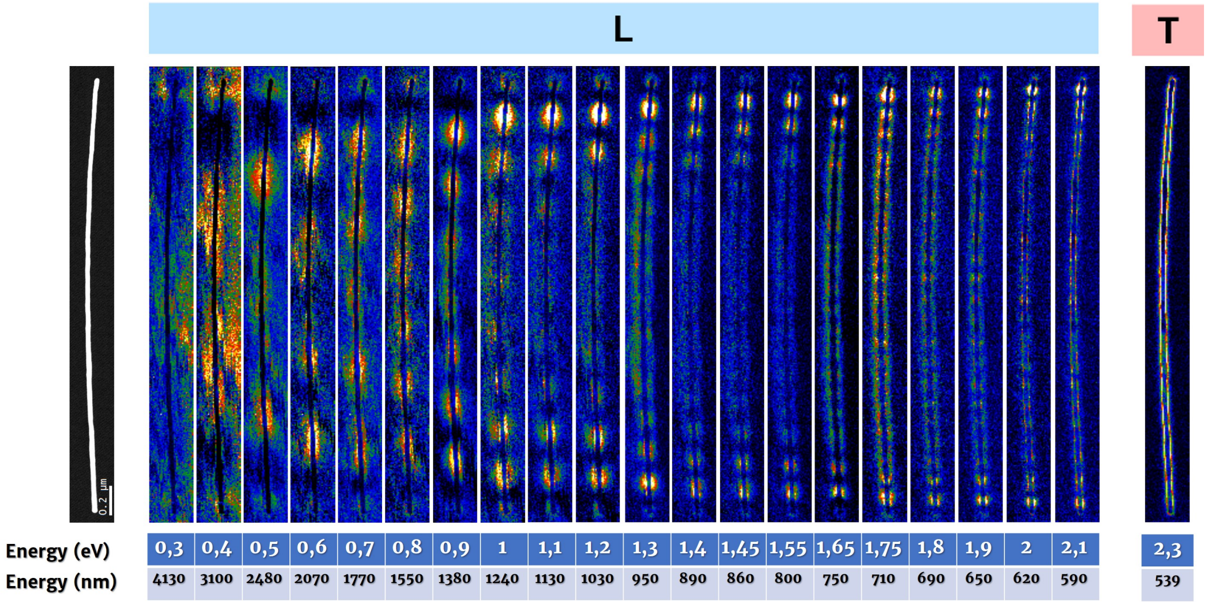

Figure 3.20: *Spatial distribution of the plasmonic modes for the Au NW. From left to right: STEM-HAADF micrograph of the area where the SPIM has been taken, spatial distribution of the different longitudinal modes in ascending order of energy of the plasmonic resonance, and spatial distribution of the transversal plasmonic mode corresponding to the NW.*

sample even more challenging, even getting to confusing them with the background noise at some points.

Even with all these challenges, the analysis manages to find plasmonic components down to 0.3 eV, which is astounding given the amount of noise in the SPIM. It also allows us to find longitudinal components up to 2.1 eV, really close to its transversal mode at 2.3 eV. Within this analysis, the differenciation of the plasmonic modes between 1.65 eV and 2 eV is especially remarkable, given the amount of noise, the proximity to the transversal plasmonic mode and the lesser number of spectra taken.

For this specific sample, since it is a homogeneous sample (that is, a single symmetric sample, with a known and homogeneous diametre an length) we can perform a study on the regularity of the wavenumber of the different longitudinal plasmonic modes in the sample. For this study, we have measured the inter-nodal distance of each mode by means of a simple intensity profile.

Since the sample is curved and intensity profiles are generally performed in a straight line, we have created a custom script that analysed the integrated signal for the whole SPIM-EELS, and discerned the region of the spim occupied by the Au NW by setting a threshold total intensity. For each measurement in the longitudinal direction of the Au NW, the three spectra gathered the closest to the interface between the sample and vacuum (where the plasmonic signal is at its highest) were taken in order to create a final intensity profile. This proved to be more effective than a regular profile, where the intensity values of the profile were not accurate due to the curvature of the sample.

In order to get the highest accuracy possible, and with the exception of the 3 nodes component at 0.3 eV, the measurements have been performed on the second-to-last node for each side of the sample since they are, in general, the most intense for each component. The wavenumber k is then obtained by using the following expression:

$$k = \frac{2 \cdot \pi}{d} = \frac{2 \cdot \pi}{\frac{d_m}{n-3}} \tag{3.32}$$

where d is the internodal distance, d_m is the distance measured between the second-to-last nodes on each side, and n is the number of nodes in that specific component.

We have compared our results to a perfect resonator, represented in this case by a line that is obtained simply by assuming a homogeneous distribution of the plasmonic modes:

$$k_L = \frac{2 \cdot \pi}{d_L} = \frac{2 \cdot \pi}{\frac{L}{n-1}} \tag{3.33}$$

where k_L is the wavenumber of a specific component with a number of nodes, d_L the ideal internodal distance for this component, L the length of our nanowire (here taken as 2.94 μm) and n again the number of nodes in this specific component.

The results for the wavenumber of the different plasmonic longitudinal components and their comparison with the light line can be seen in Figure 3.21.

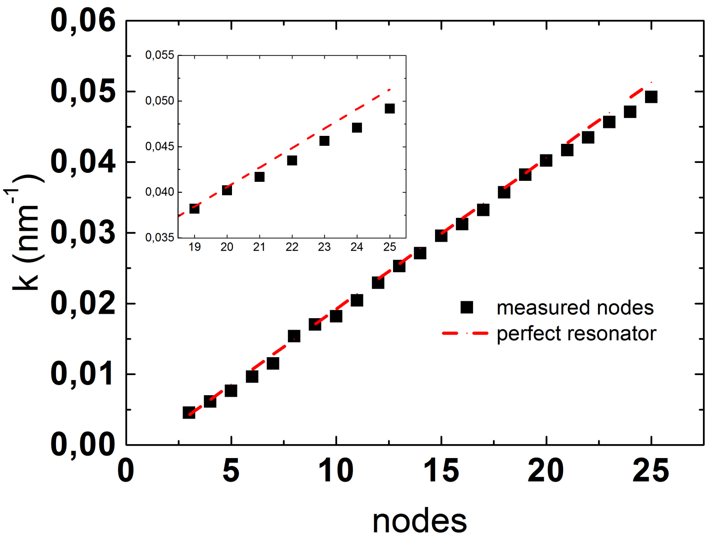

Figure 3.21: *Wavenumber analysis for the Au NW. The black dots show the wavenumbers calculated from the internodal distance measures for the different plasmonic components. The red dotted line represents the light line for this sample.*

We can see in these results that the wavenumber distribution for the different components follows the the behaviour of a perfect resonator for most of the plasmonic components analysed. However, at higher energies, these wavenumbers seem to start to stem out of this tendency, having a slightly lower value than expected.

3.4.3 Low SNR: The double Au NW, the increasing diametre NW and the Au dumbbell

Within the context of this study, some SPIMs have gathered a vast amount of experimental noise. On top of that, some of these affected SPIMs had a lower number of spectra than our high SNR one.

However, this has been a chance to test our analytic method at the most challenging conditions possible in terms of SNR. The results show that, even though not even this analysis can provide a full explanation of the plasmonic behaviour of these samples, it is possible to gather at least partial results from these SPIMs that would not have been able to be retrieved using the aforementioned traditional methods. Another option is to use parts of the analysis independently, like the NMF decomposition, to try and obtain results where the noise has difficulted the background extraction using our custom routine.

The results of these low SNR SPIMs, as well as their discussion, are shown in this section.

The double Au NW

Due to its specific SNR and its low number of spectra, this sample is unique in the way the analysis affects it. At low energies, the noise in the SPIM merges with the spectroscopic signal, making the background extraction even more challenging than the other SPIM-EELS mentioned in this section. This is the reason why, at least for low energies, the NMF decomposition does not work as well as it should after background extraction. In return, the data collected from the NMF decomposition of the SPIM with no background extraction (gathered during an initial stage of this analysis) is more accurate in depicting the different plasmonic components than the decomposition after the background extraction. At higher energies, however, the analysis with background extraction seems to yield better results, since the background extraction is less crucial for the analysis in this energy window with respect to the NMF. The results related to this analyses of the double Au NW spim are shown in Figure 3.22.

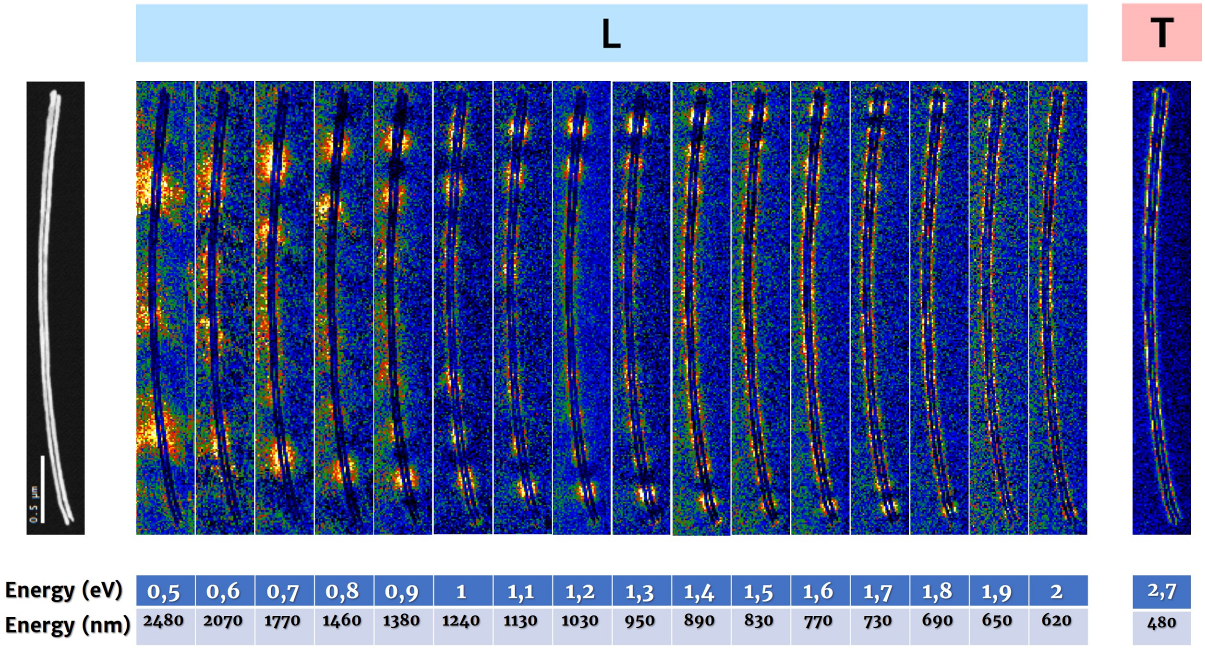

Figure 3.22: *Spatial distribution of the plasmonic modes for the double Au NW. From left to right: STEM-HAADF micrograph of the area where the SPIM has been taken, spatial distribution of the different longitudinal modes in ascending order of energy of the plasmonic resonance, and spatial distribution of the transversal plasmonic mode corresponding to the double NW.*

It seems that, even for this challenging level of noise, the results for this double Au NW are clear enough to try and make a comparative study with respect to the single Au NW, at least to some extent. However, it is true that the lowest energy to which we can get with this analysis for this SPIM is 0.5 eV, which is far worse than our results for the SPIMs with a better SNR. The spatial distribution of the longitudinal surface modes are also blurrier and noisier than their counterparts in the single NW SPIM. Nevertheless, the modes at lower energies for this sample seems to point to the fact that the longitudinal modes of these samples do not shift in energy when two different NW are joint. However, when it comes to their transversal component, where they both light up at the same energy, there is indeed a difference between the transversal resonance for a single NW (2.3 eV) and a double NW (2.7 eV). This could, in theory, indicate some sort of coupling between the two Au NW. The sample in this case could be interpreted as a single NW with a higher effective radius.

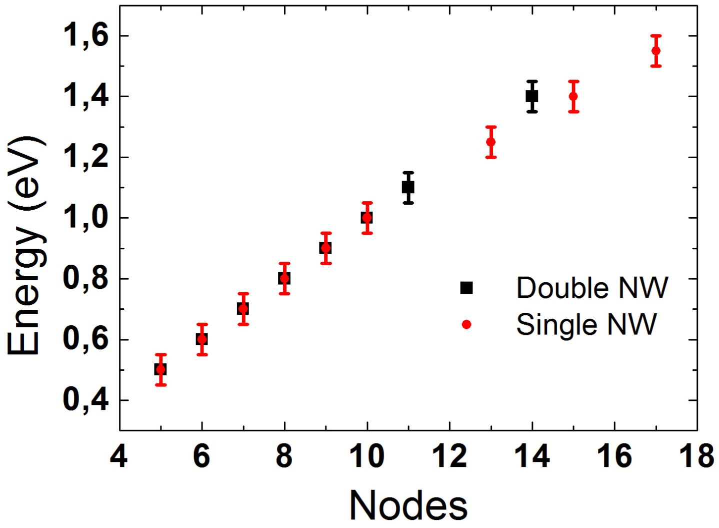

Figure 3.23: *Energy of the longitudinal plasmonic modes with the more visible nodes in the single and double NW sample for the same aspect ratio.*

However, a comparison between the plasmonic modes with the more visible nodes of the single (Figure 3.20) and double nanowires (Figure 3.22) seems to show otherwise. As it can be seen in Figure 3.23 there is a high similitude in energy for the longitudinal plasmonic modes in both samples. This seems to point out to a lack of coupling between the two NW in the double NW sample. Instead of making contact, they might be separated by a thin layer vacuum. This would be coherent with the fabrication method employed for these samples, since they come from the dispersion of an aqueous solution. A water meniscus between the two NW could result in a gap between said NW once it dried up. This hypothesis seems to be confirmed in the simulations shown in Section 3.5.2 and will be discussed in depth in said section.

As for the difference in energy in their respective transversal plasmonic features, there are two possible hypothesis that could answer this response. On the one hand, it could be possible that the transversal plasmon had a higher-range interaction than longitudinal plasmons, being able to couple even though both NW in the double NW sample do not seem to be touching each other. On the other hand, there is always a chance of it being an error coming from the high SNR or the analysis method.

All in all, the analysis has not been as accurate as the one for the single NW, mostly due to the noise present in the SPIM. However, the results obtained, like the ones shown here, are quite accurate especially taking into account the levels of noise present in the SPIM.

The increasing diametre Au NW

Results for the increasing diametre Au NW SPIM-EELS can be seen in Figure 3.24.

This sample, as it has been previously mentioned before, presents an astounding amount of

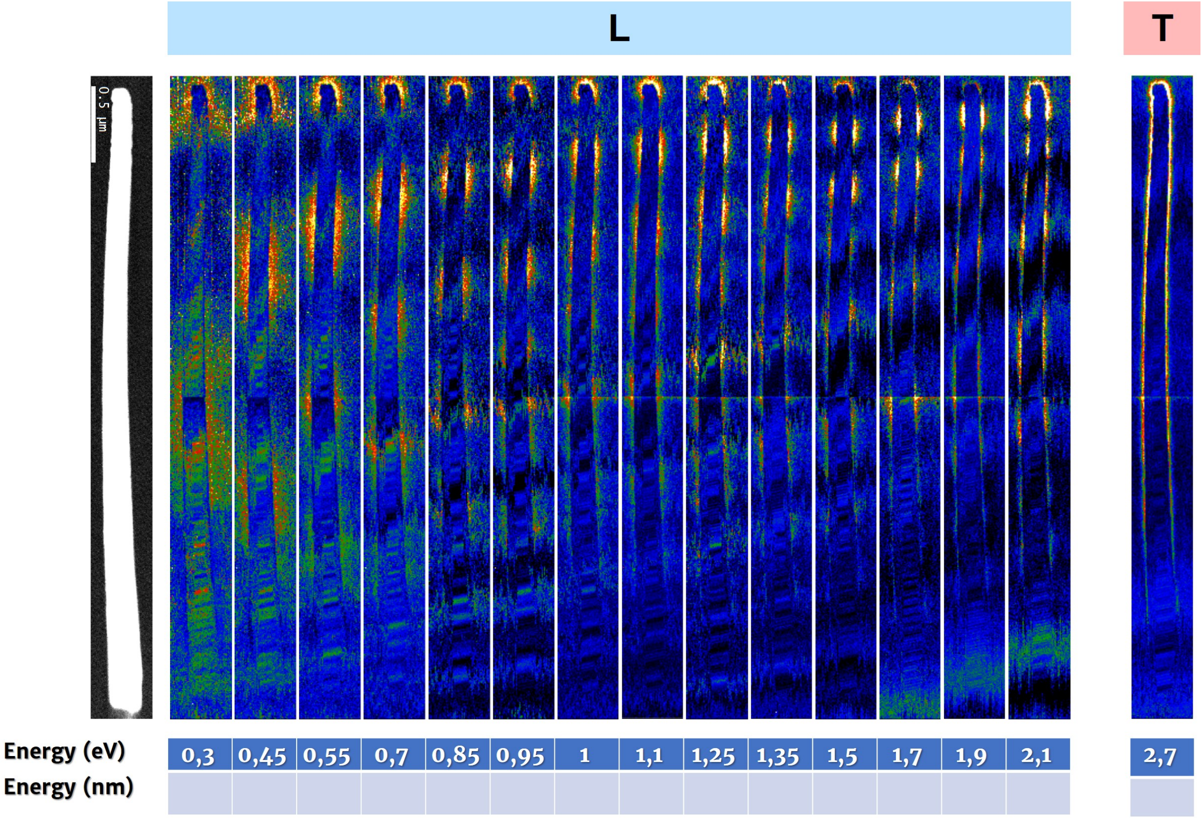

Figure 3.24: *NMF analysis of the spatial distribution of the plasmonic modes for the increasing diametre Au NW. From left to right: STEM-HAADF micrograph of the area where the SPIM has been taken, spatial distribution of the different NMF components supposedly linked to the different longitudinal modes in ascending order of energy of the plasmonic resonance, and spatial distribution of the transversal plasmonic mode corresponding to the nanostructure.*

noise, which moves somewhat homogeneously in the SPIM space when increasing the energy. This can be seen in the videos attatched as supplementary information for this chapter.

As it has been seen in Section 3.2.3, as well as in the supplementary information, this is, by far, the worst SPIM in terms of SNR out of our whole study. However, as mentioned in Section 3.11, this morphology gives us a unique opportunity to measure plasmonic components with different intensities in a SPIM with a constant amount of experimental noise. Due to the tip-induced effect shown in Section 3.11, as the diametre of the NW increases, the intensity of the components decreases, and viceversa. We relate this behaviour to the tip induced effect explained in Chapter 1, which is coherent with studies on plasmonic samples so-called "nanocarrots" [329], where modes are more intense in the thinnes parts of the samples. Since the noise level is the same for the whole SPIM, this greatly lowers the SNR, making it even more challenging for the NMF analysis. This can be observed in the sensitivity of the analysis with respect to the plasmonic modes in the thinner parts of the NW (with a higher SNR) versus the plasmonic modes in the thicker parts of the NW (with a lower SNR). In the latter, the noise levels are so high that the NMF analysis mistakes the noise for plasmonic components.

This response of the analysis implies that the results from the NMF analysis that can relate to a physical phenomenon taking place in the sample are the ones located in the thinnest part of the sample (top half of Figure 3.24).For the rest of the SPIM, the analysis mistakes the noise in the SPIM for actual plasmonic modes, which explains the erratic behaviour of this SPIM compared to the rest of the analyses performed in this study. However, this information is still quite important, since it shows in just one image the performance variation between a region with a medium-low SNR (for which this analysis can still yield some important information) and a region with a really low SNR, where a statistic method such as NMF will take the most intense components in the SPIM, in this case, the noise.

The Au dumbbell

Finally, the plasmonic components found for the Au dumbbell are displayed in Figure 3.25. As it can be seen in the video in the additional materials for this manuscript, this SPIM has an astounding amount of noise, making it almost impossible to analyse its plasmonic properties using the conventional analysis techniques. However, our analysis routine proves that, even though a complete analysis might not be possible for this SPIM, we still gather an important amount of data that is interesting both from a plasmonic and an analytic point of view:

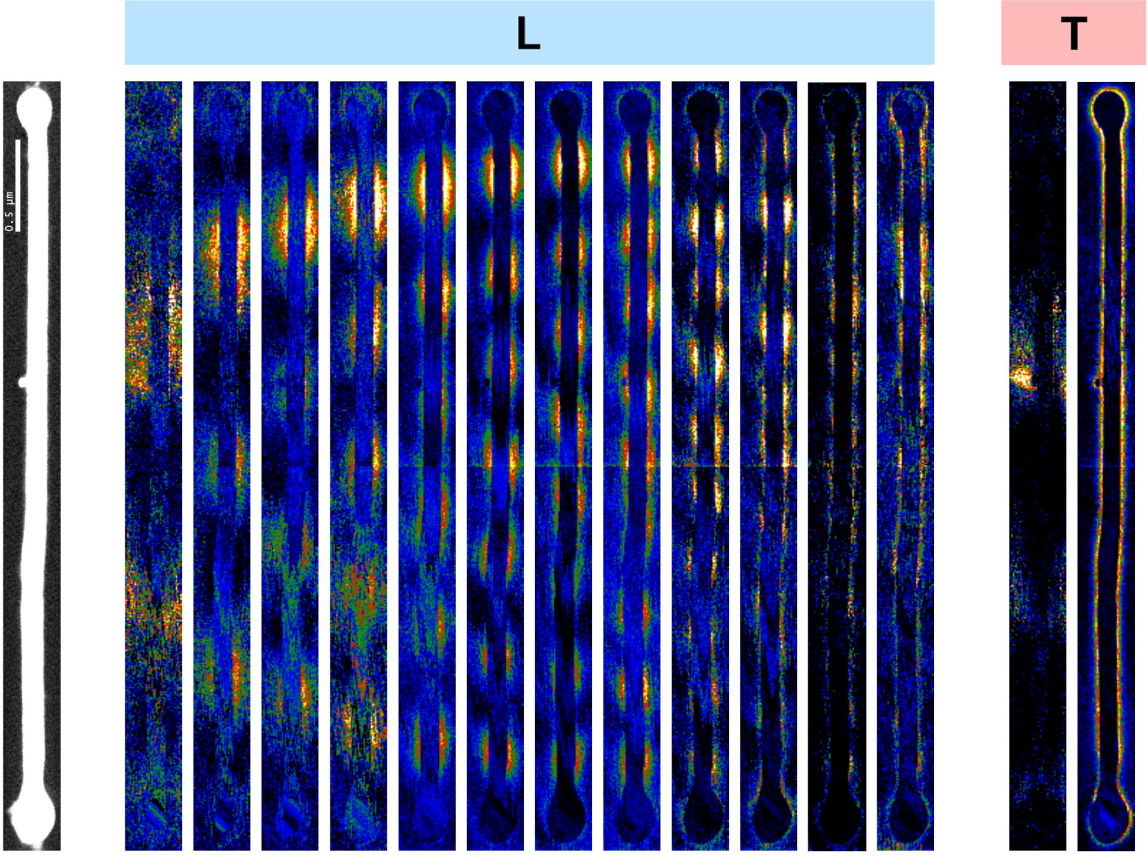

	L												T	
Energy (eV)	0,45	0,55	0,7	0,85	1	1,1	1,2	1,35	1,45	1,6	1,75	1,9	0,4	2,65
Energy (nm)	2760	2250	1770	1460	1240	1130	1030	920	860	770	710	650	3100	470

Figure 3.25: *NMF analysis of the spatial distribution of the plasmonic modes for the Au dumbbell. From left to right: STEM-HAADF micrograph of the area where the SPIM has been taken, spatial distribution of the different NMF components linked to the different longitudinal modes in ascending order of energy of the plasmonic resonance, and spatial distribution of the transversal plasmonic mode corresponding to the nanostructure.*

- The analysis can go to energies as low as 0.4 eV, even for this amount of noise

- We have been able to discern a plasmonic mode for the nanoparticle attatched to the the dumbbell from the dumbbell longitudinal mode below the resolution limit. They are located at 0.4 and 0.45 eV, respectively, which makes their discerning quite impressive given that the energy resolution was around 160 meV.
- Given the energy at which this resonance from the nanoparticle is found, our two main hypotheses are that either there is a coupling phenomenon that lowers the energy of the plasmonic resonance or the geomety is closer to that of a low aspect-ratio NW than a NP. What we can be sure of is that this small nanostructure is not just a protuberance from the NW, since we can see the surface component of the NW through the NP.
- Even for the amount of noise present in the SPIM, we still have managed to retrieve 12 different longitudinal surface plasmon modes, as well as the transversal mode of the dumbbell.
- The information gathered from the transversal plasmon in the dumbbell seems to indicate that, even though the nanoparticle in the dumbbell does not seem to be coupled with the Au NW, the nm nanoparticle seems to be so. Indeed, both transversal plasmons occur at the same energy.

3.4.4 Energy dispersion studies

In the case of the plasmonic samples where the experimental conditions have allowed for a successful measurement of the wavelength of the resonations in each plasmonic mode (single Au NW, half-dumbbell and dumbbell), we have been able to perform an experimental measurement on their characteristic energy dispersion relation.

AU NW: The results for the E-k dispersion on the Au NW can be seen in Figure 3.26.

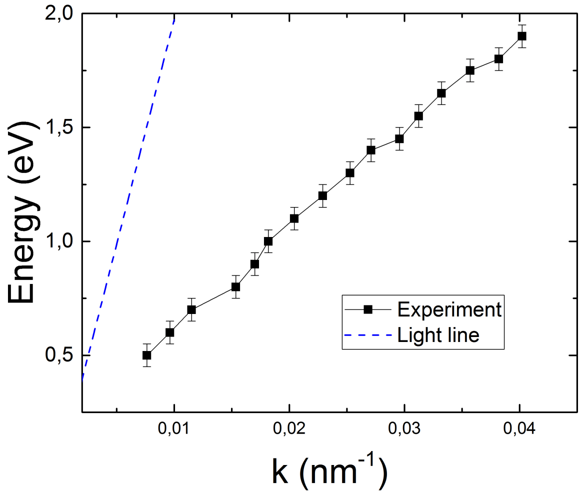

Figure 3.26: *E-k measurements for the Au single NW. The light line in vacuum is shown for reference (blue dashed line).*

These results seem to show more of a linear dependency of energy to wavenumber than the ones found in the literature [287]. This is probably due to the higher aspect-ratio of the sample, which makes it closer to an ideal resonator.

Au half-dumbbell: The experimental results regarding the E-k dispersion of the Au half-dumbbell can be seen in Figure 3.27.

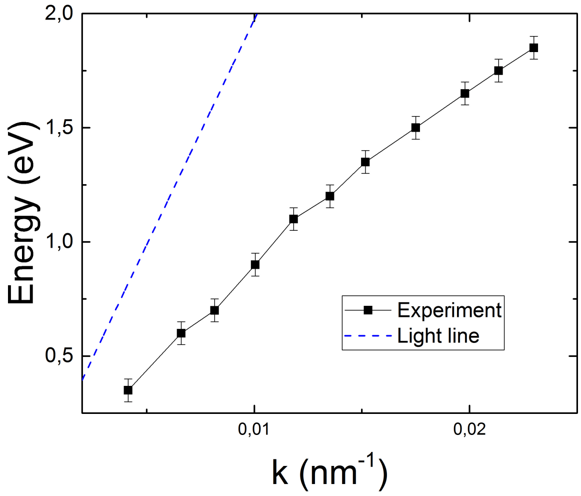

Figure 3.27: *E-k measurements for the Au half-dumbbell. The light line in vacuum is shown for reference (blue dashed line).*

This time, we do find a nanostructure that behaves in a more similar way to the one shown in the literature [287], with a curved E-k dispersion that stems further away from the light line the higher the energy. This can be due to two different factors. The first possible factor is the lower aspect-ratio of this sample with respect to the single Au NW, which would make it closer to the ones shown in section 3.1.2. The second possible factor is the presence of the Au NP. However, this possibility is less likely, since, as we have seen in this section, the NP in the half-dumbbell is not coupled to the NW.

Au dumbbell: The E-k dispersion for the Au dumbbell, as well as its comparison to the Au half-dumbbell, is shown in Figure 3.28.

Here we can see the similarities between the half-dumbbell and the dumbbell dispersions. If we take into account that both samples have a quite similar aspect ratio, we can see that, regardless of the presence of NP in the dumbbell structure and the coupling or lack thereof between the NW and the NPs, the main factor regarding the E-k dispersion of our samples is its aspect-ratio.

3.5 Theoretical calculations

For further insight on the plasmonic behaviour of these samples, simulations were performed. These simulations have two main objectives. On the one hand, confirming that our experimental data is coherent. On the other hand, seeing how close the response of these nanostructures is to their response in vacuum. These simulations have been carried out by our collaborators at the Université de Namur (Belgium), Dr. Bruno Majerus and Prof. Luc Henrard.

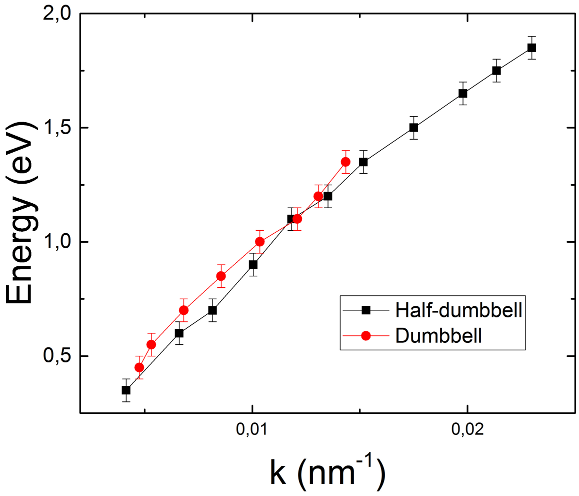

Figure 3.28: *E-k measurements for the Au dumbbell (red) and comparison to the Au half-dumbbell (black).*

3.5.1 Calculation methods: The discrete dipole approximation for electron energy loss spectroscopy

These simulations have been performed using the discrete dipole approximation for electron energy loss spectroscopy (DDEELS). This procedure, which uses the code developed by the group of Prof Henrard, divides the system being simulated into a discrete number of small (in comparison with the size of the system in question) polarizable volume elements. These volume elements produce electric dipoles under an electric field, and the electromagnetic response of the system is simulated as the interaction of all of these discreet dipoles.

The polarizability of these discrete volumes (the relation between the electric field applied to each one of these dipoles and their polarization) is calculated from the bulk dielectric function of the material in question. The total polarization of each discrete dipole is calculated by taking into account both the applied electric field and the fields radiating from the rest of the discrete dipoles in the sample.

For the modelisation of EELS experiment, the electron beam is simplified by a classical charge q moving in vacuum in the OZ-axis with a velocity dependant on the energy of the beam. By calculating the the energy exchange between the beam and each oscillating dipole system, and integrating it for the whole of a sample, we can simulate the response of a specific nanostructure in an EELS analysis. This is exquisitely explained in detail in reference [397].

In this same study, however, the influence of the substrate on which the metallic nanostructures are placed on for their EELS studies is also mentioned, since the EELS description used for these modelisations is based on an electron beam moving in vacuum. This will be a point of interest for the interpretation of the DDEELS simulations with respect to our actual results. It is possible to perform DDEELS simulations taking into account a semi-infinite substrate, but we have decided to perform them in vacuum to keep these simulations as simple as possible.

This technique had been applied to carbon nanostructures [398, 399] before being applied on plasmonic metallic nanostructures [397, 400**?**], and is now one of the main tools for the simulation of these kind of EELS experiments.

3.5.2 Theoretical simulations and comparison with the experimental results

The single Au NW

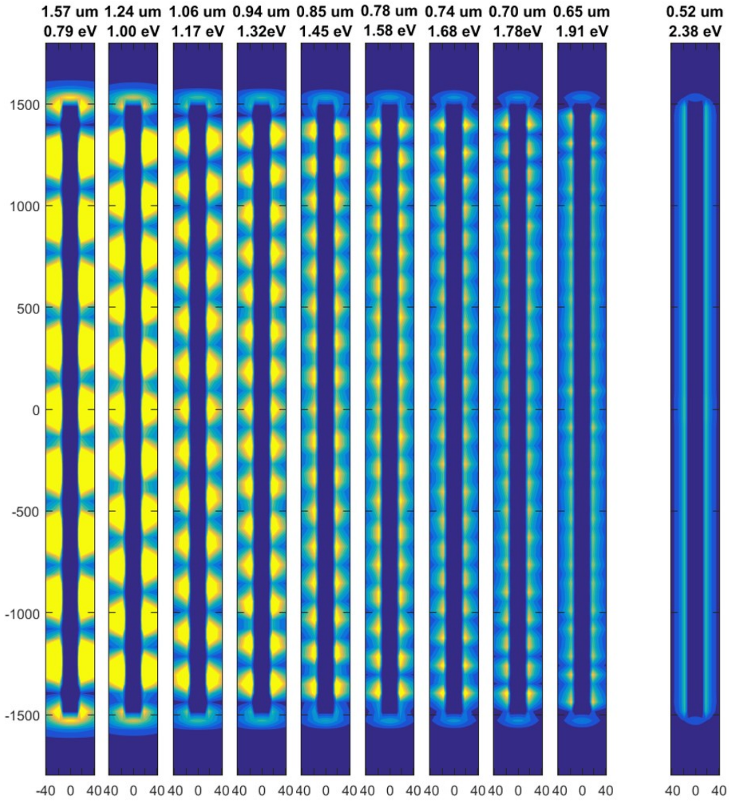

Figure 3.29: *DDEELS simulation of the plasmonic modes of the single Au NW . Spatial measurements are shown in nm. The x and y axis do not share the same scale.*

The simulation results for the single Au NW can be seen in Figure 3.29. It is important to note that these figures are not at 1:1 scale.

At first sight, we can already see a similar behaviour between the modelled and the experimental spatial distributions of the plasmonic components, which was something to be expected given that metallic NW are a kind of sample that has been extensively studied in the past [311] and due to their simple and symmetric geometry it is also an easy sample to model.

Just as we did with their experimental counterpart in Section 3.4.2, we can perform an analysis on the wavenumber of the plasmonic components that have been modelled. The results of this analysis can be seen in Figure 3.30

The direct comparison between the simulated and the experimental spatial distributions has not been possible due to the slight curvature of the NW, which difficults the comparison between both sets of maps. However, we can see that the wavenumber analysis of these model presents a very similar tendency to the one shown in Figure 3.21 for its experimental reference. This means that, even though we cannot compare the spatial distributions of the NW one by one, we know with further proof that the spatial distribution of these longitudinal plasmonic modes is very similar in the simulations and in their corresponding experimental results.

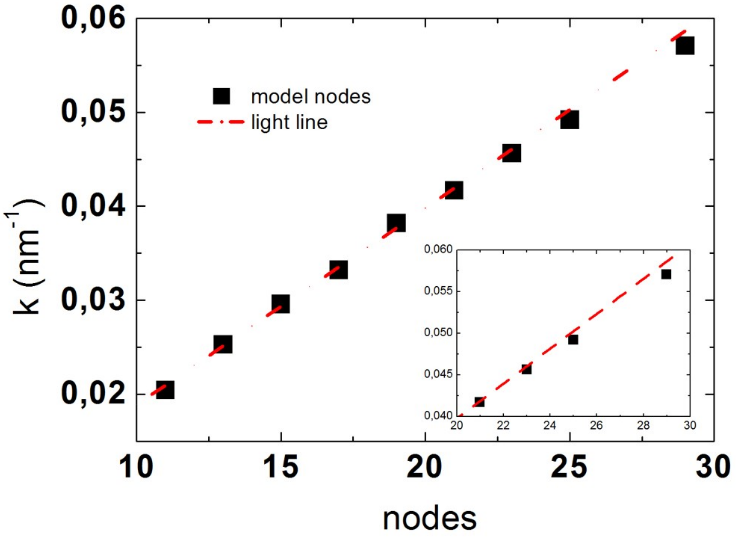

Figure 3.30: *Wavenumber analysis for the modelled Au NW. The black dots show the wavenumbers calculated from the internodal distance measures for the different plasmonic components. The red dotted line represents the light line for this sample.*

When checking these wavenumber analysis, it is clear that, even though the simulated components do step away from the light line "modellic" behaviour, they do so at much higher modes than its experimental counterpart. For an explanation on this behaviour, it is of interest to analyse the energy position of the different intensity maps related to the different plasmonic components for each specific plasmonic component (that is, for a specific number of nodes in the intensity map). This comparison is shown in Figure 3.31.

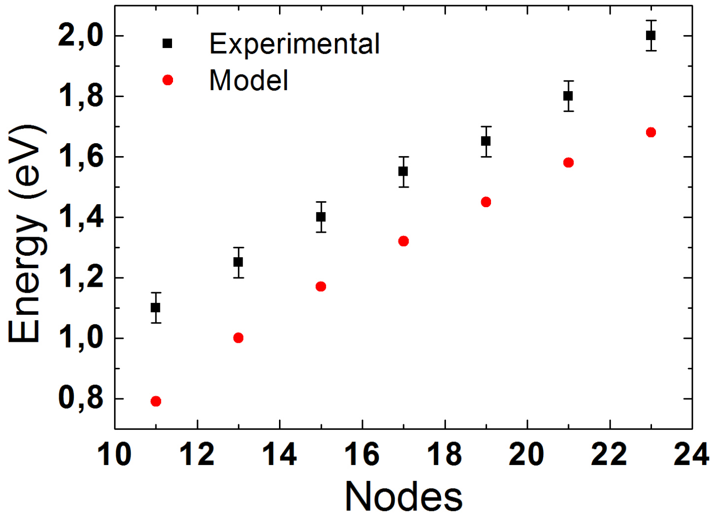

Figure 3.31: *Comparison of the energy modes of different plasmonic components. The black dots represent the experimental measured energy, while the red dots represent the model energy.*

In this figure, we can see that both the experimental and the modelled simulated components seem to show a similar trend in energy. However, it is clearly seen that there is an almost constant energy difference between the energy of a specific plasmonic mode and its simulated counterpart, with this energy being around 0.25 eV.

Our explanation for this difference in energy comes from a matter already discussed at the beginning of this section: the simulations that have been carried out have assumed a plasmonic nanostructure in vacuum, with no interaction with a substrate whatsoever. However, the interaction between our samples and the substrate they are sitting on, and the energy dispersion that is associated with it, could accurately explain the difference in energy between our experimental and our simulated results [335]. This is also the case for the behaviour of the wavenumber of our plasmonic modes: our experimental results detatch from the ideal resonator tendency at modes with lower nodes than its modelled counterparts, but the energy at which these plasmonic modes start to detatch from the light line is very close for both (∼1.7 eV)

The double Au NW

Based on our STEM data, the double Au NW has been simulated as two touching Au NW. The results for this simulation can be seen in Figure 3.32.

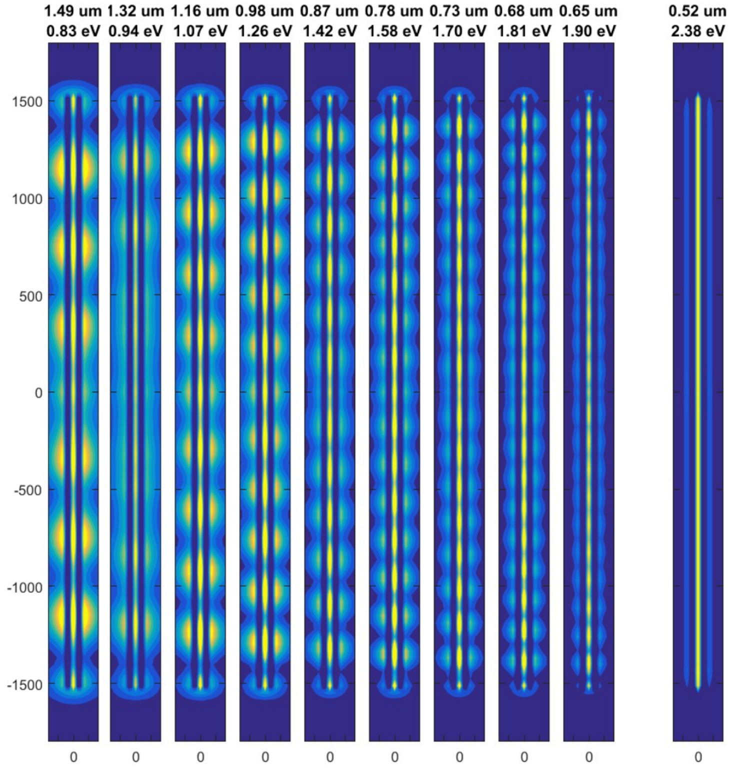

Figure 3.32: *DDEELS simulation of the plasmonic modes of the double joint Au NW. Spatial measurements are shown in nm.*

Once again, a one-by one comparison of the intensity maps of the simulated and the experimental plasmonic components is not feasible due to the slight curvature present in the former. Additionally, the noisier experimental results for the double NW make it harder as well to perform an wavenumber analysis such at the one performed for the single NW. However, the conclusions gathered from the single NW studies and simulations, presented in the previous section, seem to show enough proof that these simulations are close enough to the experimental intensity maps obtained from the STEM-EELS studies, given the geometry given as basis for the analysis is accurate. The comparisons between simulated and experimental data shown in this section for the Au half-dumbbell and the Au dumbbell seem to show further proof of this.

With respect to our hypothesis formulated in Section 3.4.3 that the two NW conforming this sample are not couple (i.e., in contact), we can look at a comparison between the simulated plasmonic modes of the single and the double NW. This comparison is shown in Figure 3.33.

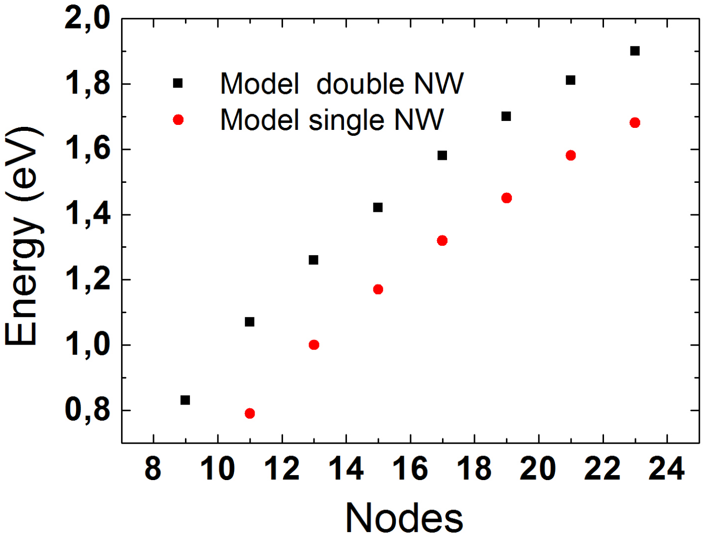

Figure 3.33: *Comparison of the longitudinal plasmonic modes of the DDEELS simulation of the single and double joint Au NW.*

As we can see in these results, there is a noticeable difference in energy between the single and the double NW simulations, something that was clearly not the case for their experimental counterparts. In the case of the simulated coupled double NW, the energy needed to reach a certain plasmonic mode is about ~0.25 eV higher than it is for the single nanowire.

Additionally, the simulated transversal plasmonic mode of the double NW, as well as half of its longitudinal modes, show something that their experimental part lacks, which is a higher intensity of the plasmonic modes in the junction between both NW.

This seems to confirm our initial hypothesis that the double NW shown in Section 3.4.3 is, in fact, two individual single NW with a very narrow gap between them. These results seem to be a better indicator, in this case, of the lack of coupling, than the presence of transversal plasmonic modes at different energies.

The Au half-dumbbell

The DDEELS simulation for the Au half-dumbel plasmonic modes can be seen in Figure 3.34.

Given the similitude between the simulated and the experimental samples, as well as the low amount of noise in the corresponding SPIM-EELS, the results of both the experimental analysis and the modelling are good enough so that we can just compare the spatial distributions of the different plasmonic modes one by one. An example of this comparison is shown in Figure 3.35.

In this comparison we can see two main characteristics. The first one is that the general

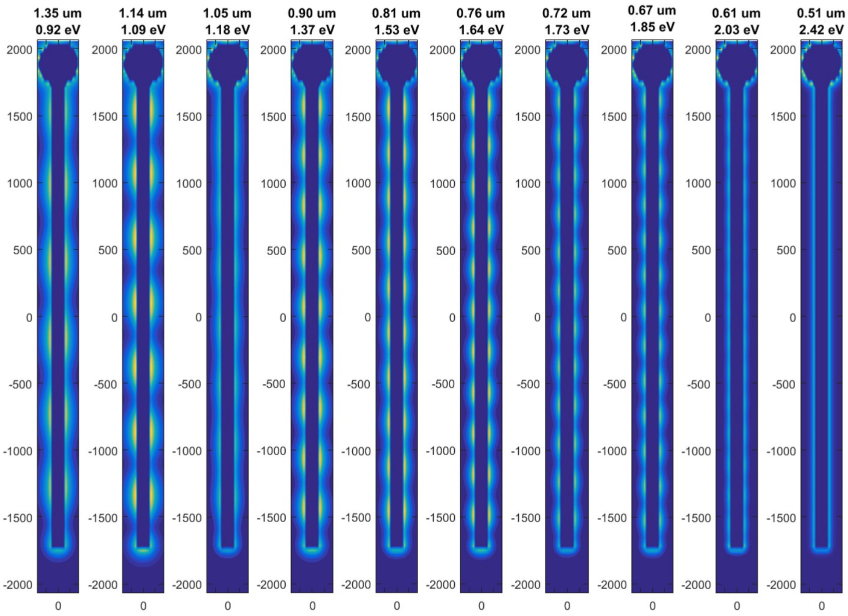

Figure 3.34: *DDEELS simulation of the plasmonic modes of the Au half-dumbbell. Spatial measurements are shown in nm.*

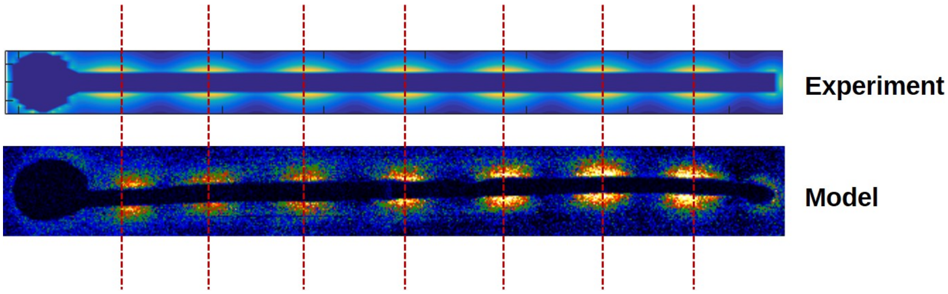

Figure 3.35: *Comparison of the experimental and modelled spatial distribution of the 8 node longitudinal plasmonic mode for the Au half-dumbbell. The energy of these modes is 1.2 eV for the experimental results and 1.09 eV for the theoretical model. Scale is as set in Figures 3.19 and 3.34.*

spatial distribution of the nodes of these plasmonic nodes seems to be coherent between the experimental results and their modelled counterpart.

Additionally, a comparison between the energy of the different modes in our experimental analysis versus our model results, which can be seen in Figure 3.36, shows an almost constant difference in energy between an experimental plasmonic mode and its corresponding model.

This difference of about 0.15 eV seems to be reminiscent of the behaviour of the Au NW (see Figure 3.31), which would lead us to attribute this energy difference to the effect of the substrate on the whole experiment. However, in this case, this energy difference seems to be visibly lower than that of the Au NW, being about half of the value for that sample.

There are two possible causes for this variation in the energy gap between experiment and models:

- On the one hand, this can be due to the different aspect-ratio of two samples. The Au NW is a much thinner sample than the half-dumbbell, and therefore the contact surface

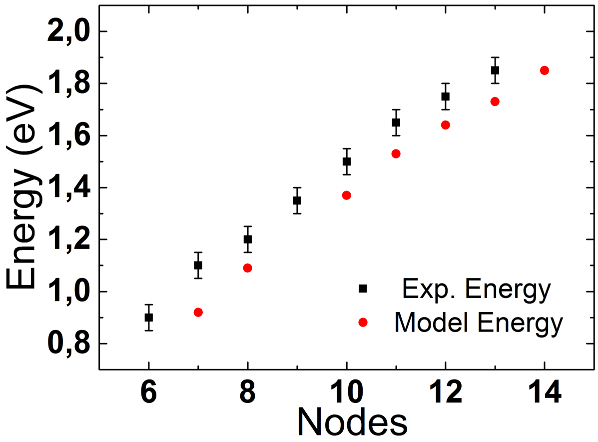

Figure 3.36: *Energy comparison between the experimental plasmonic modes of the au half-dumbbell and their simulated counterparts.*

between the NW and the substrate can represent a higher fraction of the total area of the sample, therefore increasing the coupling between sample and substrate.

- An alternative hypothesis is related to the NP in the half-dumbbell. As we have seen in section 3.11, the Au NP of the half-dumbbell is notably larger in diametre than the NW. This could mean that the NW is suspended on the NP instead of ”laying”on the substrate like the Au NW. This would reduce the contact surface and the coupling for the half-dumbbell.

The Au dumbbell

The simulated DDEELS intensity maps for several plasmonic modes of the Au dumbbell can be found in Figure 3.37.

This simulation, much like the previous one, corresponds to a geometry that is not excessively curved in the experimental section and therefore their intensity maps can be compared, as it is shown in Figure 3.38. As it can be seen here, there is a great agreement between the experimental data and their respective simulated intensity maps. The comparison of the different nodes of both maps seems to point out that, for the same mode, this model seems to simulate the position of said nodes quite accurately, which is in good agreement with all of our previous analyses.

However, once again, a comparison between the energy of the different plasmonic modes in the experimental data versus the simulated maps, which can be seen in Figure 3.39 seems to point out a constant difference in energy between the two.

This constant difference, which amounts to ~0.1 eV for this sample, seems to have the same nature as the one seen for the half-dumbbell, that is, an influence of the substrate damped either because of the aspect ratio of the NW in the dumbbell or because the dumbbell is suspended on its Au NPs and not all the way through the Au NW.

In other words, the effect we attribute to the substrate interaction can be seen for all of the samples that we have been able to analyse. However, this substrate effect does not affect all the samples the same way, with this effect being more visible for the Au NW and less visible for the sample presenting Au NPs.

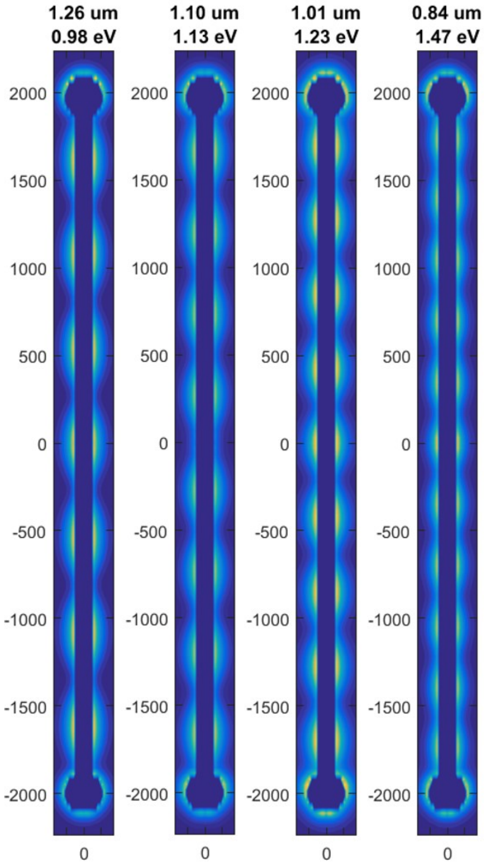

Figure 3.37: *DDEELS simulation of the plasmonic modes of the Au dumbbell. Spatial measurements are shown in nm.*

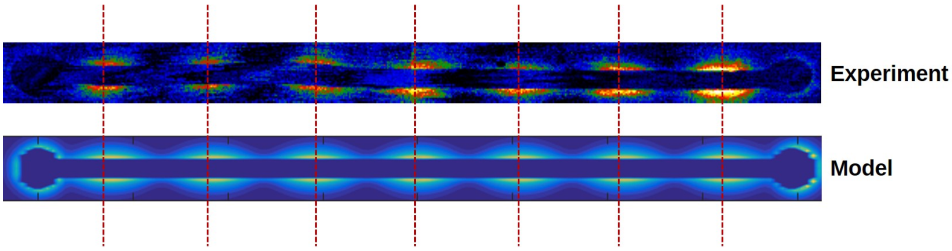

Figure 3.38: *Comparison of the experimental and simulated spatial distribution of the 7 node longitudinal plasmonic mode for the Au dumbbell. The energy of these modes is 1.1 eV for the experimental results and 0.98 eV for the theoretical model. Scale is as set in Figures 3.25 and 3.37.*

3.5.3 Energy dispersion: Experiments vs models

Since the E-k dispersions for three different samples (namely the single Au NW, the half-dumbbell and the dumbbell) have been measured in Section 3.4.4, it makes sense to observe how the modelling performed in these samples relates to these dispersions.

The modelled E-k dispersion relations, as well as their comparison to their experimental counterparts, can be seen in Figure 3.40

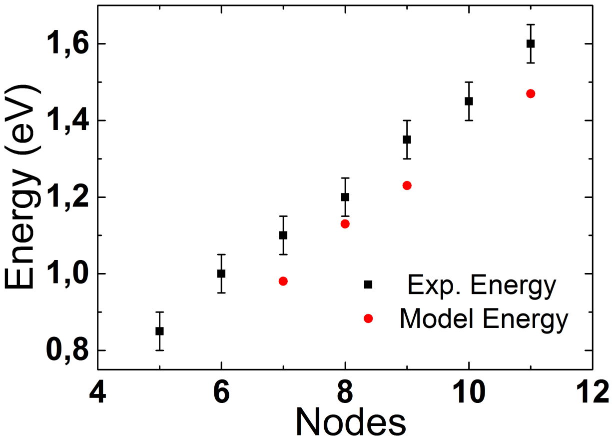

Figure 3.39: *Energy comparison between the experimental plasmonic modes of the Au dumbbell and their simulated counterparts.*

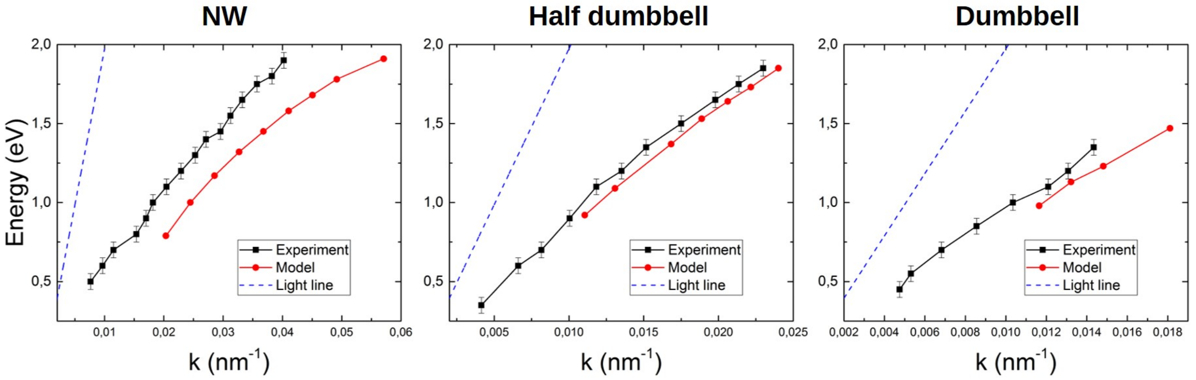

Figure 3.40: *From left to right: Experimental(black) and modelled(red) E-k dispersions for the Au NW sample, the Au half-dumbbell and the Au dumbbell. A light line is included in each plot for reference (dashed blue line).*

The main difference between the modelled and experimental results occur for the Au NW, where, on top of there being a rather high difference between the experimental and the simulated results, the tendency of the simulated results seems to follow a curve (which is coherent with the previous studies on the matter [287]) while the experimeantal results follow a somewhat linear dispersion.

Generally speaking, these results are coherent with the ones shown in the previous section. There is a significative difference in energy between the experimental and the modelled results for the Au NW, whereas for the half-dumbbell and the dumbbell there is a somewhat constant difference between the experimental and the modelled results but it is much more subtle. This resonates with the idea that the substrate plays a role in the experimental value of the energy dispersion relation, and that this role is not as important in the case of the half-dumbbell and the dumbbell. This can be either due to their lower aspect ratio when it comes to their NW, or due to them being suspended on top of the substrate instead of lying on said substrate.

3.6 Future works

The analysis presented on this chapter is quite a versatile one. It has been clear that it provides an enhancement of the accuracy when analysing plasmonic features using EELS in the abovementioned nanostructures, but its potential could be even greater.

3.6.1 Future works on high aspect-ratio NW-based structures

Other plasmonic structures

Besides the study of high aspect-ratio NW-based structures, this analysis could be used for the treatment of plasmonic data in EELS. It could provide a higher accuracy with respect to the intensity maps of the different plasmonic modes in SPIM-EELS, but, for samples such as nanoparticles and nanorods, it could also provide a quicker method for the analysis of this data.

Other types of spectroscopy

The analysis method presented in this chapter is based on Non-Negative Matrix Factorisation. As such, it is not strange to think that it could be applied to other kinds of spectroscopy based on positive components.

There are examples in the literature that use NMF for XPS analysis, which makes sense for the same reasons it makes sense to perform this analysis on EELS spectra: XPS signals are a combination of positive components. In theory, this kind of analysis could improve the accuracy of XPS analyses with respect to the currently used Gaussian multi-peak fitting.

Another technique that could benefit from NMF decompositions would be XPS. With a big enough database of a certain type of material, this analysis could, in theory, separate components coming from different physical phenomena, performing feats from chemical analysis to functional group analysis such as the one shown in Chapter 4.

The NMF method as a pre-treatment

The method stated in this chapter has proven to yield components with a physical meaning up to quite low SNR levels. However, at high levels of noise, it is clear that the components it yields are not as accurate as they are at low levels of noise. What it does yield, even for these cases, is an approximate estimation of the number of components and their approximate energy. This information could be used for an even more intricate analysis, using this method as a pre-treatment for other MVA analyses or for multi-peak fittings.

3.7 Conclusions

In this chapter, we have seen a novel method for the analysis of the plasmonic behaviour in high aspect-ratio Au nanostructures, where the characteristics of said high aspect-ratio difficult the EELS analysis of these plasmonic features.

This analysis has consisted, on the one hand, on a custom background extraction using regions from the SPIM-EELS far enough from the sample to have almost no plasmonic features. On the other hand, MVA, and more specifically, NMF has been used to discern the different plasmonic components present in each sample.

The presence of different levels of experimental noise, as well as the different morphologies of the different samples, have provided a variety of cases where we have been able to evaluate the accuracy of this analytic method.

In terms of energy resolution, this analysis has provided astounding results, being able to differentiate plasmonic components down to 0.25 eV with a resolution of 160 meV in the best of cases, and allowing for a sensible qualitative analysis of the plasmonic features in the samples even at low levels of SNR.

Finally, the DDEELS modelling and its comparison to our experimental results has provided some key information for this study:

- The components we have identified as longitudinal plasmonic modes in the different samples have been confirmed as such.
- The spatial distribution of the experimental modes is very close to that of their corresponding simulated mode. However, this model does not take into account the intensity gradient derived from the geometry of the samples such as the case of the Au half-dumbbell, which might derive from a lack of contact between the NW of the half-dumbbell and the substrate.
- The calculations on the single and double Au NW has proved that the sample we thought to be two joint Au NW is in fact two individual Au NW with a very narrow gap between them.
- We have seen, by comparison, the difference between a simulation without a substract and their corresponding experimental results. This has shone light on the influence of the substrate in this particular experiment, which is an energy difference of about 0.25 eV.

The comparison between the models and our experimental data suggests there is an energy dispersive effect coming from the substrate, which has been a recurring theme since the beginning of DDEELS modelling [397]

Furthermore, the analysis presented in this chapter opens the possibility to perform high-grade qualitative plasmonic analyses to equipments with a resolution lower than the state-of-the-art; and could possibly be extrapolated to other characterisation techniques.

4

Graphene Oxide: a TEM-EELS *in situ* thermal study

As we have seen in Section 1.7, 2D materials and its derivatives have given rise to a whole new family of materials with astounding properties, with this "*2D renaissance*" being considered to be started by the experimental discovery of graphene in 2004 [87].

It is known that nowadays one of the main challenges, if not the main challenge regarding graphene and its production, is the large-scale production as well as the lack of dispersability of the final product. This is where graphene oxide (GO) comes into play. This graphene-derived material offers large-scale production and dispersability in water and other polar solvants [401, 402]. Furthermore, the reduction of graphene oxide provides a material (reduced GO, rGO) with properties that resemble those of graphene. However, as we will see in this chapter, the actual structure and composition of GO is still up for debate nowadays, and the mechanisms behind the different kinds of GO reduction are still unknown.

In this study, we use TEM, electron diffraction, as well as low-loss and core-loss EELS to try to understand the changes that a GO sample goes through when it undergoes a thermal reduction. This study focuses on the chemical functional groups adsorbed on the sample, as well as their desorption temperature and the effects of this desorption in the material.

4.1 Introduction: Graphene Oxide and its reduction

In order to put our work into context, it is important to know what GO is, from its composition, to its structure, the properties it has and how they can be modified. This section focuses on this material in extent: from a brief historical introduction of GO as a material, to a historical discussion of the unresolved problem of GO structure, how it can be prepared and reduced, and the state of the art when it comes to spectroscopic studies on GO and rGO.

4.1.1 A brief history of Graphene oxide

The history of the oxidation of graphite begins with a study quite unknown to most on different alloys using carbon, silicon, iron and other metals [403]. In this study, while trying to find a chemical method to purify graphite, Schafhaeutl found a new reaction that he defined as "*an interesting phaenomenon*":

> *I poured [...] concentrated sulphuric acid over two grains of these purified graphite scales[...] and made the acid boil briskly over a spirit lamp. After this, I removed the*

> *crucible from the fire, till the dense fumes which arose began somewhat to cease. I then drew up [...] strong fuming nitric acid into a long small glass tube, and dropped one half of the acid rather slowly, the other half quickly, into the hot sulphuric acid, which caused the latter to boil again[...]. As soon as the boiling began to cease, I placed the crucible again over the lamp, and boiled the liquid till all the nitric acid was decomposed. I found* ***the scales of graphite so much swollen*** *as to fill up the whole lower part of the crucible, so that the liquid was no longer visible. On nearer inspection, I percceived that* ***every single leaf of those scales was converted into a spongy body****, of the lustre of coke, and of the same breadth and thickness, about the size of a pea.*

He had unknowingly fabricated for the first time the material we know nowadays as graphite oxide.

Almost twenty years later, in 1860, Sir benjamin Collins Brodie, a Professor of Chemistry in the University of Oxford, and the President of the then *Chemical Society* wrote a review paper for the *Philosophical Transactions of the Royal Society of London* [404] on the atomic weight of graphite, this term understood as a vast definition. In it, he explained his findings on the oxidation on graphite, of which we offer a freely translated quote:

> *The lamellar graphite is found in great abundance in Ceylon, whence large quantities ar annually imported into this country.[...]When Finely-divided carbon, in the form of lampblack, or charcoal from the decomposition of sugar, is heated with a mixture of 1 of nitric and 4 of sulphuric acids, the carbon is rapidly oxidized, and a black substance is formed, soluble in the concentrated acid, but precipitated on the addition of water. This substance is insoluble in acids and saline solutions, but is soluble in pure water and in alkalies. [...] When the graphite of Ceylon is treated in a similar manner, the result is very different: the graphite becomes of a beautiful purple colour, and falls to pieces in the fluid. The substance [...] has much of the appearance of the graphite itself, but is darker in colour.[...] My efforts to procure this substance of a constant composition have been unavailing;[...]When heated it undergoes a remarkable change; gasses are given off in the interior of the substance, which swells up in a most singular manner and is reduced to the minutest state of division. The residue consists of carbon, which has the appearance and the structure of the lamellar graphite. [...]These experiments established one point of importance, the existence of a peculiar compound of carbon in the form of graphite. The discovery of this substance led me to turn my attention to the oxidation of graphite.*

He had first written about his experiments on the oxidation of graphite in a much shorter publication 5 years before, in 1855 [405]. Even though Schaftaeutl had seen graphite oxide for the first time, it was Brodie who coined the term "oxidation of graphite", unknowingly opening a new branch of chemistry that would be relevant to our days. Coincidentally, he had discovered graphite oxide while developing a method to purify graphite, which by modern standards would be considered as producing graphite oxide from non-purified graphite and then reducing it thermally. This two mechanisms, the production of graphite oxide and its thermal reductions, will be delved into profoundly in sections 4.1.5 and 4.1.6.2, respectively.

Even though this article was written 160 years ago, there are plenty of ideas in this text that are worth pointing out:

- First and foremost, Brodie was the first to ever discover a method to produce graphite oxide. Other methods for its obtention will be discussed in Section 4.1.5.

- Brodie talked about the dispersibility of graphite oxide in water, which is essential to understand why GO has such a great interest within the realm of 2D materials.
- Brodie points out the chemical inhomogeneity of graphite oxide is still very much a reality, with very little accuracy on the stochiometric composition of the samples, and with variations of composition even within the same sample.
- The heating of the graphite oxide produces a change in the thickness of the sample and the expulsion of gasses. The mechanism of this process is studied in depth throughout this chapter.
- The obtention of graphite-like materials (reduced graphite oxide) after heating up the graphite oxide is also a key point as to why GO is of importance nowadays: the oxydation process for graphite, and graphene, is reversible up to a high point.

This opened up a whole new material to be studied. New, cleaner fabrication methods were developed (which will be delved into in Section 4.1.5) and the structure of graphite oxide started to be studied, giving rise to the different models on graphite oxide and thus graphene oxide (see Section 4.1.2.

The questions surrounding graphite oxide, and GO, are in many cases still the same as they were in 1859. In this chapter, we will use TEM-EELS to try to provide information to answer some of these questions.

4.1.2 Structural models of GO: a historical comparative study

The general structure of graphene oxide is understood as a combination of a somewhat graphenic structure and some sort of oxidative product. Quoting the study of Rourke *et al* from 2011 [406],

> [...] *We suggest that GO actually consists of two distinct components noncovalently complexed together: the majority by mass being large functionalized graphene-like sheets* [...] *together with small, more highly oxidized, fragments or debris (the OD).*
>
> [...] *We believe that, in acidic or neutral conditions, the debris is strongly adhered to the graphene-like sheets of GO by a combination of* $\pi - \pi$ *stacking and hydrogen bonds. The interaction between the oxidative debris and underlying covalently functionalized graphene sheet under basic con- ditions becomes repulsive because of the negative charge on the deprotonated debris. Once separated, it would appear that the two components cannot be recombined, and hence the original structure is metastable.*

For the remainder of this section, whenever we talk about the structure of GO, we will be talking about the structure of the abovementioned graphene-like layers functionalised with oxygen functional groups (OFGs). However, knowing which OFGs are present in each sample, as well as what amount of them and their distribution, is a rather complex question that has been tried to be solved for decades now.

Graphene oxide is considered to be a very inhomogeneous material, both in terms of stochiometry (the amount of oxygen in the sample depends heavily on the preparation method and is not necessarily reproducible) and in terms of structure [407] [408]. Even though the stochiometric composition of different samples of GO can be known using a variety of techniques (such an XPS, EELS or IR, a subject delved into in detail in Section 4.1.8); the general arrangement of the different atoms composing GO is still an open question.

The question of the structure of graphite oxide has been tried to be answered for at least the past 85 years, way before the concept of graphene oxide itself. The inhomogeneity of GO has played an important role in the creation of several models, the inaccuracy of such models, and the need for a model that did not try to explain graphene oxide accurately but provided an informed reasoning on all the possible OFGs present in the sample. In the following, we provide an overview of the most significant ones.

The Hofmann model

In 1934, Hofmann, Frenzel and Csalán published the first model to the structure of graphene oxide we can keep track of [401][409], where they stated that " *By oxidation, the metallic bond of the layer planes in the graphite is dissolved and oxygen is attached to the thus exposed fourth valences of the C atoms.*"(source:Hofmann *et al*[409], translated). It also stated that "*in graphitic acid*-How graphite oxide was called back then - *layer planes are only held together by intermolecular forces. The layer planes themselves are 2-dimensional macromolecules.* These 2-dimensional macromolecules are what we call graphene oxide nowadays.

They also stated something that would change graphene oxide models for years to come: given the C:O ratio in the sample, and based on their X-ray diffraction (what they called rotary crystal absorption), there was no way to confine that amount of oxygen in a standard unit cell. Their hypothesis was that the O atoms were randomly distributed among the possible lattice sites with randomly distributed gaps. Their depiction of the model for the graphene oxide can be seen in Figure 4.1

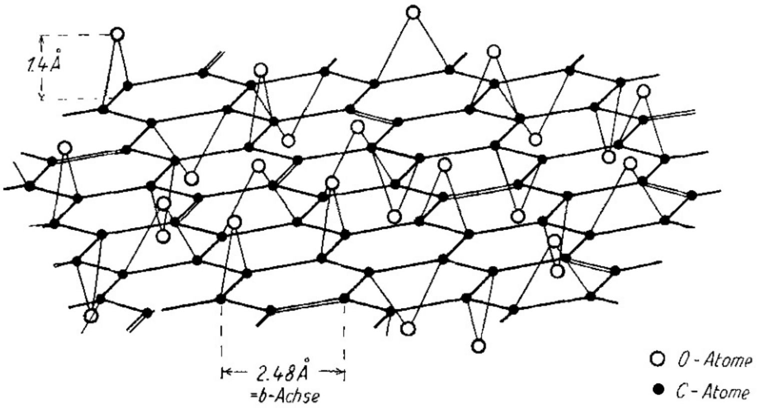

Figure 4.1: *Hofmann model for the structure of GO. Original caption (translated): "The O atoms occupy all of the sites above and below the layer plane in a statistically uniform distribution in the form of ethylene oxide-like bonding. The C atoms corresponding to the C: O atom ratio = 3 are saturated by double bonds.". Source: [409]*

When Hofmann *et al* referred to O atoms being in "ethylene oxide-like bonding" [409], they meant that the functional groups they thought to be present in the GO were in the form of epoxides exclusively. Further studies on the matter would show that this was not the case. This model also considered the GO to be completely planar, much like graphite itself, with no corrugation.

The Ruess model

In 1946, the Ruess model also brought in the presence of hydroxyls in the sample, as it can be seen in Figure 4.2. They also linked them to the oxidation process by stating that "*[...]during* *the slow oxidation of the [GO] layer planes, the oxidation mixture attacks simultaneously the layer plane edges, probably first with the formation of carboxyl groups*". [410]

In addition, as it can be seen in Figure 4.2, they no longer believed that the COC-bound oxygen was in the form of epoxides but rather ether-like oxigen bridges bound between alternate carbon atoms.

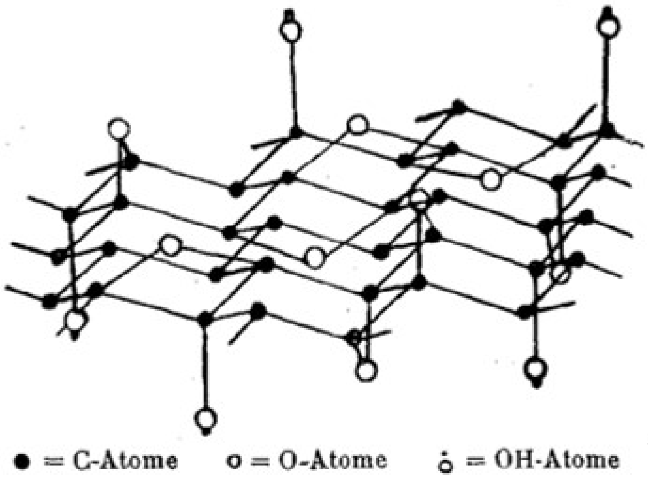

Figure 4.2: *Ruess model for graphene oxide. Translated original caption: "Structure of graphite oxyhydroxide layer (G.O. molecule). (Corrugated C plane, metastatic binding of O with simultaneous binding of OH groups at the layer plane.)". Source: [410]*

They also proposed, for the first time, the puckering of the graphene layers in GO, changing the models to come at least with respect to the general morphology of the graphene matrix in GO.

the Scholz-Boehm model

In 1969, gathering data of functional group analysis and infrared spectra of a variety of graphite oxides, Scholtz and Boehm developed a new structure model [411].

This structure model was given by the fact that they did not detect any kind of ether oxygen in the sample, but they did detect the presence of hydroxyl groups and carbonyl groups in different sourroundings. Their model can be seen in Figure 4.3.

Their answer to the general structure of the GO was that its layers were made up of mosaique domains such as the one shown in the figure with different orientations, separated by less well ordered regions. On top of this, they explained, as the previous model did, the role of the oxygen of the GO in the corrugation of the graphitic layers in the sample.

They were also responsible for introducing a seemingly obvious parameter for the measurement of the oxydation of GO, but one that had not been previously used for the study of this samples: the carbon to oxygen ratio.

The Nakajima-Matsuo model

In 1988 and 1994, two studies, one by T. Nakajima and Y. Matsuo [412] and another one by them and several other authors [413] used a different approach to try and discern the structure of GO what OFGs were present in the GO.

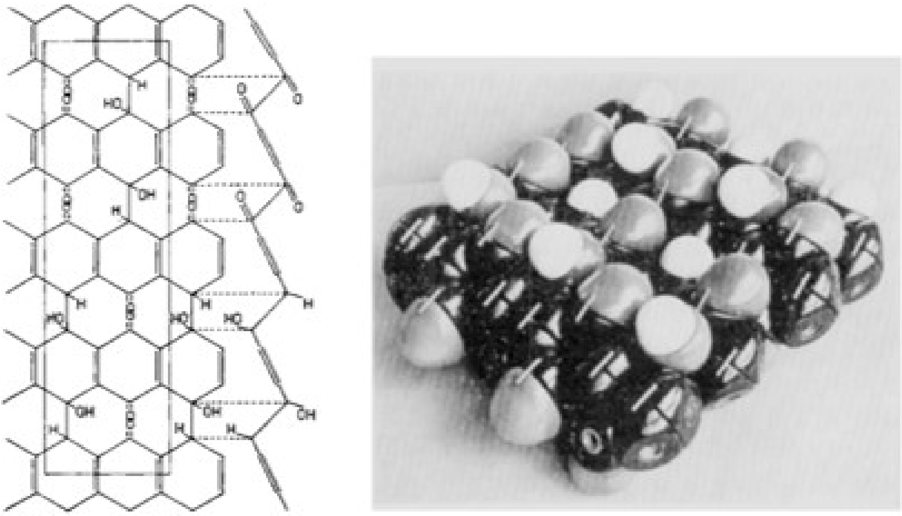

Figure 4.3: *Scholz-Boehm model for graphene oxide. Left: Schematic model. Right: ball-and-stick model. Translated caption left: "Fig. 2. Schematic representation of the structural model for graphite oxide. On the left is the top view of the layer, on the right the corresponding side view is shown". Translated caption right: "Structural model of graphite oxide constructed from Stuart and Briegleb atomic models, according to the scheme in Fig 2"(Fig 2 is the one on the left).Source: [411]*

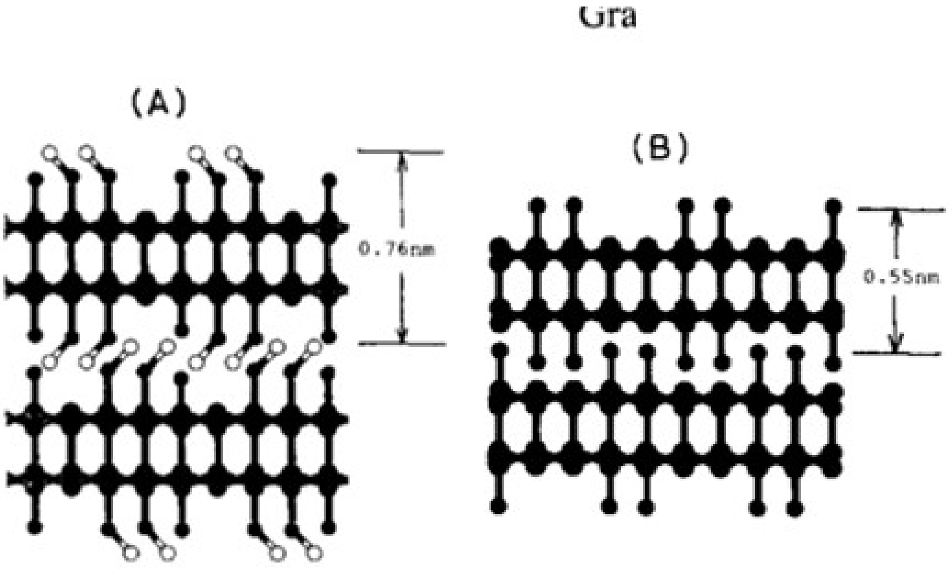

Fig. 10. Structural models of (A) hydrated and (B) dehydrated graphite oxide. : C—OH. : C$\cdots$O$^{\delta-}$.

Figure 4.4: *Nakajima-Matsuo model for GO. Caption embedded in the figure.*

On one hand, they studied the formation process of graphite oxide. They focused on the XRD of graphite oxide and the intermediate products of its oxidation for different production methods (see Section 4.1.5), and proved that graphite oxide was fabricated through a series of steps: First, the formation of graphite intercalation compounds; second, their oxidation, and finally the hydrolysis of these compounds. The interplanar distance was also measured for these intercalation compounds, resulting in a distance around 1.44 nm [413].

They also studied the structure of GO by fluorinating the graphite oxide at temperatures between 50 and 200°C. The infrared spectra of fluorinated GO was compared to that of regular GO. They concluded that the main change in the compounds were the substitution of OH groups by F atoms.

When measuring the interplanar distance of fluorinated graphite oxide, they found it was close to the interplanar distance of the structure of $(C_2F)_n$. That is why they created a model using the assumption that the structure of GO before fluorination was similar to that of $(C_2F)_n$, but with -OH groups instead of F atoms. This model can be seen in Figure 4.4.

The Lerf-Klinowski model

In 1986, an infrared spectroscopy study by Martín-Rodriguez and Valerga-Jiménez [414] studied the oxidation of graphite oxide. We will delve deeper into this study in Section 4.1.5. These works were the first to provide some sort of experimental proof that there were carboxyl groups present in GO, since their IR absorption peak was identified.

5 years later, in 1991, Mermoux *et al* published a study where they analysed graphite oxide by means of Fourier-transform infrared spectroscopy (FTIR) and Solid-state^{13}C nuclear magnetic resonance (NMR) spectra [415]. In the FTIR analysis of this study, they found proof of alcohol groups as well as carboxyl groups in the sample, although they admitted that it was possible that there were some epoxides ethers or peroxides as well.

However, according to them, the ^{13}C NMR analysis of the sample only had thre distinguishable peaks: one for the C-O-C bonds, one for the C-OH bonds and one for the C=C bonds. In this study, this analysis was proposed as proof that the Ruess model for GO was consistent with the analytical proof they provided. In turn, to adjust to this model, some of the C=C bonds in the sample would be isolated.

An analysis of the same nature, taking into account the degree of oxydation this time, was performed by Hontoria-Lucas *et al* in 1995[416]

In 1998, Lerf, He, Forster and Klinowski questioned the interpretation of the results proposed in the study by Mermoux *et al* [417]. First, they had no way to prove that the C-O-C bonds that had been found in the ^{13}C NMR analysis corresponded to 1,3-ethers, as predicted by the Ruess model. Second, they could not tell much about the disposition of the different OFGs in the sample, and finally, even though they had postulated some of the double bonds in the GO were isolated, they had no proof to back it up nor an estimate of how many.

This was the main motivation for their study of the products of the reaction of GO with potassium iodide and their thermal decomposition, using ^{13}C NMR. The GO used for this study was prepared employing a modified Hummers method, that we will delve deeper into in Section 4.1.5.

This analysis proved that there was a presence of oxide groups in the sample, since it liberated iodine when reacting with hydroiodic acid, which had been used before as a test for the presence of epoxide groups by Hofmann [409].

The results also showed that, for the reactions to be able to take place, the sample had to had alcohol OFGs attatched to the carbon rings, and at least one double bond present in the ring or formed by deoxigenation of the epoxides during the reactions. In other words, their studies confirmed the results of Mermoux *et al* concerning alcohol groups. However, their results seemed to argue for the presence of epoxides in the sample instead of ethers as suggested by Mermoux *et al.* The reactions taking place in the sample also indicated that the epoxides and the alcohols in the sample were very close to one another.

On top of this, this study also took into account the fact that carboxyl groups had been found in GO samples by means of IR absorption. It also discussed the fact that isolated double bonds could not be present in high amounts, since they are easily oxidisable. By joining all the different ideas in this section, they created a new model for GO, which is shown in Figure 4.5

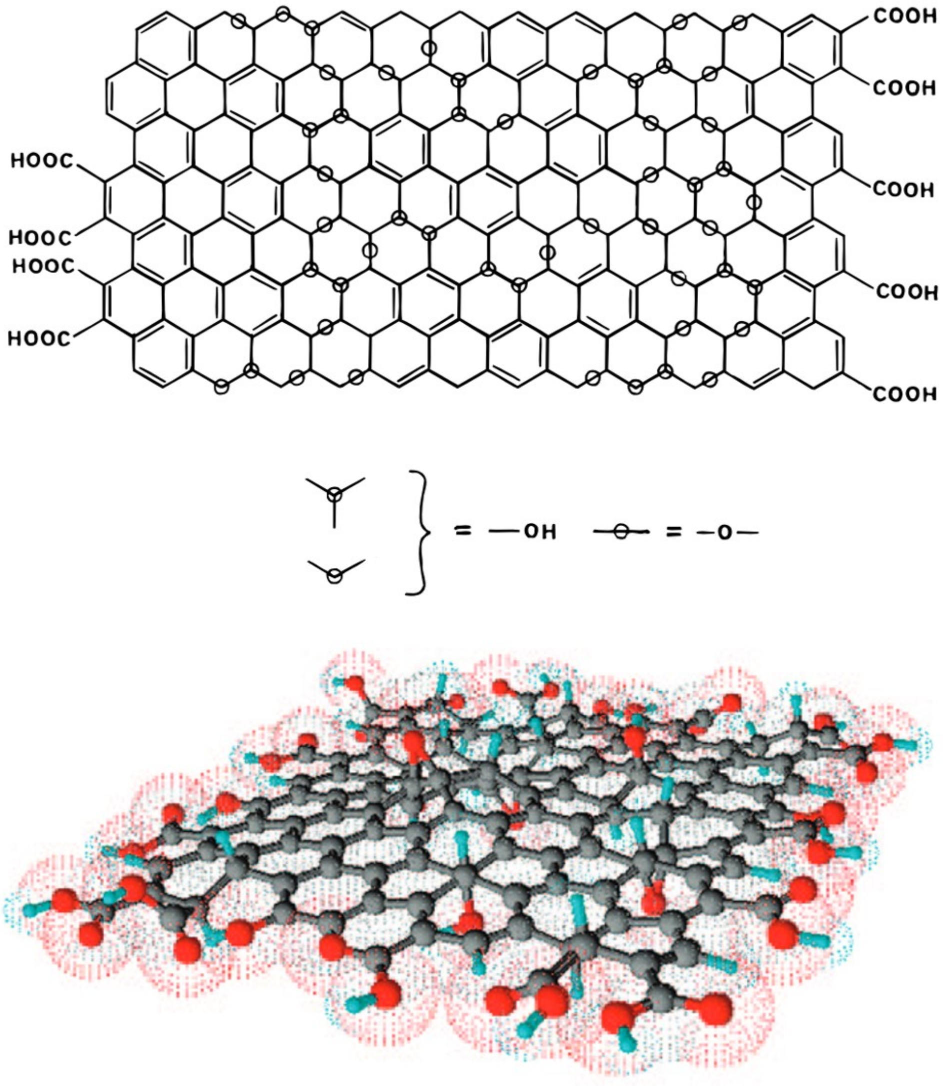

Figure 4.5: *Top: Lerf-Klinowski model for GO. Source: [417]. Bottom: 3D representation of the Lerf-Klinowski model. Source: [418]*

They created this model taking into account the inhomogeneity of GO, that is, a non-stochiometric structure. They divided the structure of GO into two sub-structures: on the one hand, aromatic (graphitic) regions with no oxygen present, and on the other hand, regions containing "*aliphatic six-membered rings*", which contain C-OH, epoxide groups and double bonds. These regions are randomly distributed[419].

By this point, the model for GO was closer to the structure we think of today as GO. However, there was still another advancement to be made, and it had a lot to do with something that had been overlooked in the Lerf-Klinowski model as well as all the previous models to that date: the defects in the graphene planes.

The Dékány model

In 2006, Szabó, Dékány *et al* published what was probably the vastest study on GO, its composition and its properties to that date, trying to challenge the contemporary models for GO [420].

It compared four different GO samples prepared using a Brodie method, which had a different oxidation degree controlled by how many times they repeated the oxydising steps from the Brodie method on each of them. These samples were labeled GO-1 to GO-4 depending on their degree of oxydation. Judging by the description of the authors, our GO should be of a similar nature to the one labeled GO-1 in the study.

Technique-wise, this article employed a miriad of techniques never seen before for GO within the same study, namely elemental analysis, transmission electron microscopy (TEM), X-ray diffraction (XRD), ^{13}C magic-angle spinning NMR (^{13}C NMR), diffuse reflectance infrared Fourier transform spectroscopy (DRIFT), X-ray photoelectron spectroscopy (XPS), and electron spin resonance (ESR). Each technique apported a new piece of information about graphene oxide.

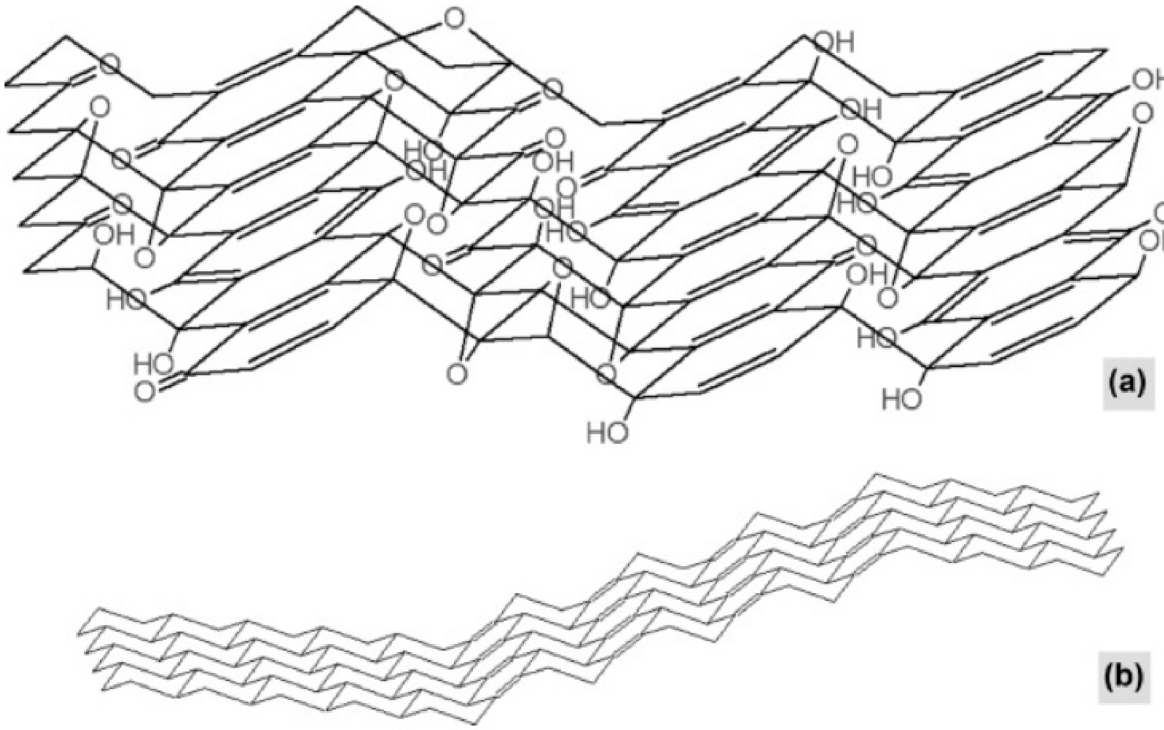

Figure 4.6: *Dékány structure model for GO. a)Surface species distribution in GO. b) Carbon skeleton. Source: [420].*

TEM imaging showed that the GO still presented a layered structure, but with some sort of wrinkling or folding that seemed to increase with the oxidation degree in the sample.

As for **XRD**, it served several purposes. First, it provided final evidence of the oxidation reaction completely taking place, since, as we will see in this section, the interlayer distance of the GO increases moderately once the sample is oxidised with respect to its pristine counterpart.

They also assumed that the lack of the XRD reflection at θ=26.28°(which relate to pristine oxide) prove the lack of any pristine graphitic areas whatsoever in the sample. To prove it, they performed the same measurements in a 1% mixture of pure graphite with a 99% mixture of heavily oxidised GO, and they could appreciate the aforementioned reflection. However, this statement can be heavily discussed, since, if the graphitic areas were small enough, the OFGs in the oxidised areas would still keep all the layers further apart from one another, even if there were some areas without any OFGs. They also performed XRD measurements on the course of hydration of dry GO, which will be discussed later in Section 4.1.3.2.

^{13}**C NMR** showed proof again of the presence of C-OH groups with a peak at 69.2 ppm, as well as aromatic functionalities and/or double bonds with their resonance at 128.2 ppm[416, 421, 417]. There were several peaks that did not have a 100% clear explanation to them, which the authors tried to explain. First, the peak at 57.6 ppm, which we have talked about before in the Lerf-Klinowski model (see previous models) that was first thought to be a 1,3-ether peak but was later described as an epoxide peak. Two more peaks were present in the sample: one at 92.9 ppm which they could not find an explanation for, and another one at 166.3 that was supposed to indicate the presence of C=O.

DRIFT spectroscopy was done in a quite novel manner. Their hypothesis was that the GO in air had such an amount of strongly bound humidity that it could result in an inaccurate interpretation of the spectra. The broad and intense OH bands could also play a part in discerning other peaks in the same spectral window.

Taking the water and the OH out of the sample was not an option, since the sample could take weeks to dehydrate and the OH groups are the most stable ones in GO [69], so, following a previous study of their own [422], they achieved an elimination of the water and OH peaks using deuterium exchange. The results of this study can be seen in Section 4.1.8. They seemed to point to the presence of C-OH, dimeric COOH, water, aromatic C=C, as well as either ketones or quinones. Another very important deduction from this set of data was the presence of phenolic moieties in the bulk of the carbon network.

XPS spectroscopy was performed on air for both bare graphite and GO. The XPS data for this study can be found in Section **??**. This study found four peaks for the less oxidised sample and three for the more oxidised sample. The extra peak for the less oxidised sample concurred with the main graphite peak so they associated it with aromatic carbon, representing a 5% of the total spectrum. The other three peaks were asigned to the bonding of C atoms with one, two and three valencies to O atoms. Since electronegative oxygen induces a partial positive charge on the carbon atoms, the more bonding to the carbon, the further up in energy the XPS peak would be. Therefore, they assigned a peak at 284.4 for aromatic carbon, one at 287.2 for single bound carbon (alcohols, phenols and ethers both 1-3 and 1-2, the latter also known as epoxides), one at 289.3 for ketones and one at 290.8 for carboxylic groups.

ESR spectroscopy proved that there were no strong resonances as there were in graphite even for the least oxidised GO, which proved there were no long-range pristine graphitic sheets in the sample.

These results were the pillars on which Szabó, Dékáný and their collaborators came up with their own model, which came to be a reinvention of the Scholz model adapting it to all the models between Scholz's and theirs, as well as adding their new results. This model can be seen in Figure 4.6.

Due to the wrinkling seen in the TEM, their model does not start with a graphitic carbon sheet but with a corrugated carbon network of flat carbon hexagons connected by C=C double bonds, linked to each other by means of periodically cleaved ribbons of cyclohexane chairs and thus forming a matrix. This is but another twist on the argument that GO is made up of two types of structures quite different among them. The distribution of the different OFGs is, according to them, as shown in the figure.

The Liu model

In 2009, a study by Gao *et al*[423] charactherised GO obtained by a modified Hummers method (see Section 4.1.5) using ^{13}C NMR. Based on their own spectra, as well as previous studies [424, 425], they found there was a feature in the spectra that had been previously been assigned to non-protonated carbons [425], but no further comment had been made on them. The main groups that could be causing this type of signal could be five- and six-membered ring lactols on the edges of the GO. For clarification, schemes of these two OFGs are shown in Figure 4.7.

This study also found the presence of carbonyls such as esters and ketones, which had been overlooked by the Lerf-Klinowski and the Dékány models.

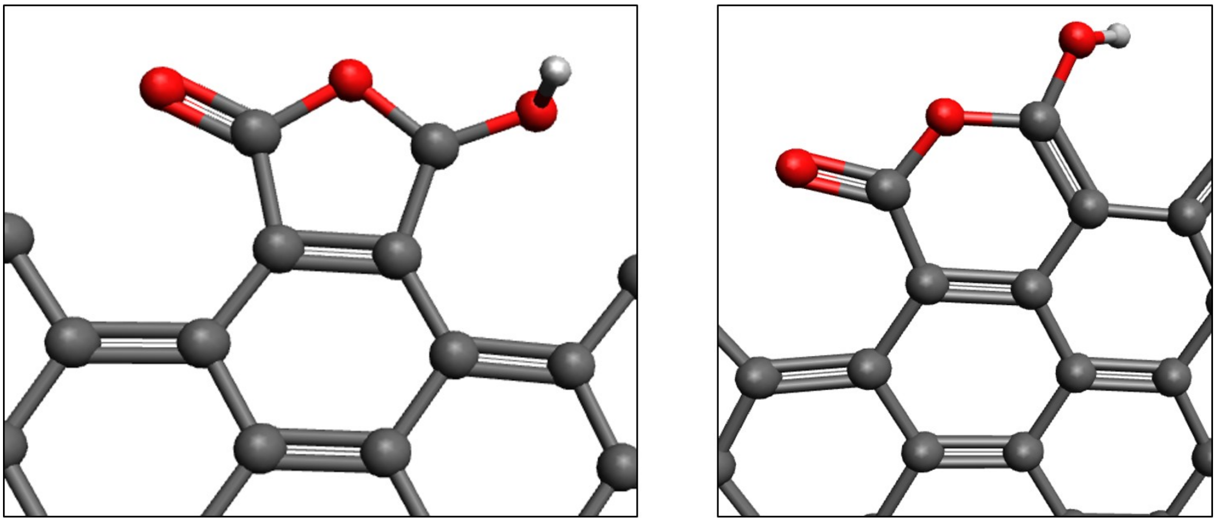

Figure 4.7: *Left: scheme of a five-membered ring lactol. Right: scheme of a six-membered ring lactol. Black atoms represent C, white represent H and red represent O. Source: Liu et al [426]*

In 2018, Liu *et al* [426] performed a study on GO with the objective of correcting the Lerf-Klinowski model, which is the one generally thought to be the most accurate, with various experimental studies confirming its accuracy, for the most part [60, 427, 408].

For this purpose, they employed XPS, Raman, FTIR and a new technique that allowed them to map the spatial distribution of C-O and C=O bonds on GO with nanometric resolution: AFM couple with infrared spectroscopy (AFM-IR) [428]. This technique allows IR spectroscopy with AFM resolution, that is, tens of nanometres of lateral resolution (40 nm for their specific setup)and 0.1 nm of resolution in z.

Using previous IR references for the different OFGs in GO, they identified the peaks in the IR spectra corresponding to OH [429], C-O groups including epoxides, hydroxyls, ethers and carboxyl groups [430, 431, 429, 432, 433], epoxides specifically [430, 431, 434, 435] and different carbonyls, including carboxyl groups, ketones, lactons and anhydrides [432, 436, 437, 438]. This will be delved deeper into in Section 4.1.8.

This identification, coupled with the novel technique of IR-AFM, allowed them to discern between different OFGs with a lateral resolution of ∼40 nm. Point spectra, spectrum profiles, as well as whole spectrum maps have been acquired. Several conclusions can be gathered from these studies:

The first study is a point spectra study comparing three different regions: a multilayer GO region (with

From this study we can deduce the following:

- The strength of the C-O peaks with respect to the rest of the peaks suggests that most of the OFGs in the ample are C-O groups, either as epoxides, hidroxyls, ethers or carboxyl groups. This peaks are more variable for monolayer GO, which is consistent with the inhomogeneity of the material.

- The peaks corresponding to C-O groups seem to indicate the main presence of an epoxide configuration.
- There is an absorption band that has previously been identified as coming from hydroxyl [429] but it is unclear if it is as an independent hydroxyl or hydroxyl in carboxyl configuration.
- There is an additional feature that appears both for multilayer and monolayer GO, that has been identified as probably the aromatic bond stretching in the carbon plane. This feature would be related to the amount of double bonds in the GO area being measure, therefore it would be weaker in more oxidised areas with a higher amount of defects. This seems like a small detail but it represents a very important part of the Liu model.
- The absorption region corresponding to C=O vibrations from carbonyls is negligible for monolayer GO in this study, which either implies that the amount of carbonyls in the monolayer is below the detection limit or that the proportion of carbonyl groups is higher for multilayers.
- The IR absorption increases proportionally with sample thickness for the absorptions related to C-O and C=O groups; with the exception of monolayers that are proportionally less oxidised than multilayers.
- Not any IR absorption was detected where the hydroxyl stretching is expected [431], which is consistent with having them between the layers and not adsorbed on the surface of the GO.

After having identified the main peaks of the IR spectrum, they could map the intensity of a specific peak with the increased spatial resolution given by the combination of IR and AFM.

A map of the C=O groups peak, along with the topography of the same region and the profiles of two regions of interest (a flake edge and a fold in a GO monolayer)can be seen in Figure 4.8

The zones 1 and 2 in Figure 4.8 correspond to a flake edge and a fold in a GO monolayer, respectively. As we can see, the intensity of the C=O stretch is considerably higher in the edges of the flakes and the folds of the GO than in the rest of the sample.

Figure 4.9 represents two maps of the same GO area, one of the intensity of the C=O peak and one of the C-O peak. These studies showed there was not only a higher proportion of C=O stretches at the GO edges and folds, but a lower proportion of C-O bonds at the areas where the C=O proportion is higher (not necessarily all folds). In other words, the higher the proportion of C=O groups, the lower the proportion of C-O groups. This would be crucial for the development of the Liu model.

Anotther important question to take into account is the existence of all the folds seen in the maps and the different points of concentration of the different OFGs. Their hypothesis is that oxygen functional groups concentrate at defective sitesin in the GO, leading to the formation of folds. This wrinkling / folding will be delved into in Section 4.1.3.1.

In order to answer all the questions that have been posed here, Liu *et al* proposed an updated structural model for GO, which would take inspiration both from the Lerf-Klinowski model and from the Dékány model.

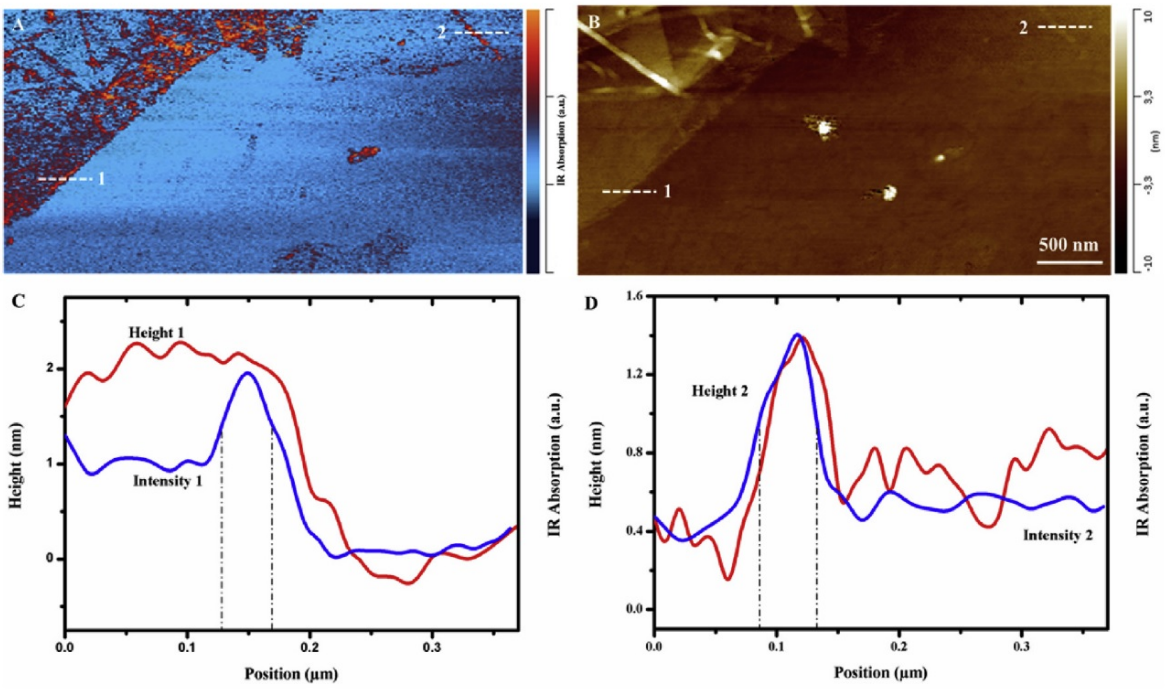

Figure 4.8: *(A) The GO IR absorption map collected at 1720 cm^{-1}, which represents the C=O stretch and (B) the AFM topography image from the same location. Feature height and IR absorption profiles were recorded along stipulated line marked by 1 (C) and marked by 2 (D). Source: [426]*

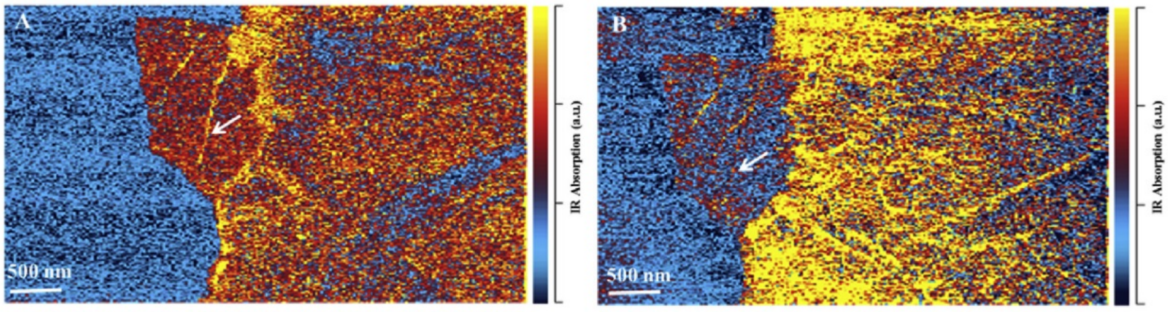

C-O mapping **C=O mapping**

Figure 4.9: *The IR absorption map from the same site at wavenumber (A) 1065 cm^{-1}, which represents the C-O stretch and (B)at 1720 cm^{-1}, the C=O stretch. The intensity in the area of the arrow suggests different distributions of C-O and C=O bonds along folds. Source: [426]*

The model itself is sort of a modification of the Lerf-Klinowski model, with the update of having C=O groups both on the edge of the GO and the basal plane. In this regard, this draws inspiration as well from the Scholz-Boehm and the Dékány model, which assumed the presence of C=O groups on the basal plane of GO. However, none of these models included carboxyl groups nor epoxides. So, in a way, the Liu model is both a correction for the Lerf-Klinowski model and for the Dékány model, making it the most unified model to date.

Much like its predecessor (The Lerf-Klinowski model), this model is also based on several types of regions within the sample. The Lerf-Klinowski model proposed an oxidised region and a pristine, graphite-like region that intertwined all through the sample. This model takes this approach a little further, and divides the GO samples in four different regions, depicted in Figure 4.10:

- The **pristine, graphite-like region** where the graphite matrix is not oxidated, much like the one proposed in the Lerf-Klinowski model.
- The **edges** (orange region). Since this experiment has proved that the edges and folds in the GO have a chemistry completely different to the rest of the sample, it makes sense that this is a part of the model proposed.
- **The non-defective oxidised region**(green region), which would correspond to the oxidised region of the Lerf-Klinowski model. That is, an oxidised platelet of graphene that has kept its carbon matrix intact despite oxidation
- **The defective oxidised region** (blue region). This is new to this model and it basically depicts an oxidised platelet of graphene with vacancy defects on it, allowing for a diffrent kind of chemistry.

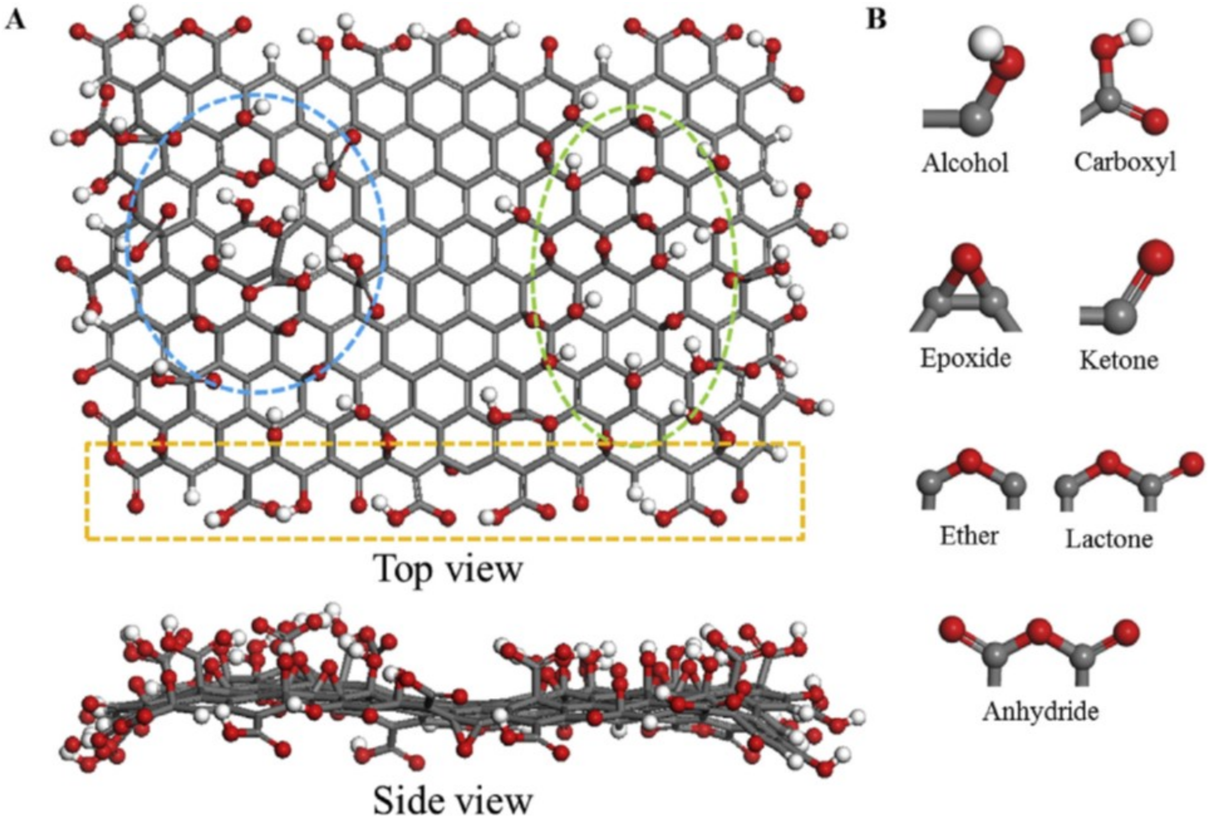

Figure 4.10: *Liu model for GO*

In order to be coherent with the data exposed here, the structural model fits several parameters:

- Having a considerable amount of disorder and defects in the GO plane, which agrees with the level of wrinkling in the images.
- C-O groups are the most present in the sample, mainly as hydroxyls and epoxides

- C=O is present as carboxyl and ketones. Lactons and anhydrides can be considered combinations of ketone and ether. This will be of importance within the context of our study.
- C-O groups are mostly on the plane (green domain in Figure 4.10)
- C=O groups are mostly on the edges and folds (orange area in Figure 4.10) but is present on the plane in the areas with structural vacancy defects (blue area in Figure 4.10).

In conclusion, this updated model seems to be the most accurate approach we have for the structure of GO. it is based on previous studies on the sample and it is a model that can work for different types of GO regardless of production method or the precursor used. The GO synthesised with different methods could have different proportions of each of these regions, but in theory any GO sample can be described with these four areas.

We will consider for the rest of this chapter that the model by Liu *et al* is the most accurate from the ones shown.

4.1.3 Composition of GO

4.1.3.1 Oxygen functional groups, their location and their role on the structure and behaviour of GO

According to Liu's model (see Figure 4.10), there are seven possible oxygen functional groups (OFGs) that can be present in the sample. We will not take the lactones and anhydrides into consideration because, on the one hand, given the oxidation of our GO the concentration of these two OFGs should be minimal and therefore not mesurable; and on the other hand, as we have seen in the previous section, lactons and anhydrides can be considered combinations of ketones and ethers. This means that, should there be any signal related to these OFGs, it will be seen as a combination of a ketone and an ether feature.

This leaves us with five possible OFGs in the samples:

- Alcohols (also called hydroxyl or OH groups).
- carboxyl groups (also called COOH groups).
- Epoxides (also called non-aromatic COC groups)
- Ketones (also called carbonyls or C=O groups)
- Ethers (also called aromatic COC groups)

We can separate these OFGs into two main groups: those that are in-plane with the graphene sheets (carboxyl groups and carbonyls) and those that are in the basal plane of the graphene sheets (alcohols and epoxides). Ketones can appartain to either group, depending whether they are located at the edge of the GO flake or at a defect in the carbon matrix. The OFGs in the basal plane are, at least partially, responsible for the increasing of the interlayer distance between graphite and graphite oxide[439]. This distance goes from ∼ 3.35 Å before oxidation to an astounding 7.37 Å after oxidation, according to the literature [440]

As we have mentioned before, these OFGs are what increases the polarity of GO, hence increasing its dispersability in polar solvants [401].

Due to the disruption of the sp^2 bonding in the graphene matrix due to oxidation in GO, it becomes an electrically insulating material [401],with a conductivity that depends on the degree of oxidation [441, 442]. However, if it is reduced, once the π-network is restored, electrical conductivity can be recovered to a high extent.

An effect of the presence of most of the OFGs is the puckering of the graphene sheets conforming the carbon matrix [439], that has been mainly attributed to the c-OH functional groups in the sample [417], resulting in a certain roughness in the carbon matrix rather than a graphitic plane.

4.1.3.2 Physisorbed water, Chemisorbed water and their role on the structure of GO

Within the context of the structure and composition of GO, the subject of water, whether physisorbed on the GO matrix or chemisorbed by hidrogen bonds to C-O-C and C-O-OH groups [433, 443, 444], has been an important one for decades. For the context of this study, we will focus on some of the main studies that have delved into the subject of intercalated water and its role either on GO or in its thermal reduction.

The first studies on intercalated water on graphite oxide date back to the 1950s, where Franklin published a study called "the role of water on the structure of graphitic acid", another name to what we call graphite oxide nowadays [445].

The role of water was relevant enough and its presence was certain enough for it to appear already on early models of graphite oxide, like the Scholz-Boehm model [411], which has been explained in detail in Section 4.1.2. By the time Nakajima presented his model in 1988 , it was widely accepted that there was water "*absorbed between graphite oxide layers*" and that the interlayer distance *increases by absorbing moisture of immersing in water*[412].

The study that prompted the Lerf-Klinowski model also played a key part in explaining the role of water in GO. First, they found there were strongly bound water molecules, "*locked in the "defects" in the layers of oxygen atoms from the C-O-C and C-OH groups*, that were, in their own words, "*an integral part of the GO structure*".

Additionally, when performing NMR spectra of hydrated GO, they found two different resonances from water. This prompted the division of the water in GO samples to be divided into two catergories: "*mobile water and strongly bound water*". This is what we know nowadays as physisorbed and chemisorbed water, respectively. They also found proof that the removal of this "strongly intercalated water" produced a disorder of sorts in the structure of GO.

In 2006, in the study by Szabó, Dékány *et al*[420], they managed to measure the water content in GO species with different levels of oxydation by measuring the mass between as-prepared, hydrated GO samples and anhydrous GO, obtained by drying GO in a dessicator over concentrated H_2SO_4 for a month. They found that the amount of water that the sample adsorbed, and the quickness to do so, was proportional to the degree of oxydation and that the interlayer space in the GO augmented with the rehydration of the sample. When it comes to IR measurements, as we will see in Section 4.1.8, they managed to distinguish the features coming from the OH groups in the GO from the water features by deuterating the sample.

A study in 2011 by Acik *et al* [433] provided an in-situ study of the desorption of water in GO by means of infared spectroscopy. The intensity of the OH vibrations in the IR spectra is dominated by three main groups: water (both physisorbed and chemisorbed), OH groups and COOH groups. By studying the behaviour of the intensity of this feature, shown in Figure 4.11, it is possible to discern the temperature at which the water is mostly desorbed, which is somewhere between 175 and 200°C. Models were created for the desorption of water using intrasheet and intersheet interactions, which are depicted in Figure 4.12.

As we can see, the presence of water is higher at thicker samples and its chemistry upon mild

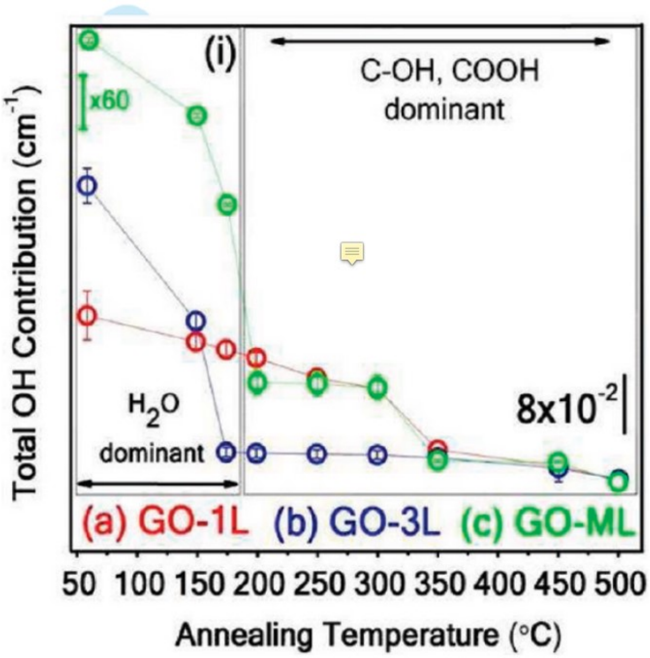

Figure 4.11: *Comparison of the integrated total OH contribution from H_2O, OH, and COOH and normalized absorbance of integrated carbonyl concentration. (i) Integrated intensities (3000-3700 cm^{-1}, std. ± 0.01-0.2%) of C-OH peak are shown as a function of temperature for GO-1 L (red), GO-3 L (blue), and GO-ML (green). Removal of H_2O up to 175 °C significantly decreases the intensity of the C-OH peak (left). After removal of H_2O, the intensities of C-OH and COOH groups are dominant (right). Source: Acik et al [433]*

heating is very different compared to monolayer GO. On top of this, this study also proved that the intercalated water in close proximity to the OFGs facilitates the creation of larger holes, indicated by the release of CO2 during the thermal treatment.

The presence of physisorbed and chemisorbed water has been since confirmed using several techniques, namely X-ray scattering [444], broadband dielectric spectro- scopies [443], or TGA[446, 444]. It was a study using the latter in 2017 [447] that decomposed the water desorption features in two distinct processes: on the one hand, the removal of physisorbed water, which took place in a temperature range from 50°C to 120°C, and on the other hand the removal of chemisorbed water, which took place in a temperature range from 120°C to 230°C. Merging this data with the one by Acik *et al* [433], the temperature range for the desorption of physisorbed water is between 50 and 120°C, and the one of chemisorbed water is between 175 and 200°C. This will be of great importance for our study.

4.1.4 Interest of GO

GO offers interesting properties that have gather research interest on it for the past decades, including its thermal properties, electrical properties and most importantly its tunability. Within this topic, the reduction of GO is by far one of the biggest interests for GO, which will be further discussed in Section 4.1.6.3

Nevertheless, one of the main interests of GO relies on its dispersibility on polar solvants, which is important for its processing as well as for its implementation at larger scales. The dispersibility of GO in solution depends on both the oxidation process and the solvent being

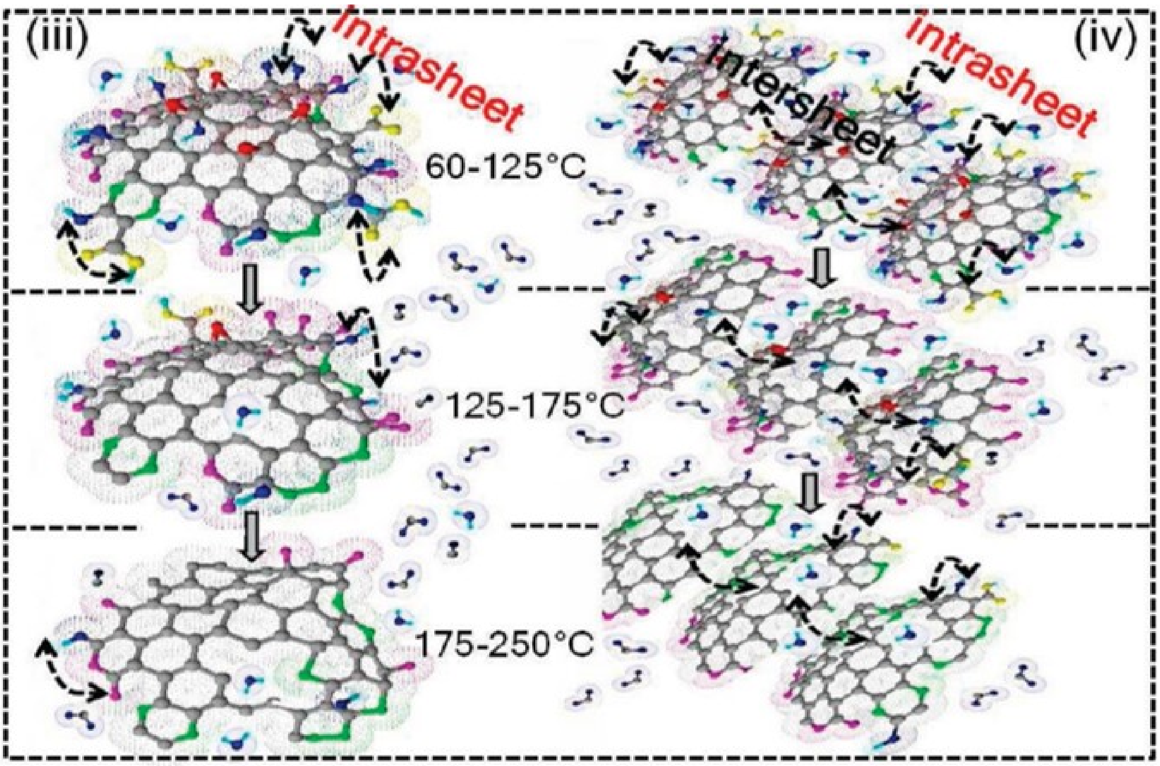

Figure 4.12: *Model structures are shown for processes involving only edge intrasheet interactions (GO-1 L) (left), and both intrasheet and intersheet interactions (GO-3 L) (right) for 60-125, 125-175, and 175-250°C. Each species is identified with specific colors: epoxides (red), ethers (green), COOH (yellow), C=C (gray), C=O (pink), H for H_2O (aqua), O for H_2O, CO, and CO_2 (blue). Source: Acik et al [433]*

used. The greater the polarity of the GO surface, the greater the dispersability. The typical values for the dispersability of GO in water range from 1 to 4 mg mL^{-1}. This dispersability can be amped up to 15 mg mL^{-1} by means of functionalisation [402].

This dispersibility is essential for the preparation of thin films using methods like Langmuir-Blodgett or Langmuir-Schaft [418, 440].

4.1.5 Preparation methods of GO

Throughout history, there have been mainly five methods for the preparation of graphite oxide, and therefore, graphene oxide [448] [449]. Examining this methods is interesting from a historical point of view, but it is also of scientific interest. This interest is due to graphene oxides prepared using different methods exhibiting different compositions and different properties. This was first shown in the study from Chua *et al* in 2012 [449] which used XPS, NMR, FTIR and Raman spectroscopy to study samples prepared using the Staudenmaier, Hummers, Hoffman and Tour methods. A summary table, extracted from the bibliography [448] can be seen in Table 4.1

The Brodie method

This preparation method was the first one ever used in 1855, since it was the very one graphite oxide was dicovered with, as it has been explained in detail in Section 4.1.1. The preparation of this graphite oxide is explained in detail in his article "On the atomic weight of graphite"[404].

In this process, a mixture by weight of 1/4 graphite and 3/4 potassium chlorate is placed in a retort, and enough fuming nitric acid is added in order to render the whole system fluid. The retort is then placed in a water bath and kept at a tempertature of 60°C for three to four days, after which it is washed in water by decantation. The sample is then dried and the oxidising process is repeated with the same proportion of $KClO_3$ and HNO_3 until no change is observed upon oxydation. Finally, the sample is dried, first *in vacuo* and afterwards at 100°C.

To the best of our knowledge, there have been no comparative studies that have checked on the differences between GO prepared using the Brodie method and other GOs. However, it is still somewhat common to find this method still being used to this day, as we can see in the literature [450] [422] [420].

The Staudenmaier method

In 1898 and 1899, with the Brodie method as a starting point, Staudenmaier improved this oxydation in order to obtain larger quantities of GO, using sulfuric acid on top of the nitric acid that Brodie had used [451] [452]. The proportions of each compound can be found in his study, of which we offer a translated excerpt:

> *2 g commercial of Ceylon graphite are grinded with the same amount by weight of potassium chloride as finely as possible, the powder was put into a mixture of 10 cc of pure concentrated sulfuric acid and 5 cc of nitric acid of 1.4% by weight, cooled to room temperature in a porcelain dish, it is stirred, and the whole content is put on a water-bath, and it is heated so that its temperature rises in one hour to 100°C, occasionally turning over. When the emission of fumes has ceased, the contents are added to water.*

Other sources [449] [448] point out that another difference that Staudenmaier established for this preparation of GO was adding the $KClO_3$ little by little instead of adding it in one take, although, to our best knowledge, that is not what is explained in the aforementioned study, although it could have been a later addition

The Hoffmann method

Several studies and reviews [449] [448] point to a study by Hofmann and König from 1937 as the starting point for a different method for the production of GO. This is quite debatable, given that,in the article cited as the source for this ”new” method, the authors themselves state that they are using the Staudenmaier method[453]. In the same study, they state that they use concentrated sulfuric and nitric acid. This means that the use of sulfuric acid in this method has gotten lost in translation for the reviews given. This has been corrected using a footnote in the caption of table 4.1.

However, it seems to be true that Hofmann was indeed the first one to use concentrated nitric acid for this procedure instead of fuming nitric acid. In other words, this method could not be considered an independent one but an important improvement on the one proposed by Staudenmaier.

The Hummers method

in 1958, Hummers and Offeman introduced a new method for the preparation of GO. Their main motivation for this method was their concern with the Staudenmaier method and the possibility of explosions it entailed [454].

For this, they used potassium permanganate as an oxidant instead of the potassium chlorate (which was used in unsafe quantities). They added the $KMnO_4$ in a mixture of concentrated sulfuric acid and sodium nitrate, which produced nitric acid in situ in stead of having to add it and the fumes this might cause. The ingredients were mixed in an ice bath, as a safety measure. Then the mixture was brought to 35 ± 3°C for 30 minutes, after which water was stirred into the paste. This caused violent effervescence and an increase in temperature up to 98°C, where it was mantained for 15 minutes before being diluted with more warm water and 3% hydrogen peroxide to reduce the residual permanganate and manganese dioxide.

It is important to notice that several modifications have been done to this method for different reasons, e.g. in order not to need the $NaNO_3$, over the years. The modification that has been used for our particular experiment can be seen in Section 4.1.5

The Tour method

A common issue for all of the abovementioned production methods is the generation of toxic gas (fumes), which come from the usage of nitric acid (HNO_3), either as a reactive in the oxidation process (as in the Brodie, Staudenmaier and Hofmann methods) or as a product of the initial reactives that oxidate the GO in a second reaction (Hummers method).

In 2010, Marcano, Kosynkin, Tour *et al* discovered a new method for the preparation of GO that did not include nitric acid in any way during the oxidation process [455]. This method consisted on increasing the amount of potassium manganate with respect to the Hummers method, not using any sodium nitrate nor nitric acid, and perfoming the reaction by adding potassium permanganate to a mixture of sulphuric and phosphoric acid as well as graphite flakes. The reaction was then heated to 50°C and stirred for 12 h. Then, it was cooled to room temperature and poured onto ice with 30% H_2O_2. This mixture was sifted, filtered, centrifuged at 4000 rpm for 4 h; and the supernatant was decanted away. After repeating this filtering process, the obtained material was coagulated with 200 mL of ether and the resulting suspension filtered. The solid obtained on the filter (the GO) was vacuum-dried overnight.

In this same study, they found that GO produced using this method was more oxidised compared to GO produced employing the Hummers method under the same external conditions. Moreover, when both were chemically reduced with hydrazine (see Section 4.1.6.1), both the GO prepared using this method and the Hummers method had a similar electrical conductivity. This, along with the lack of toxic fumes and the easy control of the temperature during the oxidation process, make of this production method a clear candidate for lage-scale production of GO. However, it is important to point out that the order of addition in this mixture is extremely important, since a different addition order could cause the $KMnO_4$ to be in high ocncentrations in the acid mixture, which could rend this mixture explosive.

Comparative studies on GOs prepared using different methods

To the best of our knowledge, the study by Chua *et al* from 2012 [449] is the most complete comparative study that has been made among graphite oxides fabricated using different preparation methods. The different graphite oxides that have been studied are the ones prepared using the Staudenmaier method (GO-ST), the Hofmann method (GO-HO), a modified Hummers (GO-HU), and a Tour (GO-TO) method.

In order to characterise these graphite oxides they use several spectroscopic methods, namely high resolution X-ray photoelectron spectroscopy (XPS), electrochemical impedance spectroscopy (EIS), NMR, Fourier transform IR (FTIR), Raman spectroscopy, electrochemical impedance spectroscopy, cyclic voltammetry, and solid-state reduction techniques. A brief run-through of each of the findings for each technique is presented here.

XPS was used to detect surface elemental composition, finding atomic C/O ratios of 2.47, 2.71, 2.05 and 1.95 for GO-ST, GO-HO, GO-HU and GO-TO, respectively. In other words, the methods that used permanganate (GO-HU and GO-TO) had a higher oxydation rate with respect to the chlorate (GO-ST GO-HO) methods. For the remainder of this section, we will refer to these methods as the permanganate methods and chlorate methods, respectively. High resolution XPS could break down the XPS signal into four Gaussian peaks correspoinding to C=C, C-O, C=O and O-C=O. They found a noticeably higher presence of C=O and O-C=O bonds in the GOs prepared with permanganate methods than the ones prepared with chlorate methods. The GO-TO had a particularly high amount of O-C=O which indicate a higher presence of carboxyl groups.

Solid-state ^{13}C NMR analyses found peaks caused by the presence of C)o, O-C=O, graphitic sp^2, C-OH and C-O-C bond types. In good agreement with the XPS results, the peaks corresponding to carbonyl and carboxyl OFGs were only present on the permanganate method GOs, confirming the previous differentiation between both sets of production methods.

FTIR studies showed the presence of preaks corresponding to O-C, C-O-C, and C=O, with the latter only appearing for the permanganate method GOs, thus confirming the previous XPS and ^{13}C NMR findings.

The authors of the study used **EIS** to determine the heterogeneous charge-transfer resistance (R_{ct}) of the different samples in a solution containing ferro/ferricyanide electrochemical probe. The complete results for this analysis can be found in table 4.1. In essence, they found a correlation between the oxydation degree of the samples and their R_{ct} values. This indicated that a portion of the OFGs in the GOs were negatively charged at the working pH of the electrochemical experiment.

Another electrochemical characterisation, **cyclic voltametry**, was used to determine the heterogeneous electron transfer (HET) rate of the different GOs in ferro/ferricyanide probe. After calculating the respective HET rates from the analysis of their data, it showed that the charge transfer rate was inversely proportional to the oxidation rate, which is in good agreement with the EIS findings.

Finally, a solid-state electrochemical reduction technique was also performed on these GO samples to try to find electrochemically reducible OFGs (mainly epoxides, carbonyls and peroxyls). Again, the results seemed to point to all of the samples having epoxide groups to some extent, but only the permanganate method GOs having carbonyl and carboxyl functional groups, which reflects in higher reduction energies.

In conclusion, the preparation method used does not only increase or decrease the oxidation rate given the same external conditions, but it also has a clear role in the OFGs in our GO. According to this study, since we have used a modified Hummers method (see Section 4.1.5), we should have carbonyls and carboxyl groups present in our sample.

The role of the precursor in the composition and properties of GO

The previous section has proved that different preparation methods yield different GOs with different compositions and properties. However, even for the exact same method, this can be the case as well. The study by Roy Chowdhury *et al* in 2014 [456] focused on the properties of the graphite oxides prepared using the same Hummers method, only with three different graphite precursors.

By means of different techniques (TGA, UV-visible spectroscopy, powder X-ray diffraction, and even some microcopy, using SEM), they were able to characterise the original graphite

Method	Oxidant	Reaction media	C/O ratio	Raman I_D/I_G ratio	R_{CT} (kΩ)	Notes
Brodie	$KClO_3$	Fuming HNO_3	1.17	0.89	1.74	-
Staudenmaier	$KClO_3$	HNO_3+H_2SO_4	-	-	-	$KClO_3$ added stepwise rather than in a single bolus
Hofmann	$KClO_3$	Non-fuming HNO_3*	1.15	0.87	1.68	-
Hummers	$KMnO_4$+ $NaNO_3$	Conc. H_2SO_4	0.84	0.87	1.98	Modifications can eliminate the need for $NaNO_3$
Tour	$KMnO_4$	H_2SO_4+H_3PO_4	0.74	0.85	2.15	-

Table 4.1: *Summary of synthetic methods used to prepare GO. R_{CT} refers to the charge-transfer resistance. Source: [448] reproduced from [449]. *According to the original study cited in the bibliography [453] , this term is incomplete and should read as "Concentrated HNO_3+H_2SO_4*

precursors and the graphite oxides prepared with them.

Their drawn conclusions show that, for larger crystallite sizes (crystallite sizes vary from graphite to graphite), and especially a longer c-axis of the crystallites, there was a higher favouring of basal plane oxidations over sheet edge oxidations. They justified this with a longer c-axis providing a higher surface area for the oxidants to react with the graphitic sheets.

Another finding of this study is that, the higher the basal plane oxidation, the higher the strain on the GO sheets and the more they would break apart. In other words, a graphite sample with larger crystallite, and especially a longer c-axis, would result in a graphite oxide sample with smaller crystallites.

For less "purely graphitic" samples of graphite, with presence of impurities such as amorphous carbon, a previous study [457] used similar techniques, as well as the study of the adsorption of ammonia, to determine that the presence of this amorphous carbon enhances oxidation defects.

Importance of our preparation method

As we have seen in this section, the preparation of GO can play a key role in its structure, composition and properties. That is why it is of vital interest to know about the specific preparation method used for our studies, as well as the possible role of this production in the final sample.

Production of our GO: modifications to the Hummers method In this study, a modified version of the Hummers method has been used.

As we have seen in this section, the amount of different OFGs in our GO should be varied, as opposed to GO prepared using Staudenmaier or Hofmann methods. This will be of use when analysing our data.

Oxidative debris It is important to notice that it has been previously seen in the bilbiography (refs) that the chemical and physical processes taking place during the preparation of GO leaves a non-negligible amount of oxidative debris, besides the one conforming the OFGs of the GO, that will play a role in the study taking place. This debris can be broken down into two different groups:

- On the one hand, there is some amount of residue product coming from the GO preparation itself, even after the washing of the sample. This oxidative debris consists of oxidative groups that are not bound to the sample and that appear in very low proportions.

- On the other hand, because we have prepared the sample using liquid exfoliation (see Section 4.3.1), it is very plausible that, during the sonication of the sample, we end up some GO-like debris on our solution; that is, GO platelets of a much smaller lateral size than our GO flakes.

This two kinds of oxidative debris are to be taken into account when performing the corresponding data analysis of our experiments.

4.1.6 The reduction of Graphene Oxide

Besides the functionalisation of GO, its other main interest with applications in mind is its reduction to a material resembling graphene as much as possible. The general materials obtained after the various processes of reduction of graphene oxide are known as reduced graphene oxide or rGO. However, much like with production methods, different reduction methdos will yield different kinds of rGO with different sets of properties.

4.1.6.1 Chemical reduction

When dispersed in a colloidal solution, a variety of chemical reductants can be used to reduce graphene oxide. It is important to notice that the main colloidal GO solution that is fabricated is a GO aqueous solution. Other polar solvants can be used as well but as it has been mentioned in Section 4.1.4, one of the main interests of GO relies on the application of its hydrophilicity. In this context, the reduction of aqueous GO dispersions with strong reductants, suchc as lithium aluminium hydride, is challenging because of their strong reactivity with water [401].

The most common reductant for GO, as well as one of the first ones to be reported, is hydrazine monohydrate(N_2H_4). The reduction of GO in aqueous solution using hydrazine hydrate was first reported in 2007 by Stankovich and collaborators [446], although the reduction of graphite oxide with hydrazine hydrate had been used even before the discovery of graphene [458]. Hydrazine hydrate is a great candidate for this kind of reaction because it does not react with water, providing a selective reduction where only the GO is affected.

They found that the product of this reduction was the aggregation and precipitation of graphene-based sheets, forming a hig surface-area black solid that was extensively characterised using a variety of elemental analysis, imaging and spectroscopic analysis, as well as electrical conductivity measurements.

SEM images of this material revealed that it contained "*randomly aggregated, thin, crumpled sheets closely associated with each other and forming a disordered solid*". Further characterisation of this material showed a very high surface area although not as high as the theoretical specific surface area for isolated graphene sheets [459]). Elemental analyses showed a decrease in oxygen content by almost an order of magnitude, and ^{13}C NMR spectra of GO and rGO showed a clear structural change after the reduction, with a single feature after the reduction that corresponds to variation of carbon atom environments. A similar behaviour can be found in the XPS spectra of the samples, where the C-C peak of the spectra change considerably, having almost no signal corresponding to OFGs after the reduction.

In other words, the rGO, however strange its morphology, seems to acquire a lot of the properties of graphene. Even though this reduction method has been vastly reproduced [460, 408, 461], the reduction mechanism is still unclear. DFT calculations have provided possible routes for the reduction of epoxides upon hydrazine treatment [460], but the reaction paths of other OFGs have not been discerned yet.

Other chemical compounds have been used to chemically reduce GO, such as sodium borohydride ($NaBH_4$)[462], which has been reported to yield better conducting rGO than its hydrazine counterpart. This could be due to hydrazine doping the final rGO sample with nitrogen atoms, thus acting as donors which compensate the hole carriers in rGO.

Vitamin C has also been, for example, a candidate for an effective reduction of GO without the use of hydrazine [463], which provide a cleaner solution for this process with a similar outcome in terms of properties of the final product.

Metal-assisted reduction An interesting case of chemical reaction was found while trying to find a cleaner method than hydrazine for the reduction of GO. It was found that, by introducing aluminum powder in an aqueous solution of GO that contained hydrochloric acid as well [**?**]. This process reduced the amount of oxygen in the sample about an 80%, with no aluminum present in the final rGO. A similar study from the same team the following year [**?**] found iron to produce the same effect on GO. It is important to notice that, at least when it comes to powder reactions, it seems that the pressence of hydrochloric acid is essential for the reduction of GO.

4.1.6.2 Thermal Reduction

Another widely used method for the reduction of GO is thermal reduction. This kind of reduction, which is the subject of these works, has also been on the research spotlight for more than a decade. It consists on heating the sample, preferably under vacuum, so that the OFGs present in the sample desorb, sometimes taking part of the carbon in the sample with them and producing CO and CO_2 [464, 465]. The processes taking place at the GO during its thermal reduction have been studied using XPS and EELS as well by D'Angelo *et al* [407, 69]. This will be delved into in detail in Section 4.1.8.

Lately, this kind of reduction has been coupled with pressuring the GO platelets to obtain a better result [466]

Other reductions

Electrochemical reduction With the pursue in mind of a faster and cleaner method than chemical reduction with hydrazine, a study in 2009 by Ramesha *et al* [467] found that it was possible to reduce GO platelets previously attatched to a cystamine-gold substrate through electrostatic interactions. This reduction took place when applying a negative potential lower than -1 V.

The resulting rGO was characterised by Raman spectroscopy, and conductive AFM. The former show a shift of the G band in the sample, which is consistent with a reduction of it. The latter shows an increase in the current flow by at least 3 orders of magnitude after the reduction of the sample, with a c:O ratio of almost 24:1.

This reduction phenomenon has been subsequently reproduced and charactersised with several different techniques, such as XPS, XRD or cyclic voltammetry, wich similar results [468, 469].

Laser reduction In a study of 2010 by Sokolov *et al*, it was proven that, by focusing either a continuous laser beam with λ=532 nm, or with a pulsed laser of either λ=355 or 532 nm (the ones that were available to them, since they used the lasers provided by their Raman equipment) it was possible to obtain rGO [470]. This was confirmed by the Raman I_D/I_{2D} ratio of the samples, proving an effective reduction in the area where the laser beam had impacted, as well as a sizable amount of degradation. The cause for this reduction is a compendium of different phenomena: the initial excitation produces electron-hole plasmas within the GO; where both electrons and holes are trapped due to the strain caused by the OFGs in the sample. All of this results in material instability as well as degradation. Phonon coupling is also a partial cause of this reduction, contributing to heating the material.

This has proven to be a very cost-effective technique for the reduction of GO, which can be applied not only to GO films but also to GO solutions [362], as well as being a great tool for the creation of patterns of rGO in GO matrices, which sound promising in terms of nanodevice engineering [471].

Substrate-assisted reduction Follwoing the studies in Section 4.1.6.1, where metals were found to be part of a reduction mechanism for GO, a study by Cao *et al* [472] proved that foils of these metals, used as a substrate that was plunged into an aqueous GO solution, can act as a reducing agent, and what is more, that the unstable environment (hydrophylicity within the solution and the zeta potential, that is, the static electrical field at the interface between the substrate and the GO solution) triggers the bonding of the different rGO layers into a continuous film. Unlike the previous studies, no HCl was needed to achieve this reduction.

Electrical reduction In the study of Ekiz *et al* in 2011, it was proved that electrical charge could act as a switch in a graphene /graphene oxide system. For this, multilayer GO was deposited on top of two contacts and a current was applied while the sample was bieng measured by means of XPS, AFM and multifrequency electrostatic force micrsocopy. Results show that, upon application of a bias potential to the contactss, the positive contact is oxidised and the negative contact is reduced. The stochiometry of the sample seems to be dependent on the distance from the contacts. This is coherent with the electronic structure of graphene and GO, since electron injection into GO should weaken the bonds of the negatively charged oxygen atoms in the OFGs.

Microbial Reduction Even though it might seem like an eccentric route, it makes sense that, given that bacteria consume oxygen, there could be a way to reduce GO using them. This is the main subject of a study of 2011 by Wang *et al*[473], where the marine bacteria *Shewanella oneidensis* has been used to successfully reduce GO in aqueous solution. The rGO resulting from this reduction has been studied using diverse techniques, such as XPS, elementary analysis or cyclic voltametry. The results gathered seem to put this rGO in a range close to the one reduced using hydrazine in terms of properties.

4.1.6.3 Our thermal reduction of GO:The need for different temperature regimes

Due to the very interesting role that adsorbed water plays in the behaviour of GO at low temperatures,as well as the rehydration of the samples, the structure of the experiment has been planned as follows:

As it has been seen in Section 4.1.3.2, there is a presence of chemisorbed and physisorbed water on the sample, which, according to the literature, should desorb at a temperature lower than 220°C. For this reason, on the first part of the study, the sample will be studied in a temperature range that will go from 70°C to 300°C. This study will focus on the desoprtion of the OFGs that leave the sample at low temperatures, as well as the physisorbed water attatched to the GO and the chemisorbed water attached to said desorbing OFGs.

It is known from previous research on the matter (refs) that physisorbed water tends to desorb from the sample at a temperature close to water boiling point (100°C)[465] whereas chemisorbed water tends to desorb from the sample at a higher temperature (between 180°C and 220°C)[447]. This is the reason why there is a region of interest in the study around 95°C and another one around 185°C. As it can be seen in Figure (reffigure), temperatures around these two points of interest have been taken into account for this study.

After these measurements - which we will name from now on LT studies for low temperature - have been performed, the sample has been taken out of the microscope and left out overnight for it to rehydrate again. The sample has then been taken back into the microscope to perform a second study from 70°C to 1200°C, which we will call HT studies for high temperature.

In principle, and according to bibliography (ref), the OFGs that the chemisorbed water is attached to get desorbed at a temperature lower than 220°C. This means that, in theory, we should only be able to find physisorbed water on the samples after the LT studies.

4.1.7 The tunability of Graphene Oxide

Graphene oxide has drawn interest not only for its ability to be reduced into rGO and therefore acquire to some extent the properties of graphene, as it has been vastly explained in the previous section, but also for the potential tunability of its properties. This can be done, for example, by modifying the chemical structure of the GO in some way; or by combining this material with other materials of interest to create composites with unique properties.

The functionalisation of graphene oxide

The chemical functionalisation of graphene oxide consists on the addition of other functional groups to GO, by either non-covalent attachment to the pristine graphitic regions of the GO, or by covalent attatchment, using some of the OFGs as anchor points. A vast review on these processes has been performed by Dreyer and coworkers [401] of which we offer a short, updated version.

Briefly speaking, the functionalisation of GO can be performed mainly at the **epoxide groups** of the GO, at the **carboxyl groups** of the GO, and as a **non-covalent functionalisation** of the graphitic platelet through $\pi - \pi$ stacking, cation-p or Van der Waals interactions. The latter is also possible for reduced graphene oxide and even graphene itself.

The functionalisation at the **epoxide groups** generally needs a ring-opening reaction to ocurr. These reactions range from the addition of octadecylamine to GO for the preparation of thin films and inks using organic solvents [402] to the stabilisation of solid-phase dispersions of GO (now chemically modified)by covalently attatching 3-amino- propyltriethoxysilane (APTS) to the GO platelets [474].

The functionalisation at the **carboxyl groups** of the GO is usually done in two different parts: first with the activation of the acid group using several chemical compounds, such as $SOCl_2$ [475], 1-ethyl-3-(3-dimethylaminopropyl)- carbodiimide (EDC)[476], N,N0-dicyclohexylcarbodiimide (DCC)[477][478], or 2-(7-aza-1H-benzotriazole-1-yl)-1,1,3,3-tetramethyluronium hexafluorophosphate (HATU)[479]. After the activation of the acid group, the addition of nucleophilic species, such as amines or hydroxyls, can produce functional groups covalently attatched to the GO. In this sense, introduction of substitued amines is the most common method for this kind of functionalisation, with applications in optoelectronics [475], drug delivery for non hydrosoluble drugs [476], and polymer composites including biocomposites [480].

All these chemical functionalisations broaden the span of the different possible applications for GO.

Graphene oxide composites

Along with the chemical functionalisation of GO, another approach for the tuning of the properties of the material has been the fabrication of composites using either GO or rGO. These composites can be made exclusively of GO, by forming GO networks with different properties than the original GO [481]. They can also be made of two or more materials, with composites ranging from GO-metal/metal oxide for water purification [482] to polyaniline/GO composites for corrosion protection [483] or even ZnO rods /rGO composites for improved sunlight photocatalysis [484].

4.1.8 Previous spectrocsopic studies on GO and RGO and State of the art

The amount of studies on graphene oxide, graphite oxide and their reduced counterparts have been extensive over the years. For this reason, we have chosen to focus, in general, on studies that fulfill at least several of the following characteristics:

- Studies that focus on graphene oxide and not just on graphite oxide
- The GO used on the study has been fabricated using the Hummers method or a modified Hummers method (they are more relevant for our study, since as we have seen in Section 4.1.5 GO fabricated using other production methods may have different properties).
- We will focus especially on studies that focus on the OFGs present in the GO using spectroscopy, and within that subject, those that use EELS.

IR spectroscopy

Infrared spectroscopy, in its many different variants, has been widely used for the study of GO and, especially, the OFGs conforming it. It was also one of the earliest techniques analysing GO that we are still using to this very day. Here we offer a brief summary of these studies.

First of all, it is important to highlight that the interpretation of the different IR spectroscopy studies has varied from study to study and that, to this very day, not all peaks are confidently assigned to a certain functional group. Some features have been asigned to one group in some studies and to another group in other studies. For this matter, we will be picking the first in-depth IR study on graphite oxide from 1955 [485], one of the most exhaustive studies on IR and GO [420], as well as a more recent study where a long discussion about previous IR studies on GO is extensively done [432].

The study from Hadzi *et al* from 1995[485] is a very advanced one for its time, and would set the initial ideas on which all other IR investigations on GO would be founded on.

Even though the GO in the study has been prepared using the Brodie method and not the Hummers method, it is important to mention the study by Szabó *et al*, previously mentioned in Section 4.1.5 [420] when it comes to the IR investigation and peak assignment of the GO samples, since it is one of the most exhaustive studies to date. In the study, both GO and deuterated GO have been studied. These results can be seen in table 4.2.

The study uses the diffuse reflectance infrared Fourier transform (DRIFT) technique. The results obtained assign the main vibrational frequencies related to C-OH, H_2O, C=O, COOH, C-C, C=C and C-O, which pretty much sum up all possible bonds within GO.

An arguably even more exhaustive study was performed 5 years later by Acik *et al*, where they did not only check the IR spectra of GO as prepared, but also studied the variation of the features of the spectra depending on the GO thickness, and they also studied in depth the thermal reduction of said GO. [432]

GO-1/H_2O	GO-1/D_2O	assignment
3630* m,sp	2680* m,sh	ν_{OH} in C-OH/ν_{OD} in C-OD/
3490* s, sp	2568 vs,br	ν_{OH} in C-OH/ν_{OD} in C-OD/
3210* s, br	2396* vs, br	ν_{OH} in H_2O/ν_{OD} in D_2O
2814 w, br	-	ν_{OH} in dimeric COOH
1714 m,sp	1716 m,sp	$\nu_{C=O}$
1616* m,sp	1196* m,sp	β_{OH} in H_2O/β_{OD} in D_2O/
1574 w,sh	1574 m,sp	aromatic $\nu_{C=C}$
1368* s, br	968* s,br	β_{OH} in C-OH/β_{OD} in C-OD
1064	1064	skeletal modes of ν_{C-C} and ν_{C-O} bonds (m, sp)
968	968	
828	828	
698	698	

Table 4.2: *IR peak positions (in* cm^{-1}*= of air-dry GO-1 (GO-1/*H_2O*) and deuterated GO-1(GO-1/*D_2O*)and their assignments. Asterisks (in the same row) designate isotopomer peak pairs. Band intensities and widths are classified as w (weak), m (medium), s (strong), vs (very strong), sh (shoulder), sp (sharp), and br (broad).Source: [420]*

The discussion of IR spectroscopy In the study by Acik *et al*, there is a very fruitful discussion about the different asignations of the peaks in IR spectroscopy. After a thorough bibliographic research up until the year 2015, this article from 2011 sums up very well the differences and advances in IR spectroscopy when it comes to GO[432]:

> *Previous IR studies have been interpreted on the basis of simple model molecules using common infrared tables. In general, conjugation and proximity effects can lead to substantial frequency shifts and need to be taken into account, which has not been the case so far. Consequently, determination of GO chemical composition has been difficult. For instance, the identification of ketone and carboxyl groups is difficult, and are mostly referred to as "carbonyls" (e.g., an intense peak at 1732* cm^{-1} *was ascribed to the stretching vibration of a carbonyl by Melucci et al. [486]) or "C=O group" (at 1750* cm^{-1} *by Nakajima et al. [413]). Although Chen et al. [487] assigned a peak at 1734* cm^{-1} *to carbonyls, they were not able to identify whether it was a carboxyl or a ketone. The overlapping spectral features in the 1650-1850* cm^{-1} *region complicate the spectral interpretations of as-synthesized GO. Therefore, it is impossible to distinguish these infrared modes without using further differentiation methods (e.g., selective removal of some species by thermal annealing). This difficulty has led to confusing assignments. For example, absorption bands at 1630* cm^{-1} *for GO and 1570* cm^{-1} *for reduced GO (rGO) were attributed to the asymmetric vibrations of the carboxylate groups[488], partly because the contribution from ketones in this region could not be distinguished. Taking into account the shifts associated with*

π-conjugation in benzene rings, the peaks at 1700 [489] and 1730 cm^{-1} [490] were both attributed to the carboxyl groups adjacent to benzene groups. Indeed, Shen et al. reported a lower frequency at 1650 cm^{-1} for noninteracting carboxyl groups [480].

Furthermore, the deformation mode of the C=O band of a carboxyl was first associated with a peak observed at 1100 cm^{-1} in a thermal annealing study monitored by thermal gravimetric analysis (TGA) [491]. Another tentative assignment of a peak at 1647 cm^{-1} to carboxyl was made for the nonoxidized graphitic domains by Kim et al.[492]

The presence of the other species, such as stretching and bending modes of hydroxyls and ethers, also complicates the identification of carboxyl groups and ketones in lower-frequency spectral regions (800-1500 cm^{-1}). Absorption features at 1414 cm^{-1} (carboxy) [493]or 1410 cm^{-1} have mostly been assigned to the deformation vibrations of C-OH groups[494], an assignment that ignores the contribution of ketones in this frequency region.

[...] Similarly, the assignment of modes at 1705, 1730, and 1750 cm^{-1} to free carboxyl groups, esters, and lactone groups, respectively, has been made for carbon fibers [495]. The assignment of the weak vibrational modes in the bending mode region for hydroxyls and carboxyl groups at lower frequencies has also been difficult. For instance, Yan et al. [496] have assigned the peak at 1365 cm^{-1} to a C-OH, while assigning only one peak to both carboxylic acid and carbonyl moieties at 1732 cm^{-1}.In other studies, the stretching modes of carboxyl groups were ignored and only a weak absorption at 1356 cm^{-1} was assigned to the stretching vibrations of carboxyl groups[497]. Nonetheless, only IR measurements are sensitive enough to determine the presence of carbonyl groups despite potentially controversial assignments.[...]

Similarly, epoxies have been identified, but the assignment of their associated vibrational modes has been unclear in most cases. [...] Some studies have avoided the 800-1330 cm^{-1} spectral region altogether because of the overlap of hydroxyl and carboxyl frequencies. Indeed, contributions in the 1000 - 1180 cm^{-1} region may arise from hydroxyls, carboxyl groups, ethers, epoxides, and ketones. A mode at 1057 cm^{-1} was attributed to a C-O in C-OH or C-O-C functional groups by Xu et al. [498], an assignment that ignores possible weak contributions from carboxyl groups and ketones. Absorption bands at 1220, 880, and 850 cm^{-1} have been assigned to the symmetric stretching, asymmetric stretching, and deformation vibrations of epoxy groups, respectively [499]. However, the band at 1220 cm^{-1} may also originate from a ketone, instead of an epoxy. In other studies, the C-OH stretch mode was placed at 1226 cm^{-1} [500],where ketone also has a weak contribution. Gonc et al. assigned the two modes at 1139 and 873 cm^{-1} to CO in epoxy groups. However, they were not able to distinguish scissor modes of water and ketone from aromatic carbon double bonds, all occurring at ~1620 cm^{-1}, [501] whereas Bon et al. interpreted a similar absorption to vibrations of nonoxidized graphitic domains [502]. In general, the identification of sp2-hybridized C=C groups at 1580-1600 cm^{-1} is also greatly complicated by the scissor mode of water (deformation vibration) at 1630-1650 cm^{-1}.

Another challenge has been the identification of C-O stretch modes of CO and CO_2in the 2200-3000 cm^{-1} region that overlaps within a broad feature with C-OH stretch modes (2800-3600 cm^{-1}), arising from a number of functionalities [503]. [...] In the work of Pham et al. [504], for instance, the observation of modes at 1703 and 3188 cm^{-1} was used to identify carboxylic groups, but additional contribution in the O-H stretch region was not taken into account. Indeed, other studies have observed

> *and assigned bands at 3616 and 3490 cm^{-1} to hydroxyl species [505].Hontoria-Lucas et al [416] first identified a broad band at 3000-3700 cm^{-1} showing two maxima at around 3190 and 3403 cm^{-1} and a shoulder at approximately 3590 cm^{-1}. These were attributed to the presence of the free and associated hydroxyl groups, due to "adsorbed and inhibited" water molecules and to the hydroxyl groups of GO.*

This exhaustive discussion comes to say that there are several modes that have been more or less assigned to certain groups, with spectral windows being assigned to two or more overlapping features. In order to have an additional certainty on the assignment of the IR features, this study provided an detailed DFT study that will be seen in Subsection 4.1.8

With this in mind, and with a more accurate assignment of the different IR features, Acik *et al* provide a very in-depth study of GO and its thermal reduction, keeping the sample thickness as a variable as well. The study is also done in two separate temperature regimes in order to study the different features taking place in each one; one from 60 to 250°C, and another one from 250 to 650°C. Figure 4.13 shows the transmission infrared absorbance at room temperature with the main OFG regions highighted, as well as the low temperature and moderate temperature results for multilayer GO on transmission infrared differential spectra, which show the strongest features. These studies have also been performed for monolayer, trilayer and 5-layer GO.

To sum up, this study offers two very distinctive sets of results. On the one hand, it offers an updated version of the studies previously performed using IR on GO, with peak assignments supported by DFT. This peak assignment, in essence, is the following:

- A hydroxyl peak,possible COOH and H_2O contribution, at 3000-3600 cm^{-1}.
- A ketone peak at ∼1750-1850 cm^{-1}.
- A peak corresponding to carboxyl groups (COOH and/or H_2O) at ∼1780-1850 cm^{-1}.
- A peak related to the in-plane stretching of the sp^2 C=C, at ∼1500-1600 cm^{-1}.
- Several epoxide features, at ∼1280-1330 and 800-900 cm^{-1}.
- All the previous OFGs have weaker features in the 900-1500cm^{-1}.

The variation of these OFGs is the one shown in Figure 4.13. Its important to notice that, even at the maximum temperature shown (650°), we cannot observe a complete reduction of GO.

A very interesting piece of data gathered in this study is that not only are OFGs desorbed during the thermal reduction of GO, but also some species were created, namely C=O.

Another important notion to take from this study is the fact that the quality of the thermal reduction of GO, in other words, the amount of oxygen that does not desorb from the sample, is dependent on the thickness of the sample. Thinner samples tend to desorb better, while thicker samples have less of its oxygen desorbed after the same thermal treatment.

Finally, as it has been seen in Section 4.10, Liu *et al* have been able to visualise the distribution of different OFGs in the GO sample, they have coupled the IR spectroscopy techniques with AFM, greatly enhancing its resolution [426]. With this new technique range we can see not only the OFGs present in the sample, but also the distribution of such OFGs along the sample and which regions have a higher concentrations of which OFGs.

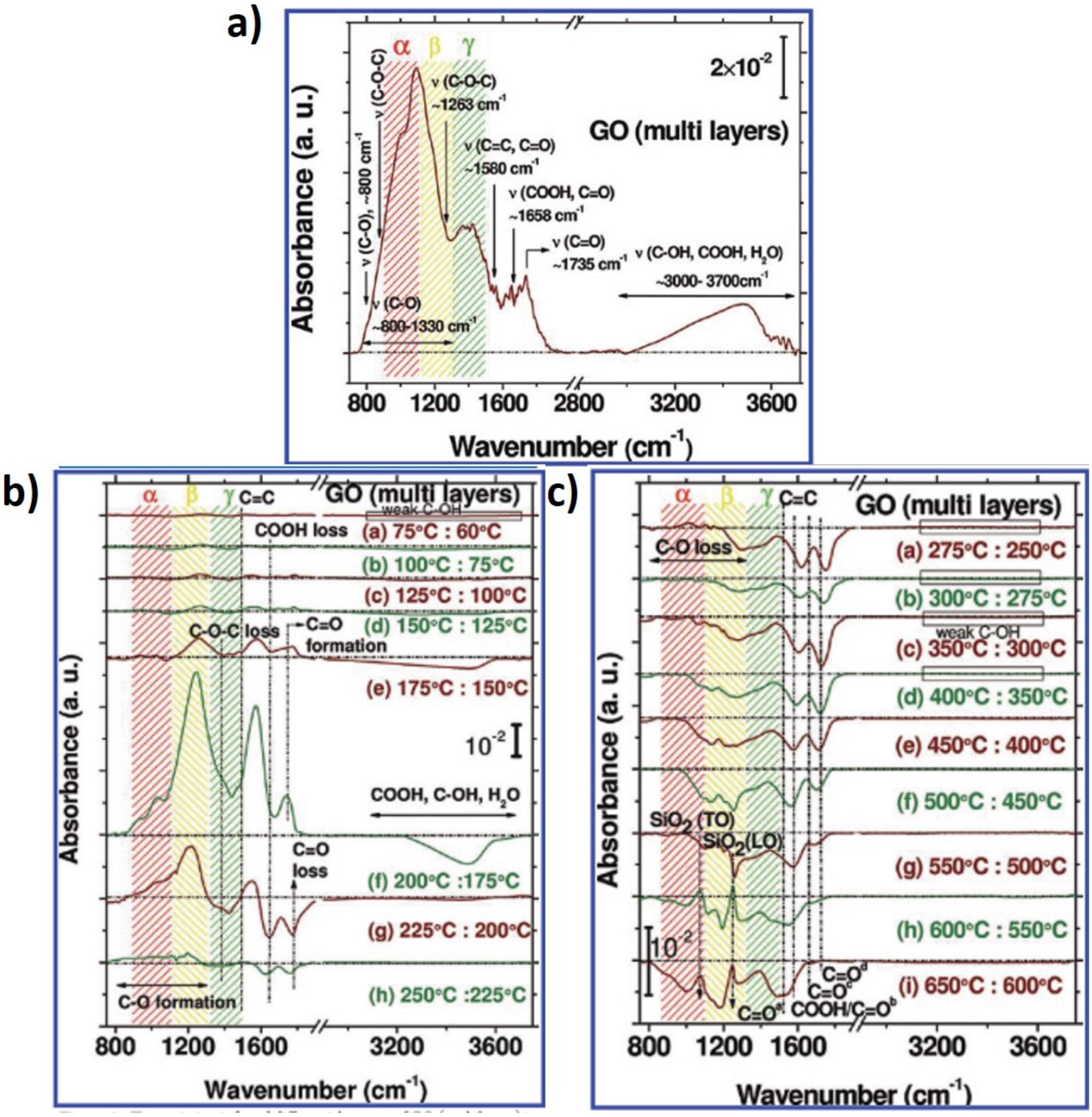

Figure 4.13: *Summary of the IR studies performed by Acik et al [432].* ***a)*** *Transmission infrared absorbance spectrum of GO (multilayers) at room temperature. Vibrational modes are shown for hydroxyls with contributions from COOH and H_2O(C-OH, 3000-3700 cm^{-1}), ketones and/or carboxyl groups within the overlapped frequency plane stretching, ~1550-1650 cm^{-1}), and epoxides (C-O-C, ~1350 range (C=O, COOH, ~1700-1900 cm^{-1}), sp^2-hybridized C=C (in-plane stretching, ~1550-1650 cm^{-1}), and epoxides (C-O-C, ~1350 and ~800-900 cm^{-1}).* ***b)*** *Transmission infrared differential spectra of GO(multilayers) in the low-temperature regime (60-250°C). Changes of functional groups are shown at the temperatures shown: The negative peaks below the baseline (black dotted lines) show the disappearance (loss) and the positive ones above it represent new formation of the functional groups with respect to each annealing temperature.****c)*** *Transmission infrared differential spectra of GO (multilayers) at moderate temperatures (250-650°C). Changes of functional groups are shown at the temperatures shown like in figure b. Vibrational modes of SiO_2 (LO and TO modes) appear at ~ 1250 and 1080 cm^{-1},respectively. For all figures, the regions labeled as α (red), β (yellow), and γ (green) refer to the chemical species for the overlapped infrared frequencies at 800-1500 cm^{-1}. Source; Acik et al [432].*

XPS

Studies of XPS on GO are of extreme importance to our works, because there is a clear correlation between the features in XPS corresponding to the different OFGs in GO, and the fine peak structures in EEL spectra, a feature we will delve into in Section 4.2.3. In this particular case, the XP spectra from the carbon 1*s* and oxygen 1*s* are correlated to the fine structure peaks present in the C-K and O-K edges of the EEL spectra.

The use of XPS for the analysis of graphite oxide was in use way before the discovery of graphene. Two interesting studies can be highlighed from these early studies, both by the same collaborators.

The study by Evans *et al* from 1972 [506] compared graphite oxide prepared using the three available methods at the moment, namely the Brodie[405], Staudenmaier[452] and Hummers[454] methods. Their results, with the resolution they had at the time, showed similar results for the three, gathering a single contribution for the oxygen present in the sample and two different components for the carbon present in the sample in aprproximately equal proportions, which they assigned to graphitic carbon and C-OH groups. This analysis was kept intact in their subsequent study on the formation of graphite oxide [507] where they measured XP spectra for GOs with different oxydation times. However, their spectra after 24 hr oxidation did seem to have several components even when looking at it with the naked eye, although the means at the time were not good enough to be able to discern said components.

With the revolution brought to research by the discovery of graphene in 2004 [87], it was only a matter of time before a way was found to exfoliate graphite oxide nanoplatelets, which nowadays could be considered few-layer GO. Several studies were focused on the exfoliation of GO and its reduction, and many of them used XPS to characterise the surface of their GO and rGO [459, 446, 508]. By this time, the resolution of XPS had improved considerably, and what's more, there was literature on other carbonaceous materials such as organic polymers [509] and organic photoconductors [510] which had been able to assign the different features in their samples to different OFGs based on the atomic charge of the atoms involved in said OFGs. This, combined with the GO models present at the time, mostly the Lerf-Klinowski one [417], paved the way for the assignation of the different features of GO in XPS to the different OFGs present in the sample. An example from the literature [459, 446], featuring both GO and rGO, can be seen in Figure 4.14

This assignation contemplates four different OFGs in the sample, coherently with what the Lerf-Klinowski model. The different peaks go up in order of relative charge in the OFG in question, since that is what causes the shifts between the different features. These features are, in ascending order of energy:

- Graphitic carbon, situated around 285.6 eV.
- C-O bonds, corresponding to C-O-C and C-OH groups, around 286.3 eV.
- C=O groups, situated at 287.8 eV.
- C-O-OH groups, situated around 289 eV.

In time, peaks associated with chemisorbed water were also added to the assigned features, such as the ones in the study by Ganguly *et al* [465], which studies the thermal reduction of GO by XPS. This study raised several important points, namely the presence of chemisorbed water in the GO and the possibility to measure it, a possible conversion of C=O groups into C-O groups at low temperatures (200°C, and the fact that, even with an annealing of the sample

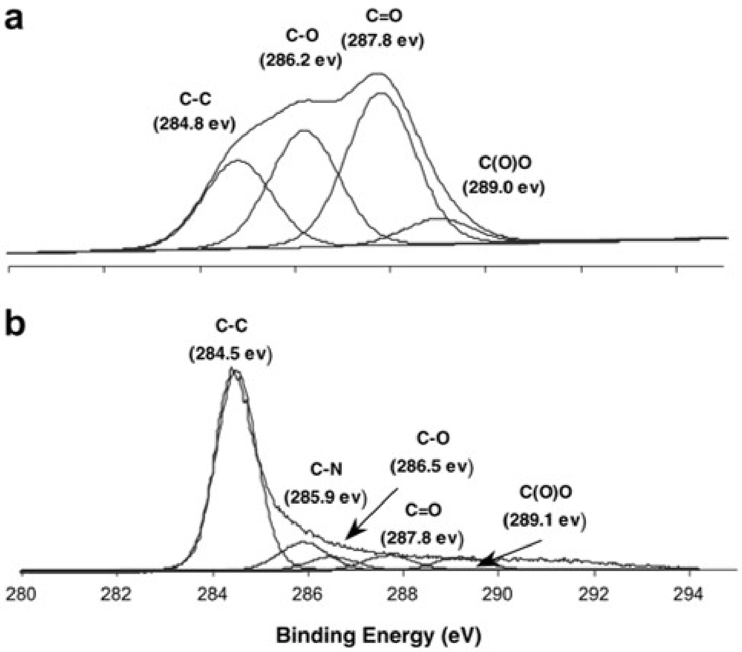

Figure 4.14: *The C1s XPS spectra of: (a) GO, (b) reduced GO. the different contributions in the peaks have been assigned to the different OFGs present in the sample. Source: [446], adapted from [459] with assignation of the peaks to the different OFGs.*

C 1s peaks	Position (eV)	O 1s peaks	Position (eV)
sp^2 C	284.2	O=C	531.0
sp^3 C	285.0	O-C	532.0
C-OH	286.0	O-C aromatic	533.0
C-O	286.8	O-H	535.0
C=O	287.7		
COOH	289.1		

Table 4.3: *XPS peak deconvolution and assignation to different OFGs in GO. Taken from D'Angelo et al [69]*

up to 1000°C, the sample could not be completely reduced, with C-OH groups being the hardest to desorb from the sample.

The study of D'Angelo *et al* in 2017 [69] provided an extended XPS/EELS analysis that will also be discussed in Section 4.1.8. When it comes to XPS, though, its main apportation to our study is the assignation of the different XPS peaks to different OFGs, which we will use as a basis for the assignation of OFGs in our own spectra. These peaks can be seen in table 4.3

An additional study that is of importance to our analysis has to do with the nitrogen dopants in the GO sample. Since the XPS studies are taken as a starting point for the assignation of the ELNES features, and we know there is a small amount of N dopants in our sample, it is important that we know the XPS peaks due to C-N bonds. The study by Wang *et al* [511] provides this information. The C 1s XPS spectra for N-doped graphene can be seen in Figure 4.15

Apart from the peak related to the π^* C atoms at 284.7 eV, this study offers two different energy values for N atoms bonded to C atoms in graphene: a feature related to N atoms bonded

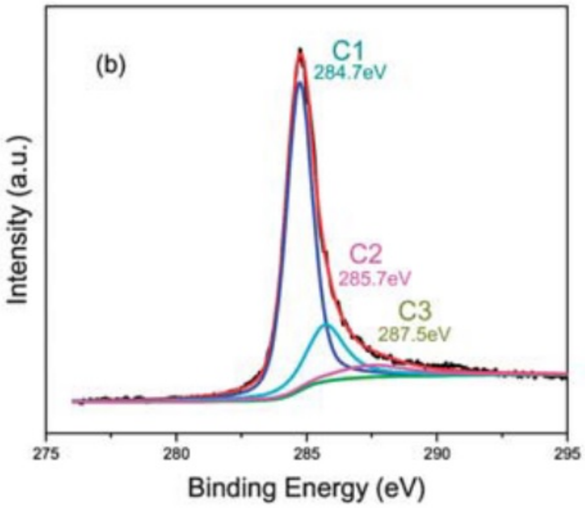

Figure 4.15: *C 1s XPS spectra and curve fitting of N-doped graphene nanosheets. Source: Wang et al [511]*

to sp^3-bonded C atoms at 285.7 eV, and a second feature for N atoms bonded to sp^2-bonded C atoms at 287.5 eV. This data will be of importance for the analysis of the C-K edge ELNES of our samples.

EELS

Electron energy loss spectroscopy (EELS) has been proven incredibly useful for this kind of studies. As it will be delved into in Section 4.2.3, EELS allow us to measure a very important number of characteristics in the material, although previous studies on GO have focused mostly on elemental analyses and the measurement and assignment of features related to different OFGs.

These kind of studies have a long history within the materials community, with the pioneers in using TEM and electron diffraction on this kind of samples being Aragon de la Cruz and Cowley [512], where electron diffraction was first used on graphite oxide showing that the material was a mixture of a crystalline material with a hexagonal layer structure with spacing a_0=1.43 . They discerned as well, based on structure, that there were hydroxyl and epoxide groups on the sample.

By the time the ”graphene revolution” took off, GO did as well to a lower extent. During this time, for example, we can find work that uses TEM as a qualitative tool to determine the level of graphitisation of a GO sample, along with other techniques such as XRD or Raman [513].

In 2009, a study by Mkhoyan *et al* [60] expanded the ability of TEM-EELS studies for this kind of sample by performing a detailed analysis of the atomic and electronic structure of GO using TEM and EELS, along with several other techniques. This study proved the non-linearity of the thickness of the GO samples with the number of layers, determined an average surface roughness of 0.6 nm, created STEM image simulations for the main OFGs, and for the first time, performed a complete EELS study on GO.

There are several aspects of this study that have influenced ours. For example, other studies have also used least-squares curve fitting for the GO spectra, decomposing said spectra into a linear sum of the spectra from graphite and amorphous carbon. This decomposition helped them calculate the amount of sp^2 bonds in the GO. This will be delved into in Section 4.3.6.4. They also tapped into the analysis of the low-loss EELS of GO in order to study its plasmonic behaviour.

This approach had already been used by Eberlein *et al* a year before [514] to characterise graphene.

The study by Erickson *et al* [427] pointed out two major topics. On the one hand, this study, along with Gomez-Navarro *et al* confirmed the structure of GO as a mixture of amorphous oxidated regions, and much less oxidated, or even pristine graphenic regions, which would pave the way for the Liu model eight years later [426]. The images from this study, with graphenic and amorphous regions highlighted, can be seen in Figure 4.16 They also studied the structure of GO and reduced and annealed GO (raGO), being able to even image and discern the presence of specific OFGs in the sample. The images of this study, along with their respective simulations, can be seen in Figure 4.16.

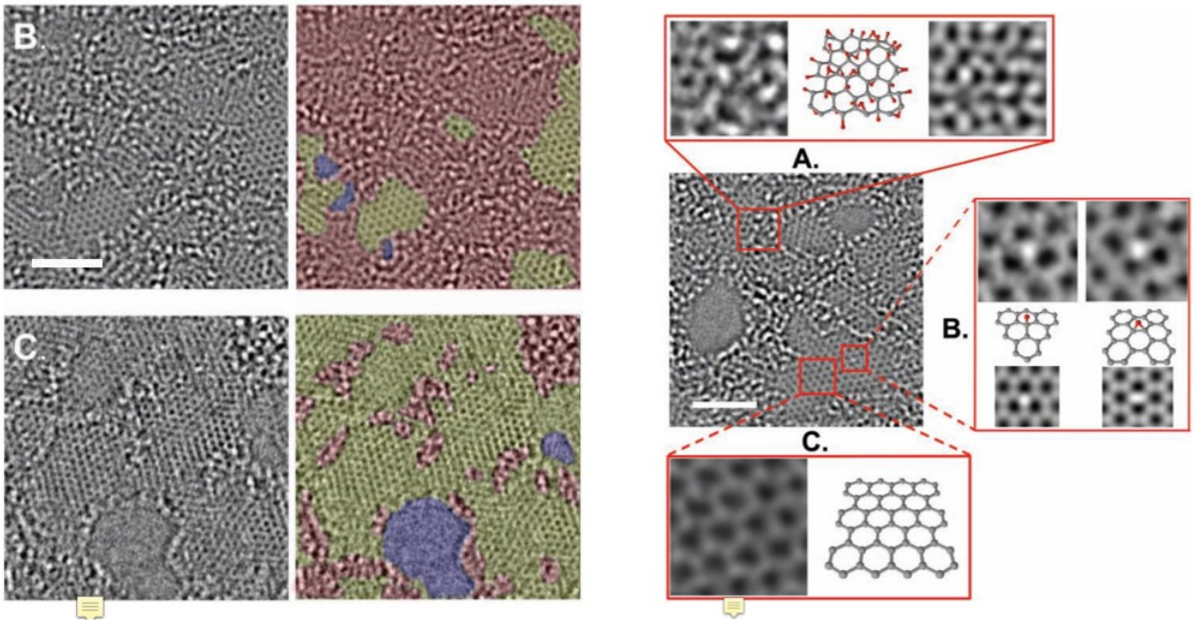

Figure 4.16: *Left: Aberration-corrected TEM images for different materials. Scale bar, denoting 2 nanometres, is valid for all images, as is the colour coding of different areas: On the right images, we offer a coloured version of the same images as on the left, where holes are indicated in blue, graphitic areas in lime green, and high contrast, disordered regions, indicating oxygen functionalities, in red. B) Single suspended sheet of GO. C) Suspended monolayer of raGO. Right: Averration-corrected TEM image of a single sheet of suspended GO. The scale bar is 2nm. Expansion (A) shows, from left to right, a 1* nm^2 *enlarged oxidized region of the material, then a proposed possible atomic structure of this region with carbon atoms in gray and oxygen atoms in red, and finally the average of a simulated TEM image on the proposed structure. Expansion (B) focuses on the white spot on the graphitic region. This spot moved along the graphitic region, but stayed stationary for 3 frames (6 seconds) at a hydroxyl position (left position of expansion (B)) and for 7 frames (14 seconds) at a 1,2-epoxy position (right portion of expansion (B)). The ball-and-stick figures below the microscopy images represent the proposed atomic structure for such functionalities. The simulated TEM image for the suggested structure agrees well with the TEM data. Expansion (C) shows a 1* nm^2 *graphitic portion from the exit plane wave reconstruction of a focal series of GO and the atomic structure of this region. Source: [427].*

The other vital point of this study was the beam resistance of GO and raGO. When exposing both materials to an electron beam for a few seconds, the latter started being etched, forming holes that grew bigger and bigger. This phenomena happened regardless of thickness, at least for low values of t. This will play a role in our study, since, based on this study at least part of the decomposition of GO in our sample will come from interactions between the beam and the sample.

In 2013, the study by Dimiev *et al* [450] used TEM imaging to prove another point that we had to take very much into account for the development of our study, which is that GO in an aqueous solution starts decomposing only weeks after its dispersion. This is due to GO generating acidic groups through interaction with water, resulting in C-C bond cleavage.

In 2014, the group of Stobinski *et al* [515] used TEM, XPS and reflective EELS (EELS using the electrons reflected by the material, therefore only those that interact with the material surface)to study both graphene oxide and reduced graphene oxide. However, they assumed fixed positions for the several features appearing at the low-loss region of the EELS spectra, which, as we will see in Section 4.2.3.1, is not the reality of the matter.

However, there was not yet an EELS analysis that could discern between different OFGs the same way we have seen XPS do in the previous section. This would change in time. In 2015, a novel study by D'Angelo *et al* [407] used DFT to calculate and simulate the EELS spectra of the C-K and O-K edges of GO functionalised, respectively, with O in bridge sites (epoxides), C-OH groups and C=O groups. These simulations, which we will approach in Section 4.1.8, gave a first impression on where the fine structure peaks of the different OFGs were located. In other words, this study proved that one could distinguish betweent the features associated with epoxide groups (a peak at ~287 eV in the C-K edge of the spectra, and a peak at ~533 eV in the O-K edge of the spectra),to hydroxyl groups(a peak at ~285.8 eV in the C-K edge), and to what they call "oxygens in vacancies", that is, esters (a peak at lower resonances than the rest at the O-K edge in the sample, located at ~530-531 eV).

The study of Tararan *et al* in 2016 [408] used monochromated EELS with a high energy resolution on GO, showing several interesting features. First, they analysed the impact of beam exposure on the oxygen content of their samples, proving that beam exposure does reduce GO to some extent, but in long periods. This is a point that we will also consider.

Furthermore, they continued the task started by D'Angelo by further assigning fine structure peaks to OFGs present in the sample. Their EEL spectra for GO and rGO can be seen in Figure 4.17.

The fine structure peaks found in the spectra are labeled A, B, C and D. Comparing with previous XANES results, absorption peaks A, B and C "*had been attributed in the literature to C-O π symmetry antibonds: lower energy peaks to single bonds and higher energy peaks to double bonds. More precisely, hydroxyl groups had been generally associated with peak A, epoxide groups to peak A or B, and carbonyl and carboxyl groups to peak B or C. In the σ^* region"*, while *"carbonyl groups have been related to peak D."*.

D'Angelo *et al* provided in 2017 a continuation of the study they had previously performed two years before, taking into account the studies that had been done up to that point. This study focused on the study of thermal reduction of GO in different environments, namely ultra-high vacuum, air, nitrogen and argon. However, the study was not really systematic in the sense that they did not study all different variables at the same temperatures. The study was not carried *in situ* either, which leaves the question of whether the transportation to and from the microscope can have an effect in the composition of the samples.

They did, however, provide a new assignation for XPS peaks and EELS peaks, which included a peak at 285.5 eV for hydroxyl groups, a peak at 287 eV for epoxides. A peak at 533 eV is associated with epoxides as well. Their XPS study, shown in Section 4.1.8, is the basis for our EELS studies as well, at least as far as OFGs go.

An additional study that is important to be mentioned here deals with the nitrogen impurities that can be found in most GO samples. These nitrogen functional groups (NFGs) act as n-dopants in the graphene matrix, and, in graphenic samples, they can be bonded to either sp^2-bonded carbon atoms, or sp^3-bonded carbon atoms.

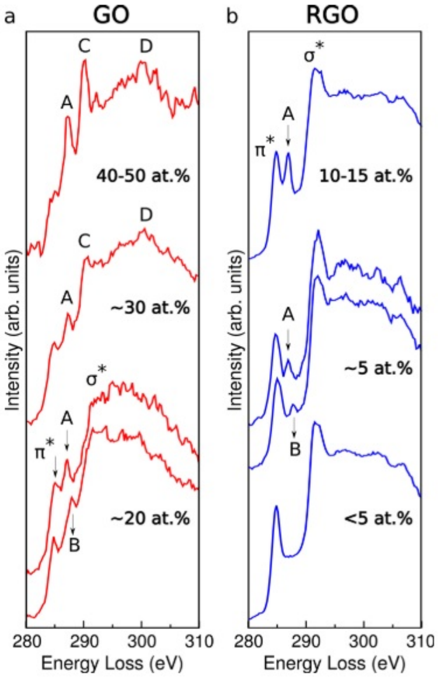

Figure 4.17: *Carbon K-edge EELS spectra of (a) GO and (b) RGO from regions with an oxygen content within the range shown. Source: Tararan et al [408].*

The EEL spectra of N-doped graphene has been studied at the nanoscale in a recent study [516]. In this study, the spectra between an N-doped region on graphene and a non-doped region have been compared, something that can be seen in Figure 4.18. In the original study, one particular feature at ∼290 eV is highlighted, although a closer look at the spectral comparison reveal two additional features at ∼286 and ∼287.5 eV. These three features have been signaled in Figure 4.18 and, even though their appearance is not very clear due to a high SNR in the spectra, these two additional features are confirmed by the additional XPS studies which we have seen in Section 4.1.8.

Raman

Raman has been a method intimately linked to the characterisation of sp^2 carbons for decades, studying 0D carbon nanomaterials (fullerenes) [517], 1D (CNTs) [518, 519], 3D (graphite) [520] and, since its discovery in 2004, graphene as well [521].

It does not come to a surprise that graphite-derived and graphene-derived materials such as graphene oxide have been the subject of Raman studies as well. These studies offer information about the vibrational and crystallographic information of the sample, as well as electron-phonon interactions. If the Raman process comes together with an optical absorption, or an emission from an excited state, this enhances the the Raman intensity to a level where it is even possible to observe the Raman signal of a single graphene monolayer. In this case, the raman reesponse is strong due to resonan enhancement caused by C-C π states, with the response of disordered carbon materials being much weaker than graphenic materials [406]. Moreover, since most sp^2 carbons do not exhibit an energy gap at the Fermi level, we always get a resonance condition for Raman spectra regardless of the laser excitation energy. [522].

The transitions taking place in the different bands of the Raman spectra have been extensively studied [523]. There are three main Raman features when it comes to 2D sp^2 carbons

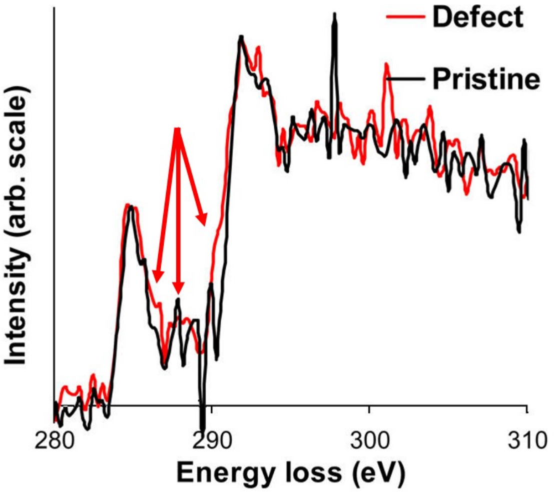

Figure 4.18: *Carbon K-edges obtained from the region surrounding a dopant atom (red) and from a region of pristine graphene (black). (The peaks in the spectra atâˆ¼297 and 302 eV are artifacts and are likely to be due to bad pixels on the CCD camera.). The three possible EEL features for the C-N ELNES features are marked with a red arrow. Edited from Nicholls et al [516].*

(other structures like nanotubes have additional features) [522, 401]:

- The G band is located around 1580 cm^{-1}. This is the dominant vibrational mode in graphenic structures.

- The G' band is located at much higher energies , with a peak value that depends on the energy of the incident laser (e.g., $\sim 2700cm^{-1}$ for a laser energy of 2.414 eV [519]). This feature, along with the G band, acts as an indicator of the stacking structure when we have a sample over one layer thick.

- We have two additional bands, called the D and D' bands, that are related to atomic defects and general disorder within the graphenic layers. These bands are closer to the G band and it are also dependent on the incident laser energy [524], with energies of 1582 and 1350 cm $^{-1}$ for a laser energy of 2.41 eV [520].

An example of these features can be seen in Figure 4.19

The D and G' bands of the sp^2 carbon Raman spectra are related to phonon modes close to the K point in the Brillouin zone [522]. These features, as well as the ratios between them, have been used to infer several properties of graphene and its derivatives.

On the one hand,the intensity ratio between the G and the G' bands, as well as the shape of the G' band, have been used to extimate the number of layers of graphene samples. This is due to monolayer graphene having less contributions to the G' band than its multilayer counterparts, with bilayer G' bands being broader than monolayer G' bands, and trilayer bands being broader than bilayer bands. An example of said bands can be seen in Figure 4.20

As we can see by the change in shape (and the corresponding change in peak intensity) of the G' band implies that both the deconvolution of this band and the ratio between the G' and the G band are valid methods for the estimation of the number of layers of atomically thin graphenic samples.

Another interesting parametre in these studies is the intensity ratio between the D and G bands. This is usually taken as a measurement of the disorder level in the sample [522, 524], in

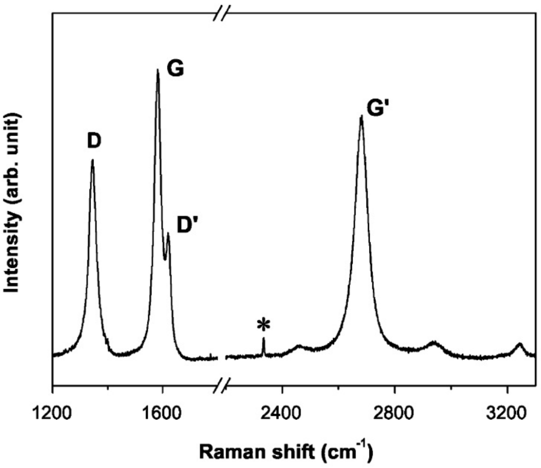

Figure 4.19: *Example Raman spectrum of a nanographite sample, showing the main Raman features, namely the D, G, D' and G' bands. The Raman spectrum was taken with a laser excitation energy of 2.41 eV. Source: Pimenta et al [520].*

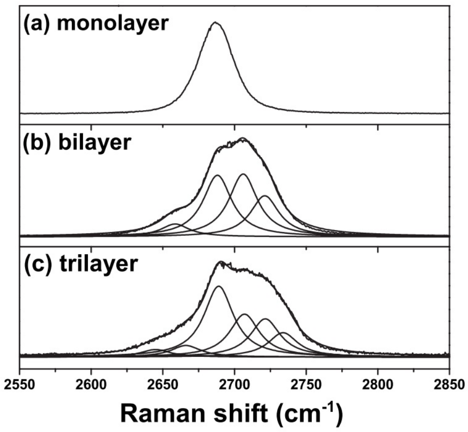

Figure 4.20: *Raman spectra of the G' band of (a) monolayer, (b) bilayer, and (c) trilayer graphenes. The analyses were performed using 2.41 eV laser energy. The G' band for monolayer, bilayer, and trilayer graphenes were fitted with one, four, and six Lorentzians, respectively, with a FWHM of 24* cm^{-1}. *Source: Malard et al [523].*

other words, the amount of edges and defects in the samples. In graphene samples, this gives an idea of the quality and homogeneity of the graphene, and its prospective electronic properties.

An additional property that can be inferred from this intensity ratio (one that is linked to the disorder in the sample) is the in-plane crystallite size L_C of graphitic/graphenic samples, that is, the average size of the finite regions containing no structural defects. This work was started in the 1970s with side-to-side comparisons of XRD diffraction patterns and Raman spectra of different graphitic samples[525, 526], and has been implemented to graphene samples as well, where the number of defects has been carefully controlled by ion radiation[521, 524].

The aforementioned studies have found that, for values of L_C over a certain threshold (a few nm), it was possible to see that the intensity D/G ratio (I_D/I_G) decreases as the crystallite size L_C increases. The exact expression relating L_C and the D/G ratio, taken from the experimental model, can be seen in the literature[521]. This has been an important remark for the study of GO and rGO.

When it comes to GO and rGO, several studies have covered this topic in relation to Raman spectroscopy. These studies focus mainly on the thickness of the samples and the structural quality of GO and rGO [446, 527, 406, 528], as well as potentially the oxydation degree in the samples [528].

The first studies conducted on GO and rGO[446, 527] considered an interpretation of the GO and rGO spectra according to what had been made for graphite and graphene until then, that is, the feature assignation shown in Figure 4.19.

Using these parametres, the first comparative studies on graphene, GO and chemically reduced GO were performed. They found that, as seen in Figure 4.21, the D/G ratio was found to be higher for rGO than for GO. The explanation given at the time was that, even though rGO was supposed to have a higher amount of ordered material (since it had a lower concentration of OFGs), the crystallites in the sample could be smaller but more numerous [446].

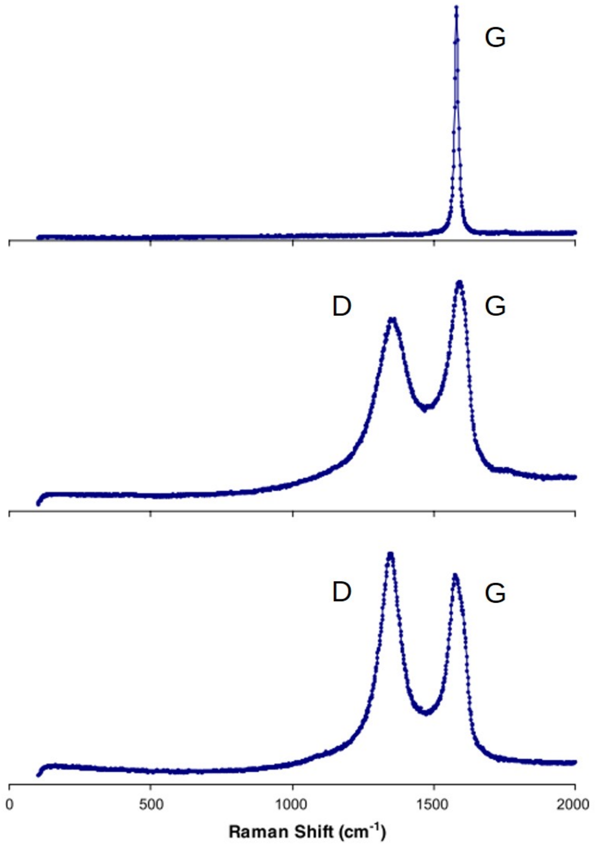

Figure 4.21: *Raman spectra of SP-1 graphite (top), GO (middle), and the reduced GO (bottom), showing the identified D and G bands when visible. Source: Stankovich et al [446].*

However, more recent analyses of the same data has shed some light into what the actual behaviour of these samples might be. In the study by King *et al* [528], a multipeak fit analysis has shown that the feature considered as the G band in the study by Stankovitch *et al* [446] might have been a combination of two different features, one related to the G band and another one related to the D' band, which would be a lot more intense than it had been expected for the GO samples going even higher than the G band itself. This can be seen in Figure 4.22.

These studies show that the D/G ratio for the original GO Raman spectra is, in fact, a lot lower that it had first been estimated, and that it did go up substantially after reducing the

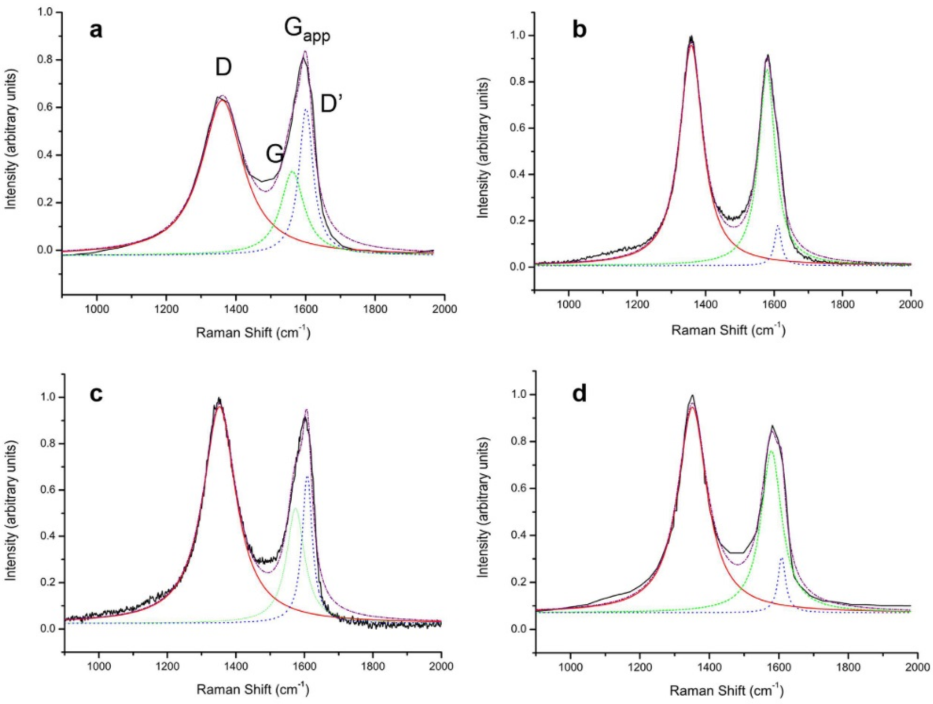

Figure 4.22: *Raman spectra of (a,b) GO before and after thermal reduction at 1,000°C respectively and (c,d) GO before and after reduction with hydrazine, respectively. A multipeak fitting has been performed and the features related in this study to the D band (red line), G band (green dotted line) and D' band (blue dotted line) are shown. Source: King et al [528], modified from Stankovich et al [446].*

GO either by thermal reduction or by chemical reduction. In other words, this meant that the rGO crystallite size would be larger than that of GO. This seems more coherent with a lower presence of OFGs in the sample, and it is also in better agreement with the results presented in our work.

DFT

Another technique that has provided key information in devising the properties of GO has been theoretical modelling, and more specifically, density functional theory (DFT).

DFT has been key in studying the atomic structure of GO, especially before studies like the one performed by Mkhoyan *et al* [60] where experimental data on GO at the atomic scale started to be available.

Different works have studied the structure of GO, from the atomic deviations due to certain OFGs and the structure of GO with one or more types of OFGs bonded to it [529, 530, 531], to the difference in structure with the oxidation levels [532, 408].

DFT has also tried to find answers to the reactions of oxidation that give rise to GO [530] and the reactions taking place in GO when reducing it [460, 533]. A myriad of studies focus as well on the position of the different OFGs with respect to the original graphene/graphite matrix [439, 532, 531, 534, 535]

Many of these studies have also focused on the binding energy of different OFGs with respect to the graphene matrix, both individually and in combination with other OFGs [529, 534, 536, 530, 533, 407, 69]. Thich gives an idea of which configurations are more energetically viable and which groups are supposed to have a weaker binding energy. This is interesting from the point of view of thermal reduction, OFGs with a weaker binding energy are prone to desorb at lower temperatures than those with stronger binding energies.

However, the use of DFT that is probably the most important with regards to these works is as a theoretical support for spectroscopic data, as it has been mentioned previously in this section.

For example, as previously stated, the studies by Acik *et al* [432] did not only focus on the structure and position of OFGs in GO, but also on the vibration energies of the different OFGs present in GO. Using these vibrational energies, it was possible to better discern the different features in IR spectroscopy with relation to each OFG as well as water, which yielded the results previously seen in Figure 4.13.

In a similar way, there have been several DFT studies that aim to simulate the EEL spectra of different kinds of GO. Out of these studies, we highlight the works by D'Angelo *et al* [407, 69]. In these works, the EEL spectra of GO samples presenting different kinds of OFGs were simulated. This has allowed us to have an estimation of the energetic order of some the different fine structure peaks both in the C-K edge and the O-K edge of our own EEL spectra, namely those related to alcohols, epoxides and ketones. A summary figure of their latest study [69] can be seen in Figure 4.23 As we can see, to an extent, these studies and the ones shown for XPS are coherent with one another, in the sense that we can order the presented OFGs in the study in ascending energy of their features. This will be key for the experimental part of these works.

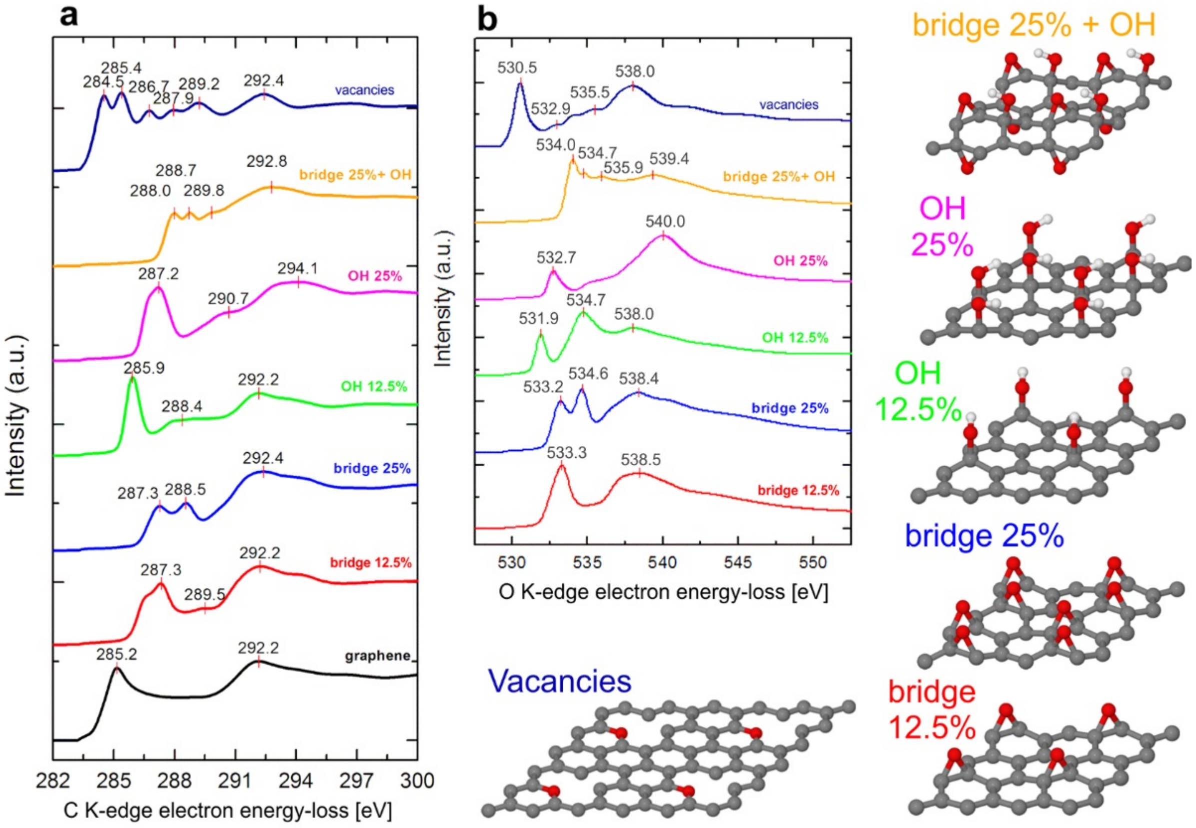

Figure 4.23: *Simulated EEL spectra of the C-K and O-K edges (a and b, respectively) of different graphene supercells. Bridge configuration represents the epoxides. The configuration labeled â€œvacanciesâ€ represent the in-plane ketones, with a an oxygen atom at a divacancy of a 3 Ã— 3 graphene supercell. Source: D'Angelo et al [69].*

4.2 Methods

In this next part of the chapter, we will delve into the methods used for these works. These methods mainly divide into two catergories: first, the device allowing for these thermal studies (the TEM heating holder) and second, the analytical methods that allow for the estimation of the atomic structure, mass density, thickness and the fraction of sp^2-bonded carbon atoms (graphitic carbon) in the sample.

4.2.1 Thermal *in situ* studies inside of a TEM: the heating holder

The experiment of this study has been carried out in a DENSSolutions Lightning biasing and heating TEM holder. This has allowed us to perform our *in situ* heating experiment with an accuracy of approximately 0.03°C. This holder allows heating between room temperature and 1300°C and can sustain pre-programmed custom heating routines, which we have used. This will be further discussed in Section 4.3.2. A sceme of this biasing and heating holder, as well as the chips used for this study, can be seen in Figure 4.24.

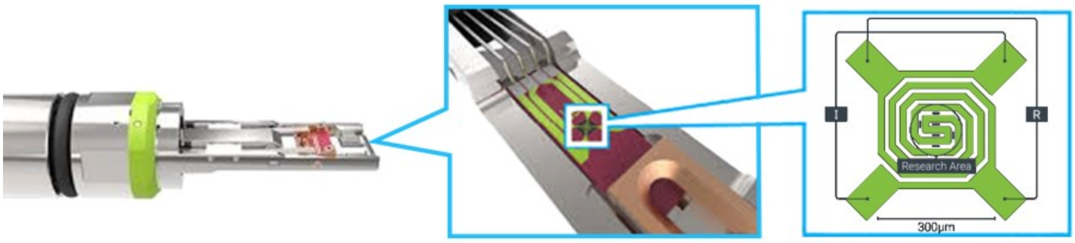

Figure 4.24: *Scheme of a DENSSolutions Lightning heating holder. Source: DENSSolutions.com (adapted)*

In heating mode, the current applied to the contacts seen in Figure 4.24 transforms into heat, that distributes along the spiral system shown in the scheme.

4.2.1.1 The chips

DENS store-bought heating chips were used for the experiments. These chips are formed by homogeneous membranes on a heating spiral circuit, as it can be seen in Figure 4.25. Although the chip membrane was supposed to be made of silicon nitride, Si_xN_y , after an EELS analysis during a first attempt for this studies, it was found out that there was also a noticeable amount of oxygen (between a 15% and a 20% according to our quantifications) that seemed to come from some form of silica. On top of that, the thickness of the membrane itself made it harder to interpret the EELS measurements from the experiment.

This is why holes were carved into the chips using Focused Ion Beam in order to measure the GO alone. These holes had diametres from 300 nm to 3 μm. Fifteen holes have been fabricated on the chips in order to have several areas where the sample can be studied after drop-casting it. A scheme of the distribution of these holes can be seen in Figure 4.25. The placement of these holes is not at random, they are located around the centre of the chip. This is due to the fact that the company that fabricates the chips advises that the most accurate values for the temperature in the chip correspond to the centre of the chips, and it diverges as one approaches the edge of the chips.

Figure 4.25: *Scheme of the holes carved into the heating holder chips using FIB.*

4.2.2 The importance of TEM imaging

Besides showing general morphology of a material [537] and helping us find the right areas to measure (holes with GO flakes on top), TEM, HRTEM and electron diffraction can be of great help to understand the nature of GO at different temperatures. As discussed in Section 1.2.3, both the Fourier transformed TEM micrographs and the electron diffraction micrographs provide important information on the internal structure of the materials at the local scale, showing spots in the k-space whenever cristalinity is observed. This, along with the sp^2 ratio in the sample, are the only two direct measurements of the graphitisation of GO during thermal reduction.

4.2.3 The importance of EELS

An extended report on the different features found in EELS spectra that are relevant for our studies has been given in the introduction of this manuscript (see Section 1.4). This section will focus on how these features can be used for the measurement of properties of interest in the sample.

4.2.3.1 The Low Loss EELS region of Graphene Oxide

The low loss EELS spectra Besides the zero loss peak mentioned in Section 1.4.3, there are several features we can find in the low loss spectra of GO, as well as other thin carbon layers, namely its π^* volume plasmon and its $\pi^*+\sigma^*$ volume plasmon. These features have been previously studies both in graphene [514] and GO [538]. An example of these spectra after ZLP removal can be seen in Figure 4.26.

The $\pi^*+\sigma^*$ volume plasmon will have a key role in determining the mass density of the sample.

Plasmons and mass density estimation As we have seen in the Section 1.4.3, the low loss EELS spectrum is proportional to the energy-loss function, $\mathrm{Im}(-1/\epsilon(E))$, where ϵ is the complex dielectric function of the GO.

According to the literature [13], the expression for the energy loss function in the case of a plasmon feature, in the free-electron limit, is:

$$\mathrm{Im}\left(-\frac{1}{\varepsilon(E)}\right) = \frac{E_p^2 \times E \times \Delta E_p}{\left(E^8 - E_p^2\right)^2 + (E \times \Delta E_p)^2} \tag{4.1}$$

Where ΔE_p is the full width at half maximum of the plasmon peak, and E_p is the plasmon energy, defined as:

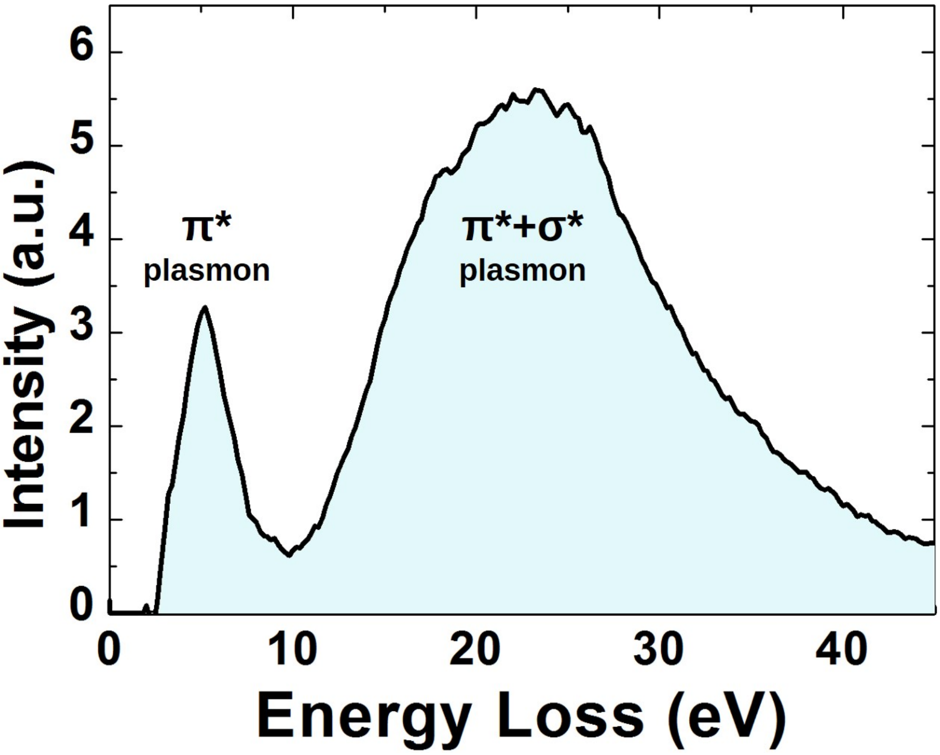

Figure 4.26: *Low loss spectrum of a GO film after zero loss peek removal. The features corresponding to the* π^* *volume plasmon and the* π^**+*σ^* *volume plasmon are highlighted.*

$$E_p = \hbar \left(\frac{n_e e^2}{\varepsilon_0 m^*} \right)^{1/2} \tag{4.2}$$

where n_e is the valence electron density and m^* is the effective electron mass, which will be delved into in the next paragraphs[65].

By assuming a contribution of four valence electrons for carbon, five for nitrogen, six for oxygen, and one for hydrogen, we can approximate the valence electron density of the material, without accounting for impurities other than nitrogen, which is usually present in this type of samples to some extent. This approximation yields the following expression:

$$n_e = 12 \frac{\rho N_A}{M_C} \left(\frac{4X_C + 5X_N + 6X_O + X_H}{12X_C + 14X_N + 16X_O + X_H} \right) \tag{4.3}$$

Where ρ is the mass density of the sample, N_A is Avogadro's number, M_C is the molecular weight of carbon, and X_i are the respective ratios of each element. We have introduced the atomic mass parameter μ and performed the approximation $M_C = 12 \times N_A \times \mu$. We also consider the fractions of nitrogen and hydrogen to be negligible with respect to the fractions of carbon and oxygen; that is, $X_C + X_O \approx 1$. With these considerations, equation 4.3 turns into the following expression:

$$n_e = \frac{\rho}{\mu} \times \frac{(4 + 2X_O)}{(12 + 4X_O)} \tag{4.4}$$

By substituting n_e in equation 4.2 we obtain:

$$E_p = \hbar \times \left(\frac{\left(\frac{\beta}{\mu} \times \frac{(4+2X_O)}{(12+4X_O)} \right) \times e^2}{\varepsilon_0 \times m^*} \right)^{1/2} \tag{4.5}$$

This equation gives an expression for ρ as a function of parametres that we can either measure or approximate:

$$\rho = \frac{E_p^2 \times m^* \times \epsilon_0 \times \mu \times (12+4X_O)}{\hbar \times e^2 \times (4+2X_O)} \tag{4.6}$$

As for the effective electron mass, there has been a previous study by Ferrari *et al* [65] where the mass density for amorphous carbon materials showing a mixture of sp^2 and sp^3 clusters was calculated using X-ray grazing-incidence x-ray reflectivity, which is also related to the mass density of the sample, and the plasmon energy. This study is shown in Figure 4.27. It yields a value of $m^* = 0.87 \times m_e$. The implementation of the estimation of the plasmon energy, as well as the derivation of the mass density from it, will be explained in Section 4.3.6.3.

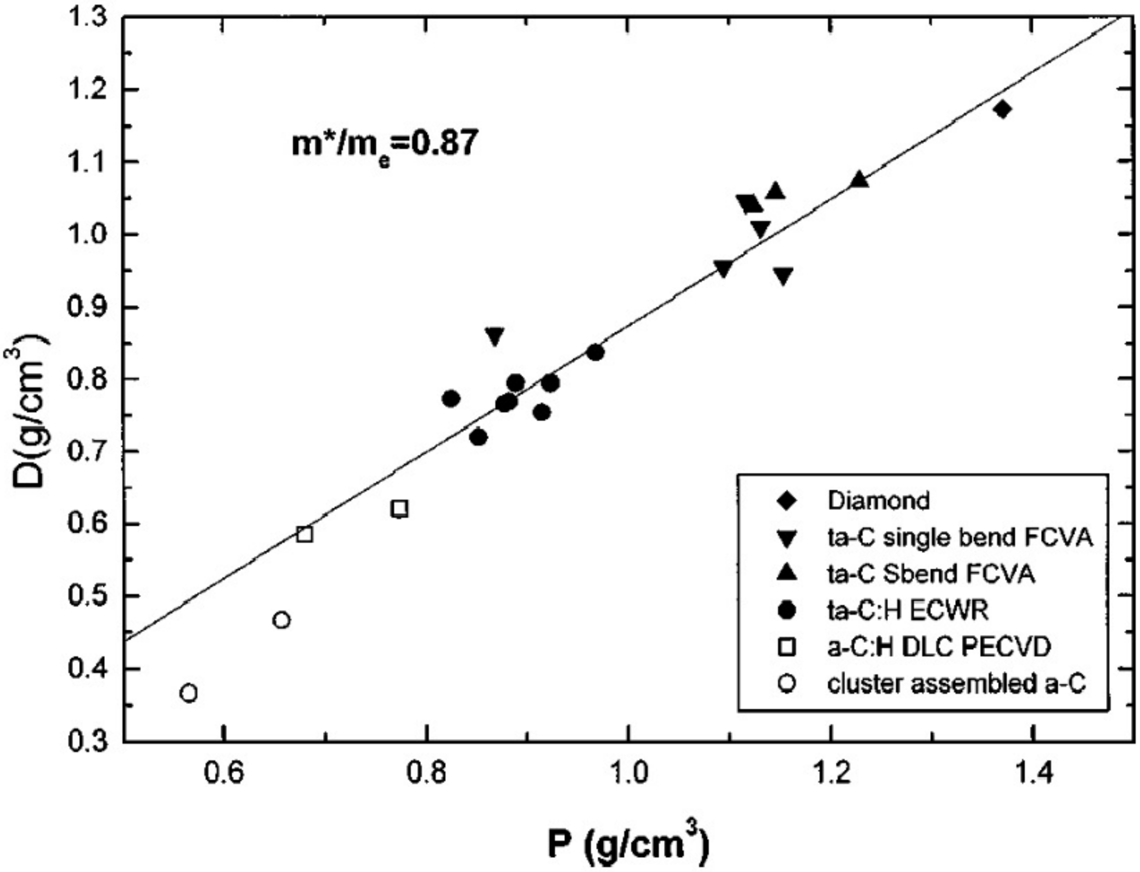

Figure 4.27: *Plot of* $D = \rho_{XRR} \times (3X_C+1)/(11X_C+1)$ *against* $P = M_c \times \varepsilon_0 \times E_p^2/(12\hbar^2 \times N_A)$ *(equivalent to a* ρ_{XRR} *vs* ρ_{EELS} *plot). The linear fit gives an average interband effective electron mass of* $m^* = 0.87 m_e$ *for amorphous carbon materials.* ***Source: Ferrari et al [65]***

Thickness estimation: the log-ratio technique It can be derived from basic optics that the transmittance of particles with no interaction in a sample of thickness t under a particle beam follows the expression in equation 4.7

$$T = \frac{I_t}{I_0} = e^{\frac{t}{\lambda}} \tag{4.7}$$

Where T is the transmittance of the sample for said beam, defined as the ratio between the transmitted intensity, I_t (that is, the intensity of the particles that have not interacted with the sample)and the incoming intensity to the sample, I_0. The parametre λ represents the inelastic mean free path (IMFP) of the beam particles in that specific sample, which, as seen in Section 1.2.1.2, is the mean distance traveled by a beam particle before interacting with the sample.

Although originally applied to optics, this expression can be applied as well to the case of an electron beam striking a sample [64]. This has been the basis of a variety of studies that have estimated the thickness of a sample by comparing the value of the trasmitted intensity I_t, which in the case of EELS is equivalent to the intensity of the ZLP, and the value of the incident intensity [13][64]. Since we assume the vast majority of the electrons going through the sample are not backscattered, we approximate the value of the incident intensity I_0 as the intensity of the whole EELS spectrum. Equation 4.7 can be written as follows:

$$\frac{t}{\lambda} = \ln\left(\frac{I_t}{I_0}\right) \tag{4.8}$$

Hence the designation of ”log ratio technique” for this measurement.

If the IMFP of the sample is unknown, the value of t/λ is known as relative thickness. However the value of the IMFP can be estimated from other parametres in the study. In 1988, Malis *et al* fitted the experimental values of λ agains several parametres such as the atomic number of the samples, the incident energy of the electrons, and the collecting angle of the microscope. This approximation is cohesive for thicknesses up to five times the IMFP, which allow most of the spectral features of the low loss to be in the first 100 eV of the spectrum[64]. This is the general case for our samples.

As for the behaviour of the mean free path with one kind of atoms, at low atomic numbers, this study provides a dependence of λ with Z as follows:

$$\lambda \propto z^{-0.28} \tag{4.9}$$

which is coherent with previous atomic models of scattering [539] that give an estimation of $\lambda \propto z^{-0.33}$.

We will be taking a proportionality exponent for z of 0.3 which is in good agreement with both values.

On the other hand, a mean free path can be expressed as the cross section (σ) of a specific type of atom for intelastic scattering;

$$\lambda = \frac{1}{n_a \times \sigma} \tag{4.10}$$

Where n_a is the amount of atoms per unit volume of the sample. According to this, $\sigma = 1/n_a\lambda$, which implies that $\sigma \propto Z^{0.3}$ Taking this into account, the effective atomic number, Z_{eff}, of a sample with several kinds of atoms would be given by:

$$\mathrm{Z_{eff}} \approx \frac{\mathrm{\Sigma_i f_i \sigma_i Z_i}}{\mathrm{\Sigma_i f_i \sigma_i}} \approx \frac{\mathrm{\Sigma_i f_i Z_i^{1+r}}}{\mathrm{\Sigma_i f_i Z_i^r}} \tag{4.11}$$

where σ_i is the cross section of element i, f_i is its fraction and Z_i its atomic number.

Using a Kramers-Kronig sum rule, the mean free path for this kind of interaction can be written as [13]:

$$\lambda = \frac{2\mathrm{a_0 T}}{(1-\mathrm{n}^{-2})} \frac{\int \frac{\mathrm{S(E)dE}}{\mathrm{E}\ln(\beta/\theta_\mathrm{E})}}{\int \mathrm{S(E)dE}} \tag{4.12}$$

Where a_0 is the Bohr radius, n is the optical refractive index of the speciment, E is the energy loss, and S(E) is the single scattering distribution (in other words, the experimental spectrum after removing plural scattering). T is proportional to the incident energy with a relativistic constant, defined by:

$$T = F \times E_0 = \frac{1+(E_0/1022)}{(1+(E_0/511))^2} \times E_0 \tag{4.13}$$

Taking into account that we are working at low energies, we can use the approximation that $\theta_E \approx E/2E_0$ [13]. For $n >> 1$, equation 4.12 can be expressed as:

$$\lambda \approx \frac{106 \times F \times E0}{E_m \times \ln\left(2\beta \times \frac{E_0}{E_m}\right)} \tag{4.14}$$

With E_m defined as:

$$E_m = \frac{\int S(E)dE}{\int E^{-1}S(E)dE} \tag{4.15}$$

After fitting the experimental values of λ of 11 different samples, an approximation of E_m was found:

$$E_m = 7.6 \times Z_{eff}^{0.36} \tag{4.16}$$

This will be the approximation we will use to estimate the value of the thickness of each sample. The implementation of this analysis will be explained in Section 4.3.6.2.

4.2.3.2 Core Loss EELS

Within the core-loss part of the EEL spectra, our works we will be focusing mainly on the EELS spectra of the C-K and O-K edges , which represent the 2p partial density of states above the Fermi level [60].

Fine structure near of the edge (ELNES) analysis As we have seen extensively in Section 1.4.4, besides the features in the spectra coming from the ionisation edges, there is a series of features in the core-loss spectra that belong to the interband transitions of atoms linked in a specific way. The analysis of these features has even been used to identify and map the different oxidation states within compounds [77]. These are the so-called fine structure peaks. They will play a critical role on this study, since we have been able to correlate specific fine structure peaks to different oxygen functional groups being linked to the sample.

When it comes to the C-K edge, there is a feature around 285.5 that sums three different overlayed individual features, according to the bibliography [540, 538, 69] First, the fine peak structure coming from the π^* transitions of sp^2 carbon; second, the fine peak structures coming from the sp^3 carbon, and finally an additional one corresponding to the -OH groups in the sample.

Next, judging by these same studies, we can find a feature corresponding to non-aromatic C-O-C at ~287 eV, a C=O feature at ~288 eV and a C-O-O-H feature at ~ 289 eV.

As for the O-K edge, There are three distinct features that have been found at ~531 eV, ~534 eV and ~540 eV for C=O, non-aromatic C-O-C and C-OH groups, respectively.

Quantification We will be using the integration quantification method delved into in Section 1.4.4. The edges used for this quantification are the C-K edge, the O-K edge, the N-K edge (a common dopant on GO) and the Ca-L_2-L_3 edges (a common trace on aqueous solutions).

sp^2 **content** The analysis of the C-K edge can be used to estimate the fraction of sp^2 bonding carbon in a thin film sample, and has been used so in many studies before [541, 542, 65, 543, 544, 538]. This estimation comes from the counts appertaining to the π^* peak in the C-K edge with respect to the whole edge is proportional to the number of π-bonded electrons in the material, that is, the fraction of sp^2 bonding [541]. In other words, for two different carbon thin films A and B, and being I the intensity summed over a peak:

$$\frac{\left[\frac{A_{\pi^*}}{A_{\pi^*+\sigma^*}}\right]_A}{\%sp^2_A} = \frac{\left[\frac{A_{\pi^*}}{A_{\pi^*+\sigma^*}}\right]_B}{\%sp^2_B} \tag{4.17}$$

provided that $A_{\pi^*+\sigma^*}$ is gathered over the same spectral window for both spectra. Introducing the variable $y' = A_{\pi^*}A_{\pi^*+\sigma^*}$, we obtain:

$$\frac{y'_A}{\%sp^2_A} = \frac{y'_B}{\%sp^2_B} \tag{4.18}$$

This means that, by having a reference sample of which we know its y' and sp^2 ratio value, we can estimate, in principle, the value of the sp^2 ratio for any sample provided that we can measure y'.

The measurement of y', specifically, has been a matter of discussion in the EELS community. Initially, a very basic method of analysis has been comparing spectral windows corresponding to the energy of the π^* and σ^* features, respectively. Gaussian fitting of the π^* and σ^* peaks using a single Gaussian for each peak has been used as well [542]. A third method used in the literature consists on fitting the carbon K-edge spectrum with three Gaussian peaks, one for the π^* peak, one for the σ^* peak, and an intermediate one that accounted for indirect transitions from the $1s$ to the π^* state [542].

A different model takes into account the density of states (DOS) of graphite, calculated using density functional theory (DFT) [544]. their calculations show a density of states for π^* that decreases in an almost exponential way but has a non-negligible intensity up until at least 10 eV after the onset of the DOS peak, well over the overlapping of the π^* and σ^* peaks. The calculation of this DOS can be seen in Figure 4.28

We assume a somewhat direct proportionality between the DOS and the EELS spectra, that is, that variations of the intensity near the ionisation threshold are proportional to the density of unoccupied states of the material [13]. This means the π^* feature of the carbon K-edge in EELS will have a similar behaviour to its density of states, which means it will have some sort of exponential decrease and a non-negligible intensity well over the overlapping edge with the σ^* peak. This means the methods previously mentioned in this section will not be accurate enough for the measuring of the sp^2 fraction in carbon materials.

However, another method has been developed in the study of Bernier *et al* [544]. To account for the initial peak of the GO and its decreasing tail, a series of successive decreasing Gaussians has been proposed as a model to fit the π^* feature. These Gaussians are spaced a parametre p from one another and have a decreasing coefficient d from one Gaussian to the one after it. This fit can be expressed as:

$$I = A \times \sum_{i=1}^{60} d^{i-1} \times e^{\frac{-\left(x-x_0-p^{i-1}\right)^2}{2\sigma^2}} \tag{4.19}$$

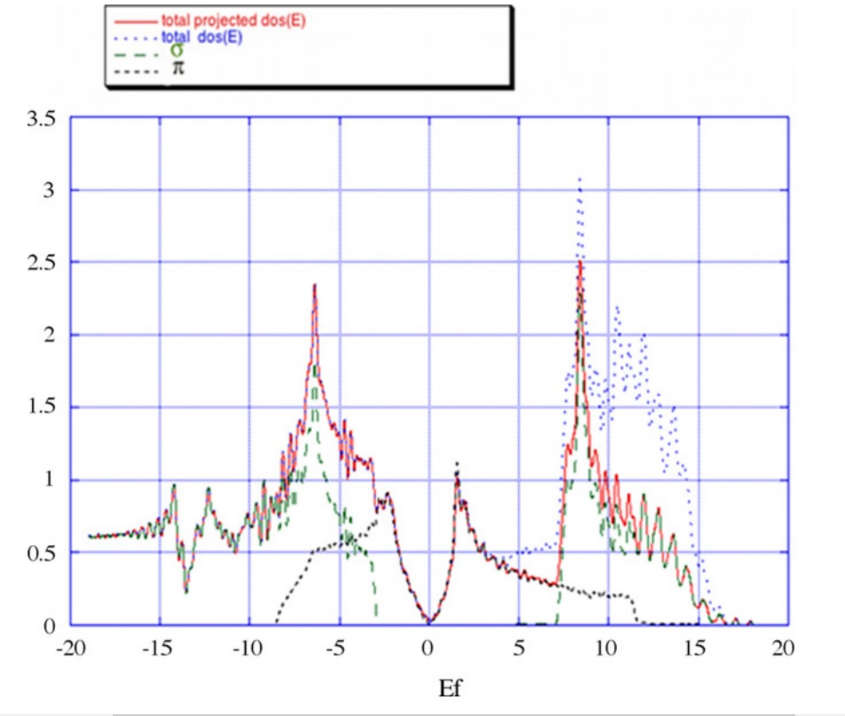

Figure 4.28: *First-principles DFT density of states (DOS) for graphite. The total projected DOS collects the s and p orbital contributions, the total DOS is calculated from the plane-waves electronic density, pi corresponds to the projection on the carbon p_z orbitals whereas σ collects all the other contributions ($s+p_x+p_y$). The π DOS can be seen to have a somewhat exponential decrease with energy. However, this contribution seems to bave a non-negligible intensity well over the overlapping edge of both peaks. Source: bibliography [544]*

.

Where A is the intensity of the first Gaussian, d is the decreasing factor between one Gaussian and the next one, x_0 is the position of the first Gaussian, σ is the FWHM of the Gaussians, and p is the energy shift between one Gaussian and the next one. The values of p and d have to agree with the context of the study. The coice of an energy shift of 0.5 eV is made for this analysis to be consistent with the smoothing used to calculate graphite DOS, which is between 0.4 and 0.5 eV [545, 546]. On the other hand, since we assume the EELS specta to be correlated to the DOS, the decreasing parameter p of the model has to be coherent with the decreasing of the DOS for the π^* feature. This yields a value of $p = 0.7$. As we can see in Figure 4.29, this fit yields a contribution for the π^* feature in the literature that es coherent with the DOS of graphite.

There is an additional issue regarding these analyses that is related to the orientation between the beam and the sample. These issues, as well as the general development of this analysis will be explained in detail in Section 4.3.6.4.

4.3 Experiment

4.3.1 Sample preparation

The GO samples for our works have been prepared by A. M. Benito and Z. W. Maser. Pristine graphite was oxidated following the modified Hummers method indicated in Subsection 4.1.5 in

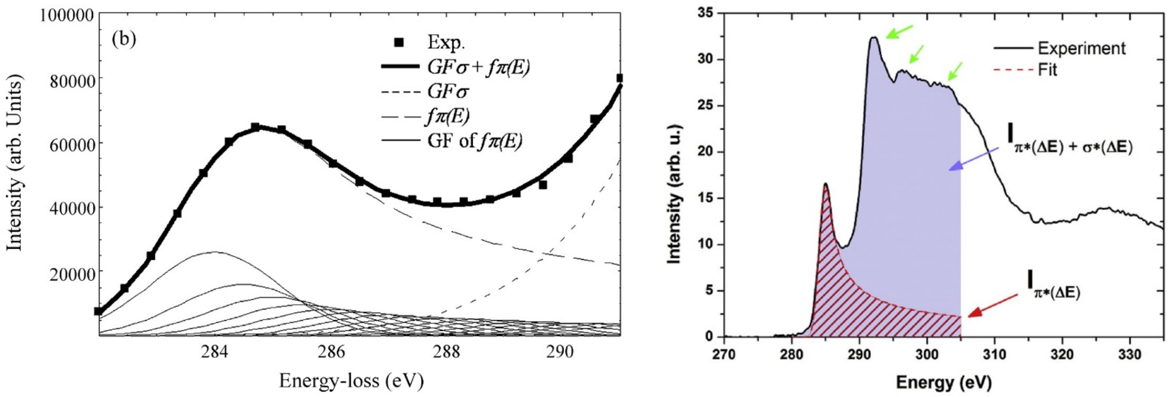

Figure 4.29: *Use of the Gaussian succession method to analyse the* π^* *contribution in carbon K-edges in EELS. Left: Gaussian succession fit applied to* sp^2*-rich carbon. This figure shows the experimental data (**Exp**), the individual successive Gaussians of the analysis (**GF of** $f\pi(E)$) and its sum ($f\pi(E)$), the single Gaussian fit for the* σ^* *contribution (**GF**sigma), and the sum of GFsigma and* $f\pi(E)$ *as the fit for the experimental spectrum. Source - bibliography [544]. Right: Gaussian succession method applied to the EELS spectrum of a graphite sample. The area highlighted in red is the* π^* *component in that range of energy. Both analyses seem to yield similar results.*

order to obtain graphite oxide, as stated in previous literature [547]. A suspension of GO sheets was obtained by liquid exfoliation, sonicating said graphite oxide in ultrapurified water in a ratio of 0.5 mg/ml for 2 hours. The resulting dispersion was then subjected to a mild centrifugation at 4500 rpm for 60 minutes in order to remove non-exfoliated materials.

This suspension was then drop-cast onto the modified DENS chips previously reported in Section 4.2.1.1 and left in an exctraction hood overnight to reduce plausible pollution of the sample while drying. The chip was then transferred to the heating holder and put into the TEM. The sample was left under high vacuum for several hours at 70°C to further prevent plausible pollution.

A reference highly oriented pyrolitic graphite (HOPG) sample was prepared as explained in Section 1.22 by mechanically exfoliating HOPG, transfering some of the exfoliated graphite flakes onto a viscoelastic stamp and then using said stamp to transfer the thin HOPG flakes onto a gold TEM grid with a 1000/2000 mesh covered with a thin layer of glue.

4.3.2 Temperature ranges

Taking into account the different processes that take place at different temperatures during the reduction of GO, delved into in Section 4.1.6.3, it seems that dividing the temperature ranges of the experiment into two different regions is of interest to study these processes in greater detail. These two regions will be called from now on the low temperature regime (70-300°C) and the high temperature regime (300-1200°C).

4.3.2.1 The low temperature regime

As previously stated in Section 4.1.6.3, the desorption of physisorbed water in the sample occurs at a temperature around 100°C, and the desorption of chemisorbed water, as well as the OFGs chemisorbed water is attached to, occurs at a temperature around 190°C. The exact temperature at which this phenomena take place can slightly differ from one sample to another due to the general inhomogeneinity of GO [427] as well as parameters such as sample thickness. This is why a temperature regime at low temperatures has been used to discern the changes surrounding these two phenomena, as well as some extra intermediate points.

Two different temperature schemes have been used for this purpose. In the first one, the main goal of the study was to discern the exact temperature at which the PW and the CW desorbed, so a second measurement was included for temperatures of interest, as we will see in Section 4.3.3. A second one was put in place where these changes were measured with an equal amount of time at each fixed temperature. The temperature changes over time for these low temperature studies can be seen in Figure 4.30.

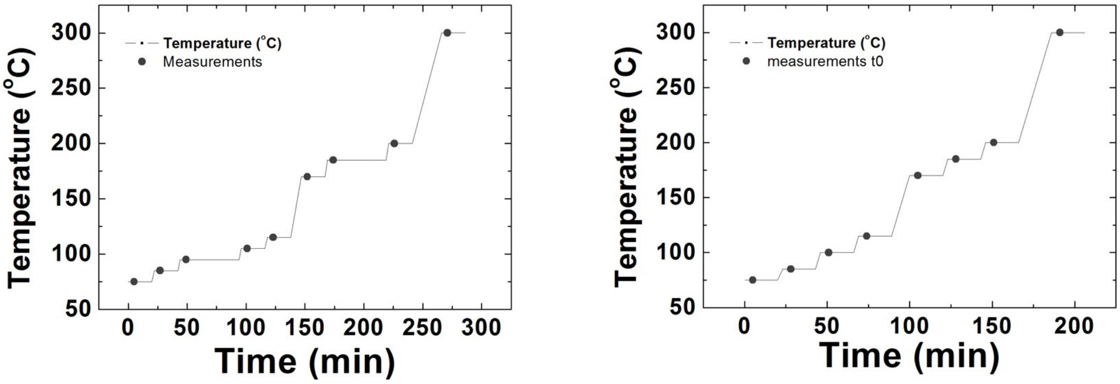

Figure 4.30: *Temperature scheme for the low temperature studies performed for these works. The black line represents the temperature the sample is being subjected to as a function of time, while the black dots represents the moments where an EELS measurement has been made. The one on the left corresponds to the early studies to find the desorption temperature and mechanism for PW and CW respectively, while the one on the right corresponds to later studies where the sample stayed at each temperature for an equal amount of time.*

4.3.2.2 The importance of rehydration

According to the literature [447], only the physisorbed water can be reversibly removed by heating. This can be deduced from the lack of interaction between the physisorbed water and specific OFGs of the GO [548]. In other words, the GO will absorb physisorbed water as long as there are any kind of OFGs in said GO. On the other hand, as it has been explained in Section 4.1.3, chemisorbed water is exclusively bonded to epoxides and carboxyl groups in the sample.

As it has been shown in Section 4.1.6.3, these two OFGs are desorbed from the sample, along with the chemisorbed water, at a temperature below 300°C. As a consequence, the removal of the chemisorbed water after the low temperature treatments is not expected to be reversible, since the OFGs chemisorbed water could form a hydrogen bond with are no longer in the sample. For this reason, we expect to have features related to both the chemisorbed and physisorbed water for the low temperature studies, but only to the latter in the high temperature ones.

4.3.2.3 High temperature

After rehydrating overnight, the sample has been introduced in the microscope again. This time around, two temperature schemes have been set to study the full reduction and graphitisation path for GO, as well as to test whether the chemisorbed water desorption has been successful. For this, temperatures between 70°C and 1200°C have been chosen. One of the temperature schemes focused more on the behaviour over time of the samples (see Section 4.3.3), especially at lower temperatures, where the data on PW and CW desorption was of special interest. The second temperature scheme focused only on the behaviour of the sample at high temperatures. The specific temperatures over time for both studies can be seen in Figure 4.31.

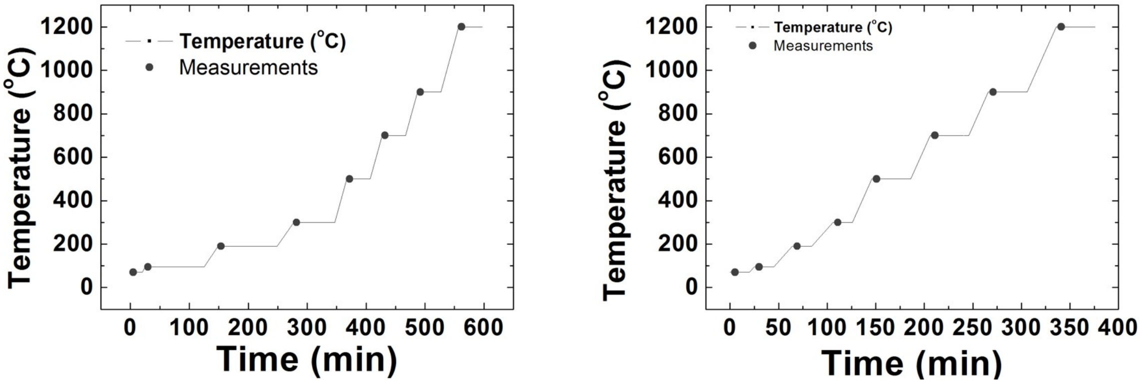

Figure 4.31: *Temperature scheme for the high temperature studies performed for these works. The black line represents the temperature the sample is being subjected to as a function of time, while the black dots represents the moments where an EELS measurement has been made. Left: Temperature scheme for studies focusing more on low temperatures. Right: temperature scheme for studies focusing more on high temperatures.*

4.3.3 Cinematic studies

As we have mentioned, on top of examining the change of different properties in the sample with temperature, it is of interest as well to study the change of said properties over time for a certain temperature. This is why second and even third measurements have been performed within the abovementioned studies to learn more about the evolution of the reduction and graphitisation at a constant temperature.

For low temperatures, this meant having an extra measurement at critical temperatures for the desorption of water, such as 100 and 175 °C, so that it was possible to provide a better tracking as to what was going on in the sample during the desorption of PW and CW, respectively. These temperature schemes can be seen in Figure 4.32

As for high temperatures, both temperature schemes show two different approaches to this study. On the one hand, one of the temperature schemes focused on the possible rehydration of PW and the success on the desorption of CW, so additional measurements had to be made at temperatures of interest regarding these phenomena. For all the other temperatures, a second measurement was set in place for a better understanding of the dynamics of the desorption of different OFGs. On the other hand, a second temperature scheme was set in place to get a better understanding of the reduction of GO at high temperatures. As we can see in Figure 4.33, only measurements for 500 and 700°C are shown. This is due to experimental problems that did not allow us to take second measurements at 900°C, as well as the degradation of the sample explained in Section 4.4.4.1

4.3.4 TEM imaging and EELS parametres

TEM images and EELS spectra in this study were acquired using the FEI Titan Cube TEM described in 1.6.1, working at 80 kV to try to minimise the effects of electron radiation. Convergence and collection angles were 6.3 and 19.7 mrad, respectively. EELS energy resolution,

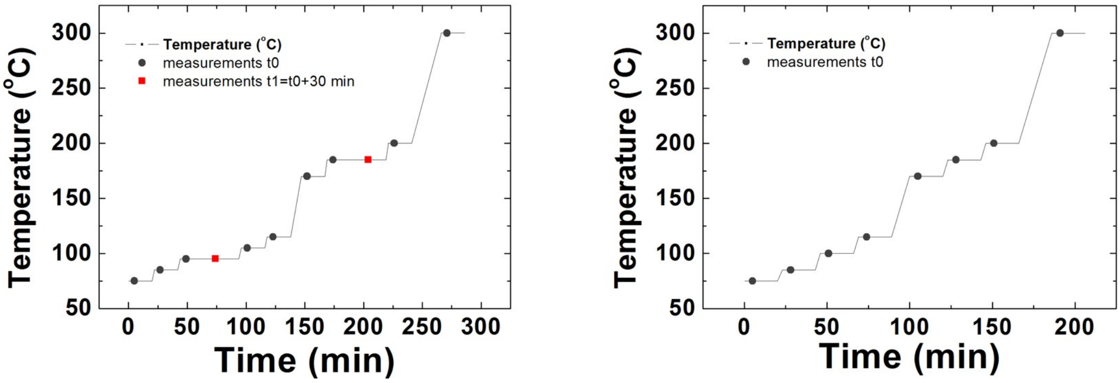

Figure 4.32: *Temperature scheme for the low temperature cinematic studies performed for these works. The black line represents the temperature the sample is being subjected to as a function of time, while the black dots represents the moments where the first EELS measurement has been made for a specific temperature and a red square represents where a second measurement has been made, 30 minutes after the first measurement. The scheme on the left corresponds to the early studies to find the desorption temperature and mechanism for PW and CW respectively, while the one on the right corresponds to later works with no cinematic studies.*

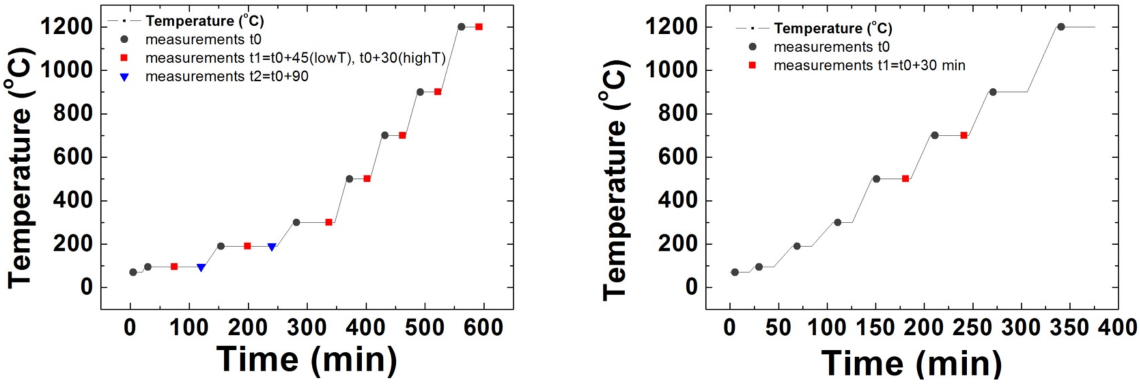

Figure 4.33: *Temperature scheme for the high temperature cinematic studies performed for these works. The black line represents the temperature the sample is being subjected to as a function of time. The black dots represents the moments where the first EELS measurement has been made for a specific temperature, a red square represents where a second measurement has been made (either 30 or 45 minutes after the first measurement), and a blue triangle represents where a third measurement has been performed, 90 minutes after the first measurement. Left: Temperature scheme for studies focusing more on low temperatures. Right: temperature scheme for studies focusing more on high temperatures.*

measured by means of full width at half maximum of the zero loss peak (ZLP) of the spectra, was under 0.8 eV. We have used an energy dispersion of 0.2 eV/channel. The EELS acquisition times were, respectively, 0.1 s for the low loss spectra, and 5 averaged frames of 2s (10 s total) for the core loss spectra; with an 8x vertical binning. The size of the analysed area was around 100 nm in diametre.

4.3.5 spectra calibration and alignment

The low-loss spectra were aligned by centering the ZLP of each spectrum taking a channel width of 0.2 eV.

The core loss spectra had their background extracted using a power law and were subsequently calibrated using a custom script that aligned the different spectra using features from the fine structures of C and O,respectively, except for the heavily reduced samples where the N has been used due to a lack of intensity in the O peaks that prevented us from being able to discern the aforementioned fine structure features.

To avoid the effects of multiscattering, a Fourier Log-ratio deconvolution has been performed to each core loss spectrum using the built-in function for this purpose. This function uses a low loss EEL spectrun taken in the same area as a point spread function of sorts and deconvolutes it from the original core loss spectrum. An example of a spectrum before and after deconvolution can be seen in Figure 4.34

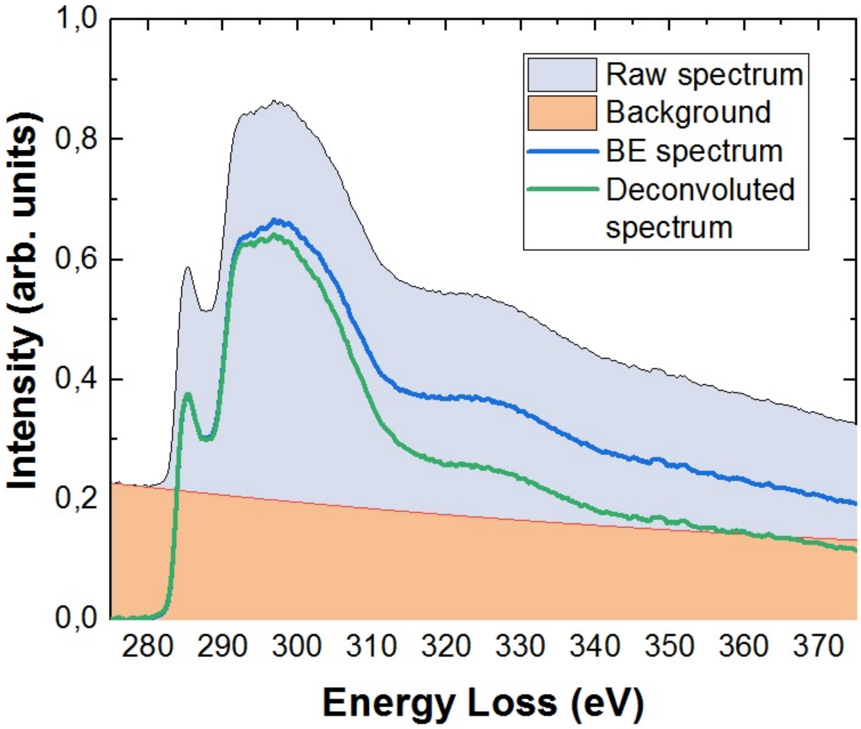

Figure 4.34: *Plural scattering treatment of core loss EEL spectra using the Fourier log-ratio deconvolution. Figure shows the core loss EEL spectra before and after background extraction, the background itself and the deconvoluted core-loss spectrum.*

4.3.6 EELS analyses

This section verses on the analysis of both the low-loss EEL spectra and the core-loss EEL spectra, which focus on four specific elements:

- EELS is a technique known bv for their applications in **chemical quantification**. With regard to GO samples, this means we have a way to calculate the **oxydation degree** of the GO as it reduces. The specifics of this quantification are shown in Section 4.3.6.1.

- The **thickness** of the sample can be estimated using the data related to the scattered and non-scattered transmitted intensities. This can be approximated using the low-loss EEL spectrum. The process for this estimation is shown in Section 4.3.6.2.
- The plasmonic features in the low-loss EEL spectra can lead to the estimation of the **mass density** of the sample. The analysis to obtain these results is explained in detail in Section 4.3.6.3.
- Finally, the features of the C-K edge of the core-loss EEL spectra can be used to estimate the fraction of the C atoms in the sample that are sp^2-bonded. This process is explained in Section 4.3.6.4.

The behaviour of these elements as a function of temperature, along with the ELNES analysis, set the experimental basis for our hypotheses about the specific changes taking place in GO as it reduces.

4.3.6.1 Chemical quantification: Oxydation degree

The integration quantification methods explained in Section 1.4.4 have been put into practice in order to analyse the relative composition of carbon, oxygen, nitrogen and calcium, according to the peaks that we have noticed in the core-loss spectra.

This measurement allows us to know the oxidation rate of the sample, taken as the normalised oxygen ratio with respect to the carbon+oxygen ratio, without taking into account the amount of other impurities. Similarly, the reduction rate can be expressed as the normalised carbon ratio with respect to the carbon+oxygen ratio:

$$\%O = \frac{[O]}{[C]+[O]} \tag{4.20}$$

$$\%C = \frac{[C]}{[C]+[O]} \tag{4.21}$$

Additionally, the amount of nitrogen present in the sample, as well as the amount of calcium we have as an impurity in the sample, have been measured as well.

4.3.6.2 Thickness estimation

As explained in Section 4.2.3.1, the parameterisation of the inelastic mean free path of electrons in our sample is given by the expression:

$$\lambda = \frac{106 \times F \times E0}{E_m \times ln\left(2\beta \times \frac{E_0}{E_m}\right)} \tag{4.22}$$

Where λ is the IMFP estimation, E$_0$ is the beam energy, F is a relativistic correction factor, β is the TEM collection semiangle, and E_m is an effective energy that amounts to $E_m = 7.6 \cdot Z^{0.36}$ [64]. For this particular experiment, we have a value of E_0=80KeV, β=19.7 mrad, and the value of Z_{eff} needed to calculate E_m (see equation 4.11) can be estimated after the chemical quantification of the sample, which has been delved into in the previous section For this particular purpose, the quantification of trace elements such as N or Ca is important in order to have the most accurate approximation possible for Z_{eff}.

For the estimation of the thickness of the samples, two different regions of the spectrum, one between -2 and 2 eV and another one between -2 and 100 eV, have been chosen as the regions corresponding to I0 and It, respectively. The choice for a 100 eV wide spectrum window has been considered valid in the literature for specimens with low atomic number like ours [13]. The corresponding regions of the spectrum can be seen in Figure 4.35. After having been cropped, these spectral regions of interest have been integrated by calculating the sum of their individual values in each point of the interest region, and then deducing the thickness of the samples by using the parametrisation for the mean free path λ found in Section 4.2.3.1.

The error in the measurement of the different intensities has been taken as the noise in the spectra, measured taking the standard deviation of the background extracted spectra as the error in the measurement of one channel of the spectra [64].

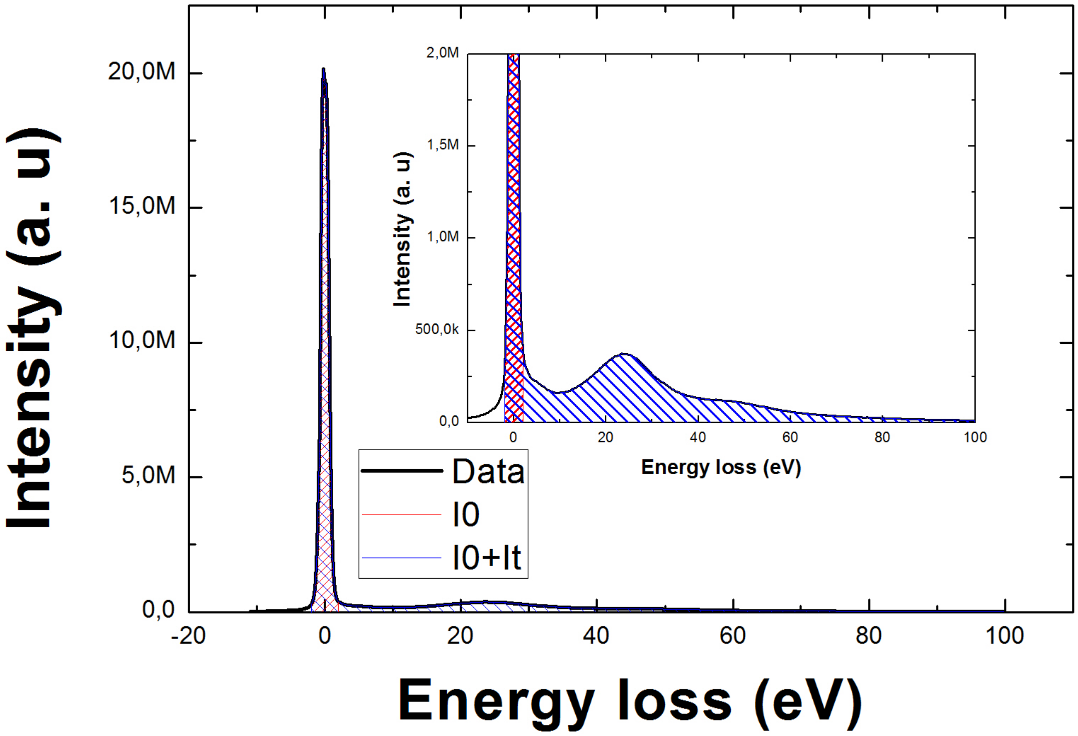

Figure 4.35: *Spectral windows for the ZLP region (I0) and a region wide enough to assume most of the plasmonic behaviour has already taken place (-2 - 100 eV, It).*

4.3.6.3 Mass density

Here we delve into the low loss EELS analysis related to the estimation of the mass density of the samples. The spectral window for this background extraction has been taken after the π^* plasmonic peak denoted in Section 4.2.3. In coherence with previous studies [538], and with the objective of obtaining a more accurate analysis, a custom script has been made using Digital Micrograph to consider only the spectral window where the intensity of the plasmon peak is 70% of its maximum or higher, providing a spectral window where the influence of other spectral features is minimal. This script has been used on the background extracted spectra and the resulting cropped spectra have been fitted using a custom fit function following the expression for the electron loss energy in the shape of the Drude model referred to in Section 4.2.3.1 [538]:

$$Im\left(-\frac{1}{\epsilon(E)}\right) = \frac{E_p^2 \times E \times \Delta E_p}{(E^2 - E_p^2) + (E \times \Delta E_p)} \tag{4.23}$$

With both E_p and ΔE_p as two different parametres to optimise. An example of this particular fit can be seen in Figure 4.36

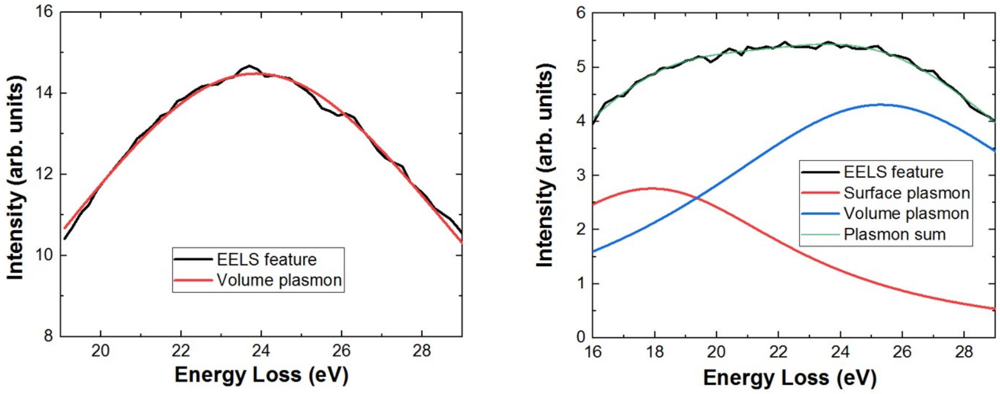

Figure 4.36: *Drude fit of a high thickness GO sample (left) and a low thickness rGO sample (right). The Drude analysis of high thickness samples is performed with a single fit for the volume plasmon, while the Drude analysis of low thickness samples needs a second fit to account for the surface plasmon contribution.*

To determine for the mass density of the sample in each of the areas studied, each low-loss spectrum has been fitted at the volume $\pi + \sigma$ plasmon spectral region. For this, after zero-loss peak removal, a spectral window around the volume plasmon region has been selected. The selection criteria for this spectral window was for energy loss to be higher higher than 70% of the maximum intensity of the volume plasmon peak [65, 13].

The value for E_p, as well as its error, are gathered from this particular fit. As expressed in Section 4.2.3.1 (see equation 4.6, the expression for the mass density estimation can be derived from the fraction of oxygen in the sample (which is known from the chemical quantification) and the value of the volume plasmon energy.

The rest of the parametres needed for the estimation of the mass density have been gathered from the experimental conditions.

Thickness issues As it can be seen in Figure 4.37, it has been previously reported in the literature [514] that, as the thickness of a graphenic sample decreases, there is a second plasmonic component related to surface in the π^*+σ^* plasmonic feature that arises in the EEL spectra. Surface plasmon features arise for values of $\frac{t}{\lambda} << 1$ [549].

This happens as well in our samples for those at high temperature with a thickness under 10 nm. In these cases, a double fit using two Drude functions is applied, one to fit the surface plasmonic feature and another one to fit the volume plasmonic feature. A comparison between a clear one-component spectrum (thick sample at low temperature) and a clear two-component spectrum (thin sample of less than 10 nm at 1200°C) with their respective fits can be seen in Figure 4.36.

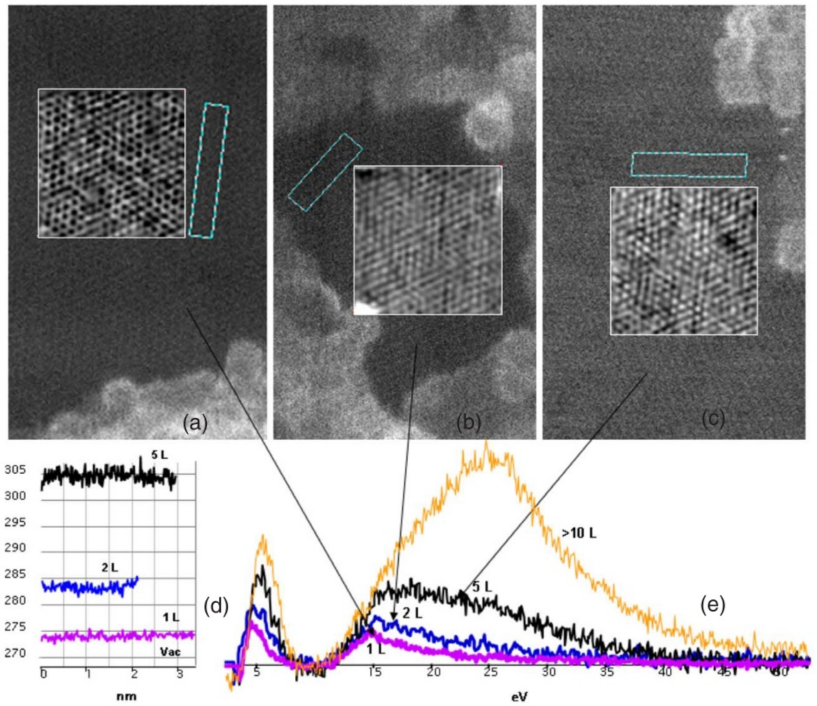

Figure 4.37: *(a)-(c)HAADF STEM images of 'pristine' regions showing one, two, and five layers of graphene. (d) Intensity traces have been gathered along the long dimensions of the rectangular cyan-framed boxes in(a)-(c); these traces have then been averaged over 40 pixels (the same width as the boxes). They show a discrete increase of the HAADF intensity correlated to the number of layers. The vacuum intensity is at 268. (e) EEL spectra of one, two, five and several layers of graphene showing the* π *and the* π*+*σ *plasmon. The spectra are taken from spectrum images; they are background subtracted and each summed over 25 pixels.* ***Source: Literature*** *[514]*

4.3.6.4 sp^2 ratio: calculation for low and high sp^2 values

In this section we focus on the different methods used for the estimation of the sp^2-bonded C atom fraction, as well as the issues regarding the accuracy of these methods.

The intensity ratio method

After the calibration and deconvolution of the core-loss spectra in order to have a single-scattering energy loss function, a custom script in Digital Micrograph has been used to crop each spectrum between 280 and 310 eV. This will be considered the spectral region for the π^* + σ^* feature , and the integration of this spectra, expressed as the sum of all the intensity channels ($S_{\pi+\sigma}$) multiplied by the width of one channel (0.2 eV) will yield the area of the π^* + σ^* feature.

At the same time, another custom-built script has been used to crop each spectrum from 280 eV to a point 3 eV over the local energy loss minimum between the π^* peak and the σ^* peak. This specific spectral window comes from previous studies proving that the analysis of the sp^2 fraction using the 60 decreasing Gaussians method explained in section [$ref section$] is stable in spectral windows going up 2 to 4 eV over the aforementioned local minimum [538].

These second cropped spectra have then been transferred to IGOR where each spectrum has been fitted using a custom-built function corresponding to the decreasing Gaussians sum introduced in Section 4.2.3.2. According to the literature, as explained in said section, The resulting expression for the custom fit developed in IGOR is:

$$I = A \times \sum_{i=1}^{60} 0.7^{i-1} \times e^{\frac{-(x-x_0-0.5^{i-1})^2}{2\sigma^2}} \tag{4.24}$$

The spectra have also been fitted using a Gaussian fit centered at 294 eV to account for the σ^* features following the same literature [538]. An example of the resulting contribution for the π^* peak can be seen in Figure 4.38. As it can be seen, it is in very good agreement with previous studies on the matter [538][544].

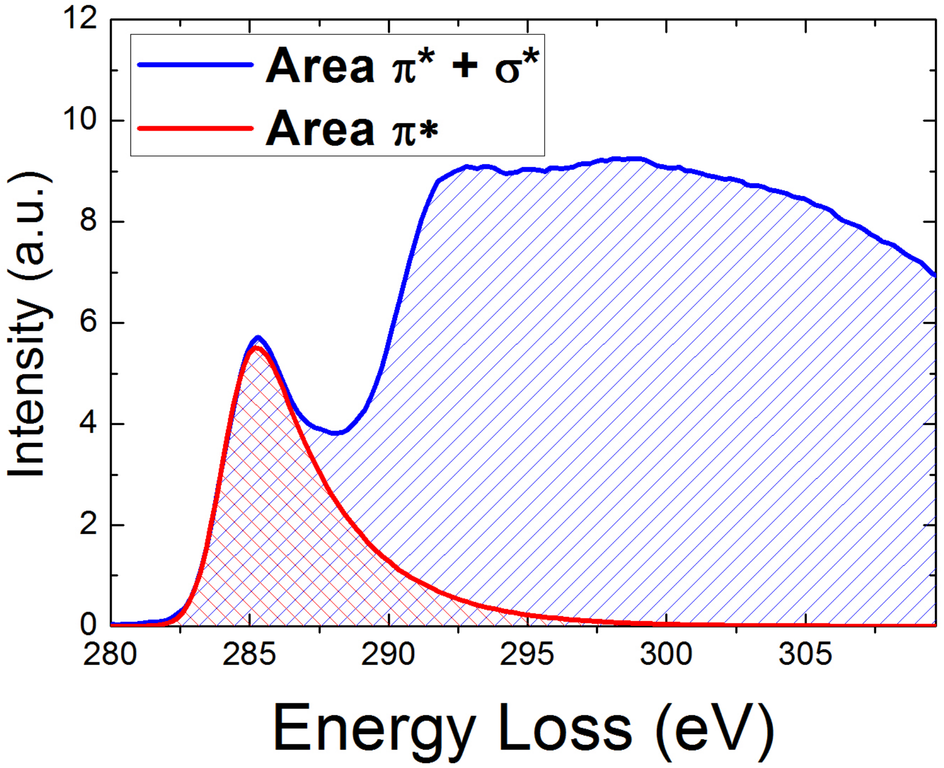

Figure 4.38: *representation of the π^* peak in a C-K edge EELS spectrum using the Gaussian succession analysis.*

The resulting 60 Gaussian fit has been considered as the π^* feature, and the integration of this fit, expressed as the value of the fit for each value of x in the spectra between 280 and 310 eV (S_π) times the width of one channel(which we can call ΔE, is considered as the area of the π^* peak.

To calculate the value of y' one only needs to divide the area of the π^* peak over the area of the $\pi^* + \sigma^*$ peak, which is equivalent to dividing its respective sums, since for each spectra the width of one channel is the same:

$$y' = \frac{A_{\pi^*}}{A_{\pi^*+\sigma^*}} = \frac{S_{\pi^*} \times \Delta E}{S_{\pi^*+\sigma^*} \times \Delta E} = \frac{S_{\pi^*}}{S_{\pi^*+\sigma^*}} \tag{4.25}$$

Finally, there are references for the value of y'_{HOPG} for experimental conditions very similar to ours (α=7.4°, β=19.7°, γ=0°, compared to our α=6.3°, β=19.7°, γ=0°)that yield a value of y' 0.2 [65]. Assuming an sp^2 ratio of a 100% for HOPG, we can simply calculate the ratio of sp^2 bonds in our sample using equation 4.26

$$\%sp^2_{GO} = \frac{y'_{GO}}{y'_{HOPG}} \times \%sp^2_{HOPG} = \frac{y'_{GO}}{0.2} \times 100 \tag{4.26}$$

The problem with oxidation

It is important to notice that this analysis uses only two different functions to fit a spectral window where more features exist besides the π^* and the σ^* K-edge features. As it has been explained in Section 4.1.8, fine peak structures corresponding to bonds other than C=C are present in the spectra as well. The analysis of spectra of slightly more oxidated samples than ours (more than a 25% oxidation rate)show that the fine peak structure features in the spectra are intense enough so that this method cannot be applied to them without using additional peaks to account for the fine peak structures in the spectra.

The anisotropy issue

It has been reported in the literature [542] that, due to its high anisotropy, graphite and graphene can lead to orientation effects in EELS. This orientation effects affect the relative intensity of the π^* and the σ^* peaks. This can be seen in Figure 4.39. In here we can see two spectra, one (left) that was taken parallel to the graphite layers (this is, the elecron beam was perpendicular to the c axis (the interplanar axis) of the HOPG; and the other taken with the electron beam parallel to the c axis.

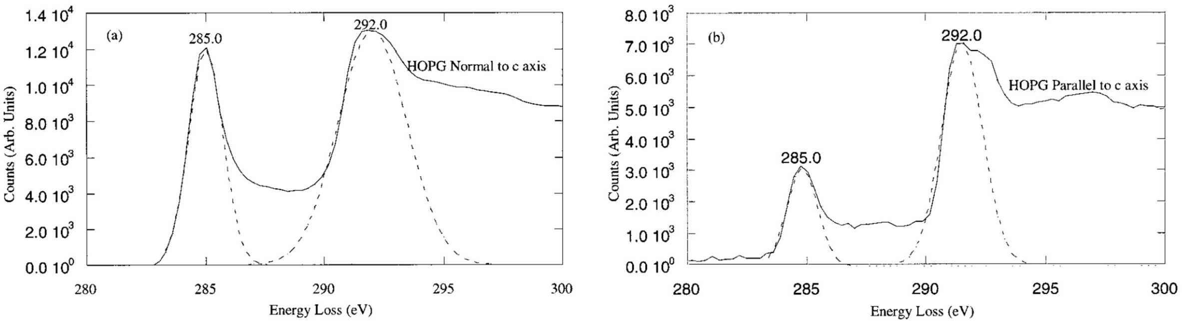

Figure 4.39: *HOPG C K-ionization EELS spectra comparison based on sample-beam orientation. Left: Sample normal to the c axis. Right: Sample parallel to the c axis.*

As our GO starts reducing and, especially, as it starts graphitising, it becomes more and more similar to graphite such as HOPG. This results on an increase of the orientation effects affecting our sample, making it impossible to gather an accurate measurement of the sp^2 fraction with the method delved into in this section, which underestimates the value of sp^2 for more graphitic samples. This has made us pursue a different path o analyse the sp^2content of highly reduced GO for the high temperature studies: the Multiple Linear Least Squares (MLLS) approach.

The low temperature studies have been analysed with the Gaussian succession analysis since, for this particular temperature regime, we have proved this method to be more accurate than the MLLS approach.

The MLLS approach

Using MLLS to determine the amount of sp^2 bonds in a carbon material had been used in previous analysis on carbon films [60], but the analysis had been deemed quite inaccurate by their own authors. Here, we postulate that, given a few modifications, this method can effectively be used for the estimation of the fraction of sp^2 bonds in carbon materials.

This analysis consisted on using the spectra of two different samples to estimate the sp^2 ratio of the sample as a linear combination of said two spectra, in their case a pure sp^2 HOPG sample, and a pure sp^3 diamond sample. In our case, we will use a different spectrum instead of the diamond one for a better accuracy. The spectrum used has been the one of GO at 70°C, that is, at the beginning of the high temperature studies.

Preparation of the spectra For this study, to avoid any problems in the analysis coming from having different intensity values for our spectra (since the dosis can vary slithgly among spectra even for similar experimental conditions)all spectra have been normalised using a custom script, which cuts the C-K edge region in the spectra (280-310 eV) and normalises the spectra by dividing them over their own sum:

$$S_{norm} = \frac{S}{\mathrm{Sum}(S)}) \tag{4.27}$$

From there, two different paths are followed. The spectra that are going to be used as model spectra are left as is (with a 30 eV spectral window. In the case of the spectra that are fitted, they are cut to the region of interest between 280 and 290 eV before being analysed. This is the window we have found to be the most coherent for our analysis, since it contains most of the π^* feature and a little bit of the σ^* and we are focusing on the shape of the π^* one.

Gaussian fit of the original spectra In order to have a more manageable fit, as well as not having noise in the spectra we were going to use as our two models for the MLLS fitting (GO at 70°C and HOPG at room temperature), a custom fit with 8 Gaussians has been applied to both spectra. This analysis has been performed for each of the areas studied. An example of one of the GO Gaussian fits and the HOPG Gaussian fit can be seen in Figure 4.40

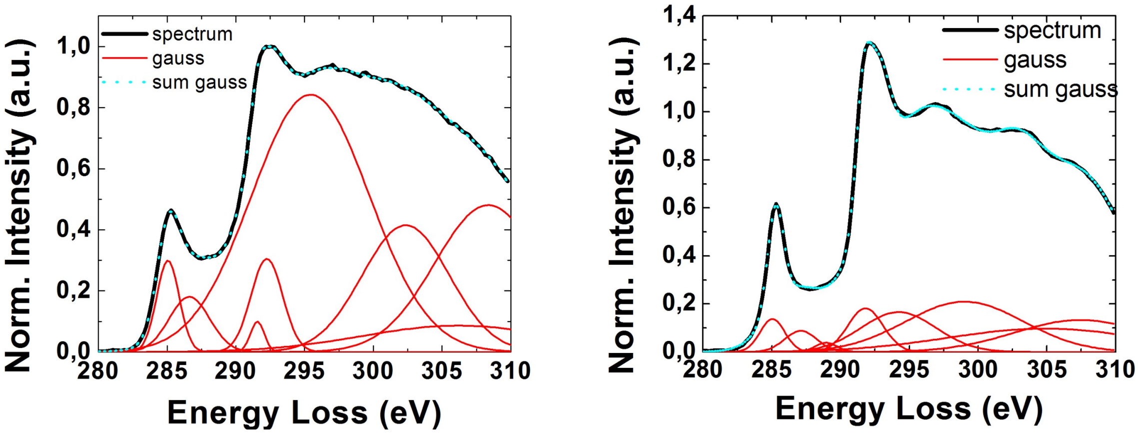

Figure 4.40: *Gaussian fit using 8 peaks for GO at 70°C (left) and HOPG at room temperature (right)*

The number of Gaussians chosen for this fit (8) comes from the fit of the curves being accurate enough.

MLLS fit and sp^2 estimation For each one of the areas studied, once the respective GO and HOPG fitting spectra have been subjected to the aforementioned Gaussian multi-peak and the spectra to be fitted have been loaded onto IGOR, it is time to create a custom fitting function for each area, where each spectra is expressed as a linear combination of the two fitting spectra or, in this case, a linear combination of their Gaussian decomposition:

$$S = a \times S_{GO} + b \times S_{HOPG} = a \times \sum_{1}^{8} G_{GO} + b \times \sum_{1}^{8} G_{HOPG}$$

(4.28)

where S is the spectra to be fitted, S_{GO} and S_{HOPG} are the corresponding spectrum of GO at 70°C and HOPG at room temperature for that specific area, G_{GO} are the Gaussians of the GO decomposition, and G_{HOPG} are the same but for HOPG. a and b are the fitting coefficients. An example of this fit can be seen in Figure 4.41 Once the fit provides us with the values for a and b, we can easily calculate the value for sp^2 from those:

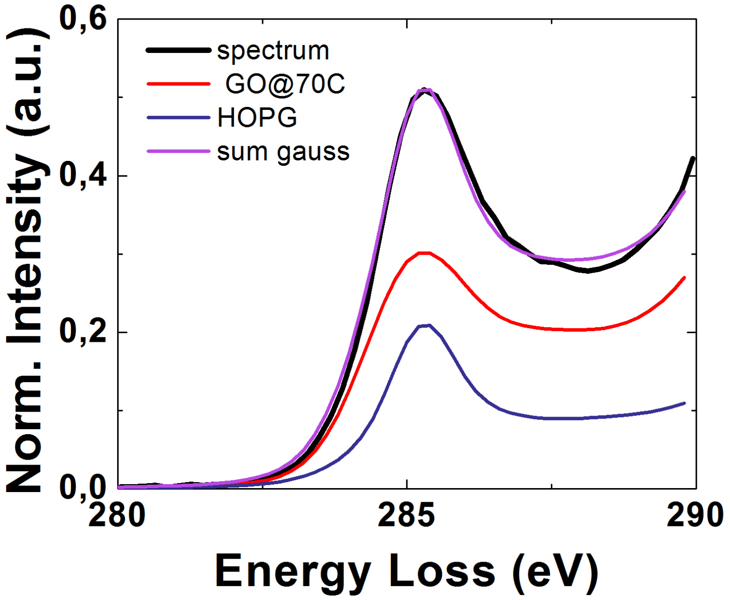

Figure 4.41: *Example of a MLLS fit using the Gaussian decomposition of a GO spectrum at 70°C and a spectrum from HOPG at room temperature.*

$$\%sp^2 = a \times \%sp^2_{GO} + b \times \%sp^2_{HOPG} \tag{4.29}$$

We assume a value of sp^2 for HOPG of 100 %. The value of sp^2_{GO} has been previously calculated using the Gaussian succession method explained in this section.

Comparison with previous method A comparison between the two methods has been made in order to determine the accuracy of the MLLS fitting. the comparison can be seen in Figure 4.42.

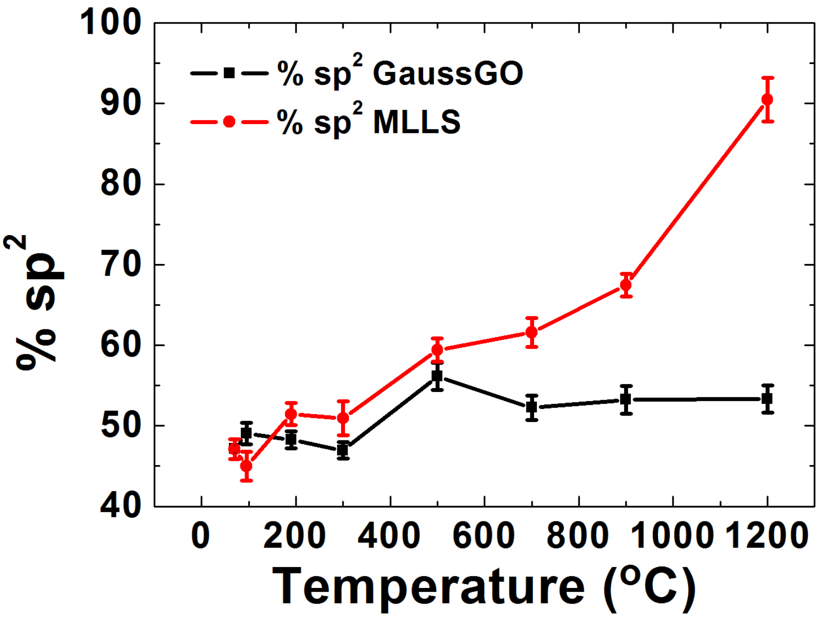

Figure 4.42: *Estimation of the sp^2 fraction using the Gaussian succession method (black) and the MLLS approach (red). The comparison shows a good agreement up until 500°C, whereas for 700°C there is a growing discrepancy.*

The underestimation of the sp^2 ratio for highly graphitised samples when using the Gaussian succession method can be observed in this figure. For temperatures under 700°C, both analyses seem to yield similar results, whereas for 700°C and up, the underestimation of the sp^2 ratio by the Gaussian succession method is more visible and so is the difference between one method an the other.

4.4 Results and discussion

4.4.1 EELS fine structure peaks analysis

A full identification of the different EELS features of each OFG is needed in order to be able to provide an explanation for the behaviour of the other preperties measured in these studies. Furthermore, both the low temperature spectra and the high temperature spectra will be analysed together, since they both help paint a more complete picture of the chemistry taking place in the sample. As it will be shown in Section 4.4.2.2, there are samples of different thicknesses in this study. We will use the thickest one for the explanation of this fine structure peaks analysis, since a thicker sample has a higher cross-section and therefore a higher signal to noise ratio (SNR) in the EELS signal.

It is important to notice that this study will be mostly focused on the presence or absence of these fine structure peaks rather than their relative intensity, so it is possible that we will be missing some features such as the formation of C=O in the sample that has previously been reported [432].

4.4.1.1 C-K edge

The identification of the fine structure peaks is based on previous studies on the subject [407, 408, 69, 538] (see Section 4.1.8) and, even though the absolute values of the different features vary along the different studies, there seems to be consensus in the rank in energy of the features of each OFG. For the C-K edge, we have, in rising order of energy, a feature due to the sp^2 C, one for the C-OH groups, one for the C-O groups (both aromatic and not), C=O groups, and COOH groups, respectively. [407, 69, 538].

With these previous studies, along with our own spectra, as well as previous studies showing which groups need a higher or lower temperature to desorb [407, 464, 533], we have estimated which features in our C-K edge spectra correspond to which OFGs. The results can be seen in Figure 4.43. Going from lower to higher energy, the identification is as follows:

- The first two features are the one corresponding to sp^2 clusters (the π^* contribution, around 284.9 eV; and the ones corresponding to alcohol (C-OH) groups at approximately 286 eV. These two features are not completely discernible from one another due to their proximity and the width of their respective peaks. We can discern the sp^2 peak at 1200°C, once the last of the -OH has desorbed going from 900°C to 1200°C.

- Up next, we have a feature at 286.6, which we have correlated to C-O bonds (both epoxides and ethers, since they both share the same feature). This feature seems to be present even after the end of the low temperature studies. However, it is true that the EELS feature seems diminished between 200°C and 300°C. As for the high temperature studies, the feature for this OFG seems to fade at around 900°C, which leads us to think this OFG desorbs to a high extent between 200°C and 300°C, but it does not fully desorb until heating up to 900°C. The behaviour of the desorption of C-O can come from the fact that this feature is due to both ethers (aromatic C-O-C) and epoxides (non-aromatic C-O-C). Our hypothesis, also based on the analysis of the O-K edge of the spectra shown in secton 4.4.1.2, is that they both desorb at different temperatures.

- At $\sim$ 287.5 eV, we find an EELS feature that appears on our spectra subtly at first, but that resists desorption all the way up to 1200°C. Based on the previously explained XPS and EELS studies on the matter [511, 516], we can convey it could be a peak corresponding to a C-N state, specifically an sp^3C bonded to a N atom. This is coherent with the fact that, even at almos complete reduction at 1200°C, we sitll have a non-negligible $\sim$4% of N in the sample.

- Going up, at 288.4 eV, we find a fine peak structure we have related to the ketone (C=O) group. It is clearly present throughout the low temperature studies, and it seems to mostly desorb between 500°C and 700°C, with a very slight amount still in the sample at 700°C that gets desorbed right away.

- Finally, there is a feature at 289.4 eV that seems to be related to carboxyl groups (COOH). This feature seems to fade in the low temperature studies at temperatures higher than 185°C. It is important to note that this feature is not visible in the high temperature studies.

4.4.1.2 O-K edge

The O-K edge in the EELS spectra is located at much higher energies and therefore has a much lower cross-section. This means our O-K edge spectra have a much lower SNR than our C-K

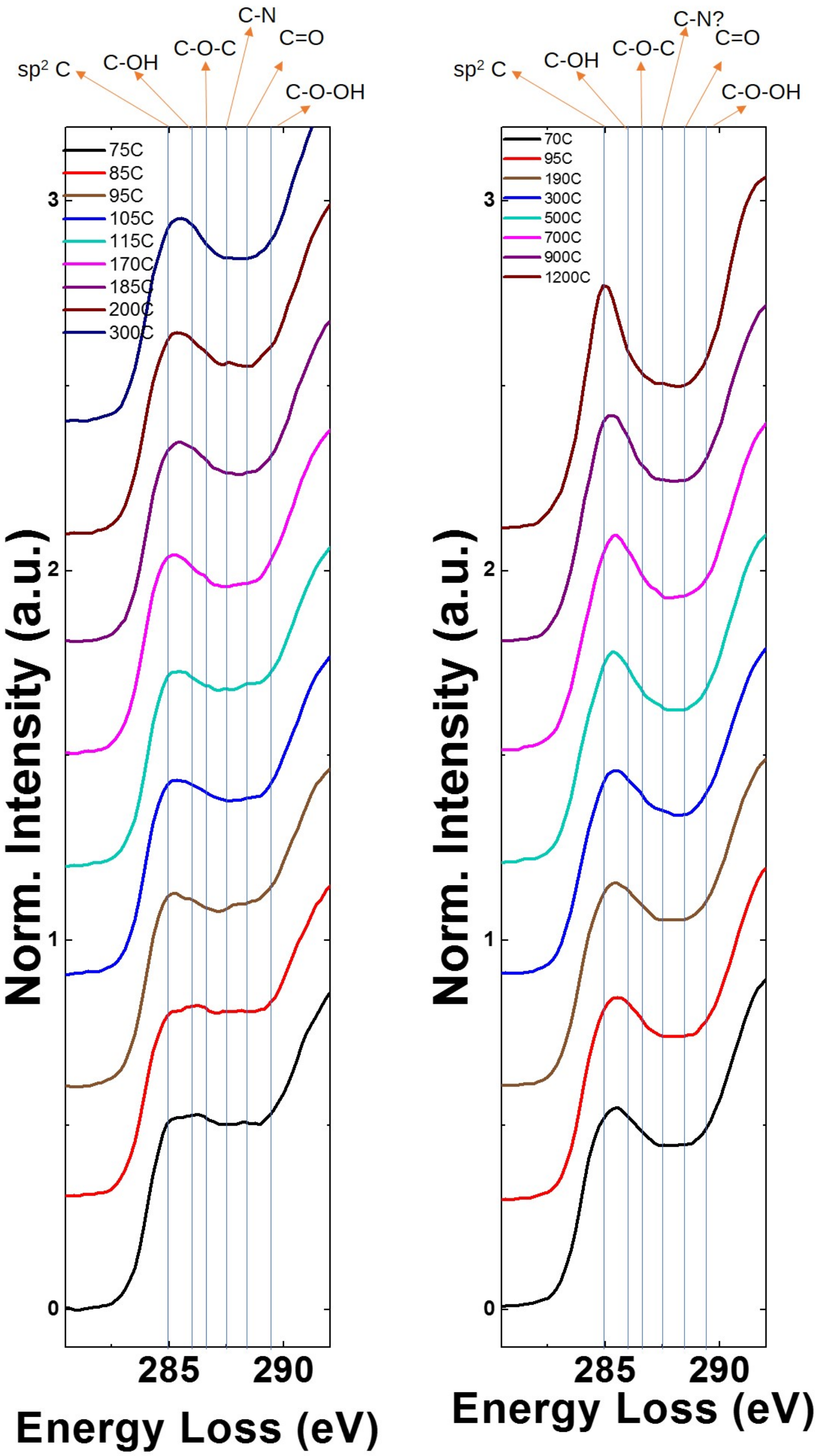

Figure 4.43: *EELS C-K edge spectra of one of our areas of interest for all temperatures in the low temperature study (left) and in the high temperature study (right). The estimated region for the features related to each OFG has been marked.*

edge spectra and therefore the results gathered from its analysis can be less accurate. Using some of the studies previously mentioned [69], we have been able to identify some of the features in the O-K edge of the EELS spectra as well, and this identification seems to further confirm the C-K feature assignments. The O-K edge of the spectra, as well as our identification of the different features which further confirm our C-K assignments, can be seen in Figure 4.44.

The in-depth analysis of these feature goes as follows:

- At ∼ 531.8 eV, we seem to have a feature that does not seem to appear in other studies, that we know of. It seems to have a first dip at ∼105°C, and a second one at ∼185°C. It also appears on the lower temperatures of the high temperature studies. Given all of this information, our hypothesis about this feature is that it is related to the physisorbed and chemisorbed water in the sample.
- At ∼533.6°C, we have found a feature that seems to correspond to C=O groups. Their desorption when heating from 500°C to 700°C (at least in this particular sample) is one of the clearest of the whole study.
- A peak can be seen at 534.9 eV, which we have correlated with the non-aromatic O-C groups. It seems that the peak fades greatly between 200 annd 300°C. As for the high temperature studies, it is hard to discern for sure whether there are still non-aromatic O-C groups on the sample because of the poor SNR.
- At a slightly highter energy, at 536.2 eV, we found a fine structure peak that we have related to aromatic C-O-C. It is worth noting that this feature can even be seen at 700°C.
- Finally, there are two features that seem to appartain to the same OFG, O-H. These features are located at 538.5 eV and 541.1 eV. The DFT calculations in the study by D'Angelo *et al* [69] does show a double feature for the O-K spectra of OH groups at low temperatures at 535 and 538 eV that could represent these two features. Both ELNES features seem to fade completely between 900 and 1200°C, which is coherent with the desorption of O-H at these temperatures.

The rest of the EELS studies on these samples will be discused in the following sections.

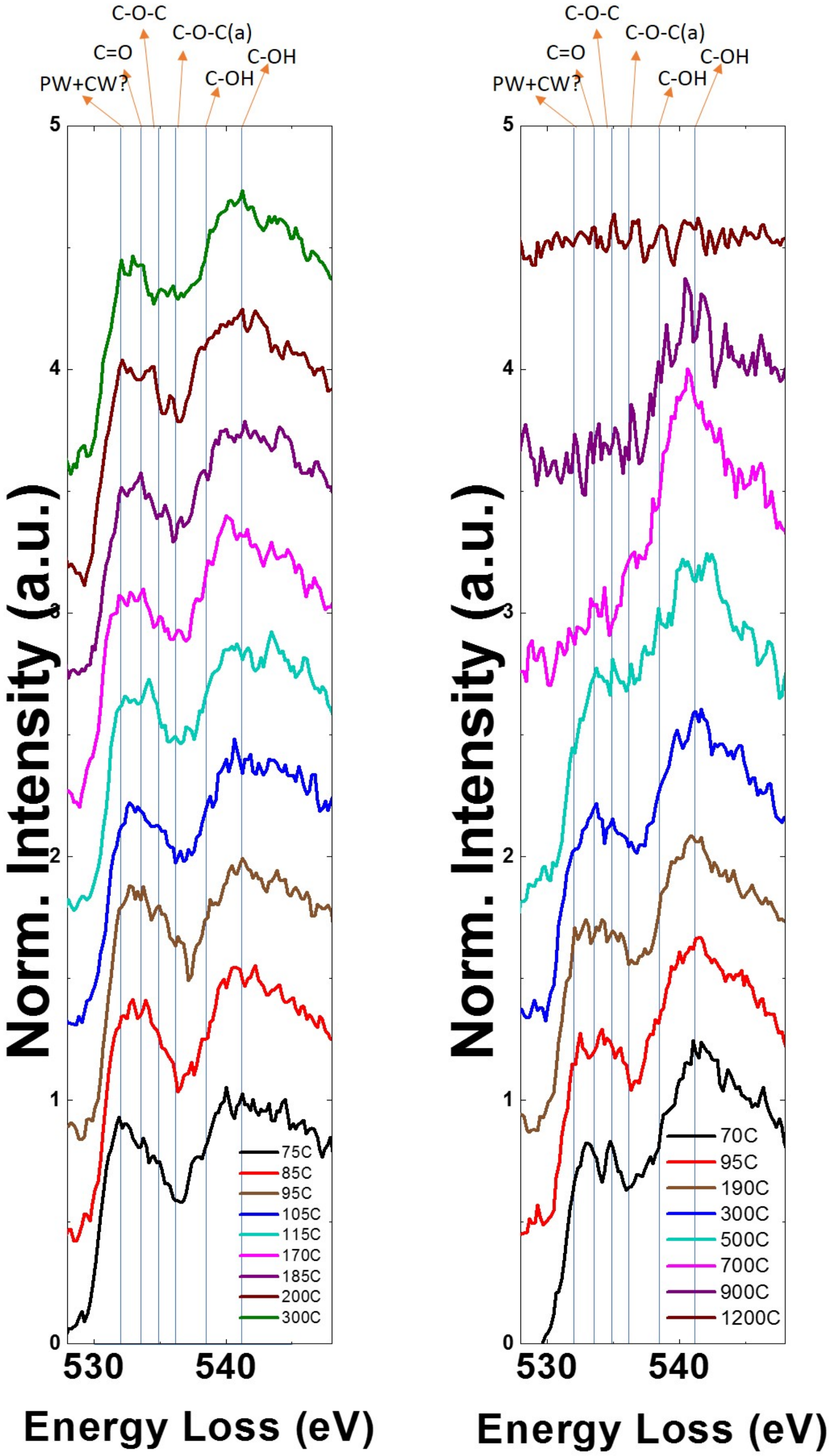

Figure 4.44: *EELS O-K edge spectra of one of our areas of interest for all temperatures in the low temperature study (left) and in the high temperature study (right). The estimated energy for the features related to each OFG has been marked.*

4.4.2 Low temperature studies

4.4.2.1 TEM imaging

In this part of the study, the TEM imaging has two main objectives. On the one hand, it helps us find the holes in the Si_xN_y membrane and discern which holes have a flake of GO on top of them. A TEM image of one of these holes can be seen in Figure 4.45

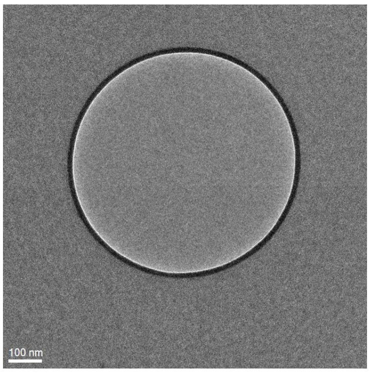

Figure 4.45: *TEM image of a hole in the Si_xN_y membrane.*

On the other hand, HRTEM imaging, as well as electron diffraction, help us discern the structure and morphology of the GO before and after the thermal treatment. In Figure 4.46, we can see, first of all, that the material presents a mostly policrystalline structure, with an amorphous ring also appearing in their diffraction pattern, if much more subtle than its policrystalline behaviour. This structure remains after the thermal treatment at low temperature.

4.4.2.2 Thickness measurements

The study of the thickness of the different samples gives a clear definition between the three studies performed, each one with a different average thickness, namely: around a few tenths of nm (study 1), around 10 nm (study 2) and around 4-5 nm (study 3). The results of the latter are not presented due to the fact that these samples were much more prone to degrade to the point of having holes at temperatures much lower than 1200°C (around 700°C). For the two remaining studies, results will be separated between thin and thick samples, since the behaviour of the samples can be dependent on the sample thickness. The **thin samples** have been labeled $\mathbf{S}_1$ and $\mathbf{S}_2$ for the remainder of the study, and the **thick samples** have been labeled $\mathbf{S}_3$ and $\mathbf{S}_4$.

The results for the sample thickness for both thin and thick samples can be seen in Figure 4.47.

Three main regions of interest appear for the behaviour of thickness as we heat up the sample: 70°C- 85°C, 85°C-100°C and 170-200°C. These regions of interest are the same for the rest of properties measured. At 70-85°C we see, first of all, an elevated initial value for t, as well as a sudden drop when heating to 85°C in all samples. This behaviour has been linked to the presence of oxidative debris in the sample at the beginning of our study, which comes from the oxidation of graphite as well as the drop-casting deposition in the chip. At 85°C (for thin samples) or 100°C (for thick samples) we encounter a sudden raise of the samples thickness, followed by a drop at $\sim$ 115°C. This is thought to be caused by the desorption of physisorbed water (PW). This PW pushes against the different graphitic layers to get to be desorbed, causing the samples to grow in thickness (a feature much more observable for thick samples, which makes sense since the growth in thickness of the sample should be in accordance with the thickness of said sample). After the desorption of PW, the sample thickness starts going down again (115°C). This effect is

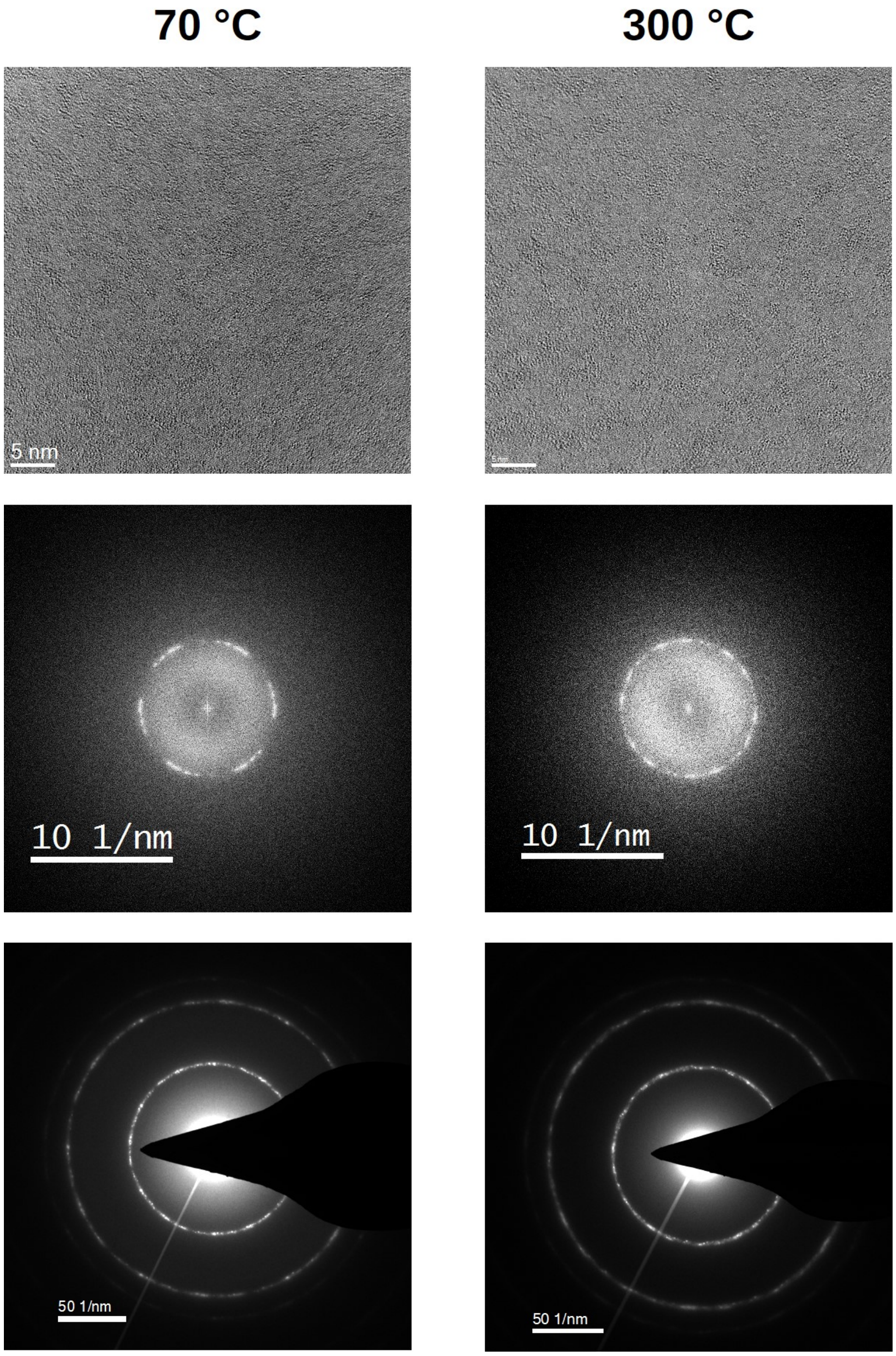

Figure 4.46: *From top to bottom: HRTEM micrographs, FFT of said HRTEM micrographs and electron diffraction images for the same area, taken at 70°C (left) and 300°C (right)*

also helped by the increasing of the degradation in these samples during or after processes that alter the carbon matrix, like the desorption of PW. A similar feature can be found in 180°C (for thin samples) and 190°C(for thick samples). The chemisorbed water (CW), as well as the OFGs it is attatched to, which are epoxides and carboxyl groups taking into account the bibliography [550]. The sample widens at first when the CW starts to desorb as it makes its way through

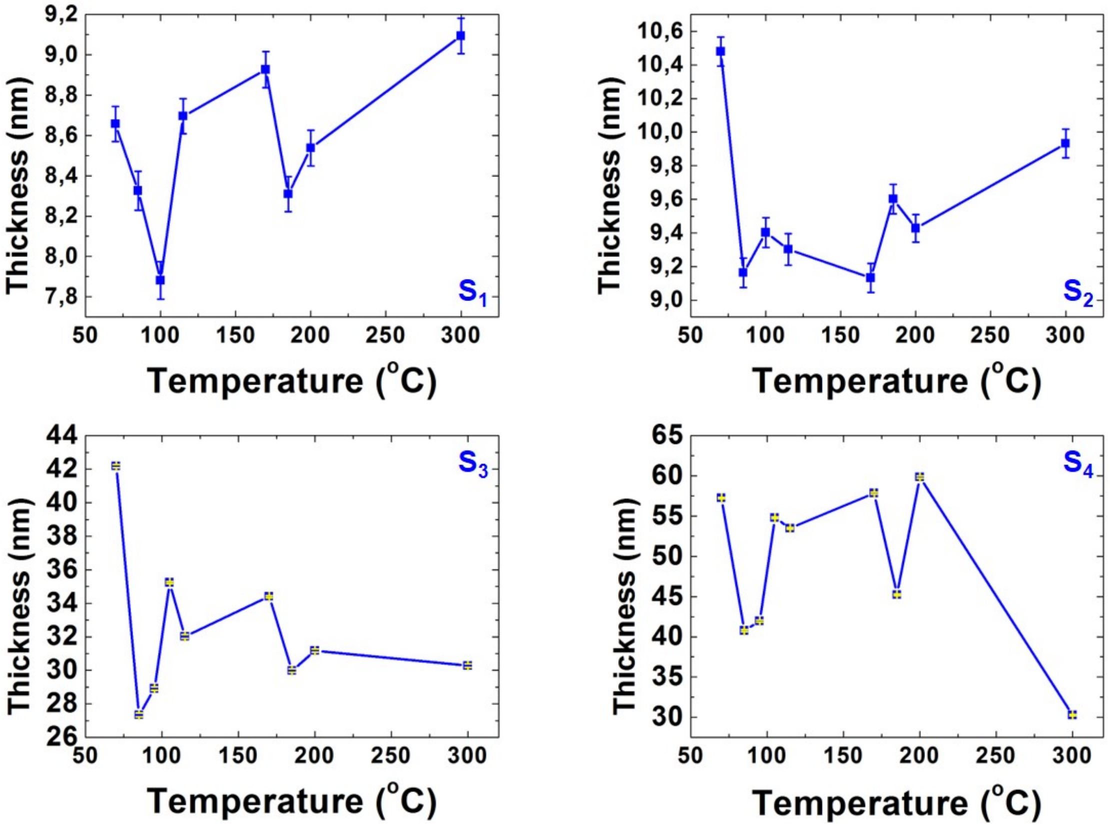

Figure 4.47: *Thickness estimation for the samples S_1 to S_4 for the temperature values in the low temperature regime.*

the graphitic layers. Once it has desorbed, at 190°C (for thin samples) and 200°C (for thick samples, the thickness goes back down. This decrease in thickness is also related to the fact that the presence of water in GO increases the interlayer distance of the sample, as we have seen in 4.1.3.2

4.4.2.3 Relative C content

The results for the [C]/[O] fraction can be found in Figure 4.48.

At first glance, there is a dip between 85°C and 100°C, corresponding to the degradation caused by the desorption of PW. When the PW desorbs, there is a raise in therelative C content at 100°C-115°C. At 170°C-185°C-200°C, there is a similar behaviour dure to the desorption of CW, epoxides and carboxyl groups. there is an initial dip due to the degradation caused by the desorption of CW and a raise (higher for the thinner samples) after the desorption of CW. this raise can be as high as a 4% for some of the thinner samples.

There is also a very big dip at 185°C for one of the samples (S_4). We initially thought it was due to the degradation of the sample due to the desorption of the CW. However, we have been measuring the amount of nitrogen and calcium there is in the sample, and for this particular spectrum the signal of the nitrogen shows 5 times the usual concentration of nitrogen. This has made us deduce that the spectra has not been taken where it shoud have (freestanding GO) but rather on the edge of the Si_xN_y membrane, which we had found to have a noticeable amount of oxygen content (see Section 4.2.1.1). This oxygen content would have falsely increased the relative amount of oxygen in the measurements, thus abruptly lowering the [C]/[O] fraction in

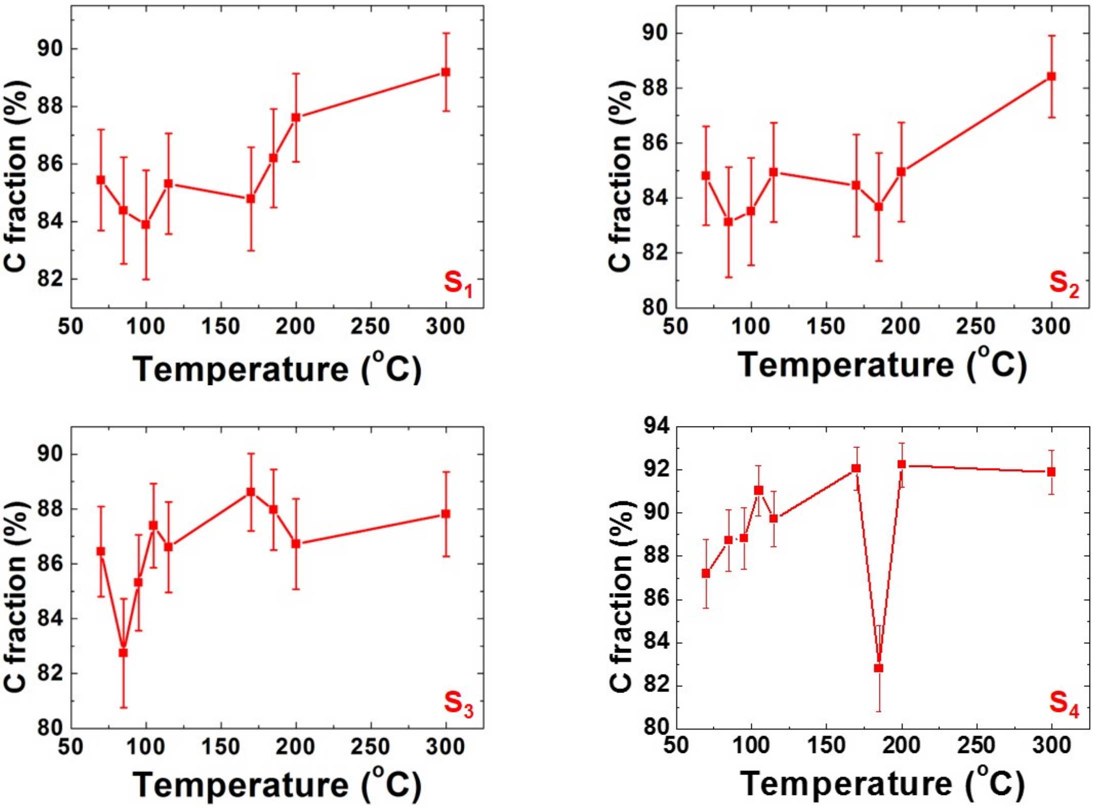

Figure 4.48: *[C]/[O] fraction for samples S_1 to S_4 for the different temperatures in the low temperature regime.*

turn.

This gives us a confirmation that all other EELS spectra recorded in this study have been successfully taken within the desired region of interest, that is, the holes in the membrane as the one shown in Figure 4.45. On top of that, this measurement has given us a clear signal of the spectrum of silicon in this kind of sample.

4.4.2.4 Mass density

Based on previous studies [65], the results for the mass density will give us an idea of how graphitic the material is, since more sp^3 bond content is known to have a lower amount of mass density [65, 551]. In this sense, GO should have a mass density ranging between somewhere near of the mass density of amorphous carbon (~1.8 g/cm^3[552, 553]) and that of graphite (2.27 g/cm^3 [554]). These results can be found in Figure 4.49.

At 70°C, there is an abnormally high initial mass density that, in some cases, even surpasses that of graphite. That can be attributed to the oxidative debris explained before in Subsection 4.4.2.2, but raises some questions about the composition and structure of this oxidative debris.

At 100°C, there is a dip in the mass density corresponding to the aforementioned degradation due to the desorption of PW that lowers the mass density of the material, in other words, makes it more amorphous. This dip is followed by a raise in mass density once the PW has been desorbed, indicating a small graphitisation after the desoprion of PW.

A similar feature occurs at 185°C-200°C due to the desorption of CW, epoxides and carboxyl groups. The raise in mass density after this desorption is specially high for the thinner samples,

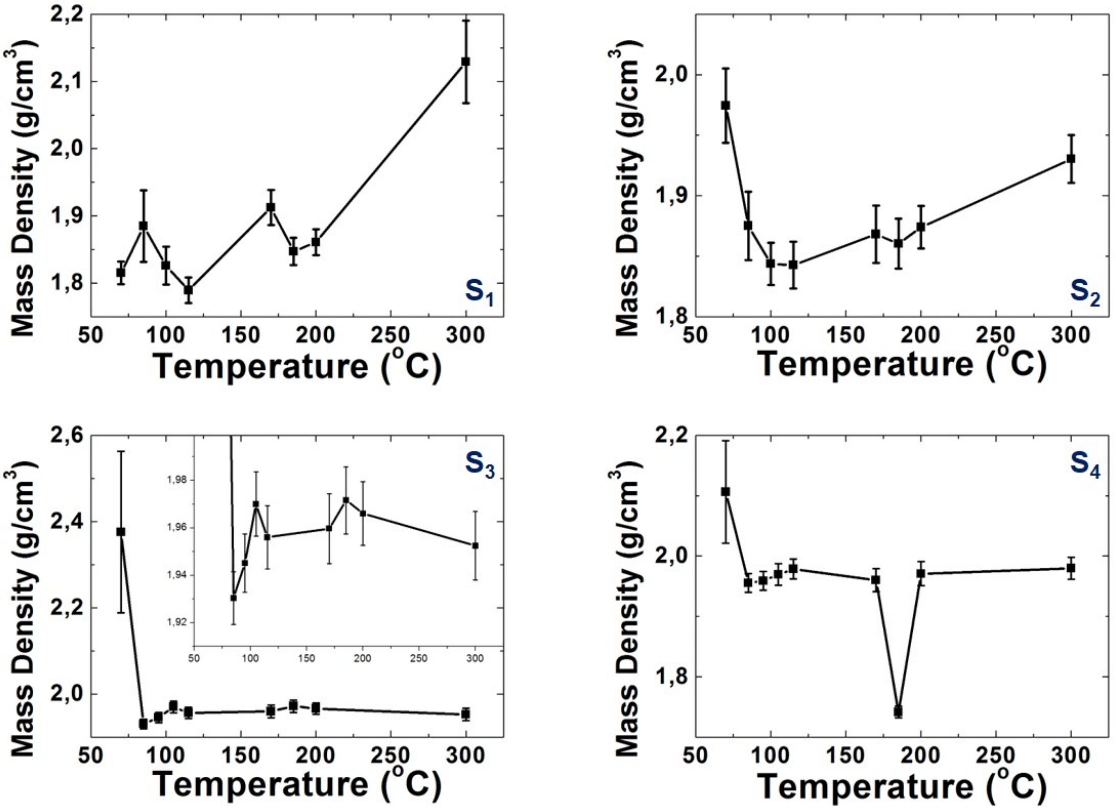

Figure 4.49: *Estimated mass density values of S_1 to S_4 for the different temperatures in the low temperature regime.*

getting to an astounding 14 %. this indicates an impressive transformation in the sample for temperatures as low as 300°C.

Additionally, there is a similar feature at 185°C for one of the thicker samples just as the one found in Subsection 4.4.2.3. This is coherent with the fact that we are measuring over the Si_xN_y membrane. The bulk density of Si_xN_y is around $\sim 3g/cm^3$. The mass density of thin films has proven to be lower [555], although no results have been found in the bibliography of a Si_xN_y membrane with a mass density as low as the values we have obtained.

However, it is important to notice that the method employed to measure the mass density is optimised to measure it on GO, as it has been explained in Section 4.2.3.1. This could imply that such a drastic change in the material being measured could yield a result lower than expected.

4.4.2.5 sp^2 fraction

The sp^2/sp^3 fraction of the C atoms in the GO samples is probably the most accurate measurement of the graphitisation of the sample, going further up as the sample becomes more graphene-like and decreasing in the event that the sample becomes more amorphous or less ordered in general. The results for this measurement can be seen in Figure 4.50.

Due to their sensitivity to the electron beam and their instability due to their thickness, these measurements are a bit challenging in thinner samples. They do not seem to increase the graphitisation in the slightest, having an almost identical initial and final sp^2 values. The thin sample represented on S_1 of Figure 4.50 seems to be the most affected by these phenomena, since no features can be seen due to the desorption of PW on this sample, which is clearly visible in

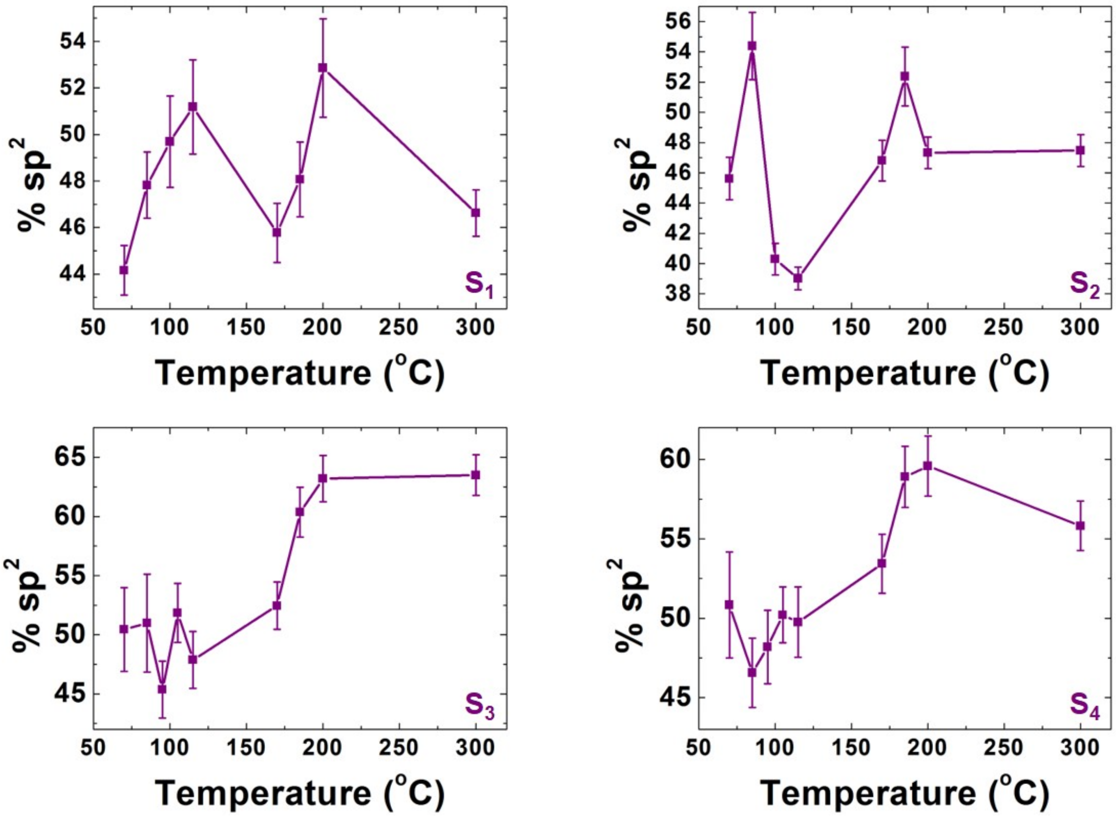

Figure 4.50: *sp^2/sp^3 ratio of the C atoms in the GO samples expressed as the % of sp^2 bound C atoms. This plot shows the results for the samples S_1 to S_4 at the temperature values on the low temperature regime.*

Figures 4.47, 4.48 and 4.49. There could be some sort of feature related to the desorption of CW (a dip followed by a steep raise at 170°C), but it seems to be in competition with a very intense degradation, which is cohesive with the low thickness of the sample. There are some really steep variations in the other thin sample (S_2 of Figure 4.50), getting to an astounding 16% decrease in sp^2 content at 100°C (probably due to the degradation due to the desorption of PW) amd a raise at higher temperatures that we can explain as two seemingly opposite effects happening at the same time: on the one hand, the graphitisation following the desorption of the CW, the epoxides and the carboxyl groups, and on the other hand the degradation in the sample, which is increased for thinner samples. At higher thicknesses, the behaviour of GO seems to be more homogeneous, at least for our experiments. As it can be seen in Figure 4.50, both spectra of thick samples show a very similar pattern. At 95-100°C, there is a dip in the sp^2 fraction that we attribute to the degradation before the desorption of PW mentioned in the previous sections. There is a slight raise right after that seems coherent with the desorption of PW and with the rest of the properties measured. The behaviour is slightly different for the desorption of CW, epoxides and carboxyl groups. It seems that in this case, these desorptions cause a very noticeable graphitisation of the sample, with increments over 15% in sp^2 fraction. it is noticeable that this graphitisation is less steep at 170°C, so that is where we locate the degradation caused by these desorptions, that do not appear as a decrease in sp^2 fraction because it is already competing with the graphitisation caused by it. It is also easy to notice that the measurement at 185°C in the S_4 sample in Figure 4.50 does not seem to be affected by the fact that, as it has been mentioned, in this particular measurement there has been a small portion of Si_xN_y membrane that has been measured along with the GO. The fact that the sp^2 content seems to follow the same behaviour as the sample with no Si_xN_y membrane in the measurements seems to point out that our explanation for the rest of the results at this temperature is correct. For all the samples, the change in sp^2 fraction between 70°C and 85°C varies greatly, which means we are not able to discern a specific value of sp^2 fraction for the oxidative debris present in the sample that has been mentioned in previous sections

4.4.2.6 Summary - low temperature regime

Based on the fine structure peaks in the spectra, and the evolution of the different properties measured, several ideas of what is going on in the sample can be taken:

- There is a clear presence of oxidative debris at the begining of our studies for both samples. This oxidative debris has a presence in the thickness of the sample as well as in the mass density of it.This debris desorbs at 85°C maximum and has probably been desorbing before the beginning of our experiments.
- The physisorbed water (PW) desorbs at $\sim$ 100°C. At the beginning of the desorption of the PW, there is a mesurable amount of degradation in the sample, which becomes more sensitive to the beam resulting in both an amorphisation of the sample and a desorption of the carbon in it.
- After the desorption of PW, the sample stabilises again.
- The chemisorbed water (CW) desorbs at $\sim$ 180°C.Similarly to PW, there is a mesurable amount of degradation in the sample at the beginning of the desorption of the CW
- After the desorption of the CW, the sample has a very noticeable amount of graphitisation, as shown in the mass density and sp^2 fracion of the samples after said desorption.

4.4.3 Low temperature: Cinematic study

For the thicker samples, a second study has been performed focusing on the behaviour of the sample over time at critical temperatures, in this case 100°C and 180°C, which are considered to be approximatively the two critical points where the PW and the CW desorb, in our case, 95 and 195 °C. For these temperatures, a second measurement has been made in the same areas 30 minutes after the first one, as shown in Figure 4.32. The results are not as many as for the previous study but it delves deeper into the main two temperatures of interest in the sample. In the following section, we present a comparative study between the measurements at t_0 (the ones we have shown in Section 4.4.2) and the measurements performed 30 minutes later for these critical temperatures.

4.4.3.1 Thickness

The representation of the thickness variation in the sample for this study can be seen in Figure 4.51.

The first thing that we can see is that the behaviour after 30 minutes in both samples seems to be quite coherent, following the same pattern. It is also coherent with respect to the different processes we have hypothesised for the evolution of GO at these temperatures.

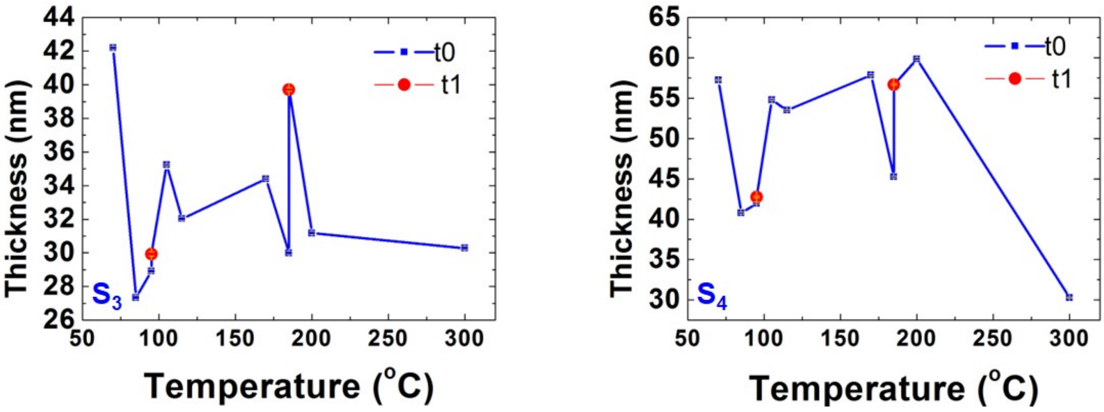

Figure 4.51: *Thickness estimation of the samples S_3 and S_4 for the cinematic studies performed in the low temperature regime. The measurements at t_0 are shown in blue, while the measurements at t_1 are shown in red.*

At 95°C, there is a very slight increase in thickness, but it barely gets to 1nm at best. It is not until the temperature of 115°C that the expansion produced by the desorption of PW starts to take in. This seems to point out that the actual temperature where the desorption of PW occurs is not 95°C, but actually a bit higher than that, which is very coherent from a plainly phyhsical point of view taking into account the boiling point of water is at 100°C.

However, it seems to be quite the contrary for the measurements at 185°C. Here, the raise in thickness due to the desorption of CW, epoxydes and carboxyl groups seems to occur at 185°C, as shown by the very impressive raise in thickness that can get to more than a 30%. After that raise in thickness, there is a decrease in it once most of the CW has desorbed. Taking the example of the sample shown in the left plot in Figure 4.51, it shows why it is of importance to perform these studies, since it provides new information of great interest.

4.4.3.2 Relative C content

The results corresponding to the [C]/[O] fraction for these cinematic studies can be seen in Figure 4.52.

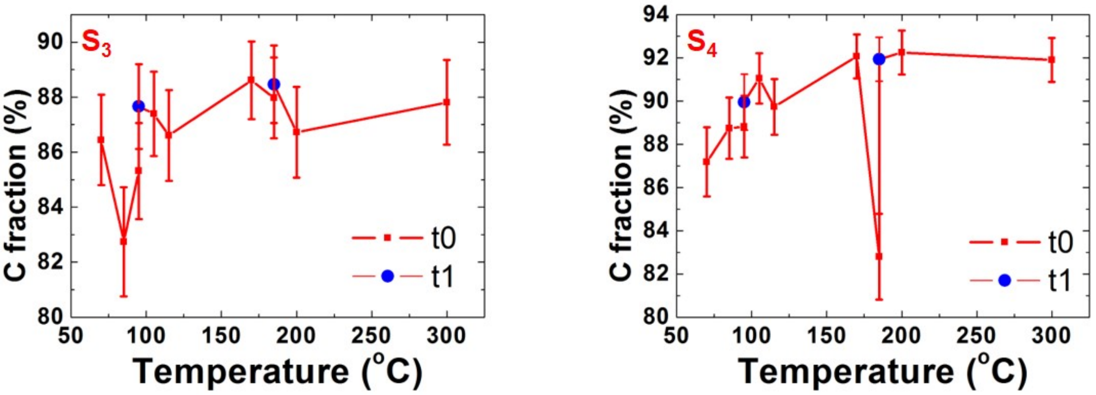

Figure 4.52: *[C]/[O] fraction estimation of the samples S_3 and S_4 for the cinematic studies performed in the low temperature regime. The measurements at t_0 are shown in red, whereas the measurements at t_1 are shown in blue.*

The results at 95°C seem to point out a decrease in oxygen content, which would be coherent with the desorption of CW at this temperature. However, the results from the thickness in Section 4.4.3.1 seem to point out that it is not until higher temperatures that the PW starts making its way through the samples and hence increasing their thickness. Nevertheless, both hypotheses would be able to coexist if the water being desorbed from the sample at 95°C were the one on the surface of the GO. This would decrease the amount of oxygen in the samples without compromising the overall thickness of the sample. Then, at 115°C, there is a raise in the thickness due to the PW making its way through the sample. This would, in turn, degrade the sample, which would be more susceptible to the electron beam, hence the decrease in relative C content at this temperature.

This hypothesis seems to be supported by what happens in the sample at 185°C. First of all, we should remember that the initial dip in the [C]/[O] fraction at 185°C for the sample on the right of Figure 4.52 is, as we have explained in previous sections, due to our measuring outside of the hole in the Si_xN_y membrane, which is corrected for the measurements 30 minutes later, so the behaviour of the sample is better shown on the S_3 sample. There is a slight increase in [C]/[O] fraction with the desorption of CW, which is consistent with the previous studies. The huge increase in thickness shown in Section 4.4.3.1 indicates a significant amount of degradation coming from the desorption of CW, epoxides and carboxyl groups. This should, in theory, make the samples more susceptible to the electron beam, hence the decrease in the [C]/[O] fraction, which would seem counterintuitive initially.

4.4.3.3 Mass density

The results for the mass density in the cinematic studies at low temperature can be seen in Figure 4.53. There are no significant changes in the mass density of the sample at 95 °C. However, there is a very clear feature for the S_3 sample at 185°C. There is a decrease in the mass density in the measurements 30 minutes later that amounts to almost a 10%.

Judging by the previous results in Section 4.4.2.4, one could think that once again we are measuring a portion of the Si_xN_y membrane along with our sample. However, there are no

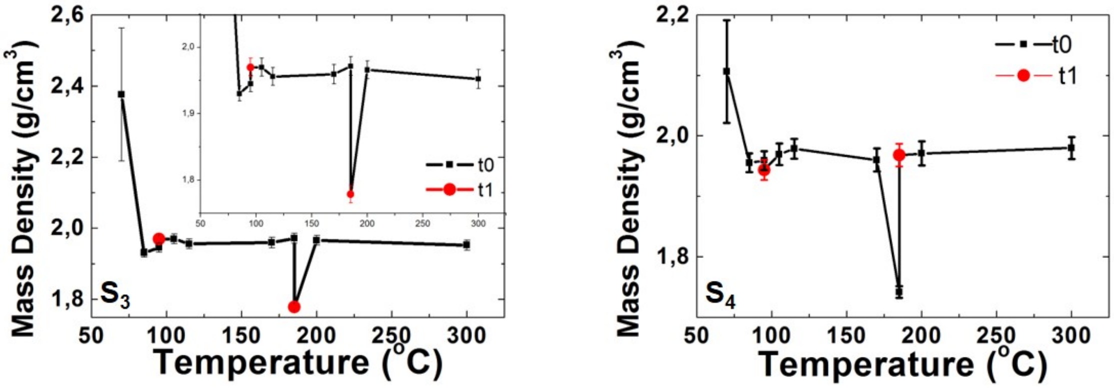

Figure 4.53: *Mass density estimation of the samples S_3 and S_4 for the cinematic studies performed in the low temperature regime. The measurements at t_0 are shown in black, whereas the measurements at t_1 are shown in red.*

sudden decreases in the [C]/[O] fraction, which would be what would happen if the measurements were not taken in the right area. This is what happened for S_4 in the measurements at t_0 (see Section 4.4.2.3) due to a presence of oxygen in the Si_xN_y membrane, as mentioned in Section 4.2.1.1.

An alternative theory would be that the desorption of CW, epoxides and carboxyl groups have caused a disruption in the structure of the GO, momentarily causing a very steep decrease of the mass density in the sample.

When it comes to S_4, what we infer from the behaviour of S_3 could mean, in principle, that the results for the mass density at 185°C in section4.4.2.4 might not have come exclusively from the mistaken measurement of a part of the Si_xN_y membrane, but also from the desorption of CW, epoxides and carboxyl groups as well.

This would explain why, for S_4, the measurements at t_1 at 185 °C show a mass density that is really close to the one estimated at t_0 for 170 and 200°C. If the desorption of CW, epoxides and carboxyl groups in S_4 happened at 185 °C before the measurements at t_1, the mass density in the sample could go back up once these OFGs were desorbed.

4.4.3.4 sp^2 fraction

The variation in sp^2/sp^3 fraction for these cinematic studies can be seen in Figure 4.54.

As it can be seen, there is a slight graphitisation at 95°C. Taking into account our previously mentioned hypothesis that, at this temperature, only the physisorbed water at the surface of the GO desorbs, this alone would not explain a raise in the sp^2 fraction. However, if a few OFGs in the surface of the GO desorbed as well at this temperature, that would definitely translate into a graphitisation of the GO. So our corrected hypothesis is that not only does PW desorb from the surface of the sample at 95°C but also a very small fraction of OFGs.

At 185°C, there is a decrease in the sp^2 fraction for both samples. This seems to be coherent with the amorphisation of the sample shown in Section 4.4.3.3, both of them being caused by the sensitivity of the sample to the beam after the disruption created by the CW, epoxides and carboxyl groups getting out of the sample; as well as the degradation that this sensitivity to the beam produces in the sample.

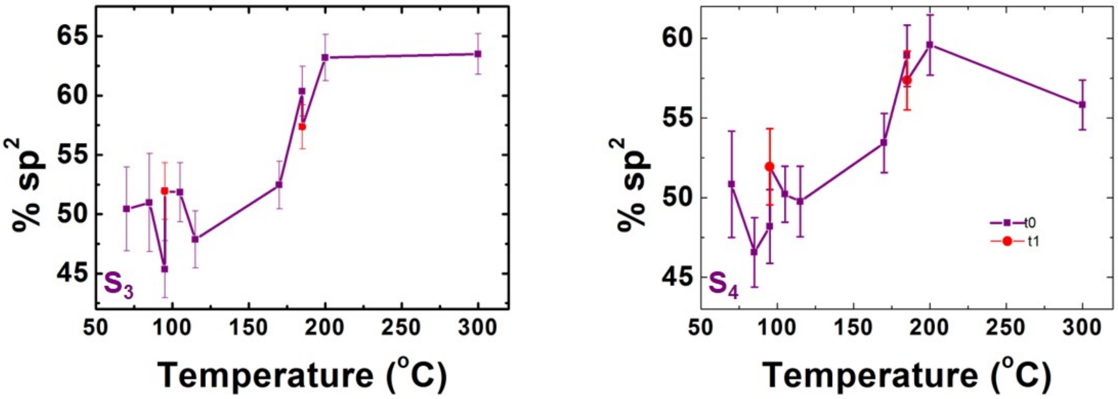

Figure 4.54: *sp^2/sp^3 ratio of the C atoms in the GO samples expressed as the % of sp^2bound C atoms. This plot shows the estimations for the samples S_3 and S_4 for the cinematic studies performed in the low temperature regime. The measurements at t_0 are shown in purple, whereas the measurements at t_1 are shown in red.*

4.4.3.5 Summary - Low T regime - Cinematic studies

This analysis might not seem vast in terms of gathered data, but it provides information that is of great interest for these studies:

- At 95 °C, there seems to be a desorption of PW from the surface of the GO but not the rest of the physisorbed water in the sample. This would explain the lack of expansion at this temperature, the raise in [C]/[O] fraction an the fact that the mass density stays the same between the measurements at t_0 and t_0+30 min. Small desorption of some OFGs in the surface of the GO might be desorbing as well, judging the raise in the sp^2fraction between both measurements.

- at 185°C, we seem to "catch" the expansion of GO due to the desorption of CW, epoxides and carboxyl groups in tall its splendor. There is a very important raise in thickness, along with a very stron decrease of the mass density and a small decrease of sp^2 that seem to point that way. The lack of an increase in the [C]/[O] fraction is explained by the fact that, at the same time as the desorption, there is also a non-negligible amount of degradation affecting the sample.

4.4.4 High temperature studies

This section focuses on the behaviour of the samples in the studies that go up to high temperatures after overnight rehydration, where the sample was put out of the microscope overnight at room conditions. This focuses on the readsorption of the PW, the success of the desorption of the CW during the low temperature studies, and the general reduction and graphitisation of GO. The specific temperatures for these studies can be found in Figure 4.31.

4.4.4.1 TEM imaging

On top of the uses mentioned in Section 4.4.2.1, HRTEM imaging has also served us in this study to identify the formation of some sort of crystalline nanoparticles on our GO, starting at 900°C. Figure 4.55 shows these micrographs, where these crystalline particles can be clearly shown. By comparing the electron diffraction pattern at 500 and 1200°C, as shown in Figure 4.56, this formation can also be observed. A new diffraction pattern appears, with a different interplanar spacing than that of graphite.

A closer inspection of our HRTEM micrographs show that this second diffraction pattern appears exclusively on the regions in the sample where the nanoparticles appear, which makes us assume they are the cause of this different structure. An example of this analysis can be seen in Figure 4.58

EELS data can also be used for the chemical identification of these nanoparticles in order to further understand them. As it has been mentioned in Sections 4.4.2 and 4.4.3, there is one point in one of the low temperature studies where a section of the $Si_xN_y + SiO_2$ membrane has been accidentally measured. This is not adequate for the temperature study itself, but it does give us a Si reference sample in this particular context.

This spectrum has shown to have intensity in the spectral region corresponding to the Si L_{2-3} edge as well as the Si L_1 edge of the EEL spectrum. if we compare this spectral region to the one measured in the GO spectra at 1200°C, it is quite clear that there is some sort of Si in both samples, although it seems to be in a rather low concentration. These spectra can be seen in Figure 4.57

This, along with the crystalline behaviour of the particles, seem to point out that we have nanoparticles of silicon carbide on top of the GO flakes, probably coming from some sort of sublimation from the membrane itself.

The low amount of Si seems to point out that the nanoparticles make up a very small part of the sample, so we have concluded that they do not interfere too much with our study, besides a very small underestimation of the O content and a slight overestimation of the sp^2 ratio.

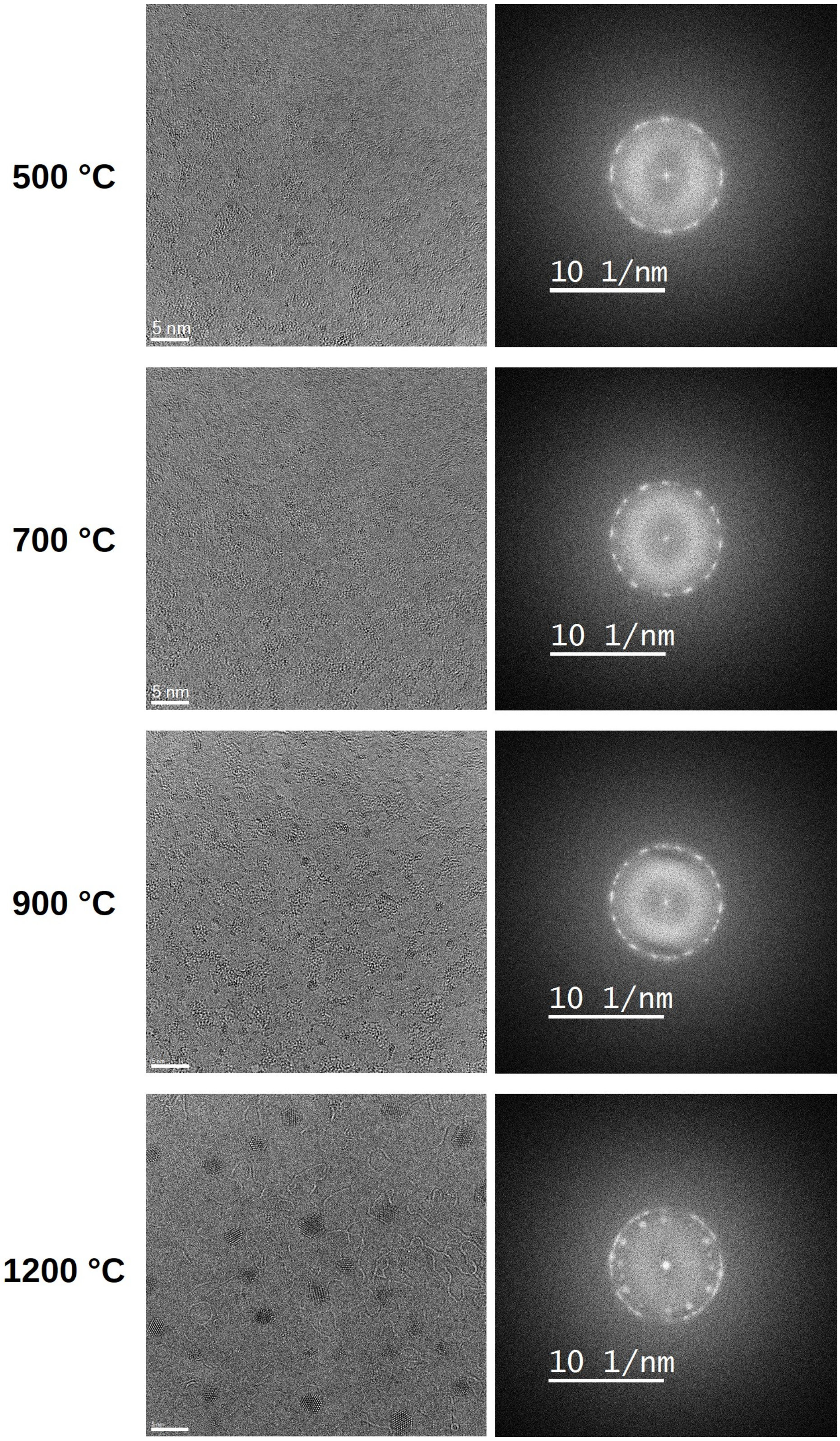

Figure 4.55: *From left to right: HRTEM micrographs and FFT of said HRTEM micrographs for the same area, taken at 500°C, 700°C, 900°C and 1200°C, respectively. The progression shows the formation of a certain sort of nanoparticle from 900°C on.*

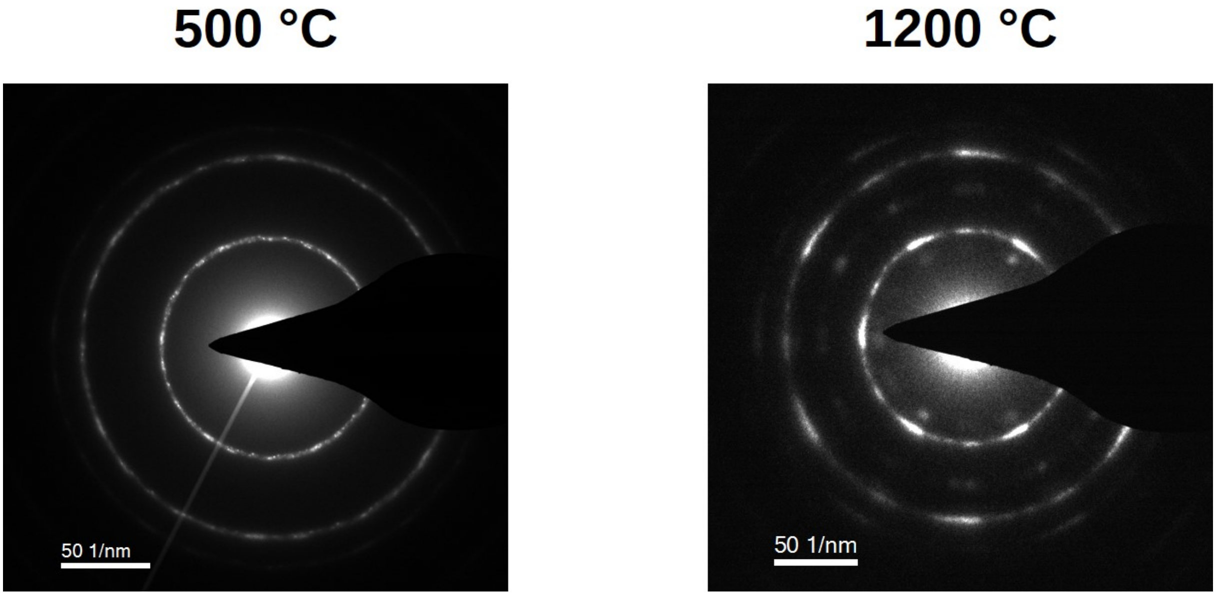

Figure 4.56: *Electron diffraction patterns of the same area of the sample at 500°C (left) and 1200°C (right).*

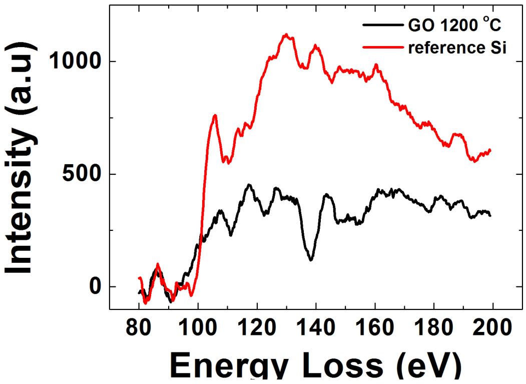

Figure 4.57: *Spectra comparison in the Si region between a spectrum of the GO sample at 1200°C and our Si reference spectrum. Both spectra seem to be in good agreement.*

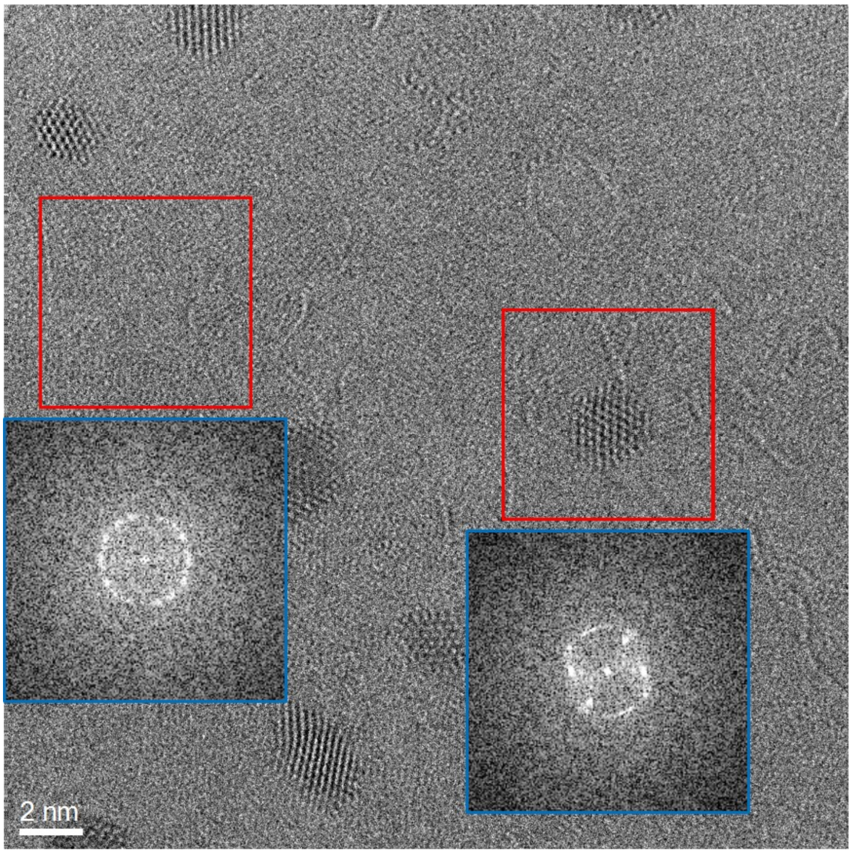

Figure 4.58: *HRTEM micrograph of the GO sample at 1200 degrees, showing several crystalline nanoparticles. FFT have been performed to the two selected areas (red), one with a nanoparticle in it and one without. The spots seen in the diffraction pattern in Figure 4.56 can only be seen for the region of interest with a nanoparticle in it.*

4.4.4.2 Thickness

The results for the variation of the thickness in the high temperature studies can be seen in Figure 4.59.

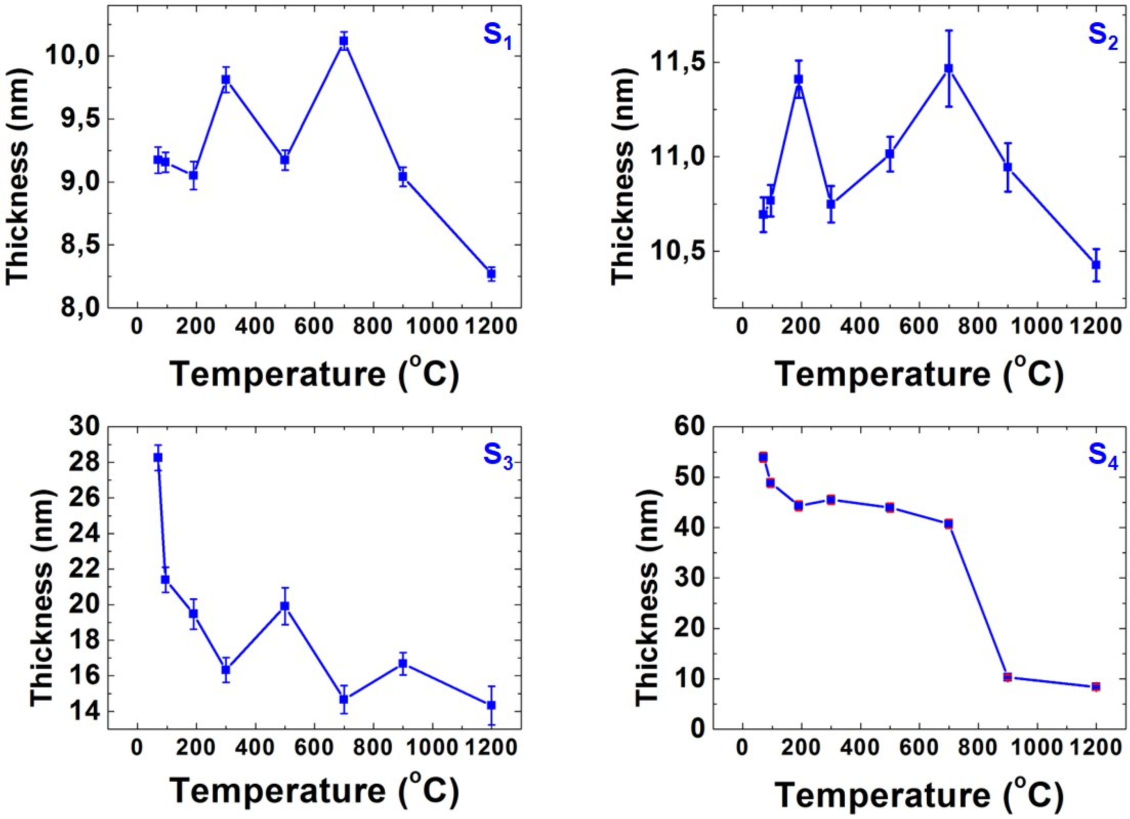

Figure 4.59: *Thickness estimation for the samples S_1 to S_4 for the temperature values in the high temperature regime.*

First and foremost, the main feature that can be seen at plain sight before a more detailed analysis is a very noticeable drop in thickness for all of the samples, getting to more than a 10% for the thinner samples and to more than a 80% for the thicker samples. This drop in thickness may have two different reasons to happen, at least according to our hypotheses. On the one hand, the desorption of the different OFGs can break the structure of the graphitic planes of the GO, making them a lot more vulnerable to the electron beam, according to the bibliography [556]. This can result in the desorption of carbon from the sample. On the other hand, we know for a fact that the OFGs in the GO increase its interlayer distance by a great deal, almost doubling it [416, 419, 557], which would make the thickness drop when desorbing these OFGs. Our take on it is that both reasons probably play a role in the drop of thickness in this study.

At a closer scale, we see different features depending on the initial thickness of the sample. At the lowest temperatures, we see a drop at 95°C for thicker samples (S_3 and S_4), as well as one of the thinner samples(S_1). We understand this initial drop in thickness as initial degradation before the desorption of PW. This desorption translates into an increase in the sample thickness that seems to occur at 100°C, but it is only visible for one of the thinner samples (S_2).

The degradation due to the desorption of the CW at 180°C can be seen not only for the thicker samples (S_3 and S_4), but one of the thinner samples as well (S_1) as a decrease in thickness after the desorption of CW and epoxides. This is coherent with the analysis of the fine peak structures with respect to the C-O bonds in the C-K edge, and they seem to indicate that the epoxides are not completely desorbed at 300°C in most cases, which provides a mean for the CW to be reabsorbed into the sample when left overnight at ambient conditions.

At 300°C, there is a dip in the thickness for the samples on the S_2 and S_3 samples of Figure 4.59. This should be due to the degradation caused by the desoprtion of ketones in the sample according to our analysis of the fine structure peaks in Section 4.4.1. In the case of the S_1 sample, there are two main options for the increase in its thickness: either the desorption of CW and epoxides happens at pretty much the same temperature, which makes it impossible to observe this phenomenon; or the desorption of ketones happens at a lower temperature for this sample because of its lower thickness, coinciding with the desorption of CW and epoxides. As for the S_3 sample, the thickness continues to decrease as the epoxides in the sample finally desorb.

At 500°C, for the S_1 sample, there is a decrease in thickness probably coming from the desorption of several OFGs, so we take the second hypothesis explained in the previous paragraph as the true one. This would mean that at this temperature, the CW, ketones and epoxides desorb. At the same time, for the thicker samples, it is now in this samples that the ketones start to desorb, resulting in a thickness increase of almost a 20% that can be seen in the S_3 sample in Figure 4.59.

At 700°C, there is a general raise in thickness for the thinner samples, corresponding to the beginning of the desorption of alcohols. At the same time, for thicker samples, there is a decrease in thickness probably caused by the desorption of ketones.

At 900°C, the alcohols seem to be desorbing well for thinner samples. That is what we gather from the decrease in thickness from the top plots in Figure 4.59. This seems to be the case, as well as an important amount of degradation, for the S_4 sample, which goes through a shrinkage of more of a 75% in a temperature span of 200°C. As for the S_3 sample, there is an increase in thickness showing that, for this sample, it is now where the alcohols start to desorb resulting in a "swelling" of the sample.

Finally, at 1200°C, there is a general decrease of the thickness of the samples, partially due to degradation from the beam at high temperatures and sublimation, and partially due to the final desorption of alcohols, leaving a quite clean carbon matrix. As it had been mentioned in Section 4.1, the OFGs inbetween the graphitic layers increase the interlayer distance considerably, so it is expected that the thickness value will go down once said OFGs are desorbed.

4.4.4.3 Relative C content

The results for the [C]/[O] fraction at high temperatures can be found in Figure 4.60.

The first piece of data that we can gather from these results is the effectiveness of the thermal reduction in terms of desorbing all the oxyger from the GO. This results in an oxygen fraction under 2% for every single sample.

The path to get to that reduction seems to be similar for most samples, even though there are clear differences.

At 95°C, there seems to be a slight reduction in the [C]/[O] fraction, probably caused by the degradation caused by the desorption of PW, which is coherent with the results of Section 4.4.4.2. This does not happen for one of the thinner samples (S_2 in Figure 4.59).

There is a disparity in behaviour at 180°C. Whereas the thinner samples have a rather steep 2-3% raise in [C]/[O] fraction, the thicker samples have either a decrease (S_3 sample) or a very slight increase (S_4 sample). This can be interpreted as degradation caused by the desorption of CW in different concentrations (a higher one on the left and a lower one on the right). It is important to notice that the sample that does not have a decrease in the [C]/[O] fraction at this temperature, and it did not have it either in the low temperature studies (see Figure 4.48).

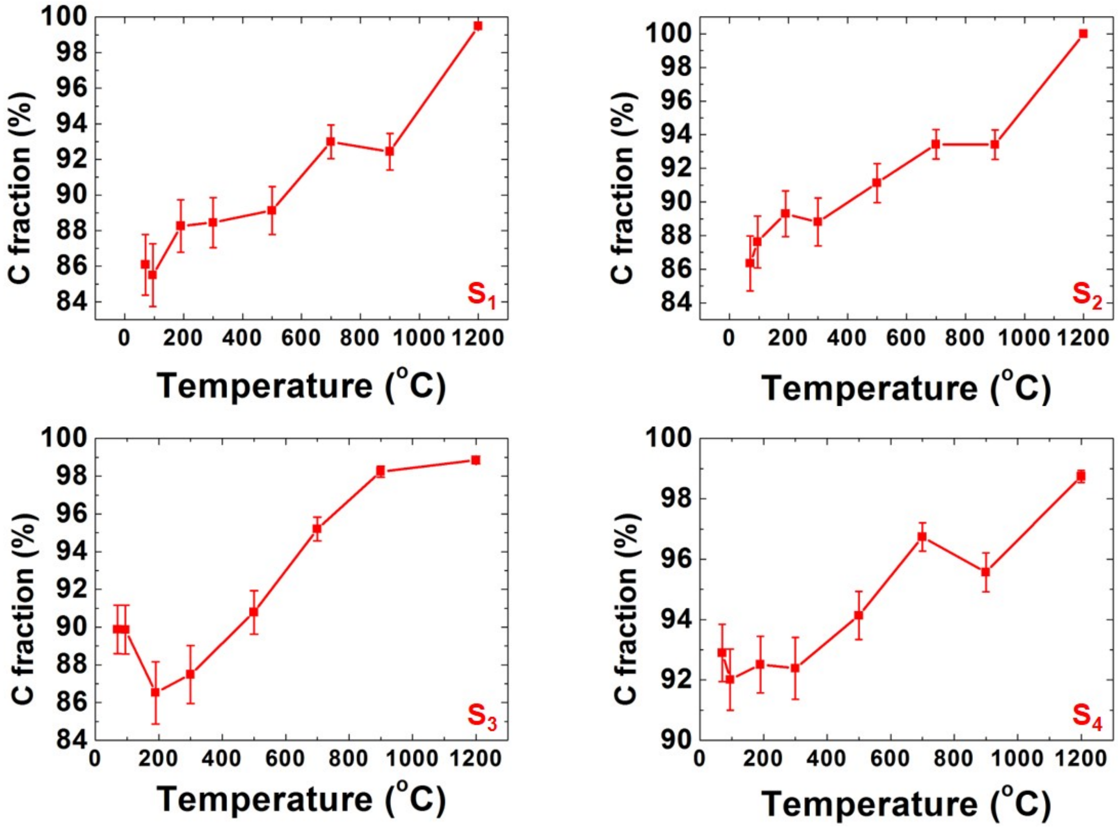

Figure 4.60: *[C]/[O] fraction for samples S_1 to S_4 for the different temperatures in the high temperature regime.*

This can be due to a chemical composition with less epoxides and carboxyl groups, which would yield a lower absorption of CW. This is coherent with the chemical inhomogeneity present in GO. As for the S_1 sample, which we have hypothesised to have at least a small portion of CW and epoxides, the raise in [C]/[O] fraction is almost the same as the one not thought to have CW. This make us hypothesise that maybe for these samples the temperature of desorption for CW is slightly lower than for thicker samples.

The desorption of ketones at 200-300°C does not seem to be very visible in terms of variations of the [C]/[O] fraction of the sample. This can be due to the degradation caused by the desorption of ketones and the desorption of CW and epoxides being very close in temperature, so their effect on the [C]/[O] fraction sort of neutralise each other.

At 500°C, there is a general increase in the [C]/[O] fraction that seems to be coherent with our hypothesis in Section 4.4.4.2 that at this temperature, the CW, epoxides and ketones desorb. It seems that, even for thicker samples, the raise in the [C]/[O] fraction shows that, even if there is some sort of degradation coming from the desorption of ketones, it is masked by the general reduction taking place at this temperature. This general increase in [C]/[O] fraction continues at 700°C.

At 900°C, there seems to be a slight decrease for most samples in the [C]/[O] fraction. This can be due to several causes, like a slight sublimation of the sample at these high temperatures, the desorption of OH and the degradation it causes to the sample or a higher sensitivity to the beam at these higher temperatures

Finally, at 1200°C there is a general increase of the [C]/[O] fraction, getting to levels close to 100%. This increase also supports our hypothesis about the composition of the nanoparticles appearing on the GO (see Section 4.4.4.1) being SiC particles. This would increase the ratio of carbon in the sample.

4.4.4.4 Mass density

The results for the mass density of the GO samples at the temperatures in the high temperature regime can be seen in Figure 4.61.

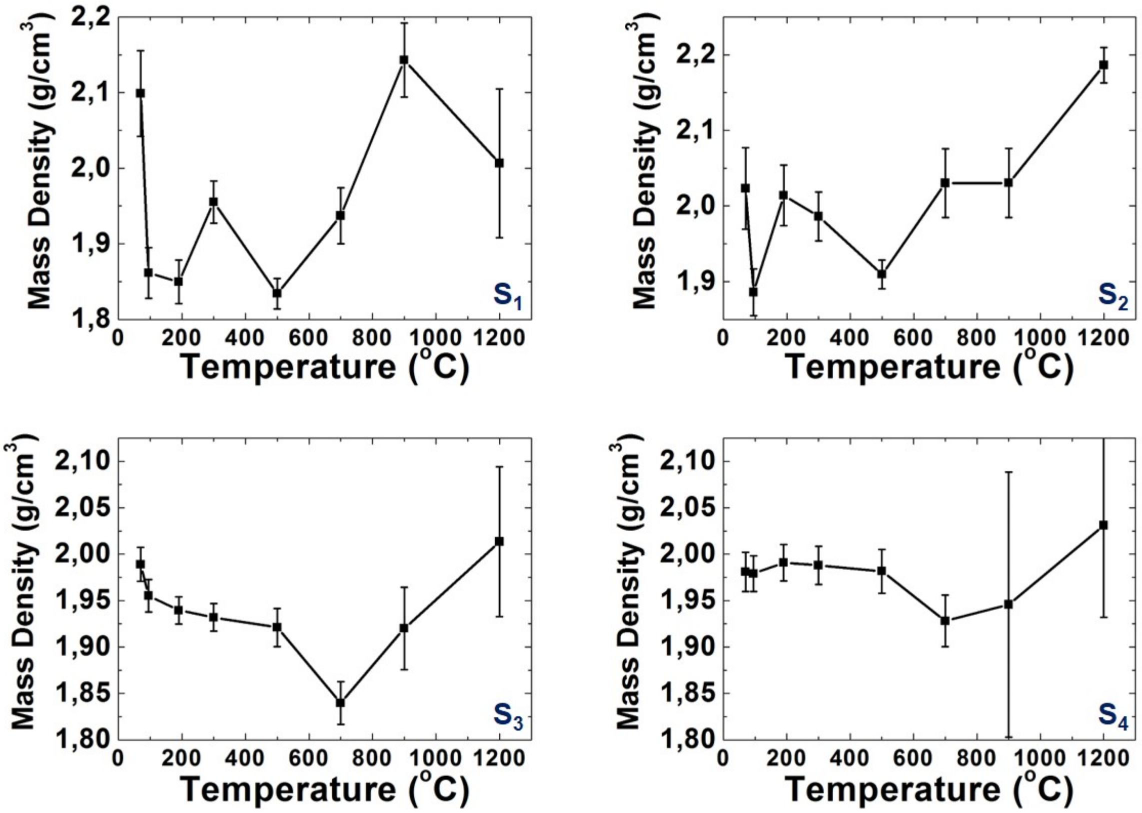

Figure 4.61: *Estimated mass density values of S_1 to S_4 for the different temperatures in the high temperature regime.*

It is easy to see that these results are the least accurate of the whole study, so the hypothesis derived from this will have to be taken accordingly. However, we can also see that, at least for one of the samples, we have achieved a mass density of almost $2.2 g/cm^3$, which according to the bibliography [554] is very close to the mass density known for bulk graphite. This seems to point out that, at least in some of the cases, the reduction and graphitisation seems to have been a success.

The behaviour of the mass density at for thicker samples is tricky to interpret, since the variation between 100°C and 500°C is smaller than the incertitude of the measurement performed. However, that is not the case for the rest of the measurements.

There is a general dip (steeper, with some decreases bigger than a 10%) of the mass density at 95°C. this seems in good agreement with our hypothesis that the PW readsorbs overnight and desorbs at ~100°C.

At 185°C, the only noticeable changes in the mass density come from the thinner samples. In one of them (S_2 in Figure 4.61, there is a clear raise in the mass density, which is consistent with the desorption of PW and a lack of CW, epoxydes or carboxyl groups. However the other one does not really experience a variation of the mass density at this temperature, which could be caused by the presence of CW in the sample or a higher sensitivity to the beam (since it is, as we have seen in Section 4.59, the thinnest sample of the ones in this study).

At 300°C, there is a raise in the mass density only for the S_1 sample, which seems to be coherent with the sample either having CW present at the beginning of the study or a higher sensitivity to the beam, taking a longer time to anneal.

At 500°C for thinner samples, and at 700°C for thicker samples, there is a decrease of the mass density that we attribute to an amorphisation caused by the degradation due to the desorption of ketones.

At 900°C, there is a general increase of the mass density. Our interpretation of this feature is that the degradation caused by the desorption of alcohols is less important in terms of mass density than the graphitisation due to the annealing temperatures and the desorption of the rest of the OFGs.

Finally, at 1200°C, there is a general raise in the mass density, caused by the general graphitisation after the desorption of alcohols and also due to the annealing temperatures, that allow the carbon material to graphitise.

4.4.4.5 sp^2 fraction

The results related to the sp^2/sp^3 fraction of the samples at high temperature can be seen in Figure 4.62.

The first general conclusion that we can gather from these results is that the graphitisation of the sample is a complete success, with over a 20% increase in sp^2 fraction at least and an astounding 45% at most, getting to values that can reach almost a 90% of sp^2 bonds in carbon. We can see as well that, even though the final values of sp^2 are different for each sample, in general terms, the behaviour among thin samples and among thick samples is roughly the same.

At 95°C, there is a dip in the sp^2 fraction for thin samples, whereas for thick samples there is an increase of said fraction. Judging by the rest of properties measured, it is reasonable to assume that, for all four samples, there is a presence of PW that desorbs at $\sim$100°C. The fact that the sp^2 decreases for thinner samples and increases for thicker samples suggests that, for thinner samples, the desorption taking place comes from the whole of the sample, producing a bigger disruption in the carbon matrix and therefore a bigger amount of degradation. For their thicker counterparts, these results could indicate that the PW being desorbed at 95°C could be located on the surface of the sample or a few layers into the sample, producing a lesser amount of degradation when desorbing. This would also explain the much bigger decrease in thickness shown for this temperature in Section 4.4.4.2.

At 190°C, there is a clear dip for thicker samples that does not appear for thinner ones. Assuming this amorphisation of the sample is caused by degradation produced by the desorption of CW, epoxides and carboxyl groups, this would be in agreement with a lack of CW and either epoxides, carboxyl groups or both in the thinner samples, and a presence of such in the thicker samples.

There is a small dip at 300°C for the S_2 sample that does not appear in the S_1 sample. This seems coherent with our hypothesis, previously established in Section 4.61, that the ketones in the thinner sample (S_1) desorb at a temperature above 300°C, while for thinner samples this desorption starts happening at 300°C, hence the amorphisation caused by the degradation of the sample.

From these temperatures and up, the sp^2 fractions seems to increase generally for all the samples. From this, we interpret that the graphitisation due to the desorption of the different

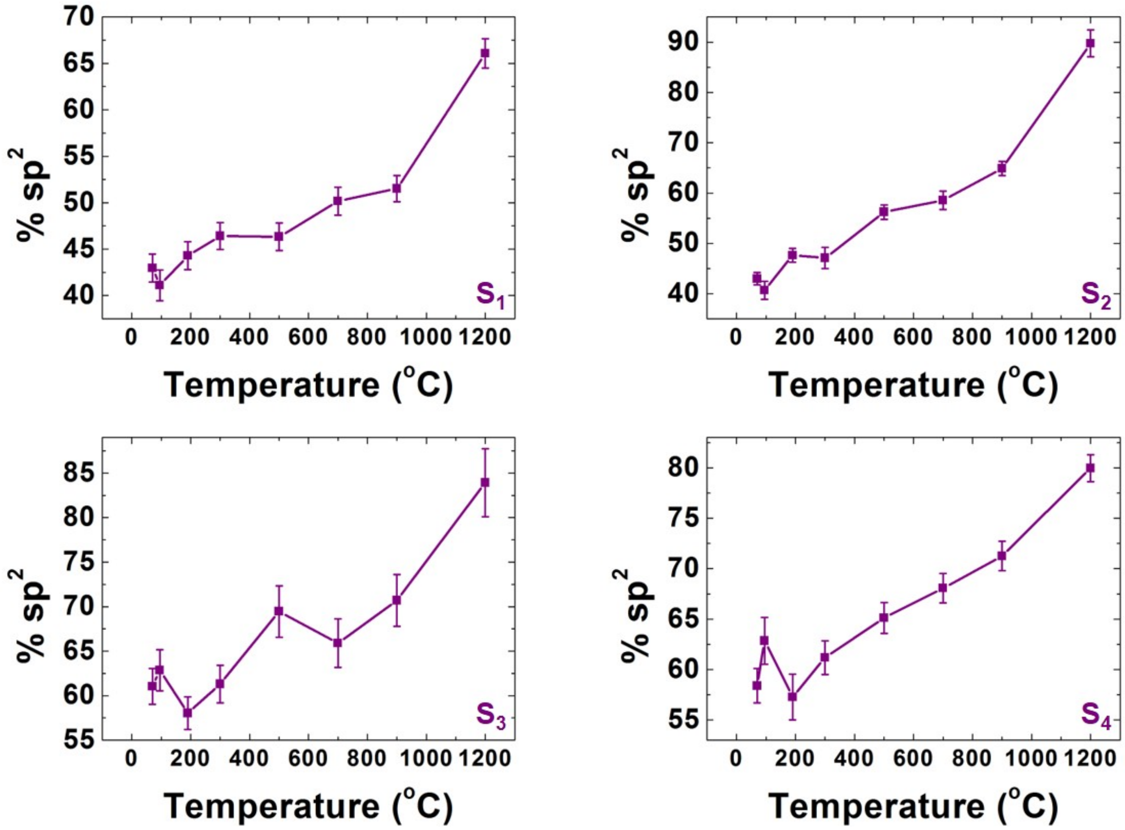

Figure 4.62: *sp^2/sp^3 ratio of the C atoms in the GO samples expressed as the % of sp^2 bound C atoms. This plot shows the results for the samples S_1 to S_4 at the temperature values on the high temperature regime.*

OFGs is stronger than the amorphisation due to the degradation of the sample. However, this amorphisation can still be quite high for some samples, such as the S_1 one. This is reflected in its low final sp^2 value at 1200°C, as well as the decrease of its mass density at high temperatures (see Figure 4.61.

There is only one exception for this general increase in sp^2, which is the dip at 700°C for the S_3 sample. The interpretation we gather from this, along with the abovementioned measurements on these samples, is that, for this sample, the degradation caused by the desorption of ketones (which has also been deduced from its mass density in Section 4.61) is higher than the graphitisation caused by the annealing and the desorption of the different OFGs at this temperature, which is not the case for the rest of the samples.

4.4.4.6 Summary - High temperature regime

Several conclusions can be drawn from these high temperature studies:

- With respect to physisorbed water, it seems quite clear that it has reabsorbed overnight when taking the sample out of the microscope. This is especially visible for the thinner samples.

- As for chemisorbed water, it is unclear whether it is reasorbed or not for the thinner samples, but it is quite clear that it is reabsorbed into the thicker samples. This points out that the desorption of epoxides and carboxyl groups on the studies performed in sections

4.4.2 and 4.4.3 might not have been complete, especially epoxides for which we seem to see a weak ELNES feature.

- The ketones in the sample seem to have different desorption temperatures depending on the thickness of the sample, desorbing between 300 and 500°C for thinner samples, and between 500 and 700°C for thicker samples.
- The desorption of hydroxyls seems to have a similar path: whereas for the thinner samples it starts around 700°C, for thicker samples it does so at 900°C.
- Some of the samples achieve, at 1200°C, characteristics that are really close to those of graphene in terms of [C]/[O] fraction, mass density and sp^2 fraction.

4.4.5 High temperature regime: Cinematic study

We have also performed cinematic studies at high temperatures, as previously mentioned in Section 4.3.2. For the thinner samples, the studies will focus on the behaviour of the samples at 500 and 700°C, a region of interest where we are not completely sure of what is going on. The measurements for the cinematic study have been performed at a time t_1 30 minutes after the initial measurements. As for the thicker samples, they have been subjected to a thorough cinematic study with measurements at different times for all of the temperatures measured. At low temperatures (95 and 190°C) there has been a second measurement taken at a time t_1 45 minutes after the initial measurement and a third measurement taken at a time t_2 90 minutes after the initial measurement. For high temperatures (300, 500, 700, 900 and 1200°C), there has been a single measurement taken at a time t_1 30 minutes after the initial measurements. The results of these analyses are shown in this section.

4.4.5.1 Thickness

The results regarding the thickness of the samples for these cinematic studies can be observed in Figure 4.63.

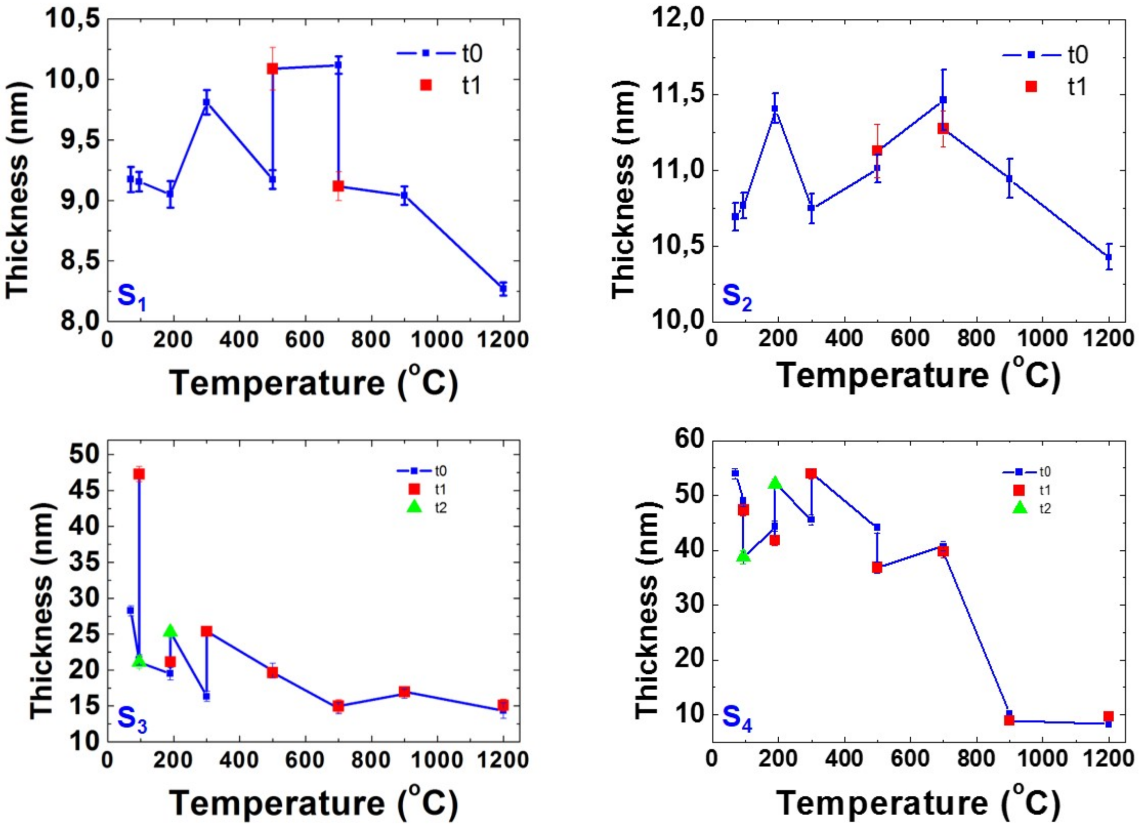

Figure 4.63: *Thickness estimation of the GO samples for the cinematic studies performed in the high temperature regime. The measurements at* t_0 *are shown in blue, while the measurements at* t_1 *are shown in red and the measurements at t2 in green.*

Thinner samples The analyses for thicker samples coincide among both samples: they both have an increase of their thickness at t_1 at 500°C, followed by a decrease at t_1 at 700°C.

Judging by the reasoning employed in previous measurements (see previous experimental sections), this would lead us to think there is some OFG that desorbs at 500°C that we have missed. However, as it will be seen in sections 4.4.5.2, 4.4.5.3 and 4.4.5.4, this expansion comes along with an increase inrelative C content, an increase in mass density and an increase in sp^2 fraction in the S_1 sample, all of which suggest the opposite of the beginning of desorption, judging by the results for all of the rest of the experiments. Our current hypothesis on the matter is simply that, at this temperature, there is an annealing of the sample as it desorbs some of its OFGs (probably some epoxide groups that had not been desorbed yet, as well as ketones, which start desorbing at 300°C), but since we do not have any electrom beam irradiation during this process (we suppose it happens between t_0 and t_1), we do not have the degradation we had before.

At 700°C, the sample decreases in thickness over time. In the rest of these studies, we have interpreted that as the end of the desorption of a certain OFG, but in this case, the values of carbon content and mass density seem to indicate otherwise, with a decrease in both at this temperature that has previously been related in this work with an amorphisation due to degradation. Our hypothesis is that, at this temperature, at least for thinner samples, the alcohol OFGs start to desorb, but they do not produce an increase in thickness, probably due to the general sublimation taking place at this temperature.

Thicker samples At 95°C we see two different behaviours in the samples, which we think correspond either to two different ways PW desorbs in our samples, or to two different moments in the desorption.

On the one hand, the S_3 sample experiences a huge increase in thickness, more than doubling in size at t_1 and then coming back to the exact same thickness at t_2. This seems to indicate that the increase in sample thickness due to the desorption of PW can be a lot higher than we expected, albeit not constant in time at all. It seems this measurement has been in the peak of said increase.

However, for the S_4 sample, the thickness measured at t_1 is pretty much the same as in t_0 and the thickness measured at t_2 is almost a 20% lower. Judging by the intense decrease inrelative C content, mass density and sp^2 fractions at t_1 for this sample, that we will delve deeper into in sections 4.4.5.2 4.4.5.3 4.4.5.4 , this seems to be a counterpart for the behaviour we have just seen in the previous paragraph. The apparent lack of change in the thickness, along with these decreases, seems to point out a desorption of PW where the water is breaching through the graphitic layers, degrading a lot more carbon than it is desorbing oxygen. After that, at t_2, it goes back to its previous C levels, mass density and sp^2 fraction, which could indicate a complete desorption of the PW.

We have established two main hypothesis regarding this difference in behaviour. Our first hypothesis is that the difference in thickness (the initial thickness of the S_3 sample is almost half of the S_4 sample) or in general composition (due to the inhomogeinity of the sample) make the samples behave differently with respect to the desorption of their PW.

Our second hypothesis is that both undergo the exact same process, just at different speeds, again due to their difference in thickness or in composition. This hypothesis sustains that the sample has two very specific moments during the desorption of PW: a first moment where the PW pushes against the graphitic layers, greatly increasing the sample thickness, and a second moment where the water finally pushes through the graphitic layers, producing a great deal of degradation.

At 190°C, we have an increase for both samples from t_0 to t_2, with S_4 taking a little longer than S_3. We have previously associated this with the beginning of the desorption of CW and epoxides.

At 300°C, we have a clear increase in thickness from t_0 to t_1 for both samples. This could indicate that the desorption of ketones might start at temperatures even lower than we thought, starting at t_1 at 300°C with the characteristic increase in thickness and then going down as it desorbs. For the S_4 sample, this also would happen between t_0 and t_1 at 500°C.

The analysis of the samples show a pretty stable behaviour for temperatures of 500°C or higher for one of the samples (S_3) and for temperatures of 700°C or more for the other one (S_4). However, this is only if we take their variation in thicknes with respect to their actual thickness, since the absolute value of the variations in thickness is quite close to that of the thinner samples at these temperatures (∼ 1-2 nm). This seems to point out that, for the desorption of OH groups, it is necessary to increase the temperature in order to obtain changes from the sample, and annealing at a certain temperature will not provide results on its own.

4.4.5.2 Relative C content

The analysis of the carbon content for these studies can be seen in Figure 4.52.

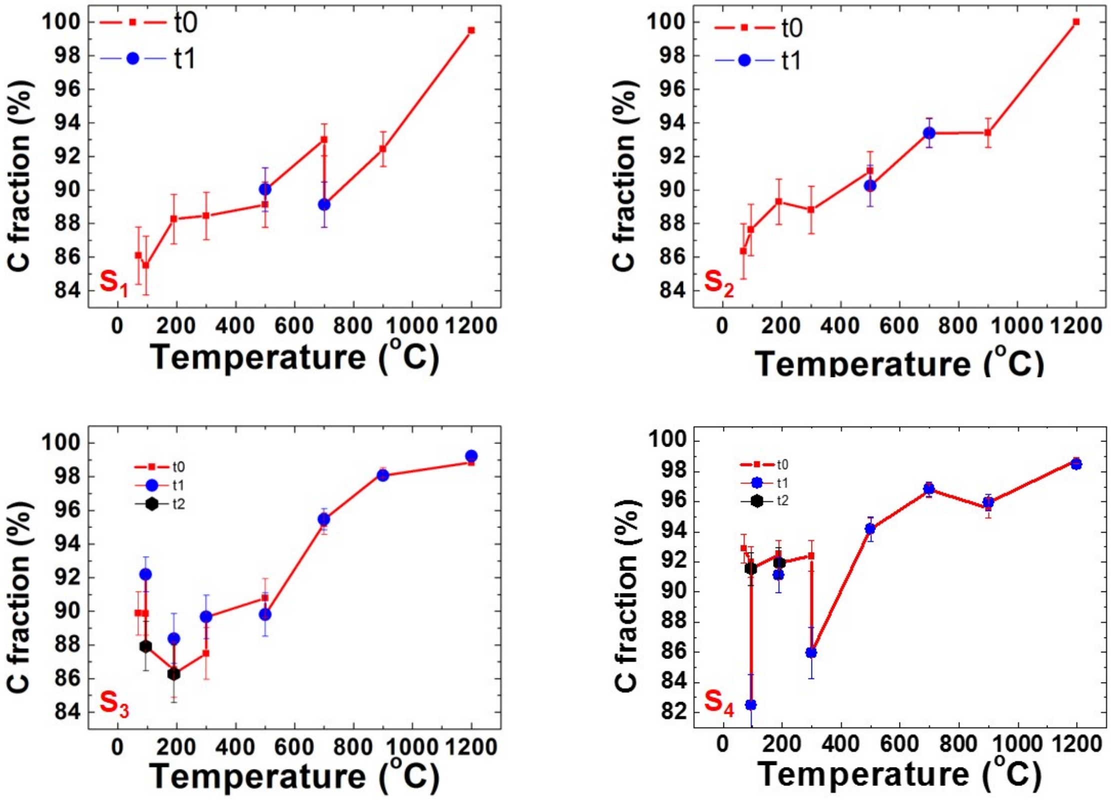

Figure 4.64: *[C]/[O] fraction of the GO samples for the cinematic studies performed in the high temperature regime. The measurements at t_0 are shown in red, while the measurements at t_1 are shown in blue and the measurements at t2 in black.*

Thinner samples

As it has previously been mentioned in Section 4.4.5.1, there is a raise in the relative C content at 500°C and a decrease at 700°C for one of the samples (S_1), while for the other one (S_2) it stays roughly the same. These variations have been explained in that section as being resulting from an annealing process with a resulting thicker structure for the changes at 500°C. At 700°C, this behaviour is thought to be coming from the desorption of OH groups and the sublimation of carbon on the edges of the sample, respectively.

Thicker samples

As it has been previously mentioned in Section 4.4.5.1, the two thick samples in this study follow two very different paths. The S_3 sample experiences an increase in its [C]/[O] fraction at t_1, folllowed by a bigger decrease (over a 4%) at t_2. On the other hand, the S_4 sample goes through a decrease in the [C]/[O] fraction over a 10% at t_1, going back up almost to its initial position at t_2. This can happen because of the same two hypothesis stated in section4.4.5.1: Either they respond differently to the desorption of PW due to their differences (thicknes, inhomogeneity, etc), with or they respond the same way to the desorption of PW, with an initial bloating of the sample followed by a decrease in thickness due to degradation, but they happen at different times due to their particular difference and we are measuring different states of the same phenomenon.

At 190°C, the S_3 sample seems to have a slight increase in [C]/[O] fraction at t_1, and it goes back down to a value very close to the initial one at t_2. As for the S_4 sample, there could be a small decrease in the [C]/[O] fraction but if there were any, it would be too small to know, since the variation in C fraciton is below the accuracy of the measurements. It is also quite hard to know for sure what is going on here. Our hypothesis is that there are two competing phenomena on the sample: on the one hand, the graphitisation and reduction coming from the desorption of PW, and on the other hand, the degradation caused by the desoprion of CW.

At 300°C, for S_4 there is a dip in the carbon fraction of the sample equivalent to a 6% of the total. This is consistent with the beginning of the desorption of epoxides at a lower temperature that we thought. This is not the case for the S_3 sample, where there is a 3% increase in the [C]/[O] fraction between t_0 and t_1. Our hypothesis is that, for this specific sample, the degradation caused by the desorptions of ketones is still lower than the loss of oxygen from the desorption of CW, epoxides and carboxyl groups.

For temperatures of 500°C and up, there are no visible differences between the measurements at t_0 and the measurements at t_1. This seems to be in good agreement with the hypothesis formulated in Section 4.4.5.1.

4.4.5.3 Mass density

The results for the mass density measured on these studies can be seen in Figure 4.65.

These are, in the case of thicker samples, the least accurate results of these studies, especially when going to high temperatures. This is due to analysis dificulties on the plasmon EELS spectra, which has been delved into in Section 4.3.6.3. They shall be examined with especial care and always taking into account the context provided by the rest of measurements.

Thinner samples Just like it was measured for the thickness and the C ratio of the sample, the mass density of the thinner samples increases at 500°C for the S_1 sample and stays the same for the S_2 sample.After that, it decreases at 700°C, with a drop of almost 6% for the S_2 sample. This is coherent with our hypothesis that, at 500°C the S_1 sample undergoes some sort of annealing with no beam irradiation in the process. The decrease in mass density at 700°C can be explained as an amorphisation caused by the beginning of the desorption of the OH groups.

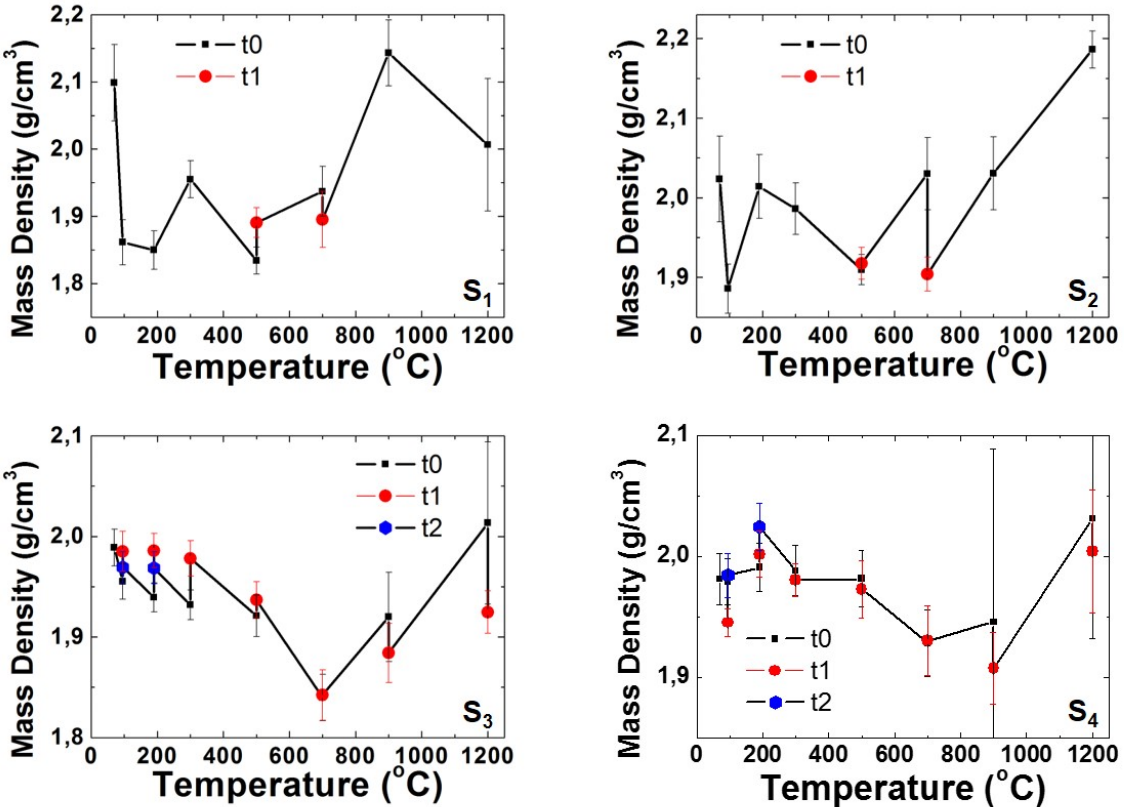

Figure 4.65: *Mass density estimation of the GO samples for the cinematic studies performed in the high temperature regime. The measurements at* t_0 *are shown in black, whereas the measurements at* t_1 *are shown in red and the ones at* t_2 *are shown in blue.*

Thicker samples At 95°C, yet again we have a different behaviour for the S_3 and S_4 samples: on the one hand, the S_3 sample seems to have a raise in mass density at t_1 followed by a drop at t_2, although the raise in mass density is in the same range as the inaccuracy of our measurements. On the other hand, the mass density in the S_4 sample has a drop of approximately a 2%, which is not huge but is noticeable enough; only to come back up to its initial level at t_2. These behaviours seem to support the hypothesis expressed in sections4.4.5.1 and 4.4.5.2.

At 190°C, we have a behaviour for both samples really similar to the previous behaviour at 95°C from the S_3 sample. The thickiness has a general raise between t_0 and t_1. Then between t_1 and t_2 the S_3 sample has an decrease in thickness and the S_4 one has an increase in thickness. We attribute these changes in mass density to the desorption of CW.

At 300°C, there is a clear increase in the mass density for the S_3 sample, corresponding with the beginning of the desoption of ketones. This seems a bit inconsistent with the studies expressed in Section 4.4.4. However, it could be that this kind of desorption during a longer time and at a stable temperature helps to anneal the sample, rendering it more graphitic. For the S_4 sample, the mass density barely changes over time.

At 500°C and 700°C, the samples do not experience any changes in their mass density between t_0 and t_1, which is coherent with what has previously been said in sections 4.4.5.1 and 4.4.5.2.

Not much can be said with certainty of the results above 700°C due to their great inaccuracy. If anything, we can see there could be a slight drop in mass density at 900°C, which would be coherent with the desorption of OH groups, but we cannot know for sure.

4.4.5.4 sp^2 fraction

The results for the sp^2 fraction in this study can be seen in Figure 4.66.

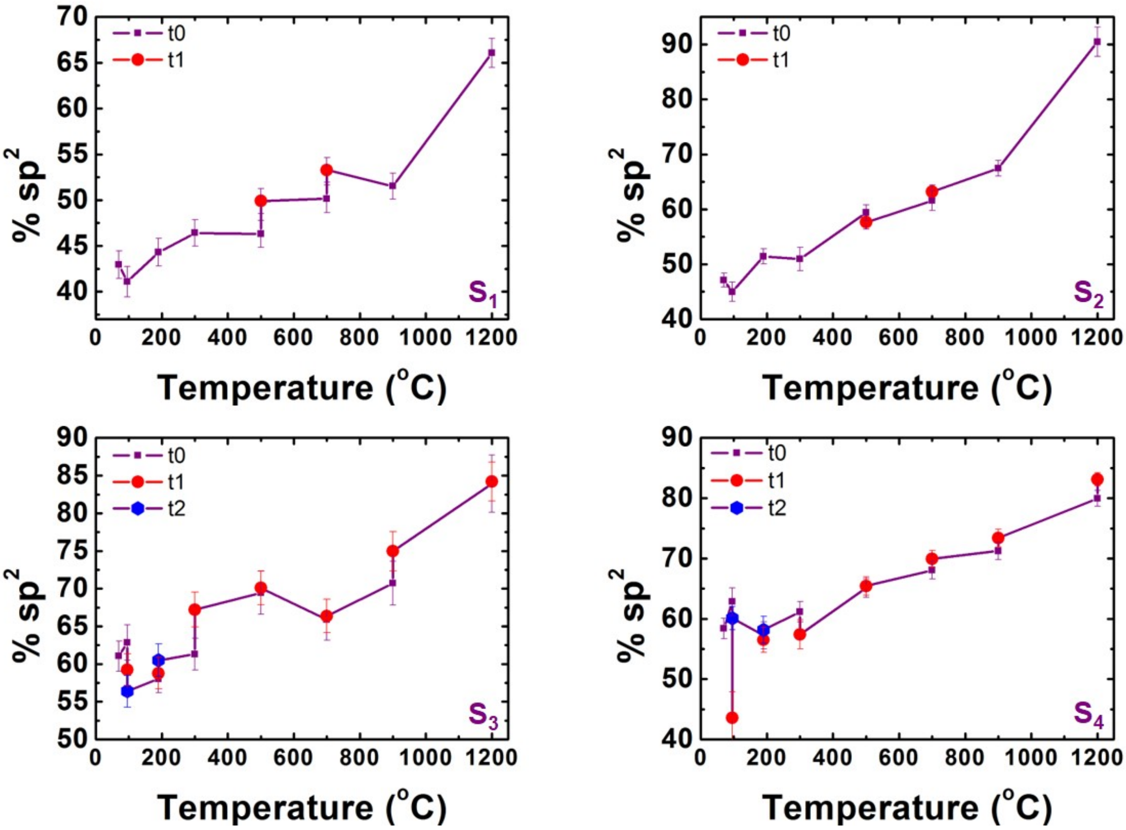

Figure 4.66: *%sp^2 sp^2/sp^3 ratio of the C atoms in the GO samples expressed as the % of sp^2 bound C atoms for the high temperature cinematic studies of the GO samples.*

Thinner samples For these samples, the sp^2 ratio goes up for the S_1 sample at 500°C and stays pretty much the same for the S_2 sample. This is consistent with the hypothesis that the S_1 sample undergoes some sort of annealing, rendering the sample more graphitic. As for the S_2 sample, there are no phenomena going on, which is supported by the rest of the properties measured in this study.

As for the behaviour at 700°C, again we find a raise in the sp^2 fraction of the S_1 sample whilst the sp^2 fraction of the S_2 sample stays more or less the same. We attribute this graphitisation to the desorption of OH groups. The S_2 sample seems to be having a bigger amount of degradation based on its mass density (see Section 4.4.5.3) so it seems reasonable that, in this case, the graphitisation and degradation cancel each other out in terms of sp^2 variation.

Thicker samples At 95°C, the sp^2 fraction in the S_3 sample drops about a 3% between t_0 and t_1, and then an additional 3% between t_1 and t_2. However, the S_4 sample drops an astounding almost 20% between t_0 and t_1, only to come back up to 60 % at t_2. This seems to be in good agreement with the hypothesis in previous sections, since an expansion of GO would decrease, even slightly, the sp^2 fraction of the sample. A degradation like the one explained in previous sections would be coherent with a drop in sp^2 fraction as big as the one the S_4 sample has experienced.

At 190°C, there seems to be a really slight increase in sp^2 fraction for the S_3 sample, as well as a slight decrease for the S_4 sample. This variation is smaller than the accuracy of the measurements so we cannot know for sure.

At 300°C, There is a clear increase between t_0 and t_1 in the sp^2 content for the S_3 sample, and a decrease for the S_4 sample. This seems to support our hypothesis, stated in Section 4.4.5.2 which is that, for the S_3 sample, the degradation produced by the desorptions of ketones is lower than the loss of oxygen from the desorption of CW, epoxides and carboxyl groups, which amounts to a positive balance in the sp^2 content.

For 500°C and up, there is not much to be told about the behaviour of these samples for the cinematic study. If anything, both samples experience a really slight increase in sp^2 fraction between t_0 and t_1 for most temperatures, probably caused by the annealing the samples are going through during this experiment.

The only other exception to this lack of behaviour is a 5% raise experienced by the S_3 sample at 900°C. This seems to be coherent with the graphitisation caused by the desorption of OH groups.

4.4.5.5 Summary - High T regime - Cinematic studies

From the cinematic studies at 500 and 700°C on the thinner samples (S_1 and S_2), we can draw the following conclusions:

- at 500°C, we have an increase in thickness between t_0 and t_1 that is accompanied by an increase or a stability in C fraction, mass density and sp^2 fraction. Our hypothesis to explain this behaviour is that there is a desorption of the carboxyl and moreover the epoxides in the sample that have not been desorbed yet, but this desorption happens purely due to thermal annealing and without any electron beam irradiation, which implies less damage and therefore less degradation in the sample.

- at 700°C, we see a decrease in thickness, along with a decrease in carbon content and mass density and an increase in the sp^2 fraction. We explain this behaviour as the beginning of the desorption of alcohol groups, which degrades the sample. Since there is a general sublimation of the sample taking place, the thickness does not increase due to this process.

On the other hand, from the cinematic studies on the thicker samples (S_3 and S_4) we gather the following conclusions:

- When it comes to the desorption of PW, it seems that S_3 and S_4 go through this desorption at a slightly different temperature, with S_3 going through the increase in thickness and decrease in all other properties that we link to the desorption process itself and S_4 having a decrease in thickness and an increase in the rest of its properties that make it seem as though during our measurements at t_1 PW has already desorbed from the sample. We think this can be due either to their different thicknesses or to inhomogeneities in the sample.

- The desorption of CW and epoxides seems to take place in a manner much more coherent with the low temperature studies, although there seems to be a much higher amount of graphitisation than there is degradation.

- Ketones start desorbing at lower temperatures than expected, with the beginning of the desorption and the degradation related to it starting at t_1 at 300°C.

- From 500°C up, there are not many big changes in the samples from t_0 to t_1. The only possible exception is a slight decrease in mass density and increase in sp^2 content at 900°C, which we relate to the beginning of the desorption of alcohols.

4.5 Future prospectives

4.5.1 I/V studies

The techniques shown in these works allow for a very complete characterisation of GO, which can be used for different kinds of *in situ* studies. Among those studies, some that have started to be performed at our institution deal with the study of the different properties of GO as it is subjected to an electric potential, and the conclusions that can be drawn from this.

4.5.2 Variability of GO

It is of importance to understand that, in this study, we have tried to give the best explanation possible to the phenomena taking place in GO that was oxydised but not saturated, with an initial relative oxygen ratio somewhere between a 12 and a 16%, while there are some GO samples in the literature with oxygen contents over 40% [416] and some prepared using different methods than the one used for our study (the Hummers method).

Oxidation rates We have covered the importance of the oxidation saturation in the structure of GO in Section 4.1.2. It could be that this might be true as well for some of the mechanisms of desorption of the different OFGs, which would explain, at least partially, the vast differences between the model of Dékány [420] versus the Lerf-Klinowski [417] and Liu [426]. In other words, our results could be different in some aspects if these experiments were repeated with GO samples having a higher concentration of oxygen. and it definitely seems like a subject worth looking into.

Preparation method In a similar fashion to the oxidation rate, we have only studied GO that has been obtained through one of the various preparation methods stated in Section 4.1.5. Just like the oxidation saturation could play play a role in the properties of the GO obtained, its structure and its behaviour, it is normal to ask ourselves if the preparation method plays a role in said characteristics as well. This would be an added explanation for the differences between the Dékány model versus the Lerf-Klinowski and Liu models.

Nevertheless, it is important to notice that the full analysis method shown in these works should, in principle, work for any kind of GO sample, with a few exceptions regarding the estimation of sp^2 carbon in heavily oxidised samples.

4.5.3 Future improvement on this study

Technique improvement The technique we have employed for this study (non-monochromated EELS) is not within the state of the art when it comes to materials spectroscopy. The use of monochromated EELS should improve both the assignment of the peaks and the quantification of the intensity of said peaks in each stage of the reduction.

Substrate improvement When it comes to the substrate for the thermal chips in the study, it has been proven (see Section 4.4.4) that the Si_xN_y in the substrate starts to sublimate and combine with our annealed rGO, probably forming SiC in the process. For this very reason, a more heat r esistant substrate could be key for future similar studies on this matter.

Other approaches for data analysis However intricate the data analysis might have been for this study, there is still room for improvement, especially when it comes to the assignment of peaks in the C-K and O-K edges of core-loss EEL spectra to the different OFGs. Two different approaches are suggested for this kind of analysis:

On the one hand, if it were possible to functionalise graphene with a single OFG, which seems plausible following what has been explained in Section 4.1.7, one could have a more accurate understanding of the fine structure peaks corresponding to said functional group. if enough of them were able to be synthesised, an MLLS analysis could be conducted using these spectra.

On the other hand, similarly to what we have seen in chapter 3, the C-K and O-K edges of the spectra are nothing but a combination of positive components, corresponding to different features (transitions, fine structure peaks, multiple scattering, etc). In theory, if we gathered enough EEL spectra in multiple, different regions of the same GO, eventually we could have enough material for a multi-variate analysis of the spectra, since what we would have would be a similar "background" spectrum with a variation of the different OFGs. This is, however, a very costly experiment due to the amount of spectra that we should have in order to obtain accurate results from a component analysis.

4.6 General Conclusion

From both the low temperature and high temperature analyses performed on these works, combining the analysis of ELNES features as well as the estimation of the [C]/[O] fraction (inverse to the oxydation degree), the thickness, the mass density and the sp^2/sp^3 ratio for the C atoms in the different samples, we have been able to gather an important amount of information regarding the thermal reduction of GO:

- At the beginning of our low temperature studies, there is a strange behaviour in the system that we have related to the presence of oxydative debris in the sample. This oxidative debris has an effect in the thickness of the samples as well as in their mass density.This debris desorbs at low temperatures, around 85°C maximum, and a part of it has probably been desorbed before the beginning of our experiments.

- The physisorbed water (PW) desorbs at a temperature around $\sim$ 100°C. This desorption seems to start with the PW adsorbed to the surface of the GO and then with the water intercalated among the graphitic layers. At the beginning of the desorption of the PW, there is a mesurable amount of degradation in the sample. This renders the sample more sensitive to the beam. The measurable effects of this is a desorption of C, resulting in a lower C fraction, an increase in thickness and an amorphisation of the sample, resulting in a lower mass density and sp^2 fraction in the C atoms.

- After the desorption of PW, the sample stabilises. These two phenomena combined imply a loss of oxygen (a higher [C]/[O] ratio), a decrease in thickness and a re-graphitisation of the sample, with the mass density and the sp^2 going back up.

- The chemisorbed water (CW) desorbs at $\sim$ 180°C, along with most of the epoxide groups and seemingly all of the carboxyl groups. Similarly to PW, there is a mesurable amount of degradation in the sample at the beginning of the desorption of the CW, which translates into the same changes in the abovementioned properties. The expansion of the samples during this desorption, which we have been able to see during the cinematic studies, has shown to be especially dramatic.

- After the desorption of the CW, most of the epoxides and all the carboxyl groups, the sample has a very noticeable amount of graphitisation, as shown in the increase in mass density and sp^2 fracion of the samples after said desorption.

- The desorption of epoxides seems to be quite effective when heating the sample up to 300°C but not completely. This is shown by the presence of epoxide groups in the ELNES analysis of the high temperature studies, as well as the presence of CW in these same studies.

- PW is shown to be readsorbed into the samples as well after leaving them overnight at ambient conditions, especially for thinner samples.

- New desorption features are seen for both PW and CW on the high temperature studies, altough the effects of the latter are a bit more subdued.

- Ketones seem to start their desorption at 300°C , at t_0 for thinner samples and after some given time for thicker samples (in our case, 30 minutes). this desorption continues up to 500°C for thicker samples.

- Alcohol groups start desorbing at 700°C for thinner samples after 30 minutes. As for thicker samples, this desorption start at 900°C.

- The GO samples undergo a graphitisation process during their thermal reduction, with some of the samples achieving a 96% fraction of sp^2-bonded C atoms. In turn, the thickness of the samples goes down not only due to the desorption of the different OFGs, but also the degradation caused by the electron beam damage and the temperature.

- Both in the case of intercalated water desorption or OFG desorption, the thickness of the sample can play a part in the temperature at which the desorption takes place and the time at a certain temperature the sample needs to start said process. The inhomogeneities in the sample can also make some of the desorptions differ from one another in the temperature or the time at which they take place. Even so, it seems the abovementioned behaviour is coherent for these specific samples and this specific kind of GO.

5

General conclusions

Throughout this manuscript, we have delved into the optoelectronic properties of atomically thin $Mo_xW_{1-x}S_2$ alloys and the plasmonic behaviour of high aspect-ratio Au nanostructures. We have also explored different properties of GO and how these properties vary when the GO is exposed to temperature raises, thus reducing and graphitising it. This section focuses on the general conclusions drawn from these experiments.

Optoelectronic properties of atomically thin $\mathbf{Mo_xW_{1-x}S_2}$ alloys When it comes to this study, there are four main results to focus on: The optical band gap, the C exciton, the α and β van Hove features.

The most prominent results have to do with the behaviour of the optical band gap, which has been obtained using a direct measurement method, instead of using the position of the A exciton peak in PL as a reference for the position of the band gap as previous studies did. Our study shows an average variation in the band gap values for different alloying degrees that is consistent with these previous studies, with a decrease in the band gap from x=1 to x=0.7 and a continous increase in the band gap value from x=0.7 to x=0. This provides not only a better understanding of the optoelectronical properties of this material, but a better guide for the tuning of the band gap in this kind of alloys, in case there was a necessity to fabricate an alloy with a specific value for its band gap.

When it comes to the C exciton features, the results within a specific alloying degree show a somewhat clear tendency for these features to decrease with the number of layers in the sample. The average position of the C exciton signature for each alloying degree seems to show a tendency for these features to decrease as the Mo content in the sample increases.

As for the α van Hove feature, within the same alloying degree there seems to be a slight decrease in this feature as the number of layers go up for high amounts of Mo. Besides that, there is a general increase of this feature with the number of layers. Regarding the average variation of this feature with the alloying degree, the average value for WS_2 is notably higher than for the rest of the alloys.

Regarding the β van Hove feature, it is clear that, for any alloying degree, the value for this feature increases with the number of layers. However, it is not possible to discern as clearly how the average value of this feature behaves as a function of the Mo content.

The theoretical simulations performed on these materials have helped us interpret our data and have confirmed our initial hypotheses.

Plasmonic properties of high aspect-ratio Au nanostructures This chapter has dealt with the analysis of the EELS data of plasmonic nanostructures that, due to their high aspect-ratio, did not allow for a conventional analysis method of their EEL spectra. A new analysis method has been used instead, which has consisted on a custom background extraction routine and a treatment using multi-variate analysis.

Out of the SPIM-EELS that have been analysed, most of them showed various amounts of experimental noise, which has served the purpose of testing our analysis routine with even more challenging datasets.

This analysis has turned out to perform remarkably well even under very challenging SNR conditions. It has been able to differentiate plasmonic components down to energies of 0.25 eV with an energy resolution of 160 meV for the most favorable samples or resolving modes below the energy resolution limit. In general, it has allowed for a very complete qualitative analysis of the plasmonic features even for the samples with a low level of SNR. We have been able to find a reasonable energy dispersion relation for these samples, furthering our knowledge about them.

The DDEELS modelling present in the chapter, as well as its comparison to our experimental results, has been very informative in terms of our experiment, and it has pointed out the possible effects of the substrate on our experiment as an energetically diffusive element.

On top of characterising these plasmonic resonators, this technique has been built in a way that could be used for other types of characterising techniques, such as XPS.

In-situ studies regarding the thermal reduction of GO Our studies regarding the thermal reduction of GO have been able to paint arguably the most complete picture to date on the thermal reduction of GO (produced using a Hummers method), investigating the different mechanisms taking place.

From both the low temperature and high temperature analyses performed, and combining the analysis of ELNES features as well as the estimation of the [C]/[O] fraction, the thickness, the mass density and the sp^2/sp^3 ratio for the C atoms in the different samples, we have been able to delve into all the stages in GO thermal reduction. These works focus on two different temperature regions; a first one ranging from 70 to 300 °C and a second one ranging from 70 to 1200 °C, with the sample being left out of the microscope overnight for rehydration purposes.Two different initial thicknesses for the samples have been considered as well, one around 10 nm and another one on the tenths of nm. The conclusions drawn from these works are as follows:

- At the beginning of our studies, we have some sort of oxydative debris in the sample. This oxidative debris has an effect in the thickness of the samples as well as in their mass density.This debris desorbs at low temperatures, around 85°C maximum.

- The physisorbed water (PW) desorbs at a temperature around $\sim$ 100°C. This desorption seems to start with the PW adsorbed to the surface of the GO and then with the water intercalated among the graphitic layers. This imply an important amount of degradation of the sample. The expansion of the samples during this desorption, which we have been able to see during the cinematic studies, has shown to be especially remarkable. After the desorption of PW, the sample stabilises.

- The desorption of carboxyl groups in the sample seems to be completely effective when heating the sample up to 300 °C, as hinted by the disappearance of its ELNES feature in the C-K EELS edge.

- The desorption of epoxides in the sample seems to be rather effective when heating up the sample up to 300 °C, but it does not work up to a full desorption. This is shown by the presence of epoxide groups in the ELNES analysis of the high temperature studies, as well as the presence of CW in these same studies.

- After leaving the sample overnight at ambient conditions, PW is shown to be readsorbed into the samples.
- New desorption features are seen for both PW and CW on the high temperature studies, altough the effects of the latter are far more subdued, which is coherent with the desorption of epoxides being only partial.
- Ketones seem to start their desorption at 300 °C , at t_0 for thinner samples and after some given time for thicker samples (in our case, 30 minutes). this desorption continues up to 500 °C for thicker samples.
- Alcohol groups start desorbing at 700 °C for thinner samples after 30 minutes. As for thicker samples, this desorption starts at 900 °C.
- The GO samples undergo a graphitisation process during their thermal reduction, with some of the samples achieving a 96% fraction of sp^2-bonded C atoms. In turn, the thickness of the samples goes down not only due to the desorption of the different OFGs, but also the degradation caused by the electron beam damage and the temperature.
- Both in the case of intercalated water desorption or OFG desorption, the thickness of the sample can play a part in the temperature at which the desorption takes place and the time at a certain temperature the sample needs to start said process. The inhomogeneities in the sample can also make some of the desorptions differ from one another in the temperature or the time at which they take place. Even so, it seems the abovementioned behaviour is coherent for these specific samples and this specific kind of GO.

These studies have improved not only what is known about the materials subject to this manuscript, but it has also pushed the techniques used for their study as well as their data analysis. This means that not only have the properties of these materials been delved into in a more complete way, but there has been a development on the data analysis for these results that will also be beneficial to new studies in the matter.

Conclusiones generales

A lo largo de este manuscrito, hemos profundizado en las propiedades optoelectrónicas de aleaciones de $Mo_xW_{1-x}S_2$ de espesor atómico (2D) y el comportamiento plasmónico de nanoestructuras de oro con una alta relación de aspecto. También hemos explorado las diferentes propiedades del óxido de grafeno y cómo estas propiedades varían cuando el GO se expone a aumentos de temperatura. Esta sección se centra en las conclusiones generales que se han sacado de estos experimentos.

Propiedades optoelectrónicas de aleaciones de $Mo_xW_{1-x}S_2$ de espesor atómico En lo que respecta a este estudio, hay cuatro resultados principales en los que centrarse: el gap óptico, el excitón C, y los picos característicos de las singularidades de Van Hove α y β.

Los resultados más notables tienen que ver con el comportamiento del gap óptico, que se han obtenido usando un método de medida directo en lugar de utilizar la posición del excitón A en PL como referencia para la posición del gap como los estudios previos. Nuestro estudio muestra una variación en la media de los valores del gap para differentes grados de aleación (cantidad de Mo) que es coherente con estos estudios previos, con un decrecimiento de los valores del gap de x=1 a x=0.7 y un crecimiento continuo en el gap para valores de x de 0.7 a 0. Esto no sólo ofrece un mejor entendimiento de las propiedades optoelectrónicas de este material, sino que también ofrece una mejor guía para el ajuste del band gap óptico en este tipo de aleaciones, en el caso de que hubiese la necesidad de fabricar una aleación con un valor específico de band gap.

En lo relativo a los picos del exciton C, los resultados para cada uno de los grados de aleación muestran una tendencia más o menos clara para estos picos para decrecer en energía cuanto mayor es el número de capas del copo analizado. La posición promedio del pico del excitón C para cada grado de aleación parece mostrar una tendencia de decrecimiento conforme la cantidad de Mo en la muestra aumenta.

Con respecto al pico de van Hove α, dentro del mismo grado de aleación parece haber un ligero decrecimiento en la posición de este pico conforme aumenta el espesor de la muestra para altos contenidos de Mo. Además, hay un aumento general de la posición de este pico con el número de capas. En cuanto al comportamiento de la posición promedio de este pico para cada grado de aleación, el valor medio para WS_2 es particularmente más alta que la del resto de aleaciones.

En lo relativo al pico β de van Hove, está claro que, para cualquier grado de aleación, la posición de este pico aumenta con el número de capas de la muestra. Sin embargo, no es posible discernir de manera tan clara cómo es el comportamiento de los valores promedio en función del contenido de Mo.

Las simulaciones teóricas realizadas para estos materiales han ayudado en la interpretación de nuestros datos y confirmado nuestras hipótesis iniciales al respecto.

Propiedades plasmónicas de nanoestructuras de oro de alta relación de aspecto Este capítulo ha lidiado con el análisis de datos de EELS de nanoestructuras plasmónicas que, debido a su alta relación de aspecto, no permitían un análisis convencional de sus espectros de EELS. Un nuevo método de análisis se ha puesto en marcha, consistente en una rutina personalizada para extraer el background del espectro, así como un tratamiento usando análisis multivariante.

De las SPIM-EELS que se han analizado, la mayoría mostraba diversos niveles de ruido experimental, lo cual ha servido para probar nuestra rutina de análisis con datos aún más complicados.

Este análisis ha resultado funcionar impresionantemente bien incluso bajo condiciones complicadas de señal sobre ruido. Ha sido posible, en los casos más favorables, identificar componentes plasmónicas a energías tan bajas como 0.25 eV, siendo la resolución energergética de 160 eV, o resolver modos por debajo del límite de resolución energéntica. En general, nos ha permitido realizar un análisis cualitativo de los modos plasmónicos muy completo, incluso para las muestras con un nivel bajo de señal sobre ruido. Hemos conseguido calcular dispersiones energénticas para estas muestras, aumentando nuestro conocimiento al respeto.

Los modelos de DDEELS que se presentan en el capítulo, así como la comparación con nuestros resultados experimentales, ha sido muy informativos en lo relativo a la coherencia de nuestro experimento, y ha señalado un posible efecto del sustrato en nuestro experimento como un elemento energéticamente difusivo.

Además de caracterizar estos resonadores plasmónicos, esta técnica de análisis ha sido construida de tal manera que podrá ser usada para otros tipos de técnicas de caracterización, como la XPS.

Estudios in situ sobre la reducción térmica del óxido de grafeno Nuestros estudios sobre la reducción térmica del GO han servido para producir la que probablemente sea la descripción más completa a día de hoy en la reducción térmica del óxido de grafeno (producido con el método de Hummers), investigando los diferentes mecanismos que tienen lugar.

Uniendo los análisis a bajas y a altas temperaturas, y combinando los análisis de los picos de ELNES así como la estimación de la fracción de [C]/[O], el espesor, la densidad másica y la proporción de enlaces sp^2/sp^3 en los átomos de carbono de las diferentes muestras, hemos sido capaces de profundizar en todos los pasos dentro de la reducción térmica del GO. Estos estudios se centran en dos regiones diferentes de temperaturas, una que va de 70 a 300 °C y otra que va de 70 a 1200 °C, y la muestra se ha sacado del microscopio durante la noche entre los estudios de una región de temperatura y los de la otra por motivos de rehidratación. Se han considerado dos regiones de espesor inicial para estos estudios, uno alrededor de 10 nm y otro en las decenas de nm. Las conclusiones que se han sacado de estos estudios son las siguientes:

- Al inicio de nuestros estudios, tenemos algún tipo de residuo oxidativo en la muestra. Este residuo oscidativo tiene un efecto en la estimación del espesor de las muestras, así como en su densidad másica. Este residuo se desorbe a bajas temperaturas, como máximo a 85 °C.

- el agua fisisorbida (AF) se desorbe a una temperatura en torno a ∼100 °C. Esta desorción parece empezar con el AF que está adsorbido a la superfice del GO y después con el agua intercalada entre las capas grafíticas. Esta degradación conlleva una cantidad importante de degradación en la muestra. La expansión de la muestra durante esta desorción, la cual hemos podido ver durante los estudios cinemáticos, ha resultado ser especialmente notable. Tras la desorción del AF, la muestra se estabiliza.

- La desorción de los grupos carboxilo de la muestra parece ser completamente efectiva al calentar la muestra hasta 400 °C, como parece indicar la desaparición de su pico ELNES en el edge K del carbono en EELS.

- La desorción de los grupos epoxi en la muestra parece ser bastante efectiva cuando calentamos la muestra hasta 300 °C, pero no llega a ser una desorción completa. Esto se ve en la presencia de grupos epoxi en los picos de ELNES de los estudios a alta temperatura, así como la presencia de agua quimisorbida (AQ) en estos mismos estudios, agua que está ligada a estos grupos.

- Tras dejar la muestra en condiciones ambientales toda la noche, el AF se readsorbe en las muestras.

- En los estudios a altas temperaturas se ven de nuevo picos relativos al AF y al AQ, aunque los efectos de la segunda son mucho menores, lo cual es consistente con que la desorción de los grupos epoxi sea sólo parcial a 300 °C
- Los grupos cetona parecen empezar a desorberse a 300 °C en t_0 para las muestras de menor espesor, y después de un tiempo (en nuestro caso, 30 minutos) para las muestras de mayor espesor. Esta desorción continua a 500 °C para las muestras más espesas.
- Los grupos alcohol empiezan a desorberse a 700 °C para las muestras menos espesas tras 30 minutos. Respeco a las muestras más espesas, esta desorción comienza a 900 °C.
- Las muestras de óxido de grafeno sufren un proceso de grafitización a lo largo de su reducción térmica, con algunas de las muestras llegando a una fracción de átomos de carbono en la muestra con enlaces sp^2 de un 96%. Por otra parte, el espesor de las muestras disminuye considerablemente no sólo por la desorción de los diferentes grupos funcionales, pero también por la degradación causada por el haz de electrones y la temperatura.
- Tanto en el caso de la desorción del agua intercalada como para los grupos funcionales, el espesor de la muestra puede ser un parámetro a considerar respecto a la temperatura a la cual comienza esta desorción y el tiempo que se necesita estar a una determinada temperatura para comenzar este proceso. Las inhomogeneidades en la muestra también pueden hacer que las desorciones difieran de muestra en muestra en la temperatura o el tiempo en el cual ocurre esta desorción. Aún así, parece ser que todos los comportamientos aquí explicados parecen coherentes para estas muestras y este tipo de GO en concreto.

Estos estudios no sólo han aumentado nuestro conocimiento sobre los materiales que son sujeto de este manuscrito, sino que también ha impulsado las téncinas usadas tanto para su estudio como para el análisis de datos. Esto quiere decir que no sólo hemos indagado en las propiedades de los materiales aquí mencionados de una forma más completa, sino que también ha habido un desarrollo en el análisis de datos para estos resultados que podrá ser beneficioso también para nuevos estudios en este tema.

Bibliography

[1] Louis De Broglie. *Recherches sur la théorie des quanta [Researches on the theory of quanta].* PhD thesis, 1924.

[2] David B. Williams and C. Barry Carter. The Transmission Electron Microscope. In *Transmission Electron Microscopy*, chapter 1, pages 3–22. Springer US, Boston, MA, 2009.

[3] H. Busch. Berechnung der Bahn von Kathodenstrahlen im axialsymmetrischen elektromagnetischen Felde. *Annalen der Physik*, 386(25):974–993, 1926.

[4] Ernst Ruska. *Über eine Berechungsmethode des Kathodenstrahloszillographen auf Grund der experimentell gefundenen Afghängigkeit des Schreibfleckdurchmessers yon der Stellung der Konzentrierspule (On a method of designing a cathode ray oscillograph on the basis of the e.* PhD thesis, Technische Hochschule Berlin, 1929.

[5] Ernst Ruska and M. Knoll. Die magnetische Sammelspule für schnelle Elektronenstrahlen. (The magnetic concentrating coil for fast electron beams.). *Z. techn. Physik*, 12:389–400, 1931.

[6] M. Knoll and E. Ruska. Das Elektronenmikroskop. *Zeitschrift für Physik*, 78(5-6):318–339, may 1932.

[7] E Driest and H. O Müller. Elektronenkikroskopische Aufnahmen (Elektronenmikrogramme) von Chitinobjecten [Electron microscopical photographs (electron micrographs) of Chitin objects]. *Z. Wiss. Mikrosk.*, 52:53–57, 1935.

[8] S. Bradbury. *The Evolution of the Microscope.* Pergamon Press, Oxford, 1 edition, 1967.

[9] O. Scherzer. Spharische und chromatische Korrektur von Elektronen-Linsen. *Optik*, (5):114–132, 1947.

[10] Harald Rose. History of Direct Aberration Correction. In *Advances in Imaging and Electron Physics*, volume 153, chapter 1, pages 3–39. Elsevier Inc., 2008.

[11] David B. Williams and C. Barry Carter. Scattering and Diffraction. In *Transmission Electron Microscopy*, chapter 2, pages 23–38. Springer US, Boston, MA, 2009.

[12] Z. L. Wang. *Elastic and Inelastic Scattering in Electron Diffraction and Imaging.* Plenum Press New York, New York, New York, USA, 1995.

[13] Ray F. Egerton. *Electron Energyâ€Loss Spectroscopy in the Electron Microscope.* Springer, 3 edition, 2011.

[14] David B. Williams and C. Barry Carter. Elastic Scattering. In *Transmission Electron Microscopy*, volume 61, chapter 3, pages 39–51. Springer US, Boston, MA, 2009.

[15] R. F. Egerton. Electron energy-loss spectroscopy in the TEM. *Reports on Progress in Physics*, 72(1), 2009.

[16] David B. Williams and C. Barry Carter. Inelastic Scattering and Beam Damage. In *Transmission Electron Microscopy*, chapter 4, pages 53–71. Springer US, Boston, MA, 2009.

[17] Stephen J. Pennycook and Peter D. Nellist. *Scanning Transmission Electron Microscopy.* Springer New York, New York, NY, 2011.

[18] Christopher Hammond. *The basics of crystallography and diffraction.* Oxford: International Union of Crystallography/Oxford University Press,, Oxford, 1 edition, 1997.

[19] David B. Williams and C. Barry Carter. Thinking in Reciprocal Space. In *Transmission Electron Microscopy*, chapter 12, pages 211–219. Springer US, Boston, MA, 2009.

[20] David B. Williams and C. Barry Carter. Electron Sources. In *Transmission Electron Microscopy*, chapter 5, pages 73–89. Springer US, Boston, MA, 2009.

[21] Zheng Long Zhang, Yu Rui Fang, Wen Hui Wang, Li Chen, and Meng Tao Sun. Propagating surface plasmon polaritons: Towards applications for remote-excitation surface catalytic reactions. *Advanced Science*, 3(1):1–14, 2016.

[22] F. Houdellier, L. de Knoop, C. Gatel, A. Masseboeuf, S. Mamishin, Y. Taniguchi, M. Delmas, M. Monthioux, M. J. Hÿtch, and E. Snoeck. Development of TEM and SEM high brightness electron guns using cold-field emission from a carbon nanotip. *Ultramicroscopy*, 151:107–115, 2015.

[23] Florent Houdellier, Aurélien Masseboeuf, Marc Monthioux, and Martin J. Hÿtch. New carbon cone nanotip for use in a highly coherent cold field emission electron microscope. *Carbon*, 50(5):2037–2044, 2012.

[24] David B. Williams and C. Barry Carter. Lenses, Apertures, and Resolution. In *Transmission Electron Microscopy*, number Vlm, chapter 6, pages 91–114. Springer US, Boston, MA, 2009.

[25] Rolf E. Hummel. Applications. In *Electronic Properties of Materials*, chapter 13, pages 263–264. Springer New York, New York, NY, 2011.

[26] J.N. Chapman, A.J. Craven, and C.P. Scott. Electron detection in the analytical electron microscope. *Ultramicroscopy*, 28(1-4):108–117, apr 1989.

[27] David B. Williams, C. Barry Carter, David B. Williams, and C. Barry Carter. How to â€˜See' Electrons. In *Transmission Electron Microscopy*, pages 115–126. Springer US, Boston, MA, 2009.

[28] Gatan Inc Website. Imaging. `https://www.gatan.com/techniques/imaging`, 2020.

[29] Wayne E. King, Geoffrey H. Campbell, Alan Frank, Bryan Reed, John F. Schmerge, Bradley J. Siwick, Brent C. Stuart, and Peter M. Weber. Ultrafast electron microscopy in materials science, biology, and chemistry. *Journal of Applied Physics*, 97(11), 2005.

[30] Ivan Lazic, Eric G.T. Bosch, Sorin Lazar, Maarten Wirix, and Emrah Yücelen. Integrated Differential Phase Contrast (iDPC)â€"Direct Phase Imaging in STEM for Thin Samples. *Microscopy and Microanalysis*, 22(S3):36–37, 2016.

[31] Eric G.T. Bosch, Ivan Lazic, and Sorin Lazar. Integrated Differential Phase Contrast (iDPC) STEM: A New Atomic Resolution STEM Technique To Image All Elements Across the Periodic Table. *Microscopy and Microanalysis*, 22(S3):306–307, 2016.

[32] M. Kociak and L. F. Zagonel. Cathodoluminescence in the scanning transmission electron microscope. *Ultramicroscopy*, 176:112–131, 2017.

[33] Peter W Hawkes and Ondrej L. Krivanek. Aberration Correctors Monochromators; Spectrometers. In Peter W. Hawkes and John C. H. Spence, editors, *Springer Handbook of Microscopy*, Springer Handbooks, chapter 13, page 625. Springer International Publishing, Cham, 2019.

[34] Ondrej L. Krivanek, Tracy C. Lovejoy, Niklas Dellby, and R. W. Carpenter. Monochromated STEM with a 30 meV-wide, atom-sized electron probe. *Journal of Electron Microscopy*, 62(1):3–21, 2013.

[35] Ondrej L. Krivanek, Jonathan P. Ursin, Neil J. Bacon, George J. Corbin, Niklas Dellby, Petr Hrncirik, Matthew F. Murfitt, Christopher S. Own, and Zoltan S. Szilagyi. High-energy-resolution monochromator for aberration-corrected scanning transmission electron microscopy/electron energy-loss spectroscopy. *Philosophical Transactions of the Royal Society A: Mathematical, Physical and Engineering Sciences*, 367(1903):3683–3697, 2009.

[36] Ondrej L. Krivanek, Tracy C. Lovejoy, Matthew F. Murfitt, Gwyn Skone, Philip E. Batson, and Niklas Dellby. Towards sub-10 meV energy resolution STEM-EELS. *Journal of Physics: Conference Series*, 522(1), 2014.

[37] David B. Williams and C. Barry Carter. The Instrument. In *Transmission Electron Microscopy*, number Chapter 5, chapter 9, pages 141–171. Springer US, Boston, MA, 2009.

[38] David B. Williams and C. Barry Carter. Amplitude Contrast. In *Transmission Electron Microscopy*, chapter 22, pages 371–388. Springer US, Boston, MA, 2009.

[39] Teen Hang Meen, Jenn Kai Tsai, Shi Mian Chao, Yu Chien Lin, Tien Chuan Wu, Tang Yun Chang, Liang Wen Ji, Walter Water, Wen Ray Chen, I. Tseng Tang, and Chien Jung Huang. Surface plasma resonant effect of gold nanoparticles on the photoelectrodes of dye-sensitized solar cells. *Nanoscale Research Letters*, 8(1):1–6, 2013.

[40] P. P. Ewald. X-ray diffraction by finite and imperfect crystal lattices. *Proceedings of the Physical Society*, 52(1):167–174, 1940.

[41] J. M. Cowley. IMAGE CONTRAST in a TRANSMISSION SCANNING ELECTRON MICROSCOPE. *Applied Physics Letters*, 15(2):58–59, 1969.

[42] Rik Brydson. *Aberration-Corrected Analytical Transmission Electron Microscopy*. John Wiley & Sons, Ltd, Chichester, UK, sep 2011.

[43] David B. Williams and C. Barry Carter. Diffraction in TEM. In *Transmission Electron Microscopy*, chapter 11, pages 197–209. Springer US, Boston, MA, 2009.

[44] David B. Williams and C. Barry Carter. Other Imaging Techniques. In *Transmission Electron Microscopy*, volume 53, chapter 29, pages 511–532. Springer US, Boston, MA, 2009.

[45] Francis Leonard Deepak, Alvaro Mayoral, and Raul Arenal. *Advanced Transmission Electron Microscopy*. Springer International Publishing, 2015.

[46] M. J. Hÿtch, E. Snoeck, and R. Kilaas. Quantitative measurement of displacement and strain fields from HREM micrographs. *Ultramicroscopy*, 74(3):131–146, 1998.

[47] Yi Jiang, Zhen Chen, Yimo Han, Pratiti Deb, Hui Gao, Saien Xie, Prafull Purohit, Mark W. Tate, Jiwoong Park, Sol M. Gruner, Veit Elser, and David A. Muller. Electron ptychography of 2D materials to deep sub-ångström resolution. *Nature*, 559(7714):343–349, 2018.

[48] M. J. Humphry, B. Kraus, A. C. Hurst, A. M. Maiden, and J. M. Rodenburg. Ptychographic electron microscopy using high-angle dark-field scattering for sub-nanometre resolution imaging. *Nature Communications*, 3:730–737, 2012.

[49] Crispin Hetherington. Aberration correction for TEM. *Materials Today*, 2004.

[50] Rolf Erni. Aberration-Corrected Imaging in Transmission Electron Microscopy. In *Aberration-Corrected Imaging in Transmission Electron Microscopy: An Introduction*, chapter 7. IMPERIAL COLLEGE PRESS, Berlin, Boston, aug 2010.

[51] Peter D. Nellist. The Principles of STEM Imaging. In *Scanning Transmission Electron Microscopy*, number i, chapter 2, pages 91–115. Springer New York, New York, NY, 2011.

[52] Angus I. Kirkland, Peter D. Nellist, Lan-Yun Chang, and Sarah J. Haigh. Aberration-Corrected Imaging in Conventional Transmission Electron Microscopy and Scanning Transmission Electron Microscopy. In *Advances in Imaging and Electron Physics*, volume 153, chapter 8, pages 283–325. Elsevier Inc., 2008.

[53] A. I. Kirkland, J. Sloan, and S. Haigh. Ultrahigh resolution imaging of local structural distortions in intergrowth tungsten bronzes. *Ultramicroscopy*, 107(6-7):501–506, 2007.

[54] R. R. Meyer, A. I. Kirkland, and W. O. Saxton. A new method for the determination of the wave aberration function for high resolution TEM: 1. Measurement of the symmetric aberrations. *Ultramicroscopy*, 92(2):89–109, 2002.

[55] Raul Arenal, Luc Henrard, Lucian Roiban, Ovidiu Ersen, Julien Burgin, and Mona Treguer-Delapierre. Local plasmonic studies on individual core-shell gold-silver and pure gold nano-bipyramids. *Journal of Physical Chemistry C*, 118(44):25643–25650, 2014.

[56] David B. Williams and C. Barry Carter. Electron Energy-Loss Spectrometers and Filters. In *Transmission Electron Microscopy*, chapter 37, pages 679–698. Springer US, Boston, MA, 2009.

[57] David B. Williams and C. Barry Carter. Fine Structure and Finer Details. In *Transmission Electron Microscopy*, chapter 40, pages 741–760. Springer US, Boston, MA, 2009.

[58] David B. Williams and C. Barry Carter. Low-Loss and No-Loss Spectra and Images. In *Transmission Electron Microscopy*, chapter 38, pages 699–713. Springer US, Boston, MA, 2009.

[59] Nigel D. Browning, Ilke Arslan, Rolf Erni, and Bryan W. Reed. Low-Loss EELS in the STEM. In *Scanning Transmission Electron Microscopy*, number i, chapter 16, pages 659–688. Springer New York, New York, NY, 2011.

[60] K Andre Mkhoyan, Alexander W Contryman, John Silcox, A Derek, Goki Eda, Cecilia Mattevi, Steve Miller, Manish Chhowalla, K Andre Mkhoyan, Alexander W Contryman, John Silcox, Derek A Stewart, Goki Eda, Cecilia Mattevi, and Steve Miller. Atomic and Electronic Structure of Graphene-Oxide. *Nano Letters*, 9(3):1058–1063, 2009.

[61] K. Dileep, R. Sahu, Sumanta Sarkar, Sebastian C. Peter, and R. Datta. Layer specific optical band gap measurement at nanoscale in MoS_2 and ReS2 van der Waals compounds by high resolution electron energy loss spectroscopy. *Journal of Applied Physics*, 119:114309, 2016.

[62] Jinhua Hong, Kun Li, Chuanhong Jin, Xixiang Zhang, Ze Zhang, and Jun Yuan. Layer-dependent anisotropic electronic structure of freestanding quasi-two-dimensional Mo S2. *Physical Review B - Condensed Matter and Materials Physics*, 93(7):1–11, 2016.

[63] Mathieu Kociak, Odile Stéphan, Michael G. Walls, Marcel Tencé, and Christian Colliex. Spatially Resolved EELS: The Spectrum-Imaging Technique and Its Applications. In *Scanning Transmission Electron Microscopy*, number i, chapter 4, pages 163–205. Springer New York, New York, NY, 2011.

[64] T. Malis, Shangcong Cheng, and R. F. Egerton. EELS log-Ratio Technique for Specimen-Thickness measurement in the TEM. *Journal of Electron Microscopy Technique*, 8:193–200, 1988.

[65] A. C. Ferrari, A. Libassi, B. K. Tanner, V. Stolojan, J. Yuan, J. Yuan, L. M. Brown, S. E. Rodil, B. Kleinsorge, and J. Robertson. Density, sp 3 fraction, and cross-sectional structure of amorphous carbon films determined by x-ray reflectivity and electron energy-loss spectroscopy. *Physical Review B - Condensed Matter and Materials Physics*, 62(16):11089–11103, 2000.

[66] David B. Williams and C. Barry Carter. High Energy-Loss Spectra and Images. In *Transmission Electron Microscopy*, chapter 39, pages 715–739. Springer US, Boston, MA, 2009.

[67] Quentin M. Ramasse. Twenty years after: How â€œAberration correction in the STEMâ€ truly placed a â€œA synchrotron in a Microscopeâ€. *Ultramicroscopy*, 180:41–51, sep 2017.

[68] Guillaume Radtke and Gianluigi A. Botton. Energy Loss Near-Edge Structures. In *Scanning Transmission Electron Microscopy*, number i, chapter 5, pages 207–245. Springer New York, New York, NY, 2011.

[69] D D 'angelo, C. Bongiorno, M. Amato, I. Deretzis, A La Magna, E. Fazio, S. Scalese, D. D'Angelo, C. Bongiorno, M. Amato, I. Deretzis, A. La Magna, E. Fazio, and S. Scalese. Oxygen Functionalities Evolution in Thermally Treated Graphene Oxide Featured by EELS and DFT Calculations. *The Journal of Physical Chemistry C*, 121(9):5408–5414, mar 2017.

[70] Philip Ewels, Thierry Sikora, Virginie Serin, Chris P. Ewels, and Luc Lajaunie. A Complete Overhaul of the Electron Energy-Loss Spectroscopy and X-Ray Absorption Spectroscopy Database: Eelsdb.eu. *Microscopy and Microanalysis*, 22(3):717–724, 2016.

[71] Haiyan Tan, Stuart Turner, Emrah Yücelen, Jo Verbeeck, and Gustaaf Van Tendeloo. 2D atomic mapping of oxidation states in transition metal oxides by scanning transmission electron microscopy and electron energy-loss spectroscopy. *Physical Review Letters*, 107(10):1–4, 2011.

[72] R. Arenal, F. de la Peña, O. Stéphan, M. Walls, M. Tencé, A. Loiseau, and C. Colliex. Extending the analysis of EELS spectrum-imaging data, from elemental to bond mapping in complex nanostructures. *Ultramicroscopy*, 109(1):32–38, 2008.

[73] Andrew L. Bleloch. Scanning Transmission Electron Microscopy and Electron Energy Loss Spectroscopy: Mapping Materials Atom by Atom. In *Advances in Imaging and Electron Physics*, volume 153, chapter 5, pages 195–223. Elsevier Inc., 2008.

[74] C. Jeanguillaume and C. Colliex. Spectrum-image: The next step in EELS digital acquisition and processing. *Ultramicroscopy*, 28(1-4):252–257, apr 1989.

[75] J.A. Hunt and D.B. Williams. Electron energy-loss spectrum-imaging. *Ultramicroscopy*, 38(1):47–73, oct 1991.

[76] D. A. Muller, L. F. Kourkoutis, M. Murfitt, J. H. Song, H. Y. Hwang, J. Silcox, N. Dellby, and O. L. Krivanek. Atomic-scale chemical imaging of composition and bonding by aberration-corrected microscopy. *Microscopy and Microanalysis*, 14(SUPPL. 2):132–133, 2008.

[77] R. Arenal, F. de la Peña, O. Stéphan, M. Walls, M. Tencé, A. Loiseau, and C. Colliex. Extending the analysis of EELS spectrum-imaging data, from elemental to bond mapping in complex nanostructures. *Ultramicroscopy*, 109(1):32–38, 2008.

[78] Andres Castellanos-Gomez, Michele Buscema, Rianda Molenaar, Vibhor Singh, Laurens Janssen, Herre S J van der Zant, and Gary a Steele. Deterministic transfer of two-dimensional materials by all-dry viscoelastic stamping. *2D Materials*, 1(1):011002, 2014.

[79] L. V. Radushkevich and V. M. Lukyanovich. On the structure of carbon formed during the thermal decomposition of carbon monoxide on an iron contact (in Russian). *Journal of Physical Chemistry (in Russian)*, 26:88–95, 1952.

[80] Mildred S. Dresselhaus and Mauricio Terrones. Carbon-based nanomaterials from a historical perspective. *Proceedings of the IEEE*, 101(7):1522–1535, 2013.

[81] M. S. Dresselhaus and G. Dresselhaus. Advances in Physics Intercalation compounds of graphite. *Advances in Physics*, 51(1):1–186, 1981.

[82] Eric A. Rohlfing, D. M. Cox, and A. Kaldor. Production and characterization of supersonic carbon cluster beams. *The Journal of Chemical Physics*, 81(7):3322–3330, oct 1984.

[83] Harold W. Kroto. C60: Buckminsterfullerene, The Celestial Sphere that Fell to Earth. *Angewandte Chemie International Edition in English*, 31(2):111–129, 1992.

[84] W. Krätschmer, Lowell D. Lamb, K. Fostiropoulos, and Donald R. Huffman. Solid C60: a new form of carbon. *Nature*, 347(6291):354–358, 1990.

[85] Neil J. Coville, Sabelo D. Mhlanga, Edward N. Nxumalo, and Ahmed Shaikjee. A review of shaped carbon nanomaterials. *South African Journal of Science*, 107(3/4):1–15, mar 2011.

[86] Sumio Iijima. Helical microtubules of graphitic carbon. *Nature*, 354(6348):56–58, nov 1991.

[87] K. S Novoselov, A.K. Geim, S. V. Morozov, D. Jiang, Y. Zhang, S. V. Dubonos, I. V. Grigorieva, and A. A. Firsov. Electric Field Effect in Atomically Thin Carbon Films. *Science*, 306(5696):666–669, oct 2004.

[88] K. Kneipp, A. Jorio, H. Kneipp, S. D.M. Brown, K. Shafer, J. Motz, R. Saito, G. Dresselhaus, and M. S. Dresselhaus. Polarization effects in surface-enhanced resonant Raman scattering of single-wall carbon nanotubes on colloidal silver clusters. *Physical Review B - Condensed Matter and Materials Physics*, 63(8):2–5, 2001.

[89] A. Jorio, R. Saito, J. H. Hafner, C. M. Lieber, M. Hunter, T. McClure, G. Dresselhaus, and M. S. Dresselhaus. Structural (n, m) determination of isolated single-wall carbon nanotubes by resonant Raman scattering. *Physical Review Letters*, 86(6):1118–1121, 2001.

[90] Rubén Mas-Ballesté, Cristina Gómez-Navarro, Julio Gómez-Herrero, and Félix Zamora. 2D materials: To graphene and beyond. *Nanoscale*, 3(1):20–30, 2011.

[91] Zhong Lin, Amber McCreary, Natalie Briggs, Shruti Subramanian, Kehao Zhang, Yifan Sun, Xufan Li, Nicholas J. Borys, Hongtao Yuan, Susan K. Fullerton-Shirey, Alexey Chernikov, Hui Zhao, Stephen McDonnell, Aaron M. Lindenberg, Kai Xiao, Brian J. Le Roy, Marija Drndić, James C.M. Hwang, Jiwoong Park, Manish Chhowalla, Raymond E. Schaak, Ali Javey, Mark C. Hersam, Joshua Robinson, and Mauricio Terrones. 2D materials advances: From large scale synthesis and controlled heterostructures to improved characterization techniques, defects and applications. *2D Materials*, 3(4), 2016.

[92] Vadym N. Mochalin, Olga Shenderova, Dean Ho, and Yury Gogotsi. The properties and applications of nanodiamonds. *Nature Nanotechnology*, 7(1):11–23, 2012.

[93] V. V. Danilenko. On the history of the discovery of nanodiamond synthesis. *Physics of the Solid State*, 46(4):595–599, 2004.

[94] K. S. Novoselov, S. V. Morozov, T. M.G. Mohinddin, L. A. Ponomarenko, D. C. Elias, R. Yang, I. I. Barbolina, P. Blake, T. J. Booth, D. Jiang, J. Giesbers, E. W. Hill, and A. K. Geim. Electronic properties of graphene. *Physica Status Solidi (B) Basic Research*, 244(11):4106–4111, 2007.

[95] Q. Wang and K. M. Liew. Mechanical properties of carbon nanotubes. *Carbon Nanotubes: New Research*, 260:157–174, 2009.

[96] Daniel R. Cooper, Benjamin D'Anjou, Nageswara Ghattamaneni, Benjamin Harack, Michael Hilke, Alexandre Horth, Norberto Majlis, Mathieu Massicotte, Leron Vandsburger, Eric Whiteway, and Victor Yu. Experimental Review of Graphene. *ISRN Condensed Matter Physics*, 2012:1–56, 2012.

[97] A. K. Geim and K. S. Novoselov. The rise of graphene. *Nanoscience and Technology: A Collection of Reviews from Nature Journals*, pages 11–19, 2009.

[98] Roscoe G. Dickinson and Linus Pauling. The crystal structure of molybdenite. *Journal of the American Chemical Society*, 45(6):1466–1471, 1923.

[99] J. A. Wilson and A. D. Yoffe. The transition metal dichalcogenides discussion and interpretation of the observed optical, electrical and structural properties. *Advances in Physics*, 18(73):193–335, 1969.

[100] Per Joensen, R. F. Frindt, and S. Roy Morrison. Single-layer MoS2. *Materials Research Bulletin*, 21(4):457–461, 1986.

[101] R. Tenne, L. Margulis, M. Genut, and G. Hodes. Polyhedral and cylindrical structures of tungsten disulphide. *Nature*, 360(6403):444–446, dec 1992.

[102] Y. Feldman, E. Wasserman, D. J. Srolovitz, and R. Tenne. High-rate, gas-phase growth of MoS_2 nested inorganic fullerenes and nanotubes. *Science*, 267(5195):222–225, 1995.

[103] B. Radisavljevic, A. Radenovic, J. Brivio, V. Giacometti, and A. Kis. Single-layer MoS_2 transistors. *Nature Nanotechnology*, 6(3):147–150, 2011.

[104] Andrea Splendiani, Liang Sun, Yuanbo Zhang, Tianshu Li, Jonghwan Kim, Chi-Yung Chim, Giulia Galli, and Feng Wang. Emerging Photoluminescence in Monolayer MoS $_2$. *Nano Letters*, 10(4):1271–1275, apr 2010.

[105] Kin Fai Mak, Changgu Lee, James Hone, Jie Shan, and Tony F. Heinz. Atomically thin MoS2: A new direct-gap semiconductor. *Physical Review Letters*, 105(13):2–5, 2010.

[106] Humberto R. Gutiérrez, Nestor Perea-López, Ana Laura Elías, Ayse Berkdemir, Bei Wang, Ruitao Lv, Florentino López-Urías, Vincent H. Crespi, Humberto Terrones, and Mauricio Terrones. Extraordinary room-temperature photoluminescence in triangular WS 2 monolayers. *Nano Letters*, 13(8):3447–3454, 2013.

[107] Chaoliang Tan and Hua Zhang. Two-dimensional transition metal dichalcogenide nanosheet-based composites. *Chemical Society Reviews*, 44(9):2713–2731, 2015.

[108] Sajedeh Manzeli, Dmitry Ovchinnikov, Diego Pasquier, Oleg V. Yazyev, and Andras Kis. 2D transition metal dichalcogenides. *Nature Reviews Materials*, 2, 2017.

[109] Manish Chhowalla, Zhongfan Liu, and Hua Zhang. Two-dimensional transition metal dichalcogenide (TMD) nanosheets. *Chemical Society Reviews*, 44(9):2584–2586, 2015.

[110] Damien Voiry, Aditya Mohite, and Manish Chhowalla. Phase engineering of transition metal dichalcogenides. *Chemical Society Reviews*, 44(9):2702–2712, 2015.

[111] Martin B. Dines. Lithium intercalation via n-Butyllithium of the layered transition metal dichalcogenides. *Materials Research Bulletin*, 10(4):287–291, 1975.

[112] B. K. Miremadi and S. R. Morrison. The intercalation and exfoliation of tungsten disulfide. *Journal of Applied Physics*, 63(10):4970–4974, 1988.

[113] Yung Chang Lin, Dumitru O. Dumcenco, Ying Sheng Huang, and Kazu Suenaga. Atomic mechanism of the semiconducting-to-metallic phase transition in single-layered MoS 2. *Nature Nanotechnology*, 9(5):391–396, 2014.

[114] Russell R. Chianelli, Mohammad H. Siadati, Myriam P. De la Rosa, Gilles Berhault, Jess P. Wilcoxon, Roby Bearden, and Billie L. Abrams. Catalytic properties of single layers of transition metal sulfide catalytic materials. *Catalysis Reviews - Science and Engineering*, 48(1):1–41, 2006.

[115] Yongfu Sun, Shan Gao, Fengcai Lei, and Yi Xie. Atomically-thin two-dimensional sheets for understanding active sites in catalysis. *Chemical Society Reviews*, 44(3):623–636, 2015.

[116] Paul D. Cunningham, Aubrey T. Hanbicki, Kathleen M. McCreary, and Berend T. Jonker. Photoinduced Bandgap Renormalization and Exciton Binding Energy Reduction inWS_2. *ACS Nano*, 11(12):12601–12608, 2017.

[117] Gerd Plechinger, Philipp Nagler, Ashish Arora, Andrés Granados Del Águila, Mariana V. Ballottin, Tobias Frank, Philipp Steinleitner, Martin Gmitra, Jaroslav Fabian, Peter C.M. Christianen, Rudolf Bratschitsch, Christian Schüller, and Tobias Korn. Excitonic Valley Effects in MonolayerWS_2 under High Magnetic Fields. *Nano Letters*, 16(12):7899–7904, 2016.

[118] Masaru Onga, Yijin Zhang, Toshiya Ideue, and Yoshihiro Iwasa. Exciton Hall effect and transport of valley exciton in monolayer MoS2. In *SAP-OSA Joint Symposia 2017 Abstracts*, Fukuoka, Japan, 2017. Japan Society of Applied Physics, Optical Society of America.

[119] Sudipta Dubey, Simone Lisi, Goutham Nayak, Felix Herziger, Van Dung Nguyen, Toai Le Quang, Vladimir Cherkez, César González, Yannick J. Dappe, Kenji Watanabe, Takashi Taniguchi, Laurence Magaud, Pierre Mallet, Jean Yves Veuillen, Raul Arenal, Laëtitia Marty, Julien Renard, Nedjma Bendiab, Johann Coraux, and Vincent Bouchiat. Weakly Trapped, Charged, and Free Excitons in Single-Layer MoS_2 in the Presence of Defects, Strain, and Charged Impurities. *ACS Nano*, 11(11):11206–11216, 2017.

[120] Kłopotowski, C. Backes, A. A. Mitioglu, V. Vega-Mayoral, D. Hanlon, J. N. Coleman, V. Y. Ivanov, D. K. Maude, and P. Plochocka. Revealing the nature of excitons in liquid exfoliated monolayer tungsten disulphide. *Nanotechnology*, 27(42), 2016.

[121] Hualin Wu, Haonan Si, Zihan Zhang, Zhuo Kang, Pingwei Wu, Lixin Zhou, Suicai Zhang, Zheng Zhang, Qingliang Liao, and Yue Zhang. All-Inorganic Perovskite Quantum Dot-Monolayer MoS_2 Mixed-Dimensional van der Waals Heterostructure for Ultrasensitive Photodetector. *Advanced Science*, 5(12), 2018.

[122] Yang Liu, Yixin Nie, Mengke Wang, Qian Zhang, and Qiang Ma. Distance-dependent plasmon-enhanced electrochemiluminescence biosensor based on MoS_2 nanosheets. *Biosensors and Bioelectronics*, 148:111823, 2020.

[123] Damien Voiry, Raymond Fullon, Jieun Yang, Cecilia De Carvalho Castro E Silva, Rajesh Kappera, Ibrahim Bozkurt, Daniel Kaplan, Maureen J. Lagos, Philip E. Batson, Gautam Gupta, Aditya D. Mohite, Liang Dong, Dequan Er, Vivek B. Shenoy, Tewodros Asefa, and Manish Chhowalla. The role of electronic coupling between substrate and 2D MoS_2 nanosheets in electrocatalytic production of hydrogen. *Nature Materials*, 15(9):1003–1009, 2016.

[124] Mit H. Naik and Manish Jain. Ultraflatbands and Shear Solitons in Moiré Patterns of Twisted Bilayer Transition Metal Dichalcogenides. *Physical Review Letters*, 121(26):266401, 2018.

[125] Miao Ling Lin, Qing Hai Tan, Jiang Bin Wu, Xiao Shuang Chen, Jin Huan Wang, Yu Hao Pan, Xin Zhang, Xin Cong, Jun Zhang, Wei Ji, Ping An Hu, Kai Hui Liu, and Ping Heng Tan. Moiré phonons in twisted bilayer MoS2. *ACS Nano*, 12(8):8770–8780, 2018.

[126] Sotiris Psilodimitrakopoulos, Leonidas Mouchliadis, Ioannis Paradisanos, George Kourmoulakis, Andreas Lemonis, George Kioseoglou, and Emmanuel Stratakis. Twist Angle mapping in layeredWS_2 by Polarization-Resolved Second Harmonic Generation. *Scientific Reports*, 9(1):1–23, 2019.

[127] Wei Yan, Lan Meng, Zhaoshun Meng, Yakui Weng, Lulu Kang, and Xing Ao Li. Probing Angle-Dependent Interlayer Coupling in Twisted BilayerWS_2. *Journal of Physical Chemistry C*, 2019.

[128] Fuyou Liao, Jianan Deng, Xinyu Chen, Yin Wang, Xinzhi Zhang, Jian Liu, Hao Zhu, Lin Chen, Qingqing Sun, Weida Hu, Jianlu Wang, Jing Zhou, Peng Zhou, David Wei Zhang, Jing Wan, and Wenzhong Bao. A Dual-Gate MoS_2 Photodetector Based on Interface Coupling Effect. *Small*, 16(1):1–7, 2020.

[129] Xiao Li and Hongwei Zhu. Two-dimensional MoS2: Properties, preparation, and applications. *Journal of Materiomics*, 1(1):33–44, 2015.

[130] K. S. Novoselov, D. Jiang, F. Schedin, T. J. Booth, V. V. Khotkevich, S. V. Morozov, and A. K. Geim. Two-dimensional atomic crystals. *Proceedings of the National Academy of Sciences*, 102(30):10451–10453, jul 2005.

[131] Xingke Cai, Yuting Luo, Bilu Liu, and Hui Ming Cheng. Preparation of 2D material dispersions and their applications. *Chemical Society Reviews*, 47(16):6224–6266, 2018.

[132] Sonia Biccai, Sebastian Barwich, Daniel Boland, Andrey Harvey, Damien Hanlon, Niall McEvoy, and Jonathan N Coleman. Exfoliation of 2D materials by high shear mixing. *2D Materials*, 6(1):015008, oct 2018.

[133] Juntan Yang, Xinpeng Shen, Cong Wang, Yang Chai, and Haimin Yao. Deciphering mechanical properties of 2D materials from the size distribution of exfoliated fragments. *Extreme Mechanics Letters*, 29:100473, 2019.

[134] Deji Akinwande, Nicholas Petrone, and James Hone. Two-dimensional flexible nanoelectronics. *Nature Communications*, 5:1–12, 2014.

[135] Viet Phuong Pham and Geun Young Yeom. Recent Advances in Doping of Molybdenum Disulfide: Industrial Applications and Future Prospects. *Advanced Materials*, 28(41):9024–9059, 2016.

[136] M.N. Nasruddin, Mula Sigiro, and Muhammad Ridwan Fahmi. Raman Scattering Characterization of $Mo_xW_{1-x}S_2$ Layered Mixed Crystals. *Applied Mechanics and Materials*, 754-755:595–601, 2015.

[137] Haotian Wang, Charlie Tsai, Desheng Kong, Karen Chan, Frank Abild-Pedersen, Jens K. Nørskov, and Yi Cui. Transition-metal doped edge sites in vertically aligned MoS_2 catalysts for enhanced hydrogen evolution. *Nano Research*, 8(2):566–575, 2015.

[138] K. K. Kam and B. A. Parkinson. Detailed photocurrent spectroscopy of the semiconducting group VI transition metal dichalcogenides. *Journal of Physical Chemistry*, 86(4):463–467, 1982.

[139] In Soo Kim, Vinod K. Sangwan, Deep Jariwala, Joshua D. Wood, Spencer Park, Kan Sheng Chen, Fengyuan Shi, Francisco Ruiz-Zepeda, Arturo Ponce, Miguel Jose-Yacaman, Vinayak P. Dravid, Tobin J. Marks, Mark C. Hersam, and Lincoln J. Lauhon. Influence of stoichiometry on the optical and electrical properties of chemical vapor deposition derived MoS2. *ACS Nano*, 8(10):10551–10558, 2014.

[140] Ana Laura Elías, Néstor Perea-López, Andrés Castro-Beltrán, Ayse Berkdemir, Ruitao Lv, Simin Feng, Aaron D. Long, Takuya Hayashi, Yoong Ahm Kim, Morinobu Endo, Humberto R. Gutiérrez, Nihar R. Pradhan, Luis Balicas, Thomas E. Mallouk, Florentino López-Urías, Humberto Terrones, and Mauricio Terrones. Controlled synthesis and transfer of large-areaWS_2 sheets: From single layer to few layers. *ACS Nano*, 7(6):5235–5242, 2013.

[141] Gang Wang, Alexey Chernikov, Mikhail M. Glazov, Tony F. Heinz, Xavier Marie, Thierry Amand, and Bernhard Urbaszek. Colloquium: Excitons in atomically thin transition metal dichalcogenides. *Reviews of Modern Physics*, 90(2):21001, 2018.

[142] Z. Y. Zhu, Y. C. Cheng, and U. Schwingenschlögl. Giant spin-orbit-induced spin splitting in two-dimensional transition-metal dichalcogenide semiconductors. *Physical Review B - Condensed Matter and Materials Physics*, 84(15):1–5, 2011.

[143] Jill A. Miwa, Søren Ulstrup, Signe G. Sørensen, Maciej Dendzik, Antonija Grubišić Čabo, Marco Bianchi, Jeppe Vang Lauritsen, and Philip Hofmann. Electronic structure of epitaxial single-layer MoS2. *Physical Review Letters*, 114(4):1–5, 2015.

[144] Hannah Catherine Nerl, Kirsten Trøstrup Winther, Fredrik S. Hage, Kristian Sommer Thygesen, Lothar Houben, Claudia Backes, Jonathan N. Coleman, Quentin M. Ramasse, and Valeria Nicolosi. Probing the local nature of excitons and plasmons in few-layer MoS2. *npj 2D Materials and Applications*, 1(1):2, 2017.

[145] M. A. Py and R. R. Haering. Structural destabilization induced by lithium intercalation in MoS 2 and related compounds. *Canadian Journal of Physics*, 61(1):76–84, jan 1983.

[146] S. Jiménez Sandoval, D. Yang, R. F. Frindt, and J. C. Irwin. Raman study and lattice dynamics of single molecular layers of MoS2. *Physical Review B*, 44(8):3955–3962, 1991.

[147] D. Yang, S. Jiménez Sandoval, W. M. R. Divigalpitiya, J. C. Irwin, and R. F. Frindt. Structure ofsingle-molecular-layer MoS2. *Physical Review B*, 43(14):12053–12056, may 1991.

[148] Zhongxin Chen, Kai Leng, Xiaoxu Zhao, Souradip Malkhandi, Wei Tang, Bingbing Tian, Lei Dong, Lirong Zheng, Ming Lin, Boon Siang Yeo, and Kian Ping Loh. Interface confined hydrogen evolution reaction in zero valent metal nanoparticles-intercalated molybdenum disulfide. *Nature Communications*, 8:1–9, 2017.

[149] P. Ganal, W. Olberding, T. Butz, and G. Ouvrard. Soft chemistry induced host metal coordination change from octahedral to trigonal prismatic in 1T-TaS2. *Solid State Ionics*, 59(3-4):313–319, 1993.

[150] Bo Shang, Xiaoqiang Cui, Lin Jiao, Kun Qi, Yingwei Wang, Jinchang Fan, Yuanyuan Yue, Haiyu Wang, Qiaoliang Bao, Xiaofeng Fan, Shuting Wei, Wei Song, Zhiliang Cheng, Shaojun Guo, and Weitao Zheng. Lattice -Mismatch-Induced Ultrastable 1T-Phase MoS 2 -Pd/Au for Plasmon-Enhanced Hydrogen Evolution. *Nano Letters*, 19(5):2758–2764, 2019.

[151] Deji Akinwande, Christopher J. Brennan, J. Scott Bunch, Philip Egberts, Jonathan R. Felts, Huajian Gao, Rui Huang, Joon Seok Kim, Teng Li, Yao Li, Kenneth M. Liechti, Nanshu Lu, Harold S. Park, Evan J. Reed, Peng Wang, Boris I. Yakobson, Teng Zhang, Yong Wei Zhang, Yao Zhou, and Yong Zhu. A review on mechanics and mechanical properties of 2D materialsâ€"Graphene and beyond. *Extreme Mechanics Letters*, 13:42–77, 2017.

[152] Pablo Solís-Fernández, Mark Bissett, and Hiroki Ago. Synthesis, structure and applications of graphene-based 2D heterostructures. *Chemical Society Reviews*, 46(15):4572–4613, 2017.

[153] Hong Wang, Fucai Liu, Wei Fu, Zheyu Fang, Wu Zhou, and Zheng Liu. Two-dimensional heterostructures: Fabrication, characterization, and application. *Nanoscale*, 6(21):12250–12272, 2014.

[154] Shengxi Huang, Liangbo Liang, Xi Ling, Alexander A. Puretzky, David B. Geohegan, Bobby G. Sumpter, Jing Kong, Vincent Meunier, and Mildred S. Dresselhaus. Low-Frequency Interlayer Raman Modes to Probe Interface of Twisted Bilayer MoS2. *Nano Letters*, 16(2):1435–1444, 2016.

[155] Efthimios Kaxiras, Jing Kong, and Han Wang. Graphene/MoS 2 Hybrid Technology for Large-Scale Two- Dimensional Electronics. (Cvd), 2014.

[156] Rong He, Jian Hua, Anqi Zhang, Chuanhao Wang, Jiayu Peng, Weijia Chen, and Jie Zeng. Molybdenum Disulfide-Black Phosphorus Hybrid Nanosheets as a Superior Catalyst for Electrochemical Hydrogen Evolution. *Nano Letters*, 17(7):4311–4316, 2017.

[157] Changxi Zheng, Qianhui Zhang, Bent Weber, Hesameddin Ilatikhameneh, Fan Chen, Harshad Sahasrabudhe, Rajib Rahman, Shiqiang Li, Zhen Chen, Jack Hellerstedt, Yupeng Zhang, Wen Hui Duan, Qiaoliang Bao, and Michael S. Fuhrer. Direct Observation of 2D Electrostatics and Ohmic Contacts in Template-Grown Graphene/WS2 Heterostructures. *ACS Nano*, 11(3):2785–2793, 2017.

[158] S. Omar and B. J. Van Wees. Graphene-WS_2 heterostructures for tunable spin injection and spin transport. *Physical Review B*, 95(8):1–5, 2017.

[159] Byungjin Cho, Jongwon Yoon, Sung Kwan Lim, Ah Ra Kim, Dong Ho Kim, Sung Gyu Park, Jung Dae Kwon, Young Joo Lee, Kyu Hwan Lee, Byoung Hun Lee, Heung Cho Ko, and Myung Gwan Hahm. Chemical Sensing of 2D Graphene/MoS2 Heterostructure device. *ACS Applied Materials and Interfaces*, 7(30):16775–16780, 2015.

[160] Phan Thi Kim Loan, Wenjing Zhang, Cheng Te Lin, Kung Hwa Wei, Lain Jong Li, and Chang Hsiao Chen. Graphene/MoS2 heterostructures for ultrasensitive detection of DNA hybridisation. *Advanced Materials*, 26(28):4838–4844, 2014.

[161] Sanjay Behura, Phong Nguyen, Songwei Che, Rousan Debbarma, and Vikas Berry. Large-area, transfer-free, oxide-assisted synthesis of hexagonal boron nitride films and their heterostructures with MoS_2 andWS_2. *Journal of the American Chemical Society*, 137(40):13060–13065, 2015.

[162] Jue Hu, Chengxu Zhang, Lin Jiang, He Lin, Yiming An, Dan Zhou, Michael K.H. Leung, and Shihe Yang. Nanohybridization of MoS_2 with Layered Double Hydroxides Efficiently Synergizes the Hydrogen Evolution in Alkaline Media. *Joule*, 1(2):383–393, 2017.

[163] Yuting Luo, Xu Li, Xingke Cai, Xiaolong Zou, Feiyu Kang, Hui Ming Cheng, and Bilu Liu. Two-Dimensional MoS_2 Confined Co(OH)2 Electrocatalysts for Hydrogen Evolution in Alkaline Electrolytes. *ACS Nano*, 12(5):4565–4573, 2018.

[164] Guoqiang Zhao, Kun Rui, Shi Xue Dou, and Wenping Sun. Heterostructures for Electrochemical Hydrogen Evolution Reaction: A Review. *Advanced Functional Materials*, 28(43):1–26, 2018.

[165] Bo Shang, Pengfei Ma, Jinchang Fan, Lin Jiao, Zijian Liu, Zheyu Zhang, Nuo Chen, Zhiliang Cheng, Xiaoqiang Cui, and Weitao Zheng. Stabilized monolayer 1T MoS$_2$ embedded in CoOOH for highly efficient overall water splitting. *Nanoscale*, 10(26):12330–12336, 2018.

[166] Wei Chen, Elton J.G. Santos, Wenguang Zhu, Efthimios Kaxiras, and Zhenyu Zhang. Tuning the electronic and chemical properties of monolayer MoS$_2$ adsorbed on transition metal substrates. *Nano Letters*, 13(2):509–514, 2013.

[167] Ziwei Li, Yu Li, Tianyang Han, Xingli Wang, Ying Yu, Bengkang Tay, Zheng Liu, and Zheyu Fang. Tailoring MoS$_2$ Exciton-Plasmon Interaction by Optical Spin-Orbit Coupling. *ACS Nano*, 11(2):1165–1171, 2017.

[168] Xin Chen and Aidan R. McDonald. Functionalization of Two-Dimensional Transition-Metal Dichalcogenides. *Advanced Materials*, 28(27):5738–5746, 2016.

[169] Damien Voiry, Anandarup Goswami, Rajesh Kappera, Cecilia De Carvalho Castro E. Silva, Daniel Kaplan, Takeshi Fujita, Mingwei Chen, Tewodros Asefa, and Manish Chhowalla. Covalent functionalization of monolayered transition metal dichalcogenides by phase engineering. *Nature Chemistry*, 7(1):45–49, 2015.

[170] Stanislav Presolski and Martin Pumera. Covalent functionalization of MoS2. *Materials Today*, 19(3):140–145, 2016.

[171] Anders Tuxen, Jakob Kibsgaard, Henrik Gøbel, Erik Lægsgaard, Henrik Topsøe, Jeppe V. Lauritsen, and Flemming Besenbacher. Size threshold in the dibenzothiophene adsorption on MoS$_2$ nanoclusters. *ACS Nano*, 4(8):4677–4682, 2010.

[172] Ruben Canton-Vitoria, Yuman Sayed-Ahmad-Baraza, Mario Pelaez-Fernandez, Raul Arenal, Carla Bittencourt, Christopher P. Ewels, and Nikos Tagmatarchis. Functionalization of MoS$_2$ with 1,2-dithiolanes: toward donor-acceptor nanohybrids for energy conversion. *npj 2D Materials and Applications*, 1(1):13, 2017.

[173] Cai Yun Luo, Wei Qing Huang, Wangyu Hu, P. Peng, and Gui Fang Huang. Non-covalent functionalization ofWS$_2$ monolayer with small fullerenes: Tuning electronic properties and photoactivity. *Dalton Transactions*, 45(34):13383–13391, 2016.

[174] Sadao Adachi. *Properties of Semiconductor Alloys: Group-IV, III-V and II-VI Semiconductors; Wiley: Chichester, U.K., 2009.* John Wiley & Sons, Ltd, 1st edition, 2009.

[175] L V Keldysh. Behavior of Non-Metallic Crystals in Strong Electric Fields. *Sov. Phys. JETP*, 6(33):763, 1958.

[176] Walter Franz. Einfluß eines elektrischen Feldes auf eine optische Absorptionskante. *Zeitschrift für Naturforschung A*, 13(6):484–489, jan 1958.

[177] G. H. Yousefi and M. K. Agarwal. Hall effect measurements of Mo1-xWxSe2 (0 â‰¤ x â‰¤ 1) dichalcogenide single crystals. *Journal of Materials Science Letters*, 12(22):1731–1732, 1993.

[178] Philippe R. Bonneau and Richard B. Kaner. High-Quality Mixed-Transition-Metal Dichalcogenides from Solid-State Exchange Reactions. *Inorganic Chemistry*, 32(26):6084–6087, 1993.

[179] R.J. Bouchard. The preparation of pyrite solid solutions of the type FexCo1-xS2, CoxNi1-xS2, and CuxNi1-xS2. *Materials Research Bulletin*, 3(7):563–570, jul 1968.

[180] Sefaattin Tongay, Hasan Sahin, Changhyun Ko, Alex Luce, Wen Fan, Kai Liu, Jian Zhou, Ying Sheng Huang, Ching Hwa Ho, Jinyuan Yan, D. Frank Ogletree, Shaul Aloni, Jie Ji, Shushen Li, Jingbo Li, F. M. Peeters, and Junqiao Wu. Monolayer behaviour in bulk ReS 2 due to electronic and vibrational decoupling. *Nature Communications*, 5:1–6, 2014.

[181] Miklos Kertesz and Roald Hoffmann. Octahedral vs. Trigonal-Prismatic Coordination and Clustering in Transition-Metal Dichalcogenides. *Journal of the American Chemical Society*, 106(12):3453–3460, 1984.

[182] Matteo Calandra. Chemically exfoliated single-layer MoS 2: Stability, lattice dynamics, and catalytic adsorption from first principles. *Physical Review B - Condensed Matter and Materials Physics*, 88(24):1–6, 2013.

[183] M Kan, J Y Wang, X. W Li, S H Zhang, Y W Li, Y Kawazoe, Q Sun, and P Jena. Structures and Phase Transition of a MoS 2 Monolayer. *The Journal of Physical Chemistry C*, 118(3):1515–1522, jan 2014.

[184] Keliang He, Charles Poole, Kin Fai Mak, and Jie Shan. Experimental demonstration of continuous electronic structure tuning via strain in atomically thin MoS2. *Nano Letters*, 13(6):2931–2936, 2013.

[185] H. Peelaers and C. G. Van de Walle. Effects of strain on band structure and effective masses in MoS <math display="inline"> <msub> <mrow/> <mn>2</mn> </msub> </math>. *Physical Review B*, 86(24):241401, dec 2012.

[186] Sheng Han Su, Yu Te Hsu, Yung Huang Chang, Ming Hui Chiu, Chang Lung Hsu, Wei Ting Hsu, Wen Hao Chang, Jr Hau He, and Lain Jong Li. Band gap-tunable molybdenum sulfide selenide monolayer alloy. *Small*, 10(13):2589–2594, 2014.

[187] Qingliang Feng, Nannan Mao, Juanxia Wu, Hua Xu, Chunming Wang, Jin Zhang, and Liming Xie. Growth of MoS2(1-x)Se2 x (x = 0.41-1.00) Monolayer Alloys with Controlled Morphology by Physical Vapor Deposition. *ACS Nano*, 9(7):7450–7455, 2015.

[188] Yifan Sun, Kazunori Fujisawa, Zhong Lin, Yu Lei, Jared S. Mondschein, Mauricio Terrones, and Raymond E. Schaak. Low-Temperature Solution Synthesis of Transition Metal Dichalcogenide Alloys with Tunable Optical Properties. *Journal of the American Chemical Society*, 139(32):11096–11105, 2017.

[189] Yifan Sun, Kazunori Fujisawa, Mauricio Terrones, and Raymond E. Schaak. Solution synthesis of few-layer WTe2 and Mo:XW1-xTe2 nanostructures. *Journal of Materials Chemistry C*, 5(43):11317–11323, 2017.

[190] Y. Lei and Mauricio Terrones. V-doped MoS_2 and V-MoS2 alloys. 2020.

[191] Ziqian Wang, Pan Liu, Yoshikazu Ito, Shoucong Ning, Yongwen Tan, Takeshi Fujita, Akihiko Hirata, and Mingwei Chen. Chemical Vapor Deposition of Monolayer $Mo_{1-x}W_xS_2$Crystals with Tunable Band Gaps. *Scientific Reports*, 6(January):2–10, 2016.

[192] Ziqian Wang, Yuhao Shen, Yoshikazu Ito, Yongzheng Zhang, Jing Du, Takeshi Fujita, Akihiko Hirata, Zheng Tang, and Mingwei Chen. Synthesizing 1T-1H Two-Phase $Mo_{1-x}W_xS_2$Monolayers by Chemical Vapor Deposition. *ACS Nano*, 12(2):1571–1579, 2018.

[193] Ilya Belopolski, Su-Yang Xu, Yukiaki Ishida, Xingchen Pan, Peng Yu, Daniel S. Sanchez, Madhab Neupane, Nasser Alidoust, Guoqing Chang, Tay-Rong Chang, Yun Wu, Guang Bian, Hao Zheng, Shin-Ming Huang, Chi-Cheng Lee, Daixiang Mou, Lunan Huang, You Song, Baigeng Wang, Guanghou Wang, Yao-Wen Yeh, Nan Yao, Julien Rault, Patrick Lefevre, François Bertran, Horng-Tay Jeng, Takeshi Kondo, Adam Kaminski, Hsin Lin, Zheng Liu, Fengqi Song, Shik Shin, and M. Zahid Hasan. Unoccupied electronic structure and signatures of topological Fermi arcs in the Weyl semimetal candidate Mo\$_x\$W\$_{1-x}\$Te\$_2\$. pages 1–24, 2015.

[194] Qi Fu, Lei Yang, Wenhui Wang, Ali Han, Jian Huang, Pingwu Du, Zhiyong Fan, Jingyu Zhang, and Bin Xiang. Synthesis and Enhanced Electrochemical Catalytic Performance of MonolayerWS_2(1-x)Se2x with a Tunable Band Gap. *Advanced Materials*, 27(32):4732–4738, 2015.

[195] He Tian, Matthew L. Chin, Sina Najmaei, Qiushi Guo, Fengnian Xia, Han Wang, and Madan Dubey. Optoelectronic devices based on two-dimensional transition metal dichalcogenides. *Nano Research*, 9(6):1543–1560, 2016.

[196] Zongyou Yin, Hai Li, Hong Li, Lin Jiang, Yumeng Shi, Yinghui Sun, Gang Lu, Qing Zhang, Xiaodong Chen, and Hua Zhang. Single-Layer MoS 2 Phototransistors. *ACS Nano*, 6(1):74–80, jan 2012.

[197] Woong Choi, Mi Yeon Cho, Aniruddha Konar, Jong Hak Lee, Gi Beom Cha, Soon Cheol Hong, Sangsig Kim, Jeongyong Kim, Debdeep Jena, Jinsoo Joo, and Sunkook Kim. High-detectivity multilayer MoS_2 phototransistors with spectral response from ultraviolet to infrared. *Advanced Materials*, 24(43):5832–5836, 2012.

[198] H. Tributsch and J. C. Bennett. Electrochemistry and photochemistry of MoS_2 layer crystals. I. *Journal of Electroanalytical Chemistry*, 81(1):97–111, 1977.

[199] Berit Hinnemann, Poul Georg Moses, Jacob Bonde, Kristina P Jørgensen, Jane H Nielsen, Sebastian Horch, Ib Chorkendorff, and Jens K Nørskov. Biomimetic Hydrogen Evolution: MoS 2 Nanoparticles as Catalyst for Hydrogen Evolution. *Journal of the American Chemical Society*, 127(15):5308–5309, apr 2005.

[200] Thomas F. Jaramillo, Kristina P. Jørgensen, Jacob Bonde, Jane H. Nielsen, Sebastian Horch, and Ib Chorkendorff. Identification of active edge sites for electrochemical H2 evolution from MoS_2 nanocatalysts. *Science*, 317(5834):100–102, 2007.

[201] Lingming Yang, Kausik Majumdar, Han Liu, Yuchen Du, Heng Wu, Michael Hatzistergos, P. Y. Hung, Robert Tieckelmann, Wilman Tsai, Chris Hobbs, and Peide D. Ye. Chloride molecular doping technique on 2D materials:WS_2 and MoS2. *Nano Letters*, 14(11):6275–6280, 2014.

[202] Haichuan Zhang, Yingjie Li, Tianhao Xu, Jiabao Wang, Ziyang Huo, Pengbo Wan, and Xiaoming Sun. Amorphous Co-doped MoS 2 nanosheet coated metallic CoS 2 nanocubes as an excellent electrocatalyst for hydrogen evolution. *Journal of Materials Chemistry A*, 3(29):15020–15023, 2015.

[203] Xiaoping Dai, Kangli Du, Zhanzhao Li, Mengzhao Liu, Yangde Ma, Hui Sun, Xin Zhang, and Ying Yang. Co-Doped MoS_2 Nanosheets with the Dominant CoMoS Phase Coated on Carbon as an Excellent Electrocatalyst for Hydrogen Evolution. *ACS Applied Materials and Interfaces*, 7(49):27242–27253, 2015.

[204] Jia Li, Yang Peng, Xianhao Qian, and Jun Lin. Few-layer Co-doped MoS 2 nanosheets with rich active sites as an efficient cocatalyst for photocatalytic H 2 production over CdS. *Applied Surface Science*, 452:437–442, 2018.

[205] Tanyuan Wang, Dongliang Gao, Junqiao Zhuo, Zhiwei Zhu, Pagona Papakonstantinou, Yan Li, and Meixian Li. Size-dependent enhancement of electrocatalytic oxygen-reduction and hydrogen-evolution performance of MoS_2 particles. *Chemistry - A European Journal*, 19(36):11939–11948, 2013.

[206] Zhebo Chen, Arnold J. Forman, and Thomas F. Jaramillo. Bridging the gap between bulk and nanostructured photoelectrodes: The impact of surface states on the electrocatalytic and photoelectrochemical properties of MoS2. *Journal of Physical Chemistry C*, 117(19):9713–9722, 2013.

[207] Anders B. Laursen, Søren Kegnæs, Søren Dahl, and Ib Chorkendorff. Molybdenum sulfidesâ€"efficient and viable materials for electro - and photoelectrocatalytic hydrogen evolution. *Energy & Environmental Science*, 5(2):5577, 2012.

[208] Yanguang Li, Hailiang Wang, Liming Xie, Yongye Liang, Guosong Hong, and Hongjie Dai. MoS2 nanoparticles grown on graphene: An advanced catalyst for the hydrogen evolution reaction. *Journal of the American Chemical Society*, 133(19):7296–7299, 2011.

[209] Lei Liao, Jie Zhu, Xiaojun Bian, Lina Zhu, Micheál D. Scanlon, Hubert H. Girault, and Baohong Liu. MoS2 formed on mesoporous graphene as a highly active catalyst for hydrogen evolution. *Advanced Functional Materials*, 23(42):5326–5333, 2013.

[210] Qiufang Gong, Liang Cheng, Changhai Liu, Mei Zhang, Qingliang Feng, Hualin Ye, Min Zeng, Liming Xie, Zhuang Liu, and Yanguang Li. Ultrathin MoS2(1-x)Se2x Alloy Nanoflakes for Electrocatalytic Hydrogen Evolution Reaction. *ACS Catalysis*, 5(4):2213–2219, 2015.

[211] Vankayala Kiran, Debdyuti Mukherjee, Ramesh Naidu Jenjeti, and Srinivasan Sampath. Active guests in the MoS2/MoSe2 host lattice: Efficient hydrogen evolution using few-layer alloys of MoS2(1-x)Se2x. *Nanoscale*, 6(21):12856–12863, 2014.

[212] Oren E. Meiron, Vasu Kuraganti, Idan Hod, Ronen Bar-Ziv, and Maya Bar-Sadan. Improved catalytic activity of Mo1-: XWxSe2 alloy nanoflowers promotes efficient hydrogen evolution reaction in both acidic and alkaline aqueous solutions. *Nanoscale*, 9(37):13998–14005, 2017.

[213] Xin Gan, Ruitao Lv, Xuyang Wang, Zexia Zhang, Kazunori Fujisawa, Yu Lei, Zheng Hong Huang, Mauricio Terrones, and Feiyu Kang. Pyrolytic carbon supported alloying metal dichalcogenides as free-standing electrodes for efficient hydrogen evolution. *Carbon*, 132:512–519, 2018.

[214] Desheng Kong, Judy J. Cha, Haotian Wang, Hye Ryoung Lee, and Yi Cui. First-row transition metal dichalcogenide catalysts for hydrogen evolution reaction. *Energy & Environmental Science*, 6(12):3553, 2013.

[215] Dustin R. Cummins, Ulises Martinez, Andriy Sherehiy, Rajesh Kappera, Alejandro Martinez-Garcia, Roland K. Schulze, Jacek Jasinski, Jing Zhang, Ram K. Gupta, Jun Lou, Manish Chhowalla, Gamini Sumanasekera, Aditya D. Mohite, Mahendra K. Sunkara, and Gautam Gupta. Efficient hydrogen evolution in transition metal dichalcogenides via a simple one-step hydrazine reaction. *Nature Communications*, 7(May):1–10, 2016.

[216] Jinsong Wang, Jia Liu, Bao Zhang, Xiao Ji, Kui Xu, Chi Chen, Ling Miao, and Jianjun Jiang. The mechanism of hydrogen adsorption on transition metal dichalcogenides as hydrogen evolution reaction catalyst. *Physical Chemistry Chemical Physics*, 19(15):10125–10132, 2017.

[217] Dequan Er, Han Ye, Nathan C. Frey, Hemant Kumar, Jun Lou, and Vivek B. Shenoy. Prediction of Enhanced Catalytic Activity for Hydrogen Evolution Reaction in Janus Transition Metal Dichalcogenides. *Nano Letters*, 18(6):3943–3949, 2018.

[218] Yanfeng Chen, Jinyang Xi, Dumitru O. Dumcenco, Zheng Liu, Kazu Suenaga, Dong Wang, Zhigang Shuai, Ying Sheng Huang, and Liming Xie. Tunable band gap photoluminescence from atomically thin transition-metal dichalcogenide alloys. *ACS Nano*, 7(5):4610–4616, may 2013.

[219] Juhong Park, Min Su Kim, Bumsu Park, Sang Ho Oh, Shrawan Roy, Jeongyong Kim, and Wonbong Choi. Composition-Tunable Synthesis of Large-Scale Mo 1â€" x W x S 2 Alloys with Enhanced Photoluminescence. *ACS Nano*, 12(6):6301–6309, jun 2018.

[220] Jeong Gyu Song, Gyeong Hee Ryu, Su Jeong Lee, Sangwan Sim, Chang Wan Lee, Taejin Choi, Hanearl Jung, Youngjun Kim, Zonghoon Lee, Jae Min Myoung, Christian Dussarrat, Clement Lansalot-Matras, Jusang Park, Hyunyong Choi, and Hyungjun Kim. Controllable synthesis of molybdenum tungsten disulfide alloy for vertically composition-controlled multilayer. *Nature Communications*, 6:1–10, 2015.

[221] A. M Fox. *Optical properties of solids.* Oxford Universitary Press, Oxford, 2002.

[222] J. Daniels, C. V. Festember, and H. Raether. *Optical constants of solids by electron spectroscopy.* Springer-Verlag, New York, 1970.

[223] S. Lazar, G. A. Botton, and H. W. Zandbergen. Enhancement of resolution in core-loss and low-loss spectroscopy in a monochromated microscope. *Ultramicroscopy*, 106(11-12 SPEC. ISS.):1091–1103, 2006.

[224] A Howie and R.H. Milne. Excitations at interfaces and small particles. *Ultramicroscopy*, 18(1-4):427–433, jan 1985.

[225] T. L. Ferrell and P. M. Echenique. Generation of surface excitations on dielectric spheres by an external electron beam. *Physical Review Letters*, 55(14):1526–1529, 1985.

[226] P. M. Echenique, A. Howie, and D. J. Wheatley. Excitation of dielectric spheres by external electron beams. *Philosophical Magazine B: Physics of Condensed Matter; Statistical Mechanics, Electronic, Optical and Magnetic Properties*, 56(3):335–349, 1987.

[227] A A Lucas. Electron Inelastic Scattering Cross Section. 49(4):2888–2896, 1994.

[228] L. Henrard, F. Malengreau, P. Rudolf, K. Hevesi, R. Caudano, P. Lambin, and T. Cabioc'h. Electron-energy-loss spectroscopy of plasmon excitations in concentric-shell fullerenes. *Physical Review B - Condensed Matter and Materials Physics*, 59(8):5832–5836, 1999.

[229] M. Kociak, O. Stéphan, L. Henrard, V. Charbois, A. Rothschild, R. Tenne, and C. Colliex. Experimental evidence of surface-plasmon coupling in anisotropic hollow nanoparticles. *Physical Review Letters*, 87(7):75501–1–75501–4, 2001.

[230] O. Stéphan, D. Taverna, M. Kociak, K. Suenaga, L. Henrard, and C. Colliex. Dielectric response of isolated carbon nanotubes investigated by spatially resolved electron energy-loss spectroscopy: From multiwalled to single-walled nanotubes. *Physical Review B - Condensed Matter and Materials Physics*, 66(15):1–6, 2002.

[231] D. Taverna, M. Kociak, V. Charbois, and L. Henrard. Electron energy-loss spectrum of an electron passing near a locally anisotropic nanotube. *Physical Review B - Condensed Matter and Materials Physics*, 66(23):1–10, 2002.

[232] R. Arenal, O. Stéphan, M. Kociak, D. Taverna, A. Loiseau, and C. Colliex. Electron energy loss spectroscopy measurement of the optical gaps on individual boron nitride single-walled and multiwalled nanotubes. *Physical Review Letters*, 95(12):1–4, 2005.

[233] R. Arenal. *Synthese de nanotubes de nitrure de bore: études de la structure et des propriétés vibrationnelles et électroniques.* PhD thesis, Université Paris XI, Orsay-France, 2005.

[234] Fengcheng Wu, Timothy Lovorn, and A. H. Macdonald. Theory of optical absorption by interlayer excitons in transition metal dichalcogenide heterobilayers. *Physical Review B*, 97(3):1–10, 2018.

[235] Maxim Trushin, Mark Oliver Goerbig, and Wolfgang Belzig. Optical absorption by Dirac excitons in single-layer transition-metal dichalcogenides. *Physical Review B*, 94(4):1–5, 2016.

[236] Yongji Gong, Zheng Liu, Andrew R. Lupini, Gang Shi, Junhao Lin, Sina Najmaei, Zhong Lin, Ana Laura Elías, Ayse Berkdemir, Ge You, Humberto Terrones, Mauricio Terrones, Robert Vajtai, Sokrates T. Pantelides, Stephen J. Pennycook, Jun Lou, Wu Zhou, and Pulickel M. Ajayan. Band gap engineering and layer-by-layer mapping of selenium-doped molybdenum disulfide. *Nano Letters*, 14(2):442–449, 2014.

[237] Sandhya Susarla, Luiz Henrique Galvão Tizei, Steffi Y. Woo, Alberto Zobelli, Odile Stephan, and Pulickel M. Ajayan. Low Loss EELS of Lateral MoS_2/WS_2 Heterostructures . *Microscopy and Microanalysis*, 25(S2):640–641, 2019.

[238] Diana Y. Qiu, Felipe H. Da Jornada, and Steven G. Louie. Optical spectrum of MoS2: Many-body effects and diversity of exciton states. *Physical Review Letters*, 111(21):1–5, 2013.

[239] Alexey Chernikov, Timothy C. Berkelbach, Heather M. Hill, Albert Rigosi, Yilei Li, Ozgur Burak Aslan, David R. Reichman, Mark S. Hybertsen, and Tony F. Heinz. Exciton binding energy and nonhydrogenic Rydberg series in monolayerWS_2. *Physical Review Letters*, 113(7):1–5, 2014.

[240] Alejandro Molina-Sánchez, Maurizia Palummo, Andrea Marini, and Ludger Wirtz. Temperature-dependent excitonic effects in the optical properties of single-layer MoS2. *Physical Review B*, 93(15):1–8, 2016.

[241] Michael Binnewies, Robert Glaum, Marcus Schmidt, and Peer Schmidt. Chemical Vapor Transport Reactions - A Historical Review. *Zeitschrift für anorganische und allgemeine Chemie*, 639(2):219–229, feb 2013.

[242] Robert Bunsen. Vulkanische Exhalationen. *Journal für Praktische Chemie*, 56(1):53–64, 1852.

[243] S. Fiechter, J. Mai, A. Ennaoui, and W. Szacki. Chemical vapour transport of pyrite (FeS_2) with halogen (Cl, Br, I). *Journal of Crystal Growth*, 78(3):438–444, 1986.

[244] J. M. Ntep, S. Said Hassani, A. Lusson, A. Tromson-Carli, D. Ballutaud, G. Didier, and R. Triboulet. ZnO growth by chemical vapour transport. *Journal of Crystal Growth*, 207(1):30–34, 1999.

[245] R. Nitsche. The growth of single crystals of binary and ternary chalcogenides by chemical transport reactions. *Journal of Physics and Chemistry of Solids*, 17(1-2):163–165, dec 1960.

[246] R. Nitsche, H.U. Bölsterli, and M. Lichtensteiger. Crystal growth by chemical transport reactionsâ€"I -Binary, tertiary and mixed-crystal chalcogenides. *Journal of Physics and Chemistry of Solids*, 21(3-4):199–205, dec 1961.

[247] D. O. Dumcenco, K. Y. Chen, Y. P. Wang, Y. S. Huang, and K. K. Tiong. Raman study of 2H-$\mathrm{Mo}_{1-x}\mathrm{W}_x\mathrm{S}_2$ layered mixed crystals. *Journal of Alloys and Compounds*, 506(2):940–943, 2010.

[248] J. B. Legma, G. Vacquier, and A. Casalot. Chemical vapour transport of molybdenum and tungsten diselenides by various transport agents. *Journal of Crystal Growth*, 130(1-2):253–258, 1993.

[249] Peer Schmidt, Michael Binnewies, Robert Glaum, and Marcus Schmidt. Chemical Vapor Transport Reactions-Methods, Materials, Modeling. In *Advanced Topics on Crystal Growth*, volume i, pages 227–305. InTech, 2013.

[250] Dumitru O Dumcenco, Haruka Kobayashi, Zheng Liu, Ying-Sheng Huang, and Kazu Suenaga. Visualization and quantification of transition metal atomic mixing in $\mathrm{Mo}_{1-x}\mathrm{W}_x\mathrm{S}_2$ single layers. *Nature Communications*, 4:1351, 2013.

[251] Ziqian Wang, Pan Liu, Yoshikazu Ito, Shoucong Ning, Yongwen Tan, Takeshi Fujita, Akihiko Hirata, and Mingwei Chen. Chemical Vapor Deposition of Monolayer $\mathrm{Mo}_{1-x}\mathrm{W}_x\mathrm{S}_2$Crystals with Tunable Band Gaps. *Scientific Reports*, 6(January):2–10, 2016.

[252] Kirsten Andersen, Karsten W. Jacobsen, and Kristian S. Thygesen. Plasmons on the edge of MoS_2 nanostructures. *Physical Review B - Condensed Matter and Materials Physics*, 90(16):1–5, 2014.

[253] Tuomas P. Rossi, Kirsten T. Winther, Karsten W. Jacobsen, Risto M. Nieminen, Martti J. Puska, and Kristian S. Thygesen. Effect of edge plasmons on the optical properties of MoS_2 monolayer flakes. *Physical Review B*, 96(15):1–10, 2017.

[254] M. M. Disko, M. M.J. Treacy, S. B. Rice, R. R. Chianelli, J. A. Gland, T. R. Halbert, and A. F. Ruppert. Spatially resolved electron energy-loss spectroscopy of MoS_2 platelets. *Ultramicroscopy*, 23(3-4):313–319, 1987.

[255] William Hadley Richardson. Bayesian-Based Iterative Method of Image Restoration. *Journal of the Optical Society of America*, 62(1):55–59, jan 1972.

[256] L. B. Lucy. An iterative technique for the rectification of observed distributions. *The Astronomical Journal*, 79(6):745, 1974.

[257] A. Gloter, A. Douiri, M. Tencé, and C. Colliex. Improving energy resolution of EELS spectra: an alternative to the monochromator solution. *Ultramicroscopy*, 96(3-4):385–400, sep 2003.

[258] Alexey Chernikov, Arend M. Van Der Zande, Heather M. Hill, Albert F. Rigosi, Ajanth Velauthapillai, James Hone, and Tony F. Heinz. Electrical Tuning of Exciton Binding Energies in MonolayerWS_2. *Physical Review Letters*, 115(12):1–6, 2015.

[259] Ming Li, Scott K. Cushing, and Nianqiang Wu. Plasmon-enhanced optical sensors: A review. *Analyst*, 140(2):386–406, 2015.

[260] S. Pillai and M. A. Green. Plasmonics for photovoltaic applications. *Solar Energy Materials and Solar Cells*, 94(9):1481–1486, 2010.

[261] Mark L Brongersma. The Case for Plasmonics. *Science*, 440(2010):10–12, 2012.

[262] Mark L Brongersma, J. W. Hartman, Harry A. Atwater, and J. Thomas. Plasmonics: Electromagnetic Energy Transfer and Switching in Nanoparticle Chain Arrays below the Diffraction Limit. In Sokrates T. Pantelides, Mark A. Reed, James S. Murday, and Ari Aviram, editors, *Materials Research Society Symposium Proceedings Volume 582,session 10.5*, Boston, Massachusetts, USA, 1999. Materials Research Society.

[263] Stefan A Maier. *Plasmonics: fundamentals and applications.* 2007.

[264] D. Funes-Hernando. *From hybrid structures to original plasmonic and optical properties.* PhD thesis, Université de Nantes, 2018.

[265] Michael Faraday. X. The Bakerian Lecture. â€"Experimental relations of gold (and other metals) to light. *Philosophical Transactions of the Royal Society of London*, 147:145–181, dec 1857.

[266] R W Wood. On a Remarkable Case of Uneven Distribution of Light in a Diffraction Grating Spectrum. *Proceedings of the Physical Society of London*, 18(1):269–275, jun 1902.

[267] A. Sommerfeld. Ueber die Fortpflanzung elektrodynamischer Wellen längs eines Drahtes. *Annalen der Physik und Chemie*, 303(2):233–290, 1899.

[268] Gustav Mie. Beiträge zur Optik trüber Medien, speziell kolloidaler Metallösungen. *Annalen der Physik*, 330(3):377–445, 1908.

[269] U. Fano. The Theory of Anomalous Diffraction Gratings and of Quasi-Stationary Waves on Metallic Surfaces (Sommerfeld's Waves). *Journal of the Optical Society of America*, 31(3):213, mar 1941.

[270] R. H Ritchie. Plasma Losses by Fast Electrons in Thin Films. *Physical Review*, 106(5), 1957.

[271] R. Ritchie, E. Arakawa, J. Cowan, and R. Hamm. Surface-Plasmon Resonance Effect in Grating Diffraction. *Physical Review Letters*, 21(22):1530–1533, nov 1968.

[272] C. J. Powell and J. B. Swan. Origin of the characteristic electron energy losses in aluminum. *Physical Review*, 115(4):869–875, 1959.

[273] Ye-Yung Teng and Edward A. Stern. Plasma Radiation from Metal Grating Surfaces. *Physical Review Letters*, 19(9):511–514, aug 1967.

[274] Nathan C. Lindquist, Prashant Nagpal, Kevin M. McPeak, David J. Norris, and Sang Hyun Oh. Engineering metallic nanostructures for plasmonics and nanophotonics. *Reports on Progress in Physics*, 75(3), 2012.

[275] Xiaohua Huang and Mostafa A. El-Sayed. Plasmonic photo-thermal therapy (PPTT). *Alexandria Journal of Medicine*, 47(1):1–9, 2011.

[276] Souhir Boujday, Marc Chapelle, Johannes Srajer, and Wolfgang Knoll. Enhanced Vibrational Spectroscopies as Tools for Small Molecule Biosensing. *Sensors*, 15(9):21239–21264, aug 2015.

[277] Ming Li, Scott K. Cushing, and Nianqiang Wu. Plasmon-enhanced optical sensors: A review. *Analyst*, 140(2):386–406, 2015.

[278] Dana Cialla, Anne März, René Böhme, Frank Theil, Karina Weber, Michael Schmitt, and Jürgen Popp. Surface-enhanced Raman spectroscopy (SERS): Progress and trends. *Analytical and Bioanalytical Chemistry*, 403(1):27–54, 2012.

[279] Aric Warner Sanders. *Optical Properties of Metallic Nanostructures.* PhD thesis, Yale University, 2007.

[280] F. J. García De Abajo. Optical excitations in electron microscopy. *Reviews of Modern Physics*, 82(1):209–275, 2010.

[281] Hiroshi Watanabe. Experimental Evidence for the Collective Nature of the Characteristic Energy Loss of Electrons in Solidsâ€“Studies on the Dispersion Relation of Plasma Frequencyâ€“. *Journal of the Physical Society of Japan*, 11(2):112–119, feb 1956.

[282] E. A. Stern and R. A. Ferrell. Surface plasma oscillations of a degenerate electron gas. *Physical Review*, 120(1):130–136, 1960.

[283] Kathryn M. Mayer and Jason H. Hafner. Localized surface plasmon resonance sensors. *Chemical Reviews*, 111(6):3828–3857, 2011.

[284] L. Piazza, T. T.A. Lummen, E. Quiñonez, Y. Murooka, B. W. Reed, B. Barwick, and F. Carbone. Simultaneous observation of the quantization and the interference pattern of a plasmonic near-field. *Nature Communications*, 6, 2015.

[285] O. A. Yeshchenko, I. S. Bondarchuk, V. S. Gurin, I. M. Dmitruk, and A. V. Kotko. Temperature dependence of the surface plasmon resonance in gold nanoparticles. *Surface Science*, 608:275–281, 2013.

[286] J. Leiro, E. Minni, and E. Suoninen. Study of plasmon structure in XPS spectra of silver and gold. *Journal of Physics F: Metal Physics*, 13(1):215–221, 1983.

[287] G. Schider, R. Krenn, A. Hohenau, H. Ditlbacher, A. Leitner, R. Aussenegg, L. Schaich, I. Puscasu, B. Monacelli, and G. Boreman. Plasmon dispersion relation of Au and Ag nanowires. *Physical Review B - Condensed Matter and Materials Physics*, 68(5):1–4, 2003.

[288] Kanglin Wang and Daniel M. Mittleman. Dispersion of surface plasmon polaritons on metal wires in the terahertz frequency range. *Physical Review Letters*, 96(15):1–4, 2006.

[289] J. R. Krenn, G. Schider, W. Rechberger, B. Lamprecht, A. Leitner, F. R. Aussenegg, and J. C. Weeber. Design of multipolar plasmon excitations in silver nanoparticles. *Applied Physics Letters*, 77(21):3379–3381, 2000.

[290] Olivia Nicoletti, Francisco De La Peña, Rowan K. Leary, Daniel J. Holland, Caterina Ducati, and Paul A. Midgley. Three-dimensional imaging of localized surface plasmon resonances of metal nanoparticles. *Nature*, 502(7469):80–84, 2013.

[291] Lindsey J.E. Anderson, Kathryn M. Mayer, Robert D. Fraleigh, Yi Yang, Seunghyun Lee, and Jason H. Hafner. Quantitative measurements of individual gold nanoparticle scattering cross sections. *Journal of Physical Chemistry C*, 114(25):11127–11132, 2010.

[292] Antonio I. Fernández-Domínguez, Francisco J. García-Vidal, and Luis Martín-Moreno. Unrelenting plasmons. *Nature Photonics*, 11(1):8–10, 2017.

[293] Steven D. Christesen. Raman cross sections of chemical agents and simulants. *Appl. Spectrosc.*, 42(2):318–321, Feb 1988.

[294] M. Fleischmann, P.J. Hendra, and A.J. McQuillan. Raman spectra of pyridine adsorbed at a silver electrode. *Chemical Physics Letters*, 26(2):163–166, may 1974.

[295] Martin Moskovits. Surface-enhanced Raman spectroscopy: A brief retrospective. *Journal of Raman Spectroscopy*, 36(6-7):485–496, 2005.

[296] Ujjal Kumar Sur. Surface-enhanced Raman spectroscopy. *Resonance*, 15(2):154–164, 2010.

[297] Paul L. Stiles, Jon A. Dieringer, Nilam C. Shah, and Richard P. Van Duyne. Surface-Enhanced Raman Spectroscopy. *Annual Review of Analytical Chemistry*, 1(1):601–626, jul 2008.

[298] Martin Moskovits, Li-Lin Tay, Jody Yang, and Thomas Haslett. SERS and the Single Molecule. *Optical Properties of Nanostructured Random Media*, 227:215–227, 2007.

[299] Ruoxi Yang and Zhaolin Lu. Subwavelength plasmonic waveguides and plasmonic materials. *International Journal of Optics*, 2012, 2012.

[300] D. Funes-Hernando, M. Pelaez-Fernandez, D. Winterauer, J. Y. Mevellec, R. Arenal, T. Batten, B. Humbert, and J. L. Duvail. Coaxial nanowires as plasmon-mediated remote nanosensors. *Nanoscale*, 10(14):6437–6444, 2018.

[301] O. L. Krivanek, N. Dellby, J. A. Hachtel, J. C. Idrobo, M. T. Hotz, B. Plotkin-Swing, N. J. Bacon, A. L. Bleloch, G. J. Corbin, M. V. Hoffman, C. E. Meyer, and T. C. Lovejoy. Progress in ultrahigh energy resolution EELS. *Ultramicroscopy*, 203(December 2018):60–67, 2019.

[302] P. E. Batson. Damping of bulk plasmons in small aluminum spheres. *Solid State Communications*, 34(6):477–480, 1980.

[303] P E Batson. Surface Plasmon Coupling in Clusters of Small Spheres. *Physical Review Letters*, 49(13):936–940, sep 1982.

[304] M. Kociak, L. Henrard, O. Stéphan, K. Suenaga, and C. Colliex. Plasmons in layered nanospheres and nanotubes investigated by spatially resolved electron energy-loss spectroscopy. *Physical Review B - Condensed Matter and Materials Physics*, 61(20):13936–13944, 2000.

[305] Mathieu Kociak, Odile Stephan, Dario Taverna, Jaysen Nelayah, and Christian Colliex. Probing surface plasmons on individual nano-objects by near-field electron energy loss spectroscopy. *Plasmonics: Metallic Nanostructures and Their Optical Properties III*, 5927:592711, 2005.

[306] Jaysen Nelayah, Mathieu Kociak, Odile Stéphan, F. Javier García De Abajo, Marcel Tencé, Luc Henrard, Dario Taverna, Isabel Pastoriza-Santos, Luis M. Liz-Marzán, and Christian Colliex. Mapping surface plasmons on a single metallic nanoparticle. *Nature Physics*, 3(5):348–353, 2007.

[307] M. Bosman, V. J. Keast, J. L. García-Muñoz, A. J. D'Alfonso, S. D. Findlay, and L. J. Allen. Two-dimensional mapping of chemical information at atomic resolution. *Physical Review Letters*, 99(8):1–4, 2007.

[308] Sean M. Collins, Emilie Ringe, Martial Duchamp, Zineb Saghi, Rafal E. Dunin-Borkowski, and Paul A. Midgley. Eigenmode Tomography of Surface Charge Oscillations of Plasmonic Nanoparticles by Electron Energy Loss Spectroscopy. *ACS Photonics*, 2(11):1628–1635, nov 2015.

[309] Aziz Genç, Javier Patarroyo, Jordi Sancho-Parramon, Raul Arenal, Martial Duchamp, Edgar E. Gonzalez, Luc Henrard, Neus G. Bastús, Rafal E. Dunin-Borkowski, Victor F. Puntes, and Jordi Arbiol. Tuning the Plasmonic Response up: Hollow Cuboid Metal Nanostructures. *ACS Photonics*, 3(5):770–779, 2016.

[310] Aziz Genç, Javier Patarroyo, Jordi Sancho-Parramon, Neus G. Bastús, Victor Puntes, and Jordi Arbiol. Hollow metal nanostructures for enhanced plasmonics: Synthesis, local plasmonic properties and applications. *Nanophotonics*, 6(1):193–213, 2017.

[311] Mathieu Kociak, Odile Stéphan, Alexandre Gloter, Luiz F. Zagonel, Luiz H.G. Tizei, Marcel Tencé, Katia March, Jean Denis Blazit, Zackaria Mahfoud, Arthur Losquin, Sophie Meuret, and Christian Colliex. Seeing and measuring in colours: Electron microscopy and spectroscopies applied to nano-optics. *Comptes Rendus Physique*, 15(2-3):158–175, 2014.

[312] G. W. Paterson, A. Karimullah, SDR Williamson, M. Kadodwala, and D. A. MacLaren. Electron Energy Loss Spectroscopy of a Chiral Plasmonic Structure. *Journal of Physics: Conference Series*, 644(1):012005, oct 2015.

[313] Surong Guo, Nahid Talebi, Wilfried Sigle, Ralf Vogelgesang, Gunther Richter, Martin Esmann, Simon F. Becker, Christoph Lienau, and Peter A. Van Aken. Reflection and Phase Matching in Plasmonic Gold Tapers. *Nano Letters*, 16(10):6137–6144, 2016.

[314] Zhizhong Han, Lili Ren, Zhihui Cui, Chongqi Chen, Haibo Pan, and Jianzhong Chen. Ag/ZnO flower heterostructures as a visible-light driven photocatalyst via surface plasmon resonance. *Applied Catalysis B: Environmental*, 126:298–305, 2012.

[315] Mathieu Kociak. Surface Plasmon Mapping of Dumbbell-Shaped Gold Nanorods: The E ff ect of Silver Coating. 2012.

[316] Raul Arenal, Luc Henrard, Lucian Roiban, Ovidiu Ersen, Julien Burgin, and Mona Treguer-Delapierre. Local plasmonic studies on individual core-shell gold-silver and pure gold nano-bipyramids. *Journal of Physical Chemistry C*, 118(44):25643–25650, 2014.

[317] Alfredo Campos, Nicolas Troc, Emmanuel Cottancin, Michel Pellarin, Hans Christian Weissker, Jean Lermé, Mathieu Kociak, and Matthias Hillenkamp. Plasmonic quantum size effects in silver nanoparticles are dominated by interfaces and local environments. *Nature Physics*, 15(3):275–280, 2019.

[318] Ye Zhu, Philip N.H. Nakashima, Alison M. Funston, Laure Bourgeois, and Joanne Etheridge. Topologically Enclosed Aluminum Voids as Plasmonic Nanostructures. *ACS Nano*, 11(11):11383–11392, 2017.

[319] Stefano Mazzucco, Nicolas Geuquet, Jian Ye, Odile Stéphan, Willem Van Roy, Pol Van Dorpe, Luc Henrard, and Mathieu Kociak. Ultralocal modification of surface plasmons properties in silver nanocubes. *Nano Letters*, 12(3):1288–1294, 2012.

[320] Jessica Rodr, Isabel Pastoriza-santos, Kevin F Macdonald, Luc Henrard, Luis M Liz-marza, Nikolay I Zheludev, Mathieu Kociak, and F Javier Garc. Plasmon Spectroscopy and Imaging of Individual Gold Nanodecahedra: A Combined Optical Microscopy, Cathodoluminescence, and Electron Energy-Loss Spectroscopy Study. *Nano letters*, 2012.

[321] Franz Philipp Schmidt, Harald Ditlbacher, Ulrich Hohenester, Andreas Hohenau, Ferdinand Hofer, and Joachim R. Krenn. Dark plasmonic breathing modes in silver nanodisks. *Nano Letters*, 12(11):5780–5783, 2012.

[322] Guillaume Boudarham, Nils Feth, Viktor Myroshnychenko, Stefan Linden, Javier García De Abajo, Martin Wegener, and Mathieu Kociak. Spectral imaging of individual split-ring resonators. *Physical Review Letters*, 105(25):1–4, 2010.

[323] Felix Von Cube, Stephan Irsen, and Stefan Linden. From isolated metaatoms to photonic metamaterials: Mapping of collective near-field phenomena with EELS. *Optics InfoBase Conference Papers*, pages 3–4, 2012.

[324] Felix Von Cube, Stephan Irsen, Richard Diehl, Jens Niegemann, Kurt Busch, and Stefan Linden. From isolated metaatoms to photonic metamaterials: Evolution of the plasmonic near-field. *Nano Letters*, 13(2):703–708, 2013.

[325] D. Rossouw, M. Couillard, J. Vickery, E. Kumacheva, and G. A. Botton. Multipolar plasmonic resonances in silver nanowire antennas imaged with a subnanometer electron probe. *Nano Letters*, 11(4):1499–1504, 2011.

[326] Olivia Nicoletti, Martijn Wubs, N. Asger Mortensen, Wilfried Sigle, Peter A. van Aken, and Paul A. Midgley. Surface plasmon modes of a single silver nanorod: an electron energy loss study. *Optics Express*, 19(16):15371, 2011.

[327] David Rossouw and Gianluigi A. Botton. Plasmonic response of bent silver nanowires for nanophotonic subwavelength waveguiding. *Physical Review Letters*, 110(6):1–5, 2013.

[328] Sean M. Collins, Olivia Nicoletti, David Rossouw, Tomas Ostasevicius, and Paul A. Midgley. Excitation dependent Fano-like interference effects in plasmonic silver nanorods. oct 2014.

[329] Hongyan Liang, David Rossouw, Haiguang Zhao, Scott K. Cushing, Honglong Shi, Andreas Korinek, Hongxing Xu, Federico Rosei, Wenzhong Wang, Nianqiang Wu, Gianluigi A. Botton, and Dongling Ma. Asymmetric silver ”nanocarrot” structures: Solution synthesis and their asymmetric plasmonic resonances. *Journal of the American Chemical Society*, 135(26):9616–9619, 2013.

[330] David Rossouw, Gianluigi A. Botton, Dongling Ma, Wenzhong Wang, Andreas Korinek, Hongxing Xu, Federico Rosei, Honglong Shi, Scott K. Cushing, Haiguang Zhao, Hongyan Liang, and Nianqiang Wu. Asymmetric Silver â€œNanocarrotâ€ Structures: Solution Synthesis and Their Asymmetric Plasmonic Resonances. *Journal of the American Chemical Society*, 135(26):9616–9619, 2013.

[331] Moussa N’Gom, Shuzhou Li, George Schatz, Rolf Erni, Ashish Agarwal, Nicholas Kotov, and Theodore B. Norris. Electron-beam mapping of plasmon resonances in electromagnetically interacting gold nanorods. *Physical Review B - Condensed Matter and Materials Physics*, 80(11):1–4, 2009.

[332] John S. Biggins, Sadegh Yazdi, and Emilie Ringe. Magnesium Nanoparticle Plasmonics. *Nano Letters*, 18(6):3752–3758, 2018.

[333] S. Mazzucco, O. Stéphan, C. Colliex, I. Pastoriza-Santos, L. M. Liz-Marzan, J. Garcia De Abajo, and M. Kociak. Spatially resolved measurements of plasmonic eigenstates in complex-shaped, asymmetric nanoparticles: Gold nanostars. *EPJ Applied Physics*, 54(3):1–9, 2011.

[334] Michel Bosman, Enyi Ye, Shu Fen Tan, Christian A. Nijhuis, Joel K.W. Yang, Renaud Marty, Adnen Mlayah, Arnaud Arbouet, Christian Girard, and Ming Yong Han. Surface plasmon damping quantified with an electron nanoprobe. *Scientific Reports*, 3:1–7, 2013.

[335] Martin Prieto, Raul Arenal, Luc Henrard, Leyre Gomez, Victor Sebastian, and Manuel Arruebo. Morphological tunability of the plasmonic response: From hollow gold nanoparticles to gold nanorings. *Journal of Physical Chemistry C*, 118(49):28804–28811, 2014.

[336] Bernhard Schaffer, Werner Grogger, Gerald Kothleitner, and Ferdinand Hofer. Comparison of EFTEM and STEM EELS plasmon imaging of gold nanoparticles in a monochromated TEM. *Ultramicroscopy*, 110(8):1087–1093, 2010.

[337] J. Nelayah, L. Gu, W. Sigle, C. T. Koch, I. Pastoriza-Santos, L. M. Liz-Marzán, and P. A. van Aken. Direct imaging of surface plasmon resonances on single triangular silver nanoprisms at optical wavelength using low-loss EFTEM imaging. *Optics Letters*, 34(7):1003, 2009.

[338] Lin Gu, Wilfried Sigle, Christoph T. Koch, Burcu Ögüt, Peter A. Van Aken, Nahid Talebi, Ralf Vogelgesang, Jianlin Mu, Xiaogang Wen, and Jian Mao. Resonant wedge-plasmon modes in single-crystalline gold nanoplatelets. *Physical Review B - Condensed Matter and Materials Physics*, 83(19):1–7, 2011.

[339] J. Nelayah, M. Kociak, O. Stéphan, N. Geuquet, L. Henrard, F. J. De García Abajo, I. Pastoriza-Santos, L. M. Liz-Marzán, and C. Colliex. Two-dimensional quasistatic stationary short range surface plasmons in flat nanoprisms. *Nano Letters*, 10(3):902–907, 2010.

[340] Alfredo Campos, Arnaud Arbouet, Jérôme Martin, Davy Gérard, Julien Proust, Jérôme Plain, and Mathieu Kociak. Plasmonic Breathing and Edge Modes in Aluminum Nanotriangles. *ACS Photonics*, 4(5):1257–1263, 2017.

[341] V. J. Keast, C. J. Walhout, T. Pedersen, N. Shahcheraghi, M. B. Cortie, and D. R.G. Mitchell. Higher Order Plasmonic Modes Excited in Ag Triangular Nanoplates by an Electron Beam. *Plasmonics*, 11(4):1081–1086, 2016.

[342] Emilie Ringe, Christopher J Desantis, Sean M Collins, Martial Duchamp, Rafal E Dunin, Rafal E Dunin-Borkowski, Sara E Skrabalak, and Paul A Midgley. Near-Field Plasmonic Behavior of Au/Pd Nanocrystals with Pd-Rich Tips. *arXiv preprint*, 5:1506, 2015.

[343] Ina Alber, Wilfried Sigle, Sven Mu, Reinhard Neumann, Oliver Picht, Markus Rauber, Peter A Van Aken, and Maria Eugenia Toimil-molares. Visualization of Multipolar Longitudinal and Transversal Surface Plasmon Modes in Nanowire Dimers. (12):9845–9853, 2011.

[344] Ming-wen Chu, Viktor Myroshnychenko, Cheng Hsuan Chen, Jing-pei Deng, Chung-yuan Mou, and F Javier García De Abajo. Probing Bright and Dark Surface-Plasmon Modes in Individual and Coupled Noble Metal Nanoparticles Using an Electron Beam 2009. 2009.

[345] Michel Bosman, Vicki J Keast, Masashi Watanabe, Abbas I Maaroof, and Michael B Cortie. Mapping surface plasmons at the nanometre scale with an electron beam. 165505.

[346] Ai Leen Koh, Antonio I Fern, David W Mccomb, Stefan A Maier, and Joel K W Yang. High-Resolution Mapping of Electron-Beam-Excited Plasmon Modes in Lithographically Defined Gold Nanostructures. pages 1323–1330, 2011.

[347] Michel Bosman and Stefan A Maier. Nanoplasmonics : Classical down to the Nanometer Scale. 2012.

[348] O Burcu, Melanie Rohm, and Peter A Van Aken. Breaking the Mode Degeneracy of Surface Plasmon Resonances in a Triangular System. 2012.

[349] Jonathan A Scholl, Aitzol Garc, Ai Leen Koh, and Jennifer A Dionne. Observation of Quantum Tunneling between Two Plasmonic Nanoparticles. 2012.

[350] Steven J. Barrow, Sean M. Collins, David Rossouw, Alison M. Funston, Gianluigi A. Botton, Paul A. Midgley, and Paul Mulvaney. Electron Energy Loss Spectroscopy Investigation into Symmetry in Gold Trimer and Tetramer Plasmonic Nanoparticle Structures. *ACS Nano*, 10(9):8552–8563, sep 2016.

[351] Matthew Rycenga, Claire M. Cobley, Jie Zeng, Weiyang Li, Christine H. Moran, Qiang Zhang, Dong Qin, and Younan Xia. Controlling the synthesis and assembly of silver nanostructures for plasmonic applications. *Chemical Reviews*, 111(6):3669–3712, 2011.

[352] Tuncay Ozel, Gilles R. Bourret, and Chad A. Mirkin. Coaxial lithography. *Nature Nanotechnology*, 10(4):319–324, 2015.

[353] Georg Haberfehlner, Franz Philipp Schmidt, Gernot Schaffernak, Anton Hörl, Andreas Trügler, Andreas Hohenau, Ferdinand Hofer, Joachim R. Krenn, Ulrich Hohenester, and Gerald Kothleitner. 3D Imaging of Gap Plasmons in Vertically Coupled Nanoparticles by EELS Tomography. *Nano Letters*, 17(11):6773–6777, 2017.

[354] Anuj Dhawan, Michael Gerhold, Andrew Madison, Jason Fowlkes, Phillip E. Russell, Tuan Vo-Dinh, and Donovan N. Leonard. Fabrication of nanodot plasmonic waveguide structures using FIB milling and electron beam-induced deposition. *Scanning*, 31(4):139–146, 2009.

[355] Joshua F. Einsle, Jean Sebastien Bouillard, Wayne Dickson, and Anatoly V. Zayats. Hybrid FIB milling strategy for the fabrication of plasmonic nanostructures on semiconductor substrates. *Nanoscale Research Letters*, 6:1–5, 2011.

[356] Sergey V. Makarov, Anastasia S. Zalogina, Mohammad Tajik, Dmitry A. Zuev, Mikhail V. Rybin, Aleksandr A. Kuchmizhak, Saulius Juodkazis, and Yuri Kivshar. Light-Induced Tuning and Reconfiguration of Nanophotonic Structures. *Laser and Photonics Reviews*, 11(5):1–25, 2017.

[357] Lina Zhou, Jinsheng Lu, Hangbo Yang, Si Luo, Wei Wang, Jun Lv, Min Qiu, and Qiang Li. Optically controllable nanobreaking of metallic nanowires. *Applied Physics Letters*, 110(8), 2017.

[358] Liaoyong Wen, Rui Xu, Yan Mi, and Yong Lei. Multiple nanostructures based on anodized aluminium oxide templates. *Nature Nanotechnology*, 12(3):244–250, 2017.

[359] Shunping Zhang, Hong Wei, Kui Bao, Ulf Håkanson, Naomi J. Halas, Peter Nordlander, and Hongxing Xu. Chiral surface plasmon polaritons on metallic nanowires. *Physical Review Letters*, 107(9):1–5, 2011.

[360] Long Gao, Li Chen, Hong Wei, and Hongxing Xu. Correction: Lithographically fabricated gold nanowire waveguides for plasmonic routers and logic gates. *Nanoscale*, 10(30):14771–14771, 2018.

[361] Qiang Li and Min Qiu. Plasmonic wave propagation in silver nanowires: guiding modes or not? *Optics Express*, 21(7):8587, 2013.

[362] Yingzhou Huang, Yuri Fang, and Mengtao Sun. Remote excitation of surface-enhanced raman scattering on single au nanowire with quasi-spherical termini. *Journal of Physical Chemistry C*, 115(9):3558–3561, 2011.

[363] Nicolas Dobigeon and Nathalie Brun. Spectral mixture analysis of EELS spectrum-images. *Ultramicroscopy*, 120:25–34, 2012.

[364] Alberto Eljarrat, Sònia Estradé, and Francesca Peiró. Low-loss EELS methods. In *Advances in Imaging and Electron Physics*, volume 209, chapter 2, pages 49–77. Elsevier Inc., 2019.

[365] Karl Pearson. LIII. On lines and planes of closest fit to systems of points in space . *The London, Edinburgh, and Dublin Philosophical Magazine and Journal of Science*, 2(11):559–572, 1901.

[366] Svante Wold, Kim Esbensen, and Paul Geladi. Principal component analysis. *Chemometrics and intelligent laboratory systems*, 2(1-3):37–52, 1987.

[367] Pierre Trebbia and Noël Bonnet. EELS elemental mapping with unconventional methods I. Theoretical basis: Image analysis with multivariate statistics and entropy concepts. *Ultramicroscopy*, 34(3):165–178, 1990.

[368] F. de la Peña, M. H. Berger, J. F. Hochepied, F. Dynys, O. Stephan, and M. Walls. Mapping titanium and tin oxide phases using EELS: An application of independent component analysis. *Ultramicroscopy*, 111(2):169–176, 2011.

[369] N Bonnet, N Brun, and C Colliex. Extracting information from sequences of spatially resolved EELS spectra using multivariate statistical analysis. *Ultramicroscopy*, 77(3-4):97–112, jul 1999.

[370] M. Bosman, M. Watanabe, D. T.L. Alexander, and V. J. Keast. Mapping chemical and bonding information using multivariate analysis of electron energy-loss spectrum images. *Ultramicroscopy*, 106(11-12 SPEC. ISS.):1024–1032, 2006.

[371] Lluís Yedra, Alberto Eljarrat, Raúl Arenal, Eva Pellicer, Moisés Cabo, Alberto López-Ortega, Marta Estrader, Jordi Sort, Maria Dolors Baró, Sònia Estradé, and Francesca Peiró. EEL spectroscopic tomography: Towards a new dimension in nanomaterials analysis. *Ultramicroscopy*, 122:12–18, 2012.

[372] M. R. Keenan and P. O. Kotula. Multivariate statistical analysis of EEL-spectral images. *Microscopy and Microanalysis*, 10(SUPPL. 2):874–875, 2004.

[373] V. Badjeck, M. G. Walls, L. Chaffron, J. Malaplate, and K. March. New insights into the chemical structure of Y2Ti2O7-δ nanoparticles in oxide dispersion-strengthened steels designed for sodium fast reactors by electron energy-loss spectroscopy. *Journal of Nuclear Materials*, 456:292–301, 2015.

[374] Christian Jutten and Jeanny Herault. Blind separation of sources, part I: An adaptive algorithm based on neuromimetic architecture. *Signal Processing*, 24(1):1–10, 1991.

[375] A. Hyvärinen and E. Oja. Independent component analysis: algorithms and applications. *Neural Networks*, 13(4-5):411–430, jun 2000.

[376] Pierre Comon. Independent component analysis, A new concept? *Signal Processing*, 36(3):287–314, apr 1994.

[377] Yu-Xiong Wang and Yu-Jin Zhang. Nonnegative Matrix Factorization: A Comprehensive Review. *IEEE Transactions on Knowledge and Data Engineering*, 25(6):1336–1353, jun 2013.

[378] Pentti Paatero and Unto Tapper. Positive matrix factorization: A nonâ€negative factor model with optimal utilization of error estimates of data values. *Environmetrics*, 5(2):111–126, 1994.

[379] Pentti Paatero. Least squares formulation of robust non-negative factor analysis. *Chemometrics and Intelligent Laboratory Systems*, 37(1):23–35, 1997.

[380] Daniel D. Lee and H. Sebastian Seung. Learning the parts of objects by non-negative matrix factorization. *Nature*, 401(6755):788–791, 1999.

[381] Daniel D. Lee and H. Sebastian Seung. Algorithms for Non-negative Matrix Factorization. *Advances in Neural Information Processing Systems*, 13, 2000.

[382] Wei Xu, Xin Liu, and Yihong Gong. Document clustering based on non-negative matrix factorization. In *Proceedings of the 26th annual international ACM SIGIR conference on Research and development in informaion retrieval - SIGIR '03*, volume 2, page 267, New York, New York, USA, 2003. ACM Press.

[383] Chris Ding, Tao Li, Wei Peng, and Haesun Park. Orthogonal nonnegative matrix tri-factorizations for clustering. *Proceedings of the ACM SIGKDD International Conference on Knowledge Discovery and Data Mining*, 2006:126–135, 2006.

[384] Taiping Zhang, Bin Fang, Guanghui He, Jing Wen, and Yuanyan Tang. Face recognition using topology preserving nonnegative matrix factorization. *Proceedings - 2007 International Conference on Computational Intelligence and Security, CIS 2007*, 17(4):405–409, 2007.

[385] Paris Smaragdis and J.C. Brown. Non-negative matrix factorization for polyphonic music transcription. In *2003 IEEE Workshop on Applications of Signal Processing to Audio and Acoustics (IEEE Cat. No.03TH8684)*, number 1, pages 177–180. IEEE, 2003.

[386] Thomas Blum, Jeffery Graves, Michael Zachman, Ramakrishnan Kannan, Xiaoqing Pan, and Miaofang Chi. Machine Learning for Challenging EELS and EDS Spectral Decomposition. *Microscopy and Microanalysis*, 25(S2):180–181, 2019.

[387] Motoki Shiga, Shunsuke Muto, Kazuyoshi Tatsumi, and Koji Tsuda. Matrix Factorization for Automatic Chemical Mapping from Electron Microscopic Spectral Imaging Datasets. *Transactions of the Materials Research Society of Japan*, 41(4):333–336, apr 2016.

[388] Motoki Shiga, Shunsuke Muto, Kazuyoshi Tatsumi, and Koji Tsuda. Matrix Factorization for Automatic Chemical Mapping from Electron Microscopic Spectral Imaging Datasets. *Transactions of the Materials Research Society of Japan*, 41(4):333–336, apr 2016.

[389] Yuki Nomura, Kazuo Yamamoto, Tsukasa Hirayama, Mayumi Ohkawa, Emiko Igaki, Nobuhiko Hojo, and Koh Saitoh. Quantitative Operando Visualization of Electrochemical Reactions and Li Ions in All-Solid-State Batteries by STEM-EELS with Hyperspectral Image Analyses. *Nano Letters*, 18(9):5892–5898, 2018.

[390] Renu Sharma, Alina Bruma, Wei-Chang (David) Yang, and Canhui Wang. Electron Energy-Loss Spectroscopy for Designing Plasmonic Catalysts. *Microscopy and Microanalysis*, 25(S2):638–639, 2019.

[391] Emilie Ringe, Christopher J. DeSantis, Sean M. Collins, Martial Duchamp, Rafal E. Dunin-Borkowski, Sara E. Skrabalak, and Paul A. Midgley. Resonances of nanoparticles with poor plasmonic metal tips. *Scientific Reports*, 5(1):17431, dec 2015.

[392] Sean M. Collins, Demie M. Kepaptsoglou, Keith T. Butler, Louis Longley, Thomas D. Bennett, Quentin M. Ramasse, and Paul A. Midgley. Subwavelength Spatially Resolved Coordination Chemistry of Metal-Organic Framework Glass Blends. *Journal of the American Chemical Society*, 140(51):17862–17866, 2018.

[393] Alberto Eljarrat, Lluís López-Conesa, Julian López-Vidrier, Sergi Hernández, Blas Garrido, César Magén, Francesca Peiró, and Sònia Estradé. Retrieving the electronic properties of silicon nanocrystals embedded in a dielectric matrix by low-loss EELS. *Nanoscale*, 6(24):14971–14983, 2014.

[394] Francisco Javier De la Peña, Vidar Tonaas Fauske, Pierre Burdet, Tomas Ostasevicius, Mike Sarahan, Magnus Nord, Joshua A. Taillon, Duncan Johnstone, Katherine E. MacArthur, Alberto Eljarrat, Stefano Mazzuco, Jan Caron, Tom Furnival, Michael Walls, Eric Prestat, Gaël Donval, Ben Martineau, Luiz F. Zagonel, Petras Jokubauskas, Thomas Aarholt, Andreas Garmannslund, and Ilya Iyengar. hyperspy: HyperSpy 0.8.5, 2016.

[395] Stijn Lichtert and Jo Verbeeck. Statistical consequences of applying a PCA noise filter on EELS spectrum images. *Ultramicroscopy*, 125(2013):35–42, 2013.

[396] Peter Bajorski. Statistical inference in PCA for hyperspectral images. *IEEE Journal on Selected Topics in Signal Processing*, 5(3):438–445, 2011.

[397] Nicolas Geuquet and Luc Henrard. EELS and optical response of a noble metal nanoparticle in the frame of a discrete dipole approximation. *Ultramicroscopy*, 110(8):1075–1080, 2010.

[398] L. Henrard and Ph Lambin. Calculation of the energy loss for an electron passing near giant fullerenes. *Journal of Physics B: Atomic, Molecular and Optical Physics*, 29(21):5127–5141, 1996.

[399] A. Rivacoba and F. J. García de Abajo. Electron energy loss in carbon nanostructures. *Physical Review B - Condensed Matter and Materials Physics*, 67(8):1–8, 2003.

[400] Martin Prieto, Raul Arenal, Luc Henrard, Leyre Gomez, Victor Sebastian, and Manuel Arruebo. Morphological tunability of the plasmonic response: From hollow gold nanoparticles to gold nanorings. *Journal of Physical Chemistry C*, 118(49):28804–28811, 2014.

[401] Daniel R Dreyer, Sungjin Park, W Bielawski, and Rodney S Ruoff. The chemistry of graphene oxide. *Chemical Society Reviews*, 39:228–240, 2010.

[402] Shuai Wang, Perq Jon Chia, Lay Lay Chua, Li Hong Zhao, Rui Qi Png, Sankaran Sivaramakrishnan, Mi Zhou, Roland G.S. Goh, Richard H. Friend, Andrew T.S. Wee, and Peter K.H. Ho. Band-like transport in surface-functionalized highly solution-processable graphene nanosheets. *Advanced Materials*, 20(18):3440–3446, 2008.

[403] C Schafhaeutl. LXXXVI. On the combinations of carbon with silicon and iron, and other metals, forming the different species of cast iron, steel, and malleable iron. *The London, Edinburgh, and Dublin Philosophical Magazine and Journal of Science*, 16(106):570–590, jan 1840.

[404] Benjamin Collins Brodie. XIII. On the atomic weight of graphite. *Philosophical Transactions of the Royal Society of London*, 149(1113):249–259, 1859.

[405] Benjamin Collins Brodie. Note sur un Nouveau Procédé pour la Purification et la Désagrégation du Graphite. *Annuaire de Chimie et Physique*, 45:351–353, 1855.

[406] Jonathan P Rourke, Priyanka A Pandey, Joseph J Moore, Matthew Bates, Ian A Kinloch, Robert J Young, and Neil R Wilson. The Real Graphene Oxide Revealed: Stripping the Oxidative Debris from the Graphene-like Sheets. *Angewandte Chemie*, 123(14):3231–3235, mar 2011.

[407] D. D'Angelo, C. Bongiorno, M. Amato, I. Deretzis, A. La Magna, G. Compagnini, S.F. Spanò, and S. Scalese. Electron energy-loss spectra of graphene oxide for the determination of oxygen functionalities. *Carbon*, 93:1034–1041, nov 2015.

[408] Anna Tararan, Alberto Zobelli, Ana M Benito, Wolfgang K Maser, and Odile Stéphan. Revisiting Graphene Oxide Chemistry via Spatially-Resolved Electron Energy Loss Spectroscopy. *Chemistry of Materials*, 28(11):3741–3748, jun 2016.

[409] Von Ulrich Hofmann, Alfred Frenzel, and E Csalán. Die Konstitution der Graphitsaure und ihre Reaktionen. *Justus Liebigs Annalen der Chemie*, 510(1):1–41, 1934.

[410] G Ruess. Über das Graphitoxyhydroxyd (Graphitoxyd). *Monatshefte für Chemie und verwandte Teile anderer Wissenschaften*, 76(3-5):381–417, 1946.

[411] W Scholz and H P Boehm. Betrachtungen zur Struktur des Graphitoxids. *Zeitschrift Fur Anorganische Und Allgemeine Chemie*, 236(369(3-6)):327–340, 1969.

[412] T. Nakajima, A. Mabuchi, and R. Hagiwara. A new structure model of graphite oxide. *Carbon*, 26(3):357–361, 1988.

[413] Tsuyoshi Nakajima and Yoshiaki Matsuo. Formation process and structure of graphite oxide. *Carbon*, 32(3):469–475, 1994.

[414] A. Martín Rodríguez and P.S. Valerga Jiménez. Some new aspects of graphite oxidation at 0Â°c in a liquid medium. A mechanism proposal for oxidation to graphite oxide. *Carbon*, 24(2):163–167, 1986.

[415] M. Mermoux, Y. Chabre, and A. Rousseau. FTIR and 13C NMR study of graphite oxide. *Carbon*, 29(3):469–474, 1991.

[416] C. Hontoria-Lucas, A.J. López-Peinado, J.de D. López-González, M.L. Rojas-Cervantes, and R.M. Martín-Aranda. Study of oxygen-containing groups in a series of graphite oxides: Physical and chemical characterization. *Carbon*, 33(11):1585–1592, 1995.

[417] Anton Lerf, Heyong He, Michael Forster, and Jacek Klinowski. Structure of Graphite Oxide Revisited —. *Journal of Physical Chemistry B*, 102(23):4477–4482, 1998.

[418] Laura J. Cote, Franklin Kim, and Jiaxing Huang. Langmuir-blodgett assembly of graphite oxide single layers. *Journal of the American Chemical Society*, 131(3):1043–1049, 2009.

[419] Heyong He, Jacek Klinowski, Michael Forster, and Anton Lerf. A new structural model for graphite oxide. *Chemical Physics Letters*, 287(1-2):53–56, apr 1998.

[420] Tamás Szabó, Ottó Berkesi, Péter Forgó, Katalin Josepovits, Yiannis Sanakis, Dimitris Petridis, and Imre Dékány. Evolution of surface functional groups in a series of progressively oxidized graphite oxides. *Chemistry of Materials*, 18(11):2740–2749, 2006.

[421] Heyong He, Thomas Riedl, Anton Lerf, and Jacek Klinowski. Solid-state NMR studies of the structure of graphite oxide. *Journal of Physical Chemistry*, 100(51):19954–19958, 1996.

[422] Tamás Szabó, Ottó Berkesi, and Imre Dékány. DRIFT study of deuterium-exchanged graphite oxide. *Carbon*, 43(15):3186–3189, 2005.

[423] Wei Gao, Lawrence B. Alemany, Lijie Ci, and Pulickel M. Ajayan. New insights into the structure and reduction of graphite oxide. *Nature Chemistry*, 1(5):403–408, 2009.

[424] A.L. Blumenfeld, V.E. Muradyan, I.B. Shumilova, Z.N. Parnes, and Yu.N. Novikov. Investigation of Graphite Oxide by Means of 13C NMR and 1H Spin-Lattice Relaxation. *Materials Science Forum*, 91-93:613–617, jan 1992.

[425] W. Cai, R. D. Piner, F. J. Stadermann, S. Park, M. A. Shaibat, Y. Ishii, D. Yang, A. Velamakanni, S. J. An, M. Stoller, J. An, D. Chen, and R. S. Ruoff. Synthesis and Solid-State NMR Structural Characterization of 13C-Labeled Graphite Oxide. *Science*, 321(5897):1815–1817, sep 2008.

[426] Zilong Liu, Kasper Nørgaard, Marc H Overgaard, Marcel Ceccato, David M A Mackenzie, Nicolas Stenger, Susan L S Stipp, and Tue Hassenkam. Direct observation of oxygen con fi guration on individual graphene oxide sheets. *Carbon*, 127:141–148, 2018.

[427] Kris Erickson, Rolf Erni, Zonghoon Lee, Nasim Alem, Will Gannett, and Alex Zettl. Determination of the local chemical structure of graphene oxide and reduced graphene oxide. *Advanced Materials*, 22(40):4467–4472, 2010.

[428] Alexandre Dazzi, Craig B. Prater, Qichi Hu, D. Bruce Chase, John F. Rabolt, and Curtis Marcott. AFM-IR: Combining atomic force microscopy and infrared spectroscopy for nanoscale chemical characterization. *Applied Spectroscopy*, 66(12):1365–1384, 2012.

[429] Karthikeyan Krishnamoorthy, Murugan Veerapandian, Kyusik Yun, and S. J. Kim. The chemical and structural analysis of graphene oxide with different degrees of oxidation. *Carbon*, 53:38–49, 2013.

[430] D. W. Lee, L. De Los Santos V., J. W. Seo, L. Leon Felix, A. Bustamante D., J. M. Cole, and C. H.W. Barnes. The structure of graphite oxide: Investigation of its surface chemical groups. *Journal of Physical Chemistry B*, 114(17):5723–5728, 2010.

[431] Te Fu Yeh, Jhih Ming Syu, Ching Cheng, Ting Hsiang Chang, and Hsisheng Teng. Graphite oxide as a photocatalyst for hydrogen production from water. *Advanced Functional Materials*, 20(14):2255–2262, 2010.

[432] Muge Acik, Geunsik Lee, Cecilia Mattevi, Adam Pirkle, Robert M. Wallace, Manish Chhowalla, Kyeongjae Cho, and Yves Chabal. The role of oxygen during thermal reduction of graphene oxide studied by infrared absorption spectroscopy. *Journal of Physical Chemistry C*, 115(40):19761–19781, 2011.

[433] Muge Acik, Cecilia Mattevi, Cheng Gong, Geunsik Lee, Kyeongjae Cho, Manish Chhowalla, and Yves J Chabal. The Role of Intercalated Water in Multilayered Graphene Oxide. *ACS Nano*, 4(10):5861–5868, oct 2010.

[434] Jesus Guerrero-Contreras and F. Caballero-Briones. Graphene oxide powders with different oxidation degree, prepared by synthesis variations of the Hummers method. *Materials Chemistry and Physics*, 153:209–220, 2015.

[435] Ali Gharib, Leila Vojdani Fard, Nader Noroozi Pesyan, and Mina Roshani. A New Application of Nano - Graphene Oxide (NGO) as a Heterogeneous Catalyst in Oxidation of Alcohols Types. *Chemistry Journal*, 1(4):151–158, 2015.

[436] E. Fuente, J. A. Menéndez, M. A. Díez, D. Suárez, and M. A. Montes-Morán. Infrared spectroscopy of carbon materials: A quantum chemical study of model compounds. *Journal of Physical Chemistry B*, 107(26):6350–6359, 2003.

[437] Chenliang Su, Muge Acik, Kazuyuki Takai, Jiong Lu, Si Jia Hao, Yi Zheng, Pingping Wu, Qiaoliang Bao, Toshiaki Enoki, Yves J. Chabal, and Kian Ping Loh. Probing the catalytic activity of porous graphene oxide and the origin of this behaviour. *Nature Communications*, 3:1298–1299, 2012.

[438] Heyun Fu, Xiaolei Qu, Wei Chen, and Dongqiang Zhu. Transformation and destabilization of graphene oxide in reducing aqueous solutions containing sulfide. *Environmental Toxicology and Chemistry*, 33(12):2647–2653, 2014.

[439] Goki Eda and Manish Chhowalla. Chemically Derived Graphene Oxide: Towards Large-Area Thin-Film Electronics and Optoelectronics. *Advanced Materials*, 22(22):2392–2415, jun 2010.

[440] Mohammad Arif Ishtiaque Shuvo, Md Ashiqur Rahaman Khan, Hasanul Karim, Philip Morton, Travis Wilson, and Yirong Lin. Investigation of modified graphene for energy storage applications. *ACS Applied Materials and Interfaces*, 5(16):7881–7885, 2013.

[441] Zhi Xu, Yoshio Bando, Lei Liu, Wenlong Wang, Xuedong Bai, and Dmitri Golberg. Electrical Conductivity, Chemistry, and Bonding Alternations under Graphene Oxide to Graphene Transition As Revealed by <i>In Situ</i> TEM. *ACS Nano*, 5(6):4401–4406, jun 2011.

[442] Inhwa Jung, Dmitriy A. Dikin, Richard D. Piner, and Rodney S. Ruoff. Tunable electrical conductivity of individual graphene oxide sheets reduced at "Low" temperatures. *Nano Letters*, 8(12):4283–4287, 2008.

[443] Silvina Cerveny, Fabienne Barroso-Bujans, Ángel Alegría, and Juan Colmenero. Dynamics of water intercalated in graphite oxide. *Journal of Physical Chemistry C*, 114(6):2604–2612, 2010.

[444] Stéphan Rouzière, J. David Núñez, Erwan Paineau, Ana M. Benito, Wolfgang K. Maser, and Pascale Launois. Intercalated water in multi-layered graphene oxide paper: an X-ray scattering study. *Journal of Applied Crystallography*, 50(3):876–884, 2017.

[445] Rosalind E. Franklin. Le rôle de l'eau dans la structure de l'acide graphitique. *Journal de Chimie Physique*, 50:C26–C26, jun 1953.

[446] Sasha Stankovich, Dmitriy A. Dikin, Richard D. Piner, Kevin A. Kohlhaas, Alfred Kleinhammes, Yuanyuan Jia, Yue Wu, SonBinh T. Nguyen, and Rodney S. Ruoff. Synthesis of graphene-based nanosheets via chemical reduction of exfoliated graphite oxide. *Carbon*, 45(7):1558–1565, jun 2007.

[447] J. D. Núñez, A. M. Benito, S. Rouzière, P. Launois, R. Arenal, P. M. Ajayan, and W. K. Maser. Graphene oxide-carbon nanotube hybrid assemblies: Cooperatively strengthened OHâ<¯O=C hydrogen bonds and the removal of chemisorbed water. *Chemical Science*, 8(7):4987–4995, 2017.

[448] Daniel R. Dreyer, Alexander D. Todd, and Christopher W. Bielawski. Harnessing the chemistry of graphene oxide. *Chemical Society Reviews*, 43(15):5288, 2014.

[449] Chun Kiang Chua, Zdeněk Sofer, and Martin Pumera. Graphite oxides: Effects of permanganate and chlorate oxidants on the oxygen composition. *Chemistry - A European Journal*, 18(42):13453–13459, 2012.

[450] Ayrat M Dimiev, Lawrence B Alemany, and James M Tour. Graphene Oxide. Origin of Acidity, Its Instability in Water, and a New Dynamic Structural Model. *ACS Nano*, 7(1):576–588, 2013.

[451] L Staudenmaier. Verfahren zur Darstellung der Graphitsäure. *Ber. Dtsch. Chem. Ges. 1898,*, 31,(3):1481–1487, 1898.

[452] L Staudenmaier. Verfahren zur Darstellung der Graphitsaure. *Berichte der Deutschen Chemischen Gesellschaft*, 32(2):1394–1399, 1899.

[453] Ulrich Hofmann and Ernst König. Untersuchungen über Graphitoxyd. *Zeitschrift für anorganische und allgemeine Chemie*, 234(4):311–336, 1937.

[454] William S. Hummers and Richard E. Offeman. Preparation of Graphitic Oxide. *Journal of the American Chemical Society*, 80(6):1339, 1958.

[455] Daniela C. Marcano, Dmitry V. Kosynkin, Jacob M. Berlin, Alexander Sinitskii, Zhengzong Sun, Alexander Slesarev, Lawrence B. Alemany, Wei Lu, and James M. Tour. Improved synthesis of graphene oxide. *ACS Nano*, 4(8):4806–4814, 2010.

[456] Debarati Roy Chowdhury, Chanderpratap Singh, and Amit Paul. Role of graphite precursor and sodium nitrate in graphite oxide synthesis. *RSC Advances*, 4(29):15138–15145, 2014.

[457] Mykola Seredych, Camille Petit, Albert V. Tamashausky, and Teresa J. Bandosz. Role of graphite precursor in the performance of graphite oxides as ammonia adsorbents. *Carbon*, 47(2):445–456, 2009.

[458] Nicholas A. Kotov, Imre Dékány, and Janos H. Fendler. Ultrathin graphite oxide-polyelectrolyte composites prepared by self-assembly: Transition between conductive and non-conductive states. *Advanced Materials*, 8(8):637–641, aug 1996.

[459] Sasha Stankovich, Richard D. Piner, Xinqi Chen, Nianqiang Wu, Sonbinh T. Nguyen, and Rodney S. Ruoff. Stable aqueous dispersions of graphitic nanoplatelets via the reduction of exfoliated graphite oxide in the presence of poly(sodium 4-styrenesulfonate). *Journal of Materials Chemistry*, 16(2):155–158, 2006.

[460] Xingfa Gao, Joonkyung Jang, and Shigeru Nagase. Hydrazine and thermal reduction of graphene oxide: Reaction mechanisms, product structures, and reaction design. *Journal of Physical Chemistry C*, 114(2):832–842, 2010.

[461] Goki Eda, Giovanni Fanchini, and Manish Chhowalla. Large-area ultrathin films of reduced graphene oxide as a transparent and flexible electronic material. *Nature Nanotechnology*, 3(5):270–274, 2008.

[462] Hyeon Jin Shin, Ki Kang Kim, Anass Benayad, Seon Mi Yoon, Hyeon Ki Park, In Sun Jung, Mei Hua Jin, Hae Kyung Jeong, Jong Min Kim, Jae Young Choi, and Young Hee Lee. Efficient reduction of graphite oxide by sodium borohydride and its effect on electrical conductance. *Advanced Functional Materials*, 19(12):1987–1992, 2009.

[463] M. J. Fernández-Merino, L. Guardia, J. I. Paredes, S. Villar-Rodil, P. Solís-Fernández, A. Martínez-Alonso, and J. M. D. Tascón. Vitamin C Is an Ideal Substitute for Hydrazine in the Reduction of Graphene Oxide Suspensions. *The Journal of Physical Chemistry C*, 114(14):6426–6432, apr 2010.

[464] Songfeng Pei and Hui-Ming Cheng. The reduction of graphene oxide. *Carbon*, 50(9):3210–3228, aug 2012.

[465] Abhijit Ganguly, Surbhi Sharma, Pagona Papakonstantinou, and Jeremy Hamilton. Probing the Thermal Deoxygenation of Graphene Oxide Using High-Resolution In Situ X-ray-Based Spectroscopies. *J. Phys. Chem. C*, 115:17009–17019, 2011.

[466] Xianjue Chen, Xiaomei Deng, Na Yeon Kim, Yu Wang, Yuan Huang, Li Peng, Ming Huang, Xu Zhang, Xiong Chen, Da Luo, Bin Wang, Xiaozhong Wu, Yufei Ma, Zonghoon Lee, and Rodney S. Ruoff. Graphitization of graphene oxide films under pressure. *Carbon*, 132:294–303, 2018.

[467] Ganganahalli K. Ramesha and Nivasan Sri Sampath. Electrochemical reduction of oriented Graphene oxide films: An in situ Raman spectroelectrochemical study. *Journal of Physical Chemistry C*, 113(19):7985–7989, 2009.

[468] Shaw Yong Toh, Kee Shyuan Loh, Siti Kartom Kamarudin, and Wan Ramli Wan Daud. Graphene production via electrochemical reduction of graphene oxide: Synthesis and characterisation. *Chemical Engineering Journal*, 251:422–434, 2014.

[469] Yuyan Shao, Jun Wang, Mark Engelhard, Chongmin Wang, and Yuehe Lin. Facile and controllable electrochemical reduction of graphene oxide and its applications. *Journal of Materials Chemistry*, 20(4):743–748, 2010.

[470] Denis A. Sokolov, Kristin R. Shepperd, and Thomas M. Orlando. Formation of graphene features from direct laser-induced reduction of graphite oxide. *Journal of Physical Chemistry Letters*, 1(18):2633–2636, 2010.

[471] Li Guo, Hao Bo Jiang, Rui Qiang Shao, Yong Lai Zhang, Sheng Yi Xie, Jian Nan Wang, Xian Bin Li, Fan Jiang, Qi Dai Chen, Tong Zhang, and Hong Bo Sun. Two-beam-laser interference mediated reduction, patterning and nanostructuring of graphene oxide for the production of a flexible humidity sensing device. *Carbon*, 50(4):1667–1673, 2012.

[472] Xuebo Cao, Dianpeng Qi, Shengyan Yin, Jing Bu, Fengji Li, Chin Foo Goh, Sam Zhang, and Xiaodong Chen. Ambient fabrication of large-area graphene films via a synchronous reduction and assembly strategy. *Advanced Materials*, 25(21):2957–2962, 2013.

[473] Gongming Wang, Fang Qian, Chad W. Saltikov, Yongqin Jiao, and Yat Li. Microbial reduction of graphene oxide by Shewanella. *Nano Research*, 4(6):563–570, 2011.

[474] Huafeng Yang, Fenghua Li, Changsheng Shan, Dongxue Han, Qixian Zhang, Li Niu, and Ari Ivaska. Covalent functionalization of chemically converted graphene sheets via silane and its reinforcement. *Journal of Materials Chemistry*, 19(26):4632–4638, 2009.

[475] Yanfei Xu, Zhibo Liu, Xiaoliang Zhang, Yan Wang, Jianguo Tian, Yi Huang, Yanfeng Ma, Xiaoyan Zhang, and Yongsheng Chen. A graphene hybrid material covalently functionalized with porphyrin: Synthesis and optical limiting property. *Advanced Materials*, 21(12):1275–1279, 2009.

[476] Zhuang Liu, Joshua T. Robinson, Xiaoming Sun, and Hongjie Dai. PEGylated nanographene oxide for delivery of water-insoluble cancer drugs. *Journal of the American Chemical Society*, 130(33):10876–10877, 2008.

[477] L. Monica Veca, Fushen Lu, Mohammed J. Meziani, Li Cao, Puyu Zhang, Gang Qi, Liangwei Qu, Mona Shrestha, and Ya-Ping Sun. Polymer functionalization and solubilization of carbon nanosheets. *Chemical Communications*, page 2565, 2009.

[478] Sumita Rani, Mukesh Kumar, Rajiv Kumar, Dinesh Kumar, Sumit Sharma, and Gulshan Singh. Characterization and dispersibility of improved thermally stable amide functionalized graphene oxide. *Materials Research Bulletin*, 60:143–149, 2014.

[479] Nihar Mohanty and Vikas Berry. Graphene-based single-bacterium resolution biodevice and DNA transistor: Interfacing graphene derivatives with nanoscale and microscale biocomponents. *Nano Letters*, 8(12):4469–4476, 2008.

[480] Jianfeng Shen, Min Shi, Bo Yan, Hongwei Ma, Na Li, Yizhe Hu, and Mingxin Ye. Covalent attaching protein to graphene oxide via diimide-activated amidation. *Colloids and Surfaces B: Biointerfaces*, 81(2):434–438, 2010.

[481] Manuela Meloni, Sandra Victor-Roman, Alice King, Giuseppe Fratta, Emin Istif, Matthew Large, Mario Pelaez-Fernandez, Sean Paul Ogilvie, Raul Arenal, Ana M Benito, and Wolfgang K Maser. Controlled assembly and reduction of graphene oxide networks for conductive composites. In American Chemical Society, editor, *Abstracts of Papers of the American Chemical Society*, 2019.

[482] T. S. Sreeprasad, Shihabudheen M. Maliyekkal, K. P. Lisha, and T. Pradeep. Reduced graphene oxide-metal/metal oxide composites: Facile synthesis and application in water purification. *Journal of Hazardous Materials*, 186(1):921–931, 2011.

[483] B. Ramezanzadeh, M.H. Mohamadzadeh Moghadam, N. Shohani, and M. Mahdavian. Effects of highly crystalline and conductive polyaniline/graphene oxide composites on the corrosion protection performance of a zinc-rich epoxy coating. *Chemical Engineering Journal*, 320:363–375, jul 2017.

[484] Hatem Moussa, Emilien Girot, Kevin Mozet, Halima Alem, Ghouti Medjahdi, and Raphaël Schneider. ZnO rods/reduced graphene oxide composites prepared via a solvothermal reaction for efficient sunlight-driven photocatalysis. *Applied Catalysis B: Environmental*, 185:11–21, may 2016.

[485] D. Hadži and A. Novak. Infra-red spectra of graphitic oxide. *Transactions of the Faraday Society*, 51:1614–1620, 1955.

[486] Manuela Melucci, Emanuele Treossi, Luca Ortolani, Giuliano Giambastiani, Vittorio Morandi, Philipp Klar, Cinzia Casiraghi, Paolo Samorì, and Vincenzo Palermo. Facile covalent functionalization of graphene oxide using microwaves: Bottom-up development of functional graphitic materials. *Journal of Materials Chemistry*, 20(41):9052–9060, 2010.

[487] Wufeng Chen, Lifeng Yan, and P R Bangal. Chemical Reduction of Graphene Oxide to Graphene by Sulfur-Containing Compounds. *The Journal of Physical Chemistry C*, 114(47):19885–19890, dec 2010.

[488] Shifeng Hou, Shujun Su, Marc L. Kasner, Pratik Shah, Krutika Patel, and Clemonne John Madarang. Formation of highly stable dispersions of silane-functionalized reduced graphene oxide. *Chemical Physics Letters*, 501(1-3):68–74, 2010.

[489] C. Nethravathi, Michael Rajamathi, N. Ravishankar, Lubna Basit, and Claudia Felser. Synthesis of graphene oxide-intercalated α-hydroxides by metathesis and their decomposition to graphene/metal oxide composites. *Carbon*, 48(15):4343–4350, 2010.

[490] Tomoki Ogoshi, Yuto Ichihara, Tada Aki Yamagishi, and Yoshiaki Nakamoto. Supramolecular polymer networks from hybrid between graphene oxide and per-6-amino-β-cyclodextrin. *Chemical Communications*, 46(33):6087–6089, 2010.

[491] Jianfeng Shen, Min Shi, Hongwei Ma, Bo Yan, Na Li, Yizhe Hu, and Mingxin Ye. Synthesis of hydrophilic and organophilic chemically modified graphene oxide sheets. *Journal of Colloid and Interface Science*, 352(2):366–370, 2010.

[492] Tae Wook Kim, Yan Gao, Orb Acton, Hin Lap Yip, Hong Ma, Hongzheng Chen, and Alex K.Y. Jen. Graphene oxide nanosheets based organic field effect transistor for nonvolatile memory applications. *Applied Physics Letters*, 97(2), 2010.

[493] Xiangbo Meng, Dongsheng Geng, Jian Liu, Mohammad Norouzi Banis, Yong Zhang, Ruying Li, and Xueliang Sun. Non-aqueous approach to synthesize amorphous/crystalline metal oxide-graphene nanosheet hybrid composites. *Journal of Physical Chemistry C*, 114(43):18330–18337, 2010.

[494] Jiali Zhang, Haijun Yang, Guangxia Shen, Ping Cheng, Jingyan Zhang, and Shouwu Guo. Reduction of graphene oxide vial-ascorbic acid. *Chemical Communications*, 46(7):1112–1114, 2010.

[495] C. Sellitti, J. L. Koenig, and H. Ishida. Surface characterization of graphitized carbon fibers by attenuated total reflection fourier transform infrared spectroscopy. *Carbon*, 28(1):221–228, 1990.

[496] Xingbin Yan, Jiangtao Chen, Jie Yang, Qunji Xue, and Philippe Miele. Fabrication of free-standing, electrochemically active, and biocompatible graphene oxide-polyaniline and graphene-polyaniline hybrid papers. *ACS Applied Materials and Interfaces*, 2(9):2521–2529, 2010.

[497] Vimlesh Chandra, Jaesung Park, Young Chun, Jung Woo Lee, In-Chul Hwang, and Kwang S. Kim. Water-Dispersible Magnetite-Reduced Graphene Oxide Composites for Arsenic Removal. *ACS Nano*, 4(7):3979–3986, jul 2010.

[498] Jingjing Xu, Kai Wang, Sheng-zhen Zu, Bao-hang Han, and Zhixiang Wei. Hierarchical Nanocomposites of Polyaniline Nanowire Arrays on Graphene Oxide Sheets with Synergistic Effect for Energy Storage. *ACS Nano*, 4(9):5019–5026, sep 2010.

[499] Joonsuk Oh, Jun Ho Lee, Ja Choon Koo, Hyouk Ryeol Choi, Youngkwan Lee, Taesung Kim, Nguyen Dang Luong, and Jae Do Nam. Graphene oxide porous paper from amine-functionalized poly(glycidyl methacrylate)/graphene oxide core-shell microspheres. *Journal of Materials Chemistry*, 20(41):9200–9204, 2010.

[500] Su Zhang, Huaihe Song, Peng Guo, Jisheng Zhou, and Xiaohong Chen. Formation of carbon nanoparticles from soluble graphene oxide in an aqueous solution. *Carbon*, 48(14):4211–4214, 2010.

[501] Gil Gonalves, Paula A.A.P. Marques, Ana Barros-Timmons, Igor Bdkin, Manoj K. Singh, Nazanin Emami, and José Grácio. Graphene oxide modified with PMMA via ATRP as a reinforcement filler. *Journal of Materials Chemistry*, 20(44):9927–9934, 2010.

[502] S. Bittolo Bon, L. Valentini, and J. M. Kenny. Preparation of extended alkylated graphene oxide conducting layers and effect study on the electrical properties of PEDOT:PSS polymer composites. *Chemical Physics Letters*, 494(4-6):264–268, 2010.

[503] Tamás Szabó, Etelka Tombácz, Erzsébet Illés, and Imre Dékány. Enhanced acidity and pH-dependent surface charge characterization of successively oxidized graphite oxides. *Carbon*, 44(3):537–545, 2006.

[504] Tuan Anh Pham, Nanjundan Ashok Kumar, and Yeon Tae Jeong. Covalent functionalization of graphene oxide with polyglycerol and their use as templates for anchoring magnetic nanoparticles. *Synthetic Metals*, 160(17-18):2028–2036, 2010.

[505] Nikolaos Karousis, Atula S.D. Sandanayaka, Taku Hasobe, Solon P. Economopoulos, Evangelia Sarantopoulou, and Nikos Tagmatarchis. Graphene oxide with covalently linked porphyrin antennae: Synthesis, characterization and photophysical properties. *Journal of Materials Chemistry*, 21(1):109–117, 2011.

[506] E. L. Evans, J. M. Thomas, H. P. Boehm, and H. Marsh. No Title. In *Extended abstracts on the Conference of Carbon of Baden-Baden 49*, 1972.

[507] E. L. Evans, J. De, A. Martin-Rodriguez, and F. Rodriguez-Reinoso. Kinetics of the formation of graphite oxide. *Carbon*, 13(6):461–464, 1975.

[508] Dongyu Cai and Mo Song. Preparation of fully exfoliated graphite oxide nanoplatelets in organic solvents. *Journal of Materials Chemistry*, 17(35):3678–3680, 2007.

[509] D. Briggs and G Beamson. High resolution XPS of organic polymers. In *The Scienta ESCA 300 Database*. John Wiley and Sons,, New York, 1992.

[510] R. J. Waltman, J. Pacansky, and C. W. Bates. X-ray Photoelectron Spectroscopic Studies on Organic Photoconductors: Evaluation of Atomic Charges on Chlorodiane Blue and p-(Diethylamino)benzaldehyde Diphenylhydrazone. *Chemistry of Materials*, 5(12):1799–1804, 1993.

[511] Haibo Wang, Chuanjian Zhang, Zhihong Liu, Li Wang, Pengxian Han, Hongxia Xu, Kejun Zhang, Shanmu Dong, Jianhua Yao, and Guanglei Cui. Nitrogen-doped graphene nanosheets with excellent lithium storage properties. *Journal of Materials Chemistry*, 21(14):5430–5434, 2011.

[512] F. Aragon De La Cruz and J. M. Cowley. Structure of Graphitic Oxide. *Nature*, 196(4853):468–469, nov 1962.

[513] G Wang, J Yang, J Park, and X Gou. Facile synthesis and characterization of graphene nanosheets. *The Journal of Physical Chemistry C*, 112(22):8192–8195, 2008.

[514] T. Eberlein, U. Bangert, R. R. Nair, R. Jones, M. Gass, A. L. Bleloch, K. S. Novoselov, A. Geim, and P. R. Briddon. Plasmon spectroscopy of free-standing graphene films. *Physical Review B*, 77(23):233406, jun 2008.

[515] L. Stobinski, B. Lesiak, A. Malolepszy, M. Mazurkiewicz, B. Mierzwa, J. Zemek, P. Jiricek, and I. Bieloshapka. Graphene oxide and reduced graphene oxide studied by the XRD, TEM and electron spectroscopy methods. *Journal of Electron Spectroscopy and Related Phenomena*, 195:145–154, 2014.

[516] Rebecca J. Nicholls, Adrian T. Murdock, Joshua Tsang, Jude Britton, Timothy J. Pennycook, Antal Koós, Peter D. Nellist, Nicole Grobert, and Jonathan R. Yates. Probing the bonding in nitrogen-doped graphene using electron energy loss spectroscopy. *ACS Nano*, 7(8):7145–7150, 2013.

[517] M. S. Dresselhaus, G. Dresselhaus, and P. C. Eklund. Raman Scattering in Fullerenes. *Journal of Raman Spectroscopy*, 27(34):351–371, 1996.

[518] A. Jorio, M. A. Pimenta, A. G. Souza Filho, R. Saito, G. Dresselhaus, and M. S. Dresselhaus. Characterizing carbon nanotube samples with resonance Raman scattering. *New Journal of Physics*, 5, 2003.

[519] Millie S. Dresselhaus, G. Dresselhaus, R. Saito, and A. Jorio. Raman spectroscopy of carbon nanotubes. *Physics Reports*, 409(2):47–99, 2005.

[520] M. A. Pimenta, G. Dresselhaus, M. S. Dresselhaus, L. G. Cançado, A. Jorio, and R. Saito. Studying disorder in graphite-based systems by Raman spectroscopy. *Physical Chemistry Chemical Physics*, 9(11):1276–1291, 2007.

[521] L. G. Cançado, A. Jorio, E. H.Martins Ferreira, F. Stavale, C. A. Achete, R. B. Capaz, M. V.O. Moutinho, A. Lombardo, T. S. Kulmala, and A. C. Ferrari. Quantifying defects in graphene via Raman spectroscopy at different excitation energies. *Nano Letters*, 11(8):3190–3196, 2011.

[522] M.S. Dresselhaus, A. Jorio, and R. Saito. Characterizing Graphene, Graphite, and Carbon Nanotubes by Raman Spectroscopy. *Annual Review of Condensed Matter Physics*, 1(1):89–108, 2010.

[523] L. M. Malard, M. H.D. Guimarães, D. L. Mafra, M. S.C. Mazzoni, and A. Jorio. Group-theory analysis of electrons and phonons in N -layer graphene systems. *Physical Review B - Condensed Matter and Materials Physics*, 79(12):1–8, 2009.

[524] K. Sato, R. Saito, Y. Oyama, J. Jiang, L. G. Cançado, M. A. Pimenta, A. Jorio, Ge G. Samsonidze, G. Dresselhaus, and M. S. Dresselhaus. D-band Raman intensity of graphitic materials as a function of laser energy and crystallite size. *Chemical Physics Letters*, 427(1-3):117–121, 2006.

[525] F. Tuinstra and J.L. Koenig. Characterization of Graphite Fiber Surfaces with Raman Spectroscopy. *Journal of Composite Materials*, 4(4):492–499, oct 1970.

[526] F. Tuinstra and J. L. Koenig. Raman Spectrum of Graphite. *The Journal of Chemical Physics*, 53(3):1126–1130, aug 1970.

[527] Dongxing Yang, Aruna Velamakanni, Gülay Bozoklu, Sungjin Park, Meryl Stoller, Richard D. Piner, Sasha Stankovich, Inhwa Jung, Daniel A. Field, Carl A. Ventrice, and Rodney S. Ruoff. Chemical analysis of graphene oxide films after heat and chemical treatments by X-ray photoelectron and Micro-Raman spectroscopy. *Carbon*, 47(1):145–152, 2009.

[528] Alice A.K. King, Benjamin R. Davies, Nikan Noorbehesht, Peter Newman, Tamara L. Church, Andrew T. Harris, Joselito M. Razal, and Andrew I. Minett. A new raman metric for the characterisation of graphene oxide and its derivatives. *Scientific Reports*, 6:1–6, 2016.

[529] Dan C. Sorescu, Kenneth D. Jordan, and Phaedon Avouris. Theoretical study of oxygen adsorption on graphite and the (8,0) single-walled carbon nanotube. *Journal of Physical Chemistry B*, 105(45):11227–11232, 2001.

[530] Je Luen Li, Konstantin N. Kudin, Michael J. McAllister, Robert K. Prud'homme, Ilhan A. Aksay, and Roberto Car. Oxygen-driven unzipping of graphitic materials. *Physical Review Letters*, 96(17):5–8, 2006.

[531] D. W. Boukhvalov and M. I. Katsnelson. Modeling of graphite oxide. *Journal of the American Chemical Society*, 130(32):10697–10701, 2008.

[532] R. J.W.E. Lahaye, H. K. Jeong, C. Y. Park, and Y. H. Lee. Density functional theory study of graphite oxide for different oxidation levels. *Physical Review B - Condensed Matter and Materials Physics*, 79(12):1–8, 2009.

[533] Min Chan Kim, Gyeong S. Hwang, and Rodney S. Ruoff. Epoxide reduction with hydrazine on graphene: A first principles study. *Journal of Chemical Physics*, 131(6):1–6, 2009.

[534] Andrei Incze, Alain Pasturel, and Christian Chatillon. Oxidation of graphite by atomic oxygen: A first-principles approach. *Surface Science*, 537(1-3):55–63, 2003.

[535] Priya Johari and Vivek B. Shenoy. Modulating optical properties of graphene oxide: Role of prominent functional groups. *ACS Nano*, 5(9):7640–7647, 2011.

[536] A. Jelea, F. Marinelli, Y. Ferro, A. Allouche, and C. Brosset. Quantum study of hydrogen-oxygen-graphite interactions. *Carbon*, 42(15):3189–3198, 2004.

[537] H. G. Richardson and G. O. Sayles. *Transmission Electron Microscopy*, volume 36 of *Springer Series in Optical Sciences*. Springer New York, New York, NY, jan 2008.

[538] L. Lajaunie, C. Pardanaud, C. Martin, P. Puech, C. Hu, M. J. Biggs, and R. Arenal. Advanced spectroscopic analyses on a:C-H materials: Revisiting the EELS characterization and its coupling with multi-wavelength Raman spectroscopy. *Carbon*, 112:149–161, 2017.

[539] Friedrich Lenz. Zur Streuung mittelschneller Elektronen in kleinste Winkel. *Zeitschrift fur Naturforschung - Section A Journal of Physical Sciences*, 9(3):185–204, 1954.

[540] S Scalese, S Baldo, S Filice, C Bongiorno, R Reitano, E Fazio, S Conoci, and A La Magna. Electrical properties and oxygen functionalities in ethanol-treated and thermally modified graphene oxide. *Journal of Applied Physics*, 1211(121):155105–155302, 2017.

[541] S D Berger, D R Mckenzie, and P J Martin. EELS analysis of vacuum arc-deposited diamond- like films. *Philosophical Magazine Letters*, 57(6):285–290, 1988.

[542] A. J. Papworth, C. J. Kiely, A. P. Burden, S. R P Silva, and G. A J Amaratunga. Electron-energy-loss spectroscopy characterization of the sp2 bonding fraction within carbon thin films. *Physical Review B - Condensed Matter and Materials Physics*, 62(19):12628–12631, 2000.

[543] J. Titantah and D. Lamoen. Technique for the sp2âˆ•sp3 characterization of carbon materials:â€fAb initio calculation of near-edge structure in electron-energy-loss spectra. *Physical Review B*, 70(7):075115, 2004.

[544] N. Bernier, F. Bocquet, A. Allouche, W. Saikaly, C. Brosset, J. Thibault, and A. Charaï. A methodology to optimize the quantification of sp2carbon fraction from K edge EELS spectra. *Journal of Electron Spectroscopy and Related Phenomena*, 164(1-3):34–43, 2008.

[545] X Gonze J-C Charlier and J-P Michenaud. First principles study of the elctronic structure of graphite. *Physical Review B*, 43(6):4579–4589, 1991.

[546] A. Allouche and Y. Ferro. First-principles study of electronic properties of hydrogenated graphite. *Physical Review B - Condensed Matter and Materials Physics*, 74(23):1–8, 2006.

[547] Cristina Vallés, J. David Núñez, Ana M. Benito, and Wolfgang K. Maser. Flexible conductive graphene paper obtained by direct and gentle annealing of graphene oxide paper. *Carbon*, 50(3):835–844, 2012.

[548] Stefano Borini, Richard White, Di Wei, Michael Astley, Samiul Haque, Elisabetta Spigone, and Nadine Harris. Ultrafast Graphene Oxide Humidity Sensors. *ACS Nano*, 7(12):11166–11173, 2013.

[549] K. Iakoubovskii, K. Mitsuishi, Y. Nakayama, and K. Furuya. Thickness measurements with electron energy loss spectroscopy. *Microscopy Research and Technique*, 71(8):626–631, 2008.

[550] J. D. Núñez, A. M. Benito, S. Rouzière, P. Launois, R. Arenal, P. M. Ajayan, and W. K. Maser. Graphene oxideâ€“carbon nanotube hybrid assemblies: cooperatively strengthened OHâ<¯O=C hydrogen bonds and the removal of chemisorbed water. *Chemical Science*, 8(7):4987–4995, 2017.

[551] L. Calliari, S. Fanchenko, and M. Filippi. Plasmon features in electron energy loss spectra from carbon materials. *Carbon*, 45(7):1410–1418, 2007.

[552] Dmitriy A. Dikin, Sasha Stankovich, Eric J. Zimney, Richard D. Piner, Geoffrey H.B. Dommett, Guennadi Evmenenko, Sonbinh T. Nguyen, and Rodney S. Ruoff. Preparation and characterization of graphene oxide paper. *Nature*, 448(7152):457–460, 2007.

[553] Xiaofei Ma, Michael R. Zachariah, and Christopher D. Zangmeister. Crumpled nanopaper from graphene oxide. *Nano Letters*, 12(1):486–489, 2012.

[554] Xu Du, Shan Wen Tsai, Dmitrii L. Maslov, and Arthur F. Hebard. Metal-insulator-like behavior in semimetallic bismuth and graphite. *Physical Review Letters*, 94(16):1–4, 2005.

[555] Robert Huszank, László Csedreki, Zsófia Kertész, and Zsófia Török. Determination of the density of siliconâ€“nitride thin films by ion-beam analytical techniques (RBS, PIXE, STIM). *Journal of Radioanalytical and Nuclear Chemistry*, 307(1):341–346, 2016.

[556] Felix Börrnert, Stanislav M. Avdoshenko, Alicja Bachmatiuk, Imad Ibrahim, Bernd Büchner, Gianaurelio Cuniberti, and Mark H. Rümmeli. Amorphous carbon under 80 kV electron irradiation: A means to make or break graphene. *Advanced Materials*, 24(41):5630–5635, 2012.

[557] Syed Nasimul Alam, Nidhi Sharma, and Lailesh Kumar. Synthesis of Graphene Oxide (GO) by Modified Hummers Method and Its Thermal Reduction to Obtain Reduced Graphene Oxide (rGO)*. *Graphene*, 06(01):1–18, 2017.